On the liquid dynamics, transition kinetics, and additive manufacturing of bulk metallic glass formers

Dissertation zur Erlangung des Grades des

Doktors der Ingenieurwissenschaften

der Naturwissenschaftlich-Technischen Fakultät der

Universität des Saarlandes

vorgelegt von

Maximilian Frey

Saarbrücken

2025

Tag des Kolloquiums:	12.12.2025
Dekan:	Prof. Dr.-Ing. Dirk Bähre
Berichterstatter:	Prof. Dr. Ralf Busch
	Prof. Dr.-Ing. Frank Mücklich
Vorsitz:	Prof. Dr.-Ing. Hans-Georg Herrmann
Akademischer Mitarbeiter:	Dr. Michael Roland

0. PRELIMINARIES

Abstract

The present cumulative PhD thesis incorporates six first author publications as well as additional results and discussions that focus on the material class of bulk metallic glasses. The first three publications investigate the dynamics of deeply supercooled metallic glass forming liquids as well as their crystallization and vitrification behavior. This includes the question of how to determine the fragility of metallic glass formers and how to model and combine respective data stemming from various experimental approaches. Furthermore, the close connection between liquid fragility and crystallization is demonstrated by determining and modelling a complete TTT diagram. Finally, first of its kind XPCS studies under temperature scanning conditions allow to firstly reveal and model the complex rivalry between two different types of atomic dynamics that arises with vitrification. The last three publications focus on the rather industry-related topic of additive manufacturing of metallic glasses via laser powder bed fusion. In this context, three different alloy families are investigated and evaluated for the additive manufacturing process. The resulting specimens can reach outstanding strengths of up to 2.5 GPa and high hardness values of almost 900 HV1. Furthermore, potential application cases for additively formed metallic glasses and a post-processing route in form of thermoplastic forming are presented and discussed.

Zusammenfassung

Die vorliegende kumulative Dissertationsschrift umfasst sechs Erstautor-Publikationen welche sich, in Kombination mit zusätzlichen Ergebnissen und Diskussionen, dem Thema der metallischen Massivgläser widmen. Die ersten drei Publikationen widmen sich dabei der Untersuchung der Dynamik, des Kristallisations- und des Vitrifizierungsverhaltens stark unterkühlter metallischer Glasformer. Im Kontext der Fragilität wird hierbei den Fragestellungen der Messung, Modellierung und Vergleichbarkeit unterschiedlicher Datensätze nachgegangen. Weiterhin wird die enge Verknüpfung zwischen Fragilität und Kristallisationsverhalten exemplarisch anhand einer experimentellen Bestimmung und Modellierung eines TTT-Diagramms aufgezeigt. Neuartige XPCS-Messungen unter kontinuierlicher Temperaturänderung mit konstanter Rate erlauben erstmalig die mit dem Glasübergang einhergehende Rivalität zweier grundlegend unterschiedlichen Arten atomarer Dynamik offenzulegen und mathematisch zu beschreiben. Die drei letzten Publikationen befassen sich mit der additiven Fertigung metallischer Gläser mittels des Pulverbett-basierten Laserstahl-Schmelzens. Dabei werden drei Legierungsfamilien hinsichtlich ihrer Prozesseignung untersucht. Die erzeugten Proben erreichen außergewöhnliche Festigkeiten von bis zu 2,5 GPa und hohe Härten von nahezu 900 HV1. Weiterhin werden mögliche Anwendungen additiv gefertigter metallischer Gläser sowie ein Nachbearbeitungskonzept auf Basis des thermoplastischen Formens präsentiert.

Acknowledgements

This thesis would not have been possible without all the help, input, and cooperation from a plethora of people, which shall be named and thanked in the following.

First of all, I would like to thank Professor Ralf Busch for giving me the opportunity to create this PhD thesis at the Chair for Metallic Materials and for providing all the freedom I needed to evolve and discover into manifold directions. Further thanks go to my PhD candidate fellows, especially to Nico Neuber (the good old roommate), Bastian Adam, Sascha Sebastian Riegler, and Lucas Ruschel, with which I fought through countless synchrotron beamtimes, but also to Amirhossein Ghavimi, Maryam Rahimi Chegeni, Ziyu Ling, Thomas Jamieson, Benedikt Bochtler, Oliver Gross, Alexander Kuball, and Simon Hechler. I really appreciate all the in-depth discussions, the teamwork, and the recreation. I also like to thank the LMW staff for the relentless support, namely Alfiya Kurt, Alexandra Hirth, and Sigrid Neusius for their administrative work, Martina Stemmler for her metallographic practice, as well as Jörg Eiden and Hermann Altmeyer for all their creative technical solutions. I further want to appreciate the steady contributions of manifold HiWis, for example Benedikt Schmidt, Fabian Vollmers, Marvin Müller, and Sergej Jakovlev. Gratitude also goes towards Dr. Frank Aubertin, Prof. Isabella Gallino, and Prof. Wulff Possart for the shared knowledge and experience.

I further want to thank all the external collaborators with which I had the pleasure of working with. Here, the additive manufacturing experts from the University Duisburg-Essen must be mentioned, namely my old companion through three AM-related projects, Dr. Jan Wegner, as well as Dr. Stefan Kleszczynski and Hanna Schönrath. Similar regards go to the powder atomization specialists Dr. Volker Uhlenwinkel, Dr. Nils Ellendt, and Dr. Erika Soares Barreto from the IWT Bremen. Together, we formed one of the most productive research teams in the field of additively manufactured metallic glasses. Moreover, I'd like to thank Dr. Daniele Cangialosi for the fruitful cooperation and for sharing his impressive expertise in terms of fast scanning calorimetry and relaxation phenomena in general. In terms of diffraction studies, I'd like to appreciate the researchers from the DESY beamlines P02.1, P10, P21.1 and P21.2 for their support and valuable knowledge, especially Dr. Fabian Westermeier. The same gratitude shall be expressed towards Dr. Fan Yang from the DLR.

Regarding the ESRF, I want to thank the XPCS specialists working at the ID10 beamline, most notably Dr. Antoine Cornet, Dr. Jie Shen, Dr. Yuriy Chushkin, and Dr. Marco Cammarata for their leading expertise and the good times in Grenoble. A special gratitude shall go to Dr. Beatrice Ruta. My work profited a lot from your experience, encyclopedia-like literature knowledge, and especially from the 'nasty questions' that were a source of steady improvement.

Most notably, I want to thank Prof. Eloi Pineda from the Universitat Politècnica de Catalunya in Barcelona, who was the initiator of our whole XPCS temperature scanning campaign. Your thoughts and interpretations were always one or even two steps ahead and I am deeply thankful you shared them with me through mentor-like advice. With brilliance and kindness, you established an ideal to strive for.

Naturally, this work would have been impossible without all the support and love of my friends and family. In particular, I thank my parents Melitta and Hans-Peter Frey. You raised me with immeasurable dedication and eventually paved the way for this very specific thesis. I also want to thank my uncle Heribert Becker and his family for all their support. Furthermore, I will be always grateful to Dr. Johannes Engel for his wisdom and father-like advice, sparking personal growth.

But above all, I would like to address my wife, Lara. While I learned about the perishableness, the 'abrupt kinetics' that may come with what one would call a scientific career, your love and loyalty always remained. As the mother of our offsprings, you are the antidote to the entropy and the love of my life.

Es macht den erheblichsten Unterschied, ob ein Denker zu seinen Problemen persönlich steht, so daß er in ihnen sein Schicksal, seine Not und auch sein bestes Glück hat, oder aber "unpersönlich": nämlich sie nur mit den Fühlhörnern des kalten, neugierigen Gedankens anzutasten und zu fassen versteht. Im letzteren Falle kommt nichts dabei heraus, so viel läßt sich versprechen.

Friedrich Nietzsche

Moritz Friedrich und Amelie Charlotte gewidmet.

Activities and Achievements

First author publications constituting this thesis

[1] 2020 (Paper I): M. Frey, N. Neuber, O. Gross, B. Zimmer, W. Possart, R. Busch, Determining the fragility of bulk metallic glass forming liquids via modulated DSC. J. Phys. Condens. Matter 32

[2] 2021 (Paper VI): M. Frey, J. Wegner, N. Neuber, B. Reiplinger, B. Bochtler, B. Adam, L. Ruschel, S. S. Riegler, H.-R. Jiang, S. Kleszczynski, G. Witt, R. Busch, Thermoplastic forming of additively manufactured Zr-based bulk metallic glass: A processing route for surface finishing of complex structures. Mater. Des. 198, 1–8

[3] 2022 (Paper III): M. Frey, N. Neuber, M. Müller, O. Gross, S. S. Riegler, I. Gallino, R. Busch, Determining and Modelling a Complete Time-Temperature-Transformation Diagram for a Pt-based Metallic Glass Former through Combination of Conventional and Fast Scanning Calorimetry. Scr. Mater. 215, 114710

[4] 2023 (Paper V): M. Frey, J. Wegner, E. S. Barreto, L. Ruschel, N. Neuber, B. Adam, S. S. Riegler, H. R. Jiang, G. Witt, N. Ellendt, V. Uhlenwinkel, S. Kleszczynski, R. Busch, Laser powder bed fusion of Cu-Ti-Zr-Ni bulk metallic glasses in the Vit101 alloy system. Addit. Manuf. 66

[5] 2025 (Paper VI): M. Frey, J. Wegner, L. M. Ruschel, E. S. Barreto, S. S. Riegler, B. Adam, N. Ellendt, S. Kleszczynski, R. Busch, Additive manufacturing of $Ni_{62}Nb_{38}$ metallic glass via laser powder bed fusion. Prog. Addit. Manuf. 101

[6] 2025 (Paper II): M. Frey, N. Neuber, S.S. Riegler, A. Cornet, Y. Chushkin, F. Zontone, L.M. Ruschel, B. Adam, M. Nabahat, F. Yang, J. Shen, F. Westermeier, M. Sprung, D. Cangialosi, V. Di Lisio, I. Gallino, R. Busch, B. Ruta, Liquid-like versus stress-driven dynamics in a metallic glass former observed by temperature scanning X-ray photon correlation spectroscopy, Nat. Commun. 16

Other first author publications

[7] 2018: M. Frey, R. Busch, W. Possart, I. Gallino, On the thermodynamics, kinetics, and sub-T_g relaxations of Mg-based bulk metallic glasses. Acta Mater. 155, 117–127

Co-authored publications

[8] 2018: J. Wegner, S. Kleszczynski, M. Frey, S. Hechler, G. Witt, R. Busch, Parameterstudie zur Verarbeitung metallischer Gläser auf Zr-Basis mit dem Laser-Strahlschmelzverfahren. in Proceedings of the 15th Rapid.Tech Conference

[9] 2019: O. Gross, N. Neuber, A. Kuball, B. Bochtler, S. Hechler, M. Frey, R. Busch, Signatures of structural differences in Pt-P- and Pd-P-based bulk glass-forming liquids. Commun. Phys. 2, 83

[10] 2019: J. Wegner, M. Frey, P. Stiglmair, S. Kleszczynski, G. Witt, R. Busch, MECHANICAL PROPERTIES OF HONEYCOMB STRUCTURED ZR-BASED BULK METALLIC GLASS SPECIMENS FABRICATED BY LASER POWDER BED FUSION. South African J. Ind. Eng. 30 (3), 32–40

[11] 2020: H. Jiang, B. Bochtler, M. Frey, Q. Liu, X. Wei, Y. Min, S. S. Riegler, D. Liang, R. Busch, J. Shen, Equilibrium viscosity and structural change in the $Cu_{47.5}Zr_{45.1}Al_{7.4}$ bulk glass-forming liquid. Acta Mater. 184, 69–78

[12] 2020: N. Neuber, M. Frey, O. Gross, J. Baller, I. Gallino, R. Busch, Ultrafast scanning calorimetry of newly developed Au-Ga bulk metallic glasses. J. Phys. Condens. Matter 32, 324001

[13] 2020: H.-R. Jiang, B. Bochtler, S. S. Riegler, X.-S. Wei, N. Neuber, M. Frey, I. Gallino, R. Busch, J. Shen, Thermodynamic and kinetic studies of the Cu–Zr–Al(–Sn) bulk metallic glass-forming system. J. Alloys Compd. 844, 156126

[14] 2020: B. Ruta, S. Hechler, N. Neuber, D. Orsi, L. Cristofolini, O. Gross, B. Bochtler, M. Frey, A. Kuball, S.S. Riegler, M. Stolpe, Z. Evenson, C. Gutt, F. Westermeier, R. Busch, I. Gallino, Wave vector dependence of the dynamics in supercooled metallic liquids. Phys. Rev. Lett. 125, 1–14

[15] 2020: J. Wegner, M. Frey, S. Kleszczynski, R. Busch, G. Witt, Influence of process gas during powder bed fusion with laser beam of Zr-based bulk metallic glasses. 11th CIRP Conference on Photonic Technologies [LANE 2020], 205–210

[16] 2021: H. R. Jiang, J. Y. Hu, N. Neuber, B. Bochtler, B. Adam, S. S. Riegler, M. Frey, L. Ruschel, W. F. Lu, A. H. Feng, R. Busch, J. Shen, Effect of sulfur on the glass-forming ability,

phase transformation, and thermal stability of Cu-Zr-Al bulk metallic glass. Acta Mater. 212, 116923

[17] 2021: J. Wegner, M. Frey, M. Piechotta, N. Neuber, B. Adam, S. Platt, L. Ruschel, N. Schnell, S. Sebastian, H. Jiang, G. Witt, R. Busch, S. Kleszczynski, Influence of powder characteristics on the structural and the mechanical properties of additively manufactured Zr-based bulk metallic glass. Mater. Des. 209, 109976

[18] 2021: E. S. Barreto, V. Uhlenwinkel, M. Frey, I. Gallino, R. Busch, A. Lüttge, Influence of Processing Route on the Surface Reactivity of $Cu_{47}Ti_{33}Zr_{11}Ni_6Sn_2Si_1$ Metallic Glass. Metals (Basel) 11, 1–13

[19] 2021: N. Neuber, O. Gross, M. Frey, B. Bochtler, A. Kuball, S. Hechler, I. Gallino, R. Busch, On the thermodynamics and its connection to structure in the Pt-Pd-Cu-Ni-P bulk metallic glass forming system. Acta Mater. 220, 117300

[20] 2021: J. Wegner, M. Frey, R. Busch, S. Kleszczynski, Additive manufacturing of a compliant mechanism using Zr-based bulk metallic glass. Addit. Manuf. Lett. 1, 100019

[21] 2022: H.-R. Jiang, J. Tseng, N. Neuber, J. Barrirero, B. Adam, M. Frey, A.-C. Dippel, S. Banerjee, I. Gallino, A.-H. Feng, G. Wang, F. Mücklich, R. Busch, J. Shen, On the devitrification of Cu–Zr–Al alloys: Solving the apparent contradiction between polymorphic liquid-liquid transition and phase separation. Acta Mater. 226, 117668

[22] 2022: L. Thorsson, M. Unosson, M. Teresa Pérez-Prado, X. Jin, P. Tiberto, G. Barrera, B. Adam, N. Neuber, A. Ghavimi, M. Frey, R. Busch, I. Gallino, Selective laser melting of a Fe-Si-Cr-B-C-based complex-shaped amorphous soft-magnetic electric motor rotor with record dimensions. Mater. Des. 215, 110483

[23] 2022: E. Soares Barreto, M. Frey, J. Wegner, A. Jose, N. Neuber, R. Busch, S. Kleszczynski, L. Mädler, V. Uhlenwinkel, Properties of gas-atomized Cu-Ti-based metallic glass powders for additive manufacturing. Mater. Des. 215, 110519

[24] 2022: S. Bechtel, R. Schweitzer, M. Frey, R. Busch, H.-G. Herrmann, Material Extrusion of Structural Polymer-Aluminum Joints - Examining Shear Strength, Wetting, Polymer Melt Rheology and Aging. Materials (Basel)

[25] 2022: N. Neuber, M. Sadeghilaridjani, N. Ghodki, O. Gross, B. Adam, L. Ruschel, M. Frey, S. Muskeri, M. Blankenburg, I. Gallino, R. Busch, S. Mukherjee, Effect of composition

and thermal history on deformation behavior and cluster connections in model bulk metallic glasses. Sci. Rep. 12, 1–14

[26] 2022: N. Neuber, O. Gross, M. Frey, B. Bochtler, A. Kuball, S. Hechler, F. Yang, E. Pineda, F. Westermeier, M. Sprung, F. Schäfer, I. Gallino, R. Busch, B. Ruta, Disentangling structural and kinetic components of the α-relaxation in supercooled metallic liquids. Commun. Phys. 5, 1–10

[27] 2023: E. S. Barreto, J. Wegner, M. Frey, S. Kleszczynski, R. Busch, V. Uhlenwinkel, L. Mädler, N. Ellendt, Influence of oxygen in the production chain of Cu-Ti-based metallic glasses via laser powder bed fusion. Powder Metall. 8, 1–12

[28] 2023: L. M. Ruschel, B. Adam, O. Gross, N. Neuber, M. Frey, H. Wachter, R. Busch, Development and optimization of novel sulfur-containing Ti-based bulk metallic glasses and the correlation between primarily crystallizing phases, thermal stability and mechanical properties. J. Alloys Compd. 960, 170614

[29] 2023: H. Jiang, J. Hu, N. Neuber, M. Frey, L. Xu, K. Sun, Y. Jia, G. Wang, R. Busch, J. Shen, Influence of sulfur addition on the glass formation, phase transformation and mechanical properties of $Cu_{50}Zr_{50}$ alloy. Acta Mater. 255, 119064

[30] 2023: A. Cornet, G. Garbarino, F. Zontone, Y. Chushkin, J. Jacobs, E. Pineda, T. Deschamps, S. Li, A. Ronca, J. Shen, G. Morard, N. Neuber, M. Frey, R. Busch, I. Gallino, M. Mezouar, G. Vaughan, B. Ruta, Denser glasses relax faster: Enhanced atomic mobility and anomalous particle displacement under in-situ high pressure compression of metallic glasses. Acta Mater. 255, 119065

[31] 2023: L. M. Ruschel, O. Gross, B. Bochtler, B. Li, B. Adam, N. Neuber, M. Frey, S. Jakovlev, F. Yang, H. Jiang, B. Gludovatz, J. J. Kruzic, R. Busch, Ni-Nb-P-based bulk glass-forming alloys: Superior material properties combined in one alloy family. Acta Mater. accepted f, 118968

[32] 2023: V. Di Lisio, I. Gallino, S. S. Riegler, M. Frey, N. Neuber, G. Kumar, J. Schroers, R. Busch, D. Cangialosi, Size-dependent vitrification in metallic glasses. Nat. Commun. 14, 4698

[33] 2024: E. S. Barreto, M. Frey, L. Matthias, J. Wegner, S. Kleszczynski, R. Busch, N. Ellendt, Gas atomization of fully-amorphous $Ni_{62}Nb_{38}$ powder. Mater. Lett. 357, 135798

[34] 2024: L. M. Ruschel, A. Kuball, B. Adam, M. Frey, R. Busch, A. Kuball, B. Adam, M. Frey, Viscosity and surface tension of the $Zr_{56.5}Ti_{13.3}Ni_{13.6}Cu_{9.6}S_7$ bulk metallic glass-forming liquid, AIP Adv. 14

[35] 2024: H. Schönrath, J. Wegner, M. Frey, E. Soares Barreto, A. Elspaß, N. Schnell, B. H. R. Erdmann, J. Neises, N. Ellendt, R. Busch, S. Kleszczynski, Analytical Modeling of Cooling Rates in PBF-LB/M of Bulk Metallic Glasses. Solid Free. Fabr. 2023 Proc.

[36] 2024: S. S. Riegler, Y. H. S. Camposano, K. Jaekel, M. Frey, C. Neemann, S. Matthes, E. Vardo, M. R. Chegeni, H. Bartsch, R. Busch, J. Müller, P. Schaaf, I. Gallino, Nanocalorimetry of Nanoscaled Ni/Al Multilayer Films: On the Methodology to Determine Reaction Kinetics for Highly Reactive Films. Adv. Eng. Mater. 2302279

[37] 2024: L. Bruckhaus, J. Wegner, N. Schnell, H. Schönrath, E. Soares, B. Maximilian, N. Ellendt, R. Busch, S. Kleszczynski, Empirical calibration method for the thermal simulation of Cu47Ti34Zr11Ni8 single tracks in laser powder bed fusion. Prog. Addit. Manuf. 9, 593–600

[38] 2024: H. Schönrath, J. Wegner, M. Frey, M. A. Schroer, X. Jin, M. Teresa, P. Prado, R. Busch, S. Kleszczynski, Novel titanium-based sulfur-containing BMG for PBF-LB/M. Prog. Addit. Manuf. 9, 601–612

[39] 2024: B. Adam, A. Kuball, L. M. Ruschel, N. Neuber, M. Frey, R. Busch, B. Adam, A. Kuball, L. M. Ruschel, N. Neuber, N. Neuber, Sulphuric precipitates in novel titanium-based, sulphur-bearing bulk metallic glass – a BMG composite? Philos. Mag. Lett., 1–11

[40] 2024: L. M. Ruschel, S. Jakovlev, O. Gross, N. Neuber, B. Adam, M. Frey, B. Schmidt, B. Bochtler, R. Busch, Unraveling the role of relaxation and rejuvenation on the structure and deformation behavior of the Zr-based bulk metallic glass Vit105. Mater. Today Adv. 23, 100522

[41] 2024: H. R. Jiang, M. Frey, N. Neuber, Y. F. Gao, B. Zhang, J. Ren, G. Wang, R. Busch, J. Shen, In-situ scattering and calorimetric studies of crystallization pathway and kinetics in a Cu-Zr-Al bulk metallic glass. J. Alloys Compd. 1006, 176243

[42] 2024: H. Schönrath, J. Wegner, M. A. Schroer, M. Frey, R. Busch, S. Kleszczynski, Impact of processing parameters on mechanical properties of additively manufactured Ti-based BMGs. MATEC Web Conf. 406

[43] 2025: B. Li, L. M. Ruschel, K. Nomoto, O. Gross, B. Adam, N. Neuber, M. Frey, S. P. Ringer, B. Gludovatz, R. Busch, J. J. Kruzic, Fracture behavior of NiNb and NiNbP bulk metallic glasses. J. Alloys Compd. 1010

[44] 2025: B. Adam, O. Kruse, L.M. Ruschel, N. Neuber, M. Frey, O. Gross, H.R. Jiang, B. Li, B. Gludovatz, J.J. Kruzic, R. Busch, Introduction of sulfur into an eutectic of the Zr-Ti-Ni-Cu system: Alloy development and characterization of the $(Zr_{50}Ti_{16.6}Ni_{18.3}Cu_{15})_{100-x}S_x$ bulk metallic glasses, J. Alloys Compd. 1025

[45] 2025: H.R. Jiang, M. Frey, N. Neuber, Q. Wang, W.F. Lu, L.M. Ruschel, G.Y. Sun, I. Gallino, B. Zhang, G. Wang, R. Busch, J. Shen, Y. Yang, Liquid-liquid phase transition and chemical phase separation in Cu-Zr-Al-Y bulk glass-forming supercooled liquid, Acta Mater. 293

Conference contributions

2017: Talk at the DPG-Meeting in Dresden, Germany, "Thermodynamic and kinetic properties as well as low temperature relaxations of Mg-based bulk metallic glasses"

2017: Talk at the 16th RQ in Leoben, Austria, "Thermodynamics, kinetics, and sub-T_g relaxations of Mg-based bulk metallic glasses"

2017: Poster at the 16th RQ in Leoben, Austria, "A comparison of thermodynamic and kinetic fragilities of bulk metallic glass forming liquids"

2019: Talk at the 17th LAM in Lyon, France, "The fragility of bulk metallic glass forming liquids studied via modulated DSC"

2023: Invited talk at the 9IDMRCS in Chiba, Japan, "X-ray photon correlation spectroscopy on metallic glass formers under non-isothermal temperature scan conditions"

2023: Poster at the 17th RQ & 27th ISMANAM in Warsaw, Poland, "X-ray photon correlation spectroscopy on a Pt-based metallic glass former under non-isothermal temperature scan conditions"

2024: Talk at the DPG-Meeting in Berlin, Germany, "X-ray photon correlation spectroscopy on metallic glass formers under non-isothermal temperature scan conditions" (talk held per proxy by Prof. Dr. Ralf Busch)

2024: Talk at the MRS in Boston, USA, “Liquid-like versus Stress-Driven Dynamics in a Metallic Glass Former Observed by Temperature Scanning XPCS”

2025: Talk at the DPG-Meeting in Regensburg, Germany, “Liquid-like versus Stress-Driven Dynamics in a Metallic Glass Former Observed by Temperature Scanning XPCS”

Research project proposals

2020: Writing the proposal of the AiF/IGF project “Laser-Strahlschmelzen amorpher Metallpulver (LaSaM) - Entwicklung einer synergetischen Wertschöpfungskette durch ganzheitliche Prozessoptimierung“ in cooperation with the LFT Duisburg-Essen (collaborator in charge: Jan Wegner) and the IWT Bremen (collaborator in charge: Dr. Nils Ellendt), founded in 2020 with a volume of 579285 € (183366 € given to the LMW Saarbrücken), project number 21227 N

2021: Writing the proposal of the DFG project “Schwefelhaltige metallische Massivgläser auf Ti-Basis für das Pulverbett-basierte Schmelzen von Metallen mittels Laser“ in cooperation with the LFT Duisburg-Essen (collaborator in charge: Jan Wegner), founded with a volume of 361316 € (181690 € given to the LMW Saarbrücken), project number 503259970

2024: Writing the proposal of the DFG project “Thermal gradients in binary Ni-Nb bulk metallic glass fabricated through Laser Powder Bed Fusion: Investigation on vitrification and residual stresses” in cooperation with the LFT Duisburg-Essen (collaborator in charge: Jan Wegner)

Managed research projects

2018 – 2020: Management of the AiF/IGF project „Laser-Strahlschmelzen metallischer Gläser - Optimierung von Werkstoff und Herstellungsverfahren (OptMetGlas)“ (in cooperation with the LFT Duisburg-Essen (collaborator in charge: Jan Wegner), project number 19927 N

2020 – 2022: Management of the AiF/IGF project “Laser-Strahlschmelzen amorpher Metallpulver (LaSaM) - Entwicklung einer synergetischen Wertschöpfungskette durch ganzheitliche Prozessoptimierung“ in cooperation with the LFT Duisburg-Essen

(collaborator in charge: Jan Wegner) and the IWT Bremen (collaborator in charge: Erika Soares Barreto), project number 21227 N

2022 – 2025: Management of the DFG project "Schwefelhaltige metallische Massivgläser auf Ti-Basis für das Pulverbett-basierte Schmelzen von Metallen mittels Laser" in cooperation with the LFT Duisburg-Essen (collaborator in charge: Hanna Schönrath), project number 503259970

Synchrotron beamtime proposals

2021: Beamtime 20200650 "In-situ structural analysis of a liquid-liquid transition in a metallic glass former during dynamic mechanical analysis", 96 h at beamline P21.1 of the Deutsches Elektronen-Synchrotron (DESY), principal investigator M. Frey, accepted

2025: Beamtime HC-5971 "Studying the (de-)vitrification, aging, and sub-T_g relaxation behavior of metallic glasses via slow temperature scanning XPCS", 144 h at beamline ID10 of the European Synchrotron Radiation Facility (ESRF), principal investigator M. Frey, accepted

Participated synchrotron beamtimes

2018: Beamtime 11004554 at beamline P02.1 (DESY)

2018: Beamtime 1105279 at beamline P02.1 (DESY)

2019: Beamtime 11006189 at beamline P10 (DESY)

2020: Beamtime 11009865 at beamline P21.2 (DESY)

2020: Beamtime 11009865 at beamline P21.2 (DESY)

2020: Beamtime 11009967 at beamline P21.2 (DESY)

2020: Beamtime 11009963 at beamline P21.1 (DESY)

2020: Beamtime HC-4260 at beamline ID10 (ESRF)

2021: Beamtime 11009169 at beamline P10 (DESY)

2020: Beamtime HC-4479 at beamline ID10 (ESRF)

2021: Beamtime 110011844 at beamline P21.1 (DESY)

2021: Beamtime 110011650 at beamline P21.2 (DESY)

2021: Beamtime 110011736 at beamline P21.1 (DESY)

2021: Beamtime HC-4529 at beamline ID10 (ESRF)

2021: Beamtime 110011947 at beamline P21.2 (DESY)

2022: Beamtime 110014637 at beamline P10 (DESY)

2022: Beamtime 110014806 at beamline P10 (DESY)

2023: Beamtime 110016133 at beamline P10 (DESY)

2023: Beamtime HC-5277 at beamline ID15B (ESRF)

2023: Beamtime 110016006 at beamline P10 (DESY)

2023: Beamtime 110016470 at beamline P21.2 (DESY)

2024: Beamtime 110019028 at beamline P21.2 (DESY)

2025: Beamtime HC-5971 at beamline ID10 (ESRF)

Supervised student theses

2019: Yang Min (master thesis), Saarland University, "Production and characterization of metallic glass ribbons by chill-block melt spinning"

2019: Patrick Stiglmair (bachelor thesis), Saarland University, "Mechanische und thermophysikalische Eigenschaften des per pulverbettbasiertem Laserstrahlschmelzen gefertigten metallischen Massivglases $Zr_{59.3}Cu_{28.8}Al_{10.4}Nb_{1.5}$"

2022: Marvin Müller (master thesis), Saarland University, "Crystallization and Physical Aging Behavior Studies on Bulk Metallic Glass Forming Liquids via Fast Differential Scanning Calorimetry" (co-supervised with Nico Neuber)

2022: Viktor Carl Harry Svenonius (master thesis), Saarland University, "Alloy development and thermophysical properties of new bulk metallic PdNiSe glasses" (co-supervised with Nico Neuber)

2024: Benedikt Schmidt (master thesis), Saarland University, “Comparative corrosion studies on bulk metallic glasses – on the influence of composition, production route, post-processing, and thermal history”

2025: Fabian Vollmers (master thesis), Saarland University, “Untersuchung von Magnesium basierten metallischen Gläsern mittels Chip-Kalorimetrie“

Educational work

2017: Supervised lab session “Praktikum Mischungswärme und Schmelzwärme“ of the Bachelor program „Materialwissenschaft und Werkstofftechnik“

2017 – 2025: Supervised lab session “Praktikum Aushärten von Aluminiumlegierungen” of the Bachelor program „Materialwissenschaft und Werkstofftechnik“

2021 – 2024: Given lecture “Amorphous Metals” of the Master programs „Materialwissenschaft” and “Werkstofftechnik“ (stand-in lecturer)

2024: Given lecture “Kinetics of Amorphous Systems” of the Master programs „Materialwissenschaft” and “Werkstofftechnik“ (principal lecturer together with Bastian Adam and Lucas Ruschel)

Author contributions to the publications constituting this thesis

In the following, the contributions of the first author (Maxmilian Frey) and the coauthors to each of the six publications included in this work will be explained in detail.

Paper I

Sample synthesis was primarily performed by Nico Neuber and Oliver Gross. Maximilian Frey conceptualized the work, performed the measurements with help of the Bettina Zimmer. Analysis and interpretation of the data was done by the Maximilian Frey with feedback from the Wulff Possart. Maximilian Frey also wrote the manuscript, reviewing and feedback was provided by all other authors.

Paper II

Sample synthesis was mainly done by Maximilian Frey and Nico Neuber. Maximilian Frey and Eloi Pineda conceptualized the work. The data was obtained by Maximilian Frey, Nico Neuber, Antoine Cornet, Yuriy Chushkin, Federico Zotone, Eloi Pineda, and Beatrice Ruta. Data analysis was mainly performed by Maximilian Frey with help of Eloi Pineda and Nico Neuber, interpretation was performed by these authors together with Beatrice Ruta and Yuriy Chushkin. Writing was mainly done by Maximilian Frey and Eloi Pineda with support from Betrice Ruta. All authors provided feedback and reviewing.

Paper III

Samples were synthesized by Maximilian Frey and Nico Neuber. Maximilian Frey created the concept, data was primarily obtained by Maximilian Frey with support from S. Riegler and M. Müller. Analysis and interpretation were primarily done by Maximilian Frey, with help from Nico Neuber and Oliver Gross. Maximilian Frey wrote the manuscript, all authors provided feedback and reviewing.

Paper IV

Sample synthesis was primarily done by Jan Wegner. Maximilian Frey and Jan Wegner conceptualized the work, experiments were performed by Maximilian Frey, Jan Wegner, Benedikt Reiplinger, Nico Neuber, Bastian Adam, Lucas Ruschel, Sascha Sebastian Riegler, and Hao-Ran Jiang. Data analysis and interpretation was done by Maximilian Frey with help of Benedikt Bochtler, Jan Wegner and Nico Neuber. Maximilian Frey wrote the article with support from Jan Wegner. All authors provided feedback and reviewing.

Paper V

Samples were primarily formed by Jan Wegner and Maximilian Frey. The work was conceptualized by Jan Wegner, Maximilian Frey, and Erika Soares Barreto. Data was obtained and analyzed by Maximilian Frey, Jan Wegner, Nico Neuber, Bastian Adam, Sascha Sebastian Riegler, Erika Soares Barreto, Lucas Ruschel, and Hao-Ran Jiang. Interpretation was mainly done by Jan Wegner and Maximilian Frey. The manuscript was written by Maximilian Frey, all authors provided feedback and reviewing.

Paper VI

Samples were primarily formed by Jan Wegner, the work was conceptualized by Maximilian Frey. Measurements as well as their analysis and interpretation were performed by Maximilian Frey, Lucas Ruschel, and Jan Wegner. The manuscript was primarily written by Maximilian Frey with assistance from Lucas Ruschel and Jan Wegner. All authors provided feedback and reviewing.

List of Figures

List of Contents

1. INTRODUCTION

With undercooling, liquid dynamics undergo a drastic, often faster than exponential slowdown over several orders of magnitude. If crystallization is avoided, this slowdown eventually leads to vitrification and a glass is formed. The term 'glass' originally stems from the old-Germanic 'glasa', which means 'the shining one' or 'the shimmering one'. As a liquid that has 'fallen out of equilibrium' [46], glass exhibits an amorphous atomic structure. 'Amorphous' etymologically translates from Greek as 'shape-less' or 'form-less', and addresses the fact that glasses lack the long-range order known from crystalline solids. Yet, atomic order is not completely absent in supercooled liquids and glasses, as they often display pronounced short-range order (SRO) and even medium-range order (MRO). Glass stands as one of humanity's oldest known and utilized materials, with its earliest production dating back at least 3500 years ago [47]. From a chemical standpoint, glasses are traditionally found in inorganic non-metallic systems, which can be further subclassified into non-oxide and oxide glasses, as well as organic systems, namely polymeric and molecular glass formers. Historically, metals were not considered as glass formers, since metallic liquids were always found to crystallize rapidly upon undercooling.

Therefore, the revelation of the first metallic glass former $Au_{75}Si_{25}$ (in at%) by W. Klement, R. H. Willens, and P. Duwez in 1960 came as a significant surprise to the physics community [48]. To achieve vitrification and prevent crystallization, the liquid had to be quenched extremely fast, with a rate equal to or higher than the so-called the critical cooling rate (R_c). Accordingly, the first metallic glass was obtained by splat-quenching a small liquid droplet into a thin flake of about 10 µm thickness. Regarding these dimensions, metallic glasses initially remained rather a scientific curiosity than a technologically meaningful material class. Yet, the glass forming ability (GFA) could be significantly improved through alloy development towards more complex, multi-component systems. Between 1974 and 1984, reports on ternary Pd- and Pt-based alloys [49–52] marked a decisive breakthrough, allowing to cast amorphous metals in bulk dimensions. These alloys constituted the novel material class of bulk metallic glasses (BMGs), which are alloys with a GFA that allows for critical casting diameter (d_c) of 1 mm or more. Due to the material costs of these noble metal compositions, technological interest still remained mediocre, which eventually changed with A. Inoue's reports on Zr-

based metallic glasses [53,54], which were the first among many other alloy systems, see Figure 1.1, to combine good GFA with acceptable material costs. Bulk metallic glasses offer exiting properties, especially regarding their mechanics. The amorphous atomic structure prohibits dislocation-based plastic deformation as it is known from crystalline metals, and hence, BMGs show high hardness, yield strengths close to the theoretical strength, and also high elastic limits of about 2% [55]. Thereby, strength and hardness roughly scale with the melting temperature. Zr-based alloys for example show strength values of roughly 2 GPa and hardness in the order of 500 HV [56,57]. Fe- and especially NiNb- or Ta-based systems surpass these values, marginalizing even most modern steels due to strengths exceeding 3.5 GPa and hardness values above 1000 HV [31,58–62]. Hence, BMGs are highly promising materials for countless applications that ask for small but resilient parts, e.g. in medicine, customer goods, jewelry, or in the defense sector [57,63,64].

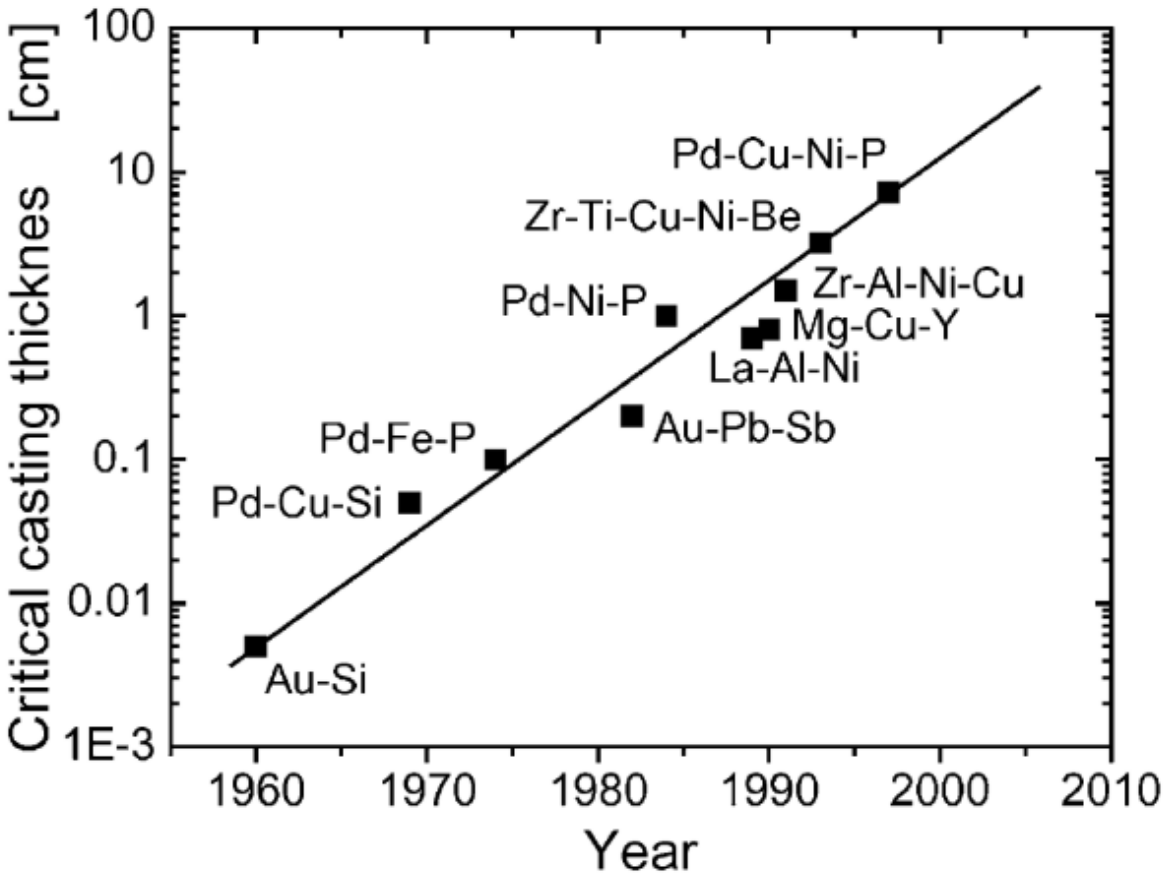

Figure 1.1: With ongoing alloy development, the critical casting diameters (here termed critical casting thickness) of metallic glass formers increase over time. Taken from J. Löffler [64].

Nevertheless, casting BMGs on an industrial scale still remains challenging as the need for a fast cooling process inherently limits the size and geometry of produced parts. Yet complex geometries can be achieved by post-processing, since BMGs offer the principal

possibility of thermoplastic forming (TPF). By heating an as-cast part above the glass transition, it can be plastically deformed and reshaped under pressure as it is known from thermoplastic polymers [65,66]. Furthermore, the rise of additive manufacturing (AM) allows to overcome the limitations of casting processes and increased the interest in BMGs [67]. Laser powder bed fusion (PBF-LB-M) leads to a fast, layer-wise, and highly localized melting and cooling, which allows to vitrify various metallic glass formers in large and complexly shaped parts that would be impossible to cast, see Figure 1.2.

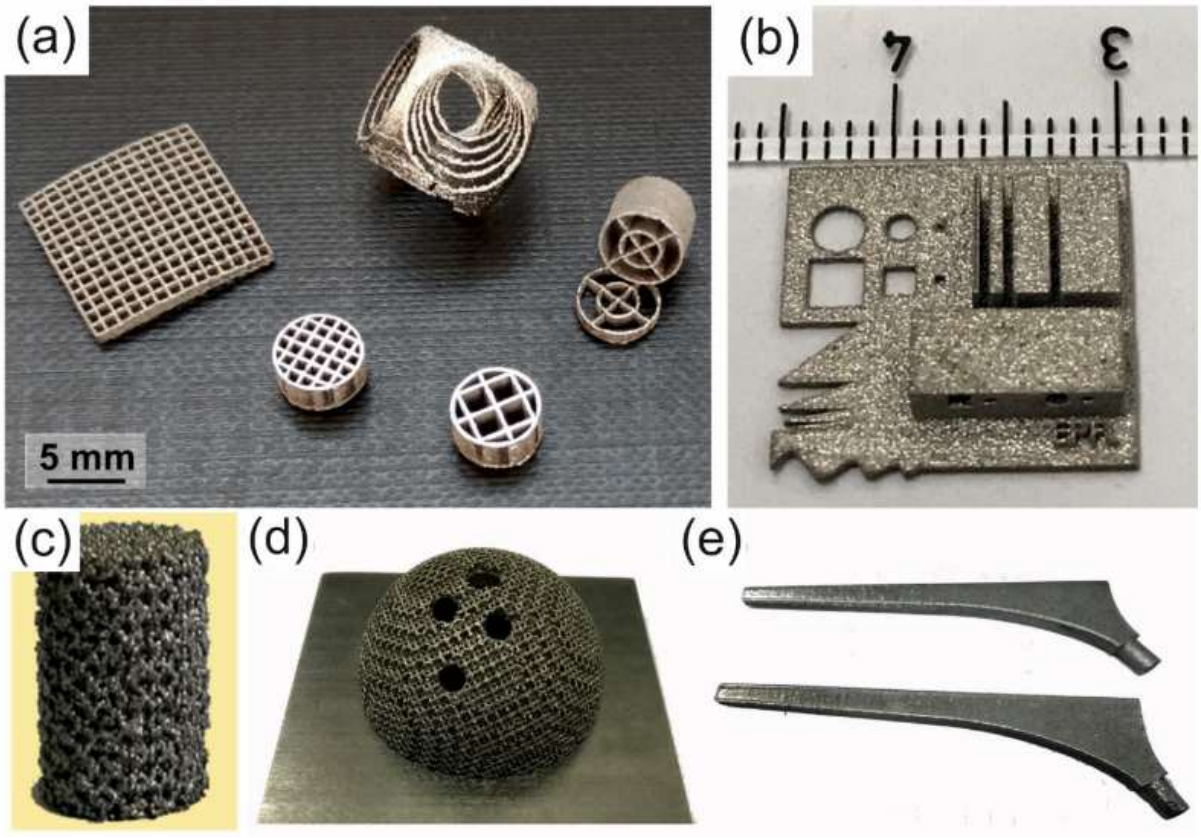

Figure 1.2: Additive manufacturing allows for complexly shaped metallic glass components. Taken from N. Sohrabi et al. [68].

This cumulative PhD thesis incorporates six publications and will comprise the broad academic field of metallic glasses in a kind of 'pincer movement'. The first three publications are dedicated to a physical, fundamental science oriented topic, namely the dynamics of supercooled metallic liquids and its impact on vitrification and crystallization. The last three publications will instead approach from a rather practical angle, taking a closer look at the processing and evaluation aspects of additive manufacturing of metallic glasses. In the following, the six publications shall be briefly introduced.

Supercooled liquids can differ drastically with respect to their dynamic's temperature dependence, which was Austen Angell's motivation to introduce his famous fragility concept [46]. It allows to categorize liquid dynamics by its degree of deviation from a classical exponential, Arrhenius-like temperature dependence. Thereby, liquids are termed 'strong' if they behave rather Arrhenius-like and are otherwise termed 'fragile' if they show distinct super-exponential behavior. Liquids dynamics and fragility directly predetermine the transition kinetics of glass formation and its 'antagonistic' process, the (primary) crystallization from the supercooled liquid. Therefore, liquid dynamics play a fundamental role for the GFA of metallic glass formers and hence, the first part of this cumulative PhD thesis will be dedicated to this important topic. More specifically, the focus will be laid on the methodological question, how to determine liquid dynamics, fragility and their direct influence on crystallization and vitrification. These aspects will be mainly demonstrated by means of the noble-metal-based $Pt_{42.5}Cu_{27}Ni_{9.5}P_{21}$ system [69], a well-established and well-studied [9,19,25,26,70,71] glass former, which excels as a model system due its excellent thermal stability against crystallization and relatively low glass transition temperature that renders it easy to characterize. Paper I [1] enters the topic by determining the alloy's fragility via a macroscopic calorimetric approach, namely modulated differential scanning calorimetry (MDSC). Here, methodological foundations will be established, discussing how to define adequate and universal ways of data handling, analysis, and data comparison. Paper II [6] leaves the macroscopic scale and focuses on the microscopic dynamics of the $Pt_{42.5}Cu_{27}Ni_{9.5}P_{21}$ system by applying a rather novel and exotic approach, namely X-ray photon correlation spectroscopy (XPCS). This diffraction method uses highly energetic, monochromatic and coherent synchrotron radiation to obtain and record specific diffraction patterns, so-called speckle patterns. These are subject to temporal changes and decorrelate with growing temporal distance to each other, thereby reflecting the dynamics of the atomic configuration on the MRO scale. By using state-of-the-art detector technology and the extremely brilliant radiation provided by the 4th generation synchrotron at ESRF, we firstly use a temperature scanning method that allows to observe the devitrification and vitrification of $Pt_{42.5}Cu_{27}Ni_{9.5}P_{21}$ in-situ. It is revealed that the observed decorrelation in the glass and glass transition region actually consists of two distinct contributions that stem from different types of atomic motion: one being (sub-)diffusive liquid-like and the other being stress-driven ballistic-like as a typical trait of the non-equilibrium glassy state. Paper III [3] finally studies the influence of liquid dynamics on the crystallization kinetics of

$Pt_{42.5}Cu_{27}Ni_{9.5}P_{21}$ by using a relatively novel calorimetric approach, the so-called fast differential scanning calorimetry (FDSC). This nano-calorimetric method uses very small specimens with masses in the order of only several ng to apply extremely rapid temperature changes. This allows to determine a complete time-temperature-transformation (TTT) diagram that describes the system's crystallization behavior.

Since a profound understanding of crystallization kinetics is of advantage for processing, Paper III can be seen as a link between the methodological, fundamental science oriented first part of the thesis and the more pragmatic, application oriented second part, in which we will focus on the additive manufacturing of metallic glasses via laser powder bed fusion (PBF-LB/M). Paper IV [2] will focus on the most established metallic glass former in additive manufacturing, the alloy $Zr_{59.3}Cu_{28.8}Al_{10.4}Nb_{1.5}$, originally termed AMZ4 [72,73] and now commercially marketed under the tradename AMLOY-ZR01 by Heraeus AMLOY [74]. While the previous parameter evaluation towards fully amorphous and highly densified samples is published in a coauthored work by J. Wegner et al. [17], Paper IV reports on the viability of post-processing of AM-formed $Zr_{59.3}Cu_{28.8}Al_{10.4}Nb_{1.5}$ parts by thermoplastic forming. TPF allows to massively reduce the AM-typical surface roughness and can be further used to apply complex µm-sized surface structures. Despite the thermal cycling brought in by such a post-processing, the amorphous state and mechanical properties can be maintained. This allows for highly robust parts with bending strength values of up to 2.1 GPa, a record value among AM-formed metallic glasses at that time [68]. Paper V [4] evaluates the impact of material toughness and thermal stability on the AM processability by microalloying the $Cu_{47}Ti_{34}Zr_{11}Ni_8$ (Vit101) alloy [75] with Si and Sn. We find that in this system, differences in the thermal stability play a minor role, while the materials toughness is decisive for crack formation and the resulting mechanical properties. Vit101 was found to further increase the record bending strength value for AM-formed BMGs to 2.5 GPa. To our knowledge, this record still stands today. Finally, Paper VI [5] reports on first PBF-LB/M parameter evaluations of the binary $Ni_{62}Nb_{38}$ bulk metallic glass former [76]. The system appears promising, since this first parameter study allows for almost fully vitrified samples with only minor crystalline fractions. NiNb-based metallic glasses are known for their extreme mechanical properties [31,58,59], which are confirmed by the AM-formed samples in Paper VI through high Vickers hardness values of almost 900 HV1. Yet, crack formation during processing remains a challenge that must be addressed in future parameter optimization attempts.

To provide the background knowledge to understand and discuss the present publications, Chapter 2, THEORY, will provide a broad and in-depth introduction to the topic of bulk metallic glasses. Here, all the dynamical, thermodynamical, and structural aspects that determine the rivalry between crystallization and glass formation in metallic systems will be explained, together with the mechanical properties of metallic glasses. Chapter 3, PROCESSING, provides an overview of the different approaches used in this work to create and post-process metallic glasses. Chapter 4, CHARACTERIZATION, explains the analysis methods used in this thesis in detail. Chapter 5, PUBLICATIONS, then lists all six paper that form the core of the present work. Chapter 6, ADDITIONAL RESULTS AND DISCUSSIONS, picks up the topics of the publications and provides further information to deepen the discussion and to highlight the given interconnections between the different subjects. Finally, Chapter 7, SUMMARY AND OUTLOOK, will briefly recapitulate the most important findings and suggest further research approaches that might be suitable for pursuing the present works.

2. THEORY

Under isobaric conditions, the Gibbs-Helmholtz equation describes that the (specific) Gibbs free energy G(T) of a system constitutes through the interplay of its enthalpy H(T) and its entropy S(T) as

$$G(T) = H(T) - T\,S(T). \tag{2.1}$$

Any system strives towards the state with the lowest overall G(T). At low temperatures, the enthalpic term dominates and a system usually prefers a highly ordered state that minimizes G(T) through a low enthalpy level. The entropic term -T S(T) dominates at higher temperatures, and hence, a rather disordered state with higher entropy is favored. This fundamental rivalry between enthalpy and entropy, i.e. between order and chaos, is the underlying principle that causes temperature dependent changes observed in all fields of nature.

In the coming chapters, we will follow a liquid, more specifically a metallic glass forming liquid, on its journey from chaos towards increasing order upon cooling from high temperatures above the liquidus temperature down into the deeply supercooled state. We will consider this process from different points of view, starting with a perspective on the liquid dynamics. Chapter 2.1 will establish the *Fundamental concepts of liquid dynamics*, which will then allow to illustrate *Liquid dynamics under changing temperatures* in Chapter 2.2. We will see that liquid dynamics slow down massively with decreasing temperature. Ultimately, this can lead to a vitrification of the liquid at the glass transition. In this context, the important difference between *Probing equilibrium dynamics via the dynamic glass transition* and the process of *Falling out of equilibrium at the kinetic glass transition* will be discussed in Chapters 2.3 and 2.4. With Chapter 2.5, we will change the perspective on the undercooling process and discuss the aspects of *Structure in metallic glass forming systems*. Finally, we will introduce a thermodynamic view on the undercooled liquid, especially in reference to the competing crystalline state. This allows to discuss the process of *Crystallization according to the classical nucleation theory* in Chapter 2.6. Vitrification and crystallization are antithetical effects, and Chapter 2.7, *Preventing crystallization and forming a glass*, will debate the conditions under which either the first or the second process occurs. The THEORY chapter will then close with a

rather practice-oriented introduction to the *Mechanical properties of metallic glasses* in Chapter 2.8.

2.1 Fundamental concepts of liquid dynamics

The liquid state is one of the four fundamental states of matter, besides the solid, gaseous, and plasma states. Liquids differ from gases in being condensed matter, therefore featuring high densities similar to the solid state. Yet, they again fundamentally differ from solids as the structural units in a liquid (atoms or molecules, further termed 'particles') are subject of permanent motion on length scales distinctly larger than vibrational movements. Therefore, particles collide randomly, rearrange, and exchange momentum. In the following, we will establish fundamental properties that describe and characterize liquid dynamics, i.e., we will consider the processes of mass transport and structural relaxation.

2.1.1 Mass transport and types of diffusion

Temporally and spatially averaged considerations about particle rearrangements can be approached by stochastic models, often using the so-called mean squared displacement (MSD), $\langle \Delta \mathbf{r}^2(t) \rangle$,

$$\langle \Delta \boldsymbol{r}^2(t) \rangle = \langle |\boldsymbol{r}(t) - \boldsymbol{r}(0)|^2 \rangle = \frac{1}{N} \sum_{i=1}^{N} |\boldsymbol{r}_i(t) - \boldsymbol{r}_i(0)|^2. \qquad (2.2)$$

Here, $\mathbf{r}_i$ is the position vector of a respective particle i at a specific time t and $\langle \dots \rangle$ indicates the ensemble average over the whole population N of considered particles. In other words, $\langle \Delta \mathbf{r}^2(t) \rangle$ provides the average squared distance a particle travels within a given time t and is therefore a property that describes microscopic mass transport. Under isothermal conditions, $\langle \Delta \mathbf{r}^2(t) \rangle$ increases with growing time according to a power law [77]

$$\langle \Delta \boldsymbol{r}^2(t) \rangle \cong K_\alpha \, t^\alpha, \qquad (2.3)$$

with the diffusion exponent α and a generalized diffusion coefficient K_α of the dimension $cm^2/s^{-\alpha}$. By means of K_α, the apparent dynamics can be categorized, as illustrated in Figure 2.1. In case of α=1, normal diffusion is observed. When α≠1, we observe so-called

anomalous diffusion. More specifically, an α<1 indicates sub-diffusive behavior, while an α>1 indicates super-diffusive behavior. In case of α=2, one speaks of ballistic dynamics.

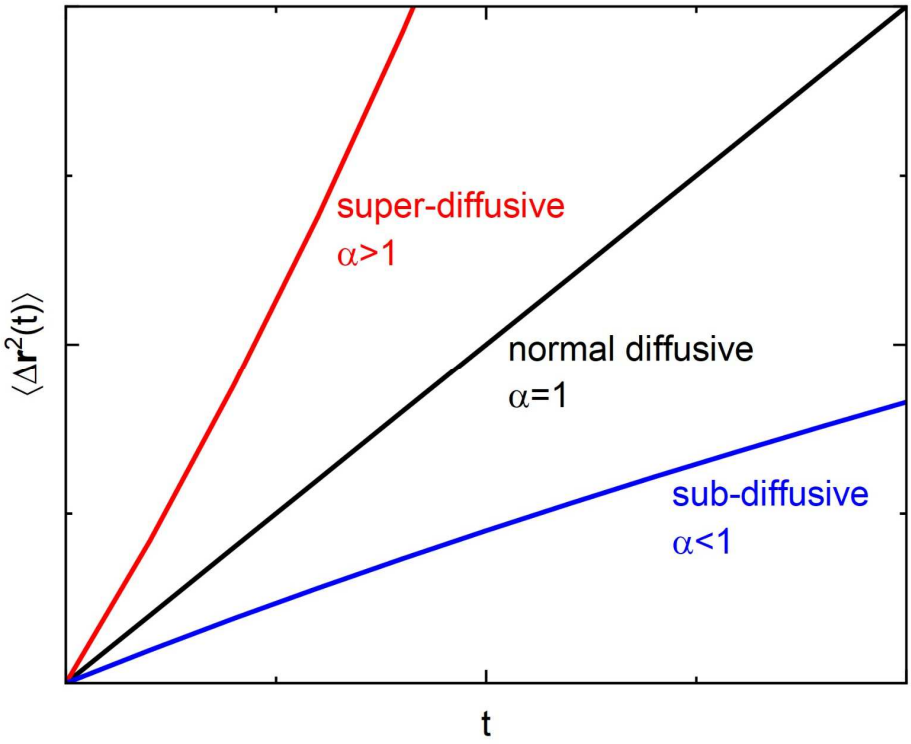

Figure 2.1: Types of diffusion can be categorized on hand of their diffusion exponent α, which determines the time dependence of the MSD. Normal diffusive behavior is characterized by α=1, super-diffusion features α>1, and sub-diffusion shows α<1.

2.1.2 α-relaxation and relaxation time

We have seen that the liquid state manifests through the ubiquity of spontaneous structural fluctuations. These thermal motion processes are generally subsumed under the term α-relaxation (or also structural relaxation) and are the primary mechanism that drives the dynamics of equilibrium liquids. We now think about a normalized structural autocorrelation function Φ(t) that quantifies how well the structural state at a given time coordinate t correlates with the structural state at t=0. Such a function can be generally modelled by the Kohlrausch-Williams-Watts (KWW) equation [78,79]:

$$\Phi(t) = \exp\left(-\left(\frac{t}{\tau}\right)^{\beta}\right). \qquad (2.4)$$

Here, τ is the relaxation time and describes the timespan after which Φ(t) has decreased to 1/e≈0.37. τ quantifies the timescale of the α-relaxation process and is therefore a

fundamental property to characterize liquid dynamics. β is termed the shape exponent. If β=1, a single exponential decay is observed. The case of β<1 is termed stretched exponential decay and in case of β>1, we speak of a compressed exponential decay. This classification resembles the one of the diffusion exponent α from equation (2.3). By considering the method of X-ray photon correlation spectroscopy introduced in Chapter 6.2.1 and discussed in detail in Chapter 6.2, we will see that this analogy is not a product of chance but related to the intuitive perception that diffusive mass transport and structural relaxation are closely interconnected.

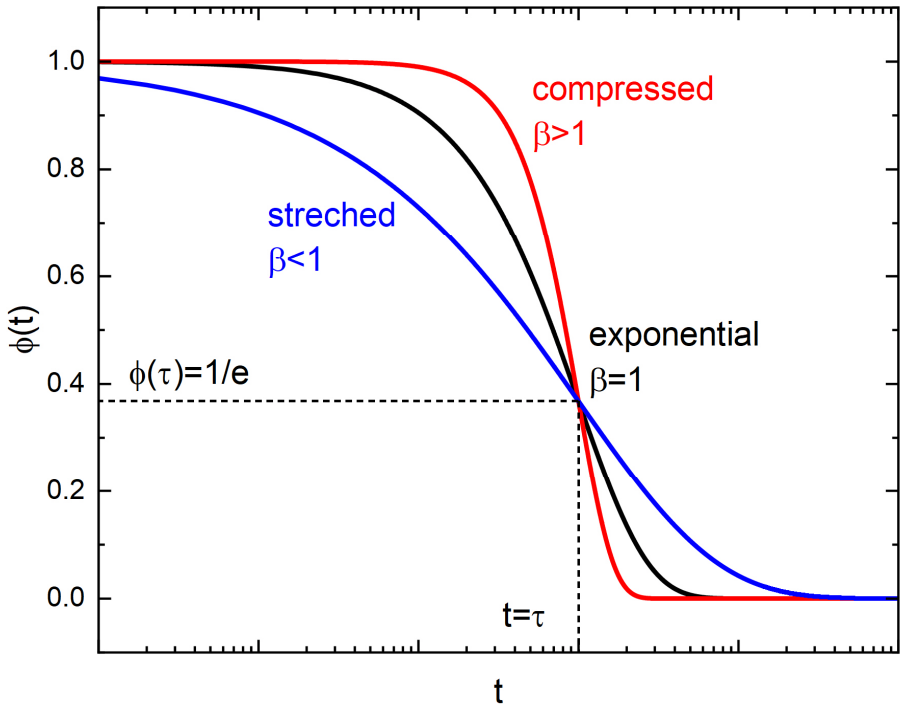

Figure 2.2: Exemplary normalized structural autocorrelation functions Φ(t) as a function of time, which illustrate the effect of the shape exponent β. A single exponential decay is characterized by β=1. A stretched decay shows a β<1 and a compressed decay a β>1. The relaxation time τ indicates the time after which Φ(t) reaches 1/e≈0.37.

2.1.3 Viscosity and the Maxwell relation

The relaxation time of a liquid directly predetermines its macroscopic rheological behavior. According to the Maxwell relation [80], τ is directly proportional to the (dynamic) viscosity η via the (high-frequency) shear modulus G:

$$\eta = G\,\tau. \tag{2.5}$$

η determines the shear rate $\dot{\gamma}$ with which the liquid responses to an applied shear stress τ_{xy} (here regarding the x-y plane):

$$\eta = \frac{\tau_{xy}}{\dot{\gamma}}. \tag{2.6}$$

Hence, the viscosity is a measure for the 'internal friction force' of a given liquid that shears under the influence of an external force. Alternatively, η can be understood as a property that quantifies the liquids ability to transfer a momentum brought in by the shear stress.

2.2 Liquid dynamics under changing temperatures

2.2.1 Homogeneous high-temperature liquids and the Stokes-Einstein relation

Liquids at and above their melting points are in a highly entropic state. They feature high levels of 'free volume', a term that refers to the concept of unoccupied excess space between particles, allowing them to move and rearrange [81,82]. Accordingly, particles can move and interact effortlessly through random walk processes. Describing the α-relaxation via the KWW model, see equation (2.4), usually provides shape exponents β near unity [83–85]. Such nearly single exponential decays suggest very narrow relaxation time spectra. High-temperature liquids are, therefore, usually seen as dynamically homogeneous and show normal diffusive behavior [83–89]. Hence, the MSD rises proportionally with time and the diffusion exponent α ranges near unity, analogous to the shape exponent β. Equation (2.3) then reduces to

$$\langle \Delta \boldsymbol{r}^2 \rangle = 6\, D\, t, \tag{2.7}$$

with D being the diffusion constant (or diffusivity) with the dimension cm^2/s as known from Fick's first and second law. It statistically describes the rapidness of mass transport through normal diffusive motions. D is inherently coupled with the (particle) mobility μ, a property that quantifies how 'effortless' an individual particle is able to move in the liquid. The Nernst-Einstein equation formulates the interplay between μ and D as

$$\mu = \frac{D}{k\, T}, \tag{2.8}$$

where k is the Boltzmann constant. By further considering a Brownian motion scenario, where a (large) particle of diameter d moves with a constant velocity v through a continuum fluid consisting of smaller particles [90,91], see Figure 2.3a), Stokes [92] showed that individual particle mobility and viscosity are inversely related according to

$$\mu = \frac{1}{3\,\pi\,d\,\eta}. \tag{2.9}$$

In combination with the Nernst-Einstein equation, we finally obtain the Stokes-Einstein relation that connects diffusion constant and viscosity in form of

$$D = \frac{k\,T}{3\,\pi\,d\,\eta}. \tag{2.10}$$

Despite being originally derived from the Brownian motion scenario, the Nernst-Einstein equation and Stokes-Einstein relation hold up well for most high-temperature liquids, see Figure 2.3b). This demonstrates the prevalence of a close relationship between microscopic mass transport and macroscopic flow.

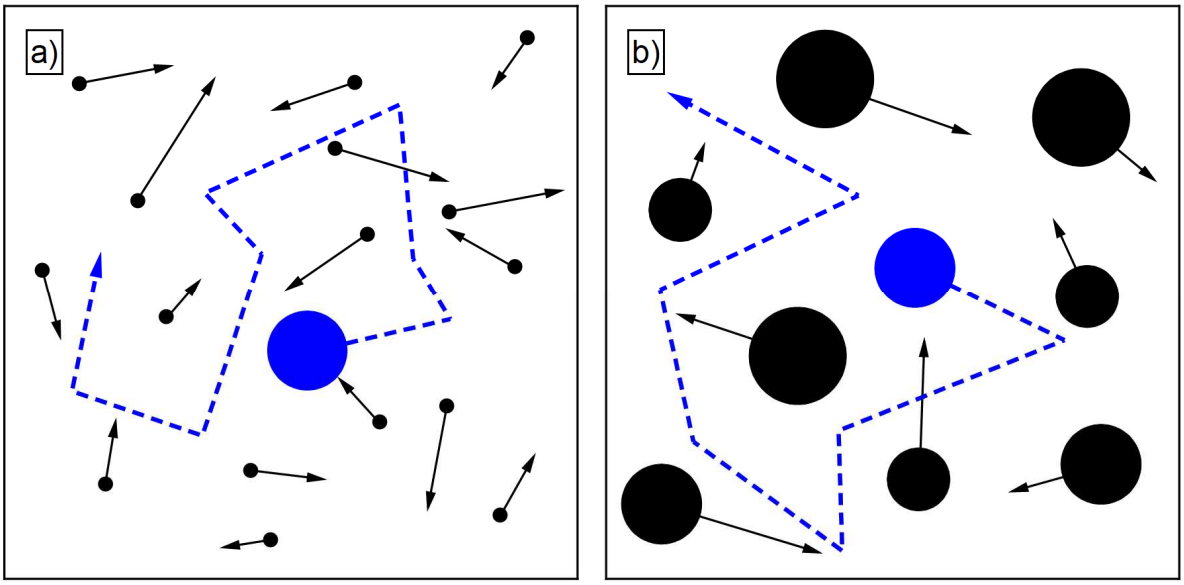

Figure 2.3: a) Illustration of the normal diffusive nature of the so-called 'Brownian motion' of a larger particle moving in a continuum fluid of smaller particles [90,91]. b) Comparable diffusive motions are found in high-temperature liquids, even though all particles feature similar sizes.

2.2.2 Heterogeneities in undercooled liquids and the Stokes-Einstein breakdown

The entropy and the free volume of an equilibrium liquid decrease with decreasing temperature and dynamics become increasingly sluggish. The resulting spatial constraints force the α-relaxation away from simple random walk motions to rely more and more on cooperative motions of groups of particles [86,87,93]. Furthermore, dynamic heterogeneities evolve with undercooling. Therefore, the ensemble-averaged α-relaxation process cannot be described by a single exponential decay anymore. Instead,

structural relaxation constitutes through a distribution $D(\tau')$ of different relaxation times. Regarding the KWW model in equation (2.4), the stretched exponential shape (β<1) of the autocorrelation function Φ(t) then results from integration over the distribution of single exponential decays with different relaxation times τ' [88,89]:

$$\Phi(t) = \int_0^\infty D(\tau') \exp\left(-\frac{t}{\tau'}\right) d\tau' = \exp\left(-\left(\frac{t}{\tau}\right)^\beta\right). \tag{2.11}$$

The shape exponent β thereby tells us how broad the relaxation times are distributed, lower β values indicate a broader spectrum and vice versa. The question arises how to visualize such a distribution of timescales. Two extreme cases can be excogitated: A 'homogeneous' and a 'heterogeneous' scenario, as schematically shown in Figure 2.4 [88,89].

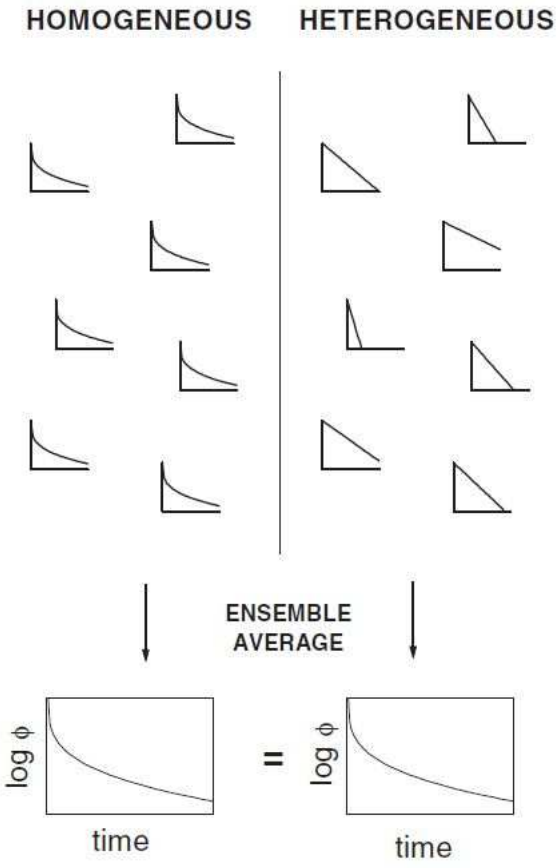

Figure 2.4: Comparison of the 'homogeneous' and 'heterogeneous' scenario of dynamic heterogeneities in liquids. In case of the former extreme, every location in the liquid features the same broad relaxation time distribution. In course of a (macroscopic) characterization of the system, one averages over the ensemble of these locations, thereby naturally reproducing the very same distribution. In case of the latter extreme, local relaxation events are not stretched but single exponential and differ massively in their relaxation times. Yet, ensemble averaging over all these locations again leads to a broad timescale distribution, as observed for the 'homogeneous' scenario. Taken from [89].

The first assumes that liquid dynamics are spatially homogeneous and feature the same distribution $D(\tau')$ at every location. Here, dynamic heterogeneity would manifest in a purely temporal manner. The latter imagines local relaxation events as single exponential decays, but with large spatial differences between varying locations. In this case, we look at a purely spatial heterogeneity scenario and the timescale distribution $D(\tau')$ stems from the volumetric ensemble averaging. From a macroscopic perspective, both approaches can equally explain an experimentally observed stretched decay, see Figure 2.4, yet, both scenarios significantly differ in terms of modelling and regarding further implications. Recent experimental studies suggest that reality manifests as a combination of both approaches, which is referred to in form of the term 'spatio-temporal' heterogeneities [88,89,94–96]. Especially the latest emergence of novel electron correlation spectroscopy (ECS) [95,96] allows to image that supercooled (metallic) liquids feature nm-scaled domains with different relaxation times and locally stretched exponential decays, which are changing and shifting with time, see Figure 2.5.

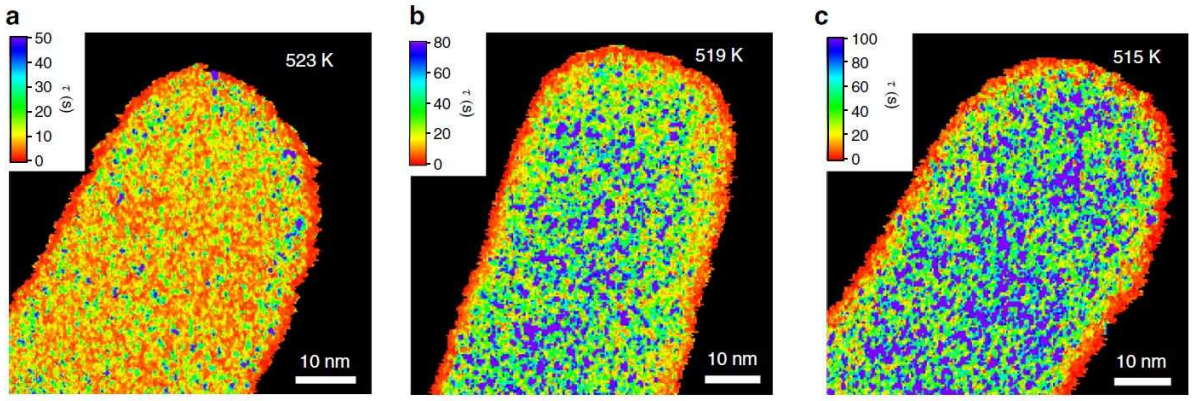

Figure 2.5: Spatial relaxation time maps of a Pt-based metallic glass forming liquid measured via ECS at three different temperatures near the glass transition. With decreasing temperature, we observe an overall decrease of relaxation times (more blue colors) and also an increase of spatio-temporal heterogeneity (larger color contrast). Taken from [96].

The reduction of free volume, rise of cooperativity, and the emergence of spatio-temporal heterogeneous dynamics naturally impede microscopic mass transport processes. As normal diffusion through random walks is suppressed, particles instead tend to show caging effects, see Figure 2.6. This means that particles can be 'trapped' inside a cage formed by their neighbors, rendering movements beyond this cage improbable [81,82]. Regarding equation (2.3), the MSD therefore rises in a less than linear manner with time, corresponding to a diffusion exponent $\alpha<1$ and indicating sub-diffusive behavior [94,97,98]. Furthermore, in liquids that incorporate different particle species, e.g. in case

of multicomponent metallic systems, the diffusivity of individual species can decouple massively by several orders of magnitude during undercooling [83,99–104]. Larger particle species can form sluggish, slow-moving sub-systems, while transport of smaller species might stay thermally activated [26,86,99,105].

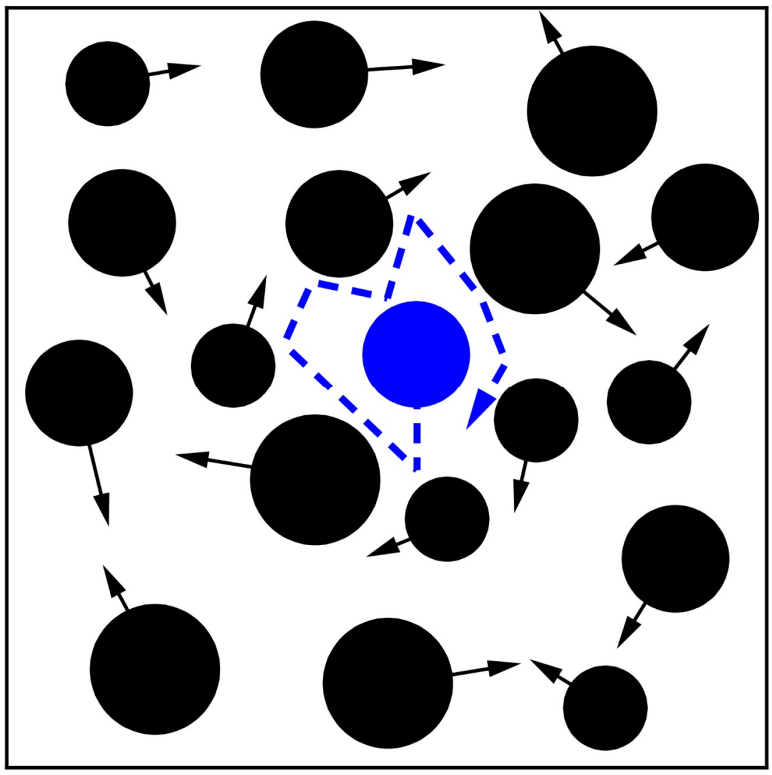

Figure 2.6: At low temperatures, particles can become trapped by their nearest neighbors, thereby limiting their mobility through the so-called caging effect and leading to sub-diffusive liquid dynamics.

All these factors culminate in a decoupling of microscopic mass transport and macroscopic flow behavior, and hence, the direct relationship between D and η described by the Stokes-Einstein relation, see equation (2.10), is losing its validity with undercooling. This widely observed effect is known as the Stokes-Einstein breakdown [83,85,99,106–108].

2.2.3 The fragility concept

Structural relaxation, viscous flow, and diffusion are thermally activated processes, and it is therefore self-evident that they slow down tremendously with decreasing temperature. In high-temperature liquids, their temperature dependence can be usually described by a simple Arrhenius equation in the general form of

$$x(T) = x_0 \exp\left(\frac{\pm E_A}{R\,T}\right). \tag{2.12}$$

Here, x(T) stand can stand e.g. for the relaxation time τ(T) or the viscosity η(T). x_0 is a preexponential scaling factor, R is the gas constant and E_A is a (temperature-invariant) activation energy that quantifies the activation barrier of structural fluctuations. In a so-called Arrhenius diagram, where x(T) is logarithmically plotted against a reciprocal temperature axis, E_A describes the slope of the Arrhenius function and hence constitutes the rate of thermal activation.

Some systems, for example SiO_2, can maintain such an Arrhenius-type temperature dependence over a broad temperature range. Yet, the previously described fundamental changes that evolve with undercooling, namely increasing cooperativity, heterogeneity, and caging effects, also affect the nature of thermal activation. Accordingly, most (glass forming) liquids develop deviations from the simple exponential Arrhenius scheme with decreasing temperature. In principle, such non-Arrhenius, super-exponential behavior can be explained by a temperature-dependent activation barrier, $E_A(T)$, that increases with decreasing temperature.

The degree of deviation varies from liquid to liquid. Austen Angell was the first to introduce a categorizing scheme based on the graveness of deviation from Arrhenius behavior, which was the birth of his famous 'fragility' concept [46,109]. Liquids whose dynamics rather follow an Arrhenius law are termed 'strong', those that show a distinct non-Arrhenius, super-exponential temperature dependence are termed 'fragile'. Angell further refined the Arrhenius plot concept by normalizing the inverse temperature axis with the respective glass transition temperature, T_g [46,109]. This way, different data sets can be plotted together and all merge at a homologous temperature of $T_g/T=1$. The approach allows for a direct visual comparison of fragilities even for glass forming liquids with vastly different temperature regimes. Figure 2.6 shows a typical Angell plot taken from [110].

We will see in the next chapter that finding a standardized definition of T_g can be challenging, as it is a kinetic effect that depends on the applied experimental conditions like e.g. the rate of temperature change. In Angell plots, T_g is often defined as the temperature at which a viscosity of 10^{12} Pa s is reached [46,111]. For this specific definition, the nomenclature T_g^* is regularly found in literature [70,112,113]. In the

timescale domain, a relaxation time of 100 s is usually used to define the glass transition [46,111].

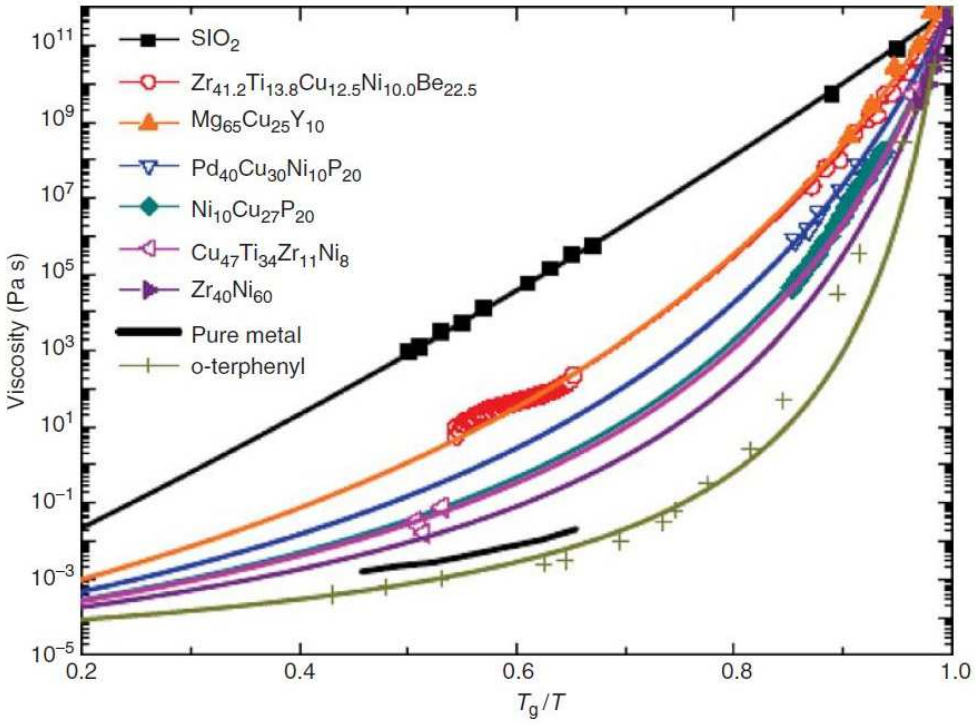

Figure 2.7: An Angell plot with mostly metallic glass formers, taken from [110]. The viscosity temperature dependencies of various (glass forming) liquids are compared by normalizing the inverse temperature axis via the glass transition temperature. Systems that show rather straight, Arrhenius-like trendlines are termed 'strong', those with curved, super-Arrhenius-like trendlines are termed 'fragile'.

While strong systems follow a rather linear Arrhenius-like course in the Angell plot, fragile systems distinctly deviate by showing a 'sagging' appearance. Here it becomes evident that the strong-fragile terminology resembles a mechanical picture, as 'strong' indicates a stiff, robust system that remains almost unaffected by stresses (alias temperature changes), while a 'fragile' system easily bends even under small stresses. The maybe simplest quantification of fragility can be found in the so-called m-fragility, also termed fragility index m. It describes the steepness of the considered property's (η, τ,…) course x(T) at the glass transition [109]:

$$m = \left. \frac{\partial \log\left(x(T)\right)}{\partial \frac{T_g^*}{T}} \right|_{T_g^*} \tag{2.13}$$

A low m-fragility indicates an Arrhenius-like course and strong behavior, a high value reflects a super-exponential course and fragile character. As shown in Figure 2.6, oxide glasses like SiO_2 or GeO_2 usually show strong behavior, with m-fragilities in the order of 15 [46,109]. The opposite extreme is found in organic liquids like o-terphenyl, featuring fragility indices of up to 200 [46,109]. Metallic glass formers show intermediate fragility with m values of roughly 50 [1,7,70,114]

2.2.4 Modelling the temperature dependence of the α-relaxation

The breakdown of the Arrhenius equation with undercooling asks for alternative functions to describe and also extrapolate the temperature dependent course of e.g. η or τ. One of the most widely used approaches is the Vogel-Fulcher-Tammann(-Hesse) equation (VFT) [46,115,116]:

$$x(T) = x_0 \exp\left(\frac{D^* T_0}{T - T_0}\right). \tag{2.14}$$

Here, D^* is the fragility parameter and T_0 is the VFT-temperature. The here shown diction of the VFT law with a nominator term $D^* T_0$ was firstly presented by Angell [46]. Earlier versions of the equation simply used a parameter $B=D^* T_0$ as nominator, which resembles an activation energy [115,116]. Angell's notion bears the advantage that the degree of deviation from Arrhenius behavior can be directly quantified on hand of the D^* parameter. High D^* values indicate strong behavior, e.g. with a value of about 100 for the archetypically strong SiO_2 system, while low values correspond to fragile behavior, for example $D^*=2$ in case of o-terphenyl [110,117]. Metallic glasses show intermediate D^* values between roughly 5 and 30 [110,117].

It shall be highlighted that the VFT equation is actually not based on a physical model but represents an empirical modification of the Arrhenius law, with the introduction of the T_0 parameter being the decisive alteration. From a mathematical perspective, T_0 changes the temperature point at which the denominator in the exponential argument equals zero. Hence, T_0 redefines the pole value where the function diverges, i.e., where viscosity and

relaxation time approach infinity. Eventually, this 'trick' allows the VFT equation to describe a curved course, therefore being also applicable for fragile systems.

The preexponential factor x_0 finally describes the high-temperature limit of the described property x, given the case that the exponential argument approaches zero. According to S. Nemilov [118], the high-temperature limit of the viscosity η_0 can be calculated as

$$\eta_0 = \frac{h\, N_A}{V_m}, \tag{2.15}$$

where h is the Planck constant, N_A is Avogadro's constant, and V_m is the average atomic volume. Applying Nemilov's formula to fix the preexponential factor reduces the amount of free fitting parameters of the VFT equation from three to two, which can have tremendous effects on the obtained results as we will see later in Paper I.

Beyond the empiric VFT equation exists manifold physically founded models that describe the super-Arrhenius temperature dependence of the α-relaxation process. Their concrete formulation depends on the chosen angle of approach and the thereby regarded physical property.

The Adam-Gibbs model regards the subject from a thermodynamic point of view and connects the temperature dependence of the dynamics to the liquid's configurational entropy $S_c(T)$. The central concept of the model is that with undercooling, less and less structural configurations are accessible due to the shrinking thermal activation, and accordingly, $S_c(T)$ decreases. The dynamic slowdown then results from the interplay between $S_c(T)$ and an effective activation energy for structural rearrangements, C, according to

$$x(T) = x_0 \ \exp\left(\frac{C}{T\, S_c(T)}\right), \tag{2.16}$$

The entropy-based approach of the Adam-Gibbs model is the basis for the MYEGA model [119] and the extended MYEGA model [120], which even allows to describe fragile-to-strong transitions occurring over large temperature spans.

An alternative approach can be found in a volumetric perspective on the problem. Since the free volume of a liquid naturally declines with decreasing temperature, viscosity and relaxation time accordingly increase. Doolittle [121] addressed this temperature

dependence to the relation between the accessible free volume $V_f(T)$ and a threshold volume V^* that must be surpassed to allow structural rearrangements as

$$x(T) = x_0 \ \exp\left(\frac{b\,V^*}{V_f(T)}\right), \tag{2.17}$$

with b being a material constant. Like the VFT model, the Doolittle equation assumes that structural relaxation processes and viscous flow vanish at a certain temperature, comparable to the T_0 temperature. The model also does not yet comment on the way the free volume is distributed in the liquid state. Based on the work of Turnbull and Cohen [81], a respective refinement was provided by Cohen and Grest [122]. Their model discards the concept of homogeneously distributed free volume and instead incorporates a spatially heterogeneous distribution, as discussed in the previous chapter. Accordingly, they differentiate between spatial regions with low free volume and slow dynamics, so-called solid-like domains (or cells), and domains with higher free volume and faster dynamics, termed liquid-like domains. With undercooling, the number of solid-like domains is thought to increase, causing the empirically observed super-Arrhenius dynamic slowdown and finally leading to the glass transition.

Lastly, the cooperative shear model by Demetriou et al. [123,124] shall be introduced here. The central idea is that flow processes in undercooled liquids occur through cooperative structural rearrangements within so-called 'shear transformation zones' (STZ), i.e., spatial regions which can incorporate some hundreds of atoms at temperatures around the glass transition [124]. By assuming an STZ activation energy that changes exponentially with temperature, the model is well-suited to describe super-Arrhenius behavior as

$$x(T) = x_0 \exp\left(\frac{T_g^*}{T}\ln\left(\frac{x_g}{x_0}\right)\ exp\left(2n\ \left(1-\frac{T}{T_g^*}\right)\right)\right). \tag{2.18}$$

Here, x_g describes the value of the modelled dynamic property at the glass transition temperature T_g^*, which is usually defined at 10^{12} Pa s or 100 s, as discussed above. n is the elastic softening index, which effectively serves as a fragility parameter: high n values indicate fragile behavior and vice versa.

2.3 Probing equilibrium dynamics via the dynamic glass transition

2.3.1 Fluctuation dissipation theorem and linear response criterion

Certain experimental approaches, for example sophisticated diffraction methods like X-ray photon correlation spectroscopy (XPCS) or electron correlation spectroscopy (ECS), can indeed determine a structural autocorrelation function that can be described by a KWW function as introduced in equation (2.4). Such approaches are therefore able to directly measure relaxation times of the thermally activated fluctuations that constitute the α-relaxation on a microscopic scale. Nevertheless, the α-relaxation can be also probed indirectly by manifold physical properties. To do so, the system must be stimulated through a (small) external perturbation P, to which it then responds as if it would respond to a 'system-internal' spontaneous thermal fluctuation. The desired information about the α-relaxation process is then encoded in the system's stimulus response R [125–127]. A suitable measurement perturbation can be brought-in for example by a periodic (also termed 'modulated') stimulus that provokes a frequency-dependent response or also by a single, step-like stimulus creating a time-dependent response. According to the fluctuation dissipation theorem [128–130], the essential precondition for the whole approach is that perturbation amplitude ΔP and response amplitude ΔR must remain (in a good approximation) proportional (i.e. linear) to each other. In other words, the perturbation should be large enough to create a detectable response but must definitively remain small enough to not permanently force the system out of its equilibrium state. This precondition to probe equilibrium dynamics is termed the 'linear response criterium' [125–127], and the principle is graphically illustrated in Figure 2.8.

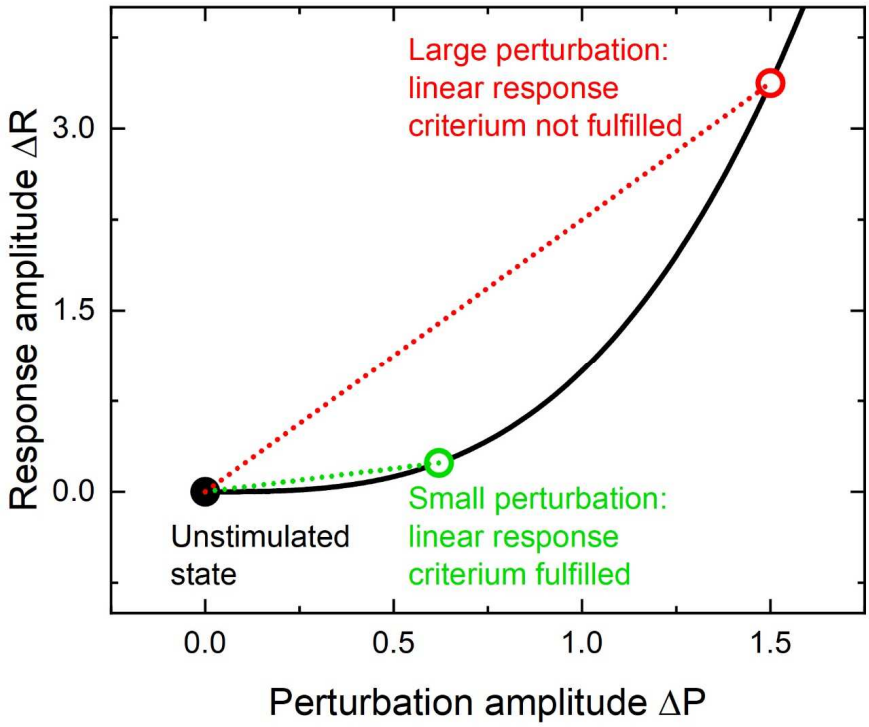

Figure 2.8: A schematic illustration of the linear response criterium. We see that the interplay between perturbation amplitude ΔP and system response amplitude ΔR can be of non-trivial (non-linear) form. Yet, as long as the assumption of a proportionality between both represents a good approximation, the linear response criterium is fulfilled. This is usually the case for small perturbation scales (green). Larger perturbations usually violate the criterium (red).

2.3.2 The difference between relaxation and retardation

At this point, the fine but sometimes decisive difference between the terms relaxation and retardation should be quickly introduced. When the perturbation is an intensive variable and the response is extensive, we perform a retardation (or recovery) experiment. An example for retardation would be a temperature perturbation (intensive) that provokes a temporally changing heat flow (extensive). When the roles are switched so that the perturbation is extensive and the measured response is intensive, we speak of a relaxation experiment. A relaxation experiment could be found in e.g. a mechanical deformation (extensive) that results in a changing stress state (intensive) [125–127].

Regarding an experiment in the time domain that fulfills the linear response criterium, a quasi-instantaneous perturbation of the amplitude ΔP creates a non-instantaneous response of the amplitude $\Delta R(t)=K(t)\,\Delta P$ with K(t) being a time-dependent proportionality factor:

$$R(t) = R_0 \pm K(t)\,\Delta P. \tag{2.19}$$

The temporal evolution of K(t) then reflects the α-relaxation process of the system and therefore resembles the stretched exponential KWW function from equation (2.4). In case of a retardation experiment (intensive perturbation, extensive response), K(t) is referred to as a compliance J(t). In case of relaxation (extensive perturbation, intensive response), it is termed modulus M(t). Hence, the τ parameter determined from a retardation approach is, technically, not a relaxation time but a retardation time [125–127]. Yet, most parts of literature use the generalized term 'relaxation time' regardless of the experimental setup. For now, we will adapt this simplified nomenclature, but we will come back to the fine difference between retardation and relaxation time later in Chapter 6.3.2, since it allows to explain offsets in experimentally determined data sets.

2.3.3 The Debora number and the dynamic glass transition

We will now consider an experimental setup that explicitly fulfills the linear response criterium, as previously described. For example, one could think about an approach using a small periodic stimulus with an angular frequency ω=2πf, with f being the frequency. We will then further regard the concept of the Deborah number, De, which was firstly introduced in 1964 by the co-founder of the term 'rheology', M. Reiner [131]. De describes the ratio between the liquid's relaxation time τ and a characteristic timeframe of experimental observation t_{exp} [131,132] as

$$De = \frac{\tau}{t_{exp}}. \tag{2.20}$$

In our modulated case, the experimental observation window is directly predetermined by the angular frequency in the form of $t_{exp}=1/\omega$. The dynamic glass transition $T_{g,dyn}$ then simply corresponds to the temperature at which $De=\omega\,\tau=1$. In other words, the timescale of external perturbation matches the internal timescale of spontaneous fluctuations. $T_{g,dyn}$ therefore characterizes the dynamics of the equilibrium liquid [125,126,132–134] and hence, determining various $T_{g,dyn}$ for different measurement frequencies ultimately allows to characterize the temperature dependence of the α-relaxation in the equilibrium liquid, i.e. its fragility.

We will later see that experimental approaches to determine $T_{g,dyn}$ often use very slow underlying temperature ramps. Since the measurement stimulus that probes the liquid dynamics is exclusively found in the modulated perturbation, these temperature changes

only serve the purpose of scanning the temperature region of interest. The rates are usually defined slow enough so that quasi-isothermal conditions can be assumed within the experimental timeframe t_{exp}. $T_{g,dyn}$ then mostly manifests as a sigmoidal-like step or a local maximum of the respectively observed physical property.

2.4 Falling out of equilibrium at the kinetic glass transition

2.4.1 The kinetic glass transition as a breaking of the linear response criterium

We will now consider an experiment in which the liquid's temperature is lowered at a constant cooling rate q_c. Here, the temperature change serves two purposes at the same time. It introduces the external perturbation required to probe the system's characteristics, but at the same time allows to continuously scan the temperature range of interest. Naturally, the α-relaxation will slow down in the course of the experiment, as previously described. When interfering effects like e.g. crystallization are excluded, such a procedure must inevitably lead, at some point, to the vitrification of the liquid, i.e., the appearance of the so-called kinetic (or thermal) glass transition $T_{g,kin}$. Here, the system cannot anymore maintain its temperature-dependent equilibrium state within the experimentally given timeframe. Hence, it gradually transforms from the equilibrium supercooled liquid state into an out-of-equilibrium state, which is the glass. Such an 'falling out of equilibrium' [46] basically acts as a large thermal perturbation inducing a large, non-linear system response. In this response, the system strives to reestablish equilibrium, and this process is termed aging. Hence, the kinetic glass transition inherently violates the earlier introduced linear response criterium, as illustrated in Figure 2.8. Accordingly, $T_{g,kin}$ is not an equilibrium property and is not covered by the term 'dynamics'. Instead, it is a transition effect that reflects non-steady-state conditions (similar to e.g. a phase transition from liquid to crystalline state) and must therefore be referred to under the term 'kinetics' [125,126,132–134].

If we consider the inverse experiment of heating a glass with a rate q, we will naturally observe the inverse effect of the vitrification, which is the devitrification of the glass towards the supercooled liquid state. Here, the system reestablishes its equilibrium in the course of the kinetic glass transition.

2.4.2 The rate dependence of the kinetic glass transition

Like other transition kinetics, vitrification kinetics show a distinct rate dependence, meaning that the temperature of $T_{g,kin}$ shifts with changing rates. To understand this aspect, we again consider the concept of the Deborah number, see equation (2.20). In our cooling experiment, the temperature within a chosen experimental timeframe t_{exp} will change by an amount dT depending on the applied cooling rate q_c as

$$-\frac{dT}{t_{exp}} = q_c. \tag{2.21}$$

The system remains in equilibrium as long as $De=\tau/t_{exp}<1$, since the liquid is able to fully relax within the experimental timeframe. Hence, the linear response criterium is still satisfied (see previous chapter) and we observe equilibrium liquid dynamics. In contrast, the glass is characterized by De>1, indicating that the system has fallen out of equilibrium through a too large thermal perturbation. Here, the system cannot establish equilibrium within the experimental timeframe anymore. $De=\tau/t_{exp}\approx1$ marks the kinetic glass transition event. At $T_{g,kin}$, deriving the expression $\tau\approx t_{exp}$ with respect to temperature and taking equation (2.21) into account then provides an alternative criterium for the kinetic glass transition in form of

$$\left.\frac{d\tau}{dT}\right|_{T_{g,kin}} = -\frac{1}{q_c}. \tag{2.22}$$

From this equation we see that a lower cooling rate corresponds to a steeper slope $d\tau/dT$. Thanks to the super-exponential temperature dependence of τ, see Chapter 2.2, this must result in a shift of $T_{g,kin}$ towards lower temperatures. Figure 2.9 illustrates the case by comparing two kinetic glass transitions occurring under different rates $q_{c,1}$ and $q_{c,2}$, with $q_{c,1} < q_{c,2}$.

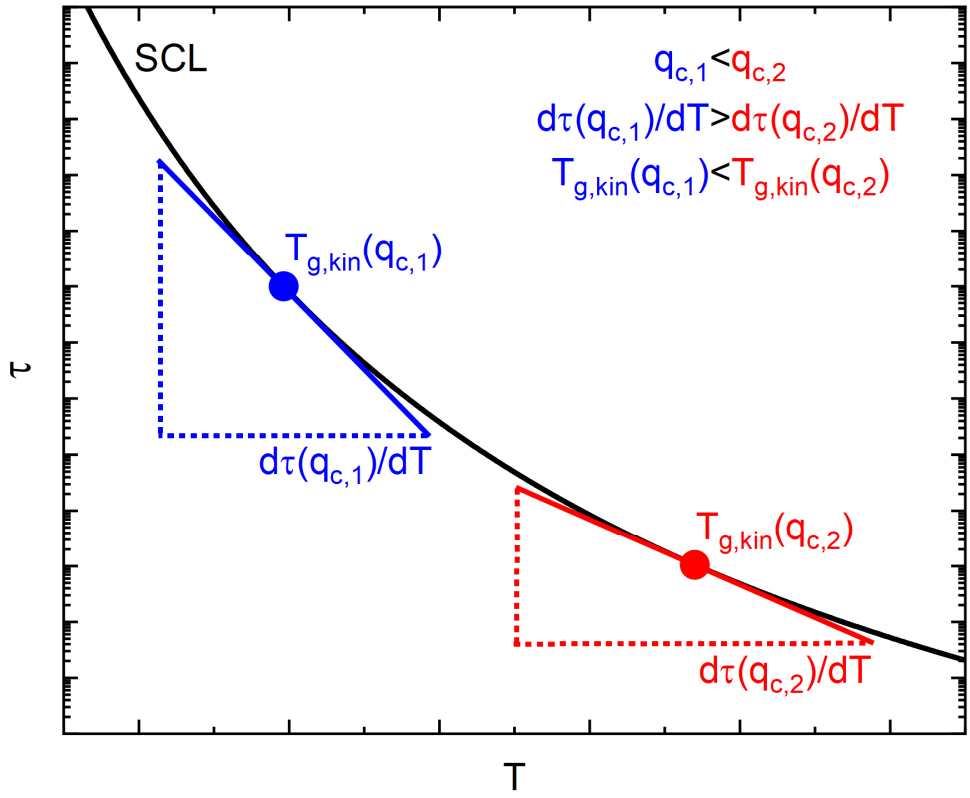

Figure 2.9: Comparing two kinetic glass transition temperatures $T_{g,kin}(q_{c,1})$ and $T_{g,kin}(q_{c,2})$ as a function of the applied cooling rates $q_{c,1}<q_{c,2}$. By taking Equation (2.22) into account, we can see that the super-exponential shape of the $\tau(T)$ curve must lead to a decrease in $T_{g,kin}$ with decreasing q_c.

2.4.3 The fictive temperature and aging

In most metallic glass literature, the general term 'glass transition' refers to the kinetic glass transition event. The publications included in this thesis also submit to this practice (if the dynamic glass transition is regarded, it is explicitly indicated as such). $T_{g,kin}$ marks the borderline between a solid-like and liquid-like empirical appearance and is therefore especially of technical importance, e.g. in case of casting processes (which are basically undercooling experiments). At $T_{g,kin}$, the highly temperature-dependent properties of the liquid, e.g. its structure, viscosity, (free) volume, enthalpy, or entropy, freeze and are 'conserved' in the glassy state. The result is a glass with properties that are a function of its thermal history, which is, here in our present undercooling experiment, determined by the applied cooling rate. An often used metric to quantify the state of the glass is the so-called fictive temperature T_{fic} [135], which refers to the temperature of the kinetic glass transition that corresponds to the present glass state. In Figure 2.10, T_{fic} is indicated for two different rates $q_{c,1}$ and $q_{c,2}$ ($q_{c,1}<q_{c,2}$), resulting in two glasses $G(q_{c,1})$ and $G(q_{c,2})$. The

exact temperature is thereby defined via a tangent method that determines the intersection between the SCL line and the glassy state trendline. In Chapter 4.1.4, we will introduce a sophisticated method to determine T_{fic} via calorimetric measurements, the so-called Moynihan approach [136].

Besides the cooling rate during vitrification, thermal history and properties of a glass can be also altered through aging. Thereby, the non-equilibrium glass evolves towards the equilibrium supercooled liquid state. Such processes can occur in vicinity of $T_{g,kin}$ (when the Deborah number is still near 1), e.g. during isotherms or when the glass is heated at a rate slower than the cooling rate with which it was initially formed. The temporal evolution of an isothermal aging process can be modelled by a KWW stretched exponential function, as introduced in Equation (2.4). Here, it must be remembered that the obtained values for β and τ do not characterize an equilibrium process, but an aging process, i.e. the isothermal kinetic glass transition. Figure 2.10 illustrates two schematic aging routes starting in the fast-quenched glass $G(q_{c,2})$. $Aging_1$ (blue) portrays an isotherm at T_a for an aging time t_1. The timespan is insufficient to completely reach the temperature-specific equilibrium liquid state, and hence, the aging process results in a new, more relaxed glassy state $G(T_a,t_1)$ of lower enthalpy, entropy and volume than the original $G(q_{c,2})$. It accordingly features a lower fictive temperature $T_{fic}(T_a,t_1)$. $Aging_2$ (blue) reflects an isotherm at T_a for an aging time t_2. This timespan is chosen as $t_2 \geq \tau_{trans}$, with τ_{trans} being the so-called transition time. It marks the minimal aging time needed to reestablish the respective equilibrium SCL state starting from a given initial glass [1,70]. Accordingly, the $aging_2$ process results in a state with a fictive temperature $T_{fic}(T_a,t_2)$ that coincides with the SCL line, showing that the initially non-equilibrium system has aged back into equilibrium again.

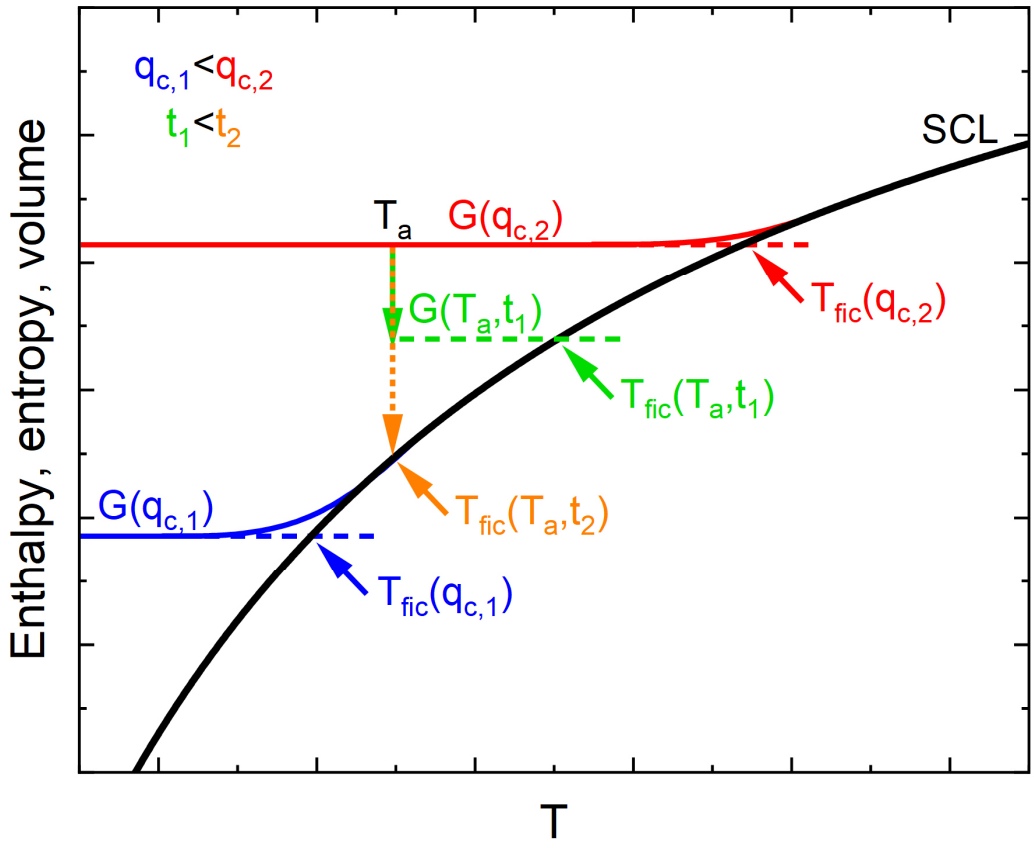

Figure 2.10: A schematic illustration of the pathways of enthalpy, entropy, or volume during vitrification upon cooling with two different cooling rates. Fast cooling leads to a glass with a high fictive temperature $T_{fic}(q_{c,2})$ (red), slower cooling creates a glass with a respectively lower fictive temperature $T_{fic}(q_{c,1})$ (blue). Isothermal aging will result in a glass with a lower fictive temperature (green), or even allow for a full isothermal glass transition (orange), depending on the aging time.

2.4.4 The Frenkel-Kobeko-Reiner relation

Despite being different effects that belong to the different fields of dynamics and kinetics, $T_{g,dyn}$ and $T_{g,kin}$ are nevertheless closely related. Equation (2.22) already foreshadows this relation as it connects the rate-dependent $T_{g,kin}$ with a dynamic property in form of the liquid's relaxation time. To further understand this equation, we assume an Arrhenius-like temperature dependence of τ for simplicity, which still can be a valid approximation for a limited temperature range of interest. Then, combining Equation (2.22) and Equation (2.13) leads to

$$\left.\frac{d\tau}{dT}\right|_{T_{g,kin}} = \tau(T_{g,kin})\frac{E_A}{R\,T_{g,kin}^2} = -\frac{1}{q} \qquad (2.23)$$

and this can be further reduced to

$$-q\,\tau\left(T_{g,kin}\right) = \frac{R\,T_{g,kin}^{2}}{E_A} = C. \tag{2.24}$$

This expression is called the Frenkel-Kobeko-Rainer (FKR) relation [132,134,137]. Since the parameter C is considered to be a constant, this fundamental equation resolves the close interplay between liquid dynamics and vitrification kinetics.

This comes to no great surprise if one considers that vitrification is basically the process of liquid dynamics falling out of equilibrium, as they just cannot completely occur anymore within the experimental timeframe. Hence, liquid dynamics must naturally predetermine the system's vitrification kinetics. Furthermore, it shall be mentioned that the close relationship between liquid dynamics and vitrification is also the reason why glasses also show spatial heterogeneous relaxation times [95,96], as earlier discussed in Chapter 2.2.2. It appears that the glassy state inherits the heterogeneous nature from its predecessor, the supercooled liquid state [88,89].

2.5 Structure in metallic glass forming systems

From a dynamical point of view, we have derived that glasses are obtained by supercooling a liquid until vitrification sets in. This process of gradually falling out of equilibrium is the reason why the structure of a glass cannot be differentiated from the structure of a liquid at the corresponding fictive temperature. Accordingly, glass is widely categorized as a form of solid matter that has inherited the amorphous atomic structure from the liquid state it stems from, thereby lacking the long-range translational order known from crystalline solids. While most dynamic and kinetic considerations from the previous chapters can be generalized for all (glass forming) liquids, structure is highly dependent on the specific type of chemical bonding and therefore differs massively among the various classes of glass formers. Other than in molecular, polymeric or oxidic systems, the smallest structural unit, also previously termed 'particle', of metallic glass forming liquids is the individual atom. The short-range order (SRO), i.e. the configuration of nearest neighbor atoms, is therefore rather unclearly defined, more fluid than in other liquid classes.

2.5.1 Short-range order in metallic liquids

One of the first attempts to visualize such SRO can be found in the topological approach of dense random packing by J. Bernal in 1959 [138–140]. Assuming a monoatomic liquid consisting of hard spheres, Bernal conceptualized local ordering via five types of irregular polyhedra [138–140]. These so-called 'Bernal's holes' are illustrated in Figure 2.11. Among them, the tetrahedron is found to be the most densely packed and most prevalent [141]. With only slight geometrical frustration, tetrahedra can furthermore arrange into an icosahedron [142], which is a highly symmetrical cluster consisting of one center atom surrounded by 12 others.

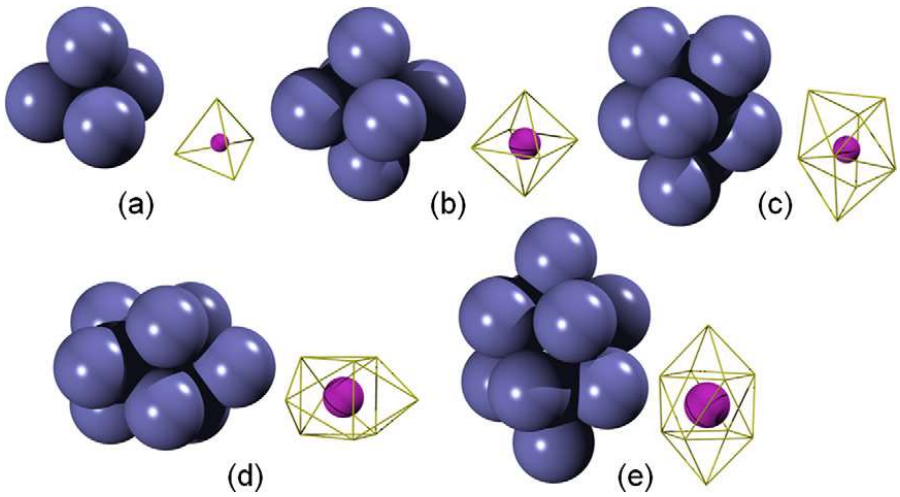

Figure 2.11: Illustrations of five typical polyhedral structures in a monoatomic liquid, termed 'Bernal's holes'. The left figure indicates the hard sphere packing, the right figure depicts the formed hole in their center. a) Tetrahedron, b) octahedron, c) tetragonal dodecahedron, d) capped trigonal prism, and e) capped Archimedean antiprism. Taken from [142].

An icosahedron shows a higher local packing fraction than e.g. a face-centered cubic (FCC) crystalline structure, therefore being an energetically favorable SRO structure in liquids as previously suggested by F. Frank [143]. The existence of icosahedral SRO has been experimentally confirmed for monoatomic melts [144] and was even imaged as a two-dimensional projection for a metallic glass [145]. Yet, icosahedra differ from crystalline packing schemes by their five-fold symmetry, which frustrates long-range transitional order. Hence, while icosahedra offer optimized packing on short scales, long-range ordered crystalline structures become energetically favorable when regarding length scales beyond the SRO. Figure 2.12 illustrates these considerations.

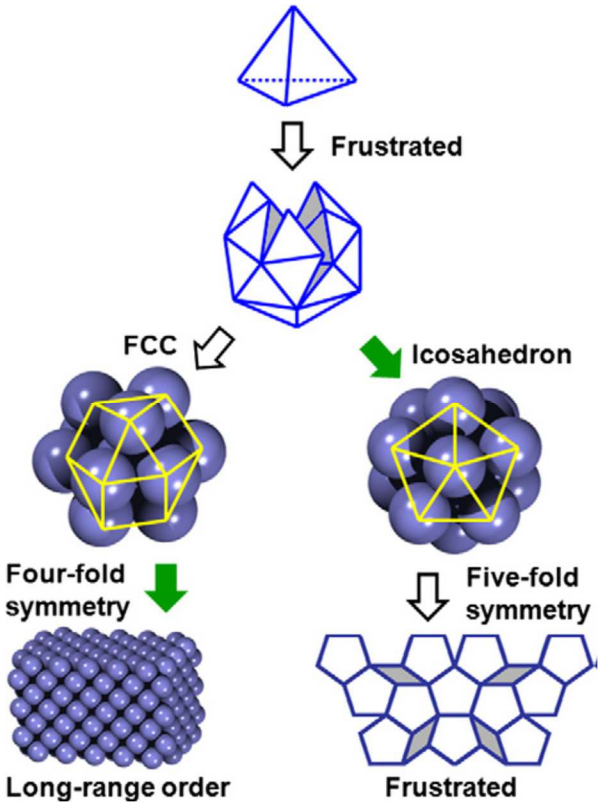

Figure 2.12: Polytetrahedral packing in monoatomic liquids consisting of hard spheres can occur through four-fold symmetry FCC packing, which is highly energetically favorable in terms of long range order, as it allows for a crystalline lattice. In contrast, five-fold symmetry icosahedrons may provide more favorable packing on short ranges, but at the cost of a frustrated long-range order that permits a crystalline structure. Taken from [142].

It has been hypothesized that high degrees of icosahedral SRO in the liquid state facilitate glass formation, since crystallization is impeded by the need for essential changes in local ordering. In other words, the fundamental differences in the SRO of liquid and crystalline state are thought to be the structural origin of the supercooling ability of metallic melts [143,146,147].

Besides such topological considerations, T. Hayes et al. [148] demonstrated the influence of chemistry on the SRO in 1978 by showing distinct deviations from the dense random packing model for a binary Pd-Ge metallic glass. Shortly afterwards, P. Gaskell substantiated the idea of chemistry-specific structure in metallic glass formers by presenting a structural model explicitly designed for metal-metalloid glass formers [149,150]. Here, SRO is seen to rather manifest via trigonal prisms as the prevalent polyhedral structure.

2.5.2 The rise of medium-range order in undercooled metallic melts and metallic glasses

We know from the Gibbs-Helmholtz formula, see Equation (2.1), that with sinking temperature, there comes an enthalpy-driven tendency towards increasing order. In case of metallic liquids, this implies an overall increase in atomic packing density with undercooling. More rigid local configurations become energetically favorable and therefore, the previously described polyhedral SRO increases in prevalence [144,151,152]. The emergence of such highly ordered local structures in an otherwise still poorly ordered liquid configuration is often interpreted as the structural origin of the dynamic slowdown and the rise of dynamic heterogeneities [88,89,122,153,154] as discussed in Chapter 2.2. The appearing SRO clusters are thought to agglomerate and interlock, thereby forming larger network-like regions of reduced mobility [152], as exemplarily described in the earlier introduced dynamical model by Cohen and Grest [122], see Chapter 2.2.4. In other words, medium-range order (MRO) rises with undercooling through the increase and agglomeration of SRO structures.

In a series of articles starting in 2003, D. Miracle [155–158] published his famous efficient cluster packing (ECP) model. This topological approach is able to describe the SRO and MRO of metallic glass formers as a function of the size and stoichiometry of the included atomic species. The species with the highest concentration is termed the solvent Ω. The model further includes up to three other atomic species, the so-called solutes α, β, and γ, which are labeled according to their atomic radii from large to small. The SRO is formed through clusters consisting of Ω atoms surrounding an α atom in the center. Thereby, the coordination number is determined by the size ratio of the α and Ω species. MRO results from arranging these clusters in an FCC or hexagonal closest packed (HCP) lattice, allowing for a high packing density. Here it shall be highlighted that despite the presence of such an ordered 'superstructure', long-range order is still frustrated by the random rotational orientation of the clusters. The clusters overlap and share atoms via vertex-, edge-, or face-connections and show differently sized interstices, which are accordingly occupied by the smaller β and γ species. Figure 2.13a) provides a two-dimensional representation by illustrating a <100> plane of an FCC lattice. In this plane, only the α and β solutes are visible, while the three-dimensional illustration in Figure 2.13b) also allows to depict the γ species. Despite the fact that the ECP model is only of topological origin, it can be nevertheless used to successfully predict compositions with good GFA [157–159].

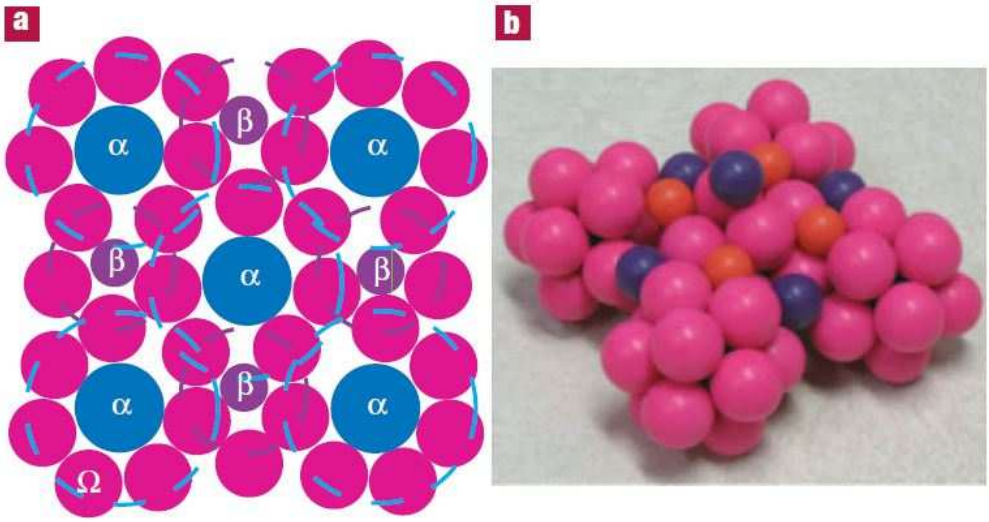

Figure 2.13: The efficient cluster packing model by Miracle. A depiction of a <100> plane of an FCC lattice is shown in a), where the solvent Ω as well as the α and β solutes are visible. The three-dimensional illustration in b) furthermore reveals the γ solute. Taken from [158].

In 2006, Sheng et al. [160] presented a refined model, which determines SRO not only through topological considerations, but also based on chemical affinities between the different atomic species. MRO then emerges from SRO clusters arranging in larger, icosahedral-like 'extended cluster' superstructures, as exemplarily shown in Figure 2.14. Sheng et al. further proposed that the configuration and interconnection of these extended clusters changes with the concentration of solutes, thereby highlighting again the complex interdependency of chemistry, topology, and structure.

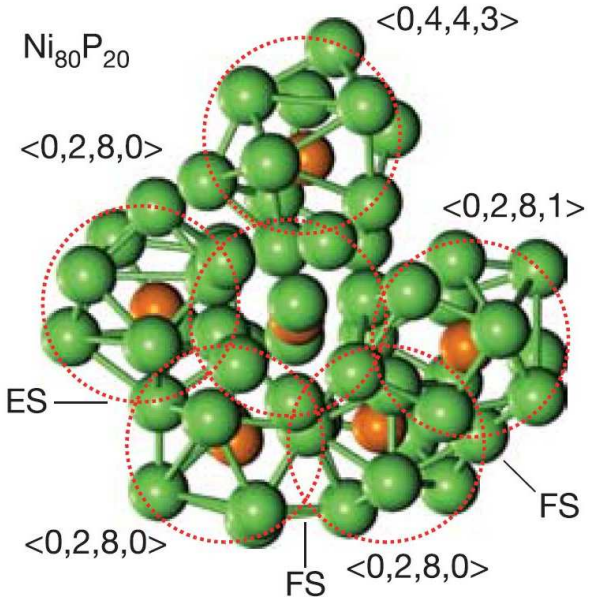

Figure 2.14: Illustration of an icosahedral-like superstructure of a $Ni_{80}P_{20}$ glass former, which consists of several solute-centered clusters. Taken from [160].

2.5.3 Structural information from diffraction studies

Despite their growing levels of sophistication, the presented theoretical models are still based on oversimplifications and often find their limitations when approaching the complex reality of metallic glass forming systems [142]. Modern electron diffraction via transmission electron microscopy (TEM) [161–163] and especially high-energy synchrotron X-ray diffraction (HESXRD) [9,164,165] allow to approach the structure of metallic glass formers from an experimental angle. While a proper theoretical and technical introduction will be provided later in Chapter 4.3, we want to highlight here a very intuitive property that can be obtained from such diffraction studies, which is the total (reduced) pair distribution function (PDF) G(r). In simplified terms, G(r) describes the probability of encountering a different atom at a distance r from a given reference atom. Figure 2.15a) illustrates the principle on hand of two g(r) curves of a metallic glass former [164]. g(r) is the total pair distribution function, which is almost identical to G(r) (the difference is that g(r) includes the number density, see later in Equation (4.31)).

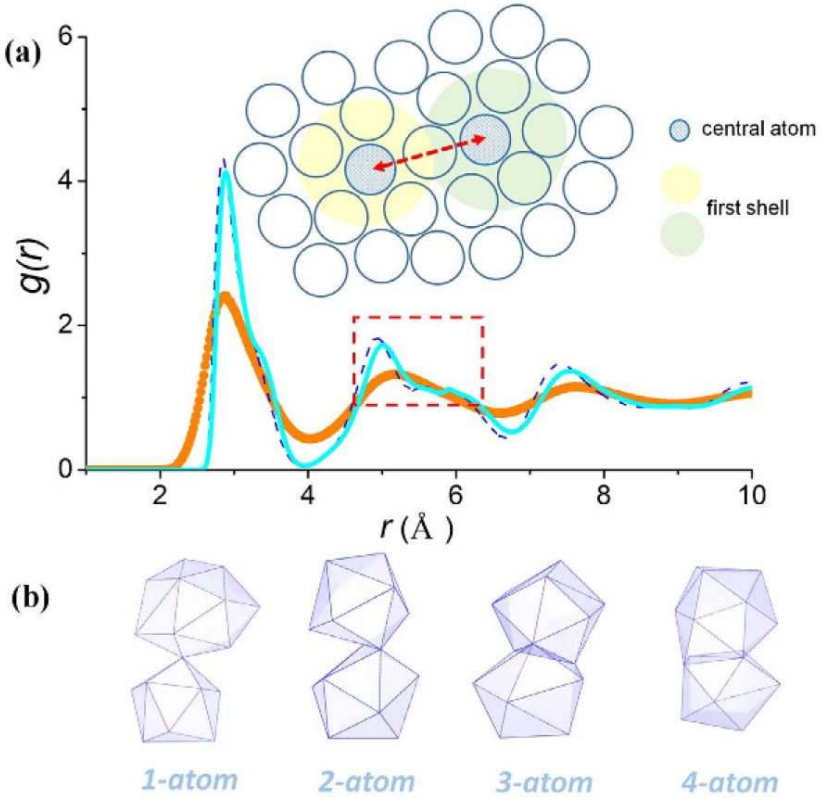

Figure 2.15: a) Total pair distribution function in a high-temperature metallic liquid (orange) and glass (cyan). The sharpened peaks in the low temperature glass state indicates the increased order. The red box highlights a typical MRO length scale, which represents cluster connections through second-nearest neighbor relations, as illustrated in the sketch. b) Schemes of different cluster connections, which differ in the number of shared atoms between both clusters. Taken from [164].

The peaks in g(r) correspond to the respective shells of atomic neighbors. For example, the red box around the second g(r) peaks reflects the shell of second-nearest neighbors, as further indicated by the red arrow in the inserted sketch of an atomic ensemble. This second-nearest neighbor region incorporates information about the MRO and the dominant cluster connection schemes [164]. Possible schemes are illustrated in Figure 2.15b) and can be based on edge-, face-, or vertex-sharing.

2.6 Crystallization according to the classical nucleation theory

We now have excessively discussed the implications of the Gibbs-Helmholtz formula, see Equation (2.1), for the evolution of the dynamics and the structure of (metallic) liquids during undercooling. Eventually, the massive dynamic slowdown and the rise of ordered local structures may lead to vitrification and the formation of a glass, i.e. a solid without long-range order. Yet, these considerations assume the absence of interfering crystallization processes. Crystallization is a first-order phase transition in which the liquid transforms into a solid state with explicit long-range order in form of a periodic lattice structure. While some material classes, like e.g. oxidic glass formers or atactic polymers, show no pronounced tendencies to crystallize or even lack the general ability to do so, undercooled metallic melts are rather prone to crystallization. Avoiding it is therefore the essential precondition for glass formation in metallic systems. In the following, we will focus on the thermodynamic and dynamic aspects that determine the crystallization behavior of undercooled metallic liquids. With the Johnson-Mehl-Avrami-Kolmogorov (JMAK) approach, we will furthermore introduce a quantitative way to model crystallization kinetics in time-temperature-transformation (TTT) diagrams.

2.6.1 Thermodynamic functions of liquid and crystalline state

A liquid becomes metastable when cooled below its liquidus temperature T_l. Accordingly, there exists a crystalline phase that features a lower Gibbs free energy than the liquid and hence, the possibility of crystallization emerges. The driving force from the metastable undercooled liquid (index l) towards the crystal (index x) is then approximated as the difference of their G(T) functions, $\Delta G_{l\text{-}x}$ as

$$\Delta G_{l-x}(T) = G_l(T) - G_x(T) = \Delta H_{l-x}(T) - T\Delta S_{l-x}(T). \qquad (2.25)$$

The thermodynamic functions $\Delta H_{l\text{-}x}$ and $\Delta S_{l\text{-}x}$ are further termed excess enthalpy and excess entropy. They can be calculated from the excess (specific and isobaric) heat capacity $\Delta c_{p,l\text{-}x}=c_{p,l}\text{-}c_{p,x}$ according to the following equations:

$$\Delta H_{l-x}(T) = \Delta H_m - \int_{T_l}^{T} \Delta c_{p,l-x}(T')\, dT', \tag{2.26}$$

$$\Delta S_{l-x}(T) = \Delta S_m - \int_{T_l}^{T} \frac{\Delta c_{p,l-x}(T')}{T}\, dT'. \tag{2.27}$$

Here, ΔH_m and ΔS_m are the enthalpy and entropy of melting, with $\Delta S_m=\Delta H_m/T$. The thermodynamic functions of $c_{p,l}$ and $c_{p,x}$ can be modelled by the so-called Kubaschewski equations [166] as

$$c_{p,l}(T) = 3R + aT + bT^{-2} \tag{2.28}$$

$$c_{p,x}(T) = 3R + cT + dT^{2}, \tag{2.29}$$

with R being the gas constant and a, b, c, and d being fitting parameters.

2.6.2 Forming a critical nucleus from a thermodynamic point of view

Figure 2.16 schematically illustrates the G(T) curves for the liquid and crystalline state. For two exemplary temperatures in the undercooled state, T_1 and T_2 with $T_2<T_1$, the thermodynamic driving forces towards crystallization $\Delta G_{l\text{-}x}(T_1)$ and $\Delta G_{l\text{-}x}(T_2)$ are indicated trough arrows. It is apparent that $\Delta G_{l\text{-}x}$ naturally increases with ongoing undercooling $\Delta T=T_l\text{-}T$. Without any inhibiting activation barrier, crystallization would occur spontaneously as soon as a liquid undershoots the liquidus temperature. Yet, massive supercooling can be possible under certain conditions, which is the precondition that potentially leads to vitrification. To resolve this apparent inconsistency, we must understand crystallization as a nucleation and growth process, where nuclei with a certain volume must form in a surrounding liquid matrix. On the one hand, any precipitating crystalline volume V_x corresponds to a favorable change in the system's Gibbs free energy $\Delta G_V=V_x\ \Delta g_{l\text{-}x}(T)$, with $\Delta g_{l\text{-}x}(T)$ being the thermodynamic driving force $\Delta G_{l\text{-}x}(T)$ from Equation (2.25) normalized to the (molar) volume V_m as $\Delta g_{l\text{-}x}(T)=\Delta G_{l\text{-}x}(T)/V_m$. On the other hand, such a crystalline volume comes with a surface, i.e. an interface A_x between the crystalline lattice structure and the surrounding amorphous liquid. It incorporates a sharp and severe change in structure and entropy, making the

interface energetically unfavorable, which is expressed by an interfacial energy $\gamma_{l\text{-}x}$. Hence, there exists a surface contribution $\Delta G_A = A_x\ \gamma_{l\text{-}x}$ that hinders the formation of a crystalline nucleus. Together, the system's overall change in Gibbs free energy through crystal nucleation ΔG constitutes from the sum of the volumetric and the surface term as

$$\Delta G = -\Delta G_V + \Delta G_A = -V_x\ \Delta g_{l-x} + A_x\ \gamma_{l-x}. \tag{2.30}$$

Nuclei are usually assumed to form in spheric shapes, since a sphere allows to minimize the amount of unfavorable interface in relation to the respective volume. Equation (2.30) can be accordingly rewritten as a function of the nucleus radius r and the temperature T:

$$\Delta G(T,r) = -\frac{4}{3}\pi\ r^3\ \Delta g_{l-x}(T) + 4\pi\ r^2\ \gamma_{l-x}. \tag{2.31}$$

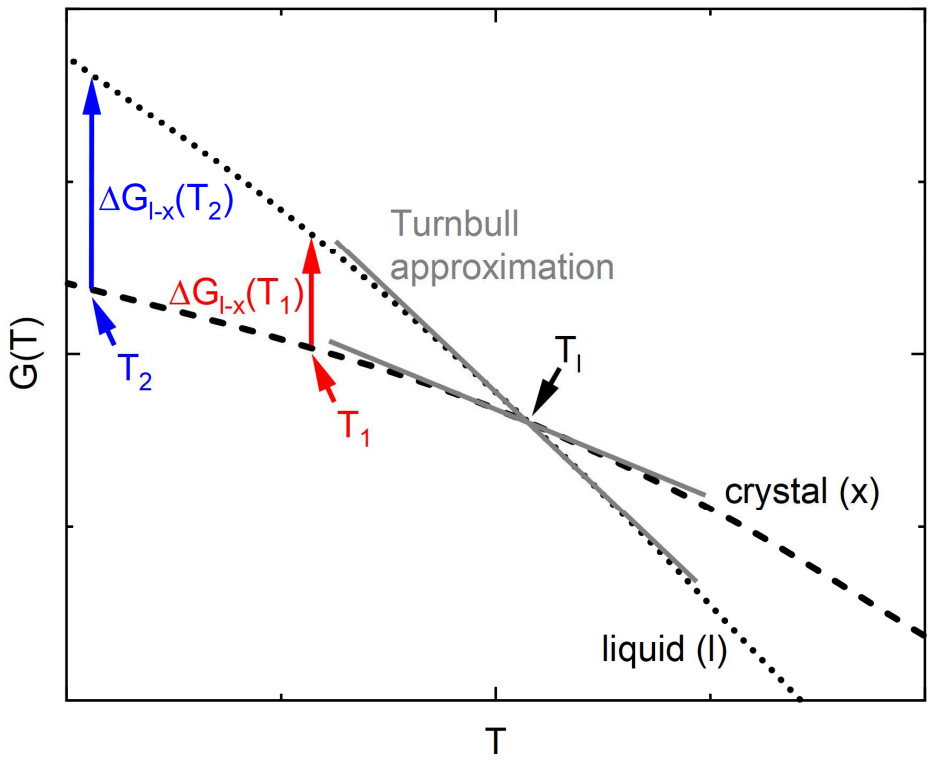

Figure 2.16: Schematic Gibbs free energy curves for the liquid and crystalline state. At the liquidus temperature, both phases are in equilibrium and their curves cross. A thermodynamic driving force towards crystallization $\Delta G_{l\text{-}x}$ rises for temperatures below T_l. The Turnbull approximation assumes linear temperature dependence for both curves, which is an adequate approach in vicinity of T_l, see the gray lines.

Nucleation occurs as a statistical process. In the course of the structural fluctuations that constitute the α-relaxation, ordered regions that resemble the structure of the crystalline lattice can spontaneously form in the undercooled liquid (we will later consider the

frequency of such an event when discussing the nucleation rate). The radii of these so-called 'embryos' decides if they are unstable or if they are persistent and able to grow. Figure 2.17a) visualizes the matter on hand of two $\Delta G(T,r)$ curves at T_1 and ΔT_2, with $T_2<T_1$ (analogous to Figure 2.16). Regarding $\Delta G(T_1,r)$, we see that for small embryo radii, the positive surface term ΔG_A dominates. Accordingly, a further growth would lead to an energetically unfavorable rise in $\Delta G(T_1,r)$ and hence the embryo will rather dissolve again. Yet, if the embryo forms with a radius that bypasses the so-called critical radius r^*, it becomes a supercritical nucleus. Here, the negative volume term ΔG_V starts to dominate and the nucleus is able to lower the system's Gibbs free energy by increasing its radius through growth. The associated value $\Delta G^*(T_1)$ can be interpreted as the respective activation barrier to form a supercritical, growth-capable nucleus at T_1.

Mathematically speaking, a critical nucleus with a radius r^* is reached at the maximum of the $\Delta G(T,r)$ curve, where the derivative of $\Delta G(T,r)$ with respect to the radius equals zero:

$$\left.\frac{d\Delta G(T,r)}{dr}\right|_{r^*} = 0. \tag{2.32}$$

Combining this condition with Equation (2.31) allows to calculate the temperature-dependent critical radius and the corresponding activation barrier for nucleation as

$$r^*(T) = \frac{2\,\gamma_{l-x}}{\Delta g_{l-x}(T)}, \tag{2.33}$$

$$\Delta G^*(T) = \frac{16\,{\gamma_{l-x}}^3}{3\,\Delta g_{l-x}(T)^2}. \tag{2.34}$$

These equations demonstrate again that the system's 'thermodynamic motivation' for nucleation stems from the antagonism of the thermodynamic driving force $\Delta g_{l\text{-}x}(T)$ and the prohibitive effect of $\gamma_{l\text{-}x}$. Since the former increases with undercooling, see Figure 2.16, while the latter is assumed to be temperature independent, $r^*(T)$ and $\Delta G^*(T)$ will decline rapidly with decreasing temperature. Comparing the curves for T_1 and T_2 in Figure 2.17 demonstrates this exemplarily.

To further specify the temperature dependence, the excess Gibbs free energy can be assumed as $\Delta G_{l\text{-}x}(T)\approx-\Delta S_m/\Delta T$ in case of a reasonably small undercooling [167]. This so-called Turnbull approximation [168] linearizes the temperature dependencies of the G(T) curves of liquid and crystal as shown by the gray lines in Figure 2.16. Equations (2.33) and (2.33) then might be reformulated as

$$r^*(T) = \frac{2\,\gamma_{l-x}\,T_m}{\Delta H_m\,\Delta T}, \tag{2.35}$$

$$\Delta G^*(T) = \frac{16\,\gamma_{l-x}{}^3}{3\,\Delta H_m\,\Delta T^2}, \tag{2.36}$$

thereby showing that $r^*(T)$ and $\Delta G^*(T)$ will decrease with ΔT^{-1} and ΔT^{-2} respectively, as further illustrated in Figure 2.17b).

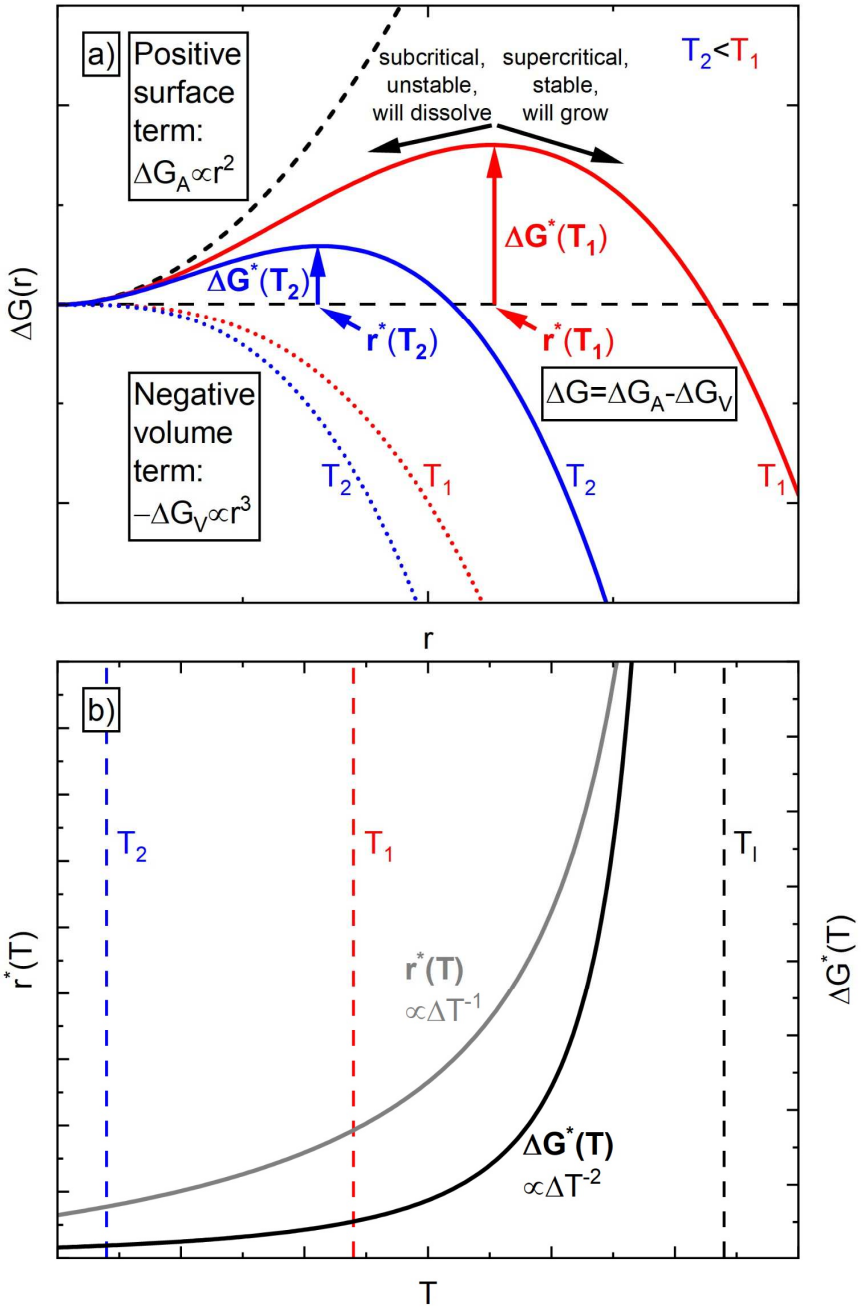

Figure 2.17: a) The overall change in Gibbs free energy as a function of crystalline embryo radius. It consists of a negative volume term and positive surface term. The temperature-dependent maximum $\Delta G^*(T)$ marks the respective critical radius $r^*(T)$ after which an embryo becomes stable and able to growth. b) Temperature dependencies of $r^*(T)$ and $\Delta G^*(T)$, both decrease rapidly with undercooling.

2.6.3 The rates of homogeneous and heterogeneous nucleation

The decrease of $r^*(T)$ and $\Delta G^*(T)$ with ongoing undercooling naturally increases the probability of critical nuclei forming spontaneously. Their average number $n^*(T)$ can be calculated at any given temperature from the absolute number of atoms in the system n_0 according to

$$n^*(T) = n_0 \exp\left(\frac{\Delta G^*(T)}{k_B T}\right). \tag{2.37}$$

Yet, in order to become supercritical, these nuclei must further increase their radius, see Figure 2.17, by adding more atoms from the surrounding liquid. This process is characterized by the so-called atomic jump frequency $\nu(T)$, which quantifies how frequently atoms from the liquid phase will attach to the crystalline lattice. $\nu(T)$ ultimately represents liquid dynamics and is closely related to dynamic properties like the atomic mobility μ and diffusivity D, see Equations (2.8) and (2.9). Hence, the homogeneous, steady-state nucleation rate I(T) with which supercritical nuclei form results from the interplay of $n^*(T)$ and $\nu(T)$ according to

$$I(T) = A\,\nu(T) \exp\left(-\frac{\Delta G^*(T)}{k_B T}\right). \tag{2.38}$$

Assuming that the Stokes-Einstein relation from Equation (2.11) is valid, Turnbull stated that $\nu(T)$ is inversely proportional to $\eta(T)$ [169]. Together with Equation (2.34), I(T) can be therefore reformulated as

$$I(T) = \frac{A_\nu}{\eta(T)} \exp\left(-\frac{16\,{\gamma_{l-x}}^3}{3\,k_B T\,\Delta g_{l-x}(T)^2}\right), \tag{2.39}$$

with A_ν being a prefactor. Here, we observe antithetical behavior. While the 'thermodynamic motivation' for nucleation, represented by $\Delta G^*(T)$ or $\Delta g_{l\text{-}x}(T)$, increases with undercooling, the accompanying slowdown of liquid dynamics acts as a deaccelerating factor.

As suggested by the term 'homogeneous nucleation rate', Equations (2.38) and (2.39) assume that supercritical nuclei form homogeneously from the liquid state, i.e. precipitate in full spheric geometry as described in the context of Equation (2.31). Yet, under the presence of any kind of crystalline interface, the formation of embryos and supercritical nuclei can be massively facilitated. Such catalyzing interfaces might be brought in by the

container wall which surrounds the melt or also through impurities like oxide particles. Mechanistically, the crystalline structure of these heterogeneous nucleation sites might resemble the structure of the nucleating crystal, resulting in a low interfacial energy between the two crystalline phases. Accordingly, embryos and nuclei can easily form by wetting the interface with a wetting angle θ and showing an only partially spherical shape as illustrated in the inset of Figure 2.18. The two ΔG(r) curves illustrate the massive decrease of the activation barrier that can be achieved through heterogeneous nucleation.

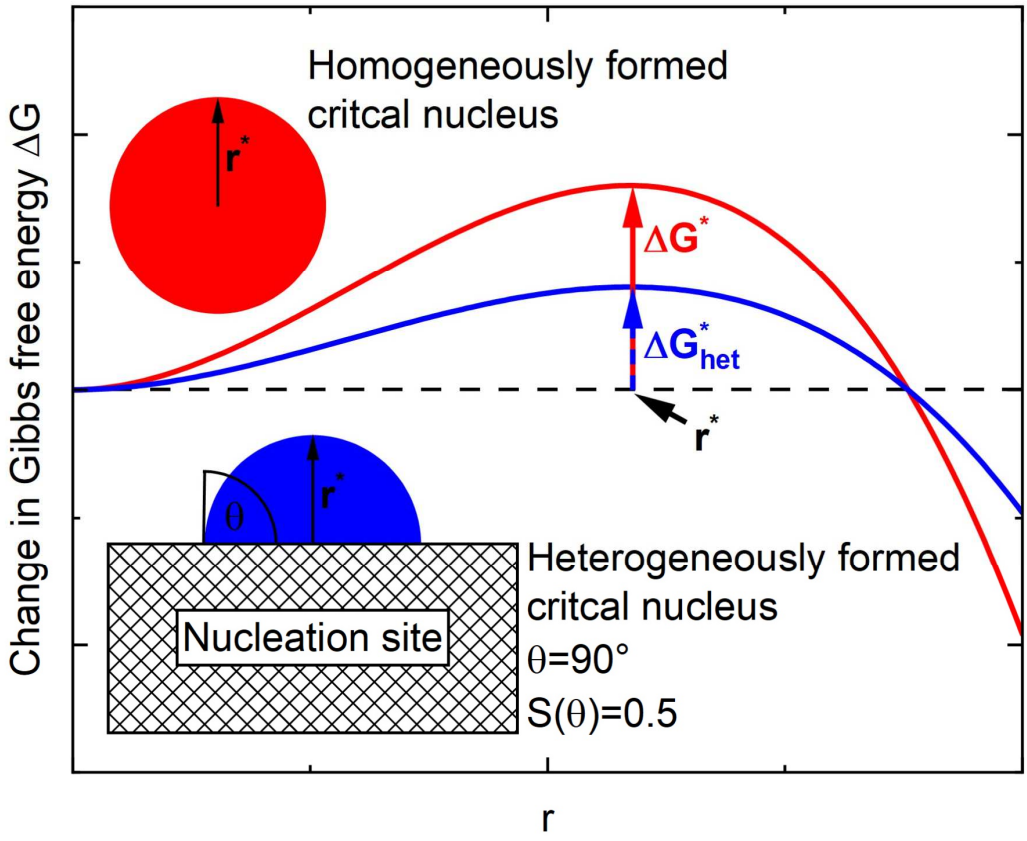

Figure 2.18: The influence of heterogeneous nucleation on the overall change in Gibbs free energy. The inset sketches a critical nucleus that forms heterogeneously on a nucleation site surface. Due to the wetting angle of 90°, only half of the crystalline volume has to be formed and the activation barrier for nucleation is halved.

This effectively lowers the nucleus volume needed to achieve supercriticality and therefore reduces the corresponding activation barrier for heterogeneous nucleation $\Delta G^*_{het}(T)$ as

$$\Delta G^*_{het}(T) = \Delta G^*(T)\, S(\theta). \tag{2.40}$$

$0 < S(\theta) < 1$ is the shape factor

$$S(\theta) = \frac{1}{4}\,(2 + \cos(\theta))\,(1 - \cos(\theta))^2, \tag{2.41}$$

which quantifies the reduction of the activation barrier as a function of the wetting angle. Figure 2.18 illustrates an exemplary case of a 90° wetting, resulting in a halving of $\Delta G^*_{het}(T)$ with respect to $\Delta G^*(T)$, i.e. $S(\theta)=0.5$.

2.6.4 The crystal growth rate

Once a supercritical nucleus has formed, it proceeds to expand with a growth rate u(T) [170] according to

$$u(T) = \frac{f\ k_B\ T}{3\ \pi\ d^2\ \eta(T)}\ \exp\left(1 - \frac{V_a\ \Delta G_{l-x}(T)}{k_B\ T}\right). \tag{2.42}$$

Here, d is the average atomic diameter, V_a is the average atomic volume, and f is a factor that quantifies the atomic-scale roughness of the crystal-liquid interface [170]. Again, thermodynamics favor crystal growth with ongoing undercooling through the increasing driving force $\Delta G_{l\text{-}x}(T)$, yet, u(T) differs from I(T) as it is not affected by the interfacial energy $\gamma_{l\text{-}x}$. Liquid dynamics are again represented by η(T) and act as a deaccelerating factor with undercooling in a similar way as found for I(T).

2.6.5 The JMAK model and the TTT diagram

We have seen that the rates of nucleation and growth both result from an interplay of thermodynamic and dynamic contributions and that these influence factors behave antagonistic in their temperature dependence. As a consequence, I(T) and u(T) do not rise monotonically with undercooling but instead increase towards maximum values to then decrease again, thereby creating nose-shaped appearances. Figure 2.19a) illustrates this behavior schematically and shows that the different mathematical conceptions of I(T) and u(T) causes them to show their maxima at different temperatures. By comparing the exponential arguments of Equations (2.39) and (2.42), it becomes evident that I(T) is decisively more dictated by thermodynamics than u(T). Accordingly, I(T) reaches its maximum at relatively low temperatures, while u(T) is rather dominated by the influence of liquid dynamics, therefore showing its maximum at higher temperatures in vicinity of T_l.

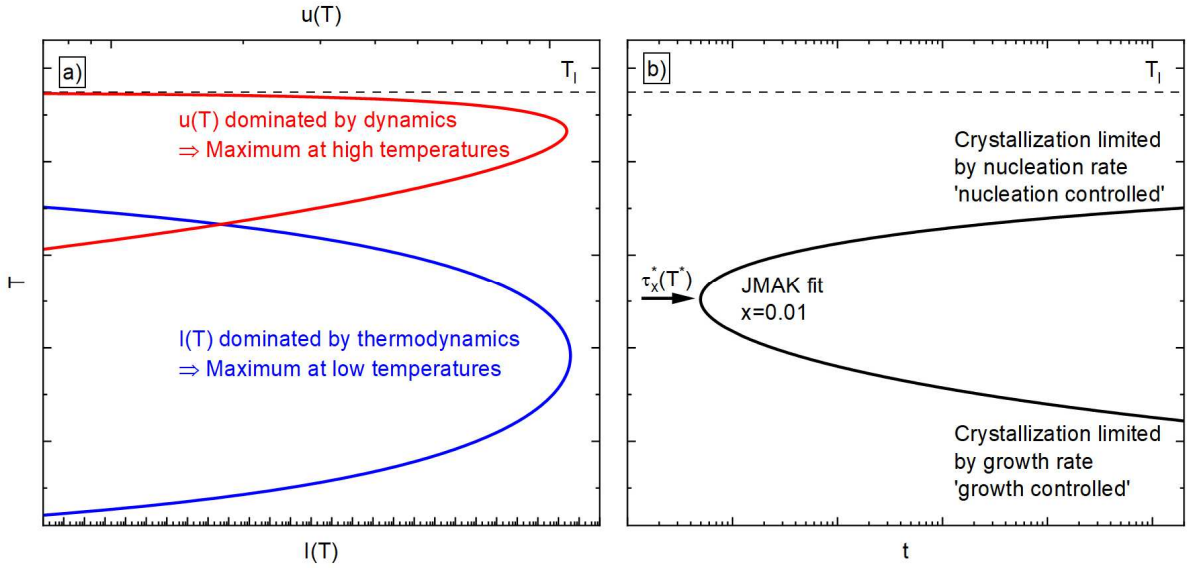

Figure 2.19: In a), the temperature dependent functions of growth rate u(T) and nucleation rate I(T) are schematically compared. While the former dominates at higher temperatures, the latter is most prominent at lower temperatures. The interplay of u(T) and I(T) eventually determines the JMAK function that describes the crystallization nose shown in the TTT diagram in b).

Crystallization occurs as a two-stage process. To initiate it, supercritical nuclei have to form first, which then are able to grow and ultimately consume all liquid volume to transform the system in a fully crystalline state. Stemming from the classical nucleation theory, the Johnson-Mehl-Avrami-Kolmogorov (JMAK) model allows to describe crystallization kinetics by combining the previously introduced expressions for I(T) and u(T), see Equations (2.39) and (2.42). Assuming a polymorphic transition and spherical growth, the crystallized fraction x(t,T) can be calculated as a function of the isothermal waiting time t [171,172] as

$$x(t,T) = 1 - \exp\left(\frac{\pi}{3} I(T)\, u(T)^3\, t^4\right). \tag{2.43}$$

This formula can be reformulated to calculate the waiting time t(x,T) after which a specific crystallized fraction x is found at a given temperature T:

$$t(x,T) = \left(\frac{-3\ln(1-x)}{\pi\, I(T)\, u(T)^3}\right)^{\frac{1}{4}}. \tag{2.44}$$

Figure 2.19b) shows a so-called time-temperature-transformation (TTT) diagram with a JMAK fit calculated for x=0.01 that results from the I(T) and u(T) curves in Figure 2.19a). Apparently, the JMAK fit also features a typical nose shape that evolves at intermediate temperatures between the maxima of I(T) and u(T). The tip of the t(x,T) nose at T^* features

a minimum crystallization time τ_x^*, indicating an optimal combination of nucleation and growth rates that leads to the fastest crystallization kinetics possible. At temperatures above the nose, crystallization is delayed due to the low thermodynamic driving force and the accordingly low nucleation rate. Here, one speaks of 'nucleation controlled' crystallization kinetics, since the initial formation of supercritical nuclei is the decisive limiting factor. Once formed, the fast growth kinetics lead to a rapid, almost 'explosive' crystallization process and a typical coarse-grained crystalline microstructure. The opposite picture is found below the nose, where crystallization kinetics are 'growth controlled', meaning that there exists an abundance of supercritical nuclei, which are however limited in their ability to growth though the overall slow liquid dynamics. These conditions lead to a typical fine-grained crystalline microstructure.

2.7 Preventing crystallization and forming a glass

2.7.1 Critical cooling rate and critical casting diameter

Despite being usually measured under isothermal conditions, the TTT diagram is a mighty and central tool to visualize and evaluate the glass forming ability of a system during undercooling. Bypassing the $\tau_x^*(T^*)$ critical point without initiating crystallization is the crucial condition for glass formation in most casting applications. The slowest (constant) cooling rate, with which crystallization can be still completely avoided, is the so-called critical cooling rate R_c. As indicated in Figure 2.20, cooling with R_c corresponds to a thermal path (blue dashed line) that grazes the tip of the crystallization nose at $\tau_x^*(T^*)$ and still allows for full vitrification at the rate-dependent $T_{g,kin}$ (gray solid line) as one would expect it from a faster cooling rate (green dashed line). Rates slower than R_c (red dashed line) cross the nose-shaped JMAK fit in the TTT diagram, and the system crystallizes. We see here that the GFA of a given alloy can be directly quantified by its critical cooling rate. A low R_c indicates high GFA and further corresponds by trend to a large τ_x^*, i.e. a high thermal stability of the supercooled liquid against crystallization. Assuming that the primary crystalline phase melts completely at T_l, R_c can be estimated from τ_x^* by a simple two-point linear equation:

$$R_c = \frac{T_l - T^*}{\tau_x^*}. \tag{2.45}$$

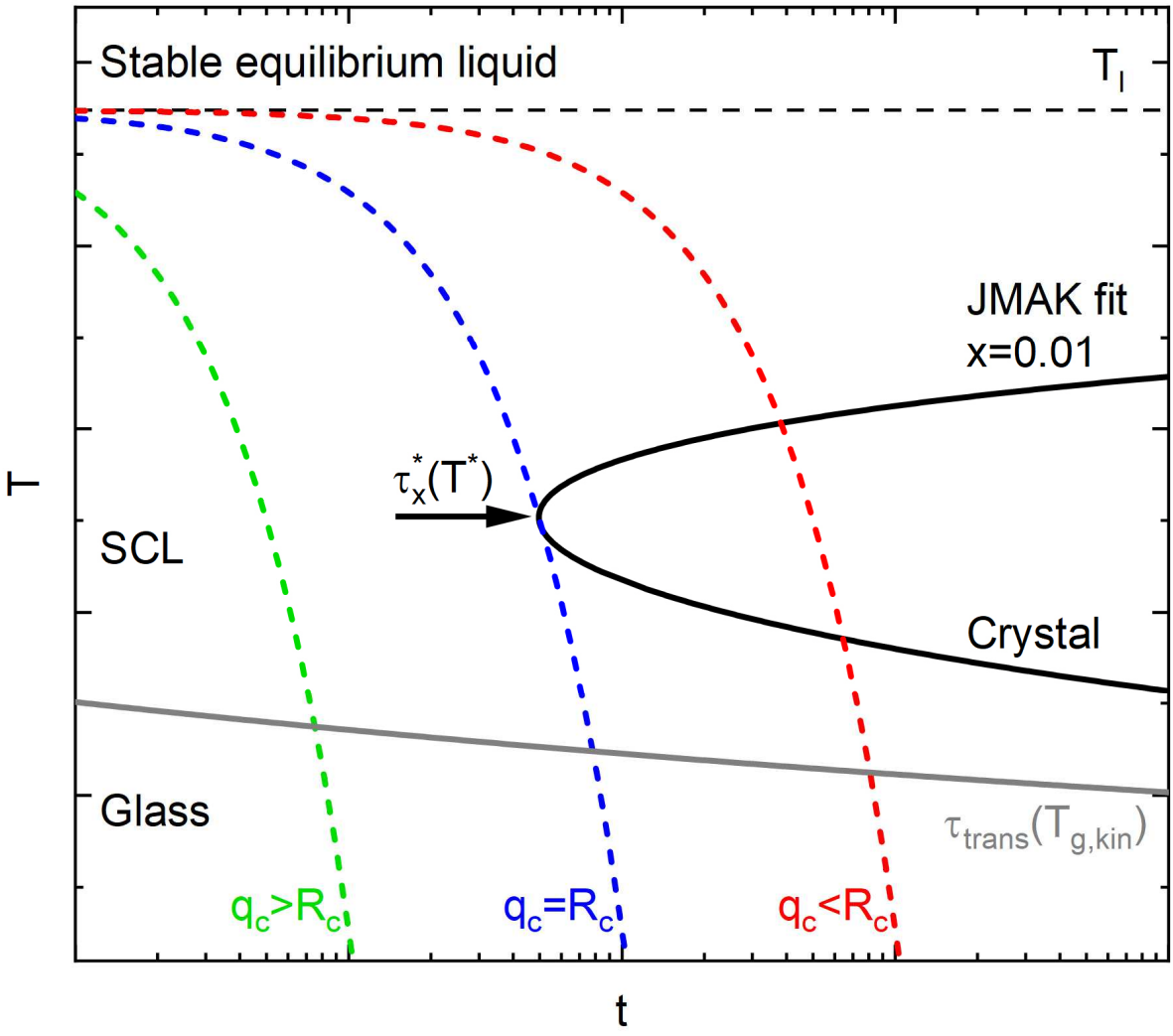

Figure 2.20: A TTT diagram that demonstrates why the GFA can be expressed through a so-called critical cooling rate R_c Undercooling the liquid with rates faster (green line) or equal to (blue line) R_c still allows glass formation as the crystallization nose is not passed. Slower cooling rates (red line) will create a thermal path that crosses the crystallization nose, leading to a (partially of fully) crystallized material.

The existence of a critical cooling rate and the limited thermal conductivity of any supercooled liquid further imply restrictions in geometry and size for the casting of fully amorphous specimen. Hence, the GFA of an alloy can be also quantified through a critical (casting) diameter d_c, which is the diameter of the largest rod-shaped sample that can be still cast in a fully amorphous state. Assuming constant heat capacity and thermal conductivity, Johnson et al. [75] estimated a rule of thumb that connects d_c (in cm) and R_c (in K/s) according to

$$d_c = \sqrt{\frac{10}{R_c}}. \tag{2.46}$$

Naturally, d_c also correlates with τ_x^*, since by trend, a higher thermal stability of the supercooled liquid allows for larger critical diameters. Johnson, Na, and Demitriou [173] established an empirical connection in the form of

$$d_c = 8.6466\ (\tau_x^*)^{0.394}. \tag{2.47}$$

From a practical perspective, d_c might be the most frequently used metric to quantify GFA. First of all, it is of fundamental and direct relevance for industrial casting processes that aim for fully amorphous parts. Secondly, it can be easily evaluated through series of casting experiments with increasing sample sizes and a subsequent screening of the microstructure. In contrast, an empirical determination of R_c requires complex in-situ monitoring of the undercooling process [174]. Evaluating the TTT diagram-based parameter τ_x^* is also rather effort consuming. It usually incorporates JMAK fitting, see Equation (2.44), of extensive data sets obtained by means of e.g. calorimetry, as later discussed in Chapter 4.1.5. Nevertheless, knowledge of the TTT diagram can turn out as crucial for advanced processing routes like thermoplastic forming or additive manufacturing, as it will be introduced in the Chapters 3.3 and 3.4.

2.7.2 The glass forming ability as an interplay of structure, thermodynamics, and dynamics

We have seen that the ability to undercool and vitrify metallic melts is a question of crystallization avoidance. The crystallization timescale must be prolongated to create the needed 'room for maneuver' for a cooling procedure that passes through the crystallization-prone undercooled liquid region until reaching the kinetic glass transition. This goal can be promoted through a stabilization of the liquid state on the one hand and a demotivation of the crystallization process itself on the other hand. In the following, we will briefly summarize the previous chapters by highlighting all the structural, thermodynamic, and dynamic aspects that favor GFA and especially, we will try to highlight the tight connections and crosslinks between these different factors.

Starting from a structural perspective, we have seen in Chapter 2.5 that a well-adjusted chemical composition can allow for increased packing density and low levels of free volume in metallic liquids. Optimized topology and chemical affinity among the included species result in pronounced order on short and medium length scales, ultimately allowing to stabilize the undercooled state against crystallization.

Regarding the Gibbs-Helmholtz formula, see Equation (2.1), such a rigid atomic structure finds its thermodynamic expression in overall low levels of Gibbs free energy of the liquid (Chapter 2.6.2) and accordingly a low driving force towards crystallization $\Delta G_{l\text{-}x}$. Furthermore, the structural motifs that establish the liquid SRO, which are prevalently icosahedra or trigonal prisms as discussed in Chapter 2.5.1, are often incompatible with the packing scheme of the rivaling crystalline state. Hence, the crystallization process must be accompanied by considerable structural rearrangements, and this facet manifests thermodynamically through the interfacial energy γ. A high interfacial energy effectively impedes the formation of critical nuclei and results in a low nucleation rate I(t), as explained in Chapter 2.6.3.

From a dynamic perspective, pronounced structural order and accordingly low levels of free volume and entropy imply highly cooperative liquid dynamics (Chapter 2.2.2) and a rather strong behavior in terms of the fragility concept. Here it shall be referred to Chapter 2.2.4, especially regarding the free volume models by Doolittle and Cohen-Grest as well as the thermodynamic Adam-Gibbs and MYEGA models. A strong liquid behavior goes hand in hand with sluggish structural relaxation processes in the crystallization-prone undercooled state. This diminishes the rates of crystal nucleation and growth as well, thereby effectively impeding crystallization kinetics as discussed in the framework of the JMAK model in Chapter 2.6.5.

Since the interplay of all these factors is highly sensitive to the respective alloy composition, different metallic glass formers will usually vary in terms of the 'main origins' of their GFA. Gross et al. [71] provided a scheme shown in Figure 2.21 that classifies BMG formers in a 'kinetically stabilized' group and a 'thermodynamically stabilized' group. The alloys of the former group gain their GFA mainly from impeded crystallization kinetics caused by strong liquid behavior and accordingly sluggish dynamics. The latter group is again subclassified in systems that are thermodynamically stabilized through a low driving force and those that show impeded crystallization due to a high interfacial energy.

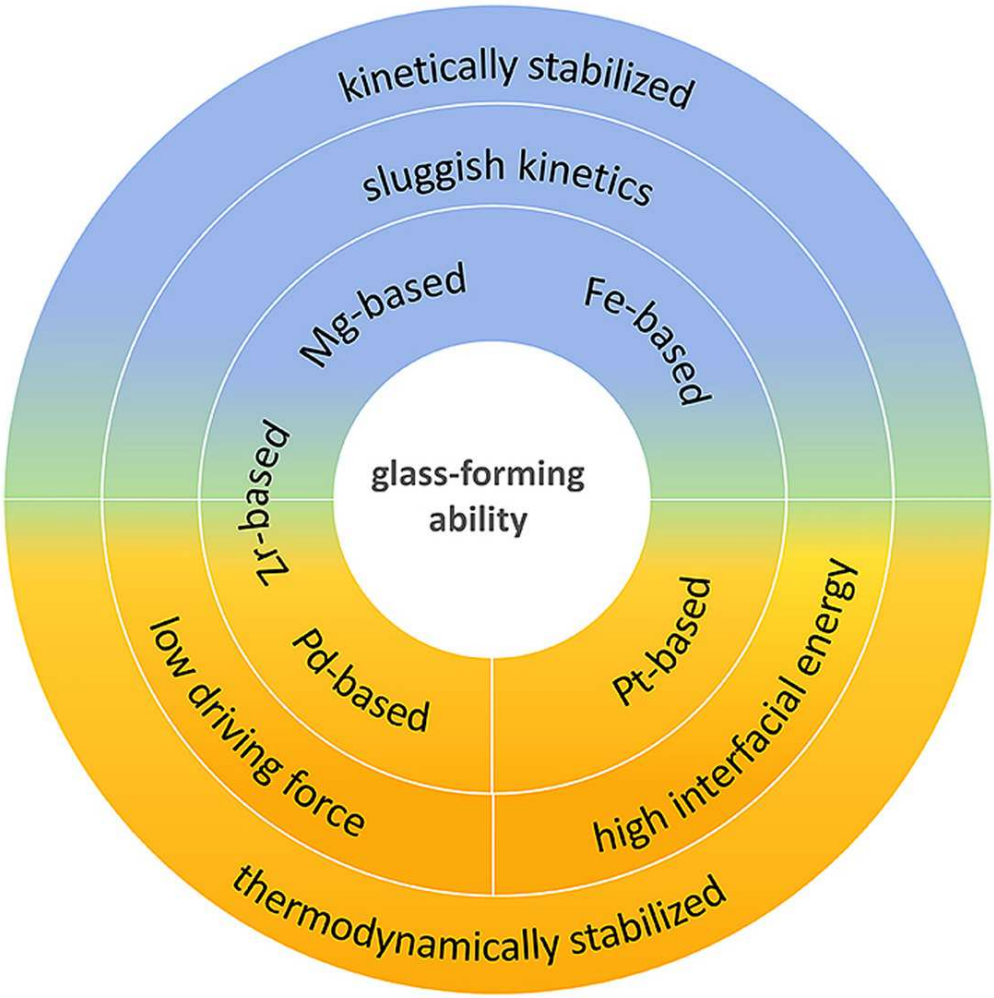

Figure 2.21: A scheme by O. Gross et al. [71] that classifies metallic glass formers according to the main factor that determines their GFA. While Pd- and Pt-based liquids are rather thermodynamically stabilized against crystallization, Zr-, Mg-, and Fe-based systems are more kinetically stabilized.

2.7.3 Practical metrics and rules for optimized glass forming ability

Besides these theoretical considerations, the following chapter will provide rather practical rules and principles that can help in alloy development attempts towards compositions with high GFA.

The term 'confusion principle' summarizes several GFA-promoting aspects that come with an increased number of atomic species in the alloy composition [175]. At first, a broad field of incorporated elements by trend increases the complexity of the primarily formed crystalline phase. This hampers crystallization, as it is now reliant on extensive structural rearrangements. Moreover, complex crystalline phases tend to be less thermodynamically stable, hence featuring a low thermodynamic driving force $\Delta G_{l\text{-}x}$ [176]. Incorporating various atomic species in different sizes further allows for efficient

and dense packing, low free volume, and accordingly sluggish liquid dynamics and crystallization kinetics as previously discussed. Inoue subsumed these considerations in his well-known criteria for good GFA [177], which are (1) having a multicomponent alloy with at least three atomic species, which show (2) relative atomic size differences of 12% or more, and (3) all-negative enthalpies of mixing among each other. The first rule directly refers to the confusion principle, while the second rule is basically an inversion of the Hume-Rothery size rule for crystalline substitutional solid solutions. The third rule further promotes dense packing through chemical affinity while also decreasing the tendency for phase separation, which is often found to be the precursor of fast crystallization processes [21].

The melting event of a given alloy is easy to characterize by calorimetry and can provide valuable insights, as it reflects the thermodynamic relationship between crystal and liquid. A low entropy of melting can indicate a highly ordered liquid state with potentially high GFA. According to the Turnbull approximation $\Delta G_{l\text{-}x}(T) \approx -\Delta S_m/\Delta T$ introduced in Chapter 2.6.2, ΔS_m represents the steepness of the $\Delta G_{l\text{-}x}(T)$ curve and is therefore a direct measure of the system's thermodynamic driving force towards crystallization [167,168]. Furthermore, a comparably low liquidus temperature speaks for a thermodynamically stable liquid, and such a condition is usually found at (near-)eutectic compositions. This is the basis of Turnbull's famous reduced glass transition concept, with T_{rg} being defined as T_g/T_l (Turnbull initially used T_m instead of T_l [169] yet T_l was later found to be a better predictor [178]). A high T_{rg} means that the critical temperature span between T_l and T_g is minimized, thereby also minimizing the 'trespassing time' that is spent in the crystallization-prone undercooled liquid state at a given cooling rate. Hence, good glass formers often show high T_{rg} values in the order of 2/3, while poor glass formers (with rather high liquidus temperatures) tend to show lower values, respectively.

Finally, it shall be referred to Chapter 2.6.3, where the crucial influence of heterogeneous nucleation on the crystallization kinetics is explained. To maximize the GFA, high levels of impurities must be avoided, since particles like e.g. high-melting oxides can act as heterogeneous nucleation sites. Alloy development attempts should therefore be conducted initially by using high-purity elements.

2.8 Mechanical properties of metallic glasses

Metallic glasses feature several properties that make them technologically relevant. The very soft-magnetic character of some Fe-based systems [22,62] or the high corrosion resistance of Ti-based [179] or Ni-based alloys [180,181] should be mentioned as examples. Yet, we will mainly focus on the mechanical performance of BMGs in the present work and the following chapter will provide an introduction to the topic. For a broader discussion of the technological potential of BMGs, the reader is referred to further literature [55,182–185].

2.8.1 On the striking elasticity of metallic glasses

The absence of long-range atomic order in form of a periodic lattice fundamentally affects the atomistic mechanisms of plastic deformation. Amorphous solids cannot accommodate applied mechanical stresses through lattice-based effects like dislocation movements, crystal twinning, or grain boundary sliding. Without such rather easily activated compensation mechanisms, plastic deformation sets in not until very high mechanical loads are reached. Hence, metallic glasses show extensive elastic deformability and reach formidable strength values close to the material's theoretical strength. The Ashby map in Figure 2.22 schematically compares usual engineering materials like steels, titanium alloys, and polymers with metallic glasses regarding their yield strength σ_y and elastic limits ε_y. We see on the one hand that BMGs show σ_y values that are at least on par with other engineering metals. Yet, Fe- and NiNb-based systems can exceed yield strengths of 3 GPa or more [31,186], and some Co-based systems outpace most crystalline metals by reaching extreme levels of up to 5.5 GPa [185,187]. This further implies impressive hardness, which can surpass values of 1000 Vickers, depending on the system [31,185–187]. On the other hand, BMGs feature elastic limits of up to 2% deformation, comparable to the much weaker material class of polymers.

These mechanical properties render BMGs as a highly promising material class for small, but extremely robust parts, e.g. customer goods, jewelry, or in the defense sector [63]. Furthermore, the combination of high yield strengths and high elastic limits implies a low damping coefficient and high elastic energy storability, since E_{el} reflects the integral over the elastic regime in a stress-strain diagram according to

$$E_{el} = \frac{1}{2}\,\sigma_y\,\varepsilon_y. \tag{2.48}$$

In principle, this establishes BMGs as superior spring materials. Yet, it must be mentioned that their humbling fatigue properties diminish the suitability for such applications and remain a challenge to be addressed [182].

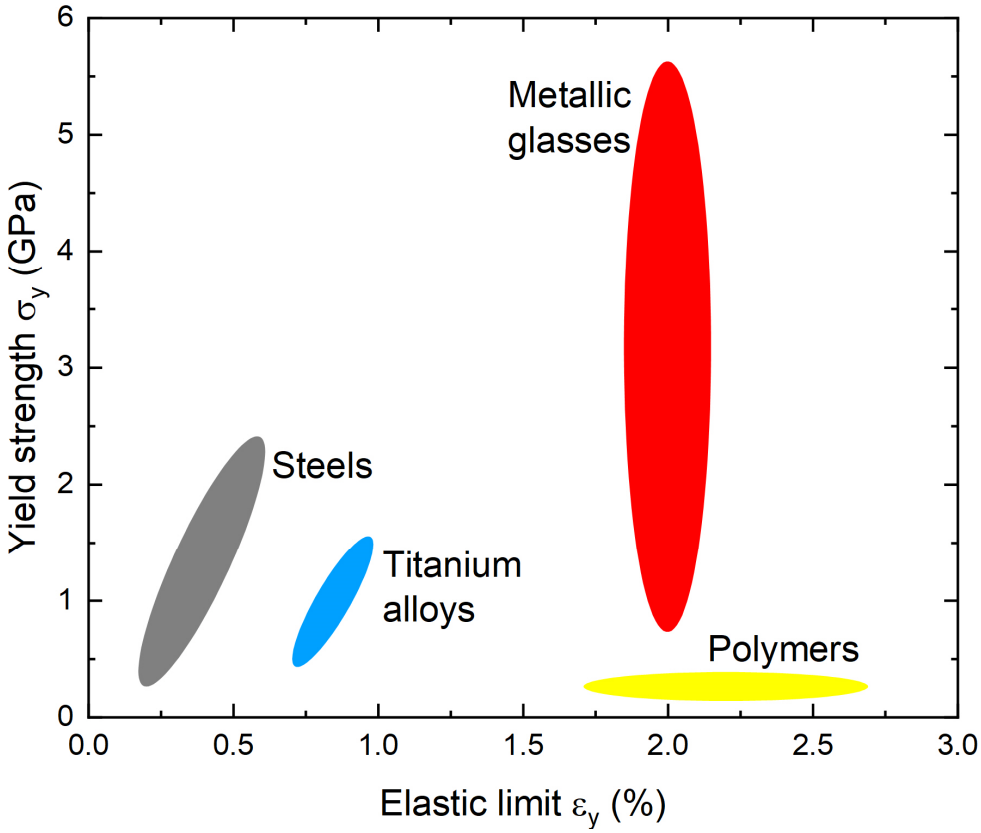

Figure 2.22: An Ashby map that compares the usual ranges of yield strength σ_y and elastic limit ε_y for major engineering material classes and metallic glasses. We see that the metallic glasses offer a very favorable combination of metal-like strength and polymer-like elastic deformability. Drawn after [184].

2.8.2 Plasticity at ambient temperatures

To understand plastic deformation of metallic glasses at temperatures far below the kinetic glass transition, we must consider the earlier discussed heterogeneous nature of the amorphous state. Plasticity occurs highly inhomogeneous as it initiates very localized in regions with increased free volume and accordingly lower resistance against viscous flow. When a certain stress threshold is bypassed, structural rearrangements are locally activated in a kind of stress-assisted nucleation process [188]. This way, a shear transformation zone (STZ) is formed, which was already introduced in the context of the

cooperative shear model of viscous flow, see Chapter 2.2.4. This activation process is dilatative [188–190] and further increases the local free volume [191–193]. Hence, localized strain softening sets in and causes self-propagating effects in which the STZs grow and merge into so-called shear bands. These usually grow from the outer surface of the part towards the inside [25], thereby orienting in direction of the highest shear stresses. The only nm-wide shear bands act as internal 'sliding surfaces' that can incorporate massive amounts of plastic deformation, while the surrounding material remains in the elastic regime. Without interfering mechanisms, even a single shear band can accumulate catastrophic deformation, causing a material fracture that appears brittle on a macroscopic scale. Such a scenario is exemplarily given under tensile stresses, which can tear a BMG sample apart as soon as the yield strength is reached. In contrast, compression loads are usually accompanied by geometrical constraints that allow the formation of manifold shear bands without catastrophic failure. Upon bending, the absence of stresses in the neutral axis stops single shear bands and can prevent early fracture, as shown in Figure 2.23. Hence, compression and bending loads allow macroscopic plasticity observed at ambient conditions for various metallic glass formers [63,188,194].

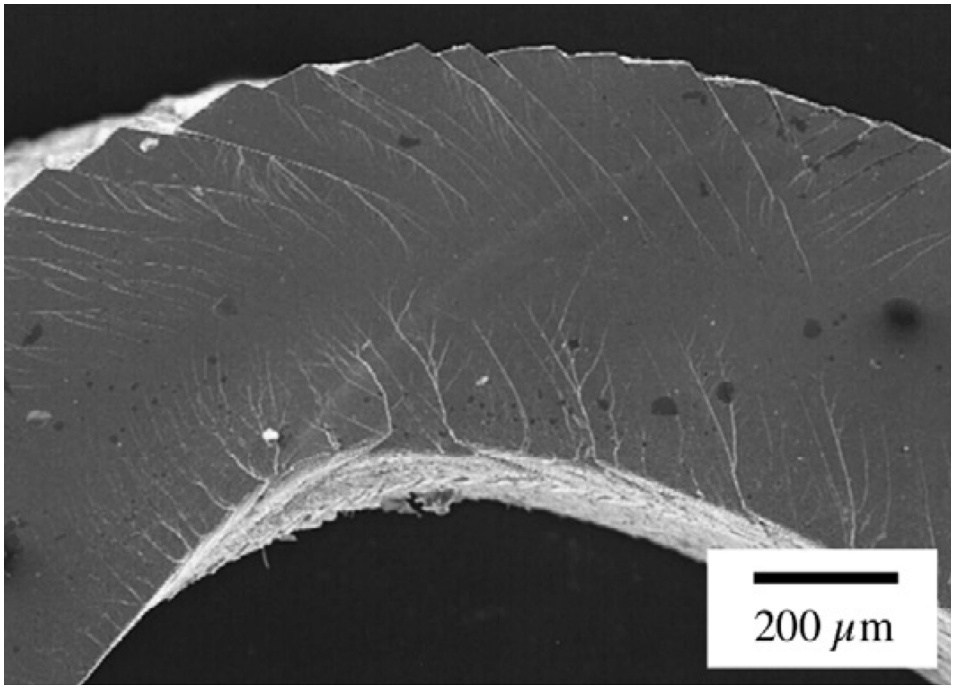

Figure 2.23: A scanning electron microscope image that shows the typical step-like appearance of shear band formation on the surface of a heavily bent Zr-based metallic glass strip. The neutral axis in the core of the specimen prevents catastrophic failure, since it prohibits the formation of a shear band that spans over the whole sample cross-section. Taken from [188].

2.8.3 Homogeneous formability at temperatures near the kinetic glass transition

If we heat a metallic glass to temperatures near the kinetic glass transition, the character of plastic deformation fundamentally changes. At these elevated temperatures, the Deborah number, see Equation (2.20), again approaches values near unity and structural relaxation becomes thermally activated in manifold STZs at once. Hence, plasticity does not manifest anymore through highly localized shear bands but occurs homogeneously through viscous flow. This so-called superplasticity allows for deformations of 1000% and more [65,188,195,196], see e.g. Figure 2.24. This is the basis for thermoplastic forming (TPF) processing routes originally known from polymers, like injection molding, blow molding or imprinting. The thermoplastic forming process will be further explained in Chapter 3.4.

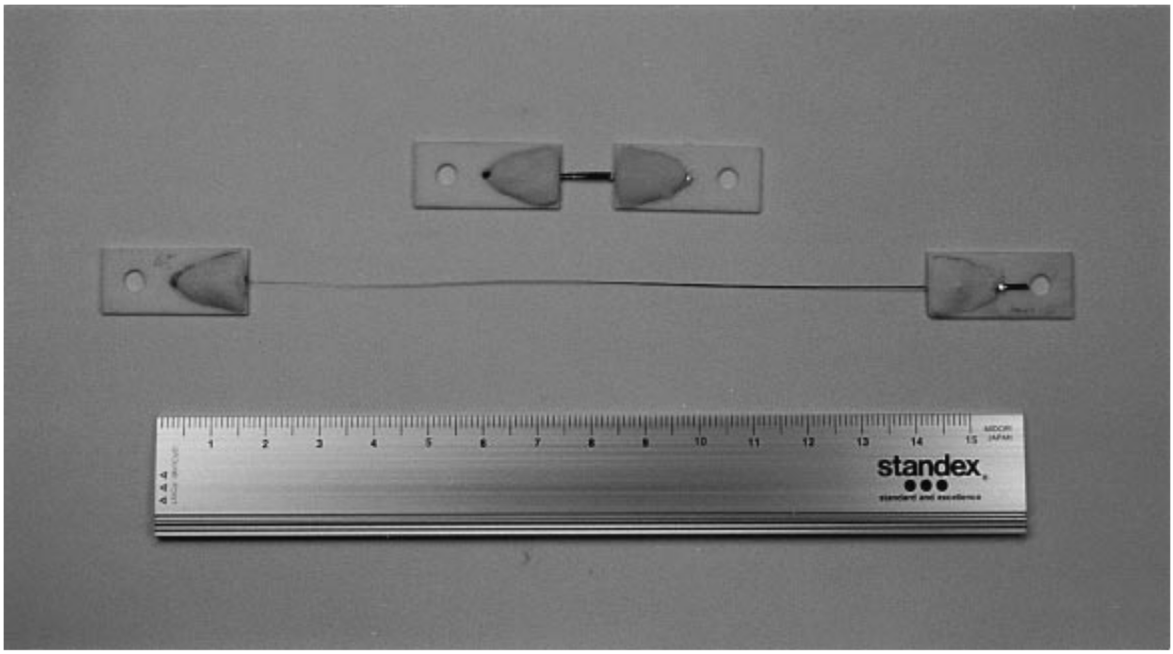

Figure 2.24: A $Pd_{40}Ni_{40}P_{20}$ metallic glass former brought to 1260% of its initial length through heating it to temperatures in the SCL state and then applying slow deformation. Taken from [196].

3. PROCESSING

The following chapter shall provide an overview of the full processing routes that lead to the specimens characterized in this work. This process starts with the initial material synthesis described in Chapter 3.1, *Alloy synthesis and feedstock production*, followed by the different routes of amorphization, namely *Conventional casting of metallic glasses* in Chapter 3.2 and *Additive manufacturing of metallic glasses* in Chapter 3.3. Chapter 3.4 finally introduces the post-processing route of *Thermoplastic forming*.

3.1 Alloy synthesis and feedstock production

Before we can focus on the synthesis routes of amorphous parts, we have to consider the formation of the therefore needed feedstock material. In the present work, such feedstock material has been formed through three different routes, namely arc melting, induction melting in combination with fluxing, as well as powder atomization. These processes will be quickly introduced in the following.

3.1.1 Arc melting

Arc melting is a widely used approach to melt metals, especially those with high melting and evaporation temperatures. Thereby, the raw elements are placed in a mold pit on a water-cooled copper plate. The setup is sealed in a vacuum chamber, which is subsequently evacuated and refilled with a high-purity argon atmosphere. An electric arc is ignited between a tip-shaped tungsten electrode and the copper plate. Initially, the arc is used to melt elemental titanium that acts as a getter material and purifies the argon atmosphere by absorbing excess oxygen from it. Then, the raw material is targeted with and molten by the electric arc, ultimately creating a homogeneous alloy that cools and solidifies rapidly onto the quasi-inert water-cooled copper to form button-shaped feedstock material. Yet, the cooling rates are usually slower than the critical cooling rate, and hence, the produced feedstock is mostly crystalline. Multiple repetitions of this process ensure compositional homogeneity. Figure 3.1 sketches the process. In the present work, arc melting is used to synthesize feedstock of the Zr-based $Zr_{59.3}Cu_{28.8}Al_{10.4}Nb_{1.5}$ alloy (AMZ4) in Paper IV, the CuTi-based $Cu_{47}Ti_{34}Zr_{11}Ni_8$ alloy (Vit101) and its derivates from Paper V, as well as the $Ni_{62}Nb_{38}$ alloy from Paper VI.

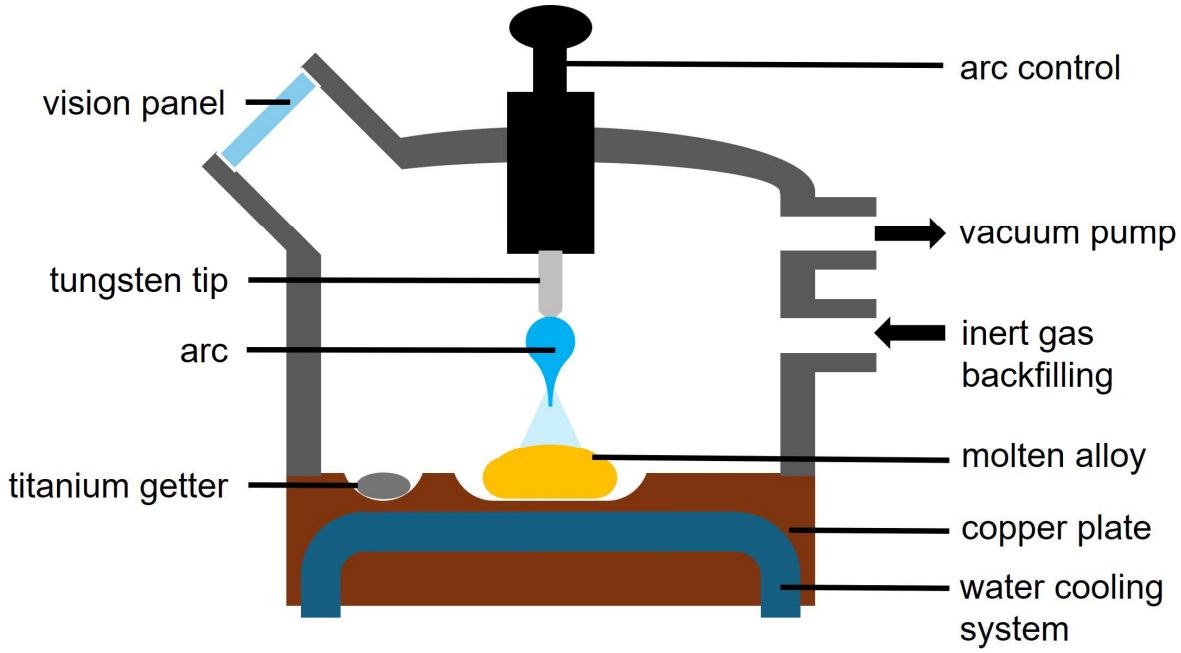

Figure 3.1: A scheme of the arc melting process. The material is molten and alloyed by an electric arc under an inert gas atmosphere. The water cooling system prohibits reactions between the melt and the copper mold.

3.1.2 Inductive melting and fluxing processes

To melt and alloy elements with lower melting and evaporation points, inductive melting can be a more gentle and careful approach, as it is able to introduce thermal energy less intensive and more homogeneous than the high-temperature electric arc. The noble-metal-based systems $Pt_{42.5}Cu_{27}Ni_{9.5}P_{21}$ (Papers I-III) and $Pd_{43}Cu_{27}Ni_{10}P_{20}$ (Paper I) are good examples, since inductive melting is well-suited to alloy the highly elusive and rather reactive phosphorus with the metallic elements. Figure 3.2 illustrates that the alloying procedure is conducted in an evacuated and high-purity argon refilled quartz tube. A more detailed process description can be found in [197,198]. After solidification, an alloy ingot in the shape of the quartz glass is obtained.

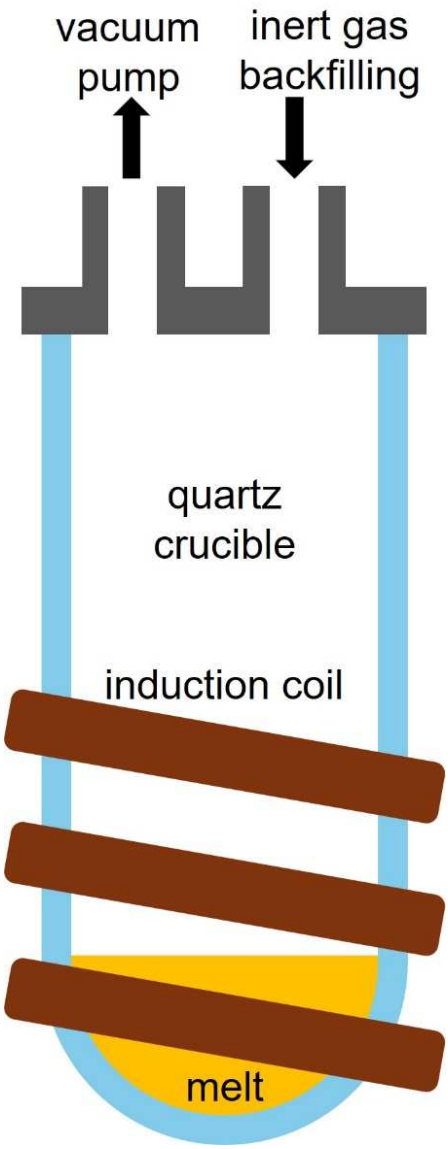

Figure 3.2: Scheme of the inductive melting and alloying process under inert gas atmosphere. A quartz tube serves as crucible.

Furthermore, it has been shown that a fluxing process allows to purify such noble-metal-based alloys and increase their GFA significantly [199]. Hence, to produce high-purity feedstock, the induction-alloyed $Pt_{42.5}Cu_{27}Ni_{9.5}P_{21}$ and $Pd_{43}Cu_{27}Ni_{10}P_{20}$ material is fluxed in liquid B_2O_3 at 1473 K for at least 16 h in a resistive furnace, as sketched in Figure 3.3.

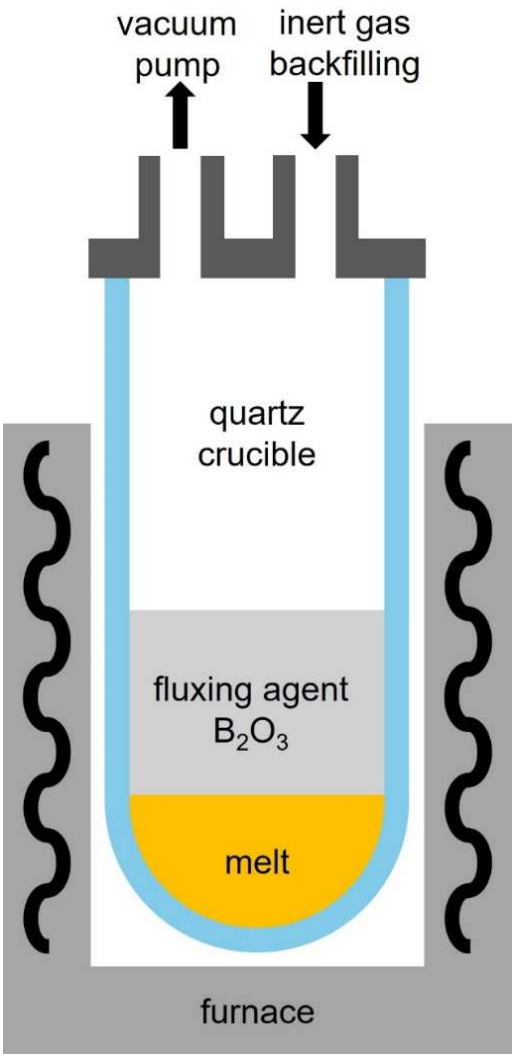

Figure 3.3: Scheme of the fluxing process. The previously alloyed feedstock is molten in a resistive furnace under an inert gas atmosphere and being covered by the fluxing agent B_2O_3.

3.1.3 Gas atomization

To produce feedstock in form of metal powder, gas atomization has emerged as a widely used technique [200]. Figure 3.4 explains the working principle. After evacuating the process chamber and refilling it with an inert atmosphere (e.g. high-purity argon), the material is inductively (or resistively) molten in a crucible and then ejected through an orifice. Gas nozzles blow inert gas jets onto the melt stream, resulting in its disintegration into fine droplets that rapidly solidify to form the powder particles. To produce feedstock for additive manufacturing purposes, close-coupled atomizers are often used [201]. This type of atomizer places the gas nozzles very close to the orifice, hence maximizing the gas velocity and the corresponding shear effects. Ultimately this allows for comparably small particles of 50 µm and below, which is often preferable for AM processes. Such small

particle sizes furthermore imply fast cooling rates, and hence, close-coupled atomization often results in fully amorphous powder feedstocks [23,33,202].

Powder atomization of the $Zr_{59.3}Cu_{28.8}Al_{10.4}Nb_{1.5}$ material used in Paper IV was done by Heraeus AMLOY. The $Cu_{47}Ti_{34}Zr_{11}Ni_8$ alloy (Vit101) and its derivates from Paper V as well as the $Ni_{62}Nb_{38}$ from Paper VI were atomized at the IWT Bremen. These atomization processes are described and evaluated in detail in the respective publications by E. Soares et al. [23,33].

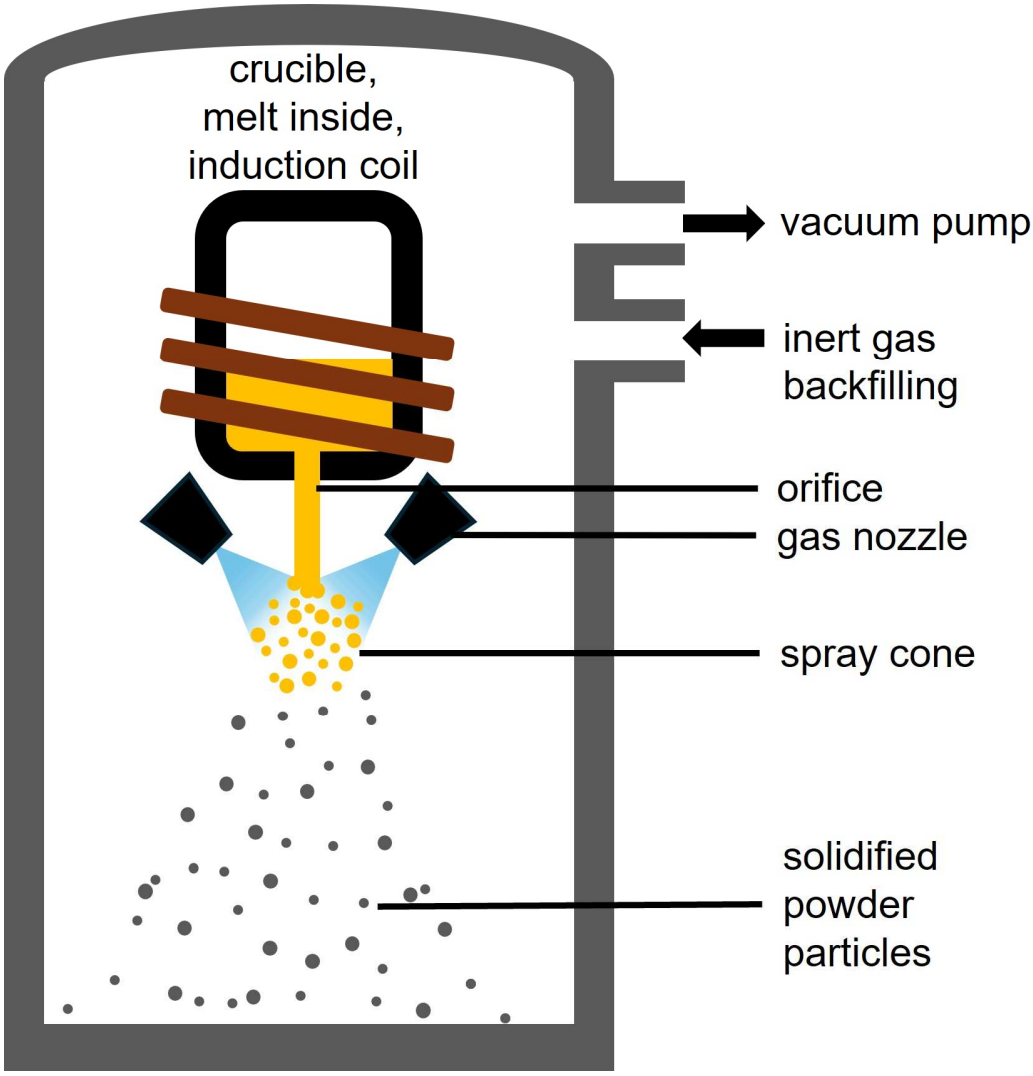

Figure 3.4: A schematic illustration of a gas atomization process under inert atmosphere. The feedstock is molten in a crucible at the top of the process chamber and then ejected through an orifice. Inert gas jets disintegrate the melt stream into small droplets that solidify rapidly on their way towards the bottom of the chamber.

3.2 Conventional casting of metallic glasses

Conventional casting routes aim to vitrify the high temperature liquid by bringing it into contact with cooler surfaces of any kind, e.g. a water-cooled crucible. These methods are among the oldest and most used approaches to create metallic glasses.

3.2.1 Melt spinning

Melt spinning is one of the oldest techniques for rapid solidification and the synthesis of metallic glasses [203,204]. Figure 3.5 illustrates the specific setup that was used to create the $Pt_{42.5}Cu_{27}Ni_{9.5}P_{21}$ ribbons measured in the Papers II and III. The process chamber is evacuated before the inductively alloyed and fluxed feedstock material is molten in a quartz crucible. Through injecting high-purity argon, the melt is ejected through a small orifice at the bottom of the crucible. The melt stream is directed to a fast rotating copper wheel. At its surface, the melt is sheared apart and forms a rapidly solidified amorphous ribbon of roughly 20 µm thickness and a width of some millimeters.

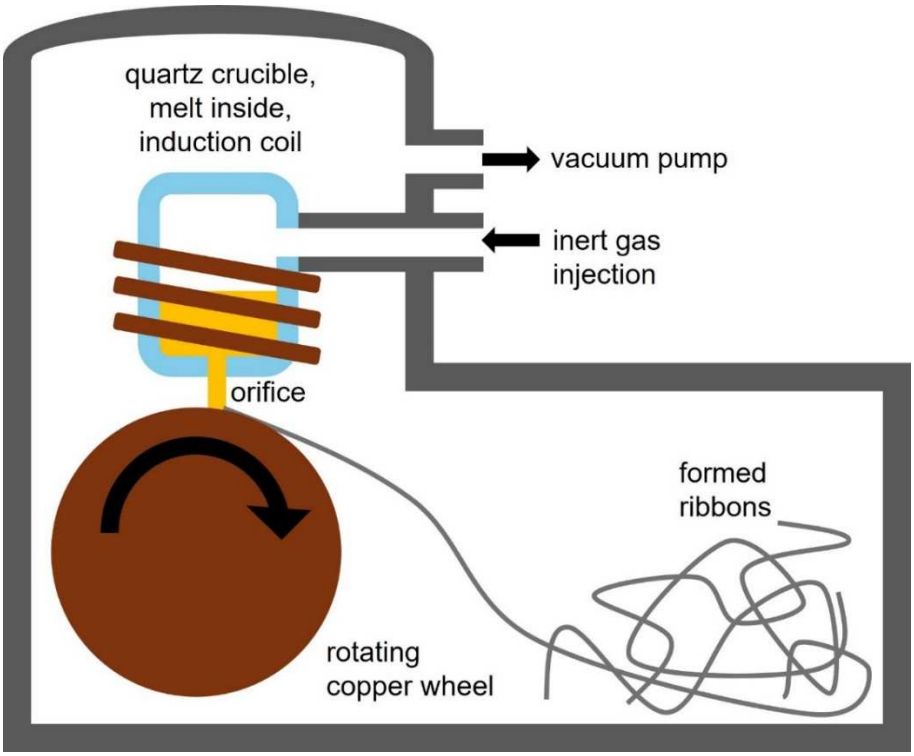

Figure 3.5: The melt spinning process schematically illustrated. Feedstock material is molten in a quartz crucible under vacuum and then ejected through a orifice by applying pressure through high purity argon injection. The melt hits a rotating copper wheel, is sheared apart and solidifies rapidly into amorphous ribbons.

With melt spinning, extremely high cooling rates of up to 10^6 K/s can be achieved. Therefore, it can be used to vitrify even bad glass formers and usually creates glasses with very high fictive temperatures (see Chapter 2.4.3).

3.2.2 Suction casting

Bulk metallic glass formers with advanced glass forming ability can vitrify in larger dimensions. Here, suction casting comes into play as a valid process route to cast BMGs in e.g. rod, plate, or paddle geometry. Figure 3.6 illustrates that the process is based on the arc melting procedure described in Chapter 3.1.1. After melting an appropriate amount of previously alloyed feedstock material, the melt is sucked into a water-cooled copper mold to form a rapidly solidified amorphous sample in the desired shape and dimension. In the Papers IV, V, and VI, suction casting is used to produce all the as-cast samples that serve as references for the evaluation of their additively formed counterparts, namely the $Zr_{59.3}Cu_{28.8}Al_{10.4}Nb_{1.5}$ alloy in Paper IV, the $Cu_{47}Ti_{34}Zr_{11}Ni_8$ alloy and its derivates in Paper V as well as the $Ni_{62}Nb_{38}$ in Paper VI.

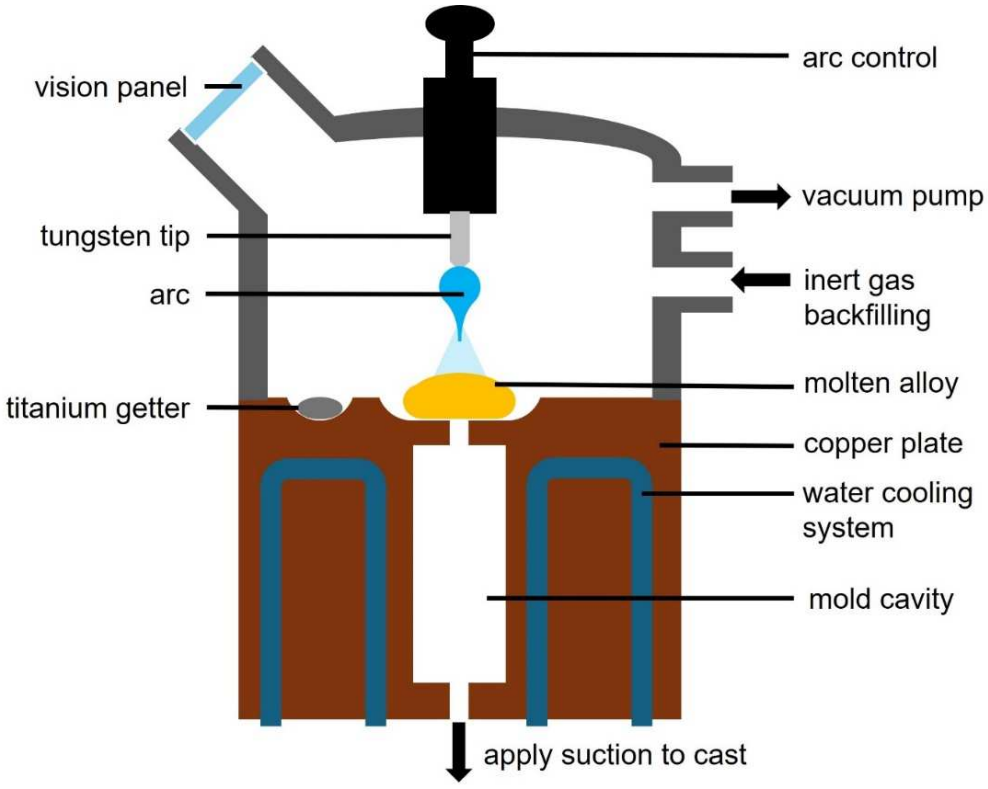

Figure 3.6: During suction casting, feedstock material is molten by an electric arc under inert gas atmosphere and then sucked into a water cooled copper mold to form a metallic glass with a specific shape.

3.2.3 Tilt casting

Tilt casting combines the gentle approach of induction melting with a cast process that is not based on an applied suction force but on gravity, as shown in Figure 3.7. The material is molten under a high-purity argon atmosphere and then poured into a water-cooled copper crucible through a tilt movement of the whole process chamber. This setup bears the advantage that the alloying, i.e. the feedstock production, and the final casting into an amorphous sample can be performed in one step. Yet, the process features inherent drawbacks in comparison to suction casting, which can be identified in the decreased form filling effectiveness and the higher tendency for sample contamination due to possible crucible reactions and the absence of a getter. In the present work, the amorphous $Au_{49}Ag_{5.5}Pd_{2.3}Cu_{26.9}Si_{16.3}$ alloy from Paper I was produced using this method.

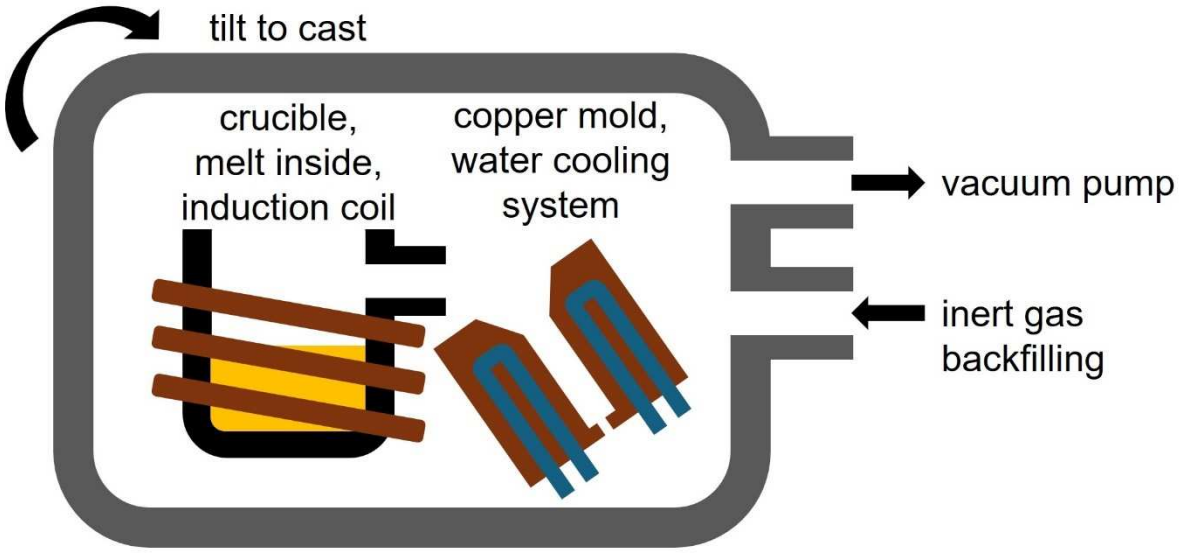

Figure 3.7: In the tilt casting process, the material is inductively heated under inert atmosphere and then poured into a water-cooled copper mold to form an amorphous specimen.

3.3 Additive manufacturing of metallic glasses

Additive manufacturing, also known as 3D printing, has drawn growing interest in recent years. As the name suggests, the basic principle is found in a step-wise build-up of the part. While filament-based 3D printing approaches are widely used for polymers, metals are often processed via powder bed methods. Thereby, layers of powder feedstock are locally compacted through melting and subsequent solidification via a concentrated energy input, which can be realized through e.g. an electron beam or also through a laser beam, as it is the focus in this work. It shall be mentioned that there exists an abundance

of different nomenclatures and abbreviations around this process. An often found notation is 'selective laser melting' (SLM), while the present publications rather use the more specific term 'laser powder bed fusion of metals', which can be abbreviated as LPBF, or more recently as PBF-LB/M (powder bed fusion – laser-based/metals).

3.3.1 Laser powder bed fusion of metals

Figure 3.8 schematically illustrates the PBF-LB/M process, which is usually performed under a controlled high-purity inert atmosphere in case of BMG processing. A recoater applies a thin powder feedstock layer on a substrate platform (build plate) with a typical layer thickness d_s of roughly 20-50 µm. A focused laser beam then scans over the regions of the powder bed that shall be compacted, creating a highly localized melt pool (about 70-200 µm in diameter, depending on the device and used process parameters [35,37]) at the respective position of the laser spot. Around the melt pool, we can further observe a region of increased temperature, a so-called heat-affected zone (HAZ). Due to the fast scan velocity v (usually more than 1000 mm/s), the once molten material cools and solidifies rapidly with rates of up to 10^6 K/s [205]. Subsequently, the build plate is lowered by d_s, a second layer of powder feedstock is applied and the laser melting process starts again. This cycle is repeated until the desired part is completely formed layer by layer.

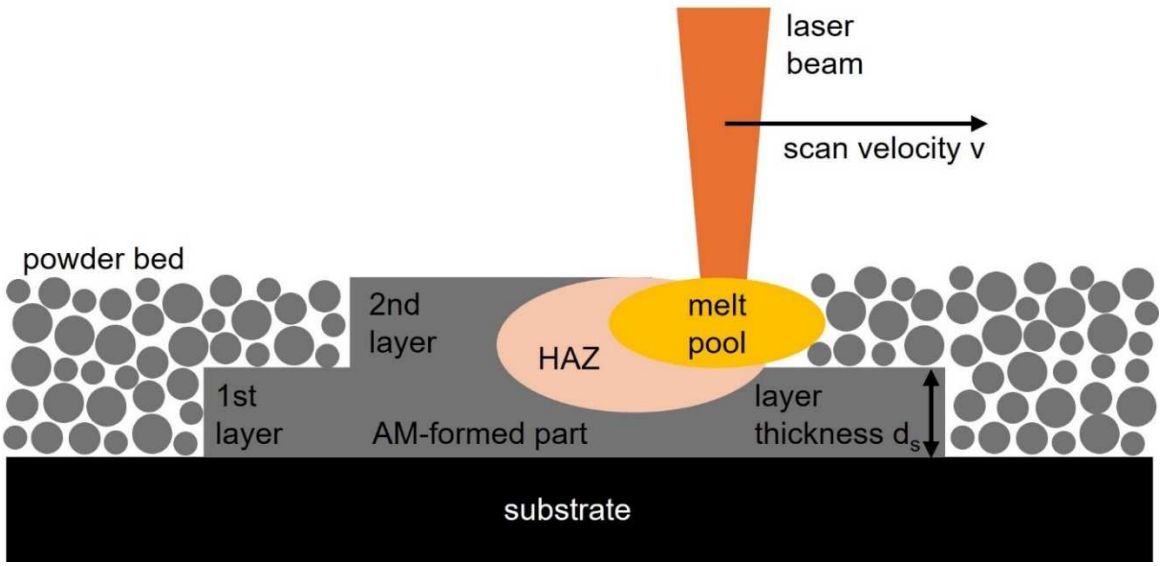

Figure 3.8: A schematic illustration of the PBF-LB/M process. The laser beam moves with a scan velocity v over the powder bed and melts the particles. The consolidated material cools rapidly to form a respective layer of the AM-formed part of thickness d_s. The process is repeated layer by layer until the desired part is created.

PBF-LB/M allows to create complex shapes that would be impossible to cast. The layer-wise, highly localized melting furthermore decouples part size and achievable cooling rate. Hence, the size limitations for amorphous parts that apply for casting processes (speaking of the critical diameter) can be overcome with this method. Yet, an optimal choice of process parameters is crucial, as discussed in the following.

3.3.2 Processing parameters and the volume energy density

To achieve highly robust AM-formed BMG parts, porosity must be minimized (hence, a high relative density must be reached) while also achieving full amorphicity. Reaching this goal is a question of the interplay between various process parameters like the laser power P, the scan velocity v, the layer thickness d_s, and the hatch distance h, which describes the distance between neighboring melt tracks. A well-established parameter that combines these aspects to describe the overall thermal energy input is the volume energy density E_V:

$$E_V = \frac{P}{v\, d_s\, h}. \tag{3.1}$$

Naturally, a too low E_V will lead to insufficient melting of the powder particles and the resulting AM-formed part will lack compaction due to irregularly shaped porosity. This defect type is known as lack of fusion (LOF). Rising E_V can decrease the LOF porosity and increase the relative density, yet this measure can also bear the issue of beginning crystallization. The TTT in Figure 3.9 illustrates two (simplified) thermal histories at a given position in the AM-formed part, which result from PBF-LB/M processing with two volume energy densities $E_{V,1}$ and $E_{V,2}$, with $E_{V,1}<E_{V,2}$. We see that the liquid in the melt pool initially cools quickly. Despite the fact that the melt pool formed with $E_{V,2}$ (red dotted line) cools somewhat slower that the one formed with the lower $E_{V,1}$ (green dashed line), both thermal paths avoid crossing the crystallization nose and lead to vitrification. Yet, we see that there exists a kind of cyclic, abating reheating effect that can be addressed to the influence of the HAZ formed due to melting in adjacent regions (e.g. neighboring melt tracks or melting in upper layers). While the overall energy input in case of $E_{V,1}$ is still low enough to prohibit crystallization, the process conducted with $E_{V,2}$ ultimately crosses the crystallization nose and creates a partially crystalline specimen. Hence, there usually exists an alloy-specific E_V range that balances the issues of LOF and crystallization and

allows for AM-formed parts with optimized technological (mechanical) properties [4,17,206–209]. The present Papers V and VI will demonstrate such process parameter optimization attempts on hand of the $Cu_{47}Ti_{34}Zr_{11}Ni_8$ alloy and its derivates as well as the $Ni_{62}Nb_{38}$ alloy. The respective parameter optimization studies for $Zr_{59.3}Cu_{28.8}Al_{10.4}Nb_{1.5}$ that create the foundation Paper IV can be found in its direct predecessor publications [8,17].

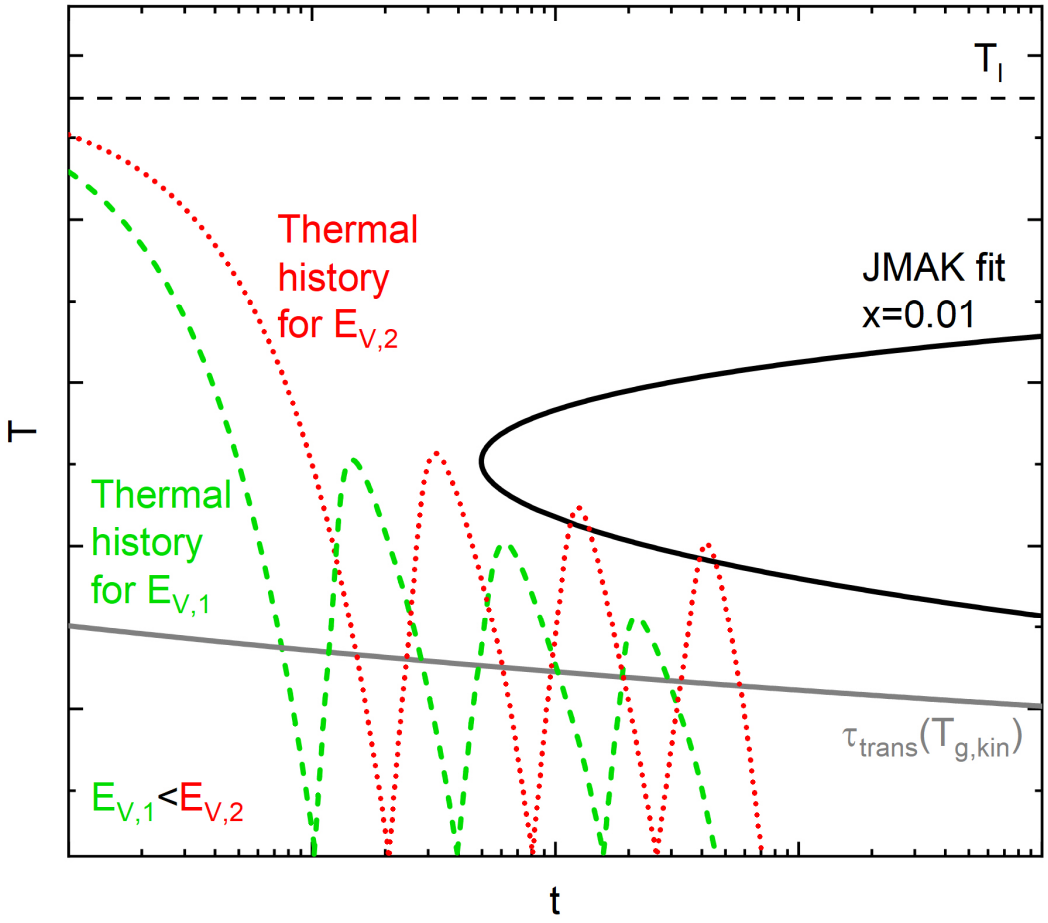

Figure 3.9: Comparing two (simplified) thermal pathways during PBF-LB/M processing with different volume energy densities $E_{V,1}<E_{V,2}$ (green dashed and red dotted lines, respectively). The initial cooling of the melt pool is fast enough to ensure vitrification for both pathways. Yet, the influence of the HAZ causes a cyclic reheating, which causes partial crystallization in case of the processing with $E_{V,2}$.

3.4 Thermoplastic forming

In Chapter 2.8.3 it is explained that metallic glasses can show superplasticity at temperatures near the thermal glass transition, and this naturally also holds true when heating directly into the supercooled liquid state. Originally known from thermoplastic polymers [210], thermoplastic forming (TPF) capitalizes on the superplasticity effect to

reshape and restructure amorphous metals into new geometries [65,66,211]. Figure 3.10 illustrates a possible TPF setup and explains the thermal protocol on hand of a TTT diagram.

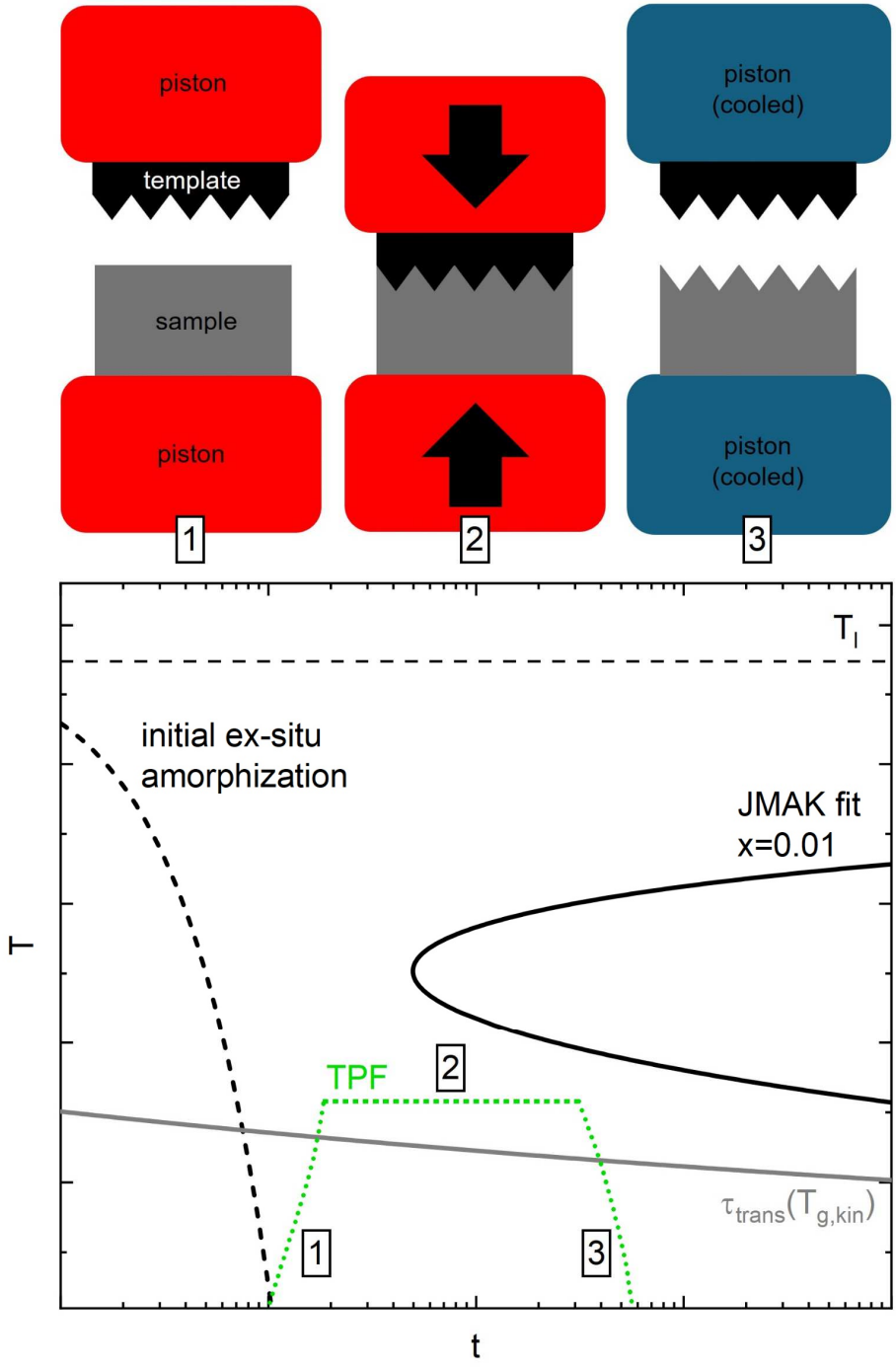

Figure 3.10: A graphical scheme of a TPF process in combination with a TTT diagram that clarifies the corresponding thermal protocol. In the first step, an ex-situ produced amorphous sample is placed between two pistons and heated into the SCL state. In the second step, the sample is pressed between the pistons to adapt the shape of a respective template while being held at an isothermal. In the third and last step, the sample is cooled back into the glass to avoid crystallization.

A fully amorphous specimen is heated into the supercooled liquid state (step 1). The actual thermoplastic forming is then conducted during an isotherm (step 2) by applying a mechanical load that shears and presses the supercooled liquid to adapt the shape of the respectively given template form (which is a simple serrated structure that imprints the part's surface in the present depiction). Finally, the material is quickly cooled back into the glass (step 3) to preserve full amorphicity, leaving us with a thermoplastically reshaped BMG part. TPF usually operates at temperatures distinctly below the crystallization nose, where the sluggish, growth-controlled crystallization kinetics allow for a certain processing time. Typically, such processing windows can reach from some seconds up to a few minutes, depending on the chosen temperature and of course the thermal stability of the respectively used alloy [211,212].

3.4.1 Thermoplastic forming of powder feedstock

In theory, TPF processing could be a viable route to overcome the size and geometry limitations of conventional casting. The basic idea would be to produce amorphous powder feedstock and then use TPF to compact it into dense parts with dimensions beyond the alloy's critical diameter. Initial studies with mm-sized pellets of a Pt-based alloy prove the principal feasibility of such a TPF compaction [65,213]. Yet, Bochtler et al. [211] showed on hand of the $Zr_{59.3}Cu_{28.8}Al_{10.4}Nb_{1.5}$ alloy that while powder consolidation into highly dense parts is possible via TPF, the achievable material strength is insufficient. Figure 3.11 indicates the reason for this issue: Due to the particle's surface oxide layers and the high viscosity at the comparably low process temperature, the powder particles cannot merge completely. Irregularly shaped porosity and the particle interfaces remain as internal stress risers, causing premature, intergranular fracture under stresses of only a third of the material's actual yield strength. Similar results were shown e.g. by Ciftci et al. [214]. Hence, PBF-LB/M remains as the only well-established processing route to create metallic glass samples with sizes beyond the critical diameter.

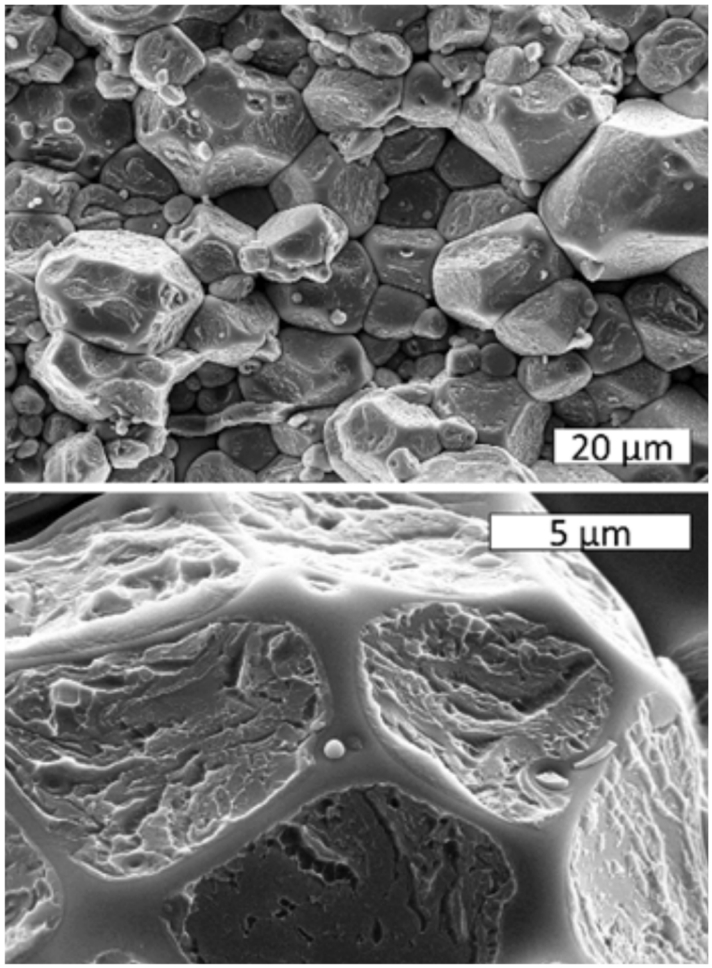

Figure 3.11: SEM images of the fracture surface (after beam bending) of an amorphous $Zr_{59.3}Cu_{28.8}Al_{10.4}Nb_{1.5}$ part that was TPF-consolidated from powder material. The granular structure of the initial powder particles is clearly visible. The lower, zoomed-in image shows that the edges of the particle surfaces were not completely connected to the other particles, resulting in irregularly shaped pores that act as stress-risers and cause premature failure under mechanical loads. Taken from [211].

3.4.2 TPF post-processing of cast and additively formed parts

TPF processing has been demonstrated in various studies to be a powerful tool for reshaping and imprinting cast metallic glasses. Due to the absence of crystalline grain structures, metallic glass formers can replicate structures even on sub-micrometer length scales [65,215], as illustrated in Figure 3.12. Furthermore, blow molding was successfully applied for metallic glass formers [216,217], a procedure that is probably best known from the industrial production of PET water bottles. Nevertheless, TPF processing of BMGs remains challenged by embrittlement problems that can stem from partial crystallization or from a very structurally relaxed glassy state [215,218,219]. In Paper IV, it will be shown for the first time that PBF-LB/M-formed BMGs, in this case the well-established $Zr_{59.3}Cu_{28.8}Al_{10.4}Nb_{1.5}$ alloy, can be successfully postprocessed via TPF, too.

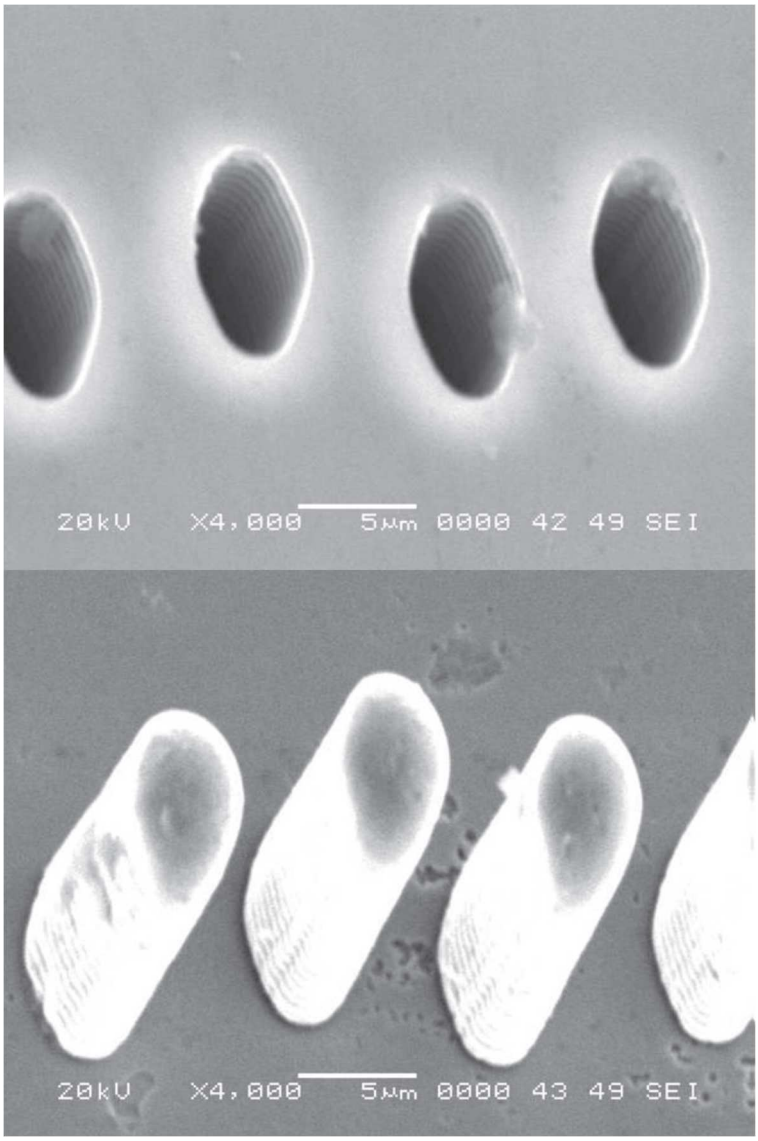

Figure 3.12: SEM images of a Pt-based metallic glass former (lower image) that replicates the fine, sub-micrometer structures of a silicon mold (upper image) after TPF processing. Taken from [65].

4. CHARACTERIZATION

All analyzing and characterizing techniques used in this work will be introduced in the following. Chapter 4.1 explains all *Calorimetry* methods and foundations, while Chapter 4.2 will do the same in terms of *Rheology*. The large topic *of X-ray diffraction* is introduced in Chapter 4.3. The Chapters 4.4 and 4.5 will then briefly explain the *Microscopy* and *Mechanical testing* approaches used. At the end of each chapter, a section named '*Experimental details*' is attached to clarify specific measurement conditions and in which context the respective technique was used.

4.1 Calorimetry

The term calorimetry describes a subfield of thermal analysis that focuses on the detection of heat flows, usually as a function of temperature or time. More specifically, the present work utilizes differential calorimetric methods that quantify the heat flows in or from the measured sample in relation to a reference [220]. Here, we differentiate between the methods of differential thermal analysis and differential scanning calorimetry. These methods and their specific subtypes will be explained in the next chapter, followed by an introduction of the different measurement types used in this work.

4.1.1 Types of differential calorimeters

In differential thermal analysis (DTA), the measurement setup consists of a furnace in which two symmetrical holders allow to position pans (also termed crucibles) of standardized weight, heat capacity, and material (aluminum, Al_2O_3, graphite, etc.). Figure 4.1 illustrates the principle. On the so-called sample side, the sample that shall be characterized is placed within the pan, the other pan on the reference side remains empty. Due to the symmetrical build and the standardized pans, it can be well-assumed that sample and reference side only differ through the presence of the sample. The temperatures on both sides are monitored by thermocouples and naturally follow the thermal changes of the furnace, e.g. upon heating at a constant rate. Under steady state conditions, the temperature on the sample side, T_S, lags behind the reference side temperature T_R due to the additional thermal mass of the sample, and a difference ΔT can be detected as [220]

$$\Delta T = T_S - T_R. \tag{4.1}$$

Any exothermic or endothermic thermal event occurring in the sample, e.g. a glass transition, or phase transitions like crystallization or melting, will provoke a respective increase or decrease in ΔT. Hence, ΔT is an indirect measure for the difference in heat flow HF between sample and reference side. Using a calibration factor K, HF can be calculated according to [220]

$$HF = \frac{dQ}{dt} = -K\,\Delta T. \tag{4.2}$$

K depends on manifold experimental factors, like the temperature, the applied rate of temperature change, or the thermal resistance of the setup. The overall robust construction of a DTA allows for a broad application range, especially for high temperatures beyond 2000 K. Yet, this comes with the drawback of a relatively high thermal resistance. Hence, the accuracy and sensitivity of a DTA is limited, in particular under faster heating and cooling rates.

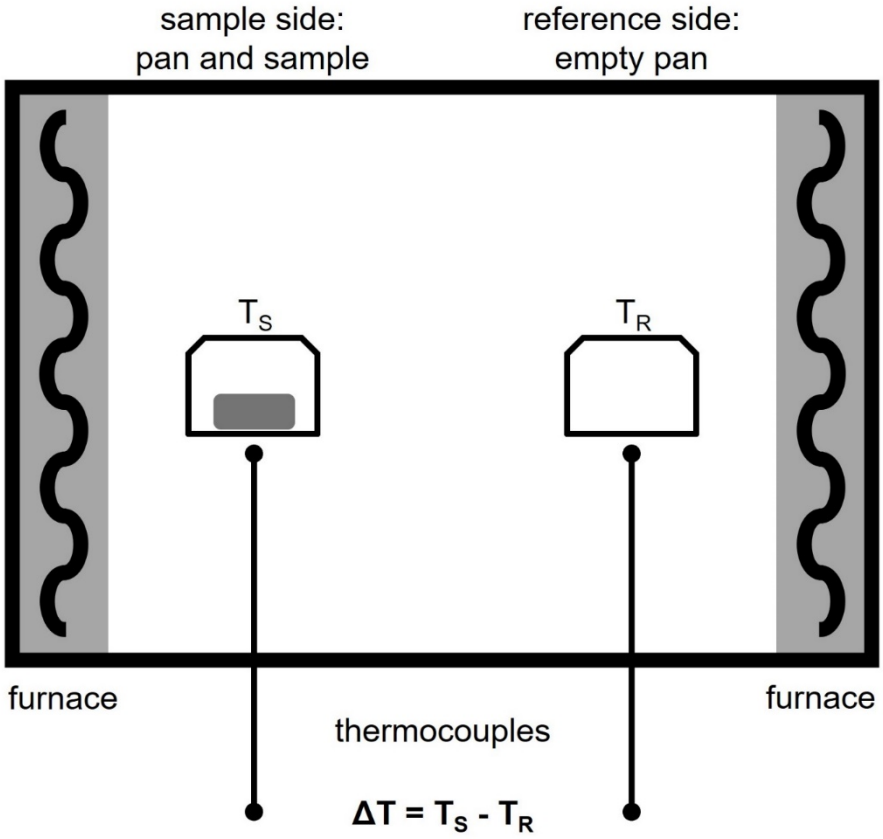

Figure 4.1: A schematic illustration of a DTA. The temperature difference between sample and reference side, ΔT, is detected through thermocouples and allows to calculate the differential heat flow HF in or from the sample.

This issue is addressed by heat flux differential scanning calorimetry (DSC), which can be seen as an enhanced derivative of the DTA. Figure 4.2 illustrates such a device built in the flux plate type setup. The measurement principle is the same as for the DTA, but the thermal resistance is massively decreased through a 'thermal bridge', the flux plate, that connects furnace, sample, and reference side and establishes a fast heat transfer. This allows for improved sensitivity and accuracy, especially under fast temperature changes. In exchange, a heat flux DSC often cannot reach the high temperatures achievable by DTA.

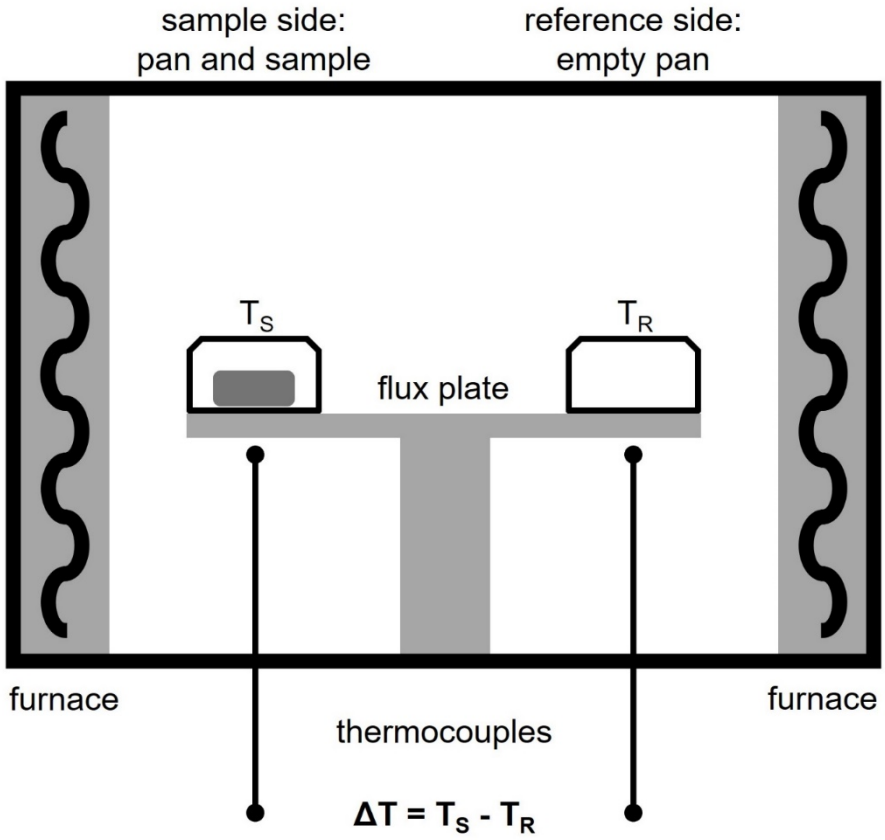

Figure 4.2: A scheme of a heat flux DSC setup. The working principle is similar to a DTA, but here, sample and reference side are connected through a flux plate, creating a much faster heat transfer and reducing the thermal resistance accordingly.

A different approach is found in a power compensated DSC, which is sketched in Figure 4.3. The sample and reference side consist of two identical furnaces with thermocouples, both isolated from each other. The furnaces are subject of the same time-temperature program, e.g. a heating scan. Instead of passively tracking the temperature difference, the device actively regulates the heating power P of both resistive furnaces in order to minimize the thermal offset, which is known as the 'null principle' ($\Delta T \cong 0$). The measurement signal of a power compensated DSC is therefore the power difference ΔP [220]:

$$\Delta P = P_S - P_R. \tag{4.3}$$

Endothermic thermal events in the sample will necessitate a higher heating power P_S to meet the null principle, while exothermic events will decrease it. ΔP is almost identical to HF, but a calibration factor K' can accommodate for effects of higher order like e.g. small asymmetries between the furnaces or slight heat flow leaks of the setup [220]:

$$HF = -K' \Delta P. \tag{4.4}$$

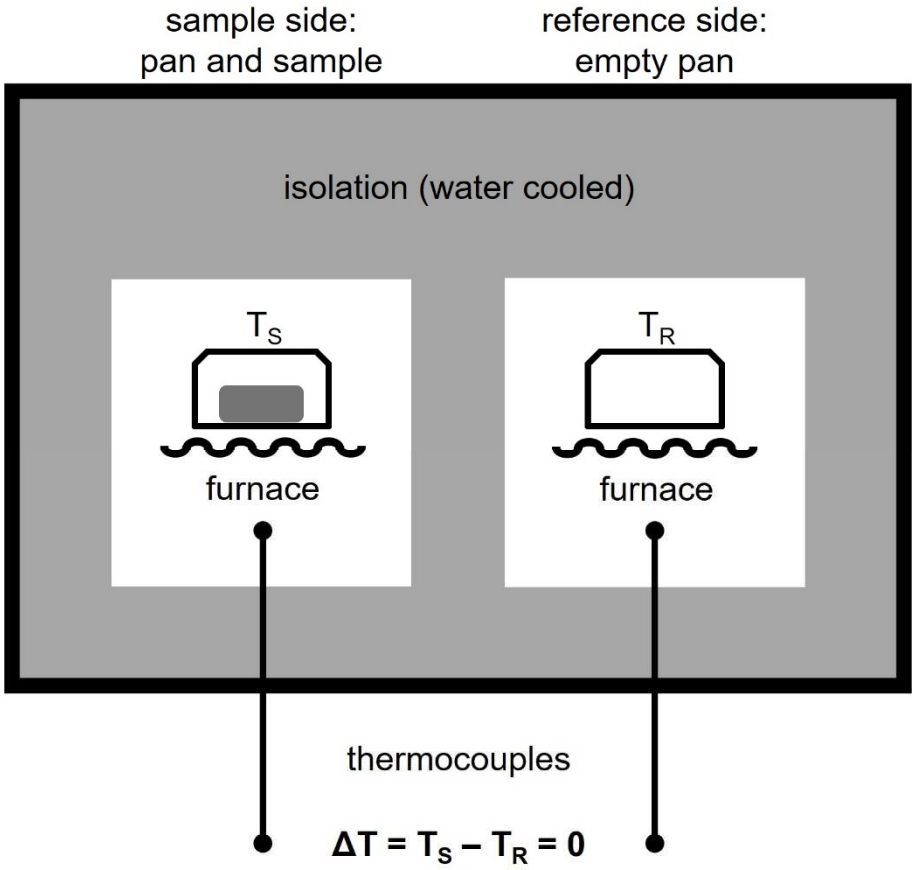

Figure 4.3: Schematical build of a powder compensated DSC. Sample and reference side are isolated from each other and heated separately. Occurring temperature differences are regulated towards zero (null principle) through a difference in heating power ΔP, which is approximately identical to the differential heat flow HF in or from the sample.

A special case of a power compensated DSC is the so-called fast scanning calorimeter (FSC). These chip-based devices allow for measurements under extremely fast temperature changes, which is achieved through a massive size reduction of the sample and the calorimeter itself [221–225]. The first commercially available FSC with a differential setup, hence being termed fast differential scanning calorimeter (FDSC), was introduced by Mettler-Toledo in 2010 in form of the FDSC1. The device allows for

temperature change rates beyond 10^4 K/s [226]. Its successor, the FDSC2+ allows to reach temperatures of up to 1273 K and further increases the achievable rates through an even smaller design of the chip calorimeter. Figure 4.4a) shows a microscopic image of the sample and reference side of the high-temperature UFH chip of the FDSC2+. The active areas (black circles) have a diameter of about 85 µm [32]. On the sample side, we see a specimen with a typical mass in the µg or even ng range, which was placed by using a manipulator device in form of a hair tip.

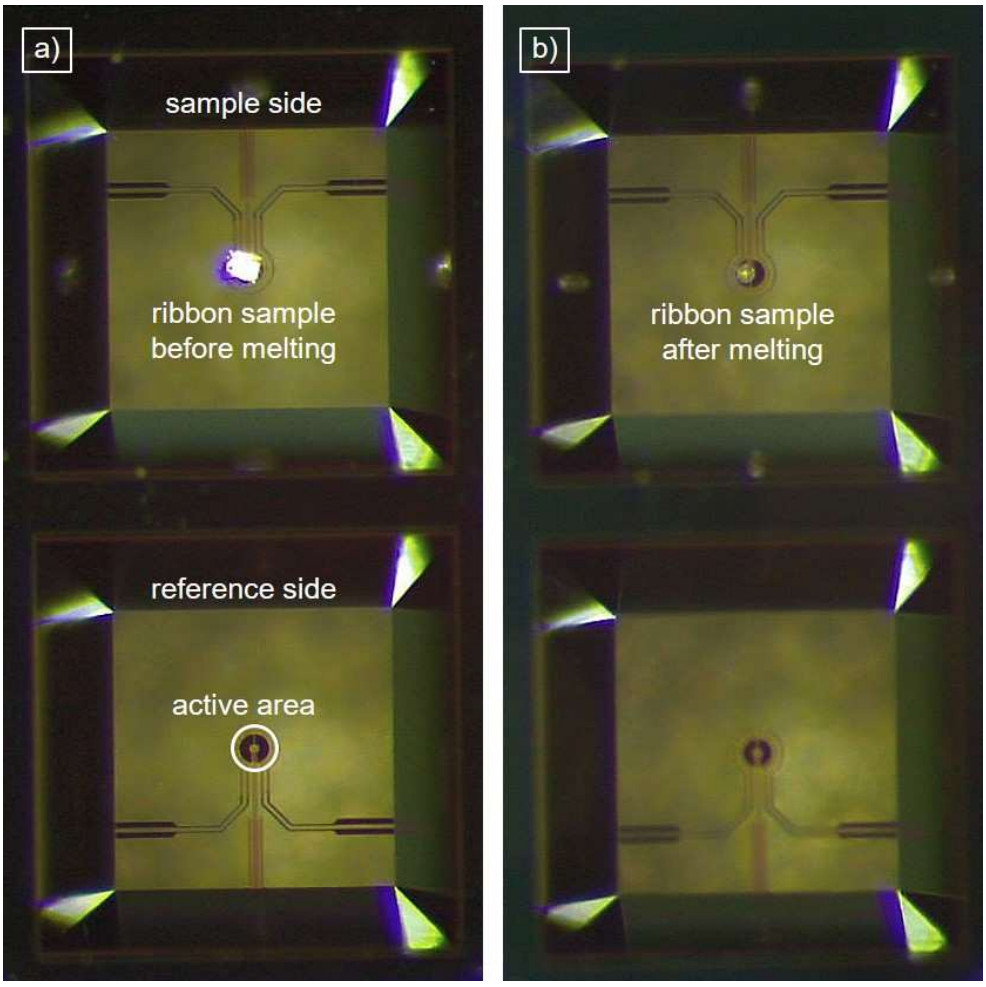

Figure 4.4: Sample and reference side of the high-temperature UFH chip of the Mettler-Toledo FDSC2+. In a), a fresh ribbon sample is placed on the active area of the sample side. On the reference side, the active area (ca. 85 µm in diameter) is exemplarily marked by a white circle. In b), the sample has been molten. It has changed to a (half-)spherical shape and formed a solid connection to the chip that allows for fast heat transfer.

Conventional DTAs and DSCs, see above, usually necessitate a new sample for each measurement, since a once crystallized metallic glass former cannot be quenched into the glass again since these devices usually lack the possibility to apply cooling rates faster than the critical cooling rate. The FDSC follows a different approach. Here, the sample is

purposely molten on the chip, see Figure 4.4b), to form a direct and solid connection that results in a fast heat transfer and a respectively low thermal resistance. From this point on, crystallization stops to be a limiting issue since the glassy state can be easily reestablished by quenching the stable equilibrium melt at rates faster than the R_c. This allows to obtain large and consistent data sets through manifold measurement runs with one and the same sample. The fast rates of the FDSC furthermore institute experimental approaches that were completely unthinkable with conventional DSCs, as will be shown in the following chapters.

4.1.2 Temperature scanning measurements

Temperature scanning measurements are among the most common experimental procedures applied with DTA and DSC devices. Thereby, the temperature is raised at a constant rate q_h (e.g. 0.333 K/s or 1K/s) in order to determine the characteristic temperatures and enthalpies of the investigated metallic glass former.

Figure 4.5a) illustrates a typical thermogram of a BMG sample measured with such a temperature scan. Like in all thermograms of this work and all included publications, the 'endo. up' convention is used, i.e., endothermal heat flows head in the positive direction. We now recapitulate from Eq. (4.2) that HF=dQ/dt and furthermore, that under isobaric conditions, a system's change in heat dQ equals its change in enthalpy dH. Hence, the integral over HF (qualitatively) corresponds to the system's enthalpic state. Accordingly, Figure 4.5b) shows a schematic enthalpy trace of the measured BMG sample, as discussed in the following.

When the sample is heated to temperatures in vicinity of the kinetic glass transition, it may start to relax towards the equilibrium SCL state. Thereby, the glass lowers its enthalpy through an exothermal effect visible in the HF signal, which is referred to as 'enthalpy relaxation' or 'undershooting' [227]. With Chapter 2.4.3 in mind, enthalpy relaxation can be understood as an aging process occurring under non-isothermal conditions. Further heating leads to the actual kinetic glass transition event, which manifests as a sigmoidal-like rise of the HF to reach the SCL level. Thereby, the end of the glass transition can be accompanied by a distinct endothermal effect, the so-called 'enthalpy recovery' or 'overshooting' [227]. Here, the system absorbs additional enthalpy to fully establish the equilibrium and reach the SCL enthalpy trendline, see Figure 4.5b).

Enthalpy relaxation and recovery are highly dependent on the experimental conditions and the thermal history of the glass, more specifically, on the interplay between the cooling rate q_c during vitrification and the applied heating rate q_h of the temperature scan experiment. If the initial glass shows a high fictive temperature due to being vitrified under a high q_c (distinctly faster than q_h of the temperature scan measurement), then we will observe excessive enthalpy relaxation. Here, the rather slow experimental timeframe provides enough time for the highly unstable glass to relax and enthalpically 'undershoot' directly below T_g. In contrast, if the initial glass is already quite relaxed with a low fictive temperature, e.g. due to a slow q_c during vitrification (slower than the q_h of the experiment), we will observe pronounced enthalpy recovery. Here, the timeframe of the experiment is too fast for the glass to adapt to the SCL enthalpy trendline directly, the relaxed glass 'overshoots' and needs to consume additional enthalpy to equilibrate. We will later see in Chapter 4.1.4 that these kinetic effects can be minimized through a so-called standard treatment, in which the glass is established with the same rate with which the heating scan is conducted, $q_c=q_h$. Upon further heating, the supercooled liquid state is abruptly terminated by the exothermal crystallization event, which lowers the system's enthalpy on the much lower crystalline level, see Figure 4.5b). Ultimately, the crystalline state transforms back into the liquid at even higher temperatures via the highly exothermal melting process. To quantify the temperatures that are associated with these events, the tangent construction method is a widely used evaluation standard. The red dotted lines in Figure 4.5a) illustrate the determination of the onset and end of the glass transition, $T_{g,ons}$ and $T_{g,end}$, the onset of crystallization T_x, as well as the lower and upper threshold of the melting event, i.e. the melting temperature T_m and the liquidus temperature T_l. The length of the supercooled liquid region, $\Delta T_x=T_x-T_{g,ons}$, is a robust measure for the alloy's thermal stability upon heating. The associated enthalpies, namely the relaxation and recovery enthalpies ΔH_{rel} and ΔH_{rec}, the crystallization enthalpy ΔH_x, and the enthalpy of melting ΔH_m are determined by integration, as marked by the dark gray areas. These characteristic enthalpies are furthermore indicated in the enthalpy trace in Figure 4.5b).

Experimental details – Temperature scans are part of every paper of this work. For the specific experimental details, please see the respective description in these publications.

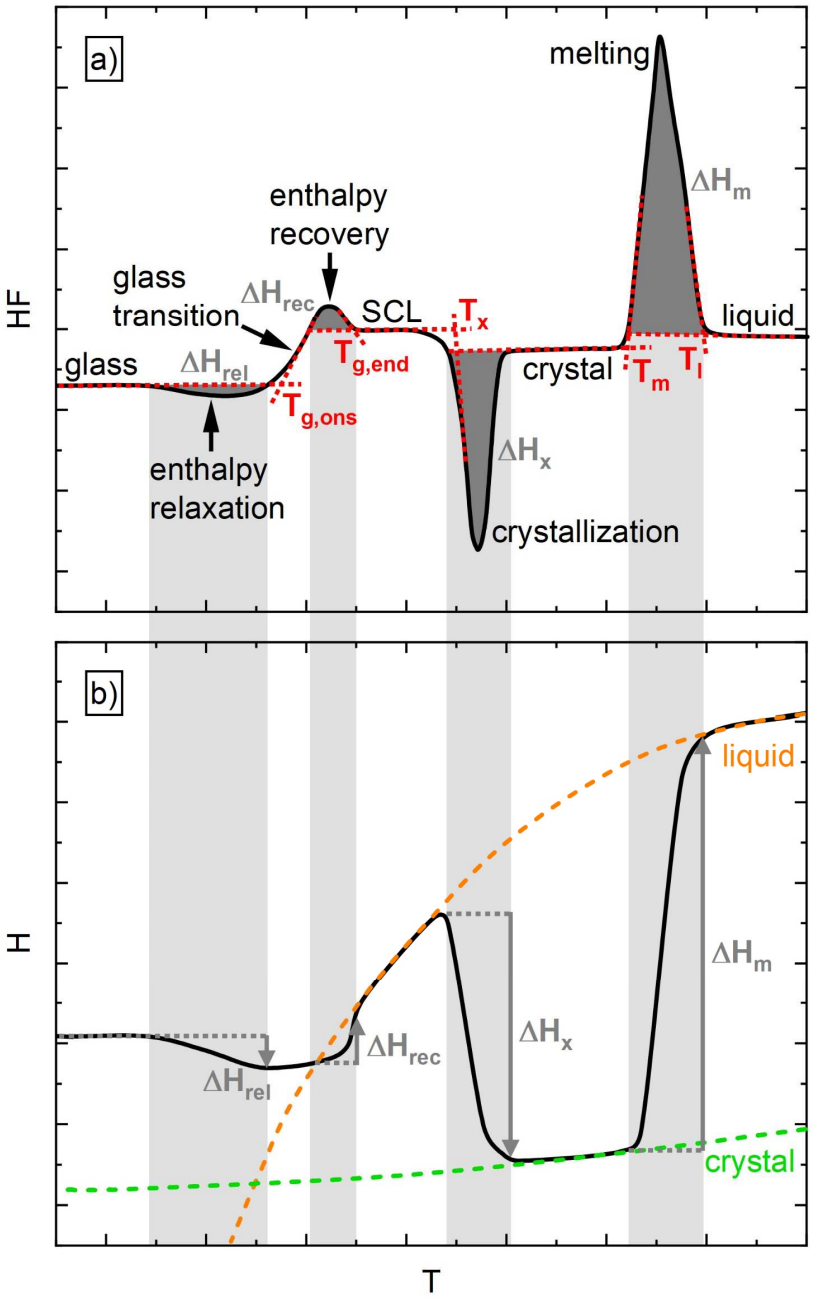

Figure 4.5: In a), the thermogram of a schematic DSC heating scan of a BMG sample is illustrated. Characteristic events are indicated, the associated temperatures are determined through tangent methods. Characteristic enthalpies are obtained through integration over the respective HF signals. In b), the enthalpy curves of the crystalline and liquid state are drawn. The black curve sketches the enthalpic trace of the DSC scan shown in a). Gray arrows and light gray backgrounds further indicate the determined characteristic enthalpies.

4.1.3 Determining the dynamic glass transition

As described in Chapter 2.3, probing the dynamic glass transition requires an experimental stimulus to provoke a respective response of the measured material while still fulfilling the linear response criterium. In terms of calorimetry, this can be achieved

through temperature modulation, which was firstly demonstrated in 1971 by Gobrecht et al. [228]. This term refers to a periodic temperature alternation pattern that is superimposed onto another temperature program, e.g. a temperature scan or sometimes on an isotherm. Respective experimental approaches can be generally subsumed under the term modulated DSC (MDSC) [229–232]. In the present work, we apply two different experimental approaches. The first one is the subject of Paper I [1], namely a conventional MDSC procedure [229,230] (further referred to as 'MDSC') using a heat flux DSC and the reversing/non-reversing analysis scheme. The second one will be a FDSC-based approach, further termed the 'step response method' [233,234], which furthermore interprets the material's heat capacity as a complex property to analyze the data.

The MDSC procedure using a conventional heat flux DSC applies a simple sinusoidal modulation. In this case, the time-temperature program T(t) of a modulated temperature scan would be

$$T(t) = T_{start} + q\ t + A_T \sin(\omega\ t) \tag{4.5}$$

and the time-dependent rate q(t) results from dT(t)/dt as

$$q(t) = q_0 + A_T\ \omega \cos(\omega\ t). \tag{4.6}$$

T_{start} describes the start temperature of the measurement, q_0 is the constant rate of the underlying temperature scan. The sinus-bearing summand describes the modulation with the temperature amplitude A_T and the angular frequency $\omega=2\pi f=2\pi/P$ (f being the frequency and P being the period of modulation). Figure 4.6a) illustrates the time-temperature program of an exemplary MDSC heating scan. The inset graphically highlights the parameters q_0, P, and A_T. Naturally, the measured BMG sample responds with a raw signal in form of a sinusoidally modulated heat flow $HF_{mod}(t)$, see Figure 4.6b). HF_{mod} transports information about the kinetic glass transition, which is dependent on the underlying rate q_0, but also about the frequency-dependent dynamic glass transition, which is determined by the applied modulation period P. To separate these effects, HF_{mod} is analyzed via a Fourier transformation over a sliding time window (in the size of P) in order to determine its amplitude A_{HF} and its average value. The latter provides us with the total heat flow HF_{tot} [232]. HF_{tot} is basically the signal one would expect from a non-modulated temperature scan at the rate q_0. Hence, the HF_{tot} curve in Figure 4.6b) shows

the typical, rate-dependent appearance of the kinetic glass transition upon heating. In contrast, A_{HF} provides knowledge about the dynamics.

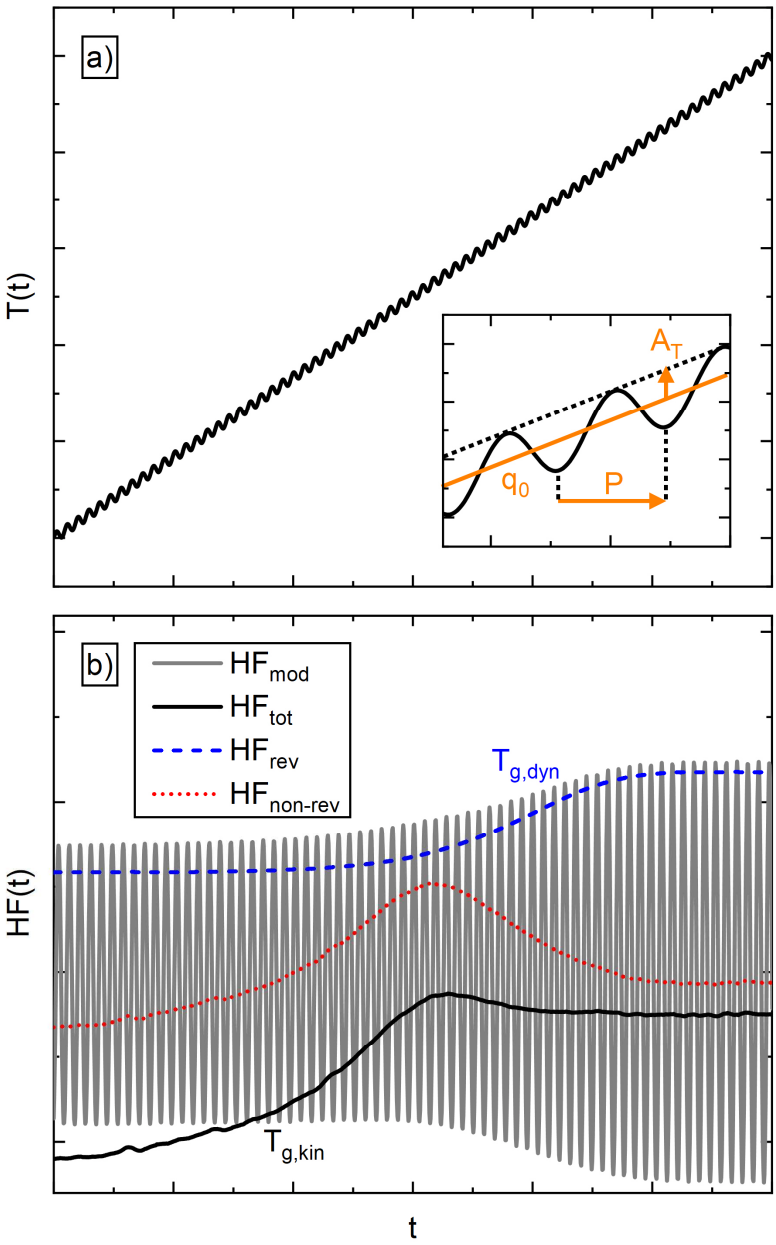

Figure 4.6: a) A modulated time-temperature program of an exemplary MDSC heating scan on a metallic glass former. The inset further provides a zoomed-in representation and clarifies the meaning of the parameters q_0, P, and A_T. b) The modulation provokes a modulated heat flow response $HF_{mod}(t)$. The total heat flow $HF_{tot}(t)$ shows a kinetic glass transition event, which is further emphasized in its 'kinetic' component, the non-reversing heat flow $HF_{non\text{-}rev}(t)$. The reversing heat flow $HF_{rev}(t)$ corresponds to the 'dynamic' component of $HF_{tot}(t)$ and shows a dynamic glass transition event at higher temperatures in form of a sigmoidal-like rise.

Recalling the Deborah number concept, De, from Equation (2.20), the period P determines the experimental time of the modulation as $t_{exp}=1/\omega=P/2\pi$. When approaching $T_{g,dyn}$, i.e. when $De=\tau/t_{exp}$ approaches unity, α-relaxation processes can occur within one

modulation timespan and A_{HF} rises accordingly. Hence, A_{HF} allows to calculate the so-called reversing heat flow HF_{rev} as [232]

$$HF_{rev}(t) = q_0 \frac{A_{HF}}{A_T \omega}. \tag{4.7}$$

HF_{rev} can be understood as the contribution of HF_{tot} that is detectable in the 'reversing' modulation component. Therefore, HF_{tot} can be written as a sum of HF_{rev} and its counterpart, the non-reversing heat flow $HF_{non\text{-}rev}$ as [232]

$$HF_{tot}(t) = HF_{rev}(t) + HF_{non-rev}(t). \tag{4.8}$$

By comparing HF_{rev} and $HF_{non\text{-}rev}$ in Figure 4.6b), we see that HF_{rev} shows the typical signal of a dynamic glass transition, namely a sigmoidal-like rise that reflects the rising amplitude of HF_{mod}, A_{HF}. It shall be mentioned that $T_{g,dyn}$ is located in the thermally equilibrated SCL state, hence, $T_{g,kin}$ has already occurred thanks to the slow underlying heating rate q_0. The kinetic features of $T_{g,kin}$, like the undershooting and, more clearly visible in Figure 4.6b), the overshooting, are then pronounced in the remaining non-reversing part of HF_{tot}. Therefore, HF_{rev} and $HF_{non\text{-}rev}$ are often referred to as the dynamic and kinetic components of the heat flow. However, this distinction should not be overinterpreted, as discussed in [232].

Figure 4.7 shows the $HF_{rev}(T)$ curves of several modulated temperature scans with various applied modulation periods (the temperature corresponds to the underlying scan at the rate q_0). We see that $T_{g,dyn}$ shifts with changing period due to the Deborah number criterium for the dynamic glass transition, $\tau\omega=1$, see Chapter 2.3.3. Hence, changing P (and therefore ω) allows to determine the temperature dependence of τ, i.e., the fragility of the liquid. Furthermore, Figure 4.7 illustrates the procedure of determining $T_{g,dyn}$. The sigmoidal rise in $HF_{rev}(T)$ forms a peak in the derivative $dHF_{rev}(T)/dT$ (gray curve). Fitting this signal with a peak function allows to determine the maximum value, which marks the inflection point of $HF_{rev}(T)$ and provides a solid and often used criterium to define the temperature value of $T_{g,dyn}$ that corresponds to the applied angular frequency ω. From the Deborah number concept in Equation (2.20) then follows that at $T_{g,dyn}(\omega)$, the relaxation time τ equals the inverse angular frequency ω according to

$$\tau\left(T_{g,dyn}(\omega)\right) = \frac{1}{2\pi f} = \frac{1}{\omega}. \tag{4.9}$$

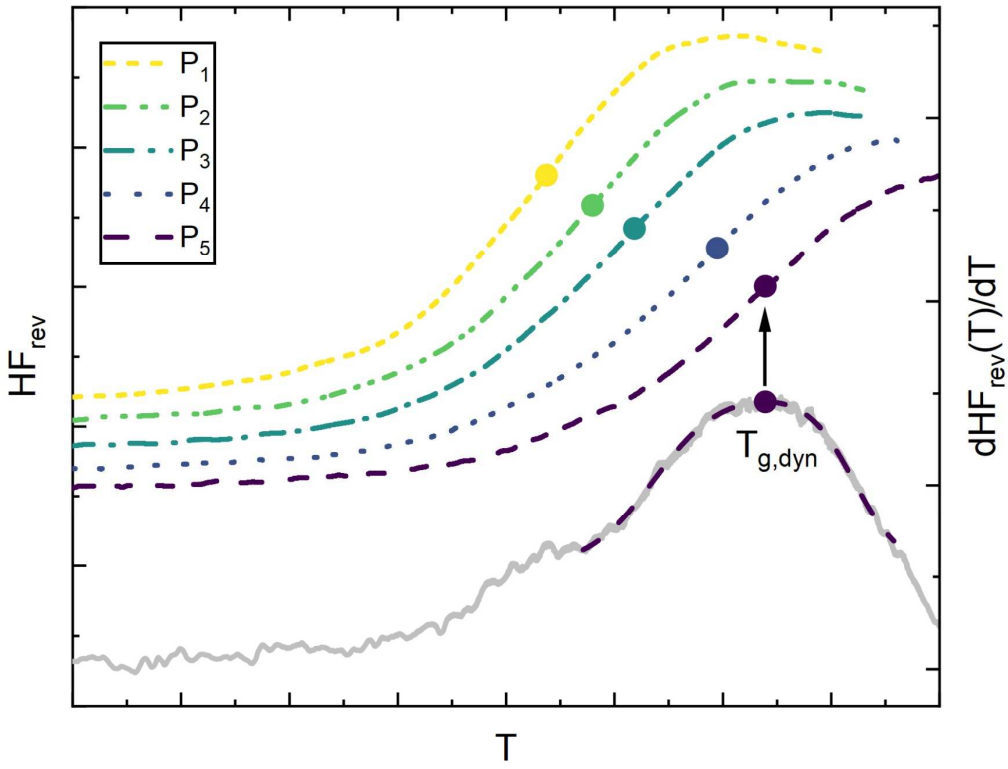

Figure 4.7: $HF_{rev}(T)$ for several MDSC heating scans on a BMG with different modulation periods applied (P_1 is the longest period, P_5 is the shortest). The temperature T thereby corresponds to the underlying rate q_0. The dynamic glass transition is determined as the inflection point of each curve by fitting the maximum of $dHF_{rev}(T)/dT$. Naturally, $T_{g,dyn}$ shifts with the applied modulation period, reflecting the fragility of the SCL.

The just introduced MDSC procedure is relatively easy to handle mathematically, since it operates with a harmonic oscillation. This means that modulation and system response (mostly) follow a sinus function characterized through a single frequency. However, temperature modulation can also be brought in by a non-sinusoidal, hence, non-harmonic stimulus, e.g. in form of a sawtooth-shaped modulation, which provokes a respective non-harmonic response. Fourier analysis allows to describe these non-harmonic signals as the sum of various sinusoidal functions with different frequencies and amplitudes. The step response analysis method utilizes such an approach to determine dynamics over a broad timescale spectrum from a single measurement. Originally applied with conventional DSC [235], step response analysis has proven as a vital tool to combine the opportunities of modulated experiments with the capabilities of the emerging FDSC technology [32,233,234,236]. The basic principle is to scan the temperature range of interest through an asymmetrical sawtooth-shaped time-temperature program, consisting of small but fast temperature steps that alternate with isothermal segments. Figure 4.8a) illustrates a single step-isotherm sequence, which is part of a larger cooling program that scans

through the SCL and the kinetic glass transition. The fast cooling step induces a corresponding exothermal spike in the heat flow (gray curve), which decays over the course of the isotherm. Fourier analysis of this heat flow signal HF(t) and the temperature change rate q(t)=dT/dt then allows to determine the complex heat capacity $c_p^*(\omega)$

$$c_p^*(\omega) = c_p'(\omega) + i\, c_p''(\omega) \tag{4.10}$$

for each isothermal temperature according to

$$c_p^*(\omega) = \frac{\sum_{k=1}^{n} HF(t_k)\cos(\omega\, t_k) - i\sum_{k=1}^{n} HF(t_k)\sin(\omega\, t_k)}{\sum_{k=1}^{n} q(t_k)\cos(\omega\, t_k) - i\sum_{k=1}^{n} q(t_k)\sin(\omega\, t_k)}. \tag{4.11}$$

Here, $c_p'(\omega)$ and $c_p''(\omega)$ refer to the real (or storage) and the imaginary (or loss) component of the heat capacity. The index k identifies each data point of the respective step-isotherm segment. From this, the reversing heat capacity $c_{p,rev}(\omega)$ can be calculated as the modulus of $c_p^*(\omega)$ according to [236]

$$c_{p,rev}(\omega) = \sqrt{c_p'(\omega)^2 + c_p''(\omega)^2}. \tag{4.12}$$

The slowest modulation that can be evaluated is the so-called base harmonic. It is determined by the duration of the isotherm, indicated by the gray background in Figure 4.8a), which equals to its base period P_1 and defines the base frequency $f_1=1/P_1=\omega_1/2\pi$ [235]. Higher frequencies are termed higher harmonics and constitute as integer multiples of f_0. Figure 4.8a) illustrates this by exemplarily marking the periods of f_1, $f_3=3f_1$, and $f_7=7f_1$. The respectively colored points and the gray background in Figure 4.8b) illustrate the (normalized) $c_{p,rev}(\omega)$ results for the three frequencies that are indicated in the single step-isotherm segment in Figure 4.8a). The entirety of step-isotherm segments in the step-wise scan procedure finally allows to establish the temperature-dependent curves for each harmonic, illustrated by the respectively colored lines. Again, we see that $T_{g,dyn}$ manifests as a frequency-dependent sigmoidal event. The corresponding temperature values are determined at the inflection point by using the derivative $dc_{p,rev}/dT$, as described above.

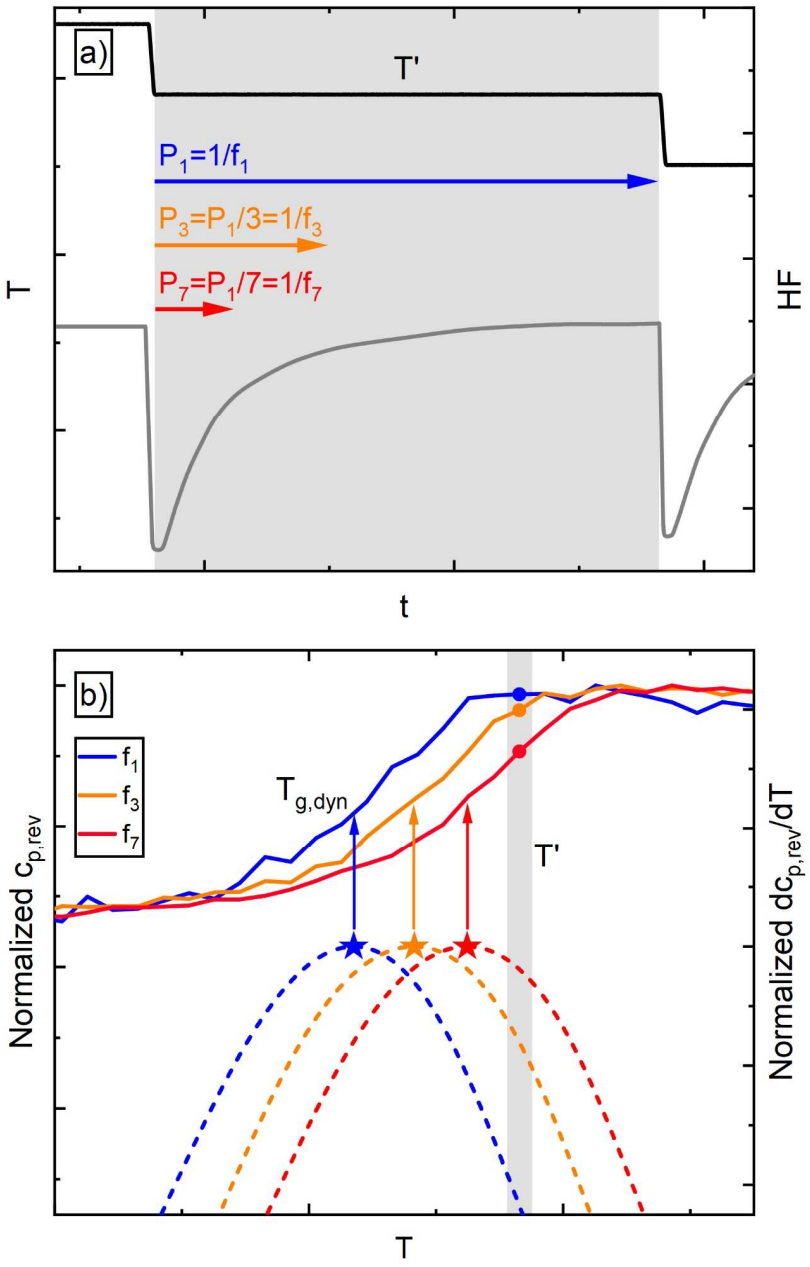

Figure 4.8: a) A part of the time-temperature program of a FDSC step response measurement. A single step-isotherm segment at the temperature T' is centered, the isothermal segment is highlighted by gray background. The blue arrow indicates the base harmonic with a period P_1 that equals the duration of the isotherm. The periods of two higher harmonics, P_3 and P_7, are also shown. In b), the temperature-dependent $c_{p,rev}$ curves (normalized to the SCL state value) for these three harmonics are shown. Colored circles and the gray background highlight the data that stems from a). The dashed curves show the peak fits of the (normalized) derivative $dc_{p,rev}/dT$, their maxima determine the dynamic glass transition for each harmonic.

Experimental details – The detailed experimental conditions and parameters of the conventional MDSC measurements shown in this work are explained in Paper I.

The step response measurements are performed with a Mettler-Toledo FDSC2+ to characterize the fragility of the $Pt_{42.5}Cu_{27}Ni_{9.5}P_{21}$ alloy. A Huber TC100 intracooler was used to create a sensor support temperature of 188 K during the experiments. A small ribbon piece was placed on a UFH1 high temperature chip and melted several times to establish a robust contact with high thermal conductivity. Prior to the step response measurement, the alloy has been heated to a maximum temperature of 973 K, roughly 100 K over the liquidus temperature, T_l= 874 K [70]. After equilibration for 10 s, the sample was cooled down to 593 K with 10000 K/s to bypass crystallization quickly [3]. Data acquisition started with the first loop, consisting of a 2 K cooling step followed by an isothermal segment. In total, 110 of such loops were repeated, across the kinetic glass transition temperature down to 373 K. Measurements were performed with two parameter combinations, namely 200 K/s cooling rate combined with a 1.014 s long isotherm and 2000 K/s cooling rate with a 0.1014 s long isotherm. Data acquisition rates were 1 kHz and 10 kHz to provide exactly k=1024 data points per step-isotherm segment. These two parameter sets allow for base frequencies of 1 Hz and 10 Hz, respectively. The sample mass was calculated to be about 350 ng from the measured enthalpy of melting [237,238]. All FDSC data was temperature corrected by using the melting event, as suggested by J. Schawe [239].

4.1.4 Measuring rate-dependent fictive temperatures

As explained through the FKR relation, see Equation (2.24) in Chapter 2.4.4, the kinetic glass transition is closely related to the dynamics of the SCL. Hence, measuring its rate dependence can serve as a measure for the system's fragility. In the following, we will discuss how to perform respective measurements with conventional DSC and FDSC experiments.

To determine a rate-dependent T_{fic} from a heating scan thermogram, Moynihan et al. [240] proposed an area matching procedure, which is illustrated in Figure 4.9 on hand of a DSC heating scan. SCL (HF_2 at T_2) are defined. The Moynihan method now allows to determine the fictive temperature of the analyzed glass through a comparison of two integral terms. The first integral, A, describes the area between the heat flow signal HF and the glassy baseline level HF_1, spanning between T_2 and T_1 as indicated by the gray background. In a first step, representative heat flow levels for the glass (HF_1 at T_1) and the equilibrium The second integral, B, describes the quadrangular area between HF_2 and

HF_1, spanning from T_2 to T_{fic} as marked by the shaded region. T_{fic} marks the temperature at which both integrals are equal, A=B, according to

$$\int_{T_2}^{T_1}(HF - HF_1)dT = \int_{T_2}^{T_{fic}}(HF_2 - HF_1)dT. \quad (4.13)$$

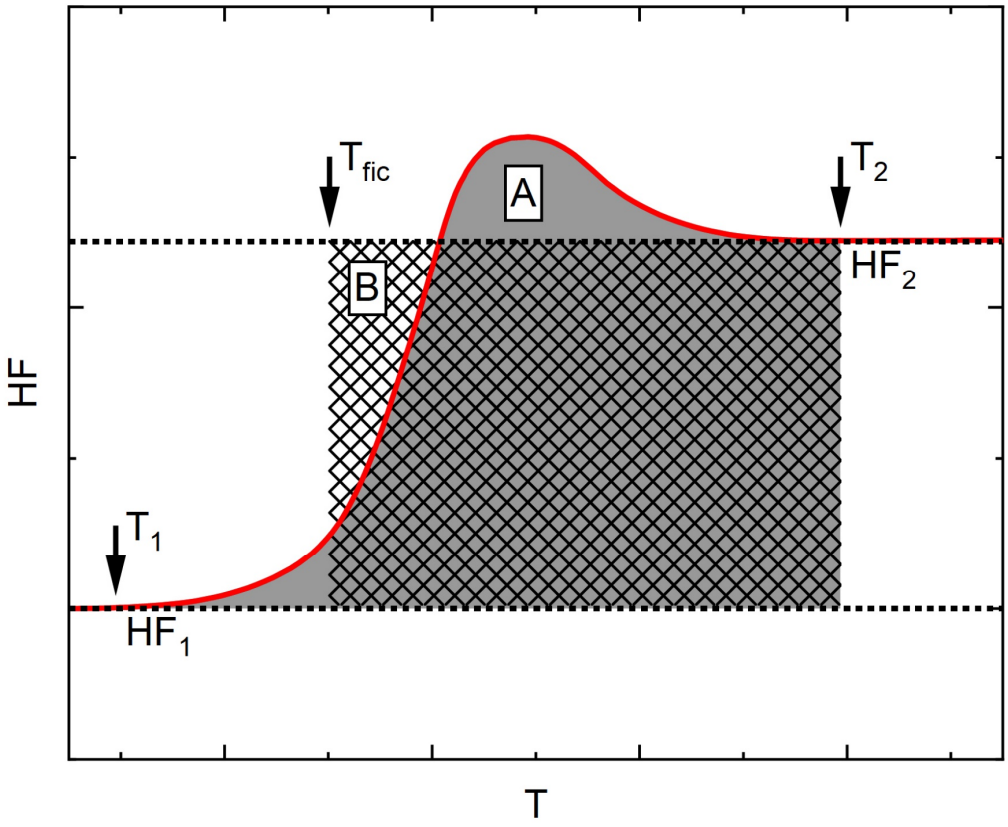

Figure 4.9: Moynihan area matching procedure to determine the fictive temperature from a DSC heating scan. Area A (gray background) is determined between the measurement curve and the glassy baseline HF_1 and in the temperature region between T_1 (glass) and T_2 (SCL). Area B (shaded) spans between the glassy baseline HF_1 and the SCL baseline HF_2, and between T_2 and T_{fic}. Through the condition A=B, T_{fic} is defined.

Evenson et al. [227] investigated the connection between the exact value of T_{fic} determined via the Moynihan method and the apparent glass transition onset $T_{g,ons}$ upon heating, which is defined through a simple tangent method, see Chapter 4.1.2. They found that under the precondition that the glass was formed under the same rate with which it was then reheated (q_c=-q_h), the effects of enthalpy relaxation and recovery can be minimized and the observed $T_{g,ons}$ upon heating equals T_{fic} (within ±1 K) [227]. This finding simplifies the determination of T_{fic} with conventional DSC devices. It further allows for the so-called T_g-shift method, in which each sample is subjected to a standard treatment protocol as demonstrated in Figure 4.10.

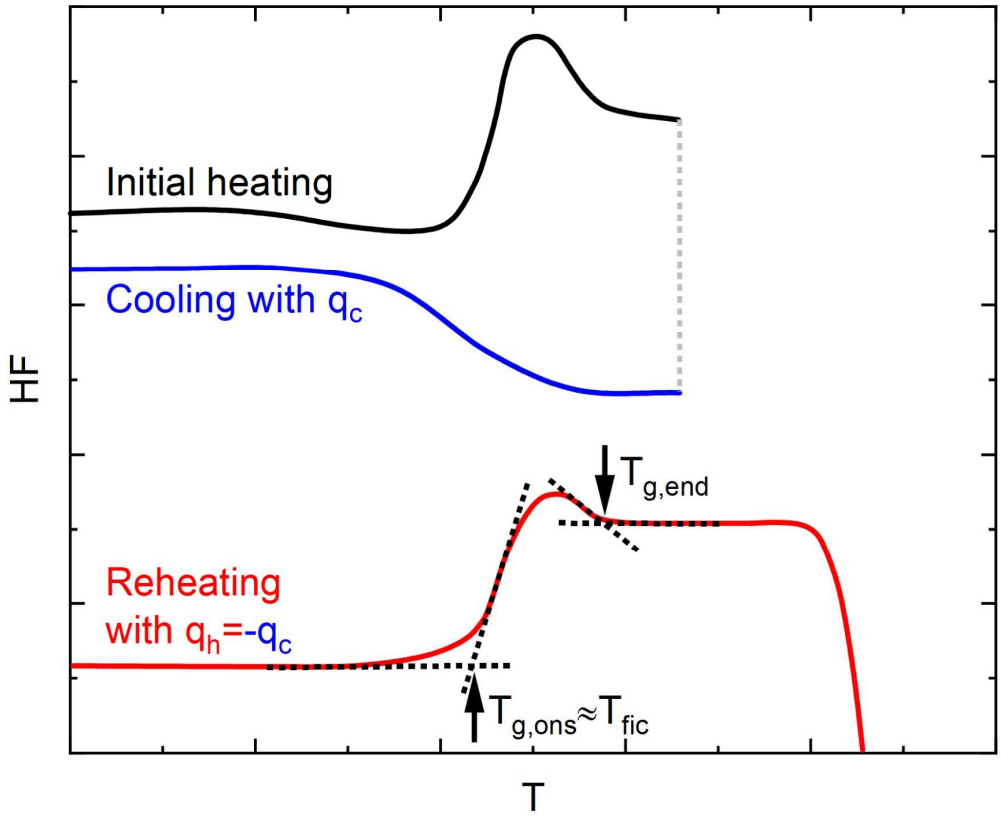

Figure 4.10: The standard treatment protocol used for T_g-shift measurements. In a first heating scan, the as-cast sample is brought in the SCL state to erase the thermal history of the cast process. Afterwards, the sample is cooled back in the glass with a rate q_c, followed by a second heating scan with q_h=-q_c. The glass transition onset of this curve then equals T_{fic}.

After heating in the SCL state, the sample is cooled back in the glass with a rate q_c and then reheated with q_h=-q_c. The glass transition onset upon heating then provides the fictive temperature that corresponds to q_c. From the temperature span of the kinetic glass transition, ΔT_g=$T_{g,end}$-$T_{g,ons}$, a transition time τ_{trans} can be calculated according to

$$\tau_{trans}(q_c) = \frac{\Delta T_g}{q_c}. \tag{4.14}$$

Applying this methodology for various rates allows to characterize the temperature-dependent (de-)vitrification kinetics, and hence, the fragility of the respective supercooled liquid. Yet, applying this T_g-shift procedure with an FDSC device would come with some drawbacks. The broad range of accessible heating rates comes hand in hand with significant differences in the signal-to-noise ratio among the obtained curves, thereby decreasing comparability. Also, largely different rates may come with large temperature offsets, making extensive calibration efforts necessary [239]. Hence, the FDSC-based T_{fic} measurements on the $Pt_{42.5}Cu_{27}Ni_{9.5}P_{21}$ alloy that are presented in this

work do not utilize the just described T_g-shift procedure but instead apply the Moynihan method.

Experimental details – An exemplary T_g-shift procedure conducted with a conventional power-compensated DSC on the $Pt_{42.5}Cu_{27}Ni_{9.5}P_{21}$ alloy can be found in [70]. The data obtained there will be used later for comparison and reference purposes.

The FDSC T_{fic} measurements are performed using the Mettler-Toledo FDSC2+ with a Huber TC100 intracooler that creates a sensor support temperature of 188 K. Each measurement run started with sample equilibration in the high-temperature melt at 973 K for 10 s, followed by cooling down to a temperature of 653 K (still in the SCL state) with 10000 K/s to evade the crystallization nose. From 653 K onwards, the sample was cooled with various cooling rates between 1000 and 5 K/s down to 193 K to vitrify the liquid with different fictive temperatures. In opposition to the T_g-shift procedure for conventional DSCs, the heating scans that follow each cooling were not conducted with $q_h=-q_c$, but with a fixed rate of 1000 K/s. This allows to consistently apply the Moynihan method in order to determine T_{fic}. The data analysis has been performed with the help of the Python program VITRIFAST, which is introduced and explained in detail in [241]. The rate-dependent transition times τ_{trans} that correspond to the different T_{fic} values again have been calculated according to Equation (4.14). As described in the previous chapter, the sample mass was estimated as 350 ng and all FDSC data was temperature corrected by using the melting event, as suggested by J. Schawe [239].

4.1.5 Determining a TTT diagram

The isothermal TTT diagram of BMGs can be determined by bringing an amorphous specimen to the temperature of interest T_{iso} and holding it for an adequate timespan to observe the complete isothermal crystallization process. The exothermal signal is analyzed through integration, as demonstrated in Figure 4.11a). Assuming a direct proportionality, the crystalline fraction x can be derived from the resulting integral curve $\Delta H_x(t)$ according to $x=\Delta H_x(t)/\Delta H_x$, where ΔH_x refers to the enthalpy change through a completed crystallization process. Figure 4.11b) illustrates the procedure, the positions of x=0.01, 0.50, and 0.99 are indicated. Measuring such isotherms at various temperatures allows to determine the shape and position of the crystallization nose in the TTT diagram. Detailed knowledge about the system's thermodynamics and dynamics furthermore

allows to model the obtained data with the JMAK model, as previously explained in Chapter 2.6.5.

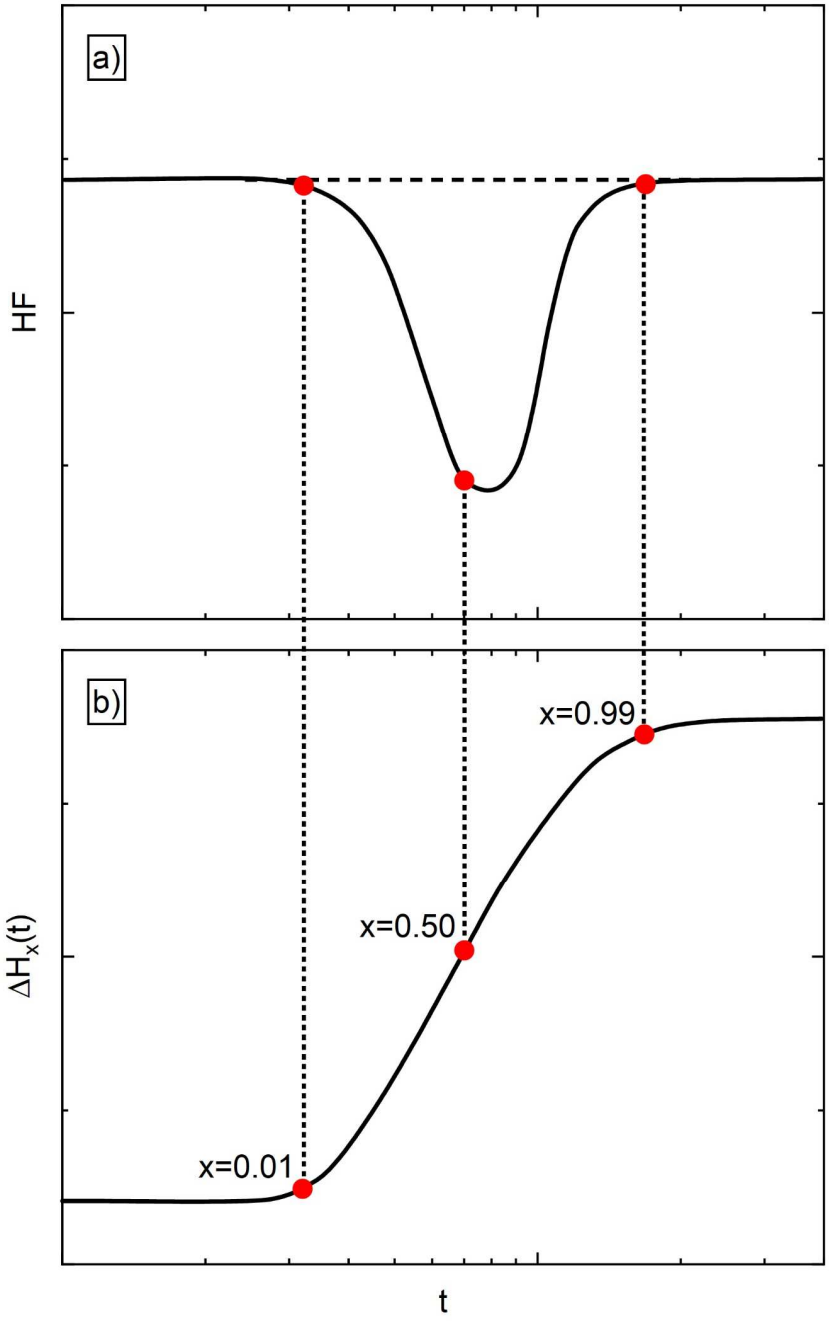

Figure 4.11: Scheme of an isothermal TTT measurement. a) Crystallization manifests as an exothermal event in the heat flow. b) Integration provides the crystallization enthalpy curve $\Delta H_x(t)$, which allows to approximate the crystalline fraction x.

Experimental details – When using a conventional DSC, two approaches are possible. As-cast amorphous samples can be heated to the desired T_{iso}. Alternatively, the sample might be equilibrated in the stable high-temperature melt before cooling down to the measurement temperature. For both approaches, the accessible T_{iso} are limited through

the achievable rates and the thermal stability of the system, since crystallization may start before the isotherm is reached. Hence, only the slower crystallization times at the lower and upper parts of the crystallization nose can be characterized via conventional DSC, the tip of the nose usually remains hidden. Gross et al. [71] exemplarily demonstrated such a conventional TTT determination on hand of the $Pt_{42.5}Cu_{27}Ni_{9.5}P_{21}$ alloy.

These incomplete $Pt_{42.5}Cu_{27}Ni_{9.5}P_{21}$ TTT data can be complemented through fast scanning calorimetry. Thanks to the possibility of ultra-fast temperature changes, isothermal FDSC studies allow to also characterize the fast crystallization kinetics at the tip of the crystallization nose, as demonstrated and explained in detail in Paper III [3].

4.2 Rheology

4.2.1 Viscosity measurements via thermo-mechanical analysis

Thermo-mechanical analysis (TMA) allows to measure dimensional changes of materials, e.g. in length or in volume, that occur as a function of temperature and applied stress. In a three-point beam bending (3PBB) setup of a thermo-mechanical analyzer as sketched in Figure 4.12, a beam-shaped sample of height h and width w is placed on two supports with a distance of L. By heating the setup to temperatures in vicinity of the glass transition and loading it with a force M, we can observe a viscous deformation over time. The resulting displacement in the center of the beam, u, is recorded. From the displacement rate $\dot{u}$=du/dt and the material's density ρ, the viscosity η of the material can be calculated as

$$\eta(t,T) = \frac{g\,L^3}{12\,w\,h^3\,\dot{u}}\left(M + \frac{5\,\rho\,w\,h\,L}{8}\right). \tag{4.15}$$

Experimental details – In the present work, equilibrium viscosity data of the $Pt_{42.5}Cu_{27}Ni_{9.5}P_{21}$ alloy from isothermal TMA experiments serves as reference for the MDSC results in Paper I, the XPCS results in Paper II as well as the extended fragility comparison in Chapter 6.3.3 of the discussion. The original TMA data was published in [71], where the details of the experiment and the evaluation can be found.

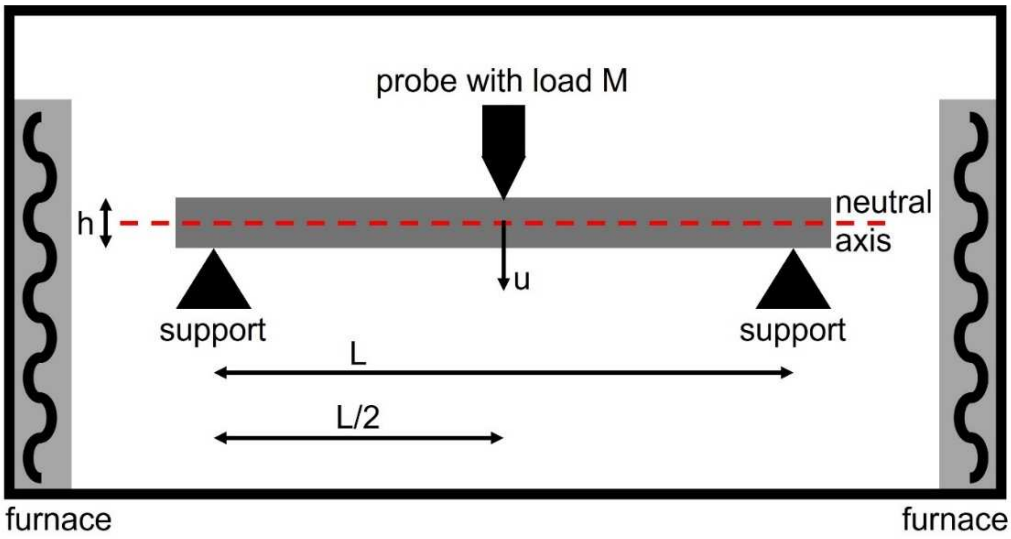

Figure 4.12: Schematic setup of a three-point beam bending TMA measurement. The beam sample is placed on two supports and its center is loaded with a loading force M. A furnace brings the sample to the desired measurement temperature, at which the sample displacement u is measured as a function of time.

4.2.2 *Dynamic-mechanical analysis to determine the dynamic glass transition*

Dynamic-mechanical analysis (DMA) is a thermal analysis method similar to TMA, but with the additional option to apply a periodic mechanical modulation to the sample [242]. Hence, DMA allows to introduce a measurement stimulus with a distinct frequency, which provokes a respective frequency-dependent material response. DMA can be therefore used to study the dynamic glass transition, in analogy to other modulated methods like the earlier introduced MDSC, see Chapter 4.1.3. Figure 4.13 illustrates a typical DMA setup in tension mode. A beam-shaped sample (e.g. a cast bulk sample or a melt-spun ribbon) is fixed between two clamps with the distance l_0. One of the clamps is stationary, the other is connected to a motor via a drivetrain, allowing to apply the mechanical stimulus. The device used in the present work is a so-called displacement-controlled DMA. This means that the sample length l(t) is modulated in a harmonic sinusoidal way (analogous to the MDSC temperature modulation) through an oscillation Δl(t) according to

$$l(t) = l_0 + \Delta l(t) = l_0 + A\sin(\omega\, t). \tag{4.16}$$

A is the modulation amplitude and ω is the angular frequency. The recorded material response is a force F(t) that opposes the length modulation as

$$F(t) = F_0 + S\,A\sin(\omega\, t - \varphi). \tag{4.17}$$

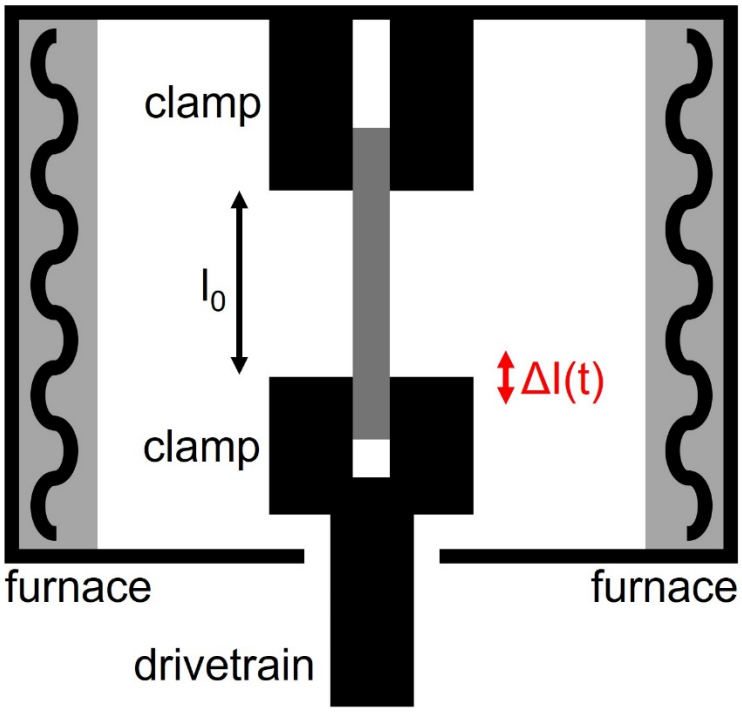

Figure 4.13: DMA measurement setup in tension mode. A beam-shaped sample is fixed between two clamps, one of which is connected to a motor via a drivetrain. The motor applies a specific mechanical length modulation Δl(t), which serves as the measurement stimulus. The material response in form of the resulting opposing force F(t) is recorded. A furnace system allows to control the temperature.

F_0 reflects a possibly applied preforce, which can prevent measurement artifacts like e.g. sample buckling in case of a thin melt-spun ribbon. S is the sample stiffness and φ describes the phase lag between the stimulus l(t) and the material response F(t). If the material behaves ideally elastic, F(t) is perfectly in phase with the imposed length protocol, hence φ=0. In case of (partially) viscous material behavior, φ is unequal to zero. Figure 4.14a) depicts exemplary l(t) and F(t) curves with an explicit phase shift. The elastic and viscous components of the material response can be expressed through the complex elastic modulus E^* as

$$E^*(\omega, T) = E'(\omega, T) + i\, E''(\omega, T). \tag{4.18}$$

The storage modulus thereby reflects the elastic component and basically corresponds to the Young's modulus one would obtain from e.g. a stress-strain diagram. Hence, E' can be calculated from the stiffness value by incorporating the sample width w and thickness t according to

$$E' = \frac{\sigma}{\varepsilon} = \frac{S\, l}{w\, t}. \tag{4.19}$$

The viscous component is reflected through the imaginary part of E*, the loss modulus E'', which is defined through the phase lag as

$$E'' = E' \tan(\varphi). \tag{4.20}$$

DMA measurements are often performed as isochronal temperature scans. Thereby, the temperature is slowly scanned with a low underlying rate while a mechanical modulation with a distinct frequency is applied. Figure 4.14b) illustrates the typical temperature behavior of E' and E'' for a BMG measured with such a procedure.

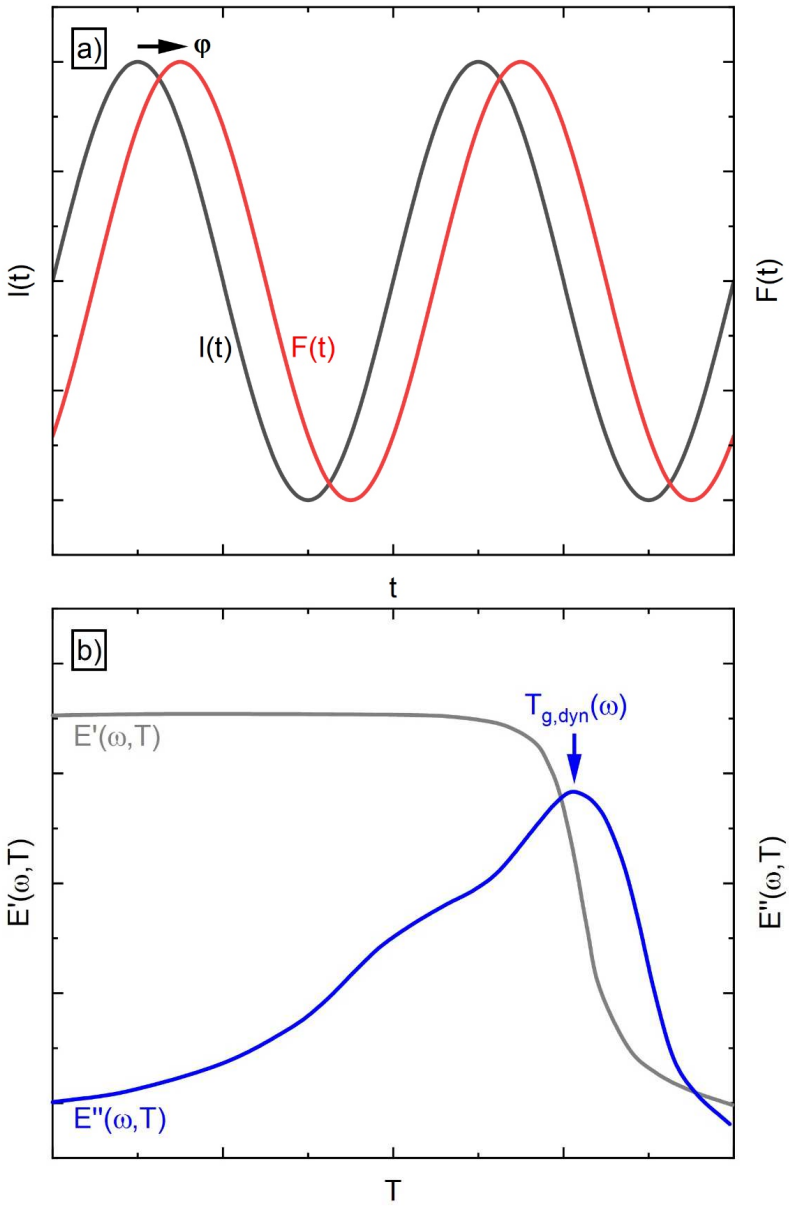

Figure 4.14: a) A typical phase lag between the length modulation l(t) and the recorded opposing force F(t) during a DMA measurement is illustrated. b) Exemplary storage and loss module curves obtained during an isochronal DMA temperature scan. At the dynamic glass transition, E' shows a sudden drop while E'' forms a maximum.

At lower temperatures in the glass, the sample behaves mainly elastic, and we observe a high and stable level of E' while E'' remains low. The material softens when approaching the supercooled liquid state, hence E' shows a sharp decrease while E'' increases. The frequency-dependent dynamic glass transition manifests as a peak in E''. Here, it follows from the Deborah number concept, see Chapter 2.3.3, that the relaxation time equals the inverse angular frequency, as described by Equation (4.9). Performing several isochronal DMA temperature scans with different ω allows to evaluate the SCL fragility, in analogy to the previously described MDSC procedure.

Experimental details – DMA temperature scans are performed by using a TA Instruments Q800 device in tension mode to characterize the fragility of the $Pt_{42.5}Cu_{27}Ni_{9.5}P_{21}$ system. Beam-shaped samples (ca. 0.3×13×2.5 mm^3) are cut from a tilt-cast plate (ca. 50×13×2.5 mm^3). A preforce F_0 of 0.25 N is used, the modulation amplitude A is 2 µm. The underlying heating rate is 3 K/min, measurement frequencies f are 0.1, 0.3, 1, 3, 10, and 30 Hz.

4.3 X-ray diffraction

If monochromatic electromagnetic radiation interacts with structures roughly in the size of the radiation's wavelength λ, diffraction can occur. This phenomenon is based on the wave-character of the radiation, which can, under certain conditions, lead to constructive or destructive interference among scattered waves, which is observed through distinct maxima in the intensity of the scattered radiation at certain angles. Due to their small wavelength, X-rays can only be diffracted by small structures on the nm or Å length scale, hence, X-ray diffraction (XRD) is a widely applied method to study atomic structures. A very fundamental model to describe XRD for crystalline structures was provided by W. H. Bragg [243]. His famous Bragg law is derived from the Huygens principle and provides a criterium for constructive interference of X-rays (i.e. Bragg peaks) that scatter at a crystalline lattice in the form of

$$2\,d\,\sin(\theta) = n\,\lambda. \tag{4.21}$$

Thereby, d describes the lattice parameter, Θ is the Bragg angle (which equals 90° minus the incidence angle), and n is the order of the maximum. Here, we can already notice an important characteristic of diffraction that will constitute a leitmotiv in the whole chapter:

structure size, here reflected through d, behaves inversely to the Bragg angle. In other words, the smaller the structure, the larger the angle under which constructive interference can be expected.

After briefly discussing the differences between conventional laboratory-scale X-ray sources on the one hand and highly sophisticated synchrotron radiation sources on the other, we will take a closer look at the theory and practice behind X-ray diffraction studies with incoherent radiation. Finally, we will concentrate on the topic of X-ray photon correlation spectroscopy, which requires coherent radiation.

4.3.1 Creating X-rays for diffraction studies

On a laboratory scale, X-rays are usually produced through X-ray tubes. The working principle is based on the thermionic effect. Under high vacuum, a cathode is heated to create free electrons through emission, which are then accelerated towards an anode made of a specific element. The electron bombardment then creates X-rays with a broad spectrum of wavelengths from the Bremsstrahlung effect but also X-rays with characteristic wavelengths. The latter are formed when an incoming electron collides with a bonded electron from an inner atomic shell, thereby ejecting it from the atom. An electron from a higher shell then captures the vacant energy level and the corresponding energy difference is emitted in form of a photon with an element-specific energy, hence the term characteristic X-rays. For most XRD applications, copper is used as an anode material, which provides a characteristic K_α radiation of 1.544 Å (8.03 keV).

Electron synchrotrons are large-scale research facilities that take X-ray creation to a completely new level in terms of experimental efforts and setup size. Figure 4.15 depicts the working principle of a synchrotron schematically. In a storage ring, often several hundreds of meters in diameter, electrons are accelerated to velocities near the speed of light and held on a circular path through complex installations of focusing and bending magnets. So-called undulators force the electrons to perform sharp directional changes through series of alternatingly polarized magnets, and these accelerations create highly energetic X-rays. This radiation is transferred to specific experiment stages, termed beamlines, that are arranged in a tangential manner around the storage ring. Here, the beam is further optimized by monochromatization and focusing before it is used for the actual experiment.

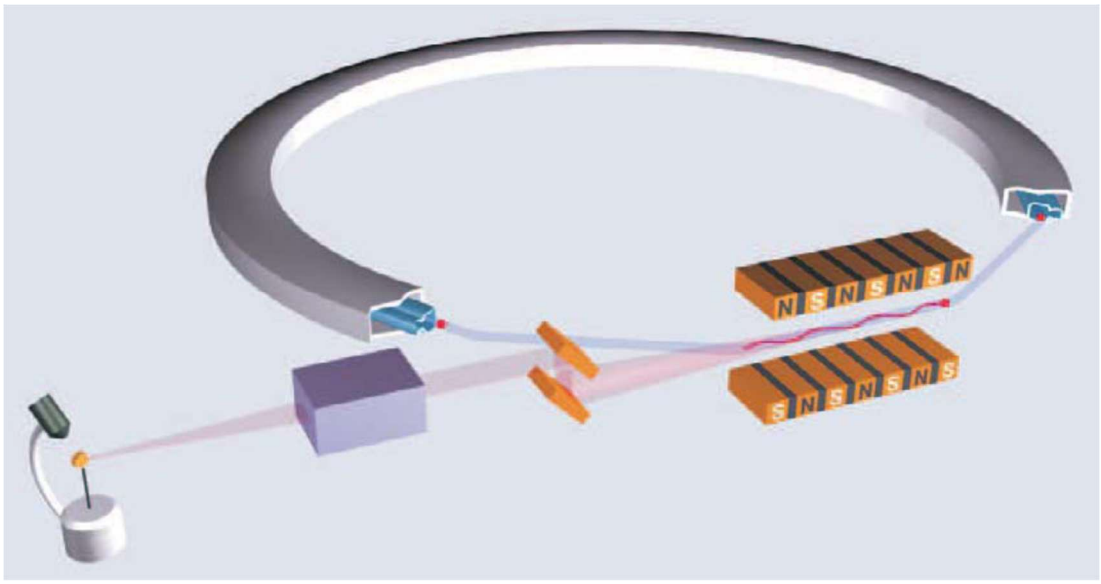

Figure 4.15: A schematic illustration of an electron synchrotron setup. Electrons are brought on a circular path in a large storage ring. An undulator accelerates these electrons to create highly energetic X-rays, which are further monochromatized and focused to be used for experiments in a beamline installation. Taken from [244].

Synchrotron-based diffraction studies allow for high beam energies in the range of 100 keV, hence, the term high-energy synchrotron XRD (HESXRD) has been established. Synchrotron radiation achieves brilliance levels that are unthinkable for conventional X-ray tubes, surpassing the latter by up to nine orders of magnitude. The brilliance B is a widely used quantity to rate the quality of a radiation source. It is calculated by normalizing the photon flux F with the beam cross-section A, the angular spread of the beam Ω, and the bandwidth $\Delta\lambda/\lambda$, which is a measure for monochromaticity according to

$$B = \frac{F}{A\,\Omega\,\frac{\Delta\lambda}{\lambda}}. \tag{4.22}$$

The extreme brilliance of synchrotron radiation allows to obtain diffraction patterns with outstanding signal-to-noise ratios within timescales of a few seconds, thereby enabling to draw meaningful conclusions about the diffracting atomic structures. Since the introduction of third generation synchrotrons, sophisticated beam optimization also allows to combine high photon flux with high levels of coherence, rendering advanced experimental approaches like X-ray photon correlation spectroscopy possible [245,246], see Chapter 4.3.3. For a deeper understanding of synchrotron technology, the reader is referred to respective literature [244,247].

4.3.2 X-ray diffraction with incoherent radiation

We start our theoretical considerations about XRD and HESXRD by envisioning that every electromagnetic wave can be described by a wave vector **k**. As a vector property, it incorporates a modulus k, termed the wave number, which basically encodes the wavelength λ, and a directional component that is oriented perpendicular to the wave front and describes the direction of wave propagation. In the following, we will only consider elastic scattering, i.e., there is no energy loss during the diffraction process. Hence, the wave number will not be altered, but the directional difference between incoming and diffracted wave with the respective wave vectors $\mathbf{k}_a$ and $\mathbf{k}_b$ is described by the diffraction vector **q** as

$$\boldsymbol{q} = \boldsymbol{k}_a - \boldsymbol{k}_b. \tag{4.23}$$

The wave number of **q** is thereby calculated according to

$$q = \frac{4\,\pi \sin(\theta)}{\lambda}. \tag{4.24}$$

Here, we see a direct link established between the diffraction vector **q** and the Bragg angle Θ from Equation (4.21). We now consider a sample volume that is irradiated with monochromatic (but incoherent) X-rays and consists of N atoms. Each atom will contribute to the overall (static) sample scattering amplitude Ψ(**q**) through its individual scattering amplitude $a_j(\mathbf{q})$ (also termed the atomic form factor) and its specific position vector $\mathbf{r}_j$ as

$$\Psi(\boldsymbol{q}) = \sum_{j}^{N} a_j(\boldsymbol{q})\ \exp\left(-i\ \boldsymbol{q}\ \boldsymbol{r}_j\right). \tag{4.25}$$

Experimentally, Ψ(**q**) is not directly accessible. Instead, any detector device records the photon counts as a function of **q**, i.e., the (static) scattering intensity I(**q**) being the squared modulus of Ψ(**q**) as

$$\begin{aligned} I(\boldsymbol{q}) &= |\Psi(\boldsymbol{q})|^2 = \Psi(\boldsymbol{q})\ \Psi^*(\boldsymbol{q}) \\ &= \sum_{j}^{N} f_j(\boldsymbol{q})\ \exp\left(-i\ \boldsymbol{q}\ \boldsymbol{r_j}\right) \sum_{k}^{N} a_j(\boldsymbol{q})\ \exp(i\ \boldsymbol{q}\ \boldsymbol{r}_k) \end{aligned} \tag{4.26}$$

$$= \sum_{j}^{N} \sum_{k}^{N} a_j(\boldsymbol{q})\, a_k(\boldsymbol{q})\ \exp\left(-i\, \boldsymbol{q}\, (\boldsymbol{r}_j - \boldsymbol{r}_k)\right),$$

with $\Psi^*(\mathbf{q})$ being the complex conjugate of $\Psi(\mathbf{q})$. We see here that $\Psi(\mathbf{q})$ predetermines at which $\mathbf{q}$ values (i.e. Bragg angles) constructive interference and the emergence of intensity maxima can be expected. Accordingly, $\Psi(\mathbf{q})$ incorporates the same information as the Bragg law in Equation (4.21), but in a quantitative, more generalized and sophisticated manner. Furthermore, $I(\mathbf{q})$ can be divided in a self part $I(\mathbf{q})_{self}$ (in case of j=k) and a distinct part (in case of j≠k) $I(\mathbf{q})_{distinct}$ as

$$I(\boldsymbol{q}) = I(\boldsymbol{q})_{self} + I(\boldsymbol{q})_{distinct}$$

$$= \sum_{j}^{N} a_j(\boldsymbol{q})^2 + \sum_{j}^{N} \sum_{k \neq j}^{N} a_j(\boldsymbol{q})\, a_k(\boldsymbol{q})\ \exp\left(-i\, \boldsymbol{q}\, (\boldsymbol{r}_j - \boldsymbol{r}_k)\right). \tag{4.27}$$

The self part reflects the sum of all individual atomic scattering intensities. Without an exponential term, it does not reflect the phase relationship among the waves scattered at the atomic structure. Hence, it does not contribute to any constructive and destructive interference that would constitute diffraction. The self part instead creates a kind of $\mathbf{q}$-dependent baseline scattering signal that is superimposed with the actual diffraction signal stemming from the distinct part. In order to concentrate on the diffraction component, $I(\mathbf{q})$ can be normalized by $I(\mathbf{q})_{self}$, which leaves us with the (static) structure factor $S(\mathbf{q})$ as

$$S(\boldsymbol{q}) = \frac{I(\boldsymbol{q})}{I(\boldsymbol{q})_{self}} = \frac{I(\boldsymbol{q})}{\langle a(\boldsymbol{q}) \rangle^2} = 1 + \frac{I(\boldsymbol{q})_{distinct}}{I(\boldsymbol{q})_{self}}. \tag{4.28}$$

Thereby, $\langle a(q) \rangle$ denotes the ensemble averaged scattering amplitude over all included atoms according to

$$\langle a(q) \rangle = \frac{1}{N} \sum_{j} a_j(\boldsymbol{q}) = \sum_{n} c_n\, a_n(\boldsymbol{q}), \tag{4.29}$$

where c_n quantifies the concentration of the atomic species n while $a_n(\mathbf{q})$ describes its respective scattering amplitude. $\Psi(\mathbf{q})$, $I(\mathbf{q})$, and $S(\mathbf{q})$ all provide structural information in the reciprocal space, see Equation (4.24). Through a Fourier transformation of $S(\mathbf{q})$, the total (reduced) pair distribution function (PDF) $G(\mathbf{r})$ can be calculated as

$$G(\boldsymbol{r}) = \frac{2}{\pi} \int_0^\infty \boldsymbol{q}\,(S(\boldsymbol{q}) - 1)\sin(\boldsymbol{q}\,\boldsymbol{r})\,d\boldsymbol{q}. \tag{4.30}$$

G(**r**) is closely related to another often used correlation function called the total pair distribution function g(**r**), which also includes the number density ρ_0 of the material as

$$g(\boldsymbol{r}) = \frac{G(\boldsymbol{r})}{4\,\pi\,r\,\rho_0} + 1. \tag{4.31}$$

G(**r**) and g(**r**) describe the atomic structure as a function of a positional vector **r**. Hence, the structural information is transferred into the real space, which might be a more intuitive and comprehensible approach for the human mind. By envisioning a sphere of radius **r** around a given atom at the center, G(**r**) or g(**r**) can be interpreted as the probability of encountering another atom at the surface of the sphere. The reader might be referred to Figure 2.15 in Chapter 2.5.3, where this aspect was initially demonstrated.

It shall be mentioned that for isotropic materials like amorphous metals, I(**q**), S(**q**), and G(**r**) are in fact not dependent on the directional components of **q** and **r** [247]. Hence, we will often use only the moduli of these vector properties, namely q and r, in the following course of this work. Figure 4.16 illustrates exemplary curves of I(q), S(q), and G(r) of a metallic glass. We see that I(q) is quantified in absolute counts, meaning that it is an extensive property with an absolute height that depends on experimental aspects like sample thickness, chemical composition, or the used acquisition time. S(q) as a normalized version of I(q) is instead an intensive property and oscillates around unity. The highest peak in I(q) and S(q) is termed the first sharp diffraction peak (FSDP). As the peak with the lowest q value, it includes the SRO, but especially the MRO of the amorphous structure. G(r) also shows its highest value at the first maximum, yet this peak corresponds to the first shell of nearest-neighbor atoms. Maxima of higher orders show a gradual decrease in height, indicating the loss of order at longer length-scales, which is the archetypical characteristic of the amorphous state. More detailed introductions to the topic can be found in the textbooks that served as basis for this chapter, namely T. Egami and S. Billinge [247] and J. Als-Nielsen and D. McMorrow [244].

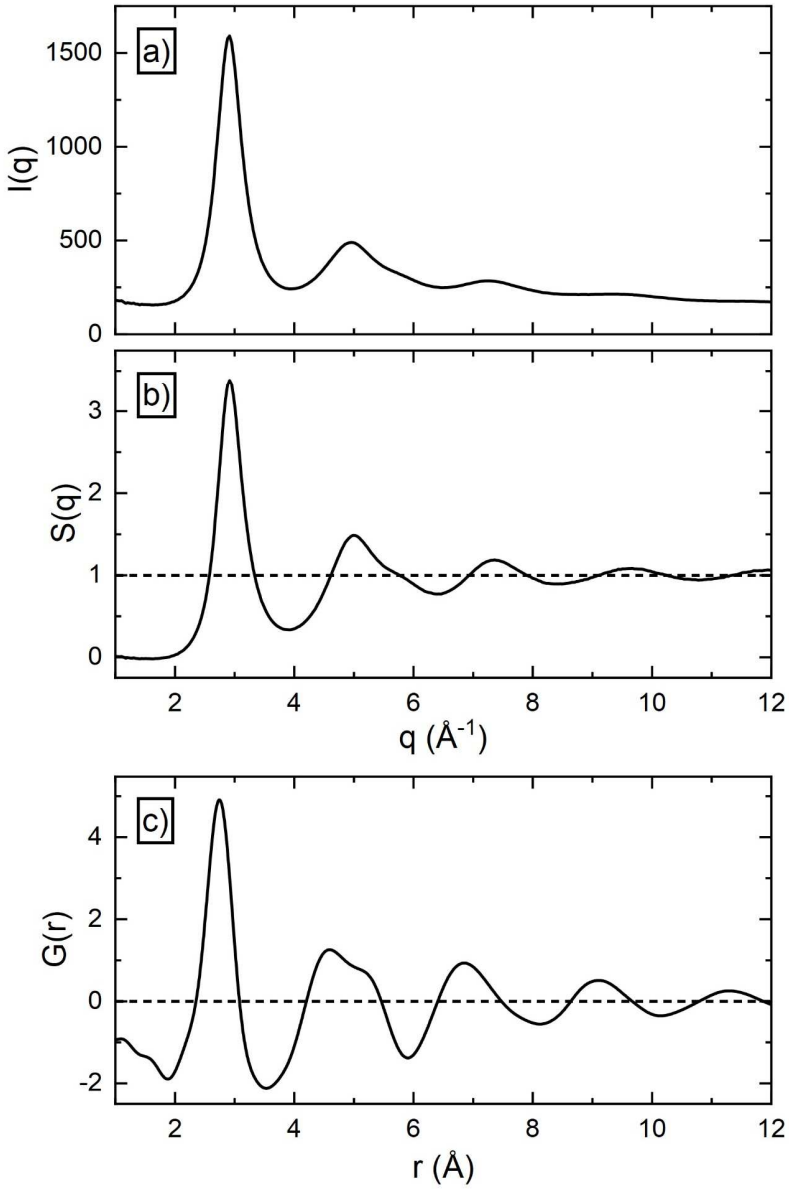

Figure 4.16: Exemplary curves for a) I(q), b) S(q), and c) G(r) for a metallic glass at room temperature. While I(q) is an extensive value that depends on experimental conditions, S(q) is a normalized property that oscillates around unity. G(r) is a real-space property that oscillates around zero.

Experimental details – In the present work, XRD measurements with radiation from conventional X-ray tubes are used as a standard analysis tool to detect potential crystallinity in especially the AM-formed samples from the Papers IV, V, and VI. The specific experimental details can be found there. Generally, commercial diffractometers built with the Bragg-Brentano geometry approach are used. Hence, radiation source and detector move on a circular path around the stationary sample in order to scan over the Bragg angles of interest. The results from these conventional XRD measurements are given in form of diffractograms that show the measured intensity as a function of 2Θ.

Isothermal room-temperature synchrotron HESXRD measurements are performed to complement the conventional XRD screening in the AM-related Papers IV and V. The extremely improved signal-to-noise ratio is used to verify sample amorphicity or to detect low crystalline fractions that are undetectable with other methods. In these HESXRD setups, the sample is irradiated in a wide-angle X-ray scattering (WAXS) setup in transmission mode. The resulting diffraction pattern is recorded by a stationary 2D-detector placed at a fixed sample-detector distance (SDD) downstream of the sample. Azimuthal integration over the detector signal with the program PyFAI integrate provides the raw intensity signal. Further data corrections, namely background subtraction, corrections for multiple scattering and inelastic Compton scattering, are performed using the PDFgetX2 program [248], which also calculates S(q) and G(r). Again, further details of the experimental setup and data treatment are described in the respective parts of the Papers IV and V. For detailed explanations regarding typical measurement setups (sample holders, heating devices for potential temperature scans, detectors) and specific data handling aspects, the reader is referred to other works [197,198,249,250].

4.3.3 X-ray photon correction spectroscopy using coherent radiation

When waves maintain a well-defined phase relationship between each other over a certain time and space (i.e. a constant phase lag), this aspect is termed coherence. So far, we have considered diffraction with monochromatic, but incoherent X-rays for XRD and HESXRD applications. Diffraction on amorphous, isotropic matter then results in a diffuse diffraction pattern as schematically shown in Figure 4.17a). The diffraction rings provide information about the average atomic distances d, as already explained on hand of the Bragg law in Equation (4.21). If we now consider monochromatic, but also coherent radiation, the appearance of the diffraction signal changes. Instead of diffuse diffraction rings, a complex ensemble of finely defined peaks can be observed, a so-called speckle pattern, see Figure 4.17b). Each speckle is an intensity maximum that results from constructive interference of the coherent radiation scattered at an atomic structure whose dimension corresponds to the radiation's wavelength. Temporal changes of these atomic structures will naturally change the appearance (intensity, position) of the speckles. Hence, temporal correlation among speckle patterns allows to study the atomic-scale dynamics of the diffracting matter.

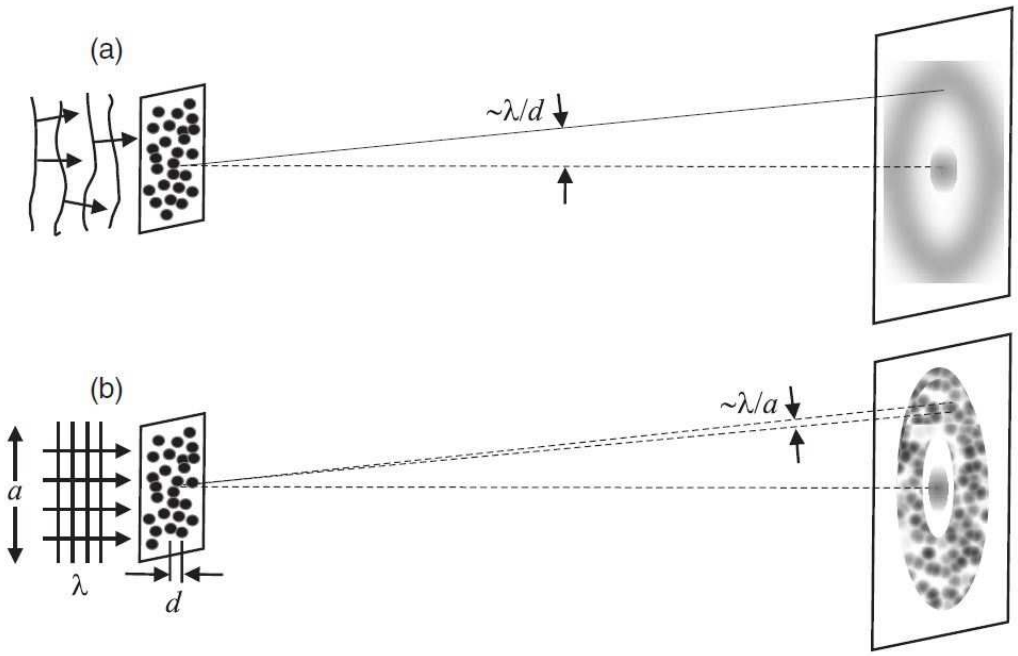

Figure 4.17: A schematic comparison between diffraction on amorphous matter with a) incoherent and b) coherent radiation. While the former creates diffuse diffraction rings, the latter generates a distinct speckle pattern. Taken from [251].

This constitutes the working principle of X-ray photon correlation spectroscopy (XPCS), a method that was firstly reported in 1991 by S. Sutton et al. [245]. The historical predecessor of XPCS can be found in the method of dynamic light scattering (DLS), which applies the same principle, but using electromagnetic radiation in the visible spectrum. Due to the lower energy and larger wavelengths, DLS cannot be used to study atomic-scale processes but rather dynamics of larger particles e.g. in colloids, clays, or concentrated emulsions [252–256].

To understand XPCS as a diffraction method using highly coherent X-rays, the static sample scattering amplitude from Equation (4.25) is not adequate anymore. Instead, the time dependence must be considered, too, leading to the dynamic sample scattering amplitude $\Psi(\mathbf{q},t)$. The underlying reason is that atomic structural rearrangements constantly change the positional vector $\mathbf{r}(t)$ of each atom, and hence, $\Psi(\mathbf{q},t)$ will change with time for any given $\mathbf{q}$. The timespan over which each speckle pattern is obtained, the so-called exposure time (or also acquisition time), therefore should be orders of magnitude shorter than the timescale on which substantial changes in the speckle pattern occur. Otherwise, temporal averaging over too long exposure times would result in pronounced smearing, ultimately leading to a diffraction pattern with diffuse rings instead of speckles, as it is obtained through incoherent radiation [257].

We now consider an evaluation window spanning over a certain amount of consecutive speckle pattern (in Paper II, this is termed an evaluation batch [6]). In principle, the correlation between speckle patterns can be quantified by comparing their dynamic sample scattering amplitudes through the intermediate scattering function (ISF) f(**q**,t). It correlates every initial value $\Psi(\mathbf{q},0)$ with its equivalent $\Psi(\mathbf{q},t)$ after an elapsed time t through a multiplication [258] in form of

$$f(\boldsymbol{q},t) = \langle \Psi(\boldsymbol{q},t)\, \Psi^*(\boldsymbol{q},0) \rangle$$
$$= \langle \sum_j^N \sum_k^N a_j(\boldsymbol{q},t)\, a_k(\boldsymbol{q},0)\ \exp\left(-i\,\boldsymbol{q}\ \left(\boldsymbol{r}_j(t) - \boldsymbol{r}_k(0)\right)\right) \rangle. \tag{4.32}$$

Ψ^*(**q**,0) is the complex conjugate of Ψ(**q**,0) and the angle brackets $\langle \dots \rangle$ indicate an averaging over all speckle pattern pairs with temporal distance t within the evaluation batch. It shall be also mentioned that the ISF can be separated into a self part (j=k) that considers the translation $\mathbf{r}_j(t)$-$\mathbf{r}_j(0)$ of particles in relation to themselves within a timeframe t, and a distinct part (j≠k) that considers the respective translation of a particle in relation to its surrounding particles.

Furthermore, the so-called first order correlation function g_1(**q**,t) results from normalizing the ISF through the static intensity I(**q**), as it has been introduced for incoherent diffraction in Equation (4.26):

$$g_1(\boldsymbol{q},t) = \frac{f(\boldsymbol{q},t)}{\langle |\Psi(\boldsymbol{q},0)|^2 \rangle}$$
$$= \frac{\langle \sum_j^N \sum_k^N a_j(\boldsymbol{q},t)\, a_k(\boldsymbol{q},0)\ \exp\left(-i\,\boldsymbol{q}\ \left(\boldsymbol{r}_j(t) - \boldsymbol{r}_k(0)\right)\right) \rangle}{\langle \sum_j^N \sum_k^N a_j(\boldsymbol{q},0)\, a_k(\boldsymbol{q},0)\ \exp\left(-i\,\boldsymbol{q}\ \left(\boldsymbol{r}_j(0) - \boldsymbol{r}_k(0)\right)\right) \rangle}. \tag{4.33}$$

Due to the multiplication in the numerator and the normalization by the denominator, g_1 quantifies the correlation among speckle patterns through values between unity and zero. Naturally, correlation reaches a maximum of 1 when t=0, hence, when each speckle pattern is compared to itself.

In practice, however, we encounter the same issue as previously found for incoherent diffraction: Ψ(**q**,t) cannot be directly measured, yet, its square value can be detected in form of a measured (dynamic) intensity I(**q**,t). By taking Equation (4.26) into account, speckle intensity correlation is performed through the intensity correlation function I_2 as

$$I_2(\boldsymbol{q},t) = \langle I(\boldsymbol{q},t)I(\boldsymbol{q},0)\rangle$$
$$= \left\langle \begin{array}{l} \sum_j^N \sum_k^N \sum_l^N \sum_m^N a_j(\boldsymbol{q},0)\, a_k(\boldsymbol{q},0)\, a_l(\boldsymbol{q},t)\, a_m(\boldsymbol{q},t) \\ \exp(-i\boldsymbol{q}\left(\boldsymbol{r}_j(0) - \boldsymbol{r}_k(0)\right) \exp(-i\,\boldsymbol{q}\,\left(\boldsymbol{r}_l(t) - \boldsymbol{r}_m(t)\right) \end{array} \right\rangle. \quad (4.34)$$

Further normalizing I_2 in an analogous way as done for the g_1 calculation then leads to the second order correlation function g_2, also termed the intensity autocorrelation function:

$$g_2(\boldsymbol{q},t) = \frac{\langle I(\boldsymbol{q},t)I(\boldsymbol{q},0)\rangle}{\langle |I(\boldsymbol{q},0)|^2\rangle}. \quad (4.35)$$

$I(\mathbf{q},0)$ refers to the static scattering intensity. Due to the normalization and the easy accessibility from the intensity signal measured by the detector, g_2 is the most widely used parameter to evaluate the speckle correlation in XPCS experiments [259–270].

The loss of correlation between speckle patterns over time is termed decorrelation. If the interference of other decorrelation mechanisms can be excluded (we will elaborate this aspect later), decorrelation reflects atomic structural rearrangements caused by the α-relaxation. Hence, the temporal decay in g_1 can be modelled by the usual KWW function as introduced in Chapter 2.1.2, Equation (2.4). Figure 4.18 illustrates a schematic speckle pattern that changes with time, together with an exemplary KWW-shaped g_1 curve that tracks the corresponding decorrelation process (black curve). g_1 and the experimentally accessible g_2 are directly related through the Siegert relation

$$g_2(\boldsymbol{q},t) = b + c\,|g_1(\boldsymbol{q},t)|^2, \quad (4.36)$$

and accordingly, g_2 can be also described by a KWW function as

$$g_2(\boldsymbol{q},t) = b + c\exp\left(-2\left(\frac{t}{\tau}\right)^{\beta}\right), \quad (4.37)$$

where b is a baseline value near unity and c is a contrast value that describes the height of the observed decay.

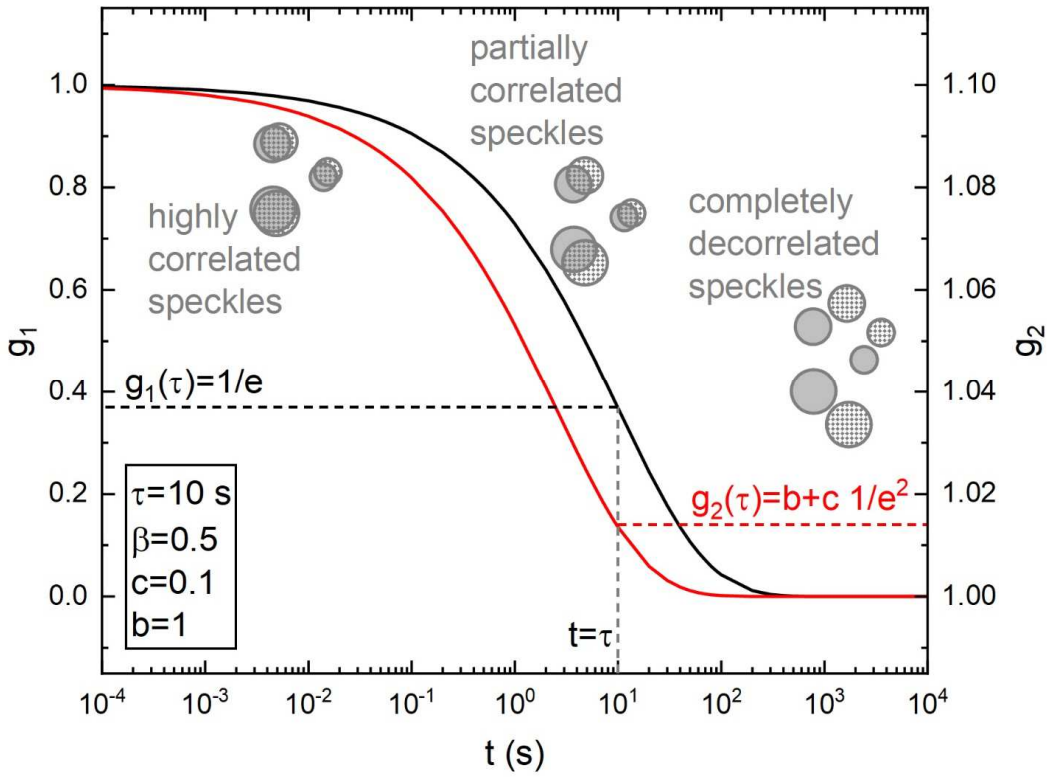

Figure 4.18: A schematic comparison between a KWW-modelled decorrelation in g_1 (black curve) and g_2 (red curve). The gray sketches illustrate speckle patterns that change over time, causing the observed decorrelation. Due to the slightly different mathematical formulation stemming from the Siegert relation, the g_2 curve decorrelates earlier than the g_1 curve.

The Siegert relation again illustrates the quadratic dependence between scattering amplitude (g_1) and intensity (g_2), as initially introduced in Equation (4.26). As a consequence, the g_2 KWW function in Equation (4.37) features an additional factor of two in the exponential argument, which shifts the whole g_2 fit to shorter times in comparison to the g_1 fit, as demonstrated by the red g_2 curve in Figure 4.18.

It shall be noted that the Siegert relation originally correlates g_2 with the ISF instead of g_1. Yet, the Equations (4.32) and (4.33) demonstrate that these functions are closely related [271] and it can be assumed that both share very similar decorrelation behavior. Hence, ISF and g_1 can be interchangeably used in terms of the Siegert relation [6,272].

Aside the g_1 and g_2 functions, decorrelation can be graphically illustrated through the two time correlation function (TTCF) $G(\mathbf{q},t_1,t_2)$, which is calculated as

$$G(\boldsymbol{q}, t_1, t_2) = \frac{\langle I(t_1) I(t_2) \rangle_p}{\langle I(t_1) \rangle_p \langle I(t_2) \rangle_p}. \tag{4.38}$$

Here, $\langle \dots \rangle_p$ indicates positional averaging over all pixels of the detector. G provides a discrete value for the correlation between two certain speckle patterns obtained at specific times t_1 and t_2. It therefore differs from all previously introduced correlation functions, which instead result from averaging over all speckle pattern correlations with a certain distance t. For a given evaluation batch, TTCFs are usually depicted in form of a color map, as exemplarily shown in Figure 4.19. Warm colors encode high correlation, cold colors indicate low correlation. The red belt along the diagonal represents self-correlation, where $t_1=t_2$. TTCFs are a helpful tool to identify (quasi-)stationary dynamics on hand of a constant width of the colored belt. Changing widths may indicate non-stationary dynamics, e.g. caused by aging effects at temperatures below the kinetic glass transition [261,262,265,273]. From a TTCF, g_2 can be calculated by respective temporal averaging, as explained above.

For further information about XPCS and the closely related method of DLS, the reader is referred to the literature that served as basis for this chapter [91,257,258,271,272,274,275].

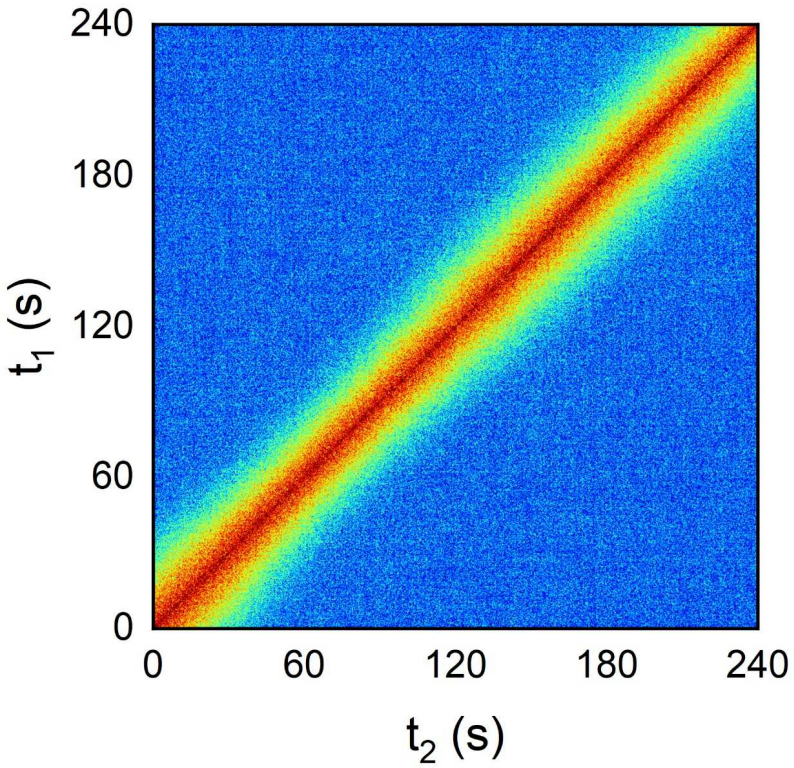

Figure 4.19: An exemplary TTCF that is also found in Paper II [6]. The evaluation window spans over a batch size of 24000 patterns obtained with 0.01 s exposure time, which equals to a batch timespan of 240 s. The warm-colored belt along the diagonal indicates high correlation. Its rather constant width further shows that (quasi-)stationary dynamics in the illustrated evaluation window can be assumed.

Experimental details – All previously published XPCS studies of metallic glass formers report on isothermal XPCS measurements. This work instead focuses on the relatively unconventional method of temperature scanning XPCS, which applies an underlying constant temperature change to scan the temperature dependence of the material's microscopic dynamics. All presented measurements used a temperature change rate of 1 K/min and were performed at the ID10 beamline of the ESRF (European Synchrotron Research Facility) in Grenoble, France. The experiments took place shortly after the EBS (Extremely Brilliant Source) upgrade in 2021, which updated the ESRF to be one of the first fourth generation synchrotrons worldwide [165,276]. Paper II reports on temperature scanning XPCS used to investigate the glass, glass transition, and SCL state of the $Pt_{42.5}Cu_{27}Ni_{9.5}P_{21}$ alloy upon heating and cooling. Experimental details can be found in the Materials and Methods section of this publication.

4.4 Microscopy

In the following, the imaging methods used in this work, namely light microscopy and scanning electron microscopy, will be introduced very briefly. For detailed information about these standard methods, the reader is referred to appropriate textbooks [277,278].

4.4.1 Light microscopy

In material science, light microscopy is a widely used method to create magnified images of surfaces and micro-scale structures. A detailed introduction to this standard method can be found in respective literature [277].

Experimental details – Light microscopy is used in Paper IV to evaluate the surfaces created through TPF post-processing of additively formed AMZ4. In the Papers V and VI, it is used to investigate porosity of AM-formed Vit101 and its derivatives as well as $Ni_{62}Nb_{38}$. The technical details can be found in the respective publications.

4.4.2 Scanning electron microscopy

Scanning electron microscopy (SEM) uses the short wavelengths of electrons to overcome the Abbe limit that restricts the resolution of conventional light microscopy. Hence, SEM

is a widely used and powerful method to image small structures on the sub-micrometer scale. Imaging can be thereby performed using eighter backscattered electrons (BSE) or secondary electrons (SE). Furthermore, SEM can be used to apply energy-dispersive X-ray spectroscopy (EDX), which allows to perform very localized chemical analysis based on the emission of element-specific characteristic X-rays. A detailed introduction to the topic can be found elsewhere [278].

Experimental details – SEM is applied in Paper IV to image the surfaces of AM-formed BMG parts that were post-processed by TPF. In Paper V, SEM imaging is used to evaluate fracture surfaces of AM-formed Vit101 and its derivatives. Paper VI reports on SEM studies to image crystalline precipitations in AM-formed $Ni_{62}Nb_{38}$. EDX mapping is further performed to obtain semi-quantitative knowledge about the chemical composition of these precipitates. Experimental details are explained in the respective articles.

4.5 Mechanical testing

4.5.1 Vickers hardness testing

The hardness of a material describes its resistance against the mechanical indentation through another (test) body. Widely applied testing approaches use standardized probes and loads to indent the material of interest in order to determine a hardness value by analyzing the created indentation. In the present work, Vickers hardness measurements [279] are performed. The indenter is a diamond in shape of a square-based pyramid with a tip angle between opposing faces of 136 °. Since hardness determination may vary with the applied load, Vickers hardness values are always specified together with the information of the used measurement force F in kilopond. For example, a Vickers hardness with a unit of HV10 was measured with F=10 kilopond=98.1 N, hence with the gravitational force of 10 kg. After loading the sample surface for 10-15 s, both diagonals of the indent, d_1 and d_2, are measured. From their average d, the Vickers hardness can be calculated as

$$HV(F) = 0.1891 \frac{F}{d^2}. \tag{4.39}$$

Experimental details – Paper VI reports HV1 hardness testing on additively formed $Ni_{62}Nb_{38}$ samples. The details can be found in the publication.

4.5.2 Stress-strain diagrams from three-point beam bending

Bending experiments are a valuable approach to determine stress-strain diagrams of metallic glass formers, especially since bending tests allow to observe potential plasticity, as explained in Chapter 2.8.2. Figure 4.20 illustrates the experimental setup in case of three-point bending (3PB). A beam-shaped sample is placed on two bearings with a distance L to each other. In the center of the beam, the sample is loaded with a probe and bent with a continuously increasing displacement motion D. The sample accordingly deforms and the thereby applied load F is recorded. Together with the width b and height h of the beam, the stress σ and strain ε at the outer surface of the beam midpoint can be calculated according to

$$\sigma = \frac{3\,F\,L}{2\,b\,h^2}, \tag{4.40}$$

$$\varepsilon = \frac{6\,D\,h}{L^2}. \tag{4.41}$$

Experimental details – In the papers IV and V, 3PB is used to determine the stress-strain diagrams of additively formed BMGs, namely AMZ4 as well as Vit101 and its derivates. The details are described in the respective sections of these publications.

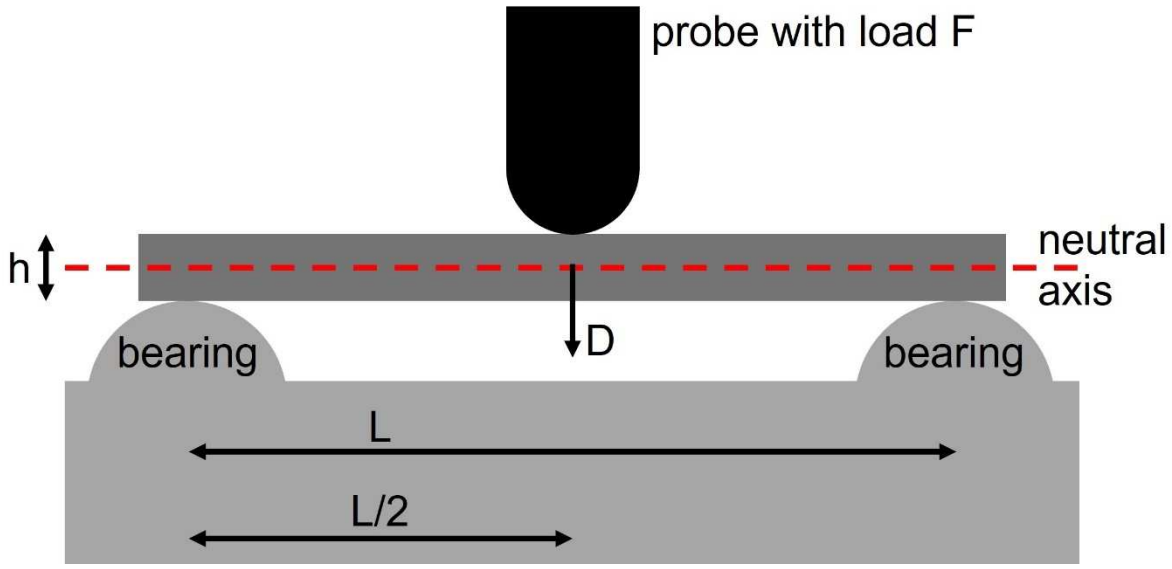

Figure 4.20: Scheme of the three-point bending procedure. The beam sample is placed on two bearings and is further loaded in the middle. Loading force F and displacement D are recorded to calculate the stress-strain diagram.

5. PUBLICATIONS

In the following, all six publications that constitute this thesis will be shown in their final published form. These are *Paper I: Determining the fragility of bulk metallic glass forming liquids via modulated DSC* in Chapter Paper I: Determining the fragility of bulk metallic glass forming liquids via modulated DSC5.1, *Paper II: Liquid-like versus stress-driven dynamics in a metallic glass former observed by temperature scanning XPCS* in Chapter 5.2, *Paper III: Determining and modelling a complete time-temperature-transformation diagram for a Pt-based metallic glass former through combination of conventional and fast scanning calorimetry* in Chapter 5.3, *Paper IV: Thermoplastic forming of additively manufactured Zr-based bulk metallic glass: A processing route for surface finishing of complex structures* in Chapter 5.4, *Paper V: Laser powder bed fusion of Cu-Ti-Zr-Ni bulk metallic glasses in the Vit101 alloy system* in Chapter 5.5, and *Paper VI: Additive manufacturing of $Ni_{62}Nb_{38}$ metallic glass via laser powder bed fusion* in Chapter 5.6. Ahead of each paper, basic information and the abstract of the article will be briefly provided.

5.1 Paper I: Determining the fragility of bulk metallic glass forming liquids via modulated DSC

Authors

Maximilian Frey, Nico Neuber, Oliver Gross, Bettina Zimmer, Wulff Possart, Ralf Busch

Publishing information

Submitted: 13.02.2020

Accepted: 31.03.2020

Published: 15.05.2020

Journal: Journal of Physics: Condensed Matter, 32 (2020), 324004

DOI: 10.1016/j.scriptamat.2022.114710

Abstract of the article

Temperature modulated DSC is used to study the fragility of three different bulk metallic glass forming liquids. Through applying various modulation frequencies, the dynamic glass transition shifts in temperature, allowing to determine the temperature dependence of the average relaxation time for each system. The resulting fragilities are compared with fragility investigations in literature obtained using thermo-mechanical analysis and the heating rate dependence of the calorimetric glass transition. Different methods to compare the data are evaluated and discussed.

IOP Publishing Journal of Physics: Condensed Matter
J. Phys.: Condens. Matter **32** (2020) 324004 (9pp) https://doi.org/10.1088/1361-648X/ab8526

Determining the fragility of bulk metallic glass forming liquids via modulated DSC

Maximilian Frey[1], Nico Neuber[1], Oliver Gross[1,2], Bettina Zimmer[3], Wulff Possart[3] and Ralf Busch[1]

[1] Chair of Metallic Materials, Saarland University, Campus C6.3, 66123 Saarbrücken, Germany
[2] Amorphous Metal Solutions GmbH, Michelinstraße 9, 66424 Homburg, Germany
[3] Chair for Adhesion and Interphases in Polymers, Saarland University, Campus C6.3, 66123 Saarbrücken, Germany

Received 13 February 2020, revised 22 March 2020
Accepted for publication 31 March 2020
Published 15 May 2020

Abstract

Temperature modulated DSC is used to study the fragility of three different bulk metallic glass forming liquids. Through applying various modulation frequencies, the dynamic glass transition shifts in temperature, allowing to determine the temperature dependence of the average relaxation time for each system. The resulting fragilities are compared with fragility investigations in literature obtained using thermo-mechanical analysis and the heating rate dependence of the calorimetric glass transition. Different methods to compare the data are evaluated and discussed.

Keywords: metallic glasses, bulk metallic glasses, relaxation, glass transition, fragility, calorimetry

(Some figures may appear in colour only in the online journal)

Introduction

Bulk metallic glasses (BMGs) are a relatively new family of materials. They are found in e.g. Zr- [1–3], Fe- [4, 5], Ti- [6, 7], Mg- [8, 9], Au- [10, 11], Pt- [12, 13], or Pd-based [14, 15] systems with usually three or more alloy components. Due to their amorphous structure and the resulting absence of dislocation movement as deformation mechanism, these materials show promising mechanical properties like high strength, hardness, and polymer-like elastic deformability of about 2%, thereby often exceeding the performance of conventional crystalline alloys [16]. To reach the glassy state, crystallization has to be bypassed during undercooling the liquid until it 'falls out of equilibrium' at the glass transition [17]. The glass forming ability (GFA) of a particular alloy is determined by thermodynamics, but also by kinetic factors. The latter are described by the equilibrium viscosity η or the relaxation time τ of the undercooled liquid, since these parameters directly affect the rate of nucleation and crystal growth. The temperature dependence of $\eta(T)$ and $\tau(T)$ can be described by e.g. the empirical VFT equation and evaluated in the framework of Angell's fragility concept [17]. Accordingly, liquids with an Arrhenius-like temperature dependence are termed strong, while those showing rather super-Arrhenius-like behavior are termed fragile liquids. One method to quantify fragility is the m-fragility approach, which defines the curve steepness of the investigated quantity $x(T)$ at $T_g{}^*/T = 1$ in an Angell plot [18] as

$$m = \left.\frac{\partial \log_{10}(x(T))}{\partial \frac{T_g^*}{T}}\right|_{T=T_g^*}. \quad (1)$$

Higher m values indicate a higher temperature sensitivity of $x(T)$ in the vicinity of T_g and therefore a more fragile liquid. In terms of viscosity, the value of $T_g{}^*$ is commonly defined at the temperature where η equals 10^{12} Pa s [19]. For timescale data, $\tau(T_g{}^*) = 100$ s is a widely used definition [18–20]. For BMG-forming liquids, a stronger behavior can enhance the GFA, since it leads to increased relaxation times and thus to sluggish atomic rearrangements in the temperature range where the supercooled liquid is prone to crystallization [17, 21]. Hence, the fragility of a glass forming liquid is a crucial factor to understand and evaluate its GFA and is therefore of interest for scientific research, but also for technological applications. Fragility can be determined

 © 2020 IOP Publishing Ltd Printed in the UK

experimentally by using thermo-mechanical analysis [5, 9, 22], dynamic-mechanical analysis [23, 24], or calorimetric methods. One calorimetric approach is the so called T_g-shift method that measures the dependence of the thermal glass transition on the applied rate of temperature change [13, 22, 25, 26]. As a different approach, (temperature) modulated differential scanning calorimetry (MDSC), introduced by Reading *et al* [27, 28], can be applied. Here, a small harmonic temperature perturbation is superimposed on an isotherm or a linear temperature scan program. The frequency of this modulation introduces a certain timescale into the experimental setup that results in a period-dependent reaction of the observed system. Besides e.g. sub-T_g effects [9, 29], hidden glass transitions [30, 31], or crystallization in polymers [32], MDSC allows to study the frequency-dependent glass transition event, also termed dynamic glass transition. This dynamic glass transition can be distinguished from the thermal, or kinetic glass transition [33], which is determined by the underlying rate of temperature change and used for the conventional T_g-shift method. Applying different modulation periods to an equilibrium liquid enables us to study the temperature dependence of the system's average relaxation time and therefore its fragility. While various studies on non-metallic systems address MDSC-based fragility analysis [20, 34–37], only a sparse amount of work on metallic glass formers can be found in literature [24, 38]. The present study aims to fill this gap by characterizing the low-temperature fragility of BMG forming liquids via the MDSC approach. In particular, the characteristics that distinguish these systems from the majority of other glass former families are considered, like the metal-typical high thermal conductivity and the limited thermal stability of the supercooled liquid state due to crystallization. For this purpose, three well-known noble metal based BMG forming liquids are investigated, which show a broad range of fragilities as well as varying thermal stabilities. The chosen systems are the Au-based $Au_{49}Ag_{5.5}Pd_{2.3}Cu_{26.9}Si_{16.3}$, the Pt-based $Pt_{42.5}Cu_{27}Ni_{9.5}P_{21}$ alloy, and the Pd-based $Pd_{43}Cu_{27}Ni_{10}P_{20}$. The results will be evaluated and compared to existing data sets obtained by, for BMGs, more commonly used techniques like thermo-mechanical analysis and rate-dependent calorimetric T_g-shift analysis.

Experimental

Plate-shaped amorphous specimens are prepared by tilt casting the melt into a water-cooled copper mold under high-purity argon atmosphere, as described in detail in [11, 13, 22, 39]. The amorphous state is verified by x-ray diffraction. Samples for calorimetry are cut with a diamond saw. The used sample weights range between 4 and 25 mg. MDSC measurements are performed in aluminum pans using a TA instruments Q100 device that was calibrated via the melting temperatures and enthalpies of indium, tin, bismuth, and lead. The samples are heated with a constant underlying rate q_0 of 1 K min^{-1} from below the thermal glass transition into the supercooled liquid (SCL) state and are subsequently cooled back into the glassy state with the same rate. Every heating-cooling sequence is superimposed by a sinusoidal temperature modulation with a respective period P and a fixed temperature amplitude A_T of 0.5 K. The used periods are 10, 12, 15, 20, 30, 45, 60, 75, 90, 105, 120, 135, and 150 s. This results in a modulated temperature change rate $q(t)$ [40]

$$q(t) = q_0 + A_T\,\omega\,\cos(\omega t), \tag{2}$$

where ω is the angular frequency of modulation with $\omega = 2\pi/P$. The Pt- and Pd-based alloys feature wide and exceptionally stable supercooled liquid regions, with $\Delta T_x = T_x - T_g$ = 83 K for a 20 K min^{-1} DSC scan [13] and ΔT_x = 131 K for a 40 K min^{-1} DSC scan [15], respectively. This allows to perform up to five heating–cooling sequences with the same sample without a detectable onset of crystallization. For the Au-based alloy, only one heating-cooling sequence per sample is performed to avoid crystallization due to the smaller supercooled liquid region ($\Delta T_x = 58$ K for a 20 K min^{-1} scan [10]). Through the fixed temperature amplitude, shorter periods lead to higher maximum values of $q(t)$ and an increased probability of critical thermal lag between sample and applied temperature program [40]. To compensate for this effect, the mass is adjusted so that short periods are measured with light samples and vice versa. Furthermore, the sample surfaces were polished for optimized heat transfer. Additionally, heating-cooling sequences with an underlying rate $q_0 = 0.1$ K min^{-1}, $A_T = 0.5$ K, and periods of 20, 30, 60, 90, and 150 s are performed for $Pd_{43}Cu_{27}Ni_{10}P_{20}$. Each sequence is measured with a new sample. Data evaluation and plotting is performed using TA Universal Analysis and Origin Pro 2019.

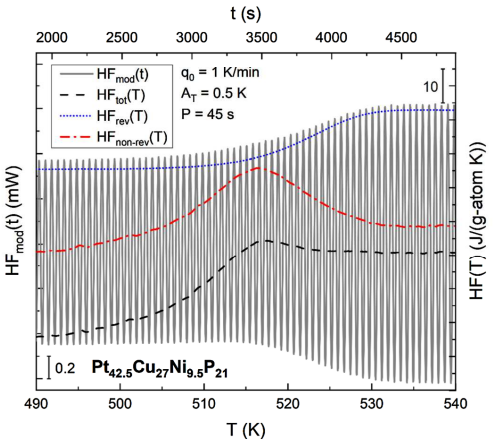

Figure 1. Modulated heat flow $HF_{mod}(t)$ induced by the modulated heating rate $q(t)$ during a heating scan on the $Pt_{42.5}Cu_{27}Ni_{9.5}P_{21}$ alloy. The total heat flow $HF_{tot}(T)$ indicates the thermal glass transition that is determined by the underlying heating rate q_0. The reversing heat flow $HF_{rev}(T)$ depicts the frequency-sensitive dynamic glass transition as an equilibrium liquid property. The excess between $HF_{tot}(T)$ and $HF_{rev}(T)$ is the non-reversing heat flow $HF_{non\text{-}rev}(T)$.

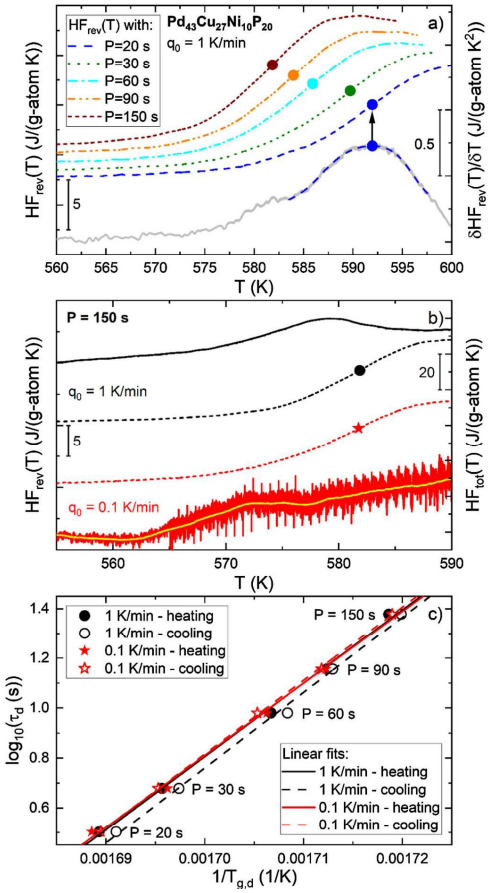

Figure 2. (a) $HF_{rev}(T)$ curves obtained by heating $Pd_{43}Cu_{27}Ni_{10}P_{20}$ samples with $q_0 = 1$ K min^{-1} and applying different modulation periods. The temperature point $T_{g,d}$ of each dynamic glass transition is defined as the inflection point in the step-like $HF_{rev}(T)$ signal by peak fitting of the maximum in the $HF_{rev}(T)$ derivative (gray curve). $T_{g,d}$ shifts to lower temperatures with increasing period. (b) For $q_0 = 1$ K min^{-1} in heating and high periods like $P = 150$ s, this results in an overlap of the dynamic glass transition in the $HF_{rev}(T)$ curve (black dashed line) and the overshoot of the thermal glass transition observed in the $HF_{tot}(T)$ signal (black solid curve). Reducing the underlying rate to $q_0 = 0.1$ K min^{-1} shifts the thermal glass transition to distinctly lower temperatures (red solid curve, smoothed signal in yellow), resulting in a more distinct separation of thermal and dynamic glass transition event. (c) In the activation diagram, $T_{g,d}$ values obtained during heating and cooling scans as well as with $q_0 = 1$ K min^{-1} and $q_0 = 0.1$ K min^{-1} show the overall same temperature dependence, albeit small offsets in the order of 1 K or below are visible.

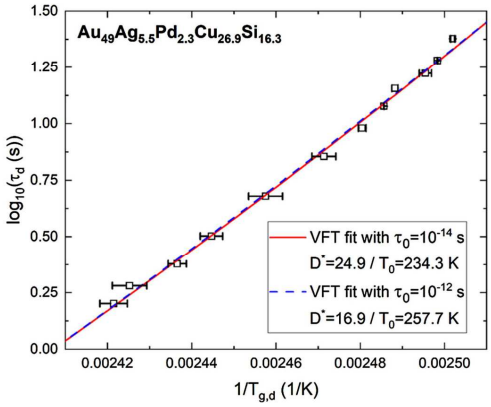

Figure 3. $\log_{10}(\tau_d)$ of the Au-based liquid over $1/T$. The temperature points reflect the average $T_{g,d}$ value for heating and cooling scans with $q_0 = 1$ K min^{-1} and with the same applied periods, the errors bars reflect the respective standard deviations. VFT fits with pre-exponential factors fixed at 10^{-14} s [45] (straight red line) and 10^{-12} s (blue dashed line) both describe the data set well, but provide completely different D^* and T_0 parameters.

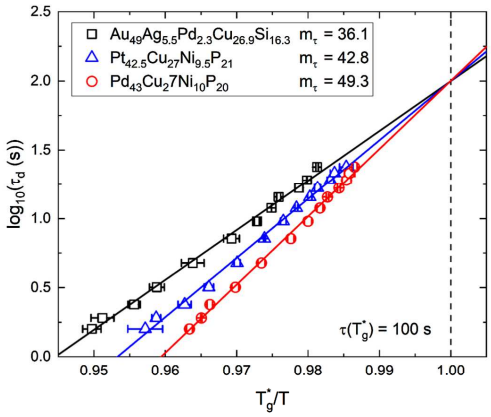

Figure 4. Linear Arrhenius fits of $\tau_d(T)$ in an Angell-type diagram for all three compositions. The linear $\tau_d(T)$ fits are extrapolated to T_g^* at $\tau_d = 100$ s to define the *m*-fragility m_τ.

Results

The modulated temperature rate $q(t)$ induces a reaction of the measured system in form of a modulated heat flow signal $HF_{mod}(t)$, as illustrated in figure 1 in the case of the $Pt_{42.5}Cu_{27}Ni_{9.5}P_{21}$ alloy. Through Fourier analysis of $HF_{mod}(t)$ over a (sliding) time window of one modulation period, the courses of average value and amplitude of $HF_{mod}(t)$ are established. With these parameters, the MDSC measurements are analyzed according to the reversing/non-reversing heat flow approach [40]. Thereby, the total heat flow $HF_{tot}(T)$ is derived from the sliding average of $HF_{mod}(t)$, where T refers to the average temperature defined by q_0. From the heat flow amplitude of $HF_{mod}(t)$, the reversing heat flow $HF_{rev}(T)$ can be

Table 1. All parameters of linear and VFT fits for MDSC, TMA [13, 39, 44] and T_g-shift [13] data. The temperature spans of data acquisition of each method are listed.

Composition	$Au_{49}Ag_{5.5}Pd_{2.3}Cu_{26.9}Si_{16.3}$	$Pt_{42.5}Cu_{27}Ni_{9.5}P_{21}$	$Pd_{43}Cu_{27}Ni_{10}P_{20}$
Temperature range of data points			
MDSC (K)	13.3	15.3	14.0
TMA (K)	24.9 [44]	33.7 [13]	30.2 [39]
T_g-shift (K)	—	21.2 [13]	—
MDSC - linear fits in time domain			
$T_g^* = T(100\text{ s})$ (K)	392.2	510.8	573.8
m_τ	36.1 ± 0.8	42.8 ± 0.9	49.3 ± 0.9
TMA - VFT fits in viscosity domain			
D^*	21.5 ± 0.7 [44]	15.3 ± 0.7 [13]	14.0 ± 0.3 [39]
T_0 (K)	244.6 ± 2.8 [44]	354.4 ± 3.5 [13]	412.4 ± 2.4 [39]
$T_g^*(10^{12}$ Pa s) (K)	383.9 [44]	498.0 [13]	565.3 [39]
m_η	45.2 [44]	56.9 [13]	60.6 [39]
MDSC - VFT fits in viscosity domain			
$G_{\tau,d-\eta}$ (Pa)	9.72×10^8	3.74×10^8	1.28×10^9
D^*	22.2 ± 0.7	15.6 ± 0.4	13.8 ± 0.3
T_0 (K)	241.5 ± 3.3	352.3 ± 3.0	414.1 ± 2.7
$T_g^*(10^{12}$ Pa s) (K)	383.5	497.9	565.4
m_d	44.3	56.1	61.3
T_g-shift - VFT fits in viscosity domain			
$G_{\tau,t-\eta}$ (Pa)	—	1.82×10^8	—
D^*	—	16.7 ± 1.5	—
T_0 (K)	—	344.4 ± 3.0	—
$T_g^*(10^{12}$ Pa s) (K)	—	496.7	—
m_t	—	53.5	—

calculated [40]. The difference between $HF_{tot}(T)$ and $HF_{rev}(T)$ is the non-reversing heat flow $HF_{non\text{-}rev}(T)$ [40]

$$HF_{tot}(T) = HF_{rev}(T) + HF_{non-rev}(T). \quad (3)$$

$HF_{tot}(T)$ corresponds to the heat flow received from a conventional DSC scan with an applied rate q_0. Hence, $HF_{tot}(T)$ in figure 1 shows a typical thermal glass transition as the heating rate-governed transition from the initially glassy state into the equilibrium supercooled liquid state. At distinctly higher temperatures, the dynamic glass transition manifests itself in the $HF_{rev}(T)$ signal as an almost sigmoidal transition from the low glassy to the higher liquid state plateau. This effect is determined by the modulation frequency instead of the underlying rate q_0 and marks the temperature region, where the average of the (enthalpy) relaxation time spectrum of the liquid $\tau_d(T)$ is in the order of the applied modulation period according to [20, 36, 41]

$$\tau_d = \frac{1}{\omega} = \frac{P}{2\pi}. \quad (4)$$

With increasing temperature, $\tau_d(T)$ decreases. This leads to a shift of the dynamic glass transition to higher temperatures for decreasing periods as shown in figure 2(a) by means of the Pd-based system. The temperature associated with the respective dynamic glass transition, $T_{g,d}$, is defined as the inflection point of the curve. It is determined by peak fitting the maximum of $\delta HF_{rev}(T)/\delta T$, see figure 2(a). For long modulation periods, the dynamic glass transition approaches the thermal glass transition event, leading to an overlap of the dynamic glass transition and the enthalpy recovery signal (overshoot) in the $HF_{tot}(T)$ signal as shown for $P = 150$ s and $q_0 = 1$ K min^{-1} in figure 2(b). By decreasing q_0 by one order of magnitude to 0.1 K min^{-1}, thermal and dynamic glass transition can be distinctly separated as the thermal glass transition decreases by roughly 10 K. Figure 2(c) compares the $T_{g,d}$ values obtained by heating and cooling with $q_0 = 1$ K min^{-1} or 0.1 K min^{-1} in an activation diagram. By trend, $T_{g,d}$ values obtained in heating are slightly higher (offsets are in the order of 0.6 K or less) than those measured in cooling when $q_0 = 1$ K min^{-1} is applied. For $q_0 = 0.1$ K min^{-1}, the offset between heating and cooling data further decreases. Even though a small difference in the order of 0.8 K or less is visible between the data sets obtained with different q_0, the linear fits in figure 2(c) reveal that the slopes of all four data sets (two different q_0 in heating and cooling setup, respectively) are basically identical within less than 5% discrepancy. For further considerations, the $T_{g,d}$ associated with an applied modulation period is defined as the average of the two values of a heating-cooling sequence with $q_0 = 1$ K min^{-1}.

The temperature dependence of equilibrium viscosity or relaxation time of metallic glass forming liquids usually shows a super-Arrhenius temperature dependence. This behavior can be mathematically described by the empirical Vogel–Fulcher–Tammann (VFT) equation [17], where $x(T)$ reflects $\tau(T)$ or $\eta(T)$, respectively:

$$x\,(T) = x_0\,\exp\left(\frac{D^*\,T_0}{T - T_0}\right), \tag{5}$$

with the fragility parameter D^*, the VFT temperature T_0 at which the function diverges, and a pre-exponential factor x_0 that defines the high-temperature minimum value of $x(T)$. High D^* parameters correspond to a rather strong behavior and vice versa. Two aspects shall be addressed at this point. At first, the divergence of $\tau(T)$ or $\eta(T)$ at low temperatures has been critically discussed in recent literature [42]. Advanced approaches like the MYEGA model [43] consider this aspect and would be more appropriate for extrapolation to extremely deep temperatures. However, since this is not an explicit goal of the present work, the still widely established VFT equation is used in the following, thus allowing a direct comparison with published VFT fit parameters [13, 39, 44]. Second, fragile-to-strong transitions are not observed in the present work and are therefore excluded from consideration. Yet, such a transition has been reported for the Au-based alloy at very low temperatures [44, 45]. Accordingly, the reported fragilities have to be handled with caution if they are used to extrapolate to temperatures distinctly beyond the investigated temperature range.

Figure 3 depicts two attempts to provide VFT fits of MDSC-defined $\tau_d(T)$ data. To obtain physically meaningful fits, τ_0 has to be assumed in the order of roughly 10^{-14} s, which is close to the inverse Debye frequency [46]. In case of $\tau_0 = 10^{-14}$ s, a D^* parameter of 24.9 is reached. However, variations in τ_0 alter D^* and T_0 massively without degrading the overall fit quality, as illustrated in figure 3 for $\tau_0 = 10^{-12}$. As the precise τ_0 value of a particular liquid is not accessible, the comparability of VFT fits of different systems in the timescale regime remains questionable.

To allow a determination of m-fragilities independent from these difficulties, linear Arrhenius-like fits of $\log_{10}(\tau_d)$ are performed. Figure 4 shows the respective fits in an Angell plot with the assumption of $\tau(T_g^*) = 100$ s. The linear curves are extrapolated to allow the definition of m_τ outside the MDSC data range as listed in table 1.

All MDSC results established in this work are further compared to equilibrium viscosity data published in earlier fragility studies [13, 39, 44]. In these works, thermo-mechanical analysis (TMA) with an isothermal three-point bending setup was used to define the temperature dependence of the equilibrium viscosity of the supercooled liquid η_{eq} in the vicinity of the glass transition. The η_{eq} data was fitted using the VFT equation. In the viscosity regime, an alloy-specific determination of the pre-exponential factor η_0 is possible according to

$$\eta_0 = \frac{h\,N_A}{v_m}, \tag{6}$$

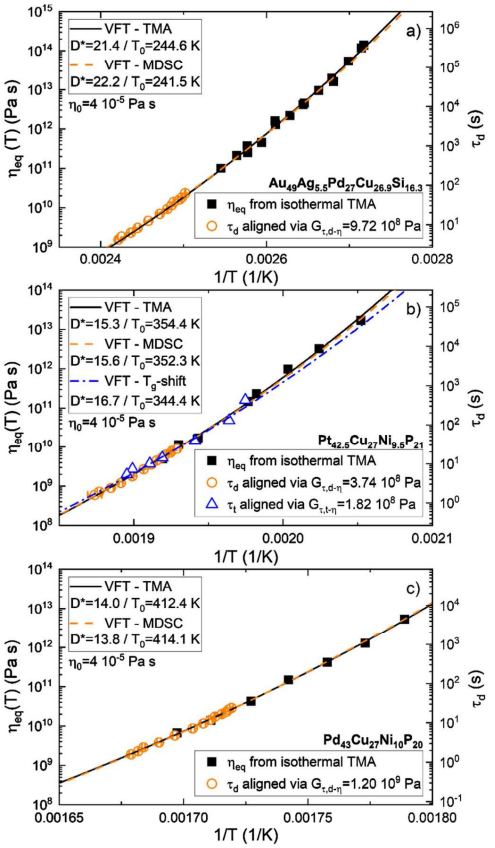

Figure 5. MDSC dynamic glass transition data (orange circles) and T_g-shift thermal glass transition data (blue triangles, only for $Pt_{42.5}Cu_{27}Ni_{9.5}P_{21}$) aligned with isothermal equilibrium viscosities obtained by isothermal TMA (black squares) for (a) $Au_{49}Ag_{5.5}Pd_{2.3}Cu_{26.9}Si_{16.3}$, (b) $Pt_{42.5}Cu_{27}Ni_{9.5}P_{21}$, and (c) $Pd_{43}Cu_{27}Ni_{10}P_{20}$. VFT fits for all three measurement methods are given and show good agreement.

where h is the Planck constant, N_A the Avogadro constant, and v_m the molar volume of the liquid [47]. For all present compositions, η_0 is calculated as 4.0×10^{-5} Pa s [13, 39, 44].

In addition, calorimetric T_g-shift measurements are available for the $Pt_{42.5}Cu_{27}Ni_{9.5}P_{21}$ alloy [13]. This approach quantifies the dependence of the fictive temperature T_f on the applied rate of temperature change. From the measured thermal glass transition width and the rate, a set of transition times τ_t is calculated that describes the average times needed to unfreeze the glassy state into the supercooled liquid state during scan conditions [13, 25].

According to the Maxwell equation, equilibrium viscosity and (shear) relaxation time are proportional to each other via the high frequency shear modulus G_∞ [48] according to

$$\eta = G_\infty \tau. \quad (7)$$

Based on this relation, the timescale data sets obtained by MDSC (τ_d) and T_g-shift (τ_t) [13] are transformed into the viscosity domain. Equations (5) and (7) are combined to fit the τ data with fixed VFT parameters (D^*, T_0, η_0) of the $\eta_{eq}(T)$ fits reported in [13, 39, 44], leaving only G as a free fitting parameter. Through the fit procedure, optimized scaling factors for MDSC relaxation times ($G_{\tau,d-\eta}$) and T_g-shift transition times ($G_{\tau,t-\eta}$) are generated to allow a direct alignment with TMA equilibrium viscosities. This way, the temperature dependencies, and therefore the fragilities, of the different data sets can be compared directly by eye or by using the VFT equation as shown in figure 5. It has to be stated that $G_{\tau,d-\eta}$ and $G_{\tau,t-\eta}$ differ from the high frequency shear modules G_∞ by about two orders of magnitude, which is further discussed in references [13, 22, 39, 49]. Table 1 lists all $G_{\tau,d-\eta}$ and $G_{\tau,t-\eta}$ scaling factors, the VFT fit parameters of TMA, MDSC and T_g-shift obtained in the viscosity regime, and the resulting m-fragilities (m_η, m_d, and m_t) defined at ${T_g}^* = T(10^{12}$ Pa s).

Discussion

For an appropriate observation of the dynamic glass transition $T_{g,d}$, several aspects need to be considered. First of all, a linear response of the investigated system has to be assumed to allow direct interpretation of data. This condition is fulfilled if the temperature fluctuations, caused by the periodic perturbation (with the temperature amplitude A_T), are small enough to have a negligible influence on the observed process as discussed in [40, 50]. For MDSC applications, temperature amplitudes up to 1 K are widely accepted to sufficiently fulfill the linear response condition [33, 51] and are frequently applied for MDSC analysis [24, 29, 34, 36]. The $A_T = 0.5$ K used in this study is therefore assumed to satisfy the linear response criterion, too. Furthermore, the measurement window to study $T_{g,d}$ is limited by technical aspects as well as by the thermophysical behavior of the sample itself. The used TA Instruments Q100 DSC can provide periods between 10 and 200 s. Shorter periods would tend to create $q(t)$ maxima too high to be realized by the heat flux DSC device. Also, thermal lag between sample and temperature program would increase massively [52]. However, the measured $T_{g,d}$ for $P = 10$ s and other short periods align well and show no noteworthy outliers in comparison to other data points, as can be seen in figures 3 and 4. Here, the quality of the measurement benefits from the fact that BMGs as metallic materials have higher thermal conductivity than e.g. polymers, therefore facilitating the thermal equilibrium between sample and applied temperature program and reducing thermal lag issues.

Regarding the upper limit of periods, two aspects shall be considered. At first, the overlap of thermal and dynamic glass transition for high periods, as described in the results section and illustrated in figure 2(b), has to be briefly discussed. $T_{g,d}$ reflects the structural α-relaxation as an equilibrium process and should therefore be determined in the thermally provided equilibrium supercooled liquid state, i.e. at temperatures above the thermal glass transition region. Upon heating, the shape and position of the dynamic glass transition event can be altered by the appearance of the thermal glass transition, which is determined by the thermal history of the previously glassy sample, see reference [38]. MDSC $T_{g,d}$ measurements in literature are therefore often found to be performed during cooling of the supercooled liquid, thereby lowering the probability of an interference with non-equilibrium effects [20, 36, 53]. Second, the relaxation time spectrum and consequently the average relaxation time change continuously due to the non-isothermal conditions of the measurements. Moreover, the Fourier analysis of $HF_{mod}(t)$ incorporates the (sliding) time window of the recently elapsed modulation period to allow the calculation of $HF_{rev}(T)$, as stated in the results section. So strictly speaking, the dynamic glass transition in $HF_{rev}(T)$ is determined by not only one discrete, but by a superposition of changing average relaxation times. This results in a 'smearing' of the timescale associated with the respective dynamic glass transition. Sequences with short modulation periods are less affected by this issue, as opposed to large periods like of $P = 150$ s and $q_0 = 1$ K min^{-1} in this work, where the Fourier analysis range extends over 2.5 K.

With these two aspects in mind, the interference of thermal and dynamic glass transition on the one hand and the smearing effect on the other hand, no striking discrepancies are observed in figures 3 and 4, where the data points of longer periods align well with those of shorter periods. Nonetheless, both aspects may induce gradual changes that are hard to detect. The decrease of the underlying rate to 0.1 K min^{-1} shifts the measurement further towards quasi-isothermal conditions and therefore allows to verify the 1 K min^{-1} data in terms of the addressed issues. Accordingly, thermal and dynamic glass transition appear to be clearly separated even for the highest applied period of 150 s as illustrated in figure 2(b). Also, the smearing effect is reduced due to the fact that for $P = 150$ s, a temperature range of only 0.25 K is utilized for Fourier analysis. The quality of the received $T_{g,d}$ data benefits from the lower q_0 in that smaller offsets between values defined in heating and cooling can be found, see figure 2(c), reflecting the quasi-isothermal measurement conditions. Even though small differences in the absolute temperature values are found, the temperature dependencies (linear fits in figure 2(c)) of the heating or cooling $T_{g,d}$ data sets for $q_0 = 1$ K min^{-1} and $q_0 = 0.1$ K min^{-1} are basically identical. Nevertheless, measuring all three alloys and periods with $q_0 = 0.1$ K min^{-1} would entail some disadvantages. Due to the less stable supercooled liquid state of $Au_{49}Ag_{5.5}Pd_{2.3}Cu_{26.9}Si_{16.3}$, the dynamic glass transition for shorter periods would more likely overlap with the onset of crystallization. Furthermore, the overall measurement time would increase (by one order of magnitude) as well as the material mass needed to compensate for the worse signal-to-noise ratio, see the $HF_{tot}(T)$ signal in figure 2(b). Thus, the practice of averaging the $T_{g,d}$ values of a heating-cooling sequence with 1 K min^{-1} used for further investigations can be seen as acceptable and practical, at least for the period range applied in this work.

The first approach to quantify fragility by means of the MDSC data sets is done by determining the fragility m_τ in the timescale regime as shown in figure 4. The linear fit lines show satisfying agreement since for the short data range of about 15 K, see table 1, the overall super-Arrhenius temperature dependence of τ_d can be considered as negligible. $Pd_{43}Cu_{27}Ni_{10}P_{20}$ is found to be the most fragile system, followed by $Pt_{42.5}Cu_{27}Ni_{9.5}P_{21}$ with a slightly stronger fragility, and $Au_{49}Ag_{5.5}Pd_{2.3}Cu_{26.9}Si_{16.3}$ is finally determined as the by far strongest system with the lowest m_τ. This hierarchy is the same as found for m_η defined by viscosity measurements in literature [13, 39, 44], as listed in table 1. Albeit, the m_η values are about 20% higher (i.e. more fragile) than the m_τ results. This effect can be tracked back to the different $T_g{}^*$ values used for m_τ and m_η that show offsets of up to 20 K, see table 1. Here, the common definition of $\eta_{eq}(T_g{}^*) = 10^{12}$ Pa s in the viscosity regime does not agree well with the frequently used timescale definition of $\tau(T_g{}^*) = 100$ s. Angell already mentioned this discrepancy between quite fragile ionic and molecular liquids on the one hand and oxide glass formers on the other hand, for which the traditional notion of $\eta_{eq}(T_g{}^*) = 10^{12}$ Pa s is appropriate [54]. Furthermore, it should be mentioned at this point that the linear fits in figure 4 are extrapolated to allow the determination of m_τ. The super-Arrhenius temperature dependence of τ_d is therefore neglected in an increased temperature span, leading to an additional systematic error. In conclusion, Arrhenius-like fitting to determine a *m*-fragility may be a straight forward and often applied method, but it finds its limitations when comparing different measuring techniques with heterogeneous definitions of $T_g{}^*$.

From these difficulties the need of a more substantiated comparison of data sets arises. Figure 4(a)–(c) illustrate all timescale data from MDSC and, in case of $Pt_{42.5}Cu_{27}Ni_{9.5}P_{21}$, T_g-shift data, aligned with TMA equilibrium viscosities as described in the results section. The MDSC data almost perfectly aligns with the equilibrium viscosities, confirmed by the resulting VFT-TMA and VFT-MDSC fits that are in good agreement. Consequently, the previously discussed discrepancy of *m*-fragilities is resolved by determining them in the same domain and with the same definition of $T_g{}^*$, as shown in table 1 for the almost identical m_η and m_d. Although the temperature range of $T_{g,d}$ data points is only about half the size of the η_{eq} data range, similar fitting errors are found, caused by the low scatter among the MDSC results. η_{eq} and τ_d are comparable to each other in that they directly characterize the equilibrium SCL state [33, 55]. In contrast, the T_g-shift method relies on measuring the rate dependence of the thermal glass transition, which does not directly describe the equilibrium state but the transition kinetics between equilibrium and non-equilibrium, i.e. the glass. Yet, according to the Frenkel–Kobeko–Rainer (FKR) relation [33, 56], dynamic and thermal glass transition are related to each other in the way that during cooling down from the SCL state with the rate q, the relaxation time at the thermal glass transition, $\tau_d(T_{g,t})$, is inversely proportional to q via a scaling factor C:

$$q\ \tau_d\left(T_{g,t}\right) = C. \tag{8}$$

The present T_g-shift measurements of $Pt_{42.5}Cu_{27}Ni_{9.5}P_{21}$ show overall agreement with TMA and MDSC results. Yet, slightly diverging VFT parameters as well as relatively high data scatter and fitting errors are present, see figure 4(b) and table 1. Here, one possible origin could be the rather error-prone analysis procedure that relies on defining the onset and end of the thermal glass transition event by tangents [25]. In direct comparison, the distinctly lower scatter observed for MDSC data sets most likely has its origin in the Fourier analysis of $HF_{mod}(t)$ that incorporates a whole modulation period as explained in the results section. This leads to a smooth $HF_{rev}(T)$ signal, see figure 2, which allows an unambiguous quantification of the dynamic glass transition event. Furthermore, proper T_g-shift measurements require a thermal standard treatment of every sample to create a glassy state with a defined thermal history [25]. As shown for the $Au_{49}Ag_{5.5}Pd_{2.3}Cu_{26.9}Si_{16.3}$ alloy, MDSC $T_{g,d}$ measurements require no such pretreatment to obtain a trustworthy fragility determination, provided an appropriate parameter set is applied as previously discussed. This can be an advantage especially for BMG formers with rather short SCL regions [5, 6, 57].

The present MDSC analysis was performed using the $HF_{rev}/HF_{non\text{-}rev}$ approach, which is the procedure originally preferred by the manufacturer of the used Q100 DSC, TA instruments. In various recent studies, the phase lag between thermal perturbation $q(t)$ and heat flow response $HF_{mod}(t)$ is further taken into account [20, 33, 50, 53]. This allows for an analysis in terms of a complex heat capacity $C_p{}^*(T)$, in analogy to other modulated techniques like dynamic-mechanical analysis [9, 23, 41, 58] or dielectric spectroscopy of polymers [20, 59, 60]. To our knowledge, a systematic comparison of the $HF_{rev}/HF_{non\text{-}rev}$ and the complex heat capacity approach for MDSC measurements on metallic glasses is still to be performed. Furthermore, the rise [61, 62] and commercial availability [63] of fast differential scanning calorimetry (FDSC) make it possible to massively enhance the data range for thermal T_g-shift measurements [64, 65] but also for modulated applications [66] in the future.

Conclusion

Modulated DSC scans on three different BMGs formers were performed with periods between 10 s and 150 s. An underlying temperature change rate of 1 K min^{-1} was found to provide satisfying results. Arrhenius-like fitting of the achieved average relaxation time data allows to qualitatively define and compare fragilities of different systems, but exposes methodical difficulties when compared to fragility results defined by other measurement methods. To overcome such problems, direct alignment of data sets from different techniques is found as an able tool and illustrates the good quantitative agreement between MDSC and e.g. thermomechanical viscosity analysis. MDSC fragility determination requires substantiated selection of measuring parameters to allow reliable results but offers several advantages over other well-established methods like thermal glass transition shift measurements or

thermo-mechanical analysis, in particular faster data acquisition and less scatter-afflicted results.

Acknowledgments

The authors would like to thank I Gallino, B Bochtler, A Kuball, and S Riegler for inspiring discussions and experimental support. Furthermore, we want to thank C. Hafner GmbH for supplying the noble metals used for alloy synthesis.

ORCID iDs

Maximilian Frey https://orcid.org/0000-0001-8602-721X
Nico Neuber https://orcid.org/0000-0002-9912-5764
Oliver Gross https://orcid.org/0000-0003-4281-6182

References

[1] Inoue A, Zhang T and Masumoto T 1990 Zr–Al–Ni amorphous alloys with high glass transition temperature and significant supercooled liquid region *Mater. Trans. JIM* **31** 177–83
[2] Heinrich J, Busch R and Nonnenmacher B 2012 Processing of a bulk metallic glass forming alloy based on industrial grade Zr *Intermetallics* **25** 1–4
[3] Kuball A, Gross O, Bochtler B and Busch R 2018 Sulfur-bearing metallic glasses : a new family of bulk glass-forming alloys *Scr. Mater.* **146** 73–6
[4] Suryanarayana C and Inoue A 2013 Iron-based bulk metallic glasses *Int. Mater. Rev.* **58** 131–66
[5] Bochtler B, Gross O, Gallino I and Busch R 2016 Thermo-physical characterization of the $Fe_{67}Mo_6Ni_{3.5}Cr_{3.5}P_{12}C_{5.5}B_{2.5}$ bulk metallic glass forming alloy *Acta Mater.* **118** 129–39
[6] Kuball A, Gross O, Bochtler B, Adam B, Ruschel L, Zamanzade M and Busch R 2019 Development and characterization of titanium-based bulk metallic glasses *J. Alloys Compd*. **790** 337–46
[7] Gross O, Ruschel L, Kuball A, Bochtler B, Adam B and Busch R 2020 Bulk metallic glass formation in the (Ti,Zr)–(Ni, Cu)-S system *J. Phys.: Condens. Matter.* **11**
[8] Inoue A, Kato A, Zhang T, Kim S G and Masumoto T 1991 Mg–Cu–Y amorphous-alloys with high mechanical strengths produced by a metallic mold casting method *Mater. Trans. JIM* **32** 609–16
[9] Frey M, Busch R, Possart W and Gallino I 2018 On the thermodynamics, kinetics, and sub-T_g relaxations of Mg-based bulk metallic glasses *Acta Mater.* **155** 117–27
[10] Schroers J, Lohwongwatana B, Johnson W L and Peker A 2005 Gold based bulk metallic glass *Appl. Phys. Lett.* **87** 404–6
[11] Gross O, Eisenbart M, Schmitt L-Y, Neuber N, Ciftci L, Klotz U E, Busch R and Gallino I 2018 Development of novel 18-karat, premium-white gold bulk metallic glasses with improved tarnishing resistance *Mater. Des.* **140** 495–504
[12] Schrocrs J and Johnson W L 2004 Highly processable bulk metallic glass-forming alloys in the Pt–Co–Ni–Cu–P system *Appl. Phys. Lett.* **84** 3666–8
[13] Gross O, Bochtler B, Stolpe M, Hechler S, Hembree W, Busch R and Gallino I 2017 The kinetic fragility of Pt-P- and Ni-P-based bulk glass-forming liquids and its thermodynamic and structural signature *Acta Mater.* **132** 118–27
[14] Inoue A and Nishiyama N 1997 Extremely low critical cooling rates of new Pd–Cu-P base amorphous alloys *Mater. Sci. Eng.* A **226–8** 401–5
[15] Lu I R, Wilde G, Görler G P and Willnecker R 1999 Thermodynamic properties of Pd-based glass-forming alloys *J. Non-Cryst. Solids* **250–2** 577–81
[16] Telford M 2004 The case for bulk metallic glass *Mater. Today* **7** 36–43
[17] Angell C A 1995 Formation of glasses from liquids and biopolymers *Science* **267** 1924–35
[18] Böhmer R, Ngai K L, Angell C A and Plazek D J 1993 Nonexponential relaxations in strong and fragile glass formers *J. Chem. Phys.* **99** 4201
[19] Angell C A 1991 Relaxation in liquids, polymers and plastic crystals—strong/fragile patterns and problems *J. Non-Cryst. Solids* **131–3** 13–31
[20] Carpentier L, Desprez S and Descamps M 2003 From strong to fragile glass-forming systems: a temperature modulated differential scanning calorimetry investigation *Phase Transit.* **76** 787–99
[21] Busch R 2000 The thermo physical properties of bulk metallic glass-forming liquids *JOM* **39** 39–42
[22] Neuber N, Gross O, Eisenbart M, Heiss A, Klotz U E, Best J P, Polyakov M N, Michler J, Busch R and Gallino I 2018 The role of Ga addition on the thermodynamics, kinetics, and tarnishing properties of the Au–Ag–Pd–Cu–Si bulk metallic glass forming system *Acta Mater.* **165** 315–26
[23] Pineda E, Serrano J, Bruna P and Crespo D 2010 Fragility measurement of Pd-based metallic glass by dynamic mechanical analysis *J. Alloys Compd*. **504** S215–8
[24] Qiao J, Casalini R, Pelletier J M and Kato H 2014 Characteristics of the structural and Johari-Goldstein relaxations in Pd-based metallic glass-forming liquids *J. Phys. Chem.* B **118** 3720–30
[25] Evenson Z, Gallino I and Busch R 2010 The effect of cooling rates on the apparent fragility of Zr-based bulk metallic glasses *J. Appl. Phys.* **107** 123529
[26] Moynihan C T, Easteal A J, Wilder J and Tucker J 1974 Dependence of the glass transition temperature on heating and cooling rate *J. Phys. Chem.* **78** 2673–7
[27] Reading M, Elliott D and Hill V L 1993 A new approach to the calorimetric investigation of physical and chemical transitions *J. Therm. Anal.* **40** 949–55
[28] Gill P S, Sauerbrunn S R and Reading M 1993 Modulated differential scanning calorimetry *J. Therm. Anal.* **40** 931–9
[29] Evenson Z, Aleway S E, Wei S, Gross O, Kruzic J J, Gallino I, Possart W, Stommel M and Busch R 2014 β relaxation and low-temperature aging in a Au-based bulk metallic glass: from elastic properties to atomic-scale structure *Phys. Rev.* B **89** 1–14
[30] Zhu M, Wang J Q, Perepezko J H and Yu L 2015 Possible existence of two amorphous phases of d -mannitol related by a first-order transition *J. Chem. Phys.* **142** 244504
[31] Lu Z P, Li Y, Ng S C, Feng Y P and Lu K 1999 Glass transition of rare-earth based metallic glasses: temperature modulated differential scanning calorimetry *J. Non-Cryst. Solids* **250–2** 689–93
[32] Righetti M C 2017 Crystallization of polymers investigated by temperature-modulated DSC *Mater.* (*Basel*) **10** 442
[33] Schawe J E K 2014 Vitrification in a wide cooling rate range : the relations between cooling rate, relaxation time, transition width, and fragility **141** 184905
[34] Kasap S O and Tonchev D 2001 Glass transformation in vitreous As2Se3studied by conventional and temperature-modulated differential scanning calorimetry *J. Mater. Res.* **16** 2399–407
[35] Fraga I, Montserrat S and Hutchinson J M 2007 TOPEM, a new temperature modulated DSC technique : application to the glass transition of polymers *J. Therm. Anal. Calorim.* **87** 119–24
[36] Carpentier L, Bourgeois L and Descamps M 2002 Contribution of temperature modulated DSC® to the study of the

molecular mobility in glass forming pharmaceutical systems *J. Therm. Anal. Calorim.* **68** 727–39
[37] Bechgaard T K, Gulbiten O, Mauro J C, Yue Y, Bauchy M and Smedskjaer M M 2019 Liquid fragility determination of oxide glass-formers using temperature-modulated DSC *Int. J. Appl. Glass Sci.* **10** 321–9
[38] Schawe J E K 1996 Investigations of the glass transitions of organic and inorganic substances: DSC and temperature-modulated DSC *J. Therm. Anal.* **47** 475–84
[39] Gross O 2018 Precious metal based bulk glass-forming liquids: development, thermodynamics, kinetics and structure *PhD Thesis* Saarland University
[40] Jiang Z, Imrie C T and IIutchinson J M 2002 An introduction to temperature modulated differential scanning calorimetry (TMDSC): a relatively non-mathematical approach *Thermochim. Acta* **387** 75–93
[41] Liu C, Pineda E and Crespo D 2015 Mechanical relaxation of metallic glasses: an overview of experimental data and theoretical models *Metals* **5** 1073–11
[42] Hecksher T, Nielsen A I, Olsen N B and Dyre J C 2008 Little evidence for dynamic divergences in ultra viscous molecular liquids *Nat. Phys.* **4** 737–41
[43] Mauro J C, Yue Y, Ellison A J, Gupta P K and Allan D C 2009 Viscosity of glass-forming liquids *Proc. Natl Acad. Sci. USA* **106** 19780–4
[44] Gallino I, Cangialosi D, Evenson Z, Schmitt L, Hechler S, Stolpe M and Ruta B 2018 Hierarchical aging pathways and reversible fragile-to-strong transition upon annealing of a metallic glass former *Acta Mater.* **144** 400–10
[45] Hechler S, Ruta B, Stolpe M, Pineda E, Evenson Z, Gross O, Bernasconi A, Busch R and Gallino I 2018 Microscopic evidence of the connection between liquid–liquid transition and dynamical crossover in an ultra viscous metallic glass former *Phys. Rev. Mater.* **2** 1–6
[46] Angell C A, Ngai K L, McKenna G B, McMillan P F and Martin S W 2000 Relaxation in glass forming liquids and amorphous solids *J. Appl. Phys.* **88** 3113
[47] Eyring H 1936 Viscosity, plasticity, and diffusion as examples of absolute reaction rates *J. Chem. Phys.* **4** 283–91
[48] Maxwell C 1867 On the dynamical theory of gases *Philos. Trans.* **157** 49–88
[49] Masuhr A, Waniuk T A, Busch R and Johnson W L 1999 Time scales for viscous flow, atomic transport, and crystallization in the liquid and supercooled liquid states of $Zr_{41.2}Ti_{13.8}Cu_{12.5}Ni_{10.0}Be_{22.5}$ *Phys. Rev. Lett.* **82** 2290–3
[50] Schawe J E K and Höhne G W H 1996 The analysis of temperature modulated DSC measurements by means of the linear response theory *Thermochim. Acta* **287** 213–23
[51] Schick C, Merzlyakov M and Hensel A 1999 Nonlinear thermal response at the glass transition *J. Chem. Phys.* **111** 2695–700
[52] Schawe J E K and Winter W 1997 The influence of heat transfer on temperature-modulated DSC measurements *Thermochim. Acta* **298** 9–16
[53] Carpentier L, Bustin O and Descamps M 2002 Temperature-modulated differential scanning calorimetry as a specific heat spectroscopy *Signals* **402** 4–11
[54] Angell C A 1988 Perspectives on the glass transition *J. Phys. Chem. Solids* **49** 863–71
[55] Busch R and Gallino I 2017 Kinetics, thermodynamics, and structure of bulk metallic glass forming liquids *JOM* **69** 2178–86
[56] Schmelzer J W P 2012 Kinetic criteria of glass formation and the pressure dependence of the glass transition temperature *J. Chem. Phys.* **136** 1–11
[57] Kuball A, Bochtler B, Gross O, Pacheco V, Stolpe M, Hechler S and Busch R 2018 On the bulk glass formation in the ternary Pd–Ni-S system *Acta Mater.* **158** 13–22
[58] Gracia-Fernández C A, Gómez-Barreiro S, López-Beceiro J, Tarrío Saavedra J, Naya S and Artiaga R 2010 Comparative study of the dynamic glass transition temperature by DMA and TMDSC *Polym. Test.* **29** 1002–6
[59] Williams G and Watts D C 1970 Non-symmetrical dielectric relaxation behaviour arising from a simple empirical decay function *Trans. Faraday Soc.* **66** 80
[60] Carpentier L, Decressain R and Descamps M 2004 Relaxation modes in glass forming meta-toluidine *J. Chem. Phys.* **121** 6470–7
[61] Zhuravlev E and Schick C 2010 Fast scanning power compensated differential scanning nano-calorimeter: 1. the device *Thermochim. Acta* **505** 1–13
[62] Zhuravlev E and Schick C 2010 Fast scanning power compensated differential scanning nano-calorimeter: 2. heat capacity analysis *Thermochim. Acta* **505** 14–21
[63] Mathot V, Pyda M, Pijpers T, Vanden G, Van De Kerkhof E, Van Herwaarden S, Van Herwaarden F and Leenaers A 2011 The Flash DSC 1, a power compensation twin-type, chip-based fast scanning calorimeter (FSC): first findings on polymers *Thermochim. Acta* **522** 36–45
[64] Schawe J E K 2015 Measurement of the thermal glass transition of polystyrene in a cooling rate range of more than six decades *Thermochim. Acta* **603** 128–34
[65] Spieckermann F, Steffny I, Bian X, Ketov S, Stoica M and Eckert J 2019 Fast and direct determination of fragility in metallic glasses using chip calorimetry *Heliyon* **5** e01344
[66] Shoifet E, Schulz G and Schick C 2015 Temperature modulated differential scanning calorimetry—extension to high and low frequencies *Thermochim. Acta* **603** 227–36

5.2 Paper II: Liquid-like versus stress-driven dynamics in a metallic glass former observed by temperature scanning XPCS

Authors

Maximilian Frey, Nico Neuber, Sascha Sebastian Riegler, Antoine Cornet, Yuriy Chushkin, Federico Zontone, Lucas Matthias Ruschel, Bastian Adam, Mehran Nabahat, Fan Yang, Jie Shen, Fabian Westermeier, Michael Sprung, Daniele Cangialosi, Valerio Di Lisio, Isabella Gallino, Ralf Busch, Beatrice Ruta, Eloi Pineda

Publishing information

Submitted: 10.05.2024

Accepted: 01.05.2025

Published: 13.05.2025

Journal: Nature Communications, 16 (2025), 4429

DOI: 10.1038/s41467-025-59767-2

Abstract of the article

Since several decades, the dynamics and vitrification kinetics of supercooled liquids are the subject of active research in science and engineering. Profiting from modern detector technology and highly brilliant fourth-generation synchrotron radiation, we apply temperature scanning X-ray photon correlation spectroscopy (XPCS) to probe the dynamics of a Pt-based metallic glass former in the glass, glass transition region, and supercooled liquid, covering up to six orders of magnitude in timescales. Our data demonstrates that the structural α-relaxation process is still observable in the glass, although it is partially masked by a faster source of decorrelation observed at atomic scale. We present an approach that interprets these findings as the superposition of heterogeneous liquid-like and stress-driven ballistic-like atomic motions. This work not only extends the dynamical range probed by standard isothermal XPCS but also adds a different view on the α-relaxation across the glass transition and provides insights into the anomalous, compressed temporal decay of the density-density correlation functions observed in metallic glasses and many out-of-equilibrium soft materials.

nature communications

Article

https://doi.org/10.1038/s41467-025-59767-2

Liquid-like versus stress-driven dynamics in a metallic glass former observed by temperature scanning X-ray photon correlation spectroscopy

Received: 10 May 2024

Accepted: 1 May 2025

Published online: 13 May 2025

Check for updates

Maximilian Frey[1] ✉, Nico Neuber[1], Sascha Sebastian Riegler[1], Antoine Cornet[2,3], Yuriy Chushkin[3], Federico Zontone[3], Lucas Matthias Ruschel[1], Bastian Adam[1], Mehran Nabahat[4], Fan Yang[5], Jie Shen[2,3], Fabian Westermeier[6], Michael Sprung[6], Daniele Cangialosi[7,8], Valerio Di Lisio[7], Isabella Gallino[9], Ralf Busch[1], Beatrice Ruta[2,3] & Eloi Pineda[4]

Since several decades, the dynamics and vitrification kinetics of supercooled liquids are the subject of active research in science and engineering. Profiting from modern detector technology and highly brilliant fourth-generation synchrotron radiation, we apply temperature scanning X-ray photon correlation spectroscopy (XPCS) to probe the dynamics of a Pt-based metallic glass former in the glass, glass transition region, and supercooled liquid, covering up to six orders of magnitude in timescales. Our data demonstrates that the structural α-relaxation process is still observable in the glass, although it is partially masked by a faster source of decorrelation observed at atomic scale. We present an approach that interprets these findings as the superposition of heterogeneous liquid-like and stress-driven ballistic-like atomic motions. This work not only extends the dynamical range probed by standard isothermal XPCS but also adds a different view on the α-relaxation across the glass transition and provides insights into the anomalous, compressed temporal decay of the density-density correlation functions observed in metallic glasses and many out-of-equilibrium soft materials.

When a liquid is undercooled, it changes from a stable to a metastable equilibrium state. Its structural dynamics undergo a drastic slowdown over several orders of magnitude. The temperature dependence of this slowdown can differ significantly among different systems, as described by Austen Angell's famous fragility concept[1] that categorizes liquid dynamics by their deviation from an exponential, Arrhenius-like temperature dependence. The dynamic slowdown of undercooled liquids is the precondition that eventually results in vitrification, where the liquid

[1]Chair of Metallic Materials, Saarland University, Saarbrücken, Germany. [2]Institut Néel, Université Grenoble Alpes and Centre National de la Recherche Scientifique, Grenoble, France. [3]European Synchrotron Radiation Facility, Grenoble, France. [4]Department of Physics, Institute of Energy Technologies, Universitat Politècnica de Catalunya—BarcelonaTech, Barcelona, Spain. [5]Institut für Materialphysik im Weltraum, Deutsches Zentrum für Luft- und Raumfahrt (DLR), Köln, Germany. [6]Deutsches Elektronen-Synchrotron DESY, Hamburg, Germany. [7]Donostia International Physics Center, San Sebastián, Spain. [8]Centro de Física de Materiales (CSIC-UPV/EHU), San Sebastián, Spain. [9]Metallic Materials, Technical University of Berlin, Berlin, Germany.
✉e-mail: maximilian.frey@uni-saarland.de

Article https://doi.org/10.1038/s41467-025-59767-2

'falls out of equilibrium'[4] and forms a non-ergodic, non-equilibrium glass. In other words, liquid dynamics predetermine vitrification kinetics. Hence, understanding the nature of the dynamic slowdown and fragility is of fundamental relevance for glass science and industry-relevant aspects like e.g., the glass forming ability of a given system.

A mighty tool to determine the dynamics of disordered materials is X-ray photon correlation spectroscopy (XPCS), a time-resolved experimental approach[2] that uses monochromatic and coherent synchrotron radiation. Coherent diffraction on amorphous matter creates a speckle pattern that reflects the configuration of the microscopic ensemble in the probed sample volume. Temporal changes in the microscopic configuration induce changes in the speckle pattern and accordingly, the correlation between two speckle patterns will decay with growing temporal distance. Analyzing the intensity autocorrelation function thus allows us to determine microscopic relaxation times. XPCS studies that resolute the atomic-scale dynamics of metallic glass formers require highly brilliant radiation to compensate the weak scattering signal of these amorphous materials and are therefore only possible since about one decade[3]. While the signal-to-noise ratio and detector technology limited the exposure time to several seconds in earlier studies[3–10], recent advances allowed exposure times in the subsecond regime[11–15].

While some non-isothermal XPCS approaches can be found in literature[15–18], XPCS studies on metallic glass formers are usually measured under isothermal conditions. In the present study, we instead perform temperature scanning XPCS, where the temperature is changed continuously with a constant rate. In order to do so, we use the high flux available at the ID10 beamline of the fourth-generation European Synchrotron Radiation Facility (ESRF) after the Extremely Brilliant Source (EBS) upgrade[19,20]. The test subject of this work is the $Pt_{42.5}Cu_{27}Ni_{9.5}P_{21}$ alloy[21]. Its excellent thermal stability against crystallization previously allowed our groups to investigate the supercooled liquid (SCL) dynamics through isothermal XPCS experiments[13]. The present work extends these studies by slowly heating and cooling the sample through the glass, the glass transition, and the SCL state.

In the equilibrium SCL, the decay of the obtained intensity autocorrelation functions can be modeled accurately by a conventional Kohlrausch-Williams-Watts (KWW) equation with stretched shape, which reflects the heterogeneous, liquid-like atomic motions of the α-relaxation process, as previously observed by isothermal XPCS[13]. Furthermore, the temperature dependence of the determined relaxation times is found to mimic the alloy's fragility measured by macroscopic viscosity measurements[22]. A different picture arises in the non-equilibrium state, i.e., in the glass and the glass transition region. Here, the conventional KWW fit fails to describe the decay of the intensity autocorrelation functions. Instead, we successfully model the complexly shaped decorrelation through a multiplication of two KWW functions. One of these features a stretched shape (KWW shape exponent <1), while the other one features a compressed shape (KWW shape exponent > 1).

Based on the long-standing concept of spatially heterogeneous dynamics, we offer a scenario that explains these findings through two different but simultaneously occurring types of atomic motion. More precisely, we interpret the vitrification process as the interlocking of nm-scale regions with slower dynamics, so termed 'rigid domains'. This jamming-like effect results in volumetric frustration and internal stress gradients, which induce ballistic-like 'microscopic drift' movements with a typical compressed decorrelation footprint. On the other hand, we attribute the stretched decorrelation component to atomic motions related to the liquid-like α-relaxation, which remains partially active in the non-equilibrium. The superposition of these two types of atomic motion finally creates the complex decorrelation shape observed in the non-equilibrium states.

Results

A first overview of the temperature scanning XPCS results

The thermal program applied during the XPCS experiments consists of a heating scan and a subsequent cooling scan, both performed with a rate of 0.0167 K s^{-1} (1 K min^{-1}). It is retraced ex-situ by differential scanning calorimetry (DSC) and the obtained heat flow signal is shown in Fig. 1A. The initial heating of the as-spun ribbon sample starts in the glassy state, passes the glass transition region between 500 K and 525 K, and enters the SCL state until the maximum temperature of 548 K is reached. In the cooling scan, the sample is cooled until vitrification occurs between 521 K and 490 K, finally reentering the glassy state. Accordingly, the thermal ranges of the glass, glass transition, and SCL regions are distinguished by gray, light gray, and white backgrounds to guide the eyes in Fig. 1A.

Two time correlation functions (TTCFs) and intensity autocorrelation functions, g_2, are evaluated in subsequent batches of 240 s duration, as further explained in the "Materials and Methods" section. To provide an overview, we focus on six of these evaluation batches in the following, numbered from B1 to B6. They are located at representative temperatures in the glass (480 K), glass transition (510 K), and SCL (541 K) upon heating and cooling, as indicated in Fig. 1A. The corresponding TTCFs are shown in Fig. 1B to give a first graphical impression of the evolution of dynamics during the temperature scanning procedure. Warm colors depict high intensity-intensity correlation between two experimental times t_1 and t_2, whereas cold colors describe low correlation. As expected, decorrelation accelerates with rising temperature, which is graphically represented by a clear narrowing of the warm-colored stripe along the diagonal of the TTCFs. The g_2 data in Fig. 1C, D mirrors this trend by showing faster decays at higher temperatures, indicating an overall acceleration of dynamics due to increased thermal motion.

Conventional KWW fitting in the equilibrium

In liquids, the temporal decay of the intermediate scattering function (ISF) and the related g_1 function is usually described by a KWW function[23]

$$|g_1(t)| = f\exp\left(-\left(\frac{t}{\tau}\right)^{\beta}\right) \tag{1}$$

and since g_1 and g_2 are connected through the Siegert relation[24,25],

$$g_2(t) = b + c\,|g_1(t)|^2 \tag{2}$$

it follows that the intensity autocorrelation function can be modeled as

$$g_2(t) = b + c\exp\left(-2\left(\frac{t}{\tau}\right)^{\beta}\right) \tag{3}$$

where f is the non-ergodicity parameter, τ is the relaxation time, β is the shape exponent, c is the experimental contrast, and b is the baseline value. The resulting KWW fits of the g_2 data are displayed by black solid curves in Fig. 1C, D. In the SCL state (B3 and B4), the KWW function models the stretched decay of g_2 quite satisfactorily, in agreement with previous findings[6,12,13,26]. A different picture arises in the non-equilibrium, i.e., in the glass transition and glass region (B1, B2, B5, and B6), where the KWW fits clearly fail to describe the complex shape of g_2. More precisely, the initial parts of the g_2 data, roughly the first three decades in timescale, from 0.01 to 10 s, behave more stretched than the overall KWW fit curve, while the later parts appear more compressed. Hence, we observe a kind of 'cut-off' behavior, where an initially stretched decay abruptly changes into a more compressed appearance.

 https://doi.org/10.1038/s41467-025-59767-2

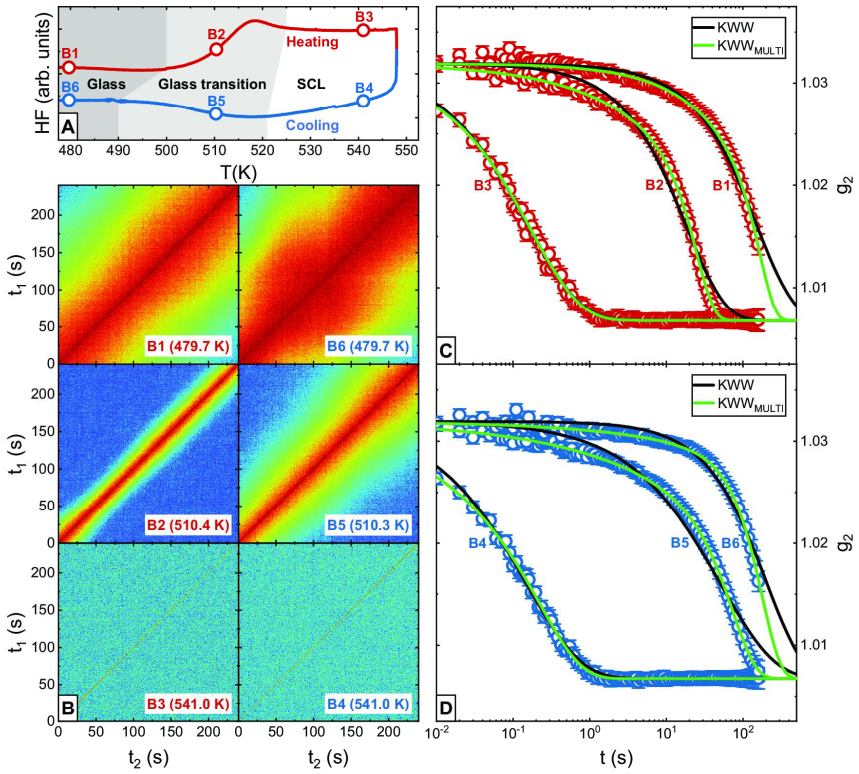

Fig. 1 | Applied thermal program, representative TTCFs and g_2 curves, as well as different fitting approaches. A Ex-situ differential scanning calorimetry (DSC) scans retrace the 0.0167 K s^{-1} heating-cooling protocol applied for the X-ray photon correlation spectroscopy (XPCS) measurements. The three thermal regions, namely glass, glass transition, and supercooled liquid (SCL), are distinguished through shaded backgrounds. Furthermore, circles highlight the temperatures of six representative g_2 evaluation batches, numbered from B1 to B6. **B** The two time correlation functions (TTCFs) of these six g_2 batches illustrate the accelerating dynamics with increasing temperature. Each TTCF includes information stemming from 24000 frames. For their respective color bars, see Supplementary Fig. 9 in the SI. The corresponding intensity autocorrelation functions are further given in (**C**, **D**). Each g_2 data set consists of 96 mean value data points, the error bars represent standard deviations. The Kohlrausch-Williams-Watts (KWW) fits and KWW_{MULTI} fits are shown as black and green lines, respectively. Both fit approaches provide satisfying and similar results in the SCL state (B3 and B4), but while the KWW approach fails to describe the shape of the g_2 decorrelation in the glass and especially in the glass transition region, KWW_{MULTI} provides meaningful results (B1, B2, B5, and B6). The fit parameters of the shown KWW and KWW_{MULTI} curves can be found in Fig. 3.

On the multiplicative KWW fitting used in the non-equilibrium

Previous XPCS studies revealed that metallic glass formers show an anomalous crossover in their microscopic dynamics. While the metastable equilibrium SCL phase typically features stretched decorrelation with β values below 1[6,12,13,26,27], compressed decorrelation with β values above 1 is found in the non-equilibrium glass[3,5,9,12,14,26,28–31]. Yet, a failure of the KWW model due to the complex superposition of stretched and compressed components as observed in the present work is, to our best knowledge, a feature that has not been reported so far. We attribute this observation to the fast exposure time of 0.01 s, which allows us to explore almost five orders of magnitude in timescale and to observe the glass transition upon temperature scanning as a gradual crossover between liquid-typical stretched and glassy-typical compressed decay. Earlier XPCS studies at third generation synchrotrons were technically limited to exposure times in the order of seconds[3,5,7,9,10,26,28,30,32–34], therefore lacking the temporal resolution to detect such features. It shall be furthermore mentioned that macroscopic approaches like e.g., stress relaxation measurements usually do not feature compressed decays[35–37], albeit exceptions were recently reported[38].

The complex decorrelation behavior in the non-equilibrium asks for an adapted fitting approach. In general, the temporal decorrelation of the ISF results from all the relative positional changes $\Delta\mathbf{r}_{j-k}(t) = \mathbf{r}_j(t) - \mathbf{r}_k(0)$ between all scattering particles N that occur within the time coordinate t[39–42]:

$$g_1(t) \propto \left\langle \sum_{j=1}^{N} \sum_{k=1}^{N} a_j(0)\, a_k(t) \exp\left(-i\,\boldsymbol{q}\,\Delta\boldsymbol{r}_{j-k}(t)\right) \right\rangle \qquad (4)$$

where a_j and a_k are the scattering factors of the respective particles. SCLs are well-known to feature heterogeneous dynamics, which implies large spatial and temporal fluctuations in $\Delta\mathbf{r}_{j-k}(t)$[43–45]. Hence, the ISF decorrelation incorporates a broad distribution $D(\tau')$ of exponential relaxations $g_{1,\tau'}(t) = \exp(-t/\tau')$ extending over several

Article https://doi.org/10.1038/s41467-025-59767-2

decades according to

$$g_1(t) = \int g_{1,\tau'}(t)\, D(\tau')\, d\tau' \tag{5}$$

and eventually, this leads to the liquid-typical stretched exponential shape[43–45].

Yet, compressed decorrelation cannot be explained by a distribution of exponential contributions. In this case, some models have demonstrated that stress-driven particle rearrangements can produce a compressed decay of the ISF[46]. Our ansatz will be the following: In the non-equilibrium state, the scattering particles can be subjected to two different types of motion, one liquid-like leading to a stretched decorrelation component (index S) and another one resulting in a compressed decorrelation component (index C), which is activated once the system is rigid enough to build the necessary stresses.

The relative positional changes of particles, therefore, result from a sum of these two types of particle movement, $\Delta\mathbf{r}_{j-k}(t) = \Delta\mathbf{r}_{j-k,S}(t) + \Delta\mathbf{r}_{j-k,C}(t)$. Hence, it follows from Eq. 4 that the global g_1 function can be approached by a factorization[41,47–49] as

$$|g_1(t)|^2 = |g_{1,S}(t)|^2\, |g_{1,C}(t)|^2. \tag{6}$$

Regarding the Siegert relation in Eq. 2, a multiplicative KWW fit function unfolds for the observed g_2 decay, termed KWW_{MULTI} in the following:

$$g_2(t)_{t_{batch}} = b + c\exp\left(-2\left(\frac{t}{\tau_S}\right)^{\beta_S}\right)\exp\left(-2\left(\frac{t}{\tau_C}\right)^{\beta_C}\right) \tag{7}$$

The KWW_{MULTI} fits of the six representative evaluation batches are shown in Fig. 1C, D as green solid lines. In the SCL state (B3 and B4), no significant increase in fit quality is gained by changing from conventional KWW to KWW_{MULTI}, since both approaches create practically overlapping curves. This changes drastically in the glass transition region (B2 and B5), where KWW_{MULTI} provides adequate fitting while the conventional KWW fails to do so. In the glassy state (B1 and B6), the misfit between g_2 data and KWW fit might be less distinct than in the glass transition region, but still, KWW_{MULTI} allows for more accurate fitting of the data.

Figure 2 focuses on batch B5 located in the glass transition region upon cooling to provide an in-depth comparison of the suboptimal KWW fit (black curve) and the well-functioning KWW_{MULTI} (green curve) approach. The orange and purple dashed curves depict the two components of the KWW_{MULTI} fit, KWW_S as well as KWW_C. Here, the rather fast ($\tau = 133$ s), but also highly compressed ($\beta = 1.61$) KWW_C provides almost no decorrelation in the first three decades below 10 s. This leads to the apparently counterintuitive result that the short-time domain is rather dominated by the slow ($\tau = 3423$ s), but quite stretched ($\beta = 0.33$) KWW_S (orange arrow and background). It is only after the initial 10 s that the compressed KWW_C gains momentum. After 57 s, it overcomes KWW_S and starts to dominate the overall g_2 decay, allowing to describe the cut-off appearance (purple arrow and background). Here, it shall be mentioned that the factorization in Eq. 6 is strictly valid only if the timescales of the two motion types are sufficiently different from each other[47] and, therefore, one of the two processes clearly dominates the decay. Hence the KWW_{MULTI} model will be an accurate approach in the short time region, the first three decades in Fig. 2, where only the fast time portion of the broad relaxation time distribution underlying the stretched decay contributes to the heterogeneous ISF. In the rather narrow timescale region dominated by the compressed cut-off decorrelation, the two sources of motion cannot be precisely disentangled, and the multiplicative approach should be interpreted as a functional shape that can adapt to model the structural dynamics participated by both sources of motion.

For the sake of completeness, we want to note that a compressed decay in g_2 can also stem, in principle, from a macroscopic sample movement relative to the incoming photon beam, called transit decorrelation[41,50]. Indeed, the constant temperature change of the temperature scanning method implies a corresponding thermal expansion of the measurement setup, which could cause such an artifact. Yet, we estimated this effect based on the conditions of the given experimental setup and found it to be negligible, as further explained in the Supplementary Information (SI).

Comparing conventional and multiplicative KWW fitting results

Introducing additional fit parameters, and, therefore, additional degrees of freedom, to a fit function easily improves its adaptivity towards a given data set. To validate the physical meaning behind the fit results, Fig. 3 compares τ and β values obtained from conventional KWW and KWW_{MULTI} during both, heating and cooling. Again, the ex-situ DSC scans are provided, see Fig. 3A, D, and the thermal ranges of the glass, glass transition, and SCL regions are separated by gray, light gray, and white backgrounds. For reasons of clarity, fit results are only displayed in the temperature regions where they appear meaningful. Hence, the KWW results are only shown in the SCL state, while the KWW_{MULTI} data is limited to the glass and glass transition region. Nevertheless, the complete data sets over the full temperature range can be found in Supplementary Fig. 2 in the SI.

Upon heating in the glass and through the full glass transition region, τ_C in Fig. 3B features a glass-typical weak temperature dependence in agreement with previous works[3,42]. While τ_S is roughly in the order of τ_C at lower temperatures in the glass, it departs from τ_C at about 480 K and starts to rise. We interpret this as aging behavior, the onset of major structural rearrangements in the proximity of the glass transition and the consequent relaxation of the system towards the SCL upon heating with a rate much slower than the fast quenching used to produce the as-spun glass[3,42]. The DSC scan in Supplementary Fig. 3 in the SI further supports this interpretation. It shows a massive exothermal signal below the glass transition, which is a well-known indication for aging. τ_S reaches a maximum in the initial part of the calorimetric glass transition at about 506 K and then adopts a steep negative temperature dependence, hence, approaching a liquid-like trendline. When entering the SCL, τ_C and τ_S merge into the conventional KWW τ curve, which continues the liquid-like temperature trend previously seen for τ_S to finally reach values as fast as 0.2 s at the maximum temperature. The shape exponents β_C and β_S depart drastically in the glass and glass transition region. With values in the order of 2, β_C is highly compressed, but abruptly drops to values around unity when reaching the SCL state. In contrast, β_S features stretched values between 0.35 and 0.7 in the whole observed temperature range. In the glass, it shows a slight downwards trend with rising temperature. Yet, at 506 K, the temperature at which τ_S enters the liquid-like trendline, β_S also starts to feature a faint upwards trend, which is in agreement with previous data obtained in the SCL by Neuber et al.[13]. This temperature behavior of β_S also resembles the one observed in macroscopic stress relaxation dynamics[35]. As an additional verification, KWW and KWW_{MULTI} fitting were also tested with fixed β and β_S values to decrease the number of parameters in the fitting routine and improve the level of confidence. Although the general interpretation is not affected, these approaches provided less optimal results as they do not take into account the small but relevant temperature trends of these shape exponents in the probed $Pt_{42.5}Cu_{27}Ni_{9.5}P_{21}$ alloy[13] (see also Supplementary Fig. 8 and the related discussion in the SI).

Regarding the results of the cooling scan in Fig. 4E, F, the τ and β values obtained in the SCL state basically show the similar temperature trends as during heating. When entering the glass transition region, τ_C and τ_S again decouple drastically. While τ_C changes to a glass-typical,

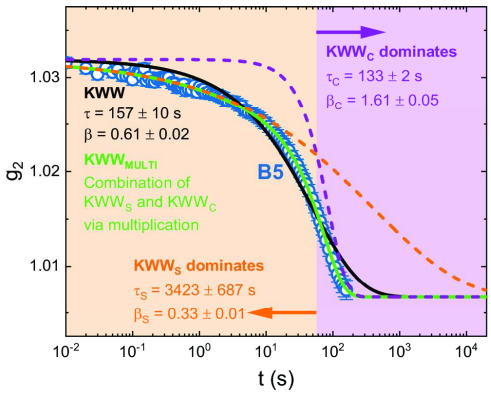

Fig. 2 | The KWW$_{MULTI}$ fitting approach in detail. Intensity autocorrelation function of the representative batch B5, located in the glass transition region upon cooling (510.3 K) as indicated in Fig. 1. The data set consists of 96 mean value data points, the error bars give the standard deviations. The black solid curve represents the conventional Kohlrausch-Williams-Watts (KWW) fit, which fails to describe the cut-off shape of the g_2 decorrelation. Instead, the KWW$_{MULTI}$ fit (green solid line) describes the decay exceptionally well. It results from a multiplication of a stretched (KWW$_S$) and a compressed (KWW$_C$) component (orange and purple dashed lines). While KWW$_S$ dominates the KWW$_{MULTI}$ fit roughly within the first 57 s (orange background and arrow), KWW$_C$ dominates at longer timescales (purple background and arrow), thereby creating the apparent cut-off appearance.

nearly temperature-insensitive course, τ_S follows the liquid-like trendline until the end of the glass transition at about 490 K, where it finally leaves the equilibrium course at high values in the order of 10^5 s. The decoupling is simultaneously observed in the shape exponents. β_C rises to highly compressed values of about 2, while β_S keeps slightly decreasing with temperature until reaching values as low as 0.3 when the glass is approached. Comparably low values of the stretching exponent in well relaxed metallic glasses are found in macroscopic relaxation dynamics and simulations[36,37].

Overall, the astonishingly good temperature agreement between calorimetric signals and changes in the KWW and KWW$_{MULTI}$ fitting parameters shall be emphasized, especially concerning the thresholds between glassy state, glass transition region, and SCL. These findings speak in favor of the applied temperature correction procedure, which is described in the "Methods" section and in the SI.

Additive KWW fitting as an alternative in the non-equilibrium

It is important to stress that the presence of multiple dynamical contributions in the ISF can be modeled also with a sum of two KWW expressions (further termed KWW$_{ADD}$) with comparable accuracy, and that the discrimination between KWW$_{ADD}$ and KWW$_{MULTI}$ is not straightforward. In literature, KWW$_{ADD}$ is usually employed when the timescales associated with the two processes are sufficiently separated, resulting in a split of the correlation curves into two distinctly separated parts and creating a step-like appearance in the decay[15,51–53] Yet, this is not observed at the atomic length scales probed in our present experiments, since we only see (cut-off) single decays as shown in Fig. 1 and Fig. 2. By its mathematical construction, KWW$_{ADD}$ therefore locates the timescale of the stretched component ($\tau_{S,ADD}$) at nearly equal or shorter times than found for the compressed component ($\tau_{C,ADD}$), see Suppementary Fig. 7 in the SI. Consequently, the main difference between KWW$_{ADD}$ and KWW$_{MULTI}$ is based on the temperature evolution of $\tau_{S,ADD}$, which features rather unphysical activation energies in the non-equilibrium glass transition and glass region. As discussed in detail in the SI, we therefore believe that the multiplicative model is more appropriate to describe the current data.

A comparison with macroscopic fragility measurements

An option to validate the temperature scanning XPCS method is to evaluate if it arrives at the same SCL fragility as determined by other experimental approaches. For this purpose, Fig. 4 compares the present KWW-fitted τ results to their equivalents from isothermal XPCS by Neuber et al.[13] as well as to equilibrium viscosities stemming from thermomechanical analysis (TMA) by Gross et al.[22]. To allow a direct comparison in the same physical quantity, the relaxation times are converted into viscosity values, $\eta(\tau)$, using the Maxwell relation $\eta = G\,\tau$[54] (G being a shear modulus) and the cooperative shear model (CSM)[55,56], as explained in detail in the "Methods" section. The data sets show broad agreement and obey the same CSM fit curve (black line), demonstrating their basically identical temperature dependence, i.e., fragility. This demonstrates that temperature scanning XPCS can provide substantial results on par with isothermal XPCS[13] and macroscopic approaches like the here shown TMA[22] or also calorimetry[22,57].

The τ_S data from the KWW$_{MULTI}$ fitting are also converted into viscosities, $\eta(\tau_S)$, and aligned in Fig. 4. $\eta(\tau_S)$ follows the CSM fit and the course of the TMA equilibrium viscosities throughout most of the glass transition region upon heating and cooling, as indicated by the arrows. This behavior confirms a trend already observed in Fig. 3, which is the KWW$_S$ component extrapolating the liquid-like dynamics from the equilibrium SCL state into the non-equilibrium glass transition region. During cooling, signs of vitrification can only be observed in the glass region, where τ_S leaves the equilibrium trendline. Upon heating, the KWW$_S$ component reflects aging of the relatively unstable as-spun glass, as τ_S gradually evolves towards the equilibrium trendline. Hence, KWW$_S$ can be seen as the KWW$_{MULTI}$ component that thaws first during heating and freezes last during cooling.

Finally, it shall be noted that instead of using the KWW relaxation times, the comparison between equilibrium viscosity and XPCS results can be also validly established using the average relaxation time $\langle\tau\rangle$[58], see Eq. (9) in the "Methods" section. This property combines the τ and β parameters from the KWW functions into a timescale parameter that also includes information about the shape of the decorrelation and hence, about the relaxation time distribution D(τ′). We see in Fig. 4 that $\eta(\langle\tau\rangle)$ and $\eta(\langle\tau\rangle_S)$ behave practically identical to $\eta(\tau)$ and $\eta(\tau_S)$, as the respective data sets show large overlap.

Discussion

The shape exponents β and β_S in Fig. 3C, F feature values distinctly below unity that reflect the stretched exponential decay typical for the heterogeneous nature of supercooled metallic glass forming liquids[6,12,13,26]. Furthermore, β and β_S decrease with decreasing temperature, as previously observed in the isothermal XPCS studies by Neuber et al.[13]. While the origin of this well-known temperature trend in the shape exponent is still subject of vital debates[59], it is often correlated with liquid dynamics becoming more temporally[60–62] and spatially[44,45,62] heterogeneous with undercooling. While the former describes a general, non-localized tendency towards a broadening relaxation time distribution, D(τ′) (see Eq. 5), the latter specifically refers to spatial fluctuations in the dynamics[45,63]. Voyles et al. recently used novel electron correlation spectroscopy (ECS)[64] to image such spatio-temporally heterogeneous dynamics in supercooled $Pt_{57.5}Cu_{14.7}Ni_{5.3}P_{22.5}$, an alloy similar to our present system[65,66]. Large differences in relaxation time of up to two orders of magnitude were observed between neighboring nm-sized domains, thus, on a length scale that is typical for the medium range order (MRO). This implies a sub-diffusive[60,67,68] structural relaxation process that is governed by cooperative atomic rearrangements and caging effects.

Article https://doi.org/10.1038/s41467-025-59767-2

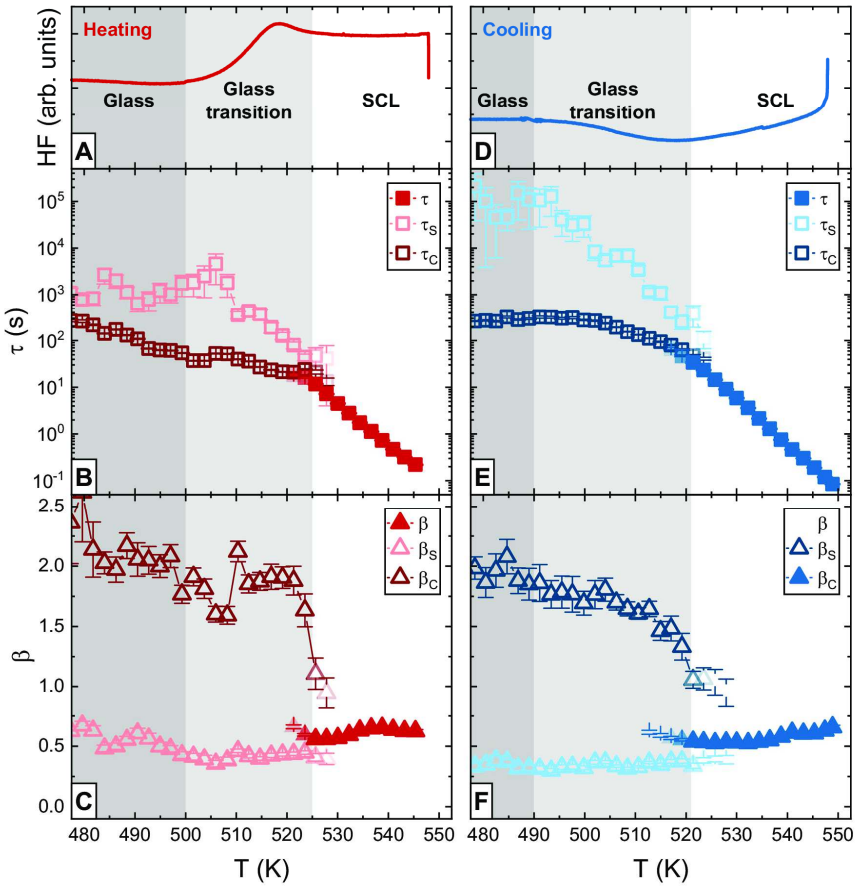

Fig. 3 | KWW and KWW_{MULTI} fit results. Reference differential scanning calorimetry (DSC) scans for heating and cooling are provided in (**A**, **D**). The temperature range is accordingly separated into three regions, glass (dark gray background), glass transition (light gray background), and SCL (white background). **B**, **C**, **E**, **F** compare the relaxation time and shape exponent data resulting from conventional Kohlrausch-Williams-Watts (KWW) and KWW_{MULTI} fitting of the g_2 data sets (each set consists of 96 mean values). The error bars represent the standard errors of the fits. As demonstrated in Fig. 1, KWW only provides meaningful results in the SCL state, while KWW_{MULTI} excels in the glass and glass transition region but appears redundant in the SCL. Accordingly, the data sets are reported only for the temperature regions where the different models provide reliable and more accurate fits (see also Supplementary Fig. 2 in the SI). The KWW fit parameters in the SCL show typical liquid behavior, namely a steep temperature dependence of τ and β values below 1. In the glass transition region, the KWW_{MULTI} approach reveals large differences between its two components KWW_C and KWW_S: While the KWW_C parameters follow glass-typical trends, in particular a relatively temperature-insensitive course of τ_C and a highly compressed shape, the KWW_S parameters show liquid-like behavior in form of a steep temperature dependence of τ_S and a stretched shape.

The KWW_C component of KWW_{MULTI} combines non-equilibrium-associated properties like highly compressed β_C values and a weak temperature dependence of τ_C in the whole glass and glass transition region, see Fig. 3. KWW_C therefore exhibits the inverse behavior of KWW_S, as it thaws last during heating and freezes first upon cooling. Similar compressed decays in photon correlation spectroscopy studies were first reported for non-equilibrium materials like jammed colloids, concentrated emulsions, and clays[46,50,69–72]. Its appearance is mostly attributed to super-diffusive dynamics in form of ballistic motions, which manifest as collective, drift-like particle movements promoted by gradients of internal stresses that arise during jamming or vitrification[69,70,73]. Later XPCS studies confirmed compressed decorrelation to be also a general feature of vitrified metallic glass formers[3,5,12,14,28–30], making a similar stress-based origin likely. Purely ballistic dynamics imply straight particle trajectories that create an archetypically compressed decay of the ISF with a β value of 2[41,50,74–76]. Furthermore, they are characterized by a $|\mathbf{q}|$-dependent relaxation time according to $\tau \propto |\mathbf{q}|^{-1}$[69]. Recent XPCS results by Cornet et al.[14] suggest a rather ballistic-like $|\mathbf{q}|$-dependence also for glassy $Pt_{42.5}Cu_{27}Ni_{9.5}P_{21}$.

To state an interim conclusion, the heterogeneous and likely sub-diffusive atomic motions of the α-relaxation process seem to survive, to some degree, in the non-equilibrium, as indicated by the presence of the typical stretched exponential decay (KWW_S). Yet, they appear superimposed by a second type of atomic motion that is characteristic for the non-equilibrium state and can be described by the compressed

Article https://doi.org/10.1038/s41467-025-59767-2

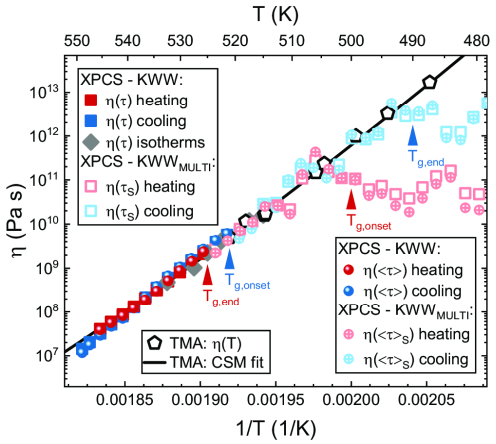

Fig. 4 | Fragility comparison. τ, τ_S,$\langle\tau\rangle$, and $\langle\tau\rangle_S$ data from Kohlrausch-Williams-Watts (KWW) and KWW_{MULTI} fitting as well as τ data from isothermal X-ray photon correlation spectroscopy (XPCS)[13] are converted into viscosity values and compared to equilibrium viscosity data determined by thermomechanical analysis (TMA)[22], which serve as a reference. All data sets are described by the same cooperative shear model (CSM) fit curve, demonstrating that the different methods observe the same fragility. The start and end temperatures of the glass transition in the XPCS heating and cooling scans are indicated by red and blue arrows, respectively.

decay component (KWW_C). This latter process arises from longer range elastic interactions leading to ballistic-like particle motions, probably related to intermittent cluster dynamics[14,77,78]. The question arises, how these stress-induced ballistic-like motions can be visualized. The present homodyne experiment observes dynamics at the $|\vec{q}|$ value of the structure factor maximum and therefore probes both, the self and the distinct part of the ISF[42], thus reflecting the temporal decorrelation of the structure not only at the particle-particle distance but also on the MRO length scale[79]. Hence, specific traits of the stress fields that cause the compressed decay, such as the length and timescale of the stress fluctuations, or the intensity of stress gradients, cannot be straightforwardly quantified from the current observations. Publications exploring the relation between the particle dynamics and the homodyne g_2 function in multicomponent systems in the non-equilibrium are still scarce[77], and therefore, we can only propose here a qualitative picture.

Nevertheless, many works interpret the glass transition in terms of heterogeneities in dynamics, structure, and density[44,45,80–86] and considering the earlier mentioned spatio-temporally heterogeneous dynamics imaged via ECS in a compositionally similar Pt-based alloy[65,66], such a scenario suggests itself in case of the present $Pt_{42.5}Cu_{27}Ni_{9.5}P_{21}$ system. We thus want to offer a picture that identifies spatial domains with slower relaxation times as the carriers of the stress-driven, ballistic-like motions. To illustrate our considerations in detail, we will focus on the cooling scan, where the SCL gently vitrifies without interfering aging effects as observed during heating. For this purpose, Fig. 5 connects the representative g_2 batches B4, B5, and B6 from Fig. 1 with simplified visualizations of the atomic dynamics at the given temperatures.

Figure 5A sketches the spatially heterogeneous dynamics of the equilibrium SCL. Here, the liquid-like and likely sub-diffusive motions of individual atoms are illustrated by orange arrows of varying lengths. Heterogeneity manifests spatially through nm-sized[65,66] domains of diverse mobility, likely corresponding to fluctuations in density or atomic packing[84,87]. Domains with slower dynamics, which will be referred to as 'rigid' in the following, are highlighted by gray shadows to guide the eyes. In the SCL, the overall fast atomic mobility still enables the system to compensate perturbations immediately without 'falling out of equilibrium'. The measured g_2 decorrelation is of stretched exponential shape, indicating a broad distribution of relaxation timescales spanning over several decades, and can be fitted by a conventional KWW model.

With ongoing cooling, the dynamic heterogeneity further increases[65,66] while the overall free volume of the system decreases. Eventually, this must lead to the glass transition, which is a gradual, rate-dependent kinetic arrest[88,89] that manifests calorimetrically as a step in the system's heat capacity beginning at about 521 K, see Fig. 1A and Fig. 3D. It can be assumed that the more rigid domains play a decisive role in this process, as their slow dynamics likely lend them rather viscoelastic than liquid-like behavior[82], therefore enabling them to bear certain stresses in a solid-like manner. Hence, we pick up an approach firstly formulated by M. Cohen and G. Grest[86] and recently applied for polymeric melts[85] and interpret vitrification as an interlocking and jamming process of the more rigid domains. The interlocked domains then act as a gradually formed backbone structure that frustrates further volume shrinkage with ongoing cooling, and so, the system starts falling out of equilibrium. The volumetric frustration causes stress gradients among the rigid domains, forcing them to perform (small-scale) ballistic-like collective motions that could be imagined as drifts or rotations, as illustrated by the purple underlying arrows in Fig. 5B. A macroscale analogy can be seen in the dynamics of drift ice, where interactions within densely packed ice floe agglomerations (representing the backbone structure formed by jammed rigid domains) create tectonic motions[90]. Eventually, the present homodyne XPCS experiment detects the velocity gradients[41] that go hand in hand with these ballistic-like 'microscopic drift' motions in form of the typical compressed decay modeled by KWW_C. Nevertheless, the gradual nature of the glass transition implies that stress-relaxation also still occurs through liquid-like α-relaxation processes that remained partially active, and therefore, the KWW_S parameters still follow their liquid-like trends. Accordingly, vitrification is characterized by rivaling types of atomic motions. This is mirrored in the ISF by different decorrelation components with roughly the same timescale, finally creating the typical cut-off appearance described by the KWW_{MULTI} model.

At about 490 K, the end of the glass transition is reached, where the heat flow signal approaches the nearly constant glassy level, as shown in Fig. 1A and Fig. 3D. Here, the last portions of liquid-like α-relaxation processes become arrested and, therefore, τ_S and β_S finally start departing from their equilibrium trendlines as seen in Fig. 3 and Fig. 4. Regarding our qualitative picture in Fig. 5C, the rigid dynamic backbone has broadly evolved, and stresses mainly relax through ballistic-like drift motions. Accordingly, the observed g_2 decorrelation is dominated by the typical compressed decay.

The vitrification in the cooling scan is a rather 'gentle' process[91–93]. The system leaves the equilibrium at a low fictive temperature thanks to the slow cooling rate. In contrast, the as-spun ribbon features a distinctly higher fictive temperature, since it has been vitrified with a rate in the order of 10^6 K s^{-1} [33]. The resulting configurational differences between the as-spun and the slowly cooled glass are observed in the particle motion component corresponding to liquid-like dynamics, KWW_S, since τ_S and β_S values significantly differ between the heating and the cooling scan (compare Fig. 3C, F). In view of our scenario, a higher fictive temperature configuration corresponds to a less rigid dynamic backbone and a faster liquid-like component. The higher atomic mobility in the as-spun glass allows for structural relaxation upon heating, as it is visible in Fig. 3B, C, where τ_S and β_S age towards equilibrium. When these parameters have reestablished their

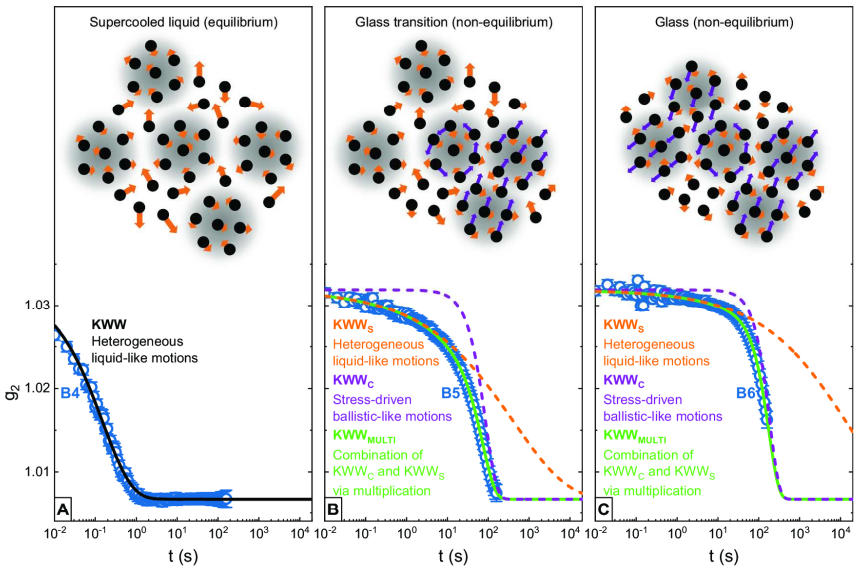

Fig. 5 | Spatial heterogeneities, stress-driven dynamics, and the glass transition. We present a possible scenario that illustrates the micro-scale dynamics during the cooling scan and connects it to the experimentally determined interplay of stretched and compressed decorrelation components. The shown g_2 curves consist of 96 mean value data points with standard deviations given by the error bars and correspond to the representative batches B4, B5, and B6 introduced in Fig. 1. Individual liquid-like atomic motions are symbolized by orange arrows. **A** In the equilibrium supercooled liquid state, spatio-temporally heterogeneous dynamics already have evolved. Regions with slower dynamics, termed rigid domains, are indicated by underlying gray shadows. The broad spectrum of relaxation times creates a stretched decay in g_2 that can be described by a conventional Kohlrausch-Williams-Watts (KWW) function. **B** Further cooling towards vitrification leads to increased spatial heterogeneity as well as volume shrinkage of the system. Accordingly, the rigid domains start to gradually interlock and jam to form a rigid dynamic backbone. Further volumetric adaptations to temperature changes are frustrated, the system falls out of equilibrium and stress gradients arise. This causes the rigid domains to push, drift, and rotate against each other (underlying purple arrows), introducing collective ballistic-like atomic motions and a typical compressed decorrelation in g_2 that competes with the stretched liquid-like decorrelation component. Hence, the conventional KWW fit fails and the KWW_{MULTI} approach is needed to model the complex shape of the g_2 decay. **C** In the glass, the rigid dynamic backbone is broadly established, and the compressed decay caused by the ballistic-like motions dominates the g_2 decorrelation. The fit parameters of the shown KWW and KWW_{MULTI} curves can be found in Fig. 3.

equilibrium trendlines, further devitrification with increasing temperature basically occurs as the inverse vitrification process, namely via a gradual dissolving of the interlocked rigid regions until a full loss of compressed decorrelation characteristics is reached when approaching the equilibrium SCL.

In summary, we used slow temperature scanning XPCS to study the micro-scale dynamics of a Pt-based metallic glass former in the glass, glass transition, and SCL state upon heating and cooling. By assuming two different types of particle motion, we describe a scenario that reduces the difference between equilibrium and non-equilibrium again to a question of crossing timescales. The system remains in equilibrium as long as liquid-like atomic motions are able to relax perturbations within the timeframe determined by the underlying thermal protocol, creating a purely stretched decorrelation of the ISF. The glass transition upon cooling initiates as soon as rigid spatial domains start to interlock, causing volumetric frustration with further decreasing temperature. The resulting stress gradients induce collective particle movements in form of ballistic-like 'microscopic drift' motions, eventually creating a compressed g_2 decorrelation component that competes with the stretched decay component stemming from the liquid-like atomic motions. The here presented KWW_{MULTI} approach allows us to model this interplay and clearly separate these coexisting decorrelation components. It shall be highlighted again that the fast exposure time of 0.01 s is the crucial technical condition to resolve the presence of such different dynamic processes, as exemplarily shown in Fig. 2. Thus, we address the fact that superimposed stretched and compressed decay was never reported in earlier XPCS studies on metallic glasses to limitations of the temporal resolution. We expect that this superposition will become a regularly observed effect with future technological advances in XPCS, but possibly also for other experimental approaches like dynamic light scattering[40,51] or ECS[64–66]. Nevertheless, we are aware that the applicability of the KWW_{MULTI} concept might be closely related to the probed length scales and experimental conditions of the present setup. Additional data at timescales at least two orders of magnitude faster than those probed here would definitely help to obtain a deeper understanding and might allow for a better discrimination between the additive and multiplicative fitting approaches. Finally, we are confident that temperature scanning XPCS will become a broadly used tool to study countless cases of non-equilibrium states[94–96] or transition effects in amorphous matter, e.g., regarding phase separations[97], liquid-liquid transitions[98], or secondary relaxations[99].

Methods

Sample preparation

The sample preparation of $Pt_{42.5}Cu_{27}Ni_{9.5}P_{21}$ consisted of inductively alloying the raw elements to obtain the master alloy, which was further purified through a fluxing treatment. An amorphous plate-shaped bulk specimen was produced from the master alloy by induction melting

and tilt-casting. For XPCS, amorphous ribbons with ~30 μm thickness were produced from this specimen by melt-spinning.

XPCS experimental procedure

XPCS was carried out at the ID10 beamline at ESRF (after the EBS update). The measured as-spun ribbon piece was sanded to a thickness of 10 μm to achieve a regular cross section and an optimized signal-to-noise ratio. The partially coherent beam with a cross section of $10 \times 10\ \mu m^2$ featured an energy of 21.0 keV and a flux of about 4.7×10^{11} photons per second. The speckle patterns were obtained in frames of 0.01 s exposure time using an Eiger 4 M CdTe detector with a sample-detector-distance of 5100 mm. All measurements were performed at a fixed wave vector of $|\mathbf{q}| = 2.86\ Å^{-1}$ ($\pm 0.05\ Å^{-1}$), directly at the first sharp diffraction peak of the structure factor[13,100]. Supplementary Fig. 5 in the SI illustrates the setup. The as-spun ribbon sample was installed in a custom-build, PID-controlled furnace to apply a temperature scan program under high vacuum. In the first step, the sample was heated with a rate of 0.0167 K s^{-1} from the glassy state into the SCL to 548 K. In the second step, the sample was subsequently cooled back into the glassy state, again with 0.0167 K s^{-1}. The TTCFs, $G(t_1, t_2)$, were calculated as

$$G(t_1, t_2) = \frac{\langle I(t_1) I(t_2) \rangle_p}{\langle I(t_1) \rangle_p \langle I(t_2) \rangle_p} \tag{8}$$

where $I(t_i)$ is the pixel intensity of the detector at the (absolute) experimental time t_i and $\langle \ldots \rangle_p$ is the average over all pixels of the detector[24,26]. Considering that the intensity fluctuations are well described by Gaussian statistics and using the Siegert relationship from Eq. 2[101,102], the intensity autocorrelation functions, g_2, were obtained from averaging over the respective TTCFs. The calculation of TTCFs and g_2 data was performed in batches of 24000 frames, corresponding to a time span of $\Delta t = 240$ s or, respectively, a temperature span of $\Delta T = 4$ K. This batch size was found to be adequate for further KWW and KWW_{MULTI} fitting as it provides enough temporal range to capture most of the decorrelation process while still retaining a reasonable error in temperature within each batch (±2 K). To achieve a sliding average effect, consecutive batches overlapped halfway, hence by 12,000 frames (120 s, 2 K).

Temperature correction procedure

To achieve a precise temperature calibration, further XPCS heating scans with the same experimental conditions as described earlier were performed on two other metallic glass forming systems, which show first signs of crystallization at about 390 K and 630 K, respectively. As soon as crystals appeared in the probed sample volume, they created quasi-stationary Bragg reflections in the speckle pattern. This leads to an abrupt and harsh increase of the g_2 baseline as shown in Supplementary Fig. 1 in the SI, allowing for a precise definition of the crystallization temperature T_x. DSC scans of these systems were performed with the same heating rate of 0.0167 K s^{-1} using a Mettler Toledo DSC3 with Al crucibles under high-purity Ar flow. Here, T_x was identified as starting point of the exothermal crystallization event in the heat flow signal, see also Supplementary Fig. 1 in the SI. Comparing the T_x values defined by calorimetry and XPCS scans allowed to define a linear two-point temperature calibration that is applied for all XPCS data shown in this article. Supplementary Fig. 1C in the SI provides the correction formula.

Ex-situ DSC scans

To provide heat flow signals for comparison and orientation, the temperature corrected heating-cooling program applied for the XPCS studies on the $Pt_{42.5}Cu_{27}Ni_{9.5}P_{21}$ ribbon was retraced ex-situ by DSC, again using the Mettler-Toledo DSC3 with Al crucibles under high-purity Ar flow. The as-spun $Pt_{42.5}Cu_{27}Ni_{9.5}P_{21}$ ribbons were heated from 463 K to 548 K and subsequently cooled back to the initial temperature of 463 K, using a rate of 0.0167 K s^{-1}. The resulting data has been evaluated and plotted using OriginPro 2021b.

KWW and KWW_{MULTI} fitting procedure

The first approach to fit the g_2 data using the KWW and KWW_{MULTI} models, see Eq. 3 and Eq. 7, would be to leave all parameters free to obtain fitting curves that describe each individual data set to the best extent. Yet, at elevated temperatures in the SCL, the fast dynamics cause significant decorrelation even within the first time increment of 0.01 s, resulting in g_2 curves with too low initial heights, as demonstrated for example in Fig. 1C, D. Here, KWW fitting with free parameters leads to an underestimation of c. In contrast, the g_2 curves at low temperatures in the glassy state may not reach full decorrelation within the correlation window as can be seen in Fig. 1C, D, resulting in a misestimation of the baseline b in case of free parameterization. To solve these problems, we define fixed values for b and c, analogous to an XPCS analysis previously described in ref. 12. For b, an average value of 1.00675 is determined from those high-temperature batches that show full decorrelation. An average c value of 0.02517 is derived from low-temperature batches that show a full initial g_2 plateau. Hence, only τ and β (or their respective counterparts from KWW_{MULTI} fitting) remain as free fitting parameters. All the data fitting procedures have been performed using OriginPro 2021b.

Furthermore, the respective average relaxation times[58] $\langle\tau\rangle$ and $\langle\tau\rangle_S$ shown in Fig. 4 can be calculated according to

$$\langle\tau\rangle = \frac{\tau}{\beta}\Gamma\left(\frac{1}{\beta}\right) \tag{9}$$

Aligning XPCS timescale data and equilibrium viscosity data

Equilibrium viscosities from TMA published in ref. 22 are shown in Fig. 4 and serve us as a reference in terms of the SCL state's fragility. To allow a direct comparison, the present τ and τ_S data from KWW and KWW_{MULTI} fitting are transferred into the viscosity domain and aligned with the TMA data. To do so, the equilibrium viscosities are fitted in a first step using the cooperative shear model (CSM)[55,56]:

$$\eta(T) = \eta_0 \exp\left(\frac{T_g^*}{T} \ln\left(\frac{\eta_g}{\eta_0}\right) \exp\left(2n\left(1 - \frac{T}{T_g^*}\right)\right)\right) \tag{10}$$

Here, η_0 is the minimum viscosity reached at high temperatures of 4×10^{-5} Pa s[22], η_g is the viscosity value of 10^{12} Pa s commonly defined by convention as the glass transition value[1] and T_g^* is the corresponding temperature value, which is 498 K in the present case. The only remaining free fit parameter n is a measure of the apparent fragility and is determined as 1.153 ± 0.030. This corresponds to an m-fragility of roughly 57[22,57] and a Vogel-Fulcher-Tammann (VFT) fragility parameter D^* of 15.3[13,22,57]. In a second step, the CSM model is combined with the Maxwell relation[54], $\eta = G\,\tau$, to be applied in the timescale domain as

$$\tau(T) = \frac{\eta_0}{G} \exp\left(\frac{T_g^*}{T} \ln\left(\frac{\eta_g}{\eta_0}\right) \exp\left(2n\left(1 - \frac{T}{T_g^*}\right)\right)\right) \tag{11}$$

Fitting the equilibrium relaxation times (hence excluding data points that indicate vitrification due to deviation from the liquid behavior) from XPCS with this equation using the fixed $n = 1.153$ from the viscosity fit leaves only the shear modulus G as a free fit parameter. The thereby determined G values are 1.815×10^8 Pa (τ, heating), 1.679×10^8 Pa (τ, cooling), 6.05×10^7 Pa (τ_S, heating), 2.66×10^7 Pa (τ_S, cooling), 1.227×10^8 Pa ($\langle\tau\rangle$, heating), 1.029×10^8 Pa ($\langle\tau\rangle$, cooling), 2.02×10^7 Pa ($\langle\tau\rangle_S$, heating), and 4.7×10^6 Pa ($\langle\tau\rangle_S$, cooling). Now, the relaxation times can be

transformed into corresponding viscosity data by means of the Maxwell relation and each respective G value. The resulting $\eta(\tau)$ and $\eta(\tau_S)$ values are depicted in Fig. 4. Their steepnesses agree well with the TMA equilibrium viscosities, indicating the same fragility among the data sets. Finally, it shall be stated that all fitting and data plotting of this study has been done using OriginPro 2021b.

Reporting summary

Further information on research design is available in the Nature Portfolio Reporting Summary linked to this article.

Data availability

The XPCS and DSC data generated in this study as well as the source files of all figures have been deposited in the figshare database under accession code https://doi.org/10.6084/m9.figshare.28855373.

References

1. Angell, C. A. Formation of glasses from liquids and biopolymers. *Science* **267**, 1924–1935 (1995).
2. Grübel, G. & Zontone, F. Correlation spectroscopy with coherent X-rays. *J. Alloy. Compd.* **362**, 3–11 (2004).
3. Ruta, B. et al. Atomic-scale relaxation dynamics and aging in a metallic glass probed by X-ray photon correlation spectroscopy. *Phys. Rev. Lett.* **109**, 1–5 (2012).
4. Zhou, H. et al. X-ray photon correlation spectroscopy revealing the change of relaxation dynamics of a severely deformed Pd-based bulk metallic glass. *Acta Mater.* **195**, 446–453 (2020).
5. Evenson, Z. et al. Comparing the atomic and macroscopic aging dynamics in an amorphous and partially crystalline Zr44Ti11Ni10-Cu10Be25 bulk metallic glass. *J. Mater. Res.* **32**, 2014–2021 (2017).
6. Hechler, S. et al. Microscopic evidence of the connection between liquid-liquid transition and dynamical crossover in an ultraviscous metallic glass former. *Phys. Rev. Mater.* **2**, 1–6 (2018).
7. Ruta, B., Giordano, V. M., Erra, L., Liu, C. & Pineda, E. Structural and dynamical properties of $Mg_{65}Cu_{25}Y_{10}$ metallic glasses studied by in situ high energy X-ray diffraction and time resolved X-ray photon correlation spectroscopy. *J. Alloy. Compd.* **615**, 45–50 (2014).
8. Soriano, D. et al. Relaxation dynamics of Pd-Ni-P metallic glass: decoupling of anelastic and viscous processes. *J. Phys. Condens. Matter* **33**, 164004 (2021).
9. Das, A., Derlet, P. M., Liu, C., Dufresne, E. M. & Maaß, R. Stress breaks universal aging behavior in a metallic glass. *Nat. Commun.* **10**, 1–9 (2019).
10. Das, A., Dufresne, E. M. & Maaß, R. Structural dynamics and rejuvenation during cryogenic cycling in a Zr-based metallic glass. *Acta Mater.* **196**, 723–732 (2020).
11. Ruta, B. et al. Wave-vector dependence of the dynamics in supercooled metallic liquids. *Phys. Rev. Lett.* **125**, 1–14 (2020).
12. Amini, N. et al. Intrinsic relaxation in a supercooled ZrTiNiCuBe glass forming liquid. *Phys. Rev. Mater.* **5**, 1–8 (2021).
13. Neuber, N. et al. Disentangling structural and kinetic components of the α-relaxation in supercooled metallic liquids. *Commun. Phys.* **5**, 1–10 (2022).
14. Cornet, A. et al. Denser glasses relax faster: enhanced atomic mobility and anomalous particle displacement under in-situ high pressure compression of metallic glasses. *Acta Mater.* **255**, 119065 (2023).
15. Jain, A. et al. Three-step colloidal gelation revealed by time-resolved x-ray photon correlation spectroscopy. *J. Chem. Phys.* **157**, 184901 (2022).
16. Lu, X., Mochrie, S. G. J., Narayanan, S., Sandy, A. R. & Sprung, M. How a liquid becomes a glass both on cooling and on heating. *Phys. Rev. Lett.* **100**, 5–8 (2008).
17. Ricci, A. et al. Intermittent dynamics of antiferromagnetic phase in inhomogeneous iron-based chalcogenide superconductor. *Phys. Rev. B* **101**, 1–6 (2020).
18. Zhang, Q. et al. Dynamic scaling of colloidal gel formation at intermediate concentrations. *Phys. Rev. Lett.* **119**, 1–6 (2017).
19. Jankowski, M. et al. The complex systems and biomedical sciences group at the ESRF: Current status and new opportunities after extremely brilliant source upgrade. *Nucl. Instrum. Methods Phys. Res. Sect. B Beam Interact. Mater. At.* **538**, 164–172 (2023).
20. Narayanan, T., Chèvremont, W., Zinn, T. & Meneau, F. Small-angle X-ray scattering in the era of fourth-generation light sources. *J. Appl. Crystallogr.* **56**, 939–946 (2023).
21. Schroers, J. & Johnson, W. L. Highly processable bulk metallic glass-forming alloys in the Pt-Co-Ni-Cu-P system. *Appl. Phys. Lett.* **84**, 3666–3668 (2004).
22. Gross, O. et al. The kinetic fragility of Pt-P- and Ni-P-based bulk glass-forming liquids and its thermodynamic and structural signature. *Acta Mater.* **132**, 118–127 (2017).
23. Kohlrausch, R. Theorie des elektrischen Rückstandes in der Leidener Flasche. *Ann. Phys.* **167**, 179–214 (1854).
24. Chushkin, Y., Caronna, C. & Madsen, A. A novel event correlation scheme for X-ray photon correlation spectroscopy. *J. Appl. Crystallogr.* **45**, 807–813 (2012).
25. Jaeschke, E. J. *Synchrotron Light Sources and Free-Electron Lasers*. *Synchrotron Light Sources and Free-Electron Lasers*. https://doi.org/10.1007/978-3-319-14394-1 (2016).
26. Ruta, B. et al. Relaxation dynamics and aging in structural glasses. *AIP Conf. Proc.* **1518**, 181–188 (2013).
27. Riechers, B., Das, A., Dufresne, E., Derlet, P. M. & Maaß, R. Intermittent cluster dynamics and temporal fractional diffusion in a bulk metallic glass. *Nat. Commun.* **15**, 1–10 (2024).
28. Giordano, V. M. & Ruta, B. Unveiling the structural arrangements responsible for the atomic dynamics in metallic glasses during physical aging. *Nat. Commun.* **7**, 1–8 (2016).
29. Evenson, Z. et al. X-ray photon correlation spectroscopy reveals intermittent aging dynamics in a metallic glass. *Phys. Rev. Lett.* **115**, 175701 (2015).
30. Wang, X. D. et al. Free-volume dependent atomic dynamics in beta relaxation pronounced La-based metallic glasses. *Acta Mater.* **99**, 290–296 (2015).
31. Riechers, B., Das, A., Rashidi, R., Dufresne, E. & Maaß, R. Metallic glasses: elastically stiff yet flowing at any stress. *Mater. Today* **82**, 92–98 (2024).
32. Xu, T. et al. Anomalous fast atomic dynamics in bulk metallic glasses. *Mater. Today Phys.* **17**, 100351 (2021).
33. Ruta, B., Baldi, G., Monaco, G. & Chushkin, Y. Compressed correlation functions and fast aging dynamics in metallic glasses. *J. Chem. Phys.* **138**, 054508 (2013).
34. Leitner, M., Sepiol, B., Stadler, L. M. & Pfau, B. Time-resolved study of the crystallization dynamics in a metallic glass. *Phys. Rev. B Condens. Matter Mater. Phys.* **86**, 1–7 (2012).
35. Duan, Y. J. et al. Intrinsic correlation between the fraction of liquidlike zones and the beta relaxation in high-entropy metallic glasses. *Phys. Rev. Lett.* **129**, 175501 (2022).
36. Duan, Y. J. et al. Connection between mechanical relaxation and equilibration kinetics in a high-entropy metallic glass. *Phys. Rev. Lett.* **132**, 1–7 (2024).
37. Sun, Y. T. et al. Distinct relaxation mechanism at room temperature in metallic glass. *Nat. Commun.* **14**, 1–8 (2023).
38. Chen, Y., Sun, Y. H. & Wang, W. H. Understanding the stretched exponential decay of strained metallic glasses by a free-volume model. *Phys. Rev. B* **110**, 1–7 (2024).
39. Pusey, P. N. Liquids, freezing and glass transition. In *Les Houches Session 51*. https://www.researchgate.net/publication/285372669_Liquids_Freezing_and_Glass_Transition (1991).

40. Pecora, R. Dynamic light scattering: applications of photon correlation spectroscopy. In *Physics and Astronomy* https://link.springer.com/book/10.1007/978-1-4613-2389-1 (2008).
41. Busch, S., Jensen, T. H., Chushkin, Y. & Fluerasu, A. Dynamics in shear flow studied by X-ray Photon Correlation Spectroscopy. *Eur. Phys. J. E* **26**, 55–62 (2008).
42. Ruta, B., Pineda, E. & Evenson, Z. Topical review: relaxation processes and physical aging in metallic glasses. *J. Phys. Condens. Matter* **29**, 503002 (2017).
43. Nagel, S. R., Angell, C. A. & Ediger Supercooled liquids and glasses. *J. Phys. Chem.* **100**, 13200–13212 (1996).
44. Ediger, M. D. Spatially heterogeneous dynamics in supercooled liquids. *Annu. Rev. Phys. Chem.* **51**, 99–128 (2000).
45. Richert, R. Heterogeneous dynamics in liquids: fluctuations in space and time. *J. Phys. Condens. Matter* **14**, R703 (2002).
46. Ferrero, E. E., Martens, K. & Barrat, J. L. Relaxation in yield stress systems through elastically interacting activated events. *Phys. Rev. Lett.* **113**, 248301 (2014).
47. Fuller, G. G., Rallison, J. M., Schmidt, R. L. & Leal, L. G. The measurement of velocity gradients in laminar flow by homodyne light-scattering spectroscopy. *J. Fluid Mech.* **100**, 555–575 (1980).
48. Arbe, A., Malo De Molina, P., Alvarez, F., Frick, B. & Colmenero, J. Dielectric susceptibility of liquid water: microscopic insights from coherent and incoherent neutron scattering. *Phys. Rev. Lett.* **117**, 1–5 (2016).
49. Arbe, A. et al. Collective dynamics and self-motions in the van der Waals liquid tetrahydrofuran from meso- to inter-molecular scales disentangled by neutron spectroscopy with polarization analysis. *J. Chem. Phys.* **158**, 184502 (2023).
50. Gabriel, J., Blochowicz, T. & Stühn, B. Compressed exponential decays in correlation experiments: the influence of temperature gradients and convection. *J. Chem. Phys.* **142**, 104902 (2015).
51. Liénard, F., Freyssingeas, É. & Borgnat, P. A multiscale time-Laplace method to extract relaxation times from non-stationary dynamic light scattering signals. *J. Chem. Phys.* **156**, 224901 (2022).
52. Parisi, D. et al. Static and dynamic properties of block copolymer based grafted nanoparticles across the non-ergodicity transition. *Phys. Fluids* **32**, 127101 (2020).
53. Marques, F. A. D. M. et al. Structural and microscopic relaxations in a colloidal glass. *Soft Matter* **11**, 466–471 (2015).
54. Maxwell, C. On the dynamical theory of gases. *Philos. Trans.* **157**, 49–88 (1867).
55. Demetriou, M. D. et al. Cooperative shear model for the rheology of glass-forming metallic liquids. *Phys. Rev. Lett.* **97**, 41–44 (2006).
56. Johnson, W. L., Demetriou, M. D., Harmon, J. S., Lind, M. L. & Samwer, K. Rheology and ultrasonic properties of metallic glass-forming liquids: A potential energy landscape perspective. *MRS Bull.* **32**, 644–650 (2007).
57. Frey, M. et al. Determining the fragility of bulk metallic glass forming liquids via modulated DSC. *J. Phys. Condens. Matter* **32**, 324004 (2020).
58. Guo, H. et al. Entanglement-controlled subdiffusion of nanoparticles within concentrated polymer solutions. *Phys. Rev. Lett.* **109**, 1–5 (2012).
59. Cangialosi, D., Alegría, A. & Colmenero, J. On the temperature dependence of the nonexponentiality in glass-forming liquids. *J. Chem. Phys.* **130**, 124902 (2009).
60. Arbe, A., Colmenero, J., Monkenbusch, M. & Richter, D. Dynamics of glass-forming polymers: "Homogeneous" versus "heterogeneous" scenario. *Phys. Rev. Lett.* **81**, 590–593 (1998).
61. Faupel, F. et al. Diffusion in metallic glasses and supercooled melts. *Rev. Mod. Phys.* **75**, 237–280 (2003).
62. Ballesta, P., Duri, A. & Cipelletti, L. Unexpected drop of dynamical heterogeneities in colloidal suspensions approaching the jamming transition. *Nat. Phys.* **4**, 550–554 (2008).
63. Richert, R. Perspective: Nonlinear approaches to structure and dynamics of soft materials. *J. Chem. Phys.* **149**, 240901 (2018).
64. He, L., Zhang, P., Besser, M. F., Kramer, M. J. & Voyles, P. M. Electron correlation microscopy: a new technique for studying local atom dynamics applied to a supercooled liquid. *Microsc. Microanal.* **21**, 1026–1033 (2015).
65. Zhang, P., Maldonis, J. J., Liu, Z., Schroers, J. & Voyles, P. M. Spatially heterogeneous dynamics in a metallic glass forming liquid imaged by electron correlation microscopy. *Nat. Commun.* **9**, 1–7 (2018).
66. Chatterjee, D. et al. Fast surface dynamics on a metallic glass nanowire. *ACS Nano* **15**, 11309–11316 (2021).
67. Chaudhuri, P., Berthier, L. & Kob, W. Universal nature of particle displacements close to glass and jamming transitions. *Phys. Rev. Lett.* **99**, 2–5 (2007).
68. Weeks, E. R., Crocker, J. C., Levitt, A. C., Schofield, A. & Weitz, D. A. Three-dimensional direct imaging of structural relaxation near the colloidal glass transition. *Science* **287**, 627–631 (2000).
69. Cipelletti, L. et al. Universal non-diffusive slow dynamics in aging soft matter. *Faraday Discuss* **123**, 237–251 (2003).
70. Trachenko, K. & Zaccone, A. Slow stretched-exponential and fast compressed-exponential relaxation from local event dynamics. *J. Phys. Condens. Matter* **33**, 315101 (2021).
71. Bouzid, M., Colombo, J., Barbosa, L. V. & Gado, E. Del. Elastically driven intermittent microscopic dynamics in soft solids. *Nat. Commun.* **8**, 1–8 (2017).
72. Bandyopadhyay, R. et al. Evolution of particle-scale dynamics in an aging clay suspension. *Phys. Rev. Lett.* **93**, 2–5 (2004).
73. Gnan, N. & Zaccarelli, E. The microscopic role of deformation in the dynamics of soft colloids. *Nat. Phys.* **15**, 683–688 (2019).
74. Sciortino, F., Fabbian, L., Chen, S. H. & Tartaglia, P. Supercooled water and the kinetic glass transition. II. Collective dynamics. *Phys. Rev. E* **56**, 5397–5404 (1997).
75. Gallo, P., Sciortino, F., Tartaglia, P. & Chen, S. H. Slow dynamics of water molecules in supercooled states. *Phys. Rev. Lett.* **76**, 2730–2733 (1996).
76. Orsi, D. et al. Controlling the dynamics of a bidimensional gel above and below its percolation transition. *Phys. Rev. E* **89**, 1–11 (2014).
77. Wang, Z., Riechers, B., Derlet, P. M. & Maaß, R. Atomic cluster dynamics causes intermittent aging of metallic glasses. *Acta Mater.* **267**, 119730 (2024).
78. Rodriguez-Lopez, G., Martens, K. & Ferrero, E. E. Temperature dependence of fast relaxation processes in amorphous materials. *Phys. Rev. Mater.* **7**, 1–19 (2023).
79. Wu, B., Iwashita, T. & Egami, T. Atomic dynamics in simple liquid: de gennes narrowing revisited. *Phys. Rev. Lett.* **120**, 135502 (2018).
80. Chang, C. et al. Liquid-like atoms in dense-packed solid glasses. *Nat. Mater.* https://doi.org/10.1038/s41563-022-01327-w (2022).
81. Wang, Q., Shang, Y. & Yang, Y. Quenched-in liquid in glass. *Mater. Futur.* **2**, 017501 (2023).
82. Wang, Z., Sun, B. A., Bai, H. Y. & Wang, W. H. Evolution of hidden localized flow during glass-to-liquid transition in metallic glass. *Nat. Commun.* **5**, 5823 (2014).
83. Qiao, J. C. et al. Structural heterogeneities and mechanical behavior of amorphous alloys. *Prog. Mater. Sci.* **104**, 250–329 (2019).
84. Tanaka, H. Two-order-parameter description of liquids. I. A general model of glass transition covering its strong to fragile limit. *J. Chem. Phys.* **111**, 3163–3174 (1999).
85. Long, D. & Lequeux, F. Heterogeneous dynamics at the glass transition in van der Waals liquids, in the bulk and in thin films. *Eur. Phys. J. E* **4**, 371–387 (2001).

86. Grest, G. S. & Cohen, M. H. Liquids, glasses, and the glass transition: a free-volume approach. *Adv. Chem. Phys.* **XLVIII**, 455–525 (1981).
87. Derlet, P. M., Bocquet, H. & Maaß, R. Viscosity and transport in a model fragile metallic glass. *Phys. Rev. Mater.* **5**, 1–7 (2021).
88. Donth, E. *The Glass Transition: Relaxation Dynamics in Liquids and Disordered Materials* Vol. 48 (Springer Science & Business Media, 2013).
89. Schmelzer, J. W. P. & Gutzow, I. S. *Glasses and the Glass Transition*. https://onlinelibrary.wiley.com/doi/book/10.1002/9783527636532 (2011).
90. Martin, T. Arctic sea ice dynamics: drift and ridging in numerical models and observations. *Univ. Brem.* **1**, 248 (2007).
91. Rodríguez-Tinoco, C. et al. Surface-bulk interplay in vapor-deposited glasses: crossover length and the origin of front transformation. *Phys. Rev. Lett.* **123**, 155501 (2019).
92. Lulli, M., Lee, C. S., Deng, H. Y., Yip, C. T. & Lam, C. H. Spatial heterogeneities in structural temperature cause Kovacs' expansion gap paradox in aging of glasses. *Phys. Rev. Lett.* **124**, 095501 (2020).
93. Ruiz-Ruiz, M. et al. Real-time microscopy of the relaxation of a glass. *Nat. Phys.* https://doi.org/10.1038/s41567-023-02125-0 (2023).
94. Leheny, R. L. XPCS: Nanoscale motion and rheology. *Curr. Opin. Colloid Interface Sci.* **17**, 3–12 (2012).
95. Angelini, R. et al. Glass-glass transition during aging of a colloidal clay. *Nat. Commun.* **5**, 1–7 (2014).
96. Ladd-Parada, M. et al. Using coherent X-rays to follow dynamics in amorphous ices. *Environ. Sci. Atmos.* **2**, 1314–1323 (2022).
97. Lan, S., Yip, Y. L., Lau, M. T. & Kui, H. W. Direct imaging of phase separation in Pd 41.25Ni 41.25P17.5 bulk metallic glasses. *J. Non Cryst. Solids* **358**, 1298–1302 (2012).
98. Tanaka, H. Liquid-liquid transition and polyamorphism. *J. Chem. Phys.* **153**, 130901 (2020).
99. Yu, H., Bin, Wang, W. H. & Samwer, K. The β relaxation in metallic glasses: an overview. *Mater. Today* **16**, 183–191 (2013).
100. Gross, O. et al. Signatures of structural differences in Pt–P- and Pd–P-based bulk glass-forming liquids. *Commun. Phys.* **2**, 83 (2019).
101. Bartsch, E., Frenz, V., Baschnagel, J., Schärtl, W. & Sillescu, H. The glass transition dynamics of polymer micronetwork colloids. A mode coupling analysis. *J. Chem. Phys.* **106**, 3743–3756 (1997).
102. Cipelletti, L. & Weitz, D. A. Ultralow-angle dynamic light scattering with a charge coupled device camera based multispeckle, multi-tau correlator. *Rev. Sci. Instrum.* **70**, 3214–3221 (1999).

Acknowledgements

We acknowledge ESRF (Grenoble, France) for providing beamtime for the proposal HC-4479. We want to thank the technicians and staff at ESRF for their support in terms of the XPCS studies. We further thank Dr. Frank Aubertin for fruitful discussions. This project has received funding (in terms of A.C., J.S., B.R.) from the European Research Council (ERC) under the European Union's Horizon 2020 research and innovation programme (Grant Agreement No 948780). E.P. acknowledges financial support by grant PID2023-146623NB-I00 and the Maria de Maeztu Units of Excellence Programme grant CEX2023-001300-M funded by MICIU/AEI/10.13039/501100011033.

Author contributions

Conceptualization: E.P., M.F. Methodology: E.P., N.N., M.F., Y.C., B.R. Validation: F.W., M.S. Formal analysis: E.P., M.F., N.N. Investigation: E.P., N.N., A.C., Y.C., F.Z., B.R., M.F. Resources: N.N., M.F. Visualization: M.F., E.P. Supervision: E.P. Writing—original draft: M.F., E.P., B.R. Writing—review & editing: N.N., S.S.R., A.C., Y.C., F.Z., L.R., B.A., M.N., F.Y., J.S., F.W., M.S., D.C., V.D.L., I.G., R.B.

Funding

Open Access funding enabled and organized by Projekt DEAL.

Competing interests

The authors declare no competing interests.

Additional information

Supplementary information The online version contains supplementary material available at https://doi.org/10.1038/s41467-025-59767-2.

Correspondence and requests for materials should be addressed to Maximilian Frey.

Peer review information *Nature Communications* thanks Qingteng Zhang and the other, anonymous, reviewer(s) for their contribution to the peer review of this work. A peer review file is available.

Reprints and permissions information is available at http://www.nature.com/reprints

Publisher's note Springer Nature remains neutral with regard to jurisdictional claims in published maps and institutional affiliations.

Open Access This article is licensed under a Creative Commons Attribution 4.0 International License, which permits use, sharing, adaptation, distribution and reproduction in any medium or format, as long as you give appropriate credit to the original author(s) and the source, provide a link to the Creative Commons licence, and indicate if changes were made. The images or other third party material in this article are included in the article's Creative Commons licence, unless indicated otherwise in a credit line to the material. If material is not included in the article's Creative Commons licence and your intended use is not permitted by statutory regulation or exceeds the permitted use, you will need to obtain permission directly from the copyright holder. To view a copy of this licence, visit http://creativecommons.org/licenses/by/4.0/.

© The Author(s) 2025

5.3 Paper III: Determining and modelling a complete time-temperature-transformation diagram for a Pt-based metallic glass former through combination of conventional and fast scanning calorimetry

Authors

Maximilian Frey, Nico Neuber, Marvin Müller, Oliver Gross, Sascha Sebastian Riegler, Isabella Gallino, Ralf Busch

Publishing information

Submitted: 21.08.2021

Accepted: 27.03.2022

Published: 01.04.2022

Journal: Scripta Materialia, 215 (2022), 114710

DOI: 10.1016/j.scriptamat.2022.114710

Abstract of the article

State of the art fast differential scanning calorimetry (FDSC) is used to complement conventional differential scanning calorimetry (DSC) studies about the isothermal time-temperature-transformation (TTT) diagram of the bulk metallic glass forming liquid $Pt_{42.5}Cu_{27}Ni_{9.5}P_{21}$ to allow a comprehensive study of the crystallization kinetics of this system over a broad temperature range. FDSC and DSC data align well in the low-temperature region of the crystallization nose but show distinct discrepancies in the high-temperature region as the FDSC studies reveal faster crystallization times. The results are mathematically described and discussed based on the Johnson-Mehl-Avrami-Kolmogorov (JMAK) equation. Thereby, either homogeneous or heterogeneous nucleation is assumed, depending on the respective experimental conditions in FDSC and DSC studies. With this approach, the complete TTT diagram can be modelled as superposition of two sequential JMAK fits.

Scripta Materialia 215 (2022) 114710

Contents lists available at ScienceDirect

Scripta Materialia

journal homepage: www.journals.elsevier.com/scripta-materialia

Determining and modelling a complete time-temperature-transformation diagram for a Pt-based metallic glass former through combination of conventional and fast scanning calorimetry

M. Frey [a,*], N. Neuber [a], M. Müller [a], O. Gross [b], S.S. Riegler [a], I. Gallino [a], R. Busch [a]

[a] Chair of Metallic Materials, Saarland University, Campus C6.3, Saarbrücken 66123, Germany
[b] Amorphous Metal Solutions GmbH, Michelinstraße 9, Homburg 66424, Germany

ARTICLE INFO

Keywords:
Bulk metallic glass
Undercooling solidification
Surface energy
Nucleation of phase transformations

ABSTRACT

State of the art fast differential scanning calorimetry (FDSC) is used to complement conventional differential scanning calorimetry (DSC) studies about the isothermal time-temperature-transformation (TTT) diagram of the bulk metallic glass forming liquid $Pt_{42.5}Cu_{27}Ni_{9.5}P_{21}$ to allow a comprehensive study of the crystallization kinetics of this system over a broad temperature range. FDSC and DSC data align well in the low-temperature region of the crystallization nose but show distinct discrepancies in the high-temperature region as the FDSC studies reveal faster crystallization times. The results are mathematically described and discussed based on the Johnson-Mehl-Avrami-Kolmogorov (JMAK) equation. Thereby, either homogeneous or heterogeneous nucleation is assumed, depending on the respective experimental conditions in FDSC and DSC studies. With this approach, the complete TTT diagram can be modelled as superposition of two sequential JMAK fits.

$Pt_{42.5}Cu_{27}Ni_{9.5}P_{21}$ is a well-known bulk metallic glass forming system that features advanced glass forming ability (GFA) with a critical diameter d_c of 20 mm [1], which is one of the best GFA found in the whole alloy system. The alloy has been subject to intense research in our group [2–6] as it differs significantly from other bulk glass-forming compositions. Within the Pt-P-based bulk glass-forming liquids developed by Schroers and Johnson [1], the $Pt_{42.5}Cu_{27}Ni_{9.5}P_{21}$ is the kinetically strongest liquid [2,3]. Additionally, only the total structure factor of the $Pt_{42.5}Cu_{27}Ni_{9.5}P_{21}$ liquid exhibits a prominent pre-peak at low scattering vectors [2,4], which is interpreted as the signature of a pronounced medium-range order that evolves upon undercooling [4,5]. Moreover, the description of the experimentally determined time-temperature-transformation (TTT) diagram with the classical nucleation theory yields a relatively high value of the interfacial energy of 0.11 $J/m^2 \pm 0.01$ J/m^2. This is considered as a key parameter explaining the high GFA of the Pt-P-based liquids despite their fragile kinetics and the relatively high driving force for crystallization, e.g. compared to Pd-P based liquids [5,6]. The previous crystallization experiments were performed in a conventional DSC, allowing only limited heating and cooling rates, prohibiting an experimental determination of the minimum crystallization time (tip of the crystallization nose). Thus, it was determined from the fit of the low- and high-temperature crystallization data. The recent developments in the field of fast differential scanning calorimetry (FDSC) now offer, for the first time, the possibility to collect crystallization data of many bulk glass-forming liquids at the tip of the crystallization nose. While the commercially available Mettler-Toledo FDSC 1 is only able to measure the TTT-diagram of glass-forming liquids with liquidus temperatures below 793 K (e.g. Au-based compositions [7,8]), the latest version, the FDSC 2+, can achieve temperatures up to 1273 K [9], giving access to a broad field of different alloy systems. Therefore, the authors chose the $Pt_{42.5}Cu_{27}Ni_{9.5}P_{21}$ bulk glass-forming system as a model system to verify the predictions of our previous study by closing the data-gap between high and low temperatures and to identify the influence of the different experimental conditions in the FDSC 2+ on the crystallization process.

The FDSC studies were performed using a Mettler-Toledo FDSC2+ equipped with a MultiSTAR UFH 1 high-temperature chip sensor with silicon nitride (Si_3N_4) surface, allowing for maximum temperatures up to 1273 K [9]. To provide fast cooling rates, a Huber HC100 intracooler was used to hold the sensor support temperature at 188 K. High-purity argon gas flow of 60 ml/min was used to prevent oxidation effects. Two samples were subsequently measured on two different chip sensors for improved statistics. Each sample was cut from the same melt spun ribbon and placed on the respective sensor area, followed by melting via

* Corresponding author.
E-mail address: maximilian.frey@uni-saarland.de (M. Frey).

https://doi.org/10.1016/j.scriptamat.2022.114710
Received 21 August 2021; Received in revised form 17 February 2022; Accepted 27 March 2022
Available online 1 April 2022
1359-6462/© 2022 The Author(s). Published by Elsevier Ltd on behalf of Acta Materialia Inc. This is an open access article under the CC BY license (http://creativecommons.org/licenses/by/4.0/).

several heating scans to temperatures above T_l to obtain good and stable thermal contact between sample and sensor. Measuring the enthalpy of melting upon heating and comparing it to the literature value [2] allows to estimate the sample masses to be roughly 430 ng and 350 ng, respectively [10,11]. These relatively high masses are chosen to avoid sample size effects on the thermal stability [10,12]. Prior to each isothermal measurement, the sample was equilibrated at 973 K (about 100 K above T_l) for several seconds, followed by fast cooling to the respective temperature of isothermal measurement with 10,000 K/s. Every isothermal temperature step was measured at least three times. The inset in Fig. 1 exemplarily depicts a typical heat flow signal obtained at 703 K. The exothermal crystallization event was integrated to obtain the times at which 1%, 50%, and 99% of the heat release has occurred (dashed line). All averaged data points corresponding to these percentage-values are shown in the main window of Fig. 1, thereby forming a typical crystallization nose shape. The standard deviations are given as error bars. At lower temperatures below 613 K, the measurement window is limited by the small sample mass, as the growth-controlled crystallization event smears out over long timescales, thereby getting undetectable due to the deteriorated signal-to-noise ratio [7,13]. At elevated temperatures above 763 K, the nucleation-controlled crystallization event exhibits the trend to shift to longer timescales, exceeding the time limit for data acquisition [7].

The low-temperature (LT) and high-temperature (HT) DSC measurements previously published in [6] were performed using a conventional Perkin-Elmer DSC 8500. For LT-DSC measurements, as-cast bulk samples were heated in aluminum pans with 2 K/s from the glassy state to the respective isotherm above T_g under high-purity argon flow. HT-measurements were performed by equilibrating the alloy in the equilibrium liquid state at the maximum operation temperature of the device of 973 K (about 100 K above the liquidus temperature of 874 K) and subsequent cooling to the respective measurement temperature below T_m with 2 K/s. The samples were measured under high-purity argon flow in graphite pans and embedded in molten B_2O_3 flux. Several HT-measurements were performed for each temperature. Fig. 2 combines the FDSC data of this work with the DSC data from [6]. In order to harmonize the appearance of the TTT diagram, the original HT-DSC datapoints [6] are averaged for each respective temperature step. Standard deviations in form of error bars are only shown for 1% data points to assure the clarity of the plot. While LT-DSC and low-temperature FDSC data align quite well, a distinct mismatch in timescales is found between the HT-DSC data and the overlapping high-temperature FDSC data, as the latter shows relatively short crystallization times. To further quantify this offset, the Johnson-Mehl-Avrami-Kolmogorov (JMAK) equation is used [14–18]. This mathematical approach based on classical nucleation theory describes the temperature dependency of steady state crystallization kinetics and can be utilized to model the crystallization nose in a TTT diagram. At a given temperature, the time t(T) until a portion x of the undercooled liquid is crystallized is calculated as

$$t(T) = \left(-\frac{3\,\ln(1-x)}{\pi\, I(T)\, u(T)^3} \right)^{1/4}. \tag{1}$$

The homogeneous nucleation rate $I_{hom}(T)$ and the crystal growth rate u(T) are determined as:

$$I_{hom}(T) = \frac{A_v}{\eta(T)}\, exp\left(-\frac{16\,\pi}{3\,k_B\,T}\, \frac{\gamma^3}{\Delta g_{l-x}(T)^2} \right), \tag{2}$$

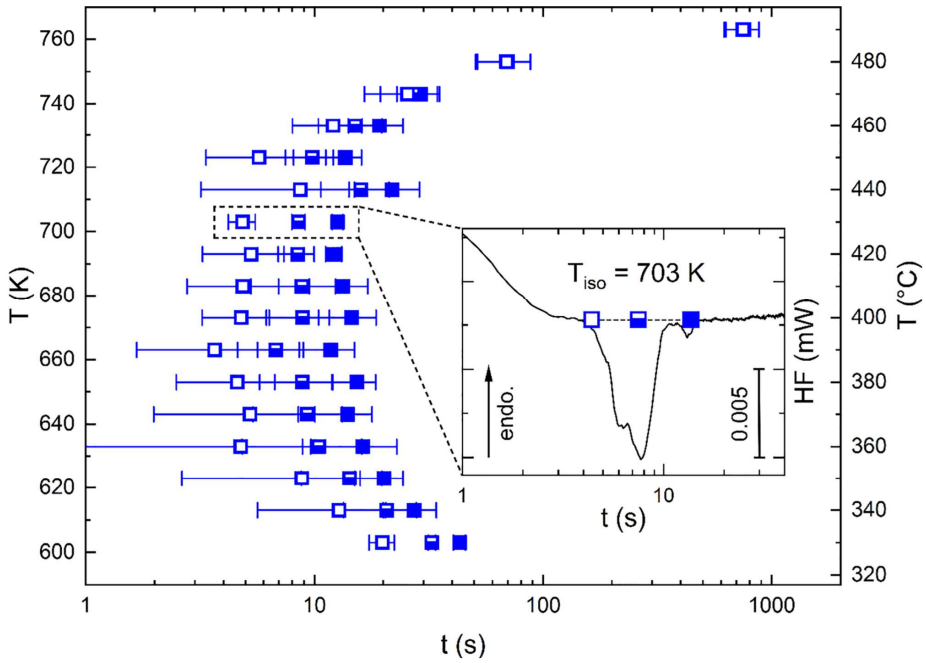

Fig. 1. Results of isothermal FDSC crystallization studies. The inset shows an exemplary measurement at 703 K. In the main window, averaged crystallization times for 1% (open squares), 50% (half-filled squares), and 99% (filled squares) of the occurred crystallization enthalpy are displayed. The standard deviations are given as error bars.

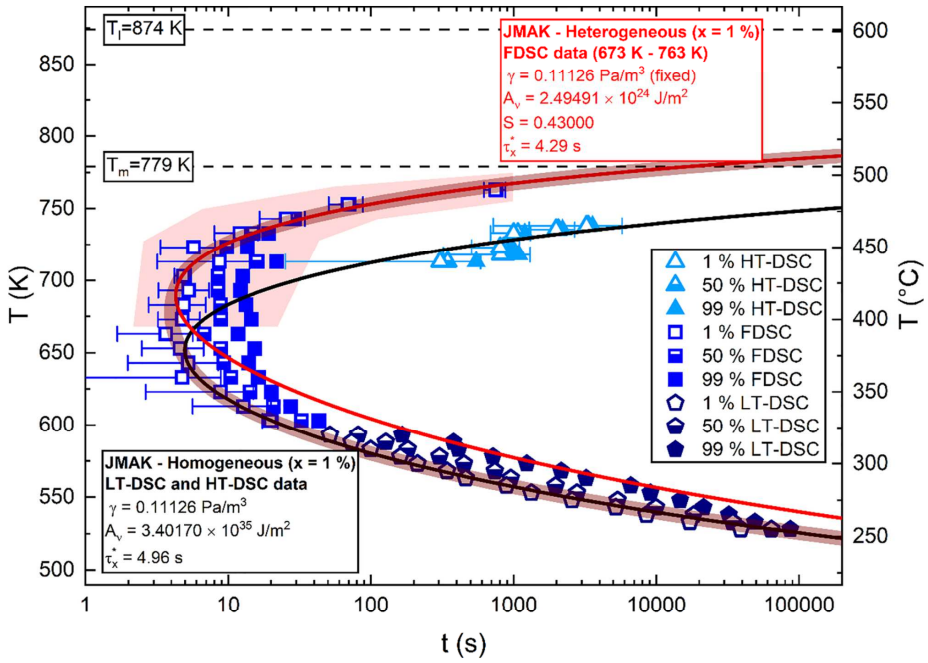

Fig. 2. Complete isothermal TTT diagram of the $Pt_{42.5}Cu_{27}Ni_{9.5}P_{21}$ alloy consisting of LT-DSC [6], HT-DSC [6], and FDSC crystallization data. Until about 668 K (below the transparent red area), LT-DSC and FDSC results show good alignment. In contrast, HT-DSC data and high-temperature FDSC data show drastic disagreement, the FDSC studies reveal crystallization times about two orders of magnitude faster than the HT-DSC data. This discrepancy is underlined by the JMAK fit of the LT- and HT-DSC data that assumes homogeneous crystallization (black solid line). Using the modification for heterogeneous crystallization, the red solid line indicates the JMAK fit of the FDSC data above 668 K (transparent red area), allowing to mathematically describe the upper FDSC crystallization nose. Consequently, the combined data set of FDSC and LT-DSC can be modeled by a superposition of both JMAK fits, as indicated by the broad transparent line (For interpretation of the references to color in this figure legend, the reader is referred to the web version of this article).

$$u(T) = \frac{k_B}{3\,\pi\,a_0^2}\,\frac{T}{\eta(T)}\left(1 - exp\left(\frac{n}{k_B}\frac{\Delta g_{l-x}(T)}{T}\right)\right) \tag{3}$$

with a preexponential factor A_ν, the volume-specific free energy difference between liquid and crystalline state $\Delta g_{l\text{-}x}(T)$, the interfacial energy between liquid and crystalline state γ, the average atomic diameter a_0, the average atomic volume n, and the temperature-dependent equilibrium viscosity $\eta(T)$. $\Delta g_{l\text{-}x}(T)$ is calculated from molar heat capacity data $\Delta C_{p,l\text{-}x}(T)$, density ρ, molar mass M, as well as the molar values of enthalpy and entropy of fusion, ΔH_f and ΔS_f [19] as

$$\Delta g_{l-x}(T) = \frac{\rho}{M}\Delta G_{l-x}(T) = \frac{\rho}{M}\left(\Delta H_f + \int_{T_l}^{T}\Delta C_{p,l-x}(T')\,dT' - T\left(\Delta S_f + \int_{T_l}^{T}\frac{\Delta C_{p,l-x}(T')}{T}\,dT'\right)\right). \tag{4}$$

The viscosity data is described by the Vogel-Fulcher-Tammann (VFT) equation [20] as

$$\eta(T) = \eta_0\ exp\left(\frac{D^*\ T_0}{T - T_0}\right), \tag{5}$$

with the high-temperature limit of viscosity η_0, the fragility parameter D^* and the VFT-temperature T_0 published in [2,3]. Most of the applied thermodynamic and kinetic parameters in these equations are empirically defined and are taken from [2,3,6], as listed in Table 1 (the parameters a, b, c, and d are the fitting parameters used to model the heat capacity as described in e.g. [21]). Only A_ν and γ are left as free fitting parameters. Here, it should be noted that the heat capacity data used for calculations represents the equilibrium crystalline mixture, which does not necessarily reflect the thermodynamic conditions of initial nucleation but serves as a lower estimate of the actual driving force for crystallization of the primary phase.

In a first step, the JMAK equation with assumed homogeneous crystallization is used to explicitly fit the LT- and HT-DSC data without taking FDSC results into account, in analogy to the fitting procedure in [6]. For a crystalline fraction of $x = 0.01$ (open symbols), an A_ν value of 3.40170×10^{35} Pa/m^3 and a γ value of 0.11126 J/m^2 are provided. These parameters are almost identical to the ones published in [6], only

Table 1
JMAK parameters provided by empirically studies and through fitting procedure.

Thermodynamic parameters taken from [2,6]	
a	9.61384×10^{-3} J/(g-atom K^2)
b	5.52829×10^{6} J K/g-atom
c	-6.14630×10^{-3} J/(g-atom K^2)
d	1.64663×10^{-5} J/(g-atom K^3)
T_l	874 K
ΔH_f	10.5 J/g-atom
ΔS_f	12.01 J/(g-atom K)
Kinetic parameters taken from [2,3]	
η_0	4×10^{-5} Pa s
D*	15.3
T_0	354.4 K
JMAK fit of DSC data (homogeneous nucleation assumed)	
A_ν	3.40170×10^{35} Pa/m^3
γ	0.11126 ± 0.00092 J/m^2
τ_x*	4.96 s
d_c (calculated from τ_x*)	16.2 mm
JMAK fit of FDSC data (heterogeneous nucleation assumed, 673 K–763 K)	
A_ν	2.49491×10^{24} Pa/m^3
γ	0.11126 J/m^2 (fixed)
S(θ)	0.43000 ± 0.01838
Θ	$84.6° \pm 1.4°$
τ_x*	4.29 s
d_c (calculated from τ_x*)	15.3 mm

slight deviations arise from the fact that the HT-DSC data was not averaged for fitting in the original article. The corresponding fit curve is displayed in Fig. 2 as a black solid line. The minimal crystallization time given by the fit curve, the so-called nose time τ_x*, is 4.96 s. Johnson et al. [22] derived an empirical equation that connects the crystallization nose time τ_x* with the critical casting diameter d_c (in mm) as

$$\tau_x^* = 0.00419\ (d_c)^{2.54}. \tag{6}$$

Accordingly, the nose time interpolated by the DSC JMAK fit would correspond to a d_c value of 16.2 mm. This is in reasonable agreement with the experimentally confirmed d_c of 20 mm [1]. These samples were produced by water quenching the equilibrium liquid under a protective environment of B_2O_3 flux in a quartz tube. The use of a fluxing agent drastically reduces the probability of heterogeneous nucleation, as it purifies the melt from oxidic contaminations and shields it to some degree from external nucleation sites [6,8,23,24]. The HT-DSC measurements mimic these conditions since the studied sample is also submerged in a B_2O_3 flux, thereby decreasing the probability of interfering reactions with gaseous impurities or the crucible pan. Indeed, the large scatter in HT-DSC crystallization times (see error bars in Fig. 2) speaks for the typical stochastic nature of a crystallization process controlled by (homogeneous) nucleation at these elevated temperatures. Thus, albeit heterogeneous nucleation cannot be completely excluded, it seems to play no major role in the crystallization behavior of the HT-DSC measurements. In case of the LT-DSC studies, the beneficial influence of a fluxing agent is absent, yet, the critical nuclei size at such low temperatures is already very small, so that the liquid does not lack on overcritical nuclei. Instead, the crystallization times are mainly dominated by the sluggish kinetics. Hence, the influence of the nucleation rate, and therefore of heterogeneous nucleation effects, on the crystallization kinetics becomes less pronounced at these low temperatures. The crystallization is rather growth-controlled as pointed out in numerous studies [6,8,13,24]. This leads to reproducible crystallization times with crystallization events stretched over large time spans, as demonstrated by the LT-DSC data in Fig. 2. Based on these considerations, two assumptions are made. First, it seems reasonable that heterogeneous nucleation plays no crucial role for the observed crystallization kinetics of all the DSC data, leaving the assumption of homogeneous nucleation for JMAK fitting as a valid approach. Second, it is assumed that DSC data and the resulting JMAK fit correspond relatively well to the crystallization conditions present for the fluxed and quenched samples reported in [1].

Comparing DSC-JMAK fit and FDSC data, excellent agreement is found in the low temperature part of the crystallization nose, but deviations increase for temperatures above the nose tip (above about 668 K), indicated by the transparent red area in Fig. 2. This trend finds its climax in the FDSC data at the highest temperatures, where crystallization events occur about two orders of magnitude faster than in HT-DSC measurements under fluxing conditions. DSC-based isothermal TTT studies on a Pd-based bulk metallic glass former [25] reported a quite similar behavior by comparing the crystallization times of fluxed and unfluxed samples. While no strong discrepancy was found in the low-temperature regime, the unfluxed samples showed distinctly shorter crystallization times in the high-temperature region above the tip of the crystallization nose, which was addressed to heterogeneous nucleation effects on the sample surface. For the present FDSC studies, the sample is molten directly on the UFH 1 sensor to form a rigid connection that permits fast temperature changes, but also increases the possibility of heterogeneous nucleation on the silicon nitride surface of the sensor.

With these aspects in mind, modifications that take heterogeneous nucleation effects into account might provide a more suitable approach for JMAK fitting of the FDSC crystallization nose. In case of heterogeneous nucleation, the free energy barrier to form a critical nucleus is gradually reduced, which can be mathematically expressed by a shape factor S(θ) included for the heterogeneous nucleation rate $I_{het}(T)$ [26]:

$$I_{het}(T) = \frac{A_\nu}{\eta(T)}\ exp\left(-S(\theta)\ \frac{16\ \pi}{3\ k_B\ T}\ \frac{\gamma^3}{\Delta g_{l-x}(T)^2}\right), \tag{7}$$

where S(θ) formally corresponds to a wetting angle θ between the formed nucleus and the substrate surface [26] as

$$S(\theta) = \frac{1}{4}\ (2+cos(\theta))\ (1-cos(\theta))^2. \tag{8}$$

This modified JMAK equation now features three fitting parameter A_ν, γ, and S(θ), instead of two. One of them must be fixed to avoid an overparameterization of the fit. To solve this apparent problem, we assume in the following that for LT-, HT-DSC, and FDSC data, the very same primary crystalline phase nucleates. Only in the nucleation-controlled high-temperature region of the FDSC data set, the crystallization kinetics accelerate due to the mentioned experimental conditions and the resulting increased effect of heterogeneous nucleation. With this approach, the interfacial energy can be fixed to the value found for the homogeneous DSC JMAK fit (0.11126 J/m^2).

In a first attempt, the heterogeneous JMAK fit fails to provide satisfying results for the combined LT-DSC and FDSC data ($x = 0.01$). The fit massively underestimates the nose time, visible in the orange solid line in Fig. A in the Supplementary Information. Similar problems evolve when only the FDSC data is fitted this way (brown dashed line). Here, the JMAK fit fails to describe the rather blunt shape of the FDSC crystallization nose data, since the whole set of empirically given thermodynamic and kinetic parameters predetermines a relatively sharp and narrow nose geometry [5]. To avoid this, only the FDSC data ($x = 0.01$) that deviates from the course of the homogeneous DSC JMAK fit is fitted, i.e. for temperatures above 668 K (the FDSC data in the transparent red area). This fit (red solid line in Fig. 2) allows a good mathematical description of the upper part of the FDSC crystallization nose and provides a S(θ) value of 0.43000, which formally corresponds, according to Eq. (8), to a wetting angle θ of 84.6°, a reasonable value for heterogeneous nucleation processes [27–29]. Geometrically, this would imply an almost half-spherical crystalline nucleus that forms onto the surface of the heterogeneous nucleation site. Albeit the nose tip of heterogeneous FDSC JMAK fit is about 50 K higher than for the homogeneous DSC JMAK fit, the nose time remains with 4.29 s basically unchanged and corresponds, according to Eq. (6), to a d_c of 15.3 mm. So, while the thermal stability in the high-temperature region of the FDSC

crystallization nose is distinctly affected, the GFA, defined by τ_x* and the resulting critical cooling rate and critical diameter, remains almost unaffected. This is a promising result for industry-relevant processing routes of $Pt_{42.5}Cu_{27}Ni_{9.5}P_{21}$, where rather suboptimal conditions (no fluxing, shear flow) are present, e.g. in case of die casting or suction casting processes. Still, it should be considered that the impact of heterogeneous nucleation quantified in this work is only valid for the present setup and can change massively under different conditions.

In summary, the use of the FDSC 2+ allows to bridge the gap in the TTT diagram between LT- and HT-DSC and to directly observe the kinetics at the crystallization nose. In the upper part of the FDSC crystallization nose, crystallization timescales decouple from the HT-DSC results and show distinctly shorter crystallization times. This is traced back to the absence of a fluxing agent in case of the FDSC setup, leaving the alloy prone to increased heterogeneous crystallization effects that catalyze crystallization. The JMAK equation is used to sequentially model crystallization kinetics under homogeneous and heterogeneous nucleation conditions with satisfying agreement. Combined LT-DSC and HT-DSC data can be well described using a single homogeneous JMAK fit, as the fluxing conditions of HT-DSC measurements effectively frustrate heterogeneous nucleation at elevated temperatures. In case of an unfluxed sample environment, where heterogeneous nucleation effects gain influence with rising temperature, the combined FDSC and LT-DSC data set can be modeled through a superposition of homogeneous JMAK fitting at low temperatures and heterogeneous JMAK fitting for higher temperatures above the crystallization nose, as indicated by the broad transparent line in Fig. 2. To our knowledge, this is the first time such a combination of homogeneous and heterogeneous JMAK fitting is used to describe the isothermal crystallization behavior of a metallic glass former. This approach allows to obtain geometrical information about the heterogeneously formed nucleus in terms of the calculated wetting angle θ of 84.6°. Assuming that the heterogeneous nucleation occurs in the sample sensor interface, the present study could be seen as a starting point for a systematic study on different sensor materials (or sensor surface coatings) and their influence on heterogeneous nucleation effects. Due to the extensive amount of accessible data, the $Pt_{42.5}Cu_{27}Ni_{9.5}P_{21}$ alloy would make a good model system, here. Such extensive studies would further benefit from imaging methods like SEM or TEM to verify the used assumption that the same primary crystalline phase forms in case of homogeneous and heterogeneous nucleation.

Moreover, another valuable approach would be a systematic study of the effect of changed overheating in the equilibrium liquid state on the crystallization kinetics of $Pt_{42.5}Cu_{27}Ni_{9.5}P_{21}$, as encouraged by earlier works [6,30].

The authors want to thank B. Adam and L. Ruschel for fruitful discussions. We declare no competing interests concerning this work. This research did not receive any specific grant from funding agencies in the public, commercial, or not-for-profit sectors.

Declaration of Competing Interest

The authors declare that they have no known competing financial interests or personal relationships that could have appeared to influence the work reported in this paper.

Supplementary materials

Supplementary material associated with this article can be found, in the online version, at doi:10.1016/j.scriptamat.2022.114710.

References

[1] J. Schroers, W.L. Johnson, Appl. Phys. Lett. 84 (2004) 3666–3668.
[2] O. Gross, B. Bochtler, M. Stolpe, S. Hechler, W. Hembree, R. Busch, I. Gallino, Acta Mater. 132 (2017) 118–127.
[3] M. Frey, N. Neuber, O. Gross, B. Zimmer, W. Possart, R. Busch, J. Phys. Condens. Matter 32 (2020) 1–9.
[4] O. Gross, N. Neuber, A. Kuball, B. Bochtler, S. Hechler, M. Frey, R. Busch, Commun. Phys. 2 (2019) 83.
[5] O. Gross, Precious Metal Based Bulk Glass-Forming Liquids: Development, Thermodynamics, Kinetics and Structure, Saarland University, 2018.
[6] O. Gross, S.S. Riegler, M. Stolpe, B. Bochtler, A. Kuball, S. Hechler, R. Busch, I. Gallino, Acta Mater. 141 (2017) 109–119.
[7] N. Neuber, M. Frey, O. Gross, J. Baller, I. Gallino, R. Busch, J. Phys. Condens. Matter (2020) 1–8.
[8] S. Pogatscher, P.J. Uggowitzer, Appl. Phys. Lett. 104 (2014) 1–5.
[9] O. Haruyama, T. Makimura, T. Miyakawa, K. Sugiyama, High Temp. Mater. Process. 29 (2010) 381–392.
[10] S. Pogatscher, D. Leutenegger, A. Hagmann, P.J. Uggowitzer, J.F. Löffler, Thermochim. Acta 603 (2015) 46–52.
[11] J.Q. Wang, Y. Shen, J.H. Perepezko, M.D. Ediger, Acta Mater. 104 (2016) 25–32.
[12] N. Sohrabi, J.E.K. Schawe, J. Jhabvala, J.F. Löffler, R.E. Logé, Scr. Mater. 199 (2021), 113861.
[13] C. Wrana, J.E.K. Schawe, Thermochim. Acta 690 (2020).
[14] A.N. Kolmogoroff, Izv. Akad. Nauk SSSR. Seriya Mat. 1 (1937) 355–359.
[15] M. Avrami, J. Chem. Phys. 7 (1939) 1103–1112.
[16] M. Avrami, J. Chem. Phys. 8 (1940) 212–224.
[17] M. Avrami, J. Chem. Phys. 9 (1941) 177–184.
[18] J.W. Christian, The Theory of Transformations in Metals and Alloys, Elsevier Ltd., 2002.
[19] I. Gallino, J. Schroers, R. Busch, J. Appl. Phys. 108 (2010).
[20] C.A. Angell, Science 267 (1995) 1924–1935 (80-.).
[21] M. Frey, R. Busch, W. Possart, I. Gallino, Acta Mater. 155 (2018) 117–127.
[22] W.L. Johnson, J.H. Na, M.D. Demetriou, Nat. Commun. 7 (2016).
[23] H.W. Kui, A.L. Greer, D. Turnbull, Appl. Phys. Lett. 45 (1984) 615–616.
[24] J. Schroers, Y. Wu, R. Busch, W.L. Johnson, Acta Mater. 49 (2001) 2773–2781.
[25] J. Schroers, Y. Wu, W.L. Johnson, Philos. Mag. A 82 (2002) 1207–1217.
[26] D.A. Porter, K.E. Easterling, Phase Transformations in Metals and Alloys, Chapman & Hall, 1992.
[27] D. Turnbull, J. Chem. Phys. 20 (1952) 411–424.
[28] K.L. Moazed, J.P. Hirth, Surf. Sci. 3 (1965) 49–61.
[29] S. Krüger, J. Deubener, Front. Mater. 3 (2016) 1–9.
[30] S. Mukherjee, Z. Zhou, J. Schroers, W.L. Johnson, W.K. Rhim, Appl. Phys. Lett. 84 (2004) 5010–5012.

5.4 Paper IV: Thermoplastic forming of additively manufactured Zr-based bulk metallic glass: A processing route for surface finishing of complex structures

Authors

Maximilian Frey, Jan Wegner, Nico Neuber, Benedikt Reiplinger, Benedikt Bochtler, Bastian Adam, Lucas Ruschel, Sascha Sebastian Riegler, Hao-Ran Jiang, Stefan Kleszczynski, Gerd Witt, Ralf Busch

Publishing information

Submitted: 28.09.2020

Accepted: 29.11.2020

Published: 30.11.2020

Journal: Materials & Design, 198 (2021), 109368

DOI: 10.1016/j.matdes.2020.109368

Abstract of the article

Additive manufacturing of bulk metallic glasses (BMGs) through laser powder bed fusion (LPBF) has drawn growing interest in the last years, especially concerning industry-relevant alloys based on iron or zirconium. The process-inherent high cooling rates and localized melting pools allow to overcome geometrical restrictions given for the production of BMGs by classical casting routes. Yet, the achievable surface qualities are still limited, making an adequate post-processing necessary. In this work, we report on applying thermoplastic forming on LPBF-formed parts for the first time to decrease surface roughness and imprint finely structured surface patterns without the need for complex abrasive machining. This BMG-specific post-processing approach allows to functionalize surface areas on highly complex LPBF-formed specimens, which could be of interest especially for medical or jewelry applications.

Materials and Design 198 (2021) 109368

Contents lists available at ScienceDirect

Materials and Design

journal homepage: www.elsevier.com/locate/matdes

Thermoplastic forming of additively manufactured Zr-based bulk metallic glass: A processing route for surface finishing of complex structures

Maximilian Frey [a,*], Jan Wegner [b], Nico Neuber [a], Benedikt Reiplinger [a], Benedikt Bochtler [a,c], Bastian Adam [a], Lucas Ruschel [a], Sascha Sebastian Riegler [a], Hao-Ran Jiang [a,d], Stefan Kleszczynski [b], Gerd Witt [b], Ralf Busch [a]

[a] Chair of Metallic Materials, Saarland University, Campus C6.3, 66123 Saarbrücken, Germany
[b] Chair of Manufacturing Technology, University Duisburg-Essen, Lotharstraße 1, 47057 Duisburg, Germany
[c] Amorphous Metal Solutions GmbH, Michelinstraße 9, 66424 Homburg, Germany
[d] School of Materials Science and Engineering, Tongji University, 4800 Caoan Road, 201804 Shanghai, China

HIGHLIGHTS

- LPBF-formed AMZ4 metallic glass provides enough thermal stability for thermoplastic forming without harsh crystallization.
- With adequate process parameters, thermoplastic forming has no influence on the mechanical properties of LPBF-formed AMZ4.
- Thermoplastic forming allows to massively reduce the surface roughness of additively formed metallic glass specimen.
- Finely structured surface pattern can be imprinted on additively formed metallic glass parts via thermoplastic forming.

GRAPHICAL ABSTRACT

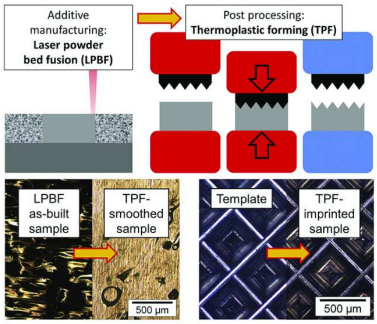

ARTICLE INFO

Article history:
Received 28 September 2020
Received in revised form 11 November 2020
Accepted 29 November 2020
Available online 30 November 2020

Keywords:
Bulk metallic glasses
Additive manufacturing
Laser powder bed fusion
Post-processing
Thermoplastic forming
Mechanical properties

ABSTRACT

Additive manufacturing of bulk metallic glasses (BMGs) through laser powder bed fusion (LPBF) has drawn growing interest in the last years, especially concerning industry-relevant alloys based on iron or zirconium. The process-inherent high cooling rates and localized melting pools allow to overcome geometrical restrictions given for the production of BMGs by classical casting routes. Yet, the achievable surface qualities are still limited, making an adequate post-processing necessary. In this work, we report on applying thermoplastic forming on LPBF-formed parts for the first time to decrease surface roughness and imprint finely structured surface patterns without the need for complex abrasive machining. This BMG-specific post-processing approach allows to functionalize surface areas on highly complex LPBF-formed specimens, which could be of interest especially for medical or jewelry applications.

© 2020 The Authors. Published by Elsevier Ltd. This is an open access article under the CC BY license (http://creativecommons.org/licenses/by/4.0/).

* Corresponding author.
E-mail address: maximilian.frey@uni-saarland.de (M. Frey).

https://doi.org/10.1016/j.matdes.2020.109368
0264-1275/© 2020 The Authors. Published by Elsevier Ltd. This is an open access article under the CC BY license (http://creativecommons.org/licenses/by/4.0/).

1. Introduction

Bulk metallic glasses (BMGs) are a relatively new class of engineering materials. Their combination of high strength and hardness on the one hand and elastic limits up to 2% similar to polymers on the other hand offers significant advantages over crystalline metals [1]. BMGs are produced by rapid cooling from the equilibrium liquid state to avoid crystallization until vitrification occurs at the glass transition temperature. Massive alloy development efforts resulted in various multicomponent alloys with high glass forming ability (GFA). A parameter that directly defines the GFA of a given system is the critical cooling rate (CCR), which is the slowest rate that ensures glass formation without crystallization effects during undercooling. BMGs are mostly produced via classical casting routes, where the high-temperature melt is poured, injected, or sucked into a (water-cooled) metallic mold. As the glassy specimen is monolithically produced by dissipating the heat of the liquid through the mold interface, the achievable cooling rates in the inner volume of a cast part decrease with sample thickness. This results in an upper size boundary for fully amorphous cast specimen that can be quantified by the critical casting thickness, which is the maximum diameter in which an amorphous rod-shaped sample can be cast. This size limitation, in combination with the typical geometric limitations of a casting process, hinders the industrial applicability of this material class until today. A novel approach to overcome these restrictions is the additive manufacturing of metallic glasses by laser powder bed fusion (LPBF) [2–5]. The layer-wise manufacturing approach with very small and localized melt pools, features high cooling rates up to 10^6 K/s [6]. This allows to create large and complexly shaped parts that cannot be produced by casting. Besides this advantage of LPBF-produced BMGs over cast specimens, the powder based process also inheres some drawbacks. The achievable surface quality is limited due to the powder feedstock material, staircase effects resulting from the layer-wise built-up, and sintered particles at the interface between the powder bed and the part. The resulting surface roughness limits the spectrum of possible applications, especially in the biomedical sector, where precisely defined surfaces are often needed [7]. Therefore, functional surfaces of LPBF-manufactured parts generally have to be post-processed to meet the requirements. In this context, several techniques such as electro-polishing [8] or abrasive flow machining [9] are subjects to current research. However, the achievable finish quality is often limited and can be detrimental for certain surface topographies such as open cavities and edges. Therefore, the development of adequate post-processing routes for complex surface structures is in high demand.

An interesting advantage of BMGs over common crystalline metals is the possibility of thermoplastic forming (TPF). Thereby, an initially glassy specimen is heated into the supercooled liquid state, where the viscosity ranges between roughly 10^{12} to 10^5 Pa s [10]. These conditions allow viscoplastic deformation through applied mechanical loads in analogy to thermoforming or blow molding processes known from thermoplastics or silicate glasses. The specimen can be formed into a desired geometry, followed by quick cooling into the glassy state to prevent undesired crystallization. High surface qualities are possible since even structures on the nanoscopic scale can be imprinted [11,12]. Recent studies about viscoplastic deformation of a LPBF-formed BMG have sparked interest to functionalize TPF post-processing for additive manufacturing [13]. Thus, the aim of this study is to demonstrate the possibility of combining both processes to synergize the geometrical freedom given by LPBF with the high-quality surface post-processing achievable by TPF.

2. Materials and methods

Gas-atomized powder of the commercially available glass forming alloy AMZ4 [14] (composition in at.%: $Zr_{59.4}Cu_{28.8}Al_{10.4}Nb_{1.5}$) with an oxygen content of about 1580 μg/g and a mean particle diameter x_{50} of 37.8 μm was provided by Heraeus Amloy Technologies GmbH. Beam-shaped samples ($1.9 \times 2.8 \times 25.2$ mm^3) and cylindrical specimen (12 mm diameter, 3 mm height) were produced under argon gas atmosphere using an eos M100 LPBF device that features a fiber laser with a wavelength of 1064 nm. The process parameters were set according to two previous studies by Wegner et al. to reach a volume energy density of 25 J/mm^3 and allow to produce samples with optical relative densities in the order of 99.5% or above [15,16].

For TPF processing, samples were heated in a custom build TPF apparatus under vacuum to the desired processing temperature (between 703 K and 723 K), at which AMZ4 reaches the highly viscous supercooled liquid (SCL) state. The samples were held isothermally for a defined time while the applied pressure caused viscous flow and plastic deformation. Subsequently, the samples were cooled back into the glassy state with the help of a Peltier element reaching cooling rates in the order of 10 K/s [17,18]. The maximum pressing force of the device is F = 4500 N. Details about the technique and the apparatus as well as a sophisticated study of TPF process parameters for cast AMZ4 samples can be found in previous works [10,18]. In the present study, three setups are tested. An overview of the setups, used sample geometries, and applied analysis methods can be found in Fig. 1.

For setup (A), beam-shaped samples were loaded with a comparably low pressing force of F = 500 N for $t = 30$ s at a temperature of $T = 713$ K to test, in principle, the influence of TPF on the thermophysical and mechanical properties. The relatively low force caused only slight deformation of the sample and allows subsequent mechanical testing of the beam.

In setup (B), the possibility to increase the surface quality of as-built LPBF samples was tested. Thereby, cylindrical specimens were placed in a suitable setup consisting of a casing and two pistons, schematically illustrated in Fig. 1, to prevent massive deformation through viscous flow and were loaded to smoothen the rough upskin surface. The process parameters were set to F = 4500 N, $t = 40$ s, and $T = 723$ K.

In setup (C), a finely structured hard metal template, provided by Olympus Surgical Technologies Europe, was pressed into a sanded beam sample to demonstrate the possibility to imprint a complex surface pattern, as shown in principle in Fig. 1. In this case the used processing parameters were F = 3000 N, $t = 30$ s, and $T = 703$ K.

Mechanical testing of beam-shaped LPBF-formed samples in as-built condition (LPBF-AB) and after TPF post-processing according to setup (A) (LPBF-TPF) was performed in three-point bending (3PB) mode to obtain stress-strain curves using a Shimadzu testing machine, as described in [16]. The surfaces of the beams to be tested were sanded to achieve a well-defined geometry and surface roughness. The amorphous state of LPBF-AB and LPBF-TPF samples was verified by calorimetry and X-ray diffraction. A power compensated Perkin Elmer DSC 8000 was used to perform temperature scan measurements with a constant heating rate of 1 K/s between 373 and 853 K in aluminum pans under argon flow to allow the quantification of the glass transition temperature T_g, the starting temperature of crystallization T_x, and the enthalpy of crystallization ΔH_x. X-ray diffraction was performed in a range of angles (2θ) between 20° and 80° with a PANalytical X'Pert Pro diffractometer using Cu-K_α radiation. Furthermore, high-energy synchrotron X-ray diffraction (HESXRD) of an as-cast reference as well as a LPBF-AB and LPBF-TPF sample was measured at the P21.2 beamline facility of PETRA III of the Deutsche Elektronen-Synchrotron (DESY). Measurements at room temperature were performed with a wavelength of 0.177138 Å (70 keV) in transition mode, using a VAREX XRD4343CT detector (2880×2880 pixels). The two dimensional diffraction pattern were integrated using PyFAI and further processed using the PDFgetX2 software to obtain the total structure factor S(Q).

Testing of surface roughness of the upper surface of the cylindrical samples before and after TPF-treatment according to setup (B) was done by a tactile method, using a Mitutoyo SJ-400 device in analogy with the DIN EN ISO 4288 standard. Yet, the dimensions of the sample limited the evaluation length to the sample diameter of 12 mm. Optical microscopy was performed using an Olympus BX51 device. Thereby, the

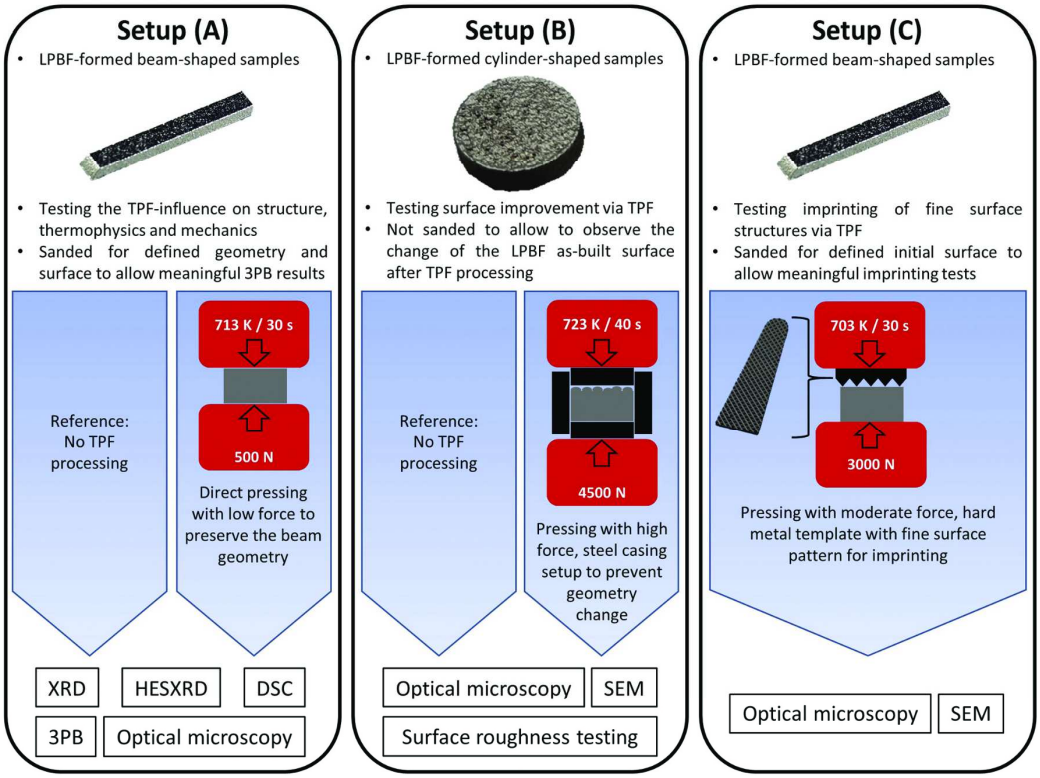

Fig. 1. Overview of the three TPF processing setups, the sample geometries with their respective surface treatment, and the subsequently used analysis methods.

optical density of LPBF-formed beams was determined using the Stream software provided by Olympus GmbH. Scanning electron microscopy was done using a Zeiss Sigma VP device in secondary electron imaging mode.

3. Results

The relative density analysis via optical microscopy reveals that the beam samples before and after TPF setup (A) feature high and basically identical densities of 99.62 ± 0.2% and 99.66 ± 0.2%, respectively. Remaining porosity appears to be mostly spherical gas pores, as can be seen in Fig. A of the Supplementary material.

Fig. 2 compares DSC, XRD, and 3PB results of an as-built LPBF-formed beam (termed LPBF-AB, black curves) and an identical LPBF-formed beam after TPF (termed LPBF-TPF, red curves) according to setup (A). Both diffractograms that are displayed in Fig. 2a do not show Bragg peaks which would reflect a major volume fraction of crystals in the specimens. Instead the diffractograms show a typical broad halo, indicating an overall amorphous structure within the detection limits of this method. In Fig. 2b, both DSC curves show a glass transition from the initial glassy state into the supercooled liquid state at glass transition temperatures T_g of 683 K (LPBF-AB) and 680 K (LPBF-TPF). Crystallization occurs for both samples at $T_x = 758$ K, integration over the respective exothermal events reveals the enthalpies of crystallization ΔH_x that are found to be 4.02 kJ/g-atom (LPBF-AB) and 3.91 kJ/g-atom (LPBF-TPF). The results are relatively similar and reflect a typical ΔH_x value for amorphous AMZ4, further validating the overall amorphous nature of the beams [16]. Differences can be found in the slightly differing shape of the crystallization signal as well as in the sub-T_g behavior of both samples. While the LPBF-AB sample indicates distinct structural relaxation in form of an exothermal signal below T_g, such an effect cannot be observed for the LPBF-TPF sample, revealing different relaxation states. In Fig. 2c, the stress-strain curves of both samples show an almost identical behavior with a Young's modulus of about 81 GPa, a fracture strength σ_f of roughly 2.1 GPa, and no observable plastic deformation. In contrast, an AMZ4 sample cast from high-purity material (the oxygen content of the used Zr is about 13 µg/g [19]) shows pronounced plasticity, combined with a Young's modulus of about 76 GPa and a yield stress σ_y of about 2.1 GPa (gray dotted line, taken from reference [18]).

Fig. 3 shows the HESXRD S(Q) results of a high purity as-cast reference AMZ4 sample, a beam-shaped LPBF-AB sample and a LPBF-TPF sample treated according to setup (A). While the as-cast sample shows no Bragg peaks, the LPBF-AB sample features slight reflexes, indicating the presence of a small amount of crystalline fraction in an overall amorphous structure. The LPBF-TPF sample still shows an overall amorphous structure but with a further increased amount and intensity of crystalline reflexes.

Fig. 4a depicts the casing and pistons used to improve the surface roughness of as-built LPBF-samples according to setup (B). The surfaces of a LPBF-AB and a post-processed LPBF-TPF cylinder are compared in

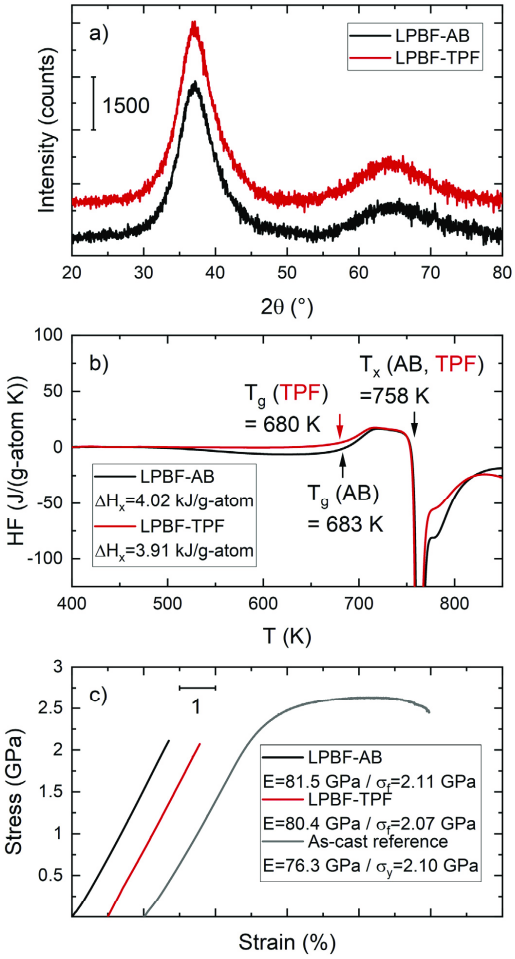

Fig. 2. a) XRD diffractograms of an as-built additionally formed beam-shaped sample (LPBF-AB) and a TPF post-processed (LPBF-TPF) beam, according to setup (A). Both samples show the typical halo, indicating an amorphous structure without crystallites. b) DSC scans of the LPBF-AB and the LPBF-TPF sample. Both of them show a glass transition at about 700 K, followed by the supercooled liquid state and crystallization at roughly 750 K with almost identical crystallization enthalpy ΔH_x. c) Results of the three-point bending mechanical testing. LPBF-AB and LPBF-TPF samples show a similar fracture strength σ_f of about 2.1 GPa without ductile behavior. In contrast, an as-cast reference beam sample reaches its yield strength at 2.1 GPa, followed by remarkable plastic deformation.

Fig. 4b and c. Here, a drastic reduction of surface roughness through the TPF post-processing is visible. This is further quantified by the results of the roughness testing. Without TPF, the R_a and R_z values are 14.2 ± 0.3 µm and 99.4 ± 13.8 µm. After TPF post-processing, these values are reduced by about one order of magnitude to 1.1 ± 0.4 µm and 10.2 ± 3.1 µm, respectively. The TPF-imprinted beam from setup (C) is shown in Fig. 4d, together with the used hard metal template. Due to the lack of containment in contrast to setup (B), bulging through plastic deformation is visible on the side faces of the TPF-pressed part. The surfaces of template and beam are shown in detail in Fig. 4e and with further magnification in the SEM images in Fig. 4f. The overall surface topology of the hard metal template is mirrored on the beam surface. Thereby, even the fine milling cuts of the template are reproduced on the imprinted surface of the BMG part.

4. Discussion

In the present study, the viability to produce amorphous AMZ4 samples using LPBF is confirmed by the XRD and DSC results within the detection limits of these analysis methods. This generally agree with earlier studies published so far [15,16,20–22]. The same applies for the LPBF-TPF sample, demonstrating the applicability of TPF post-processing without major loss of the desired glassy state of the material, if the processing window is judiciously chosen. Mechanical testing reveals that the LPBF-AB and the LPBF-TPF sample are both able to reproduce the yield strength of the high-purity as-cast reference sample. Yet, while the cast sample allows for considerable plastic deformation, the LPBF-formed ones show brittle behavior, causing the yield point and fracture point to coincide. Furthermore, the additively manufactured samples show a slightly higher Young's modulus than the cast reference. Bordeenithikasem et al. [20] reported fracture stresses of about 1.3 GPa for LPBF-formed AMZ4, which is distinctly below the yield strength of the alloy. This effect was i.a. attributed to the presence of irregularly shaped gas pores that act as crack initiation sites and lead to premature sample failure, a commonly observed mechanism in metallic glasses [23–26]. Yet, since very high optical densities above 99.6% with mostly spherically shaped pores are present, as previously reported in [15,16], and since the LPBF-formed AMZ4 in this study shows no premature failure before the yield stress is reached, porosities are not identified as a crucial threat to the mechanical integrity, as previously suggested in reference [16].

Conventional XRD is known to only provide information about the average structure of the investigated sample, thereby leaving small crystalline fractions or especially nano-crystals possibly undetected [27]. At this point, the extremely high flux used for HESXRD helps to detect smaller crystalline fractions, as shown in Fig. 3. The LPBF-AB sample features slight Bragg peaks in the HESXRD S(Q) data, which is in agreement with Pacheco et al., who recently found that small degrees of nano-crystallinity are a common feature of LPBF-formed AMZ4 [22]. Comparing the HESXRD total structure factors of LPBF-AB and the LPBF-TPF sample, the TPF process is found to further increase the degree of crystallinity. This is not surprising as TPF is performed in the supercooled liquid state, where the increased atomic mobility allows crystal nucleation and growth [28]. Based on previous works [29–31], nano-crystalline Zr_4Cu_2O has been identified as the primary crystalline phase that forms during heating of LPBF-formed AMZ4, followed by Al_3Zr_4 and Zr_2Cu [22]. Thus, the same types of nano-crystalline phases can be assumed to be present in a small degree in the LPBF-TPF sample, although the low amount and intensity of the Bragg peaks in Fig. 2 prohibit a clear phase identification. Yet, the increase in crystallinity is still low enough to be concealed by the detection limit of conventional XRD, see Fig. 2a. The change in the DSC crystallization signal shape, see Fig. 2b, and the slightly reduced ΔH_x value seem to reflect the TPF-induced crystallization, yet, it has to be noted that the observed ΔH_x difference of about 0.1 kJ/g-atom is well within the method-typical measurement uncertainty [32–34]. The gradually increased crystallinity of the LPBF-TPF sample seems to be still uncritical in terms of the mechanical properties as no decrease in strength is observed in comparison to the LPBF-AB sample, see Fig. 2c. Schroers et al. recently found that small crystalline fractions in Zr-based BMGs only have marginal influence on the mechanical properties, allowing for robust parts even after TPF processing [28].

In the present work, the absence of ductility can be mainly addressed to intrinsic brittleness of the material due to the high oxygen content, as various studies have demonstrated the increase of brittleness and

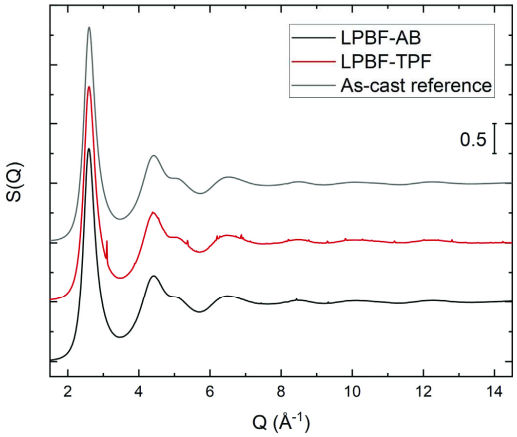

Fig. 3. High-energy synchrotron XRD total structure factors of an as-cast AMZ4 sample, an as-built (LPBF-AB) and a TPF processed (LPBF-TPF) additively formed beam-shaped sample, according to setup (A). The as-cast sample shows a fully amorphous halo without Bragg peaks, while the LPBF-AB sample features three small reflexes, indicating a slight amount of crystalline fraction. The LPBF-TPF sample still shows a mainly amorphous structure, but features an increased amount of Bragg peaks, indicating a higher degree of crystallization in comparison to the as-built sample.

stiffness of Zr-based BMGs through oxygen contamination [35–40]. Oxygen is found to change the short- and medium-range order in the way that shear processes and the formation of multiple shear bands are impeded, thus provoking catastrophic failure [38,40]. The oxygen contamination issue can be traced back to the inherent characteristics of the used powder feedstock, as it features an extremely high surface-to-volume ratio that leads to increased absorption of oxygen during the atomization process [41,42]. Also, oxygen uptake during the LPBF process itself, due to residual oxygen in the build chamber and through residual humidity in the powder feedstock, further contributes to the oxygen contamination [41–43]. Combined, powder atomization and LPBF processing increase the oxygen level massively, up to values of several hundreds or even thousands of μg/g, while Zr-based metallic glasses produced by casting usually feature oxygen levels in the order of only 80 μg/g [42,44]. The obvious difference in terms of ductility between as-cast and LPBF-formed AMZ4 should be interpreted in this context. In principle, TPF processing may lead to a further increase in oxygen contamination. Yet, by taking the rather low processing temperatures in the supercooled liquid state and consequentially sluggish diffusion processes into account, the influence of the TPF process should rather be neglectable. This approach seems valid as the mechanical performance is not harshly altered by TPF at all.

The exothermal structural relaxation signal found for the LPBF AB sample in Fig. 2b is a typical result of a fast cooling process present during vitrification [45], which is not surprising if taking the process-typical high cooling rates of up to 10^6 K/s into account [6]. In contrast, the LPBF-TPF sample does not feature a significant structural relaxation signal, reflecting the much slower cooling rate of roughly 10 K/s that is achievable with the used device [17,18] and by conductive cooling through the sample volume itself.

Thermoplastic forming has been reported to have a negative influence on the ductility of BMGs since slowly cooled glasses are structurally more relaxed, corresponding to a lower free volume and a lower enthalpic state [45,46], and therefore tend to show increased brittleness [47–49]. Yet, the present findings suggest that the influence of the relaxation state is rather neglectable as the oxygen embrittlement dominates the mechanical behavior, before and after TPF post-processing. So, in case of the present alloy and process conditions, the mechanical properties before and after TPF can be assumed to be identical, thereby simplifying the overall prediction of expectable mechanical performance of a post-processed part. This decoupling of mechanical performance and the TPF process further underlines its applicability as a viable post-processing route.

First tests to increase the surface quality of an LPBF-formed sample in setup (B), see Fig. 4b and c, show promising results by drastically lowering the roughness. Yet, residual artifacts remain visible, most likely caused by initial irregularities in the LPBF-formed surface that were too massive to be smoothed out in the present experimental setup. Here, further testing campaigns for parameter optimization are needed. Pretreating the LPBF surface before starting the TPF process by e.g. grit blasting or sanding could erase protruding irregularities and, thus, increase the surface quality achievable by TPF. The potential of such an approach is shown by the results of setup (C) in Fig. 4e and f. The previously sanded beam precisely reproduces the TPF-imprinted template and demonstrates the generally known net-shape formability of BMGs [48,50] for the first time in case of an additively formed part.

A more complex TPF template form that combines the given part containment from setup (B) with the fine structure pattern of setup (C) could be used to add a functional surface to a LPBF-formed part without changing its overall geometry through undesired plastic deformation. Such a production route would allow to combine the geometrical freedom of additive manufacturing with a tailorable application-oriented surface optimization in part regions where it is explicitly needed. This is of interest especially for components that are too complex to be formed by casting and require surface qualities that are difficult to achieve by machining. Examples can be found in medical applications, e.g. for technology used for minimal-invasive surgeries. Fig. 5 schematically demonstrates such a LPBF-TPF production route for a minimal-invasive clamp device. For this application, both clamp halves have to provide form closure, and therefore demand for a precisely defined surface pattern with low tolerances, which is applied by a local TPF post-treatment.

If only a relatively small area with a defined surface pattern is needed, an even more straight forward approach could be found that renounces the use of a complex containment setup. Thereby, a small heated template piston is to be pressed onto the respective area. The surface is locally heated into the supercooled liquid state and is imprinted by the piston template, while the surrounding volume remains cold and in the undeformed glassy state. After imprinting, the piston template is removed, and the deformed surface area is cooled quickly by the ambient material. Such a localized approach is especially suitable for jewelry applications, where e.g. complexly skeletonized LPBF parts could be surface finished or even personalized (similar to an embossing process) through imprinting. Here, Pt-based BMG systems would be promising candidates, since they combine high thermal stability against crystallization, ductile mechanical behavior even after slow cooling, and a high resistance against oxygen absorption due to the noble metal character [49,51].

Furthermore, a recent study by Bochtler et al. demonstrated the principal possibility to use TPF for consolidation of AMZ4 powder to highly dense bulk material with a low minimal porosity [18]. In the present study, the density measurements suggest that the LPBF-formed samples already show a porosity level low enough to remain unchanged after TPF processing, most likely since closed gas pores embedded in the bulk material cannot easily be erased through pressing in the supercooled liquid state. Yet, the results by Bochtler et al. [18] suggest that TPF could be a valid option to increase the relative density of additively formed BMG-parts with higher degrees of porosity, leaving this approach as a possible topic of future studies. A similar post-processing technique is already established for crystalline additively formed metals in form of hot isostatic pressing (HIP) [52,53].

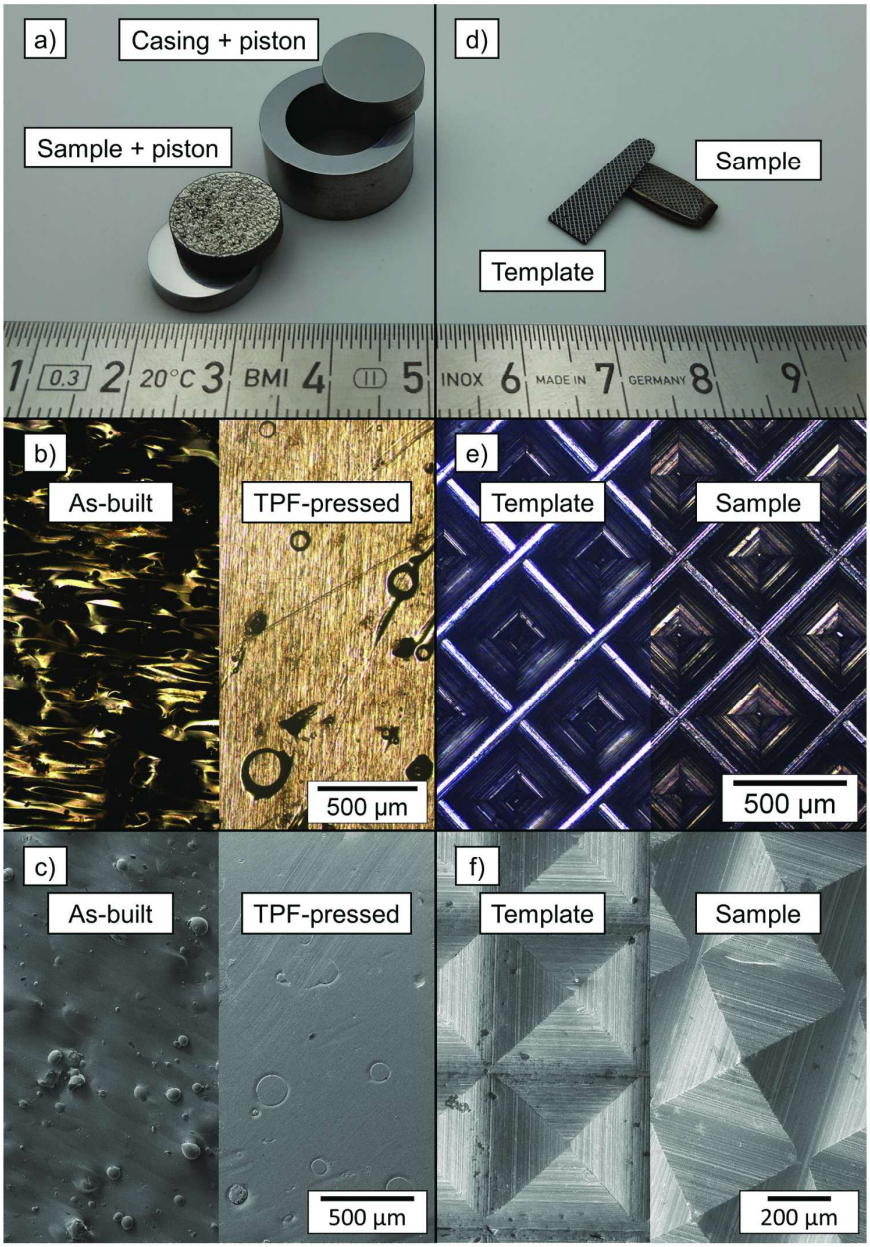

Fig. 4. a) Piston set used for TPF setup (B), consisting of two polished pistons and a cylinder casing, that allows to press and smoothen the rough surface of an LPBF as-built cylinder (placed on top of the lower piston) without severe change of geometry through plastic deformation. Optical microscopy image, b), and SEM secondary electron contrast image, c), of the as-built (left) and TPF-pressed cylinder surfaces in direct comparison. d) Hard metal template (left) and imprinted LPBF-formed beam (right) from setup (C). e) The surface structure of the template shows a periodic structure with fine milling cuts (left), which is directly mirrored on the imprinted beam (right). The respective SEM secondary electron images, f), confirm the remarkable surface reproduction.

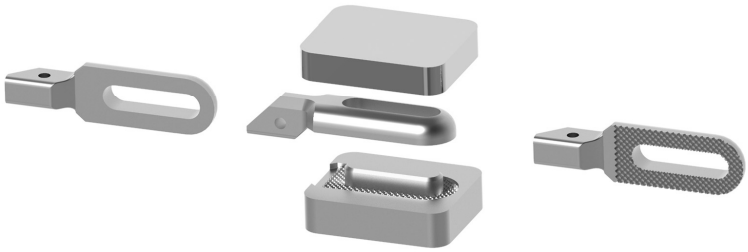

Fig. 5. TPF post-processing can be used to add finely structured surface patterns to additively formed BMG parts in regions that demand special surface requirements. In this schematic example, a LPBF-formed half of a clamp device used for minimal-invasive surgery is locally imprinted with a fine grit pattern using a template that features the negative shape of the desired pattern. Due to local containment around the TPF-processed region, severe geometry change through plastic deformation is avoided.

5. Conclusion

Overall amorphous AMZ4 specimens were produced by LPBF additive manufacturing according to previous studies. The possibility of TPF post-processing of these samples is explored in the present work, leading to three conclusions: 1) In principle, LPBF-formed AMZ4 provides enough thermal stability to withstand TPF without severe crystallization effects. Synchrotron XRD may allow to detect small degrees of crystallinity induced by TPF, but the mechanical properties remain mostly unchanged on a high level and encourage industrial applications. 2) The typical surface roughness of as-built LPBF-formed samples can be drastically reduced through TPF, albeit preliminary steps like sanding or sand blasting might be needed to get completely rid of remaining surface artifacts. 3) Imprinting of sanded LPBF-formed AMZ4 can create TPF-typical near-perfect surface pattern.

Due to their unique amorphous structure, BMGs are the only metallic materials that offer the possibility to apply thermoplastic forming. The present study provides the proof of principle that this net-shape creating method can be used to post-process additively formed metallic glasses. This is a distinct advantage over additively formed crystalline alloys and allows for novel production routes, especially for medical and jewelry applications.

Data availability

The raw/processed data required to reproduce these findings cannot be shared at this time as the data also forms part of an ongoing study.

Declaration of Competing Interest

The authors declare that they have no known competing financial interests or personal relationships that could have appeared to influence the work reported in this paper.

Acknowledgements

The authors want to thank Moritz Stolpe from Heraeus Amloy Technologies GmbH for providing powder material. We further acknowledge DESY (Hamburg, Germany), a member of the Helmholtz Association HGF, for the provision of experimental facilities. Parts of this research were carried out at PETRA III and we would like to thank Malte Blankenburg and Ulrich Lienert for assistance in using the P21.2 beamline facility. This research was funded by the German Federal Ministry for Economic Affairs and Energy (BMWi) within the Promotion of Joint Industrial Research Programme (IGF) due to a decision of the German Bundestag. It was part of the research projects 19927N (OptMetGlas) and 21227N (LaSaM) by the Association for Research in Precision Mechanics, Optics and Medical Technology (F.O.M.) under the auspices of the German Federation of Industrial Research Associations (AiF).

Appendix A. Supplementary data

Supplementary data to this article can be found online at https://doi.org/10.1016/j.matdes.2020.109368.

References

[1] M. Telford, Materialstoday 7 (2004) 36–43.
[2] S. Pauly, L. Löber, R. Petters, M. Stoica, S. Scudino, U. Kühn, J. Eckert, Mater. Today 16 (2013) 37–41.
[3] X.P. Li, M.P. Roberts, S. O'Keeffe, T.B. Sercombe, Mater. Des. 112 (2016) 217–226.
[4] Z. Mahbooba, L. Thorsson, M. Unosson, P. Skoglund, H. West, T. Horn, C. Rock, E. Vogli, O. Harrysson, Appl. Mater. Today 11 (2018) 264–269.
[5] E. Williams, N. Lavery, J. Mater. Process. Technol. 247 (2017) 73–91.
[6] P.A. Hooper, Addit. Manuf. 22 (2018) 548–559.
[7] M. Lowther, S. Louth, A. Davey, A. Hussain, P. Ginestra, L. Carter, N. Eisenstein, L. Grover, S. Cox, Addit. Manuf. 28 (2019) 565–584.
[8] V. Urlea, V. Brailovski, J. Mater. Process. Technol. 242 (2017) 1–11.
[9] N. Mohammadian, S. Turenne, V. Brailovski, J. Mater. Process. Technol. 252 (2018) 728–738.
[10] B. Bochtler, O. Kruse, R. Busch, J. Phys. Condens. Matter 32 (2020) 1–11.
[11] Y. Saotome, Y. Fukuda, I. Yamaguchi, A. Inoue, J. Alloys Compd. 434–435 (2007) 97–101.
[12] G. Kumar, A. Desai, J. Schroers, Adv. Mater. 23 (2011) 461–476.
[13] K. Kosiba, L. Deng, S. Scudino, Materials (Basel) 13 (2020).
[14] J. Heinrich, R. Busch, B. Nonnenmacher, Intermetallics 25 (2012) 1–4.
[15] J. Wegner, S. Kleszczynski, M. Frey, S. Hechler, G. Witt, R. Busch, Proc. 15th Rapid. Tech Conf, 2018.
[16] J. Wegner, M. Frey, P. Stiglmair, S. Kleszczynski, G. Witt, R. Busch, South African J. Ind. Eng. 30 (3) (2019) 32–40.
[17] M. Kelkel, Master Thesis (2016) 111.
[18] B. Bochtler, M. Stolpe, B. Reiplinger, R. Busch, Mater. Des. 140 (2018) 188–195.
[19] J. Heinrich, Massivglasbildende Metallische Legierungen Als Konstruktionswerkstoff Materialoptimierung Und Technologieentwicklung Zur Herstellung Und Verarbeitung, 2012.
[20] P. Bordeenithikasem, M. Stolpe, A. Elsen, D.C. Hofmann, Addit. Manuf. 21 (2018) 312–317.
[21] J.J. Marattukalam, V. Pacheco, D. Karlsson, L. Riekehr, J. Lindwall, F. Forsberg, U. Jansson, M. Sahlberg, B. Hjörvarsson, Addit. Manuf. 13 (2020) 101124.
[22] V. Pacheco, D. Karlsson, J.J. Marattukalam, M. Stolpe, B. Hjörvarsson, U. Jansson, M. Sahlberg, J. Alloys Compd. 825 (2020).
[23] C.J. Lee, Y.H. Lai, J.C. Huang, X.H. Du, L. Wang, T.G. Nieh, Scr. Mater. 63 (2010) 105–108.
[24] J. Zhang, D. Estévez, Y.Y. Zhao, L. Huo, C. Chang, X. Wang, R.W. Li, J. Mater. Sci. Technol. 32 (2016) 129–133.
[25] A. Kuball, B. Bochtler, O. Gross, V. Pacheco, M. Stolpe, S. Hechler, R. Busch, Acta Mater. 158 (2018) 13–22.
[26] A.S. Nouri, X.J. Gu, S.J. Poon, G.J. Shiflet, J.J. Lewandowski, Philos. Mag. Lett. 88 (2008) 853–861.
[27] C. Suryanarayana. A. Inoue. Bulk Metallic Glasses. CRC Press. 2011.
[28] J. Ketkaew, Z. Liu, W. Chen, J. Schroers, Phys. Rev. Lett. 115 (2015) 1–6.
[29] J. Eckert, N. Mattern, M. Zinkevitch, M. Seidel, Mater. Trans. JIM 39 (1998) 623–632.
[30] M.F. De Oliveira, W.J. Botta, M.J. Kaufman, C.S. Kiminami, J. Non. Cryst. Solids 304 (2002) 51–55.
[31] M.F. de Oliveira, M.J. Kaufman, W.J. Botta Filho, C.S. Kiminami, Mater. Sci. Forum 386–388 (2002) 53–58.

[32] N. Neuber, O. Gross, M. Eisenbart, A. Heiss, U.E. Klotz, J.P. Best, M.N. Polyakov, J. Michler, R. Busch, I. Gallino, Acta Mater. 165 (2018) 315–326.
[33] M. Frey, R. Busch, W. Possart, I. Gallino, Acta Mater. 155 (2018) 117–127.
[34] O. Gross, B. Bochtler, M. Stolpe, S. Hechler, W. Hembree, R. Busch, I. Gallino, Acta Mater. 132 (2017) 118–127.
[35] V. Keryvin, C. Bernard, J.C. Sanglebœuf, Y. Yokoyama, T. Rouxel, J. Non, Cryst. Solids 352 (2006) 2863–2868.
[36] Y. Yokoyama, A. Kobayashi, K. Fukaura, A. Inoue, Mater. Trans. 43 (2002) 571–574.
[37] X.H. Lin, W.L. Johnson, W.K. Rhim, Mater. Trans. JIM 38 (1997) 473–477.
[38] Z.P. Lu, H. Bei, Y. Wu, G.L. Chen, E.P. George, C.T. Liu, Appl. Phys. Lett. 92 (2008) 1–4.
[39] J.P. Best, H.E. Ostergaard, B. Li, M. Stolpe, F. Yang, K. Nomoto, M.T. Hasib, O. Muránsky, R. Busch, X. Li, J.J. Kruzic, Addit. Manuf. (2020) 101416.
[40] J.P. Best, J. Ast, B. Li, M. Stolpe, R. Busch, F. Yang, X. Li, J. Michler, J.J. Kruzic, Mater. Sci. Eng. A 770 (2020) 138535.
[41] J.H. Tan, W.L.E. Wong, K.W. Dalgarno, Addit. Manuf. 18 (2017) 228–255.
[42] L. Deng, K. Kosiba, R. Limbach, L. Wondraczek, U. Kühn, S. Pauly, J. Mater. Sci. Technol. 60 (2021) 139–146.
[43] K. Dietrich, J. Diller, S. Dubiez-Le Goff, D. Bauer, P. Forêt, G. Witt, Addit. Manuf. 32 (2020).
[44] S. Pauly, C. Schricker, S. Scudino, L. Deng, U. Kühn, Mater. Des. 135 (2017) 133–141.
[45] Z. Evenson, I. Gallino, R. Busch, J. Appl. Phys. 123 (2010) 529.
[46] A. van den Beukel, J. Sietsma, Acta Metall. Mater. 38 (1990) 383–389.
[47] G. Kumar, D. Rector, R.D. Conner, J. Schroers, Acta Mater. 57 (2009) 3572–3583.
[48] J. Schroers, Adv. Mater. 22 (2010) 1566–1597.
[49] G. Kumar, P. Neibecker, Y.H. Liu, J. Schroers, Nat. Commun. 4 (2013) 1536.
[50] J. Schroers, J. Miner. Met. Mater. (2005) 35–39.
[51] O. Gross, S.S. Riegler, M. Stolpe, B. Bochtler, A. Kuball, S. Hechler, R. Busch, I. Gallino, Acta Mater. 141 (2017) 109–119.
[52] C.B. Finfrock, A. Exil, J.D. Carroll, L. Deibler, Metallogr. Microstruct. Anal. 7 (2018) 443–456.
[53] W. Tillmann, C. Schaak, J. Nellesen, M. Schaper, M.E. Aydinöz, K.P. Hoyer, Addit. Manuf. 13 (2017) 93–102.

5.5 Paper V: Laser powder bed fusion of Cu-Ti-Zr-Ni bulk metallic glasses in the Vit101 alloy system

Authors

Maximilian Frey, Jan Wegner, Erika Soares Barreto, Lucas Ruschel, Nico Neuber, Bastian Adam, Sascha Sebastian Riegler, Hao-Ran Jiang, Gerd Witt, Nils Ellendt, Volker Uhlenwinkel, Stefan Kleszczynski, Ralf Busch

Publishing information

Submitted: 29.10.2022

Accepted: 23.02.2023

Published: 25.02.2023

Journal: Additive Manufacturing, 66 (2023), 103467

DOI: 10.1016/j.addma.2023.103467

Abstract of the article

Laser powder bed fusion (PBF-LB/M) of bulk metallic glasses (BMGs) has experienced growing scientific and industrial interest in the last years, with a special focus on application relevant systems based on zirconium. The high cooling rates and the layer-wise build-up process allow overcoming size and geometry limitations typical for conventional casting routes. Yet, the novel production approach requires different alloy characteristics than casting processes. The present work reports for the first time on the PBF-LB/M-processing of three CuTi-based bulk metallic glass formers in the Vit101 system, allowing to exceed the mechanical performance of most additively formed Zr-based BMGs. Furthermore, the influence of alloy properties like thermal stability and toughness on the PBF-LB/M applicability are systematically studied. Thermal stability plays a minor role to produce amorphous specimen, while notch toughness is found to be a more crucial aspect to achieve parts with low defect density and resulting high mechanical performance. The results suggest fundamentally different alloy development strategies adapted to the needs of the PBF-LB/M-process, leaving classical casting-based

optimization of glass forming ability behind and evolving towards a rather toughness-oriented optimization.

Additive Manufacturing 66 (2023) 103467

Contents lists available at ScienceDirect

Additive Manufacturing

journal homepage: www.elsevier.com/locate/addma

Laser powder bed fusion of Cu-Ti-Zr-Ni bulk metallic glasses in the Vit101 alloy system

Maximilian Frey [a,*], Jan Wegner [b], Erika Soares Barreto [c], Lucas Ruschel [a], Nico Neuber [a], Bastian Adam [a], Sascha Sebastian Riegler [a], Hao-Ran Jiang [d], Gerd Witt [b], Nils Ellendt [c], Volker Uhlenwinkel [c], Stefan Kleszczynski [b], Ralf Busch [a]

[a] Chair of Metallic Materials, Saarland University, Campus C6.3, 66123 Saarbrücken, Germany
[b] Chair of Manufacturing Technology, University Duisburg-Essen, Lotharstraße 1, 47057 Duisburg, Germany
[c] Leibniz Institute for Materials Engineering - IWT, Badgasteiner Str. 3, 28359 Bremen, Germany
[d] Materials Genome Institute, Shanghai University, Shanghai 200444, China

ARTICLE INFO

Keywords:
Bulk Metallic Glasses
Amorphous Metals
Additive Manufacturing
Laser Powder Bed Fusion
Mechanical Properties

ABSTRACT

Laser powder bed fusion (PBF-LB/M) of bulk metallic glasses (BMGs) has experienced growing scientific and industrial interest in the last years, with a special focus on application relevant systems based on zirconium. The high cooling rates and the layer-wise build-up process allow overcoming size and geometry limitations typical for conventional casting routes. Yet, the novel production approach requires different alloy characteristics than casting processes. The present work reports for the first time on the PBF-LB/M-processing of three CuTi-based bulk metallic glass formers in the Vit101 system, allowing to exceed the mechanical performance of most additively formed Zr-based BMGs. Furthermore, the influence of alloy properties like thermal stability and toughness on the PBF-LB/M applicability are systematically studied. Thermal stability plays a minor role to produce amorphous specimen, while notch toughness is found to be a more crucial aspect to achieve parts with low defect density and resulting high mechanical performance. The results suggest fundamentally different alloy development strategies adapted to the needs of the PBF-LB/M-process, leaving classical casting-based optimization of glass forming ability behind and evolving towards a rather toughness-oriented optimization.

1. Introduction

Bulk metallic glasses (BMGs) are a novel class of engineering materials. They combine the high strength and hardness of metals with elastic limits of up to 2 % usually only known from polymers, making them highly interesting materials for manifold industrial applications [1]. BMGs can be produced by rapid cooling of the equilibrium liquid to bypass crystallization and achieve vitrification at the glass transition temperature. The glass forming ability (GFA) of a given BMG-forming alloy can be quantified by its critical cooling rate (CCR), which defines the lowest cooling rate that allows suppressing crystallization to form a fully amorphous specimen. For conventional casting processes, the CCR imposes limitations in geometry and size, expressed by the critical diameter (d_c), which is the maximum diameter that permits full vitrification of a rod-shaped cast sample. Such limitations for conventional casting processes hinder the industrial application of BMGs until today.

Additive manufacturing (AM) through laser powder bed fusion (PBF-LB/M) of metals bears the potential to overcome the size and geometry constraints of casting processes. The layer-wise build-up principle with its small melt pool dimensions incorporates highly localized melting and solidification processes with extremely fast cooling rates of up to 10^6 K/s [2], which is far beyond the usual CCRs of modern BMGs, which range in the order of roughly 100 K/s. Studies have demonstrated the possibility to produce amorphous Fe-, Ti-, Cu-, and especially Zr-based metallic glasses [3–12] via PBF-LB/M. Complex geometries that are difficult or impossible to cast have been realized, e.g., scaffold structures [3], topology optimized structures [8], honeycomb structures for lightweight applications [13], or even compliant mechanisms [14]. Furthermore, additively formed BMGs can be post-processed by thermoplastic forming (TPF) [15], allowing to apply advanced surface finishing and structurization in a direct and efficient manner, unfeasible for crystalline

* Corresponding author.
E-mail address: maximilian.frey@uni-saarland.de (M. Frey).

https://doi.org/10.1016/j.addma.2023.103467
Received 29 October 2022; Received in revised form 23 February 2023; Accepted 23 February 2023
Available online 25 February 2023
2214-8604/© 2023 Published by Elsevier B.V.

metallic materials [16].

A major drawback of metallic glasses produced via PBF-LB/M is still found in their mechanics. Effects like porosity, (nano-)crystallization, structural relaxation, and chemical impurities usually lead to brittle fracture below the material's yield strength [17–20]. One of the few exceptions is found in the commercially available Zr-based system $Zr_{59.3}Cu_{28.8}Al_{10.4}Nb_{1.5}$ (trade name AMZ4 or Zr01 [21]) that has shown to reproducibly reach the alloy's yield strength of about 2.1 GPa for AM samples before failure in (macroscopic) bending tests [13,16,18]. Yet, the oxygen affinity of the Zr-based alloy together with the oxygen-triggered crystallization kinetics [22] necessitates rather high-purity powder feedstock to reach such high strengths combined with robust process stability [18]. Here, CuTi-based alloys like Vit101 ($Cu_{47}Ti_{34}Zr_{11}Ni_8$) [23] might emerge as a promising alternative, as they feature low material costs, increased strength, and smaller sensitivity to oxygen compared to most Zr-based alloys [24]. G. Garrett et al. [25] showed that microalloying of Vit101 with Si ($Cu_{47}Ti_{33}Zr_{11}Ni_8Si_1$ [26], further termed Vit101Si) and a combination of Si and Sn ($Cu_{47}Ti_{33}Zr_{11}Ni_6Si_1Sn_2$ [27], further termed Vit101SiSn) leads to three main effects. Firstly, the GFA increases from a critical diameter of 4 mm for Vit101 to 7.4 mm for Vit101Si and 6 mm for Vit101SiSn. Secondly, the width of the supercooled liquid (SCL) region increases, making Vit101Si and especially Vit101SiSn thermally more stable against crystallization in the low-temperature regime around the glass transition. Thirdly, the mechanical properties change in the way that the alloys become harder, yet increasingly brittle with an increasing degree of microalloying. Hence, alloying with Si and Si-Sn was found to be a double-edged sword in terms of industrial applicability. On the one hand, establishing a fully amorphous state through casting is facilitated through the increased GFA, also, TPF processability is improved through the enhanced thermal stability. On the other hand, the glassy state is found to be intrinsically more brittle, leaving produced parts less resilient against crack propagation and catastrophic failure. This ambivalent effect of microalloying also applies for PBF-LB/M processing: The higher thermal stability should toughen the material against crystallization caused by the process-typical cyclic remelting and annealing, but the increased brittleness could provoke crack formation and diminish the mechanical performance of manufactured parts.

Recently, Barreto et al. [28] have demonstrated that fully amorphous, PBF-LB/M-applicable powders of Vit101, Vit101Si, and Vit101SiSn can be atomized from commercial grade elements. The present work continues this research by evaluating the microalloying-induced trade-off between thermal stability and fracture toughness of these CuTi-based compositions during PBF-LB/M processing. In this matter, an PBF-LB/M parameter study was carried out to determine the processability in view of the fabrication of amorphous, dense, and mechanically resilient samples, heading towards a deeper understanding of specific requirements and challenges to adapt BMG compositions for AM.

2. Materials and methods

Fully amorphous powders of Vit101, Vit101Si, and Vit101SiSn with oxygen contents of 760 ± 22, 750 ± 10, and 737 ± 35 µg/g, respectively, and particle diameters between 20 and 63 µm were prepared by close-coupled gas-atomization (CCA) as described in [28]. Cuboid-shaped samples (2.5 × 5 × 5 mm^3, height × width × length) were additively manufactured under Argon gas atmosphere using an SLM 280 HL incorporating two 700 W fiber lasers with spot diameters of 70 µm. All samples were processed on top of preheated Ti6Al4V substrates at 373 K with a layer thickness d_s of 20 µm and a hatch distance h of 70 µm. The cuboid samples were produced for all three alloys with varying values of laser power and scan speed to define a range of parameters for fully amorphous samples with optimized relative density. The laser power P was changed in 10 W steps from 50 W to 80 W, which is taken into account in the sample notation by groups of samples being termed A (50 W), B (60 W), C (70 W), and D (80 W). Within these groups, the scan speed v_s was changed from 1600 mm/s to 2200 mm/s in 200 mm/s steps, indicated by the numbers 1–4. The volume energy density E_V of each sample can be calculated as

$$E_V = \frac{P}{v_s d_s h}. \quad (1)$$

Table 1 summarizes laser powers, scan speeds and the resulting volume energy densities for all samples, which range between 16.2 and 35.7 J/mm^3. Besides the cuboid samples, beam-shaped samples for mechanical testing (1.9 × 2.8 × 25.2 mm^3) were built using the medium-energy parameter set C3 (70 W, 2000 mm/s, 25.0 J/mm^3) and the high-energy parameter set D1 (80 W, 1600 mm/s, 35.7 J/mm^3). The reason for choosing these parameters will be justified later.

Cuboid samples were mechanically removed from the substrate for further analysis. Sample preparation consisted of wet cutting the cuboids in half along the build direction and hot embedding one half in epoxy resin (Technotherm 3000). The microsections were then sanded and polished to analyze the relative optical density via light microscopy using an Olympus BX51M device. Complementary, porosity and microstructure of two polished Vit101Si microsections formed with the low-energy parameter set A3 (50 W, 2000 mm/s, 17.9 J/mm^3) and the high-energy parameter set D2 (80 W, 1800 mm/s, 31.7 J/mm^3) were studied via a Zeiss Sigma VP scanning electron microscope (SEM) in secondary electron (SE) imaging mode and back-scattered electron (BSE) imaging mode.

The remaining cuboid halves were analyzed in terms of their structural and thermophysical properties using X-ray diffraction (XRD) and differential scanning calorimetry (DSC). Both methods investigate a relatively large sample region or volume, and therefore provide averaged information over a large number of additively formed layers. XRD-measurements on the sanded center area of the cuboid halves were carried out with a Bruker D8-A25 diffractometer applying the K_α-radiation of Cu with a wavelength of 1.5406 Å. For calorimetry, the cuboid halves were again cut along the build direction to achieve samples with masses in the order of 25 mg. DSC temperature scans were performed with a Perkin-Elmer DSC8000 under high-purity Ar flow in copper crucibles. The samples were heated from 323 K to 973 K with a heating rate of 1 K/s.

High-energy synchrotron X-ray diffraction (HESXRD) was performed on the samples with the highest volume energy density (D1) to clarify if small crystalline fractions are present, that cannot be resolved with conventional laboratory-scale methods. The room temperature measurements in transmission mode were performed at P21.2 beamline facility of PETRA III of the Deutsche Elektronen-Synchrotron (DESY). Radiation with a wavelength of 0.177138 Å (70 keV) was used, the beam size was 500 × 500 μm^2. The setup featured a sample detector distance of 949 mm and was geometrically calibrated via the diffraction

Table 1
Process parameters and resulting volume energy densities of the PBF-LB/M-formed cuboid samples. Each combination of scan speed and laser power leads to a specific volume energy density, which is given in the respective cell of the table. The corresponding sample notation is added in the right lower corner of each cell.

Volume energy density (J/mm^3) *(Sample notation)*		Laser power P (W)			
		50 *(A)*	60 *(B)*	70 *(C)*	80 *(D)*
Scan speed (mm/s)	1600 *(1)*	22.3 *(A1)*	26.8 *(B1)*	31.3 *(C1)*	35.7 *(D1)*
	1800 *(2)*	19.8 *(A2)*	23.8 *(B2)*	27.8 *(C2)*	31.7 *(D2)*
	2000 *(3)*	17.9 *(A3)*	21.4 *(B3)*	25.0 *(C3)*	28.6 *(D3)*
	2200 *(4)*	16.2 *(A4)*	19.5 *(B4)*	22.7 *(C4)*	26.0 *(D4)*

pattern of CeO_2. A VAREX XRD4343CT detector (2880 × 2880 pixels) recorded the two-dimensional dark-image-corrected diffraction pattern that was recorded with an acquisition time of 5 s per sample. The pattern was further integrated using PyFAI and then processed with the PDFgetX2 software [29] to obtain the background-corrected scattering intensity I(Q). Furthermore, the two-dimensional pattern were also caked in 8 pieces with an azimuthal range of 45° to check for crystalline reflexes with a further improved signal-to-noise ratio.

Macroscopic mechanical testing of the beam samples was performed in a three-point-beam bending (3PBB) setup with a Shimadzu testing machine as described in detail in [13]. Due to the large interface area between sample and substrate, the beams were removed by electric discharge machining (EDM). The surface of the beams was sanded (1200 grid) to exclude the influence of surface roughness acting as crack initiation sites [30] and to achieve a well-defined geometry. Four to five specimens per alloy and parameter set allowed for statistics. The engineering stress σ and strain ε on the specimen surface are calculated as

$$\sigma = \frac{3FL}{2bh^2} \tag{2}$$

and

$$\varepsilon = \frac{6Dh}{L^2}. \tag{3}$$

Here, F is the applied force, L is the support span of 20 mm, b is the sample width, h is the sample height, and D is the displacement at the sample center. Complementary, the morphology of fracture surfaces was further analyzed via SEM imaging (SE) as described above.

Besides the AM samples, as-cast beam-shaped samples in the same geometry as the additively manufactured beams were produced to serve as references for DSC and mechanical analysis. In a first step, high-purity raw elements were arc-melted and mixed under a Ti-gettered high-purity Argon atmosphere on a water-cooled copper plate. Several remelting steps ensure the formation of a homogeneous yet still crystalline master alloy. In a second step, the material was remelted by arc-melting and subsequently suction cast in a water-cooled copper mold to form a completely amorphous beam. A detailed description can be found in e. g. [31,32].

The oxygen contents of AM beam-shaped samples manufactured with the parameter set D1 as well as the as-cast beam references were measured via hot gas carrier extraction (ELTRA ONH-2000) using helium (99.999 %). Five specimens per sample were measured and the results were averaged.

3. Results

3.1. Light microscopy

In a first step to assess the applicability of the three alloys for the PBF-LB/M process, the process stability and crack formation in the cuboid samples are qualitatively evaluated. As often described by literature [10,18], lack of fusion (LOF) defects decrease with increased volume energy density (at least for moderately high energy densities as investigated in this study), as clearly visible in Figure A in the Supplementary Material. This tendency will be later quantified by optical density results in subsection 3.2. Furthermore, a clear trend is observable as process-induced cracking and porosity are promoted by an increasing number of microalloying components. In Fig. 1, representative light microscopy images of the D1 samples with the highest volume energy density (35.7 J/mm^3) of all three alloys are compared. Vertical cracks are visible in the Vit101 and Vit101Si microsections. The cracks initiated from the base of the samples previously in contact with the build platform, which is known to be a weak spot region in PBF-LB/M processing of BMGs [33]. This is likely to be caused by the dissimilar pairing of the CuTi-based BMGs and the Ti6Al4V substrate plate. The mismatch of the thermal expansion coefficients induces thermal stresses. Additionally, the intermixing of the alloys may lead to the weakening of the interface region due to the formation of intermetallic phases [34,35]. Nonetheless, the bulk material seems to withstand the apparent residual stresses during the consecutive build-up. On the contrary, Vit101SiSn reveals horizontal and vertical cracks in the prepared cross-sections. Horizontal cracks are initiated by in-plane residual stresses that originate from the rapid solidification. The thermal gradients between the exposed and the solidified layer typically induce large tension stresses during cooling, which mostly dominate the residual stresses in PBF-LB/M [36–38]. Apparently, the residual stresses exceed the strength of the PBF-LB/M processed Vit101SiSn which leads to the observed cracking in the bulk sample volume. Yet, Vit101 and Vit101Si withstand the in-plane stresses for the given conditions. The crack formation applies to the majority of Vit101SiSn samples, resulting in numerous losses of samples through harshly ruptured cuboids. Eventually, sample fragments interfered with the powder deposition and led to increased LOF.

As no meaningful set of specimens could be obtained, Vit101SiSn was excluded from further analysis. Besides these composition-specific effects, it is found for all three alloys that samples manufactured with the highest scan speed of 2200 mm/s (parameter set "4") tend to feature an unstable sample-substrate connection. This results in relatively frequent sample losses during processing. Accordingly, the lost samples are also not part of further analysis.

3.2. Diffraction, calorimetry, and density studies

Figs. 2(a) and (b) display all XRD results of the Vit101 and Vit101Si cuboid samples. The different colors indicate the laser power used to manufacture the respective specimen. For all investigated samples, the broad diffraction halo typical for amorphous materials together with the absence of crystalline reflexes can be observed. For e.g., an PBF-LB/M-formed Zr-based BMG (AMZ4), it has been demonstrated that a too high laser energy input can lead to thermally induced crystallization [10,18]. As small (nano-)crystalline fractions can be easily overlooked by conventional XRD due to the method's resolution limits [16,39], the samples with the highest E_V value of 35.7 J/mm^3 (D1) are double-checked via HESXRD. This method allows the detection of smaller crystalline fractions due to the extremely brilliant synchrotron

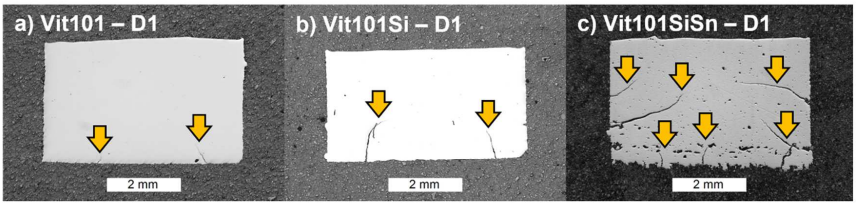

Fig. 1. Representative light microscopy images of the cuboid samples of all three compositions produced with the highest volume energy density of 35.7 J/mm^3 (D1). The build direction is from the bottom towards the top. With growing degree of microalloying, the tendency to form defects like pores and cracks increases.

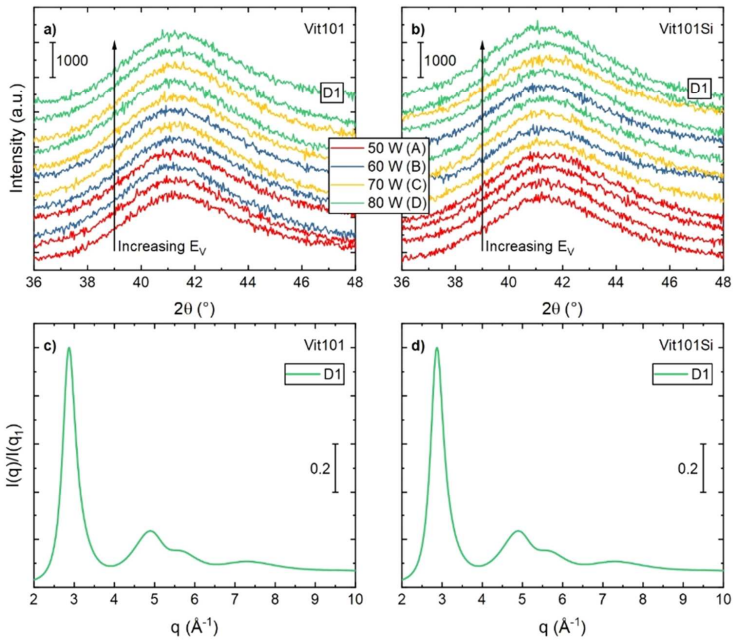

Fig. 2. In (a) and (b), all XRD diffractograms of the Vit101 and Vit101Si cuboid samples formed with different parameter sets are given. The applied E_V increases from the bottom to the top, the different colors indicate the applied laser power. No crystalline reflexes can be observed. The samples with the highest E_V (D1) are furthermore analyzed via HESXRD, the normalized background-corrected scattering intensities are given in (c) and (d). Again, crystalline reflexes are completely absent.

source and the resulting exceptional signal-to-noise ratio. Figs. 2(c) and 2(d) show the normalized background-corrected scattering intensity I(q)/I(q_1) of the D1 cuboids, which lack any crystal reflexes, thereby underlining the synchrotron-amorphous state of these samples. Also, the caking approach does not reveal reflexes, see Figure C in the Supplementary material. Hence, thermally induced crystallization effects can be mostly excluded for Vit101 and Vit101Si samples manufactured in the parameter range investigated in this work.

As reported in [28], the powder feedstock features 760 and 750 µg/g oxygen for Vit101 and Vit101Si, respectively. In the present work, the samples additively manufactured from this powder material with parameter set D1 (35.7 J/mm^3) show values of 857 ± 14 and 883 ± 16 µg/g oxygen contamination. In contrast, the high-purity as-cast samples only feature 168 ± 5 and 173 ± 7 µg/g oxygen for Vit101 and Vit101Si.

Complementary to the oxygen measurements, Figs. 3(a) and (b) display the DSC traces of the Vit101 and Vit101Si powder feedstock material (previously published in [28]), the D1 AM-samples as well as the as-cast references. For all Vit101 samples, the onset of the glass transition, T_g, occurs at about 690 K, followed by a short supercooled liquid (SCL) region of about 60 K length that is terminated by the onset of crystallization T_x at roughly 750 K. In contrast, the Vit101Si samples feature a 10 K longer SCL with a T_g of about 705 K and a T_x of roughly 775 K, confirming the previously reported increased thermal stability due to the Si addition [25,26,28]. For both alloys, neither the length of the SCL (i.e., the thermal stability) nor the shape, size, or position of the crystallization peaks appears to be strongly affected by the processing route and resulting oxygen content of the different DSC samples. The enthalpies of crystallization ΔH_x of all analyzed samples are determined by integration over the crystallization signal. Figs. 3(c) and 3(d) show ΔH_x for each AM cuboid as a function of E_V. Samples manufactured with the same laser power feature the same color. The ΔH_x values of the high-purity as-cast samples are found to be − 6980 J/g-atom for Vit101 and − 6810 J/g-atom for Vit101Si, exhibiting typical values for fully amorphous samples of the present compositions [27,40]. These values serve as reference marks for the AM samples and are indicated as dashed lines. For both alloys, the reference ΔH_x values are quite well reproduced by the high-laser-power parameter sets ("C" with 70 W and "D" with 80 W) with volume energy densities above roughly 25 J/mm^3. Samples with lower E_V (especially parameter sets "A" and "B") tend to show deviations in form of less intense crystallization events with ΔH_x values of up to − 6000 J/g-atom.

In Figs. 3(e) and 3(f), the relative optical densities as a function of E_V are shown. Low E_V values lead to insufficient densification due to LOF and resulting porosity, especially for the low-laser-power parameter set "A" (50 W). LOF typically originates from an insufficient overlap of adjacent weld tracks, and thus, incomplete melting of the powder layer. The size of the melt pools correlates with the applied laser energy. Since multiple parameters (e.g., laser power, scan speed, or hatch spacing) affect the energy input, the volume energy density is often used as a measure for different parameter settings [41]. With rising E_V, densification improves towards a relatively stable plateau with more than 99 % densification for volume energy densities above roughly 25 J/mm^3. Hereafter, the density only slightly increases with further rise of E_V. For both alloys, the highest densification is achieved with the highest E_V of 35.7 J/mm^3 (D1), with 99.92 ± 0.03 % for Vit101 and 99.87 ± 0.09 % for Vit101Si. Figure A in the Supplementary material exemplarily demonstrates the trend from LOF-porosity to high-density with increasing E_V.

3.3. Scanning electron microscopy

Sample densification is further studied via SEM imaging of representative Vit101Si cuboids formed with the low-energy parameter set A3 and the high-energy parameter set D2, both highlighted in gray in Fig. 3 (f). The A3 sample features a low optical density of 88.72 ± 1.15 %,

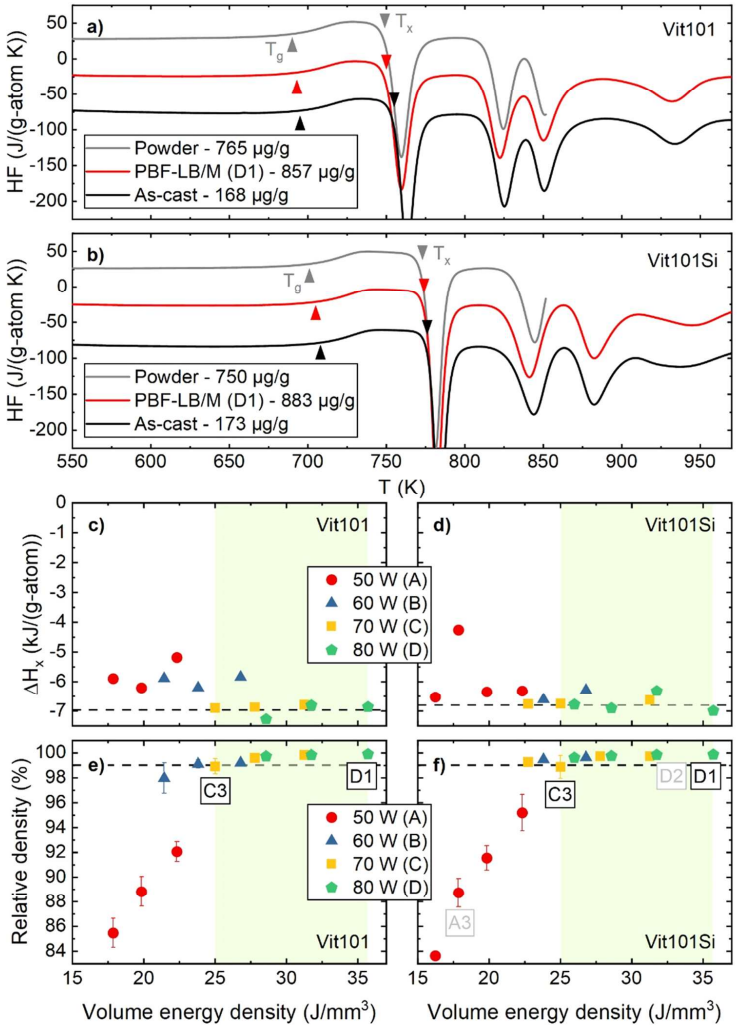

Fig. 3. In (a) and (b), DSC scans of powder material, representative samples PBF-LB/M-formed with the parameter set D1, and high-purity as-cast samples are shown for Vit101 and Vit101Si. The oxygen content of the samples is given in the captions. The powder DSC scans are taken from [28]. The crystallization enthalpy of all cuboid samples is determined by integration and displayed in (c) and (d) as a function of the applied volume energy density. Above about 25 J/mm^3, ΔH_x stabilizes at the level of the as-cast references (dashed lines). In (e) and (f), the respective relative optical densities are given, also as a function of the applied volume energy density (the error bars reflect the standard deviation). Low E_V results in insufficient densification, but above 25 J/mm^3, densities higher than about 99 % (dashed line) are reached. Hence, the optimized parameter window lies between the parameter sets C3 and D1 (highlighted), corresponding to an E_V range from 25 J/mm^3 to 35.7 J/mm^3, as indicated by the light green background. The cuboid samples A3 and D2 further analyzed by SEM imaging are highlighted in gray.

which is directly reflected by the SE image in Fig. 4a), where a large degree of porosity can be identified. Figs. 4(b) and 4(c) show higher-magnification SE and BSE images of representative pores, as indicated by the white frame in Fig. 4(a). These are irregular in shape and incorporate unmolten or only partially molten particles typical for LOF defects. The defects feature a slightly horizontal orientation, reflecting the layer-wise build process. Yet, no signs of crystallization in the form of a phase-contrast can be detected in the BSE image. In contrast, Fig. 4 (d) shows the SE image of the D2 sample that features a high optical density of 99.85 ± 0.01 %. Besides a distinct crack that originates from the sample-substrate interface, only sporadic pores can be identified, which show spherical geometry typical for gas enclosures.

3.4. Mechanical testing and fractography

Fig. 5 presents the three-point beam bending results. In Fig. 5(a), the as-cast specimen of Vit101 is depicted as black solid curves with a Young's modulus of 103.7 GPa and yield strength in the order of 2.5 GPa. A maximum strength of 3.30 GPa and a significant plastic regime of more than 3 % are observed. In the case of the high-energy parameter set D1, the additively formed Vit101 samples reach a Young's modulus of 100.1 ± 2.0 GPa and a maximum strength of 2.47 ± 0.05 GPa, while lacking significant plastic deformation. Contrastingly, the Vit101 samples formed with the medium-energy parameter set C3 show a distinctly lower Young's modulus of 85.8 ± 3.1 GPa, coupled with a relatively low maximum strength of 1.72 ± 0.17 GPa on average. Remarkably, the C3 samples show a higher scatter than the D1 samples, especially in terms of maximum strength. The as-cast Vit101Si sample in

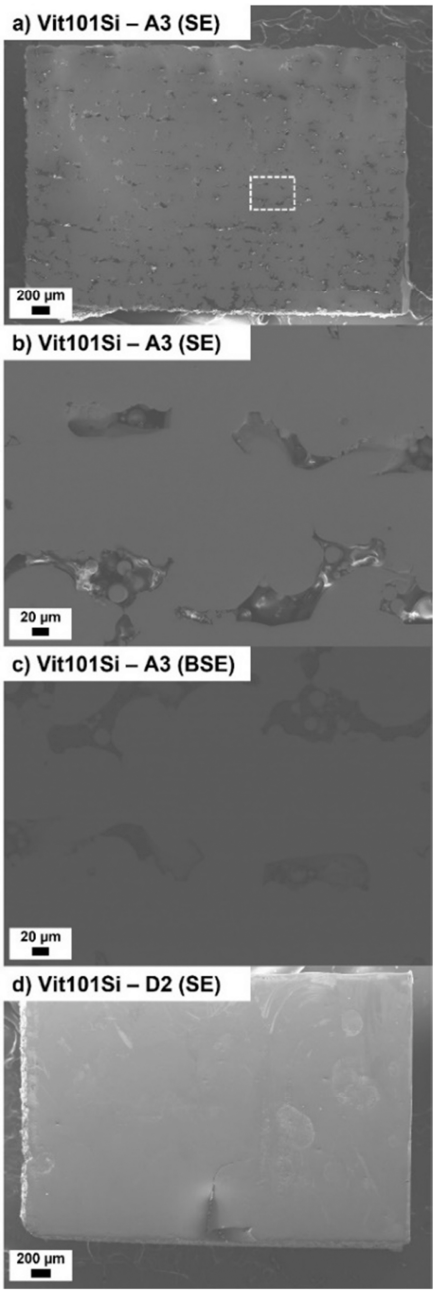

(caption on next column)

Fig. 4. SEM imaging of two representative cuboid samples. The build direction is always from the bottom towards the top. In (a), the low-energy sample A3 with a relative optical density of 88.72 ± 1.15 % is fully displayed via SE imaging. The irregularly shaped LOF-porosity is clearly visible. The region in the white rectangle is zoomed in in (b), where non-molten powder particles inside the pores can be recognized. (c) shows the same region imaged via BSE, no phase-contrast occurs. In contrast, (d) depicts the SE image of the D2 high-energy sample with a relative optical density of 99.85 ± 0.01 %. Besides a crack in the lower part, only sporadic and rounded gas pores are visible.

Fig. 5(b) behaves almost identically to the as-cast Vit101 sample, only with a reduced plastic deformation regime of about 1.5 %. Vit101Si samples additively formed with both parameter sets show a similar behavior as the Vit101 C3 samples: A noticeably decreased Young's modulus paired with a scatter-afflicted maximum strength below the reference's yield strength.

Fig. 6 provides SEM images (SE) of the fracture surfaces of Vit101 and Vit101Si D1 beams after 3PBB testing. Both fractograms in Figs. 6(a) and 6(b) show a similar appearance. A rather smooth and straight region is formed at the top of the samples (the region that experiences the highest tension stress, as the samples are loaded from below), which is often addressed to shear band forming and delamination [42]. The remaining majority of the fracture surfaces feature a rough appearance, typical for rapid fracture [42]. In this rough rapid fracture region, river-like structures can be observed, as shown in Figs. 6(c) and 6(d). Within these, typical dimple patterns are present, as shown in the zoomed-in regions in Figs. 6(e) and 6(f). For Vit101, homogeneous river structures with relatively pronounced and large-scale dimples are visible. In contrast, Vit101Si features rather heterogenous river structures, with less evolved dimples that show smaller scales than the ones observed for Vit101.

4. Discussion

4.1. Oxygen influence

The oxygen contamination of the present PBF-LB/M-formed specimens is roughly five times higher in comparison to the as-cast reference specimens. The reason can be found in the processing route itself: the AM samples are made from powder feedstock of industrial-grade purity with a high surface-to-volume ratio, which allows for a large oxygen absorption. Reviewing oxygen contaminations in comparable systems, Wang et al. [7] reported on PBF-LB/M-manufacturing of Ti-based metallic glass ($Ti_{47}Cu_{38}Zr_{7.5}Fe_{2.5}Sn_2Si_1Ag_2$) with 1250 µg/g oxygen content made from powder feedstock with 930 µg/g oxygen. PBF-LB/M-formed $Zr_{52.5}Cu_{17.9}Ni_{14.6}Al_{10}Ti_5$ metallic glass was reported to feature 920 µg/g oxygen, while the used powder includes 487 µg/g oxygen [43]. In the case of the commercially available $Zr_{59.4}Cu_{28.8}Al_{10.4}Nb_{1.5}$ (AMZ4), oxygen contents of powder feedstock can vary over a broad range from about 600 up to 2292 µg/g [18]. The comparability of these values might be limited due to various factors like the purity of the initially used raw elements, the choice of the powder atomization process, the respective process atmosphere, or also the particle fraction used, as smaller powder particles feature a larger surface-to-volume ratio and therefore a higher oxygen uptake [28]. Still, it can be claimed that the present CuTi-based alloy powders and AM-samples feature relatively moderate oxygen contaminations of about 750 and 850 µg/g, respectively, although the large content of Ti and Zr (together about 45 at%) would predetermine a strong oxygen affinity.

For Zr-based BMGs, it is well known that oxygen alters the crystallization mechanism by changing the primary phase and therefore decreases the GFA and thermal stability [21,44–47], and accordingly the robustness against thermally induced crystallization during PBF-LB/M processing [18,22]. In contrast, the GFA of Vit101 and its derivatives is reported to be relatively resistant against its deterioration through

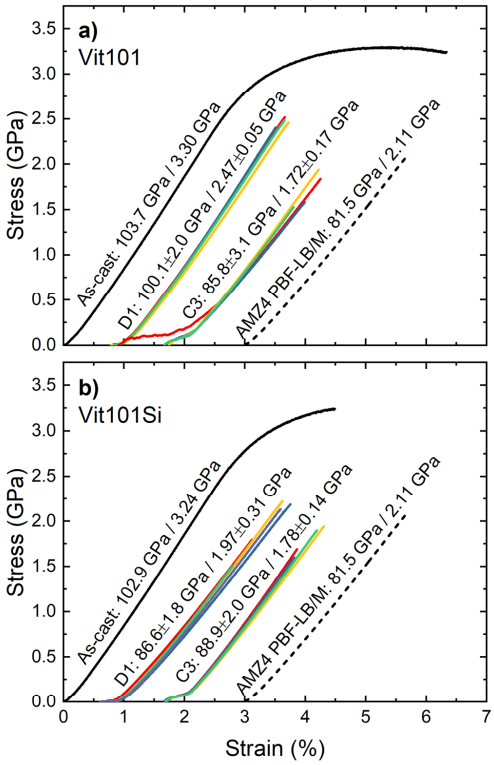

Fig. 5. Stress-strain curves determined by 3PBB mechanical testing for (a) Vit101 and (b) Vit101Si. The first value written on the curves reflects the Young's modulus, the second gives the maximum strength. The provided error values reflect the standard deviations. The as-cast curves are shown in black and serve as references. For comparison, the curves of PBF-LB/M-formed AMZ4, a Zr-based metallic glass former, are taken from [16,18] and added as black dashed lines. Only the D1 parameter sample set of Vit101 allows reaching the as-cast Young's modulus as well as its yield strength of about 2.5 GPa before brittle fracture occurs. All other parameter sets lead to a decreased Young's modulus as well as brittle fracture before the materials yield strength is reached. For some curves, the testing device causes artifacts in the low-strain regions, which are excluded for defining the Young's modulus.

impurities and especially oxygen contaminations, as no difference in critical casting diameter was found for samples cast from high-purity and industrial-grade material [24]. The presented DSC scans reveal that the length of the SCL, crystallization event morphology, and crystallization enthalpies of Vit101 and Vit101Si are practically unaffected by processing route and oxygen content, rendering the alloy system as a robust and well-suited candidate for the rather contamination-affected PBF-LB/M process.

4.2. PBF-LB/M parameter evaluation and microstructural aspects

While the XRD results in Fig. 2 suggest complete vitrification within the investigated parameter range, the ΔH_x values of low-energy samples built with low laser power (50 W and 60 W) and an E_V of less than roughly 25 J/mm^3 are distinctly higher (indicating a less intense crystallization event) than the fully amorphous reference, suggesting a partially crystalline structure, see Fig. 3. In the same E_V range below 25 J/mm^3, the optical density measurements reveal insufficient densification of less than 99 %. Both effects, the decreased crystallization enthalpy and the insufficient densification, might be linked in the way that cracks and high LOF-porosity could promote heat accumulations caused by decreased thermal dissipation, leading to localized crystallization effects. The cuboid samples further investigated via SEM imaging in Fig. 4 were chosen accordingly to verify this hypothesis. The high-energy parameter set D2 serves as a highly dense and fully amorphous (in terms of XRD and DSC) reference, while the low-energy A3 sample shows substantially lower density and the lowest measured crystallization enthalpy. The SE images in Figs. 4(a) and 4(b) allow to clearly characterize the LOF-porosity of the A3 sample, yet, signs of crystallization cannot be identified due to the lack of phase contrast, as shown by the representative BSE image in Fig. 4(c).

Glade et al. [48] have studied the isothermal crystallization behavior above T_g of Vit101. It was shown that phase separation and subsequent crystallization results in nanocrystals of only several nm in size. Bochtler suggested that the primary crystallization species of Vit101 upon heating and cooling is probably a $ZrTiCu_2$ laves phase, which features a marginal structural fingerprint even when analyzed with the excellent signal-to-noise ratio of HESXRD, as demonstrated by B. Bochtler in [24]. Hence, the small crystal size as well as the rather marginal diffraction signal of the primary crystallization phase seem to leave conventional SEM and XRD as unpreferable methods with too low resolution to identify partial crystallization in the present alloys. ΔH_x screening via DSC scans appears to be a more sensitive approach to resolve small nanocrystallization effects, as previously reported in [16]. Interestingly, the Zr-based AMZ4 does not show a comparable loss of ΔH_x when low E_V values create insufficient density and LOF, as exemplarily shown by Wegner et al. [18]. Therefore, the observed decrease in ΔH_x for low-E_V samples due to possible nanocrystallization might be an alloy-specific effect, which shall be investigated separately via high-resolution methods like TEM or broader use of HESXRD studies.

Besides such instabilities in the low-density parameter range below about 25 J/mm^3, XRD, DSC, and HESXRD show no signs of crystallization for Vit101 as well as Vit101Si, even for the highest E_V of 35.7 J/mm^3. This is a partially astonishing result, as Vit101Si features a significantly more stable SCL region in DSC scans than Vit101 with its only marginal SCL stability. Theoretically, the difference in thermal stability should result in a distinct advantage of Vit101Si in terms of robustness against higher E_V values, since it renders the alloy more resilient against the process-inherent cyclic thermal loads in the heat-affected zone of the melt pool. Yet, within the present parameter window, no differences can be identified, postponing the definition of the limiting E_V thresholds for retaining fully amorphous specimens to a successive study with larger laser intensities applied.

4.3. Mechanical performance

Summing up, an E_V range for the PBF-LB/M processing of highly dense and fully amorphous samples can be defined between about 25 and at least 35.7 J/mm^3, indicated by a light-green background in Figs. 3(c) – 3(f). The lower and upper boundaries of this process window are marked by the parameter sets C3 (2000 mm/s, 70 W) and D1 (1600 mm/s, 80 W), respectively. Previous studies on the Zr-based AMZ4 [16,18] showed that fully amorphous and density-optimized PBF-LB/M samples can reach the alloy's yield strength before brittle fracture without observable (macroscopic) plasticity occurs. Accordingly, the process window defining parameters C3 and D1 were chosen to build samples for the three-point bending tests.

The results in Fig. 5 reveal that only Vit101 manufactured with the high-energy parameter set D1 reaches the Young's modulus and the yield strength of the as-cast reference with an exceptional maximum strength of about 2.5 GPa. To our knowledge, this sets a new record for additively formed BMGs measured in (macroscopic) beam bending, outperforming the previous record-holder AMZ4 [16,18] by about

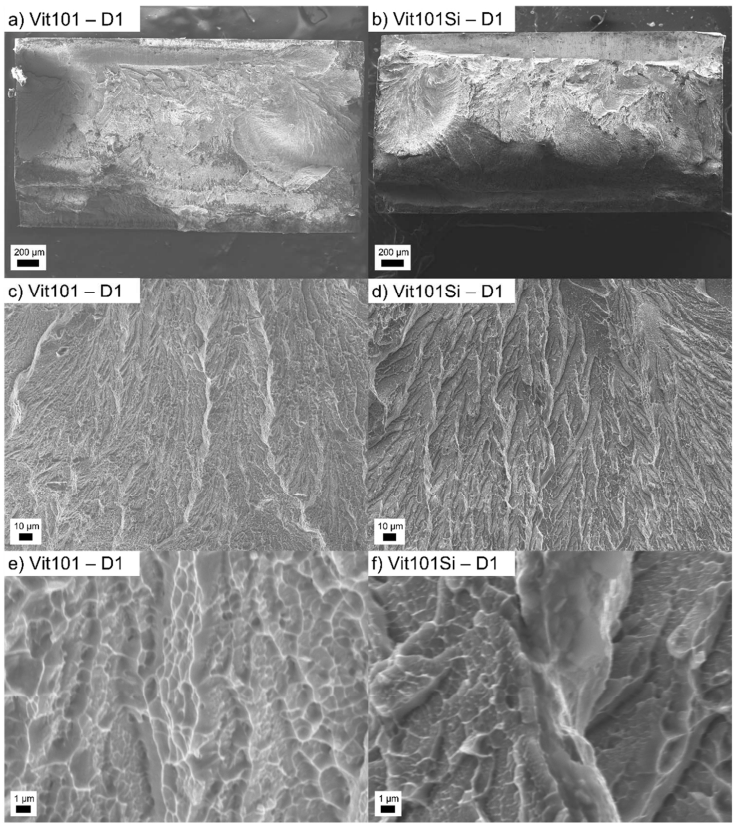

Fig. 6. SEM imaging (SE) of the fracture surfaces of tested D1 beams. (a) and (b) give an overview over the whole fracture surfaces of the Vit101 and Vit101Si samples. The beams were loaded from below, resulting in tension stress in the upper part. For both samples, a small portion on the top of the surface shows a flat appearance, most probably corresponding to the initial step of shear band forming and delamination [42]. The rest of the fracture appears rather rough, indicating a rapid fracture as a second step [42] with typical river-like pattern highlighted in (c) and (d). Zoomed-in images of the river-like structures in (e) and (f) reveal dimple pattern, which show a larger and more homogeneous structure in case of Vit101.

0.4 GPa (an increase of about 19 %) as shown in Fig. 5. The other three batches, the medium-energy C3 beams made from Vit101 as well as both Vit101Si parameter sets, show significantly lower Young's moduli and fracture strength of less than 2 GPa with large scatter among the different curves. As discussed above, crystallization can be ruled out for C3 and D1 sets as the origin of such suboptimal performance.

Regarding the results of the two Vit101 parameter sets D1 and C3 allows to directly identify the relative density as a main factor that determines the mechanical performance. The medium-energy set C3 features an 1% lower relative density than the highly densified D1 set (98.92 ± 0.61 % and 99.92 ± 0.03 %, respectively), corresponding to a higher number of remaining defects like pores or cracks. These act as stress risers and therefore lead to premature fracture before the alloy's yield strength is reached, as previously highlighted in various studies [18,49,50]. The reduced Young's modulus of the C3 set may also be explained by relative density considerations, as Shi et al. [19] have recently demonstrated that increased porosity in PBF-LB/M-formed AMZ4 leads to a decrease in Young's modulus.

The Vit101Si C3 samples also feature a suboptimal relative density (98.87 ± 0.91 %) due to the applied medium-energy parameter set. Here, the negative influence of remaining defects can be seen as origin for the diminished mechanical performance, too.

A different picture is found when comparing the D1 sets of Vit101 and Vit101Si. Both sample sets feature maximized and basically identical relative densities of 99.92 ± 0.03% and 99.87 ± 0.09 %, respectively. Accordingly, differences in relative density are ruled out as origin of the diminished performance of the Vit101Si D1 samples. Instead, the alloy-specific fracture toughness can be identified as the second main factor that determines the mechanics. Garrett et al. [25] revealed that microalloying with Si and Sn leads to embrittlement in the Vit101 system. The notch toughness K_Q of high-purity as-cast specimens was reported to decrease from 103.40 MPa $m^{1/2}$ for Vit101 to 90.92 MPa $m^{1/2}$ for Vit101Si and even 54.84 MPa $m^{1/2}$ for Vit101SiSn. Here, the circle closes towards the initially presented light microscopy results for the D1 cuboids in Fig. 1 and the cuboid overview in Figure A in the Supplementary material. Vit101Si and especially Vit101SiSn show increased crack formation, most probably since their lower toughness renders them more vulnerable to thermally induced stresses during PBF-LB/M processing. Finally, the reduced toughness leaves the Vit101Si D1 beam samples less resilient against such PBF-LB/M-typical defect sites, resulting in premature failure during the 3PBB measurements.

Xi et al. [51] have demonstrated that the size scale of viscous features like vein pattern and dimples observed in the fracture surface correlates directly with the fracture toughness of the respective BMG. Ductile BMGs tend to form homogeneous pattern with microscale sizes, while brittle systems feature smaller structures like nano-waves [42,52]. The fractograms in Fig. 6 reveal that Vit101 shows larger and more

homogeneous dimple structures in the rough rapid fracture surface region than Vit101Si, thereby well reflecting the toughness difference between the two alloys within the size scale concept introduced by Xi et al. [51].

4.4. Industrial relevance

The present evaluation process demonstrates that the non-microalloyed base alloy Vit101 is the most suitable of the three investigated systems for PBF-LB/M applications. The relatively high toughness of Vit101 allows for minimizing crack formation, resulting in superior mechanical performance, while the relatively low thermal stability plays a surprisingly neglectable role as it does not lead to unfavorable effects like thermally induced crystallization.

From an economic point of view, Vit101 ($Cu_{47}Ti_{34}Zr_{11}Ni_8$) features the advantage that it consists of relatively cheap and broadly used industry metals, mainly Cu and Ti. The small amount of the higher-priced Zr does not harshly increase the overall raw material expenses. Furthermore, it was systematically evaluated by Barreto et al. [28] that industrial-grade elemental metals can be used for successful powder atomization in just one processing step, without the need for any kind of prealloying. The present study uses exactly this industry-attractive powder produced by Barreto et al. [28] and demonstrates its applicability to additively form highly performant parts. Vit101 is therefore a possible competitor for the commercially available and already established Zr-based AMZ4 alloy. Both systems feature similar T_g, yet, as demonstrated in Fig. 5(a), additively formed Vit101 is stronger and stiffer than AMZ4. As-cast Vit101 also features a higher hardness of 576 HV5 [24] than as-cast AMZ4 with 467 HV5 [53]. Finally, AMZ4 as a Zr-based system is prone to oxygen that can, in case of high contamination levels, deteriorate the PBF-LB/M processing window as well as the mechanical performance [18]. In contrast, Vit101 has proven to be robust against oxygen contamination effects in the present study. On the other hand, the relatively high amount of Cu leaves Vit101 less resistant against corrosive attacks [31,54,55], Also, Ni might be problematic in terms of biocompatibility [31,56]. Furthermore, Vit101 still shows a certain tendency towards process-induced crack formation, while nothing comparable was reported for AMZ4 in various studies [10,13,16,18,50]. Best et al. [30] showed that as-cast AMZ4 features a K_Q of up to 138.0 MPa $m^{1/2}$, while Garrett et al. [25] reported 103.40 MPa $m^{1/2}$ for Vit101. The comparability between the notch toughness values obtained in the two different studies should be seen with caution, as K_Q depends on the tested sample dimensions and other experimental conditions, unlike the normed fracture toughness K_{IC}. Still, the difference in toughness between AMZ4 and Vit101 is also qualitatively visible in the stress-strain diagram of as-cast samples in Figure B in the Supplementary material, where AMZ4 shows distinctly higher ductility than Vit101 and the even more brittle Vit101Si. Hence, for Vit101 as the stronger, but also less tough system in the comparison, it is of special importance to minimize defect density in form of pores and cracks during PBF-LB/M processing to emphasize its superior mechanical performance.

5. Conclusion

Three CuTi-based bulk metallic glass formers, Vit101 ($Cu_{47}Ti_{34}Zr_{11}Ni_8$), Vit101Si ($Cu_{47}Ti_{33}Zr_{11}Ni_8Si_1$), and Vit101SiSn ($Cu_{47}Ti_{33}Zr_{11}Ni_6Si_1Sn_2$) were evaluated in terms of their applicability to form highly dense, amorphous, and mechanically robust PBF-LB/M parts. The Vit101 base alloy was found to be the most promising and potent alloy for PBF-LB/M processing. The addition of Si and especially Si-Sn increased thermally induced crack formation and process instability to a point that led to the exclusion of Vit101SiSn from the screening due to frequent sample loss. Vit101Si was able to form amorphous samples with low porosity over a broad parameter window, yet, the relatively low notch toughness and the tendency to form cracks prohibited optimized strength values. Vit101 showed the same robust parameter window for fully amorphous and highly dense processing but was able to reach an outstanding bending strength of about 2.5 GPa, as it features the highest toughness of the three systems.

The present work underlines that the PBF-LB/M process asks for different alloy properties than conventional casting routes to produce fully amorphous and mechanically well performing parts. GFA, conventionally defined in terms of the critical casting diameter, loses its significance in the face of a layer-wise, highly dynamic, and localized melting and vitrification process. Also, thermal stability, classically expressed via the length of the SCL region upon heating, seems to play a minor role, at least for the relatively good glass formers investigated in the present study. Instead, notch toughness and robustness against thermally induced crack formation are found as key parameters to avoid brittle products and processing issues due to structures sheared apart. Hence, future glass forming alloy development and optimization for PBF-LB/M applications should lay focus on the later aspects instead of classical casting-oriented GFA optimization.

Funding

This research was funded by the German Federal Ministry for Economic Affairs and Energy (BMWi) within the Promotion of Joint Industrial Research Program (IGF) due to a decision of the German Bundestag. It was part of the research project 21227 N (LaSaM) by the Association for Research in Precision Mechanics, Optics and Medical Technology (F.O.M.) under the auspices of the German Federation of Industrial Research Associations (AiF).

CRediT authorship contribution statement

Neuber Nico: Writing – review & editing, Methodology, Investigation, Formal analysis, Data curation. **Adam Bastian:** Writing – review & editing, Investigation, Formal analysis, Data curation. **Barreto Erika Soares:** Writing – review & editing, Project administration, Methodology, Investigation, Formal analysis, Data curation, Conceptualization. **Ruschel Lucas:** Writing – review & editing, Methodology, Investigation, Formal analysis, Data curation. **Riegler Sascha Sebastian:** Writing – review & editing, Investigation, Formal analysis, Data curation. **Jiang Hao-Ran:** Writing – review & editing, Investigation, Data curation. **Witt Gerd:** Supervision. **Kleszczynski Stefan:** Writing – review & editing, Supervision, Project administration, Funding acquisition. **Frey Maximilian:** Writing – original draft, Project administration, Methodology, Investigation, Funding acquisition, Formal analysis, Data curation, Conceptualization. **Busch Ralf:** Writing – review & editing, Supervision, Funding acquisition. **Wegner Jan:** Writing – review & editing, Project administration, Methodology, Investigation, Funding acquisition, Formal analysis, Data curation, Conceptualization. **Ellendt Nils:** Writing – review & editing, Supervision, Project administration. **Uhlenwinkel Volker:** Writing – review & editing, Supervision, Project administration, Funding acquisition.

Declaration of Competing Interest

The authors declare that they have no known competing financial interests or personal relationships that could have appeared to influence the work reported in this paper.

Data availability

Data will be made available on request.

Acknowledgments

Instrumentation and technical assistance for this work were provided by the Service Center X-ray Diffraction, with financial support from Saarland University and German Science Foundation (project number

INST 256/349–1). The authors thank Dr. Oliver Janka for the support in collection of the X-ray diffraction data presented in this paper. We want to acknowledge DESY (Hamburg, Germany), a member of the Helmholtz Association HGF, for the provision of experimental facilities. Parts of this research were carried out at PETRA III and we would like to thank Malte Blankenburg and Ulrich Lienert for assistance in using the P21.2 beamline facility.

Appendix A. Supporting information

Supplementary data associated with this article can be found in the online version at doi:10.1016/j.addma.2023.103467.

References

[1] M. Telford, The case for bulk metallic glass, Mater. Today 7 (2004) 36–43, https://doi.org/10.1016/S1369-7021(04)00124-5.
[2] U. Scipioni Bertoli, G. Guss, S. Wu, M.J. Matthews, J.M. Schoenung, In-situ characterization of laser-powder interaction and cooling rates through high-speed imaging of powder bed fusion additive manufacturing, Mater. Des. 135 (2017) 385–396, https://doi.org/10.1016/j.matdes.2017.09.044.
[3] S. Pauly, L. Löber, R. Petters, M. Stoica, S. Scudino, U. Kühn, J. Eckert, Processing metallic glasses by selective laser melting, Mater. Today 16 (2013) 37–41, https://doi.org/10.1016/j.mattod.2013.01.018.
[4] H.Y. Jung, S.J. Choi, K.G. Prashanth, M. Stoica, S. Scudino, S. Yi, U. Kühn, D. H. Kim, K.B. Kim, J. Eckert, Fabrication of Fe-based bulk metallic glass by selective laser melting: a parameter study, Mater. Des. 86 (2015) 703–708.
[5] L. Thorsson, M. Unosson, M. Teresa Pérez-Prado, X. Jin, P. Tiberto, G. Barrera, B. Adam, N. Neuber, A. Ghavimi, M. Frey, R. Busch, I. Gallino, Selective laser melting of a Fe-Si-Cr-B-C-based complex-shaped amorphous soft-magnetic electric motor rotor with record dimensions, Mater. Des. 215 (2022), 110483, https://doi.org/10.1016/j.matdes.2022.110483.
[6] X. Lu, M. Nursulton, Y. Du, W. Liao, Structural and mechanical characteristics of Cu50Zr43Al7 bulk metallic glass fabricated by selective laser melting, Materials 12 (2019), https://doi.org/10.3390/ma12050775.
[7] P. Wang, S. Pauly, L. Deng, S. Wang, P. Wang, U. Kühn, S. Pauly, Selective laser melting of a Ti-based bulk metallic glass, Mater. Lett. 212 (2017) 346–349, https://doi.org/10.1016/j.matlet.2017.10.130.
[8] X.P. Li, M.P. Roberts, S. O'Keeffe, T.B. Sercombe, Selective laser melting of Zr-based bulk metallic glasses: processing, microstructure and mechanical properties, Mater. Des. 112 (2016) 217–226, https://doi.org/10.1016/j.matdes.2016.09.071.
[9] S. Pauly, C. Schricker, S. Scudino, L. Deng, U. Kühn, Processing a glass-forming Zr-based alloy by selective laser melting, Mater. Des. 135 (2017) 133–141.
[10] J.J. Marattukalam, V. Pacheco, D. Karlsson, L. Riekehr, J. Lindwall, F. Forsberg, U. Jansson, M. Sahlberg, B. Hjörvarsson, Development of process parameters for selective laser melting of a Zr-based bulk metallic glass, Addit. Manuf. 13 (2020), 101124, https://doi.org/10.1016/j.addma.2020.101124.
[11] J. Wegner, S. Kleszczynski, S. Hechler, G. Witt, R. Busch, Parameter study about processing Zr-based bulk metallic glass with Laser beam melting, in: G. Witt (Ed.), Rapid.Tech - Int. Trade Show Conf. Addit. Manuf., Carl Hanser Verlag GmbH & Co. KG, München, 2017.
[12] J. Wegner, M. Frey, S. Kleszczynski, R. Busch, G. Witt, Influence of process gas during powder bed fusion with laser beam of Zr-based bulk metallic glasses. Proceedings of the 11th CIRP Conference on Photonic Technology, Elsevier B.V.,, 2020, pp. 205–210, https://doi.org/10.1016/j.procir.2020.09.039.
[13] J. Wegner, M. Frey, P. Stiglmair, S. Kleszczynski, G. Witt, R. Busch, Mechanical properties of honeycomb structured ZR-based bulk metallic glass specimens fabricated by laser powder bed fusion, South Afr. J. Ind. Eng. 30 (3) (2019) 32–40.
[14] J. Wegner, M. Frey, R. Busch, S. Kleszczynski, Additive manufacturing of a compliant mechanism using Zr-based bulk metallic glass Chair of Manufacturing Technology, University Duisburg-Essen, 47057 Duisburg, Lotharstraße 1, Germany Chair of Metallic Materials, Saarland University, Campus C6. 3, Addit. Manuf. Lett. (2021), 100019, https://doi.org/10.1016/j.addlet.2021.100019.
[15] K. Kosiba, L. Deng, S. Scudino, Viscous flow of supercooled liquid in a Zr-based bulk metallic glass synthesized by additive manufacturing, Materials 13 (2020), https://doi.org/10.3390/MA13173803.
[16] M. Frey, J. Wegner, N. Neuber, B. Reiplinger, B. Bochtler, B. Adam, L. Ruschel, S. S. Riegler, H.-R. Jiang, S. Kleszczynski, G. Witt, R. Busch, Thermoplastic forming of additively manufactured Zr-based bulk metallic glass: a processing route for surface finishing of complex structures, Mater. Des. 198 (2021) 1–8, https://doi.org/10.1016/j.matdes.2020.109368.
[17] N. Sohrabi, J. Jhabvala, R.E. Logé, Additive manufacturing of bulk metallic glasses - process, challenges and properties: a review, Metals 11 (2021).
[18] J. Wegner, M. Frey, M. Piechotta, N. Neuber, B. Adam, S. Platt, L. Ruschel, N. Schnell, S. Sebastian, H. Jiang, G. Witt, R. Busch, S. Kleszczynski, Influence of powder characteristics on the structural and the mechanical properties of additively manufactured Zr-based bulk metallic glass, Mater. Des. 209 (2021), 109976, https://doi.org/10.1016/j.matdes.2021.109976.
[19] J. Shi, S. Ma, S. Wei, J.P. Best, M. Stolpe, B. Markert, Connecting structural defects to tensile failure in a 3D-printed fully-amorphous bulk metallic glass, Mater. Sci. Eng. A 813 (2021), 141106, https://doi.org/10.1016/j.msea.2021.141106.
[20] J.P. Best, J. Ast, B. Li, M. Stolpe, R. Busch, F. Yang, X. Li, J. Michler, J.J. Kruzic, Relating fracture toughness to micro-pillar compression response for a laser powder bed additive manufactured bulk metallic glass, Mater. Sci. Eng. A 770 (2020), 138535, https://doi.org/10.1016/j.msea.2019.138535.
[21] J. Heinrich, R. Busch, B. Nonnenmacher, Processing of a bulk metallic glass forming alloy based on industrial grade Zr, Intermetallics 25 (2012) 1–4, https://doi.org/10.1016/j.intermet.2012.02.011.
[22] V. Pacheco, D. Karlsson, J.J. Marattukalam, M. Stolpe, B. Hjörvarsson, U. Jansson, M. Sahlberg, Thermal stability and crystallization of a Zr-based metallic glass produced by suction casting and selective laser melting, J. Alloy. Compd. 825 (2020), https://doi.org/10.1016/j.jallcom.2020.153995.
[23] X.H. Lin, W.L. Johnson, Formation of Ti-Zr-Cu-Ni bulk metallic glasses, J. Appl. Phys. 78 (1995) 6514–6519, https://doi.org/10.1063/1.360537.
[24] B. Bochtler, Thermophysical and structural investigations of a CuTi- and a Zr-based bulk metallic glass, the influence of minor additions, and the relation to thermoplastic forming, 2019.
[25] G.R. Garrett, M.D. Demetriou, J. Chen, W.L. Johnson, Effect of microalloying on the toughness of metallic glasses, Appl. Phys. Lett. 101 (2012) 101–104, https://doi.org/10.1063/1.4769997.
[26] H. Choi-Yim, R. Busch, W.L. Johnson, The effect of silicon on the glass forming ability of the Cu47Ti34Zr11Ni8 bulk metallic glass forming alloy during processing of composites, J. Appl. Phys. 83 (1998) 7993–7997, https://doi.org/10.1063/1.367981.
[27] E.S. Park, H.K. Lim, W.T. Kim, D.H. Kim, The effect of Sn addition on the glass-forming ability of Cu-Ti-Zr-Ni-Si metallic glass alloys, J. Non Cryst. Solids 298 (2002) 15–22, https://doi.org/10.1016/S0022-3093(01)01047-X.
[28] E.S. Barreto, M. Frey, J. Wegner, A. Jose, N. Neuber, R. Busch, S. Kleszczynski, L. Mädler, V. Uhlenwinkel, Properties of gas-atomized Cu-Ti-based metallic glass powders for additive manufacturing, Mater. Des. 215 (2022), 110519, https://doi.org/10.1016/j.matdes.2022.110519.
[29] X. Qiu, J.W. Thompson, S.J.L. Billinge, PDFgetX2: A GUI-driven program to obtain the pair distribution function from X-ray powder diffraction data, J. Appl. Crystallogr 37 (2004) 678, https://doi.org/10.1107/S0021889804011744.
[30] J.P. Best, H.E. Ostergaard, B. Li, M. Stolpe, F. Yang, K. Nomoto, M.T. Hasib, O. Muránsky, R. Busch, X. Li, J.J. Kruzic, Fracture and fatigue behaviour of a laser additive manufactured Zr-based bulk metallic glass, Addit. Manuf. (2020), 101416, https://doi.org/10.1016/j.addma.2020.101416.
[31] A. Kuball, O. Gross, B. Bochtler, B. Adam, L. Ruschel, M. Zamanzade, R. Busch, Development and characterization of titanium-based bulk metallic glasses, J. Alloy. Compd. 790 (2019) 337–346, https://doi.org/10.1016/j.jallcom.2019.03.001.
[32] O. Gross, L. Ruschel, A. Kuball, B. Bochtler, B. Adam, R. Busch, Bulk metallic glass formation in the (Ti,Zr)-(Ni,Cu)-S system, J. Phys. Condens. Matter 32 (2020) 1–8, https://doi.org/10.1088/1361-648X/ab7c15.
[33] N. Sohrabi, J. Jhabvala, G. Kurtuldu, M. Stoica, A. Parrilli, S. Berns, E. Polatidis, S. Van Petegem, S. Hugon, A. Neels, J.F. Löf, R.E. Logé, Characterization, mechanical properties and dimensional accuracy of a Zr-based bulk metallic glass manufactured via laser powder-bed fusion, 199 (2021). https://doi.org/10.1016/j.matdes.2020.109400.
[34] Y. Li, Y. Shen, C. Chen, M.C. Leu, H.L. Tsai, Building metallic glass structures on crystalline metal substrates by laser-foil-printing additive manufacturing, J. Mater. Process. Technol. 248 (2017) 249–261, https://doi.org/10.1016/j.jmatprotec.2017.05.032.
[35] Y. Li, Y. Shen, M.C. Leu, H.L. Tsai, Mechanical properties of Zr-based bulk metallic glass parts fabricated by laser-foil-printing additive manufacturing, Mater. Sci. Eng. A 743 (2019) 404–411, https://doi.org/10.1016/j.msea.2018.11.056.
[36] P. Mercelis, J.P. Kruth, Residual stresses in selective laser sintering and selective laser melting, Rapid Prototyp. J. 12 (2006) 254–265, https://doi.org/10.1108/13552540610707013.
[37] C. Li, J.F. Liu, X.Y. Fang, Y.B. Guo, Efficient predictive model of part distortion and residual stress in selective laser melting, Addit. Manuf. 17 (2017) 157–168, https://doi.org/10.1016/j.addma.2017.08.014.
[38] A. Hussein, L. Hao, C. Yan, R. Everson, Finite element simulation of the temperature and stress fields in single layers built without-support in selective laser melting, Mater. Des. 52 (2013) 638–647, https://doi.org/10.1016/j.matdes.2013.05.070.
[39] C. Suryanarayana, A. Inoue, Bulk Metallic Glasses, CRC Press, 2011.
[40] E.S. Park, D.H. Kim, T. Ohkubo, K. Hono, Enhancement of glass forming ability and plasticity by addition of Nb in Cu-Ti-Zr-Ni-Si bulk metallic glasses, J. Non Cryst. Solids 351 (2005) 1232–1238, https://doi.org/10.1016/j.jnoncrysol.2005.02.019.
[41] M. Tang, P.C. Pistorius, J.L. Beuth, Prediction of lack-of-fusion porosity for powder bed fusion, Addit. Manuf. 14 (2017) 39–48, https://doi.org/10.1016/j.addma.2016.12.001.
[42] G.N. Yang, Y. Shao, K.F. Yao, Understanding the fracture behaviors of metallic glasses-an overview, Appl. Sci. 9 (2019), https://doi.org/10.3390/app9204277.
[43] L. Deng, K. Kosiba, R. Limbach, L. Wondraczek, U. Kühn, S. Pauly, Plastic deformation of a Zr-based bulk metallic glass fabricated by selective laser melting, J. Mater. Sci. Technol. 60 (2021) 139–146.
[44] X.H. Lin, W.L. Johnson, W.K. Rhim, Effect of oxygen impurity on crystallization of an undercooled bulk glass forming Zr–Ti–Cu–Ni–Al alloy, Mater. Trans.\ 38 (1997) 473–477, https://doi.org/10.2320/matertrans1989.38.473.
[45] D.V. Louzguine-Luzgin, C. Suryanarayana, T. Saito, Q. Zhang, N. Chen, J. Saida, A. Inoue, Unusual solidification behavior of a Zr–Cu–Ni–Al bulk glassy alloy made from low-purity Zr, Intermetallics 18 (2010) 1531–1536.
[46] A. Gebert, J. Eckert, L. Schultz, Effect of oxygen on phase formation and thermal stability of slowly cooled Zr65Al7.5Cu17.5Ni10 metallic glass, Acta Mater. 46 (1998) 5475–5482.

[47] C.T. Liu, M.F. Chisholm, M.K. Miller, Oxygen impurity and microalloying effect in a Zr-based bulk metallic glass alloy, Intermetallics 10 (2002) 1105–1112.
[48] S.C. Glade, J.F. Löffler, S. Bossuyt, W.L. Johnson, M.K. Miller, Crystallization of amorphous Cu47Ti34Zr11Ni8, J. Appl. Phys. 89 (2001) 1573–1579, https://doi.org/10.1063/1.1332089.
[49] J. Wegner, M. Frey, P. Stiglmair, S. Kleszczynski, G. Witt, R. Busch, Mechanical properties of honeycomb structured ZR-based bulk metallic glass specimens fabricated by laser powder bed Fusion, South Afr. J. Ind. Eng. 30 (2019).
[50] N. Sohrabi, A. Parrilli, J. Jhabvala, A. Neels, R.E. Logé, Tensile and impact toughness properties of a Zr-based bulk metallic glass fabricated via laser powder-bed fusion, Materials 14 (2021), https://doi.org/10.3390/ma14195627.
[51] X.K. Xi, D.Q. Zhao, M.X. Pan, W.H. Wang, Y. Wu, J.J. Lewandowski, Fracture of brittle metallic glasses: brittleness or plasticity, Phys. Rev. Lett. 94 (2005) 25–28, https://doi.org/10.1103/PhysRevLett.94.125510.
[52] C.A. Schuh, T.C. Hufnagel, U. Ramamurty, Mechanical behavior of amorphous alloys, Acta Mater. 55 (2007) 4067–4109, https://doi.org/10.1016/j.actamat.2007.01.052.
[53] B. Bochtler, M. Stolpe, B. Reiplinger, R. Busch, Consolidation of amorphous powder by thermoplastic forming and subsequent mechanical testing, Mater. Des. 140 (2018) 188–195, https://doi.org/10.1016/j.matdes.2017.11.058.
[54] C. Qin, K. Asami, T. Zhang, W. Zhang, A. Inoue, Corrosion behavior of Cu-Zr-Ti-Nb bulk glassy alloys, Mater. Trans. 44 (2003) 749–753, https://doi.org/10.2320/matertrans.44.749.
[55] H.B. Lu, L.C. Zhang, A. Gebert, L. Schultz, Pitting corrosion of Cu-Zr metallic glasses in hydrochloric acid solutions, J. Alloy. Compd. 462 (2008) 60–67, https://doi.org/10.1016/j.jallcom.2007.08.023.
[56] Y. Guo, I. Bataev, K. Georgarakis, A.M. Jorge, R.P. Nogueira, M. Pons, A.R. Yavari, Ni- and Cu-free Ti-based metallic glasses with potential biomedical application, Intermetallics 63 (2015) 86–96, https://doi.org/10.1016/j.intermet.2015.04.004.

5.6 Paper VI: Additive manufacturing of $Ni_{62}Nb_{38}$ metallic glass via laser powder bed fusion

Authors

Maximilian Frey, Jan Wegner, Lucas Matthias Ruschel, Erika Soares Barreto, Sascha Sebastian Riegler, Bastian Adam, Nils Ellendt, Stefan Kleszczynski, Ralf Busch

Publishing information

Submitted: 08.03.2024

Accepted: 30.01.2025

Published: 26.02.2025

Journal: Progress in Additive Manufacturing, 101 (2025)

DOI: 10.1007/s40964-025-01007-6

Abstract of the article

The binary $Ni_{62}Nb_{38}$ bulk metallic glass exhibits attractive mechanical properties like a yield strength of more than 3 GPa and a hardness of more than 900 Vickers. Due to its limited glass forming ability in casting processes, industrial applications of this impressive material are still pending. Additive manufacturing via laser powder bed fusion (PBF-LB/M) can allow to overcome these limitations. Therefore, we present the first PBF-LB/M parameter study on $Ni_{62}Nb_{38}$. We are able to achieve high densification and almost fully amorphous samples, thereby demonstrating the general applicability of PBF-LB/M to process binary amorphous Ni–Nb alloys. Furthermore, two challenges can be identified, which have to be addressed before additively formed $Ni_{62}Nb_{38}$ can be considered for commercial use. Future parameter fine-tuning must lead to fully vitrified samples, and one must also find a way to avoid crack formation during processing, which was found to be one of the main issues in the present study.

Progress in Additive Manufacturing
https://doi.org/10.1007/s40964-025-01007-6

FULL RESEARCH ARTICLE

Additive manufacturing of $Ni_{62}Nb_{38}$ metallic glass via laser powder bed fusion

Maximilian Frey[1] · Jan Wegner[2] · Lucas Matthias Ruschel[1] · Erika Soares Barreto[3,4] · Sascha Sebastian Riegler[1] · Bastian Adam[1] · Nils Ellendt[3,4] · Stefan Kleszczynski[2,5] · Ralf Busch[1]

Received: 8 March 2024 / Accepted: 30 January 2025
© The Author(s) 2025

Abstract
The binary $Ni_{62}Nb_{38}$ bulk metallic glass exhibits attractive mechanical properties like a yield strength of more than 3 GPa and a hardness of more than 900 Vickers. Due to its limited glass forming ability in casting processes, industrial applications of this impressive material are still pending. Additive manufacturing via laser powder bed fusion (PBF-LB/M) can allow to overcome these limitations. Therefore, we present the first PBF-LB/M parameter study on $Ni_{62}Nb_{38}$. We are able to achieve high densification and almost fully amorphous samples, thereby demonstrating the general applicability of PBF-LB/M to process binary amorphous Ni–Nb alloys. Furthermore, two challenges can be identified, which have to be addressed before additively formed $Ni_{62}Nb_{38}$ can be considered for commercial use. Future parameter fine-tuning must lead to fully vitrified samples, and one must also find a way to avoid crack formation during processing, which was found to be one of the main issues in the present study.

Keywords Metallic glass · Amorphous metal · Additive manufacturing · Selective laser melting · Laser powder bed fusion

1 Introduction

Bulk metallic glasses (BMGs) feature favorable material properties that result from their amorphous structure. High strength, hardness, and, for metals, exceptionally large elastic limits of about 2% constitute a disruptive potential for structural applications [1]. To obtain a metallic glass, the high-temperature melt must be quenched fast enough to ensure complete vitrification without crystallization. The slowest cooling rate that avoids crystallization is termed the critical cooling rate R_C, which is a direct measure of the alloys glass forming ability (GFA). In terms of classical casting routes, geometry-dependent heat dissipation implies that the R_C results in a critical casting thickness, D_C, the largest diameter, to which a fully amorphous rod can be cast. For most BMGs, D_C is of the order of several millimeters [1], which limits the industrial applicability of BMGs. Yet, advances in process engineering have opened a new range of possibilities. Laser powder bed fusion of metals (PBF-LB/M) is a layer-wise additive manufacturing technique that uses rapid laser scanning to locally melt powder material and compact it during solidification. The process features small melt pools with diameters of about 100 µm and is associated with cooling rates of about 10^6 K/s [2, 3]. Hence, cooling and vitrification are decoupled from the size of the final part, allowing to overcome the geometrical limitations of cast BMGs as demonstrated by various studies presenting large and complex shapes [4–8]. However, previous investigations on PBF-LB/M processing of BMGs predominantly targeted the fabrication of established glass formers such as Zr- [5, 9–14], Ti- [15], CuTi- [16], or Fe-based [4, 8] BMGs. For example, AMZ4 [17] ($Zr_{59.3}Cu_{28.8}Al_{10.4}Nb_{1.5}$, also termed Zr01) and Vit101 ($Cu_{47}Ti_{34}Zr_{11}Ni_8$) can reproducibly reach their yield strength before brittle fracture occurs, but BMGs are still mediocre with strength values of, respectively, 2.1

✉ Maximilian Frey
maximilian.frey@uni-saarland.de

[1] Chair of Metallic Materials, Saarland University, Saarbrücken, Germany

[2] Chair of Manufacturing Technology, University of Duisburg-Essen, Duisburg, Germany

[3] Leibniz Institute for Materials Engineering—IWT, Bremen, Germany

[4] Faculty of Production Engineering, University of Bremen, Bremen, Germany

[5] Center for Nanointegration Duisburg-Essen (CENIDE), Duisburg, Germany

Published online: 26 February 2025

[11, 18] and 2.5 GPa [16] in bending. At this point, Ni–Nb alloys [19] appear as promising candidates to exceed these numbers considerably. The simple binary $Ni_{62}Nb_{38}$ system exhibits a D_C of 2 mm [20] and can reach a yield strength between 3 and 3.5 GPa [21], thereby outperforming Zr- and CuTi-based systems by about 1 GPa. Combined with the exceptional elastic limit typical for BMGs and hardness values of more than 900 Vickers [21–23], Ni–Nb-based metallic glasses outrival most metallic materials, including high-performance steels [24]. The comparably low GFA of the Ni–Nb system prohibited vitrification in an earlier additive manufacturing approach using laser based direct energy deposition (LB-DED), a method that features cooling rates in the order of 10^2 to 10^4 K/s [25]. In the present work, we provide the first attempt to use laser powder bed fusion (PBF-LB/M) to process the binary $Ni_{62}Nb_{38}$ alloy. Thereby, we try to find processing parameters that result in highly dense, crack-free, and fully amorphous samples, since only this combination will allow for the most mechanically robust and performant parts [11, 16, 26]. Due to the small amount of powder feedstock that is available from the atomization process [27], we are limited to a first preliminary parameter evaluation. Nevertheless, we will show that we are able to reach almost fully amorphous samples, demonstrating the applicability of PBF-LB/M processing of amorphous $Ni_{62}Nb_{38}$ alloys. Furthermore, we can identify main issues that have to be addressed in the future before the system can be introduced to industrial applications. In particular, crack formation has to be diminished to allow for robust parts.

2 Experimental

The atomization and evaluation of the powder feedstock that is used in the present study are described in detail in a previous study by Barreto et al. [27]. To quickly recapitulate, elemental Ni (99.95 wt%) and Nb (99.9 wt%) were weighed to match the desired composition of $Ni_{62}Nb_{38}$ (at%) and were further pre-alloyed by arc-melting under Ti-gettered Ar atmosphere. To ensure chemical homogeneity, the ingots were flipped and remelted at least five times. The ingots were then gas-atomized into about 500 g of powder feedstock using graphite crucibles. The powder was sieved and a size distribution of 20–63 µm was chosen for further use. PBF-LB/M processing was conducted on an SLM 280 HL Twin laser system. The operating 700 W lasers have a focal diameter of about 70 µm. Argon was used as the shielding gas, resulting in a residual oxygen concentration of 0.05 vol.% in the chamber. No heating of the build plate was applied. The process parameters were evaluated by varying the scan speed, v, and the laser power, P, to form cuboid samples ($4 \times 6.5 \times \sim 1$ mm). Layer height, d, and hatch distance, h, were held constant at $d = 40$ µm and $h = 100$ µm. The resulting volume energy densities, E_V, can be calculated as:

$$E_V = \frac{P}{vdh}$$

Cuboids were created with E_V values ranging between 13.3 and 49.3 J/mm^3, as listed in Table 1 (one 100 W parameter combination was excluded from the list and from further analysis due to extreme brittleness and sample loss). A detailed explanation of the principles of the PBF-LB/M process can be found in [26].

Each parameter setting was investigated for two different scanning strategies. For the first one, parallel scanning vectors to the sample edges were applied. Hence, the laser tracks of subsequent layers share the same orientation. The second sample set was processed using a rotating scanning strategy, which shifts the vector orientation by 67° in reference to the previous layer. Figure 1 shows the manufactured samples on the build plate and further explains both scanning strategies.

The processed samples were cut in half, perpendicular to their building direction. One half was embedded, sanded, and polished for optical microscopy and optical relative density determination, which was performed using an Olympus BX51M and the image analysis software Stream essentials version 1.9.4. Some of these samples were further characterized by micro-hardness testing (HV1) using a Zwick Z3212 (Zwick Roell) hardness tester. Five indents per sample allow for statistics. The second half was investigated with X-ray diffraction (XRD) and differential thermal analysis (DTA). For the XRD analysis, a Bruker D8-A25-Advance diffractometer was used applying Cu-K_α-radiation with a wavelength of 1.5406 Å between the angles (2θ) of 20° to 80°. DTA temperature scans on selected cuboids were performed in Y_2O_3 coated carbon crucibles using a Netzsch STA 449 F3 Jupiter device applying heating scans with a rate of 0.33 K/s from 293 to 1050 K under high-purity argon flow. Scanning electron microscopy (SEM) was performed on polished sample surfaces using a Zeiss Sigma VP device. Thereby, energy-dispersive X-ray spectroscopy (EDX) was

Table 1 Process parameters used for PBF-LB/M

P (W)	v (mm/s)	E_V (J/mm^3)
100	530	47.2
100	940	26.6
150	760	49.3
150	1190	31.5
150	2110	17.8
200	1350	37.0
200	2100	23.8
200	3750	13.3

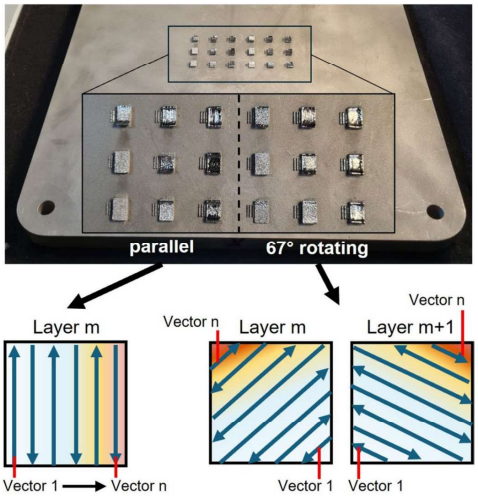

Fig. 1 A photo of the manufactured samples. Both scanning strategies are explained below. While the parallel vectors strategy uses the same scanning pattern for every layer, the rotating vectors strategy changes the vector orientation between consecutive layers through a 67° rotation

performed in area scanning mode to allow for elemental mapping.

3 Results and discussion

3.1 Density and hardness evaluation

Figure 2a displays the cross-sectional optical micrographs of three parallel vector cuboids, which represent the whole spectrum of used volume energy densities (49.3, 31.5, and 17.8 J/mm^3, respectively). As expected, the overall sample density rises with increasing E_V (the used energy range was not high enough to observe a density decrease due to keyholing). The higher energy input allows to eliminate lack of fusion, resulting in decreased porosity due to improved compaction of the molten powder material, as reported in a number of earlier studies [28–31]. Yet, with rising E_V and increased density, a tendency to form cracks is also observed in the samples, see e.g. the 31.5 J/mm^3 sample in Fig. 2a. This can be mainly attributed to the temperature gradients that arise during PBF-LB/M processing. These predominantly create in-plane residual stresses [32, 33], and hence, most of the cracks are oriented horizontally. Figure 2b shows the optically determined relative density (blue circles) and HV1 hardness (red squares) of the parallel vector cuboids as a function of the applied E_V. Both parameters increase with increasing E_V, reflecting the improved material compaction, which leads to relative densities of up to 99.9%. By

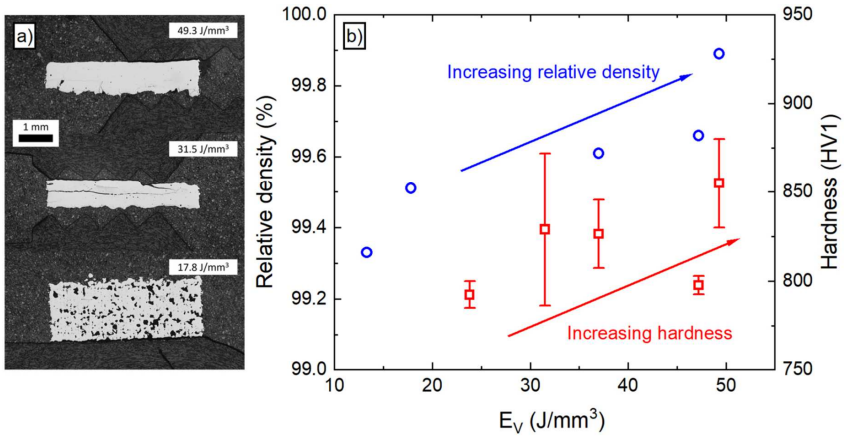

Fig. 2 **a** Optical micrographs of cross-sections of three representative parallel vector cuboids with different volume energy densities. Porosity decreases with increasing E_V, yet crack formation is observed in the more compacted samples. **b** A comparison of relative density (blue circles) and HV1 hardness (red squares) of the parallel vector cuboids. Both quantities rise with increasing E_V, allowing for densities of up to 99.9% and hardness values of almost 900 HV1. (Due to sample loss through brittle fracture, the shown data sets are incomplete)

approaching levels of 900 HV1, the samples feature the typical extreme hardness of Ni-Nb-based metallic glass formers [21–23].

3.2 *Amorphicity screening* via *X-ray diffraction*

A first screening in terms of the amorphous state of the samples is given in Fig. 3, where the diffractograms of cuboids formed with parallel and rotating vectors are compared. In the case of parallel vectors, broad diffraction halos suggest mostly amorphous samples, except for the sample with the highest E_V of 49.3 J/mm^3, which indicates partial crystallization in the form of arising Bragg reflections. Here, the high energy input appears to promote crystal formation, as previously reported by various studies [5, 10, 11]. In contrast, the cuboids formed with rotating vectors seem to be more prone to crystallization. On the one hand, the sample produced with a high E_V value of 49.3 J/mm^3 features more distinct Bragg reflections as its parallel vector counterpart, suggesting a larger crystalline fraction. On the other hand, the low-energy rotating vector samples (13.3 and 17.8 J/mm^3) also show distinct reflections. We interpret this as the result of two effects. First, the high degree of porosity of these low-E_V cuboids (see Fig. 2) might decrease the overall heat dissipation capability of the sample, resulting in local heat accumulations that promote crystallization. Similar observations have been reported in the case of CuTi-based samples formed by PBF-LB/M [16]. Yet, the low-E_V parallel vector cuboids in Fig. 3a do not show Bragg reflections, and therefore, we assume, secondly, that the rotating vector strategy induces additional overheating at the edges of the cubic samples due to shorter vector lengths, which would then lead to the higher degree of crystallinity in those samples. In Fig. 3c, we take a closer look at the samples that show the most prominent Bragg reflections, namely the rotating vector cuboids formed with 49.3 J/mm^3, 17.8 mm^3, and 13.3 mm^3. The peaks can be mostly attributed to the crystalline equilibrium phases Ni_6Nb_7 and Ni_3Nb that appear in the binary Ni–Nb phase diagram [34]. Furthermore, Ni_2O_3 can be identified, which is likely a consequence of the relatively high oxygen content of the used powder feedstock (863 ± 9 wt-ppm as reported in [27]).

3.3 Identification of crystalline precipitations through electron microscopy

We further investigate the formed crystalline phases in the 13.3 J/mm^3 rotating vector cuboid, the one with the most intense Bragg reflections in Fig. 3, by SEM analysis. Figure 4a provides a back-scattered electron (BSE) image that features apparent amorphous regions, which can be identified by their homogeneous, contrast-free appearance, and regions of crystalline precipitates with two distinctly

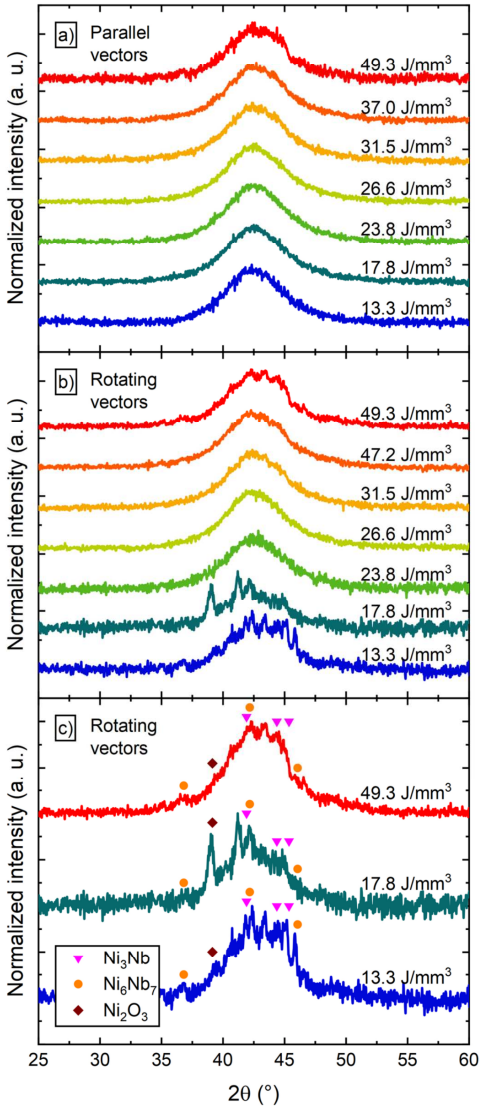

Fig. 3 Screening of the structure via XRD. **a** Parallel vector cuboids show mostly Bragg reflection-free diffractograms with broad, glass-typical halos, only the cuboid with the highest E_V shows slight reflections that indicate crystallinity. **b** Rotating vector samples show slightly more Bragg reflections for low and high E_V values, indicating higher loads of crystallinity. **c** The rotating vector cuboids with the most distinct reflections are shown here in detail to identify the crystalline compounds

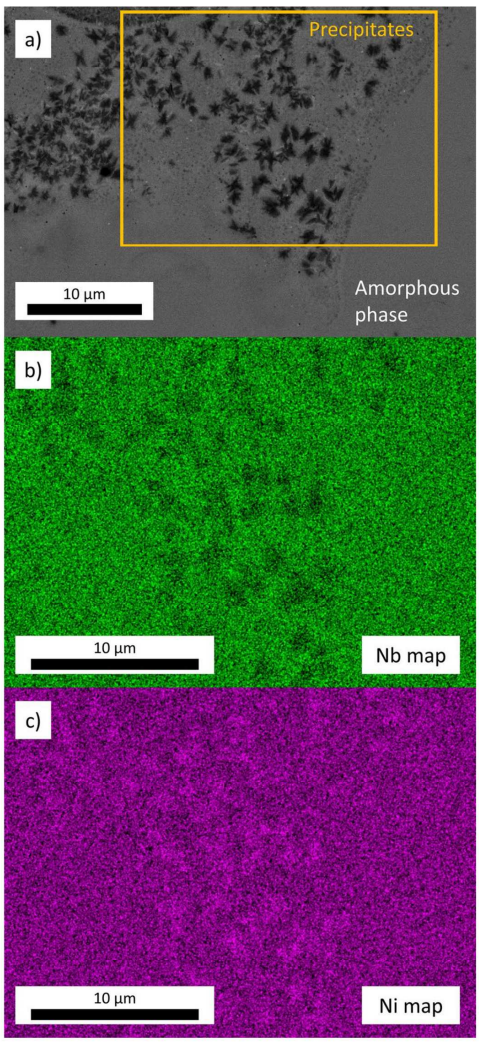

Fig. 4 SEM pictures taken on the 13.3 J/mm^3 rotating vector sample that was shown to feature distinct Bragg reflections in **b** and **c**. **a** A BSE picture of an amorphous region (homogenous) next to a group of nm-scale crystalline precipitates. The elemental maps in **b** and **c** indicate Nb depletion and Ni enrichment in these, which hinds towards the XRD-confirmed Ni_3Nb as composition

different size distributions. More precisely, equiaxed dendritic precipitates of up to 2 µm in size are embedded in a dense field of nano-precipitations that appear as black dots. All crystals are too small for proper chemical analysis by EDX, yet elemental mapping allows at least a qualitative investigation of the larger dendrites. Therefore, the region marked by the yellow frame in Fig. 4a is further EDX scanned, the resulting elemental maps for Ni and Nb are given in Fig. 4b, c. The dendritic precipitates clearly show a depletion of Nb and enrichment in Ni, rendering the XRD-confirmed Ni_3Nb as the most probable composition.

The relatively large precipitation size further indicates that they formed at elevated temperatures, where the fast dynamics of the liquid allowed for pronounced crystal growth [35]. Hence, these larger precipitates likely formed either during the initial cooling of the melt or in the 'inner region' of the heat affected zone, in direct contact with the melt pool. Both possibilities could be promoted by the earlier discussed heat accumulation effects in this 13.3 J/mm^3 sample. Such a formation of Ni_3Nb precipitates at elevated temperatures would be consistent with in-situ HEXRD undercooling experiments on levitated droplets of $Ni_{62}Nb_{38}$, in which Ni_3Nb appears as the primary phase [21]. It would also align with CALPHAD calculations of the Ni–Nb system, which show that the driving force for primary crystallization from liquid $Ni_{62}Nb_{38}$ is much larger for the Ni_3Nb phase than for the Ni_6Nb_7 phase [36]. In contrast, the smaller, nm-sized precipitates, visible in Fig. 4a, rather suggest crystallization at lower temperatures, where crystal growth is kinetically limited. Hence, these nanocrystals most likely form in the 'outer regions' of heat affected zone, with larger distance to the melt pool [10, 12, 37].

3.4 Narrowing down the optimal parameter range by calorimetric screening

Based on the XRD results, parallel vectors appear to be the more promising scanning strategy to achieve fully amorphous $Ni_{62}Nb_{38}$ samples, since it appears to create less heat accumulation than the rotating vectors strategy. Hence, we focus on the parallel vector samples in the following and use DTA temperature scanning to investigate the amount of amorphous phase in the printed samples quantitatively. The results are presented in Fig. 5. The black and grey DTA curves in Fig. 5a are taken from [27] and represent an as-cast reference formed by conventional suction casting as well as the powder feedstock material used for PBF-LB/M with a fraction of 20–63 µm. The crystallization enthalpies, ΔH_x, are determined by integration over the exothermal crystallization event (dotted lines) and are found to be virtually identical with a value of about − 4.60 kJ/g-atom, as it is typical for fully amorphous $Ni_{62}Nb_{38}$ [21]. The DTA curves of the powder and the as-cast material are further compared with the two PBF-LB/M-formed cuboids that show the highest and lowest measured crystallization enthalpies, which are the 17.8 J/mm^3 cuboid and the 49.3 J/mm^3 cuboid. The first one features a ΔH_x of − 4.08 kJ/g-atom, the second one

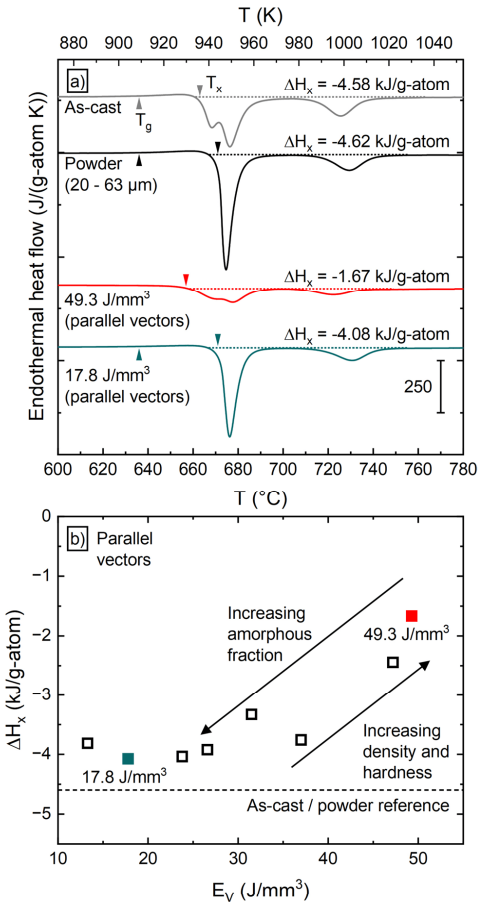

Fig. 5 **a** DTA temperature scans of an as-cast reference and the used powder, taken from [27], in comparison to the scans of the 49.3 and 17.8 J/mm^3 parallel vector cuboids. T_g and T_x are determined by the tangent method (arrows), ΔH_x is determined by integration (dotted lines). **b** All determined ΔH_x values of the parallel vector cuboids as a function of E_V. The cuboids known from **a** are highlighted by color. With values of about 20 J/mm^3, the PBF-LB/M samples reach almost 90% of the reference ΔH_x of − 4.60 kJ/g-atom (dashed line), indicating mostly amorphous samples. With rising E_V, relative density and hardness might increase (see Fig. 2), yet, crystallinity also increases

a ΔH_x of only − 1.67 kJ/g-atom. This corresponds to 89% and 36% of the reference crystallization enthalpy (4.60 kJ/g-atom), accordingly implying crystalline fractions of 11% and 64%. Considering the mostly peak-free diffractograms in Fig. 3a, the DTA findings demonstrate again that calorimetry can provide better sensitivity and resolution than conventional XRD to detect the presence of (nano-)crystalline fractions in additively formed BMGs [11, 16, 38]. This can be explained by the usually weak scattering signal of nanocrystallites as well as by the fact that calorimetric analysis incorporates the whole sample volume, therefore leading to a more representative, volume-averaged picture than the surface-localized XRD analysis.

While the rather crystal-loaded 49.3 J/mm^3 sample shows no detectable glass transition in the DTA scan, the as-cast, powder, and 17.8 J/mm^3 samples all show a glass transition onset, T_g, of 909 K, as indicated by the arrows in Fig. 5a. Yet, the powder material and the almost fully amorphous 17.8 J/mm^3 parallel vector cuboid are distinctly more thermally stable against crystallization upon heating than the high-purity as-cast reference, since their onset temperature of crystallization, T_x, is 8 K higher (942 K) as in case of the as-cast sample (936 K). Here, the oxygen content plays a decisive role. While the as-cast material shows low levels of oxygen contamination (191 wt-ppm), powder and PBF-LB/M-formed samples feature distinctly higher contamination (863 wt-ppm and above) due to the high oxygen uptake that stems from the large surface-to-volume ratio of the powder particles [27]. Upon heating from the glassy state, the primary crystallization of high-purity Ni–Nb metallic glasses is usually attributed to a metastable crystalline M-phase [36, 39], corresponding to the first separate crystallization event of the as-cast reference in Fig. 5a. As discussed in [27], the increased oxygen content in the powder and AM-formed parts seems to destabilize the primary M-phase, therefore, delaying its formation upon heating, which increases the thermal stability of the supercooled liquid (SCL). Such SCL stabilization effects are well-known from other BMG microalloying approaches with small-size atomic species like Si in CuTi-based systems [40], S in several BMG formers [41, 42], or P in the present Ni–Nb system [21]. The oxygen-driven destabilization of the M-phase renders it possible that Ni_3Nb also becomes the primary phase upon heating, since it was already shown to be the second phase in high-purity $Ni_{62}Nb_{38}$ after the M-phase has formed [39]. Hence, it could be speculated that the nanocrystalline precipitates shown in Fig. 4a next to the large equiaxed Ni_3Nb dendrites consist of the Ni_3Nb phase as well.

Figure 5b summarizes the DTA screening of the parallel vector sample set by plotting ΔH_x as a function of E_V to determine the amount of amorphous phase in the printed samples. The 17.8 J/mm^3 and 49.3 J/mm^3 samples are highlighted in their respective colors from Figs. 3a and 5a. On the one hand, the largest amount of amorphous phase of up to 89% can be found for lower E_V values of roughly 20 J/mm^3. Higher volume energy densities promote increased crystallinity as previously suggested by the XRD results. On the other hand, increased E_V values are needed to achieve full compaction and optimized hardness, as demonstrated in Fig. 2.

3.5 Recapitulatory considerations

We demonstrate that the binary $Ni_{62}Nb_{38}$ BMG former can be processed successfully by PBF/LB-M additive manufacturing, reaching exceptional hardness levels and amorphization degrees of almost 90%. Furthermore, the present parameter study allows us to formulate two main issues that future PBF-LB/M studies must solve to establish PBF-LB/M-formed $Ni_{62}Nb_{38}$ for practical use. First, process parameter optimization has to achieve full amorphization while also ensuring high sample density. While the present results may render both aspects to be antagonistic, it shall be recalled that the low amount of available powder [27] restricts the parameter optimization to first order approaches, here performed in form of a simple variation of E_V. Larger amounts of powder feedstocks will allow advanced processing approaches like two-step scanning [43], which separates material densification and vitrification in two different scanning steps. Second, crack formation can be identified as a major issue for additively formed $Ni_{62}Nb_{38}$. Thereby, the material-typical high modulus and hardness inevitably go hand in hand with increased brittleness, rendering the PBF/LB-M-formed samples prone to crack formation due to process-induced internal stresses [16]. Here, optimization approaches like the already mentioned two-step scanning [43] or changes regarding the used substrate material [9] might help to reduce stress states. Also, the comparably high T_g of Ni–Nb-alloys might induce increased stresses between sample and substrate, necessitating more in-depth testing of different substrate preheating approaches to diminish these stresses, as reported in [16].

4 Conclusions

To sum up, the present parameter study allows to create almost fully amorphous $Ni_{62}Nb_{38}$ samples via PBF-LB/M, which is a quite promising result considering the system's relatively low critical casting thickness of 2 mm. Nevertheless, porosity and crack formation are challenges that need to be solved and balanced through advanced processing approaches tested in follow-up studies. After resolving these issues, amorphous $Ni_{62}Nb_{38}$ will constitute an extremely potent choice for the additive manufacturing of highly robust products, due to the system's outstanding strength and hardness.

Acknowledgements We would like to thank Martina Stemmler for her assistance regarding SEM and XRD analysis. Instrumentation and technical assistance for this work were provided by the Service Center X-ray Diffraction, with financial support from Saarland University and German Science Foundation (project number INST 256/349-1).

Funding Open Access funding enabled and organized by Projekt DEAL.

Data availability All data needed to evaluate the conclusions in the paper are present in the paper. Additional data related to this work may be requested from the authors.

Declarations

Conflict of interest On behalf of all authors, the corresponding author states that there is no conflict of interest.

Open Access This article is licensed under a Creative Commons Attribution 4.0 International License, which permits use, sharing, adaptation, distribution and reproduction in any medium or format, as long as you give appropriate credit to the original author(s) and the source, provide a link to the Creative Commons licence, and indicate if changes were made. The images or other third party material in this article are included in the article's Creative Commons licence, unless indicated otherwise in a credit line to the material. If material is not included in the article's Creative Commons licence and your intended use is not permitted by statutory regulation or exceeds the permitted use, you will need to obtain permission directly from the copyright holder. To view a copy of this licence, visit http://creativecommons.org/licenses/by/4.0/.

References

1. Telford M (2004) The case for bulk metallic glass. Mater Today 7:36–43. https://doi.org/10.1016/S1369-7021(04)00124-5
2. Scipioni Bertoli U, Guss G, Wu S et al (2017) In-situ characterization of laser-powder interaction and cooling rates through high-speed imaging of powder bed fusion additive manufacturing. Mater Des 135:385–396. https://doi.org/10.1016/j.matdes.2017.09.044
3. Hooper PA (2018) Melt pool temperature and cooling rates in laser powder bed fusion. Addit Manuf 22:548–559. https://doi.org/10.1016/j.addma.2018.05.032
4. Pauly S, Löber L, Petters R et al (2013) Processing metallic glasses by selective laser melting. Mater Today 16:37–41. https://doi.org/10.1016/j.mattod.2013.01.018
5. Li XP, Roberts MP, O'Keeffe S, Sercombe TB (2016) Selective laser melting of Zr-based bulk metallic glasses: processing, microstructure and mechanical properties. Mater Des 112:217–226. https://doi.org/10.1016/j.matdes.2016.09.071
6. Wegner J, Frey M, Stiglmair P et al (2019) Mechanical properties of honeycomb structured zr-based bulk metallic glass specimens fabricated by laser powder bed fusion. South Afr J Ind Eng 30(3):32–40. https://doi.org/10.7166/30-3-2265
7. Wegner J, Frey M, Busch R, Kleszczynski S (2021) Additive manufacturing of a compliant mechanism using Zr-based bulk metallic glass. Addit Manuf Lett 1:100019. https://doi.org/10.1016/j.addlet.2021.100019
8. Thorsson L, Unosson M, Teresa Pérez-Prado M et al (2022) Selective laser melting of a Fe-Si-Cr-B-C-based complex-shaped amorphous soft-magnetic electric motor rotor with record dimensions. Mater Des 215:110483. https://doi.org/10.1016/j.matdes.2022.110483
9. Wegner J, Kleszczynski S, Frey M, et al (2018) Parameterstudie zur Verarbeitung metallischer Gläser auf Zr-Basis mit dem Laser-Strahlschmelzverfahren. In: Proceedings of the 15th Rapid. Tech Conference
10. Marattukalam JJ, Pacheco V, Karlsson D et al (2020) Development of process parameters for selective laser melting of a Zr-based

bulk metallic glass. Addit Manuf 13:101124. https://doi.org/10.1016/j.addma.2020.101124
11. Wegner J, Frey M, Piechotta M et al (2021) Influence of powder characteristics on the structural and the mechanical properties of additively manufactured Zr-based bulk metallic glass. Mater Des 209:109976. https://doi.org/10.1016/j.matdes.2021.109976
12. Pacheco V, Karlsson D, Marattukalam JJ et al (2020) Thermal stability and crystallization of a Zr-based metallic glass produced by suction casting and selective laser melting. J Alloys Compd 825:8. https://doi.org/10.1016/j.jallcom.2020.153995
13. Sohrabi N, Jhabvala J, Kurtuldu G, et al (2021) Characterization, mechanical properties and dimensional accuracy of a Zr-based bulk metallic glass manufactured via laser powder-bed fusion. 199:8. https://doi.org/10.1016/j.matdes.2020.109400
14. Li B, Yakubov V, Nomoto K et al (2024) Superior mechanical properties of a Zr-based bulk metallic glass via laser powder bed fusion process control. Acta Mater 266:119685. https://doi.org/10.1016/j.actamat.2024.119685
15. Wang P, Pauly S, Deng L et al (2017) Selective laser melting of a Ti-based bulk metallic glass. Mater Lett 212:346–349. https://doi.org/10.1016/j.matlet.2017.10.130
16. Frey M, Wegner J, Barreto ES et al (2023) Laser powder bed fusion of Cu-Ti-Zr-Ni bulk metallic glasses in the Vit101 alloy system. Addit Manuf 66:8. https://doi.org/10.1016/j.addma.2023.103467
17. Heinrich J, Busch R, Nonnenmacher B (2012) Processing of a bulk metallic glass forming alloy based on industrial grade Zr. Intermetallics 25:1–4. https://doi.org/10.1016/j.intermet.2012.02.011
18. Frey M, Wegner J, Neuber N et al (2021) Thermoplastic forming of additively manufactured Zr-based bulk metallic glass: a processing route for surface finishing of complex structures. Mater Des 198:1–8. https://doi.org/10.1016/j.matdes.2020.109368
19. Ruhl RC, Giessen BC, Cohen M, Grant NJ (1967) New microcrystalline phases in the NbNi and TaNi systems. Acta Metall 15:1693–1702. https://doi.org/10.1016/0001-6160(67)90060-0
20. Xia L, Li WH, Fang SS et al (2006) Binary Ni-Nb bulk metallic glasses. J Appl Phys 99:58–61. https://doi.org/10.1063/1.2158130
21. Ruschel LM, Gross O, Bochtler B et al (2023) Ni-Nb-P-based bulk glass-forming alloys: superior material properties combined in one alloy family. Acta Mater 6:118968. https://doi.org/10.1016/j.actamat.2023.118968
22. Choi-Yim H, Xu D, Johnson WL (2003) Ni-based bulk metallic glass formation in the Ni-Nb-Sn and Ni-Nb-Sn-X (X = B, Fe, Cu) alloy systems. Appl Phys Lett 82:1030–1032. https://doi.org/10.1063/1.1544434
23. Hu HT, Chen LY, Wang XD et al (2008) Formation of Ni-Nb-Zr-X (X = Ti, Ta, Fe, Cu, Co) bulk metallic glasses. J Alloys Compd 460:714–718. https://doi.org/10.1016/j.jallcom.2008.01.075
24. Tian J, Jiang Z (2021) Exploring new strategies for ultrahigh strength steel via tailoring the precipitates. Front Mater 8:1–7. https://doi.org/10.3389/fmats.2021.797798
25. Jones MR, DelRio FW, Pegues JW et al (2021) Additive manufacturing of high-strength multiphase nanostructures in the binary Ni–Nb system for the discovery of new types of superalloys. J Mater Res 36:3167–3181. https://doi.org/10.1557/s43578-021-00290-7
26. Sohrabi N, Jhabvala J, Logé RE (2021) Additive manufacturing of bulk metallic glasses—process, challenges and properties: a review. Metals (Basel) 11:8
27. Barreto ES, Frey M, Matthias L et al (2024) Gas atomization of fully-amorphous Ni62Nb38 powder. Mater Lett 357:135798. https://doi.org/10.1016/j.matlet.2023.135798
28. Mukherjee T, DebRoy T (2018) Mitigation of lack of fusion defects in powder bed fusion additive manufacturing. J Manuf Process 36:442–449. https://doi.org/10.1016/j.jmapro.2018.10.028
29. Oliveira JP, LaLonde AD, Ma J (2020) Processing parameters in laser powder bed fusion metal additive manufacturing. Mater Des 193:1–12. https://doi.org/10.1016/j.matdes.2020.108762
30. Shrestha S, Chou K (2022) Formation of keyhole and lack of fusion pores during the laser powder bed fusion process. Manuf Lett 32:19–23. https://doi.org/10.1016/j.mfglet.2022.01.005
31. Mojumder S, Gan Z, Li Y et al (2023) Linking process parameters with lack-of-fusion porosity for laser powder bed fusion metal additive manufacturing. Addit Manuf 68:103500. https://doi.org/10.1016/j.addma.2023.103500
32. Mercelis P, Kruth JP (2006) Residual stresses in selective laser sintering and selective laser melting. Rapid Prototyp J 12:254–265. https://doi.org/10.1108/13552540610707013
33. Shiomi M, Osakada K, Nakamura K et al (2004) Residual stress within metallic model made by selective laser melting process. CIRP Ann - Manuf Technol 53:195–198. https://doi.org/10.1016/S0007-8506(07)60677-5
34. Okamoto H (2008) Nb-Ni (Niobium–Nickel). J Phase Equilibria Diffus 29:210–210. https://doi.org/10.1007/s11669-008-9277-0
35. Schroers J, Busch R, Masuhr A, Johnson WL (1999) Continuous refinement of the microstructure during crystallization of supercooled Zr41Ti14Cu12Ni10Be23 melts. Appl Phys Lett 74:2806–2808. https://doi.org/10.1063/1.124020
36. Stanojevic S, Gallino I, Aboulfadl H et al (2016) Oxidation of glassy Ni-Nb-Sn alloys and its influence on the thermodynamics and kinetics of crystallization. Acta Mater 102:176–186. https://doi.org/10.1016/j.actamat.2015.09.009
37. Yang Z, Markl M, Körner C (2022) Predictive simulation of bulk metallic glass crystallization during laser powder bed fusion. Addit Manuf 59:8. https://doi.org/10.1016/j.addma.2022.103121
38. Wegner J, Frey M, Kleszczynski S, et al (2020) Influence of process gas during powder bed fusion with laser beam of Zr-based bulk metallic glasses. In: 11th CIRP Conference on Photonic Technologies [LANE 2020]. Elsevier B.V., pp 205–210
39. Collins LE, Grant NJ, Vander Sande JB (1983) Crystallization of amorphous Ni60Nb40. J Mater Sci 18:804–814. https://doi.org/10.1007/BF00745579
40. Choi-Yim H, Busch R, Johnson WL (1998) The effect of silicon on the glass forming ability of the Cu47Ti34Zr11Ni8 bulk metallic glass forming alloy during processing of composites. J Appl Phys 83:7993–7997. https://doi.org/10.1063/1.367981
41. Jiang HR, Hu JY, Neuber N et al (2021) Effect of sulfur on the glass-forming ability, phase transformation, and thermal stability of Cu-Zr-Al bulk metallic glass. Acta Mater 212:116923. https://doi.org/10.1016/j.actamat.2021.116923
42. Kuball A, Gross O, Bochtler B, Busch R (2018) Sulfur-bearing metallic glasses: a new family of bulk glass-forming alloys. Scr Mater 146:73–76. https://doi.org/10.1016/j.scriptamat.2017.11.011
43. Żrodowski Ł, Wróblewski R, Leonowicz M et al (2023) How to control the crystallization of metallic glasses during laser powder bed fusion? Towards part-specific 3D printing of in situ composites. Addit Manuf 76:8. https://doi.org/10.1016/j.addma.2023.103775

Publisher's Note Springer Nature remains neutral with regard to jurisdictional claims in published maps and institutional affiliations.

6. ADDITIONAL RESULTS AND DISCUSSIONS

While the six just presented publications incorporate the major experimental results and most parts of the discussion of this work, the present chapter will aim to complement these findings by providing additional experimental data, analysis approaches, and discussions. These aspects will help to connect all the different topics by embedding them into a larger context.

The XPCS results from Paper II are the most scientifically relevant and disruptive parts of this work and are therefore complemented through two chapters. Chapter 6.1, *Temperature scanning XPCS: Methodological considerations and experimental artifacts,* will focus on methodological aspects of temperature scanning XPCS. Chapter 6.2, *Multiplicative versus additive KWW approaches to describe XPCS decorrelation in the non-equilibrium state,* then provides an in-depth explanation of the KWW_{MULTI} model introduced in Paper II and discusses a possible alternative in form of the KWW_{ADD} model.

Chapter 6.3 will focus *On the equilibrium supercooled liquid fragility of* $Pt_{42.5}Cu_{27}Ni_{9.5}P_{21}$. In combination with additional DMA and FDSC results, a large-scale data comparison will provide deeper insights into the fragility and the question of how to properly model it.

After this we will change the attention towards the more practical part of the work, namely the additive manufacturing of metallic glasses via PBF-LB/M. Chapter 6.4 will summarize the major findings on the *Mechanical properties of metallic glasses additively formed via laser powder bed fusion*, especially regarding the various factors that determine the achievable maximum strengths. Chapter 6.5 will finally offer an outlook on *Potential application cases of additively formed metallic glasses*.

6.1 Temperature scanning XPCS: Methodological considerations and experimental artifacts

XPCS is a relatively novel method [245], and this applies in particular for the idea of performing this kind of diffraction studies under temperature scanning conditions [6,280–283]. Such a non-isothermal approach comes with its own set of methodological aspects and possible measurement artifacts, which must be considered before one can commence a meaningful interpretation of underlying physical effects. The following chapters shall provide the necessary understanding for these aspects, namely the influence of evaluation window

size explained in Chapter 6.1.1, the highly important transit decorrelation effect in Chapter 6.1.2, and the issue of temperature correction, which will be considered in Chapter 6.1.3.

6.1.1 On the effects of changing the evaluation window size

In Chapter 2.3.3, we have seen that the experimental determination of dynamics often relies on temperature scanning approaches. Here, choosing an adequate rate of temperature change is crucial, since the data evaluation occurs by taking a specific time window into account. Too fast rates lead to large temperature changes within the evaluation timespan, which can result in smearing effects. In other words, the underlying dynamics change significantly within the evaluation window, producing blurred, smeared out results. On the other hand, we have seen in Paper II that a certain evaluation window size is needed to resolve the g_2 decorrelation of slower dynamics properly, hence, a compromise must be found.

Figure 6.1 illustrates g_2 curves from the XPCS cooling scan on the $Pt_{42.5}Cu_{27}Ni_{9.5}P_{21}$ alloy from Paper II. The same representative temperature points as used in the publication are shown, namely 479.7 K in the glass, 510.3 K in the glass transition region, and 541.0 K in the equilibrium SCL state. For each temperature point, g_2 data sets stemming from evaluation window sizes of 60 s, 120 s, and 240 s are compared to each other. The 240 s g_2 data batches thereby correspond to those shown in Paper II, which are there termed as B4, B5, and B6. As reported in the article, the black curve further depicts the 240 s KWW fit in the SCL state, while the green curves represent the non-equilibrium state KWW_{MULTI} fits to the 240 s batches. Expectably, the g_2 curves from different evaluation window sizes show very good overlap. Yet, in the non-equilibrium states, the system's dynamics become so slow that especially the short 60 s evaluation window is unable to incorporate most parts of the decorrelation process. Here, larger window sizes must be chosen.

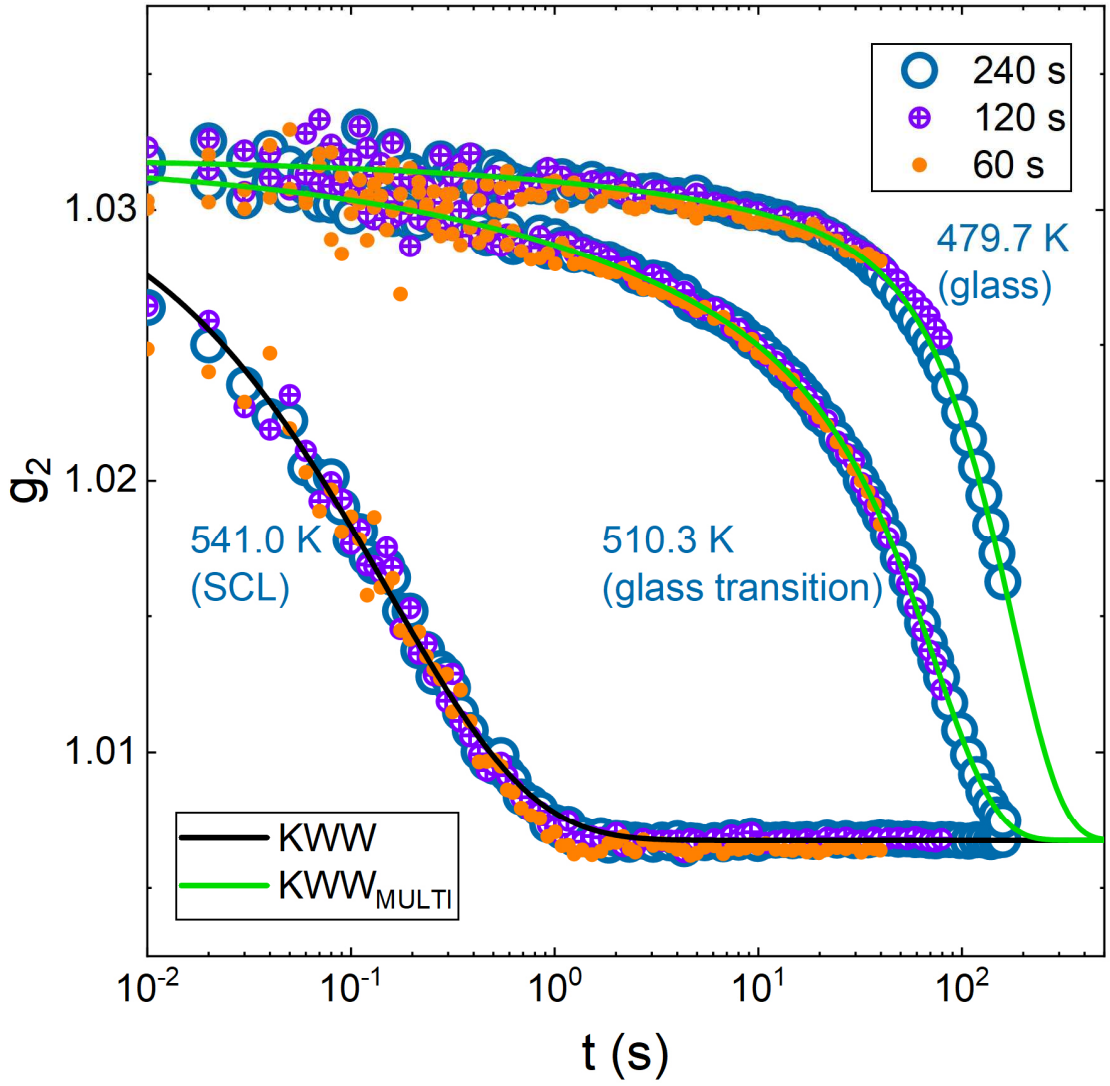

Figure 6.1: A comparison of g_2 curves obtained from evaluation windows of 240 s, 120 s, and 60 s in size. The three chosen temperature points thereby represent the glass, the glass transition, and the SCL state upon cooling with 1 K/min (compare the batches B4-B6 from Paper II). While coequal results are found in the SCL, an adequate resolution of the decorrelation requires larger batch sizes of 120 s or even 240 s in the glass transition and the glass.

Figure 6.2 compares the KWW_{MULTI} fitting results from 120 s and 240 s window sizes. Both show very similar outcomes, yet the larger temporal range of the 240 s g_2 data sets allows for better statistics and hence less scatter-prone results. Accordingly, the 240 s evaluation window was chosen for the publication. Coming back to Figure 6.1 and regarding the SCL state, we see that the fast dynamics can be quantified through all three evaluation window sizes. Yet, the aforementioned smearing effect must be considered and is therefore highlighted in Figure 6.3. While the relaxation times obtained from the 60 s and 240 s window sizes are practically identical, smearing manifests in a distinct offset of roughly 0.1 in the shape exponent.

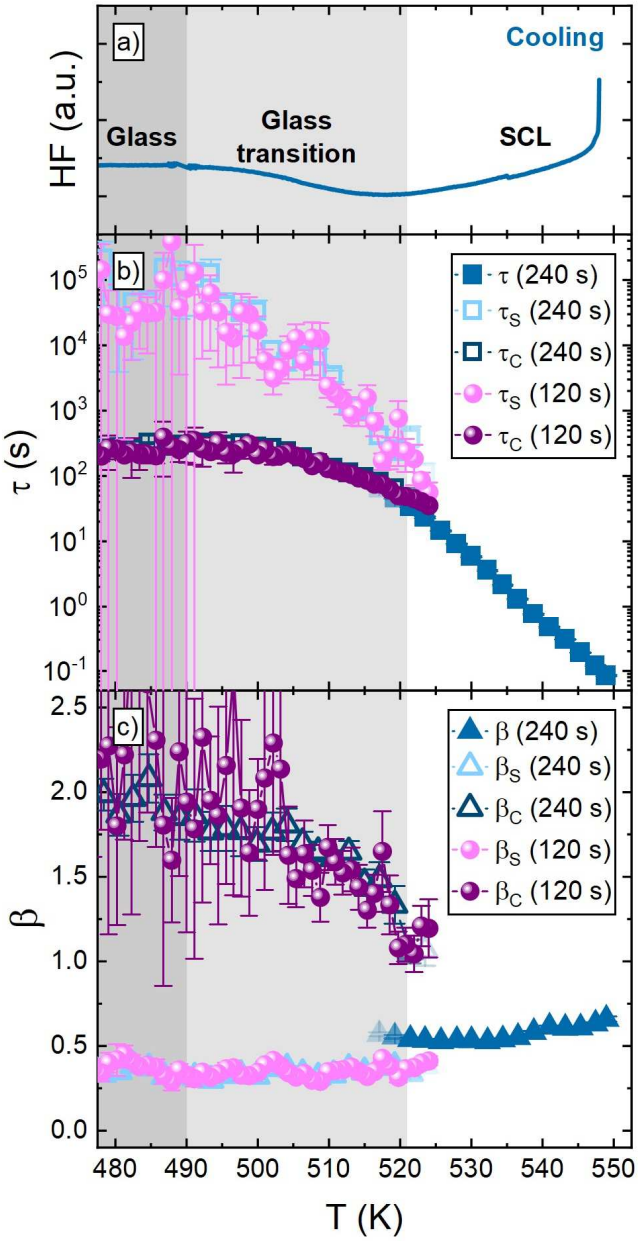

Figure 6.2: A comparison of the KWW_{MULTI} fitting results for g_2 data obtained with 240 s and 120 s evaluation window size. Both create comparable results, yet the 120 s window size feature increased scatter.

Here, the large evaluation window size of 240 s in combination with the underlying temperature change leads to a broader relaxation time spectrum that contributes to the determined g_2 decorrelation, and hence, the decay appears to be more stretched with accordingly lower β values. Smearing issues must be taken into account if absolute β values shall be compared yet Figure 6.3 demonstrates that qualitative comparisons are still appropriate since both β data sets show rather constant offsets and hence share the same temperature trends.

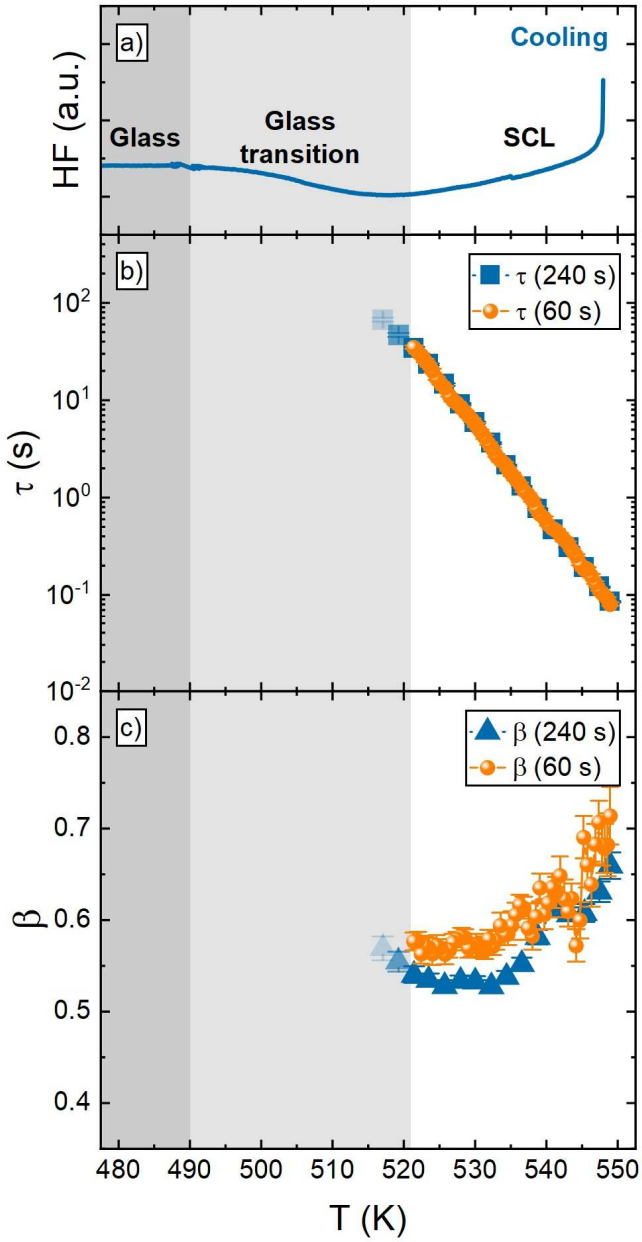

Figure 6.3: Comparing the KWW fitting results from for g_2 data obtained with 240 s and 120 s evaluation window size in the SCL state (in the non-equilibrium, KWW fitting is found to be inadequate, see Paper II). While the obtained relaxation times are basically identical, the shape exponents show significant offsets due to the increased smearing effect in the 240 s g_2 data.

6.1.2 Sample transit decorrelation as a measurement artifact

XPCS measurements are highly sensitive to positional changes of the measured material. To understand this, we must consider that the photon flux intensity within the beam spot is not evenly distributed. Instead, it is usually approximated through a Gaussian distribution [254,272,284], meaning that it features a maximum in the beam center which decays radially towards the edges, as sketched in Figure 6.4. Hence, any sample material

displacement in a direction perpendicular to the incoming X-ray beam changes the photon intensity with which each atom is radiated. This is schematically illustrated in Figure 6.4 on hand of the solid and dotted gray lines. Accordingly, the individual scattering amplitude $a_j(\mathbf{q})$ of each atom j in the ensemble is altered (a higher incoming photon intensity increases $a_j(\mathbf{q})$ and vice versa). On the edges of the beam spot, atoms even may enter or leave the spot completely, as demonstrated through the lower atom in Figure 6.4. This causes a 'refilling' of the sample volume irradiated by the beam spot. Constant motion of sample material will then lead to a complete exchange of the scattering ensemble after a certain time. This will naturally lead to an observable decorrelation, the so-called transit decorrelation, which has been demonstrated by e.g. XPCS studies on a flowing colloid solution by S. Busch et al. [272] or also by DLS studies by J. Gabriel et al. [254].

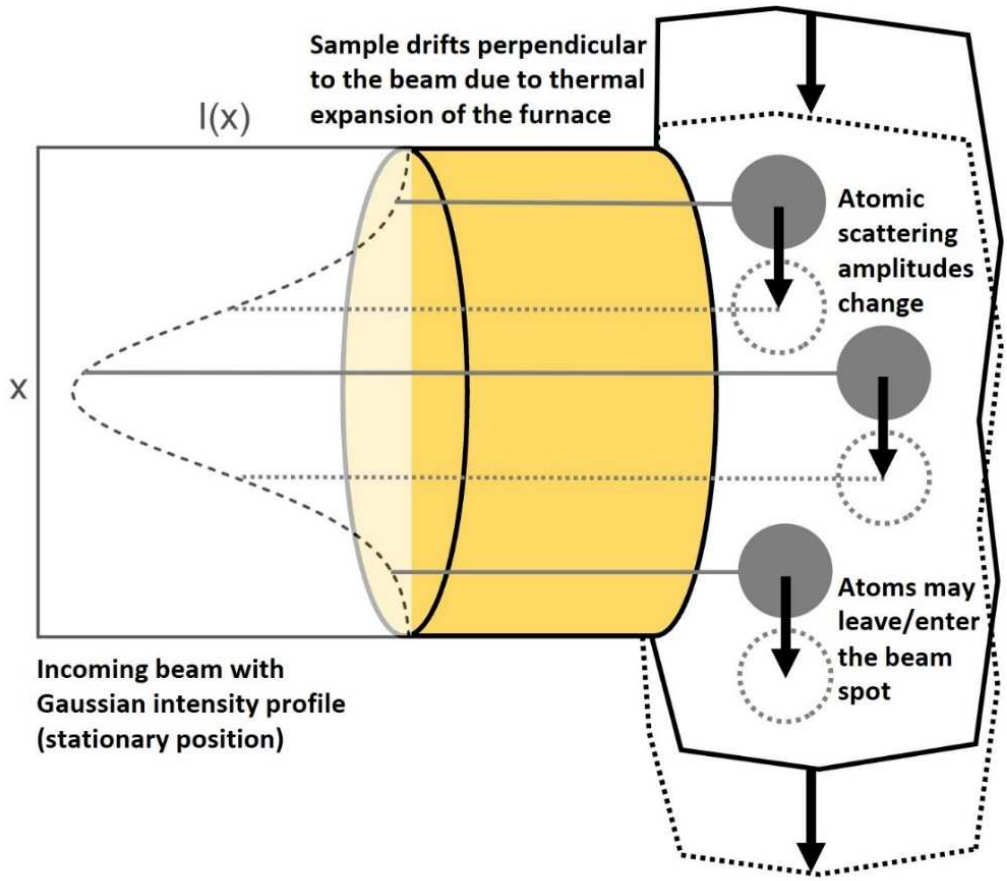

Figure 6.4: The underlying mechanism of the sample transit decorrelation effect schematically explained. The X-ray beam features a highly stabilized position. Its radial distribution of photon intensity follows a Gaussian function. Hence, a perpendicular motion of the sample in relation to the beam leads to a change of the individual scattering amplitudes of each atom. Atoms can even enter or leave the volume illuminated by the beam spot, as indicated by the lowest atom.

Reconsidering the mathematical formulations of the first order correlation function g_1 and the intensity autocorrelation function g_2 in the Equations (4.33), (4.34), and (4.35),

we see that transit decorrelation manifests through the pre-exponential factor $\sum_j^N \sum_k^N a_j(\mathbf{q}, t)\, a_k(\mathbf{q}, 0)$. Due to the multiplicative formulation, the aforementioned changes in the individual scattering amplitudes will lead to a decrease of this pre-exponential factor towards zero over time, ultimately causing a complete decorrelation in g_1 and g_2. S. Busch et al. [272] suggest to factorize the observed $g_2(t)$ decay into an actual atomic dynamics contribution $g_{2,Dynamics}$ (reflecting e.g. α-relaxation processes or stress-driven ballistic-like atomic motions as discussed in Paper II) and a macroscopic sample transit contribution $g_{2,Transit}$ as

$$g_2(t) = g_{2,Dynamics}(t)\; g_{2,Transit}(t). \tag{6.1}$$

The transit decorrelation stemming from a macroscopic sample material motion perpendicular to the beam with a constant velocity can be calculated by envisioning that the atoms 'scan' through the Gaussian intensity profile of the beam spot of width h with the drift velocity ν, as sketched in Figure 6.4 [91]. Mathematically, this is handled through an integration over the Gaussian intensity peak function. The result is an error function expression, which basically resembles a KWW equation with a shape exponent of exactly 2 [254,272]:

$$g_{2,Transit}(t) = b + c \exp\left(-\left(\frac{t}{\tau_{Transit}}\right)^2\right). \tag{6.2}$$

The parameter $\tau_{Transit}$ then characterizes the decorrelation timescale and corresponds to the time it takes one atom to travel through the beam spot as

$$\tau_{Transit} = \frac{h}{\nu}. \tag{6.3}$$

The temperature scanning XPCS studies reported in Paper II were performed using a custom oven made from nickel, which is placed perpendicular to the incoming beam. The continuous heating or cooling thus leads, in a first order approximation, to a typical sample transit scenario with constant drift velocity ν. Combining Equation (6.1), Equation (6.2), and the KWW_{MULTI} fit approach from Paper II would then lead to a general three component fit to describe the g_2 decay as

$$\begin{aligned} &g_2(t) \\ &= b + c\left[\exp\left(-2\left(\frac{t}{\tau_S}\right)^{\beta_S}\right) \exp\left(-2\left(\frac{t}{\tau_C}\right)^{\beta_C}\right) \exp\left(-\left(\frac{t}{\tau_{Transit}}\right)^2\right)\right]. \end{aligned} \tag{6.4}$$

Figure 6.5 illustrates the interplay, or, more precisely, the rivalry between these three decorrelation mechanisms. We can see that fast temperature changes can lead to thermal expansion motions that constitute a critical experimental artifact. According to Equation (6.2), a too high thermal drift velocity would decrease $\tau_{Transit}$ to a point where it dominates the observed g_2 data and leads to a premature decorrelation that renders it impossible to study the slower timescales of the actual atomic dynamics.

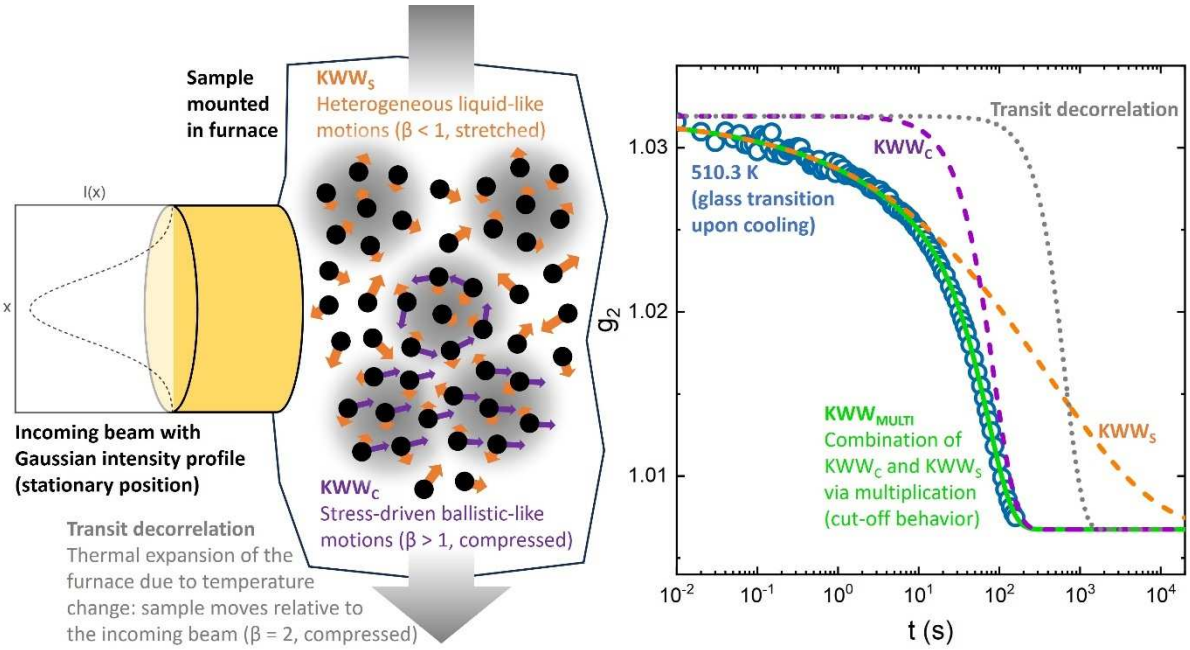

Figure 6.5: Schematic illustration of all three decorrelation contributions that compete in a g_2 data set stemming from the continuous cooling XPCS measurement at 510.3 K (glass transition region, see batch B5 in Paper II). The KWW_S and KWW_C components reflect atomic dynamics, while the transit decorrelation stems from a macroscopic drift motion of the sample due to thermal expansion.

Furthermore, the compressed shape of the transit decorrelation resembles the compressed nature of the KWW_C component that reflects the stress-driven ballistic-like atomic motions. Too similar values of $\tau_{Transit}$ and τ_C would make a separation between both effects difficult, leaving the interpretation questionable. Thus, $\tau_{Transit}$ must be taken into account, as it is described in the Supplementary Materials of Paper II. The thermal drift velocity can be estimated from the length L of the oven (about 7 cm), the thermal expansion coefficient α of Nickel (1.3×10^{-5} K^{-1}) and the used (heating and cooling) rate q_h of 1 K/min according to

$$v = L\,\alpha\,q_h. \tag{6.5}$$

Equation (6.2) then leads to a $\tau_{Transit}$ estimation of 658 s. Figure 6.6 picks up the g_2 data from the six representative evaluation batches from Paper II (located in the glass, glass

transition, and SCL for heating and cooling scan, respectively) and compares the KWW and KWW_{MULTI} fits with the transit decorrelation. Thanks to the highly compressed shape and the relatively high $\tau_{Transit}$, all major decorrelation stemming from the thermally induced sample transit occurs outside the temporal range of the evaluated g_2 data. Consequently, the transit decorrelation plays no major role and can be neglected for further interpretation, as it is done in Paper II.

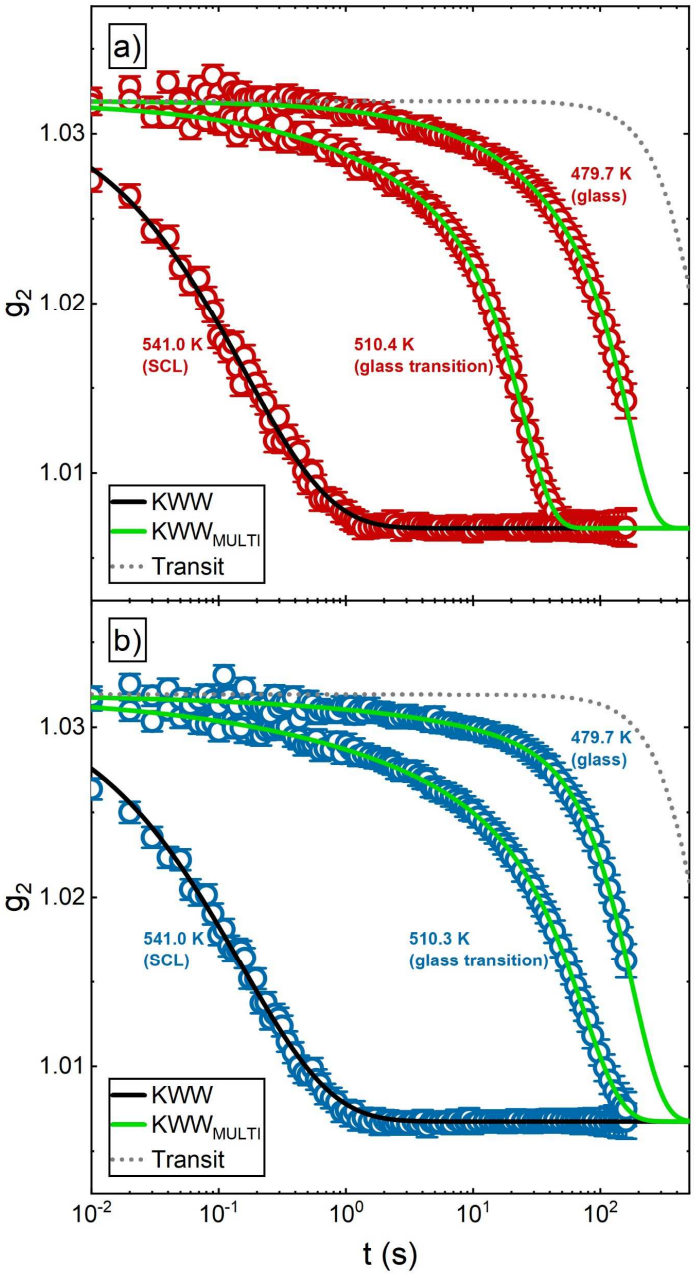

Figure 6.6: The g_2 data six representative 240 s evaluation batches located in the glass, the glass transition, and the SCL state upon a) heating and b) cooling with 1 K/min (compare the batches B1-B6 from Paper II). The respective KWW and KWW_{MULTI} fits as well as the estimated transit decorrelation are indicated. Transit decorrelation occurs mainly outside of the temporal range of the evaluation window and can be therefore neglected.

These findings demonstrate that the ultimately chosen evaluation window size of 240 s constitutes a robust compromise that balances the aspects of required temporal resolution and smearing (see previous chapter) while still holding the transit decorrelation artifact at bay, hence allowing to draw meaningful conclusions about the actual atomic dynamics. Yet, the results also highlight the methodical restrictions of temperature scanning XPCS. The underlying temperature change rates must always be adapted to the framework of the experimental setup as well as to the timescales of the dynamics that shall be observed. It should be mentioned that the here discussed transit decorrelation experiences may have contributed to the latest innovations at the ESRF ID10 beamline, namely the construction of a less temperature-sensitive furnace device [285].

6.1.3 Correcting the temperature of temperature scanning XPCS measurements

Finally, the issue of temperature correction shall be addressed. Temperature management at synchrotron beamlines often relies on custom-built heating devices, which might feature significant offsets between the set temperature and the actual temperature. Here, temperature scanning XPCS offers a methodological advantage, as it bears the possibility to perform temperature corrections based on the observation of the rate-dependent crystallization onset. The underlying principle is found in the rigid nature of the forming crystallites. Their ordered structure is very unsensitive to thermally activated structural rearrangements, i.e., rather invariant in relation to the fast dynamics of the surrounding liquid. The crystalline precipitates create distinct Bragg peaks which can be identified in the raw signal of the detector, namely as regions of increased intensity within the speckle patterns. Figure 6.7a) illustrates this for an Au-based metallic glass that has undergone significant crystallization during a XPCS heating scan experiment with a rate of 1 K/min. Naturally, the highly stationary Bragg peaks increase correlation among consecutive speckle patterns, and we observe massively rising g_2 levels as soon as crystallization sets in, see Figure 6.7b). As shown in Figure 6.7c), this effect can be clearly quantified on hand of the minimum g_2 value of each evaluation batch.

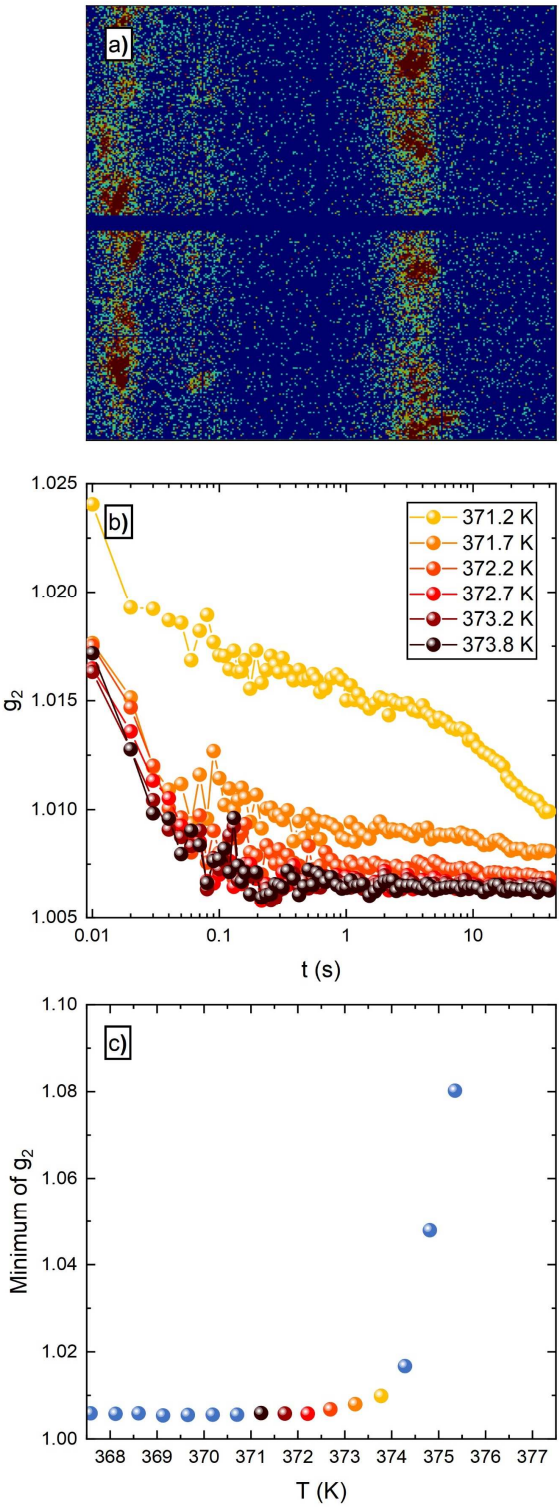

Figure 6.7: a) Distinct Bragg peaks in the speckle pattern of a XPCS heating scan on an Au-based metallic glass former after primary crystallization has occurred. b) As soon as these Bragg peaks arise, the absolute g_2 values increase significantly, which can be quantified on hand of the minimum g_2 value of each batch, as illustrated in c). The g_2 minima corresponding to the curves shown in b) are here highlighted in their respective colors.

Comparing the massive crystallization signal from the g_2 minimum values with ex-situ DSC scans performed with the same heating rate of 1 K/min then allows determine the

temperature offset of the XPCS setup in relation to the (calibrated) DSC device. Figure 6.8 illustrates this on hand of the already introduced Au-based system as well as a Pd-based glass former with a distinctly higher crystallization temperature.

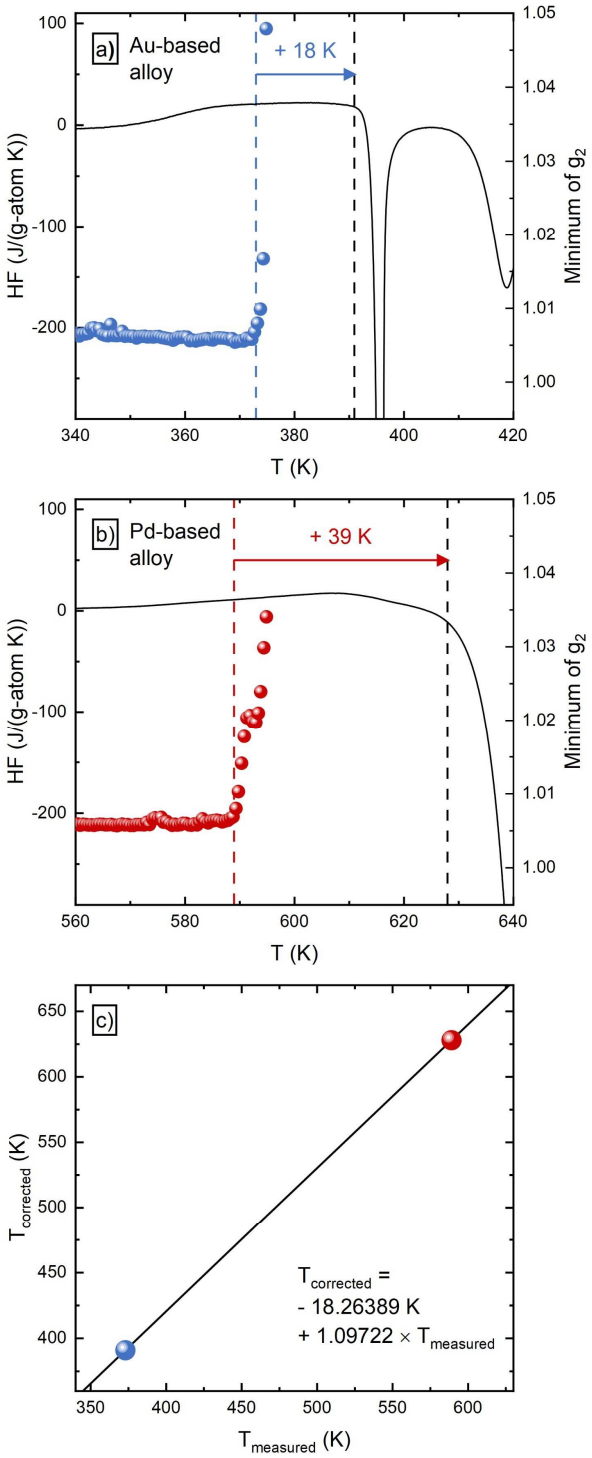

Figure 6.8: A comparison for a) an Au-based BMG former and a b) Pd-based BMG former between the g_2 minima from XPCS heating scans (red and blue points) and ex-situ DSC scans, all performed with a rate of 1 K/min. The crystallization onsets are marked by dashed lines, the arrows indicate the temperature offsets. In c), these temperature offsets are used to create a temperature correction for the temperature scanning XPCS data shown in this work and in Paper II.

Both systems are measured with 1 K/min heating scans in the present XPCS setup as well as by DSC. The dashed lines indicate the onsets of crystallization in the minimum g_2 results and the DSC scan, the arrows indicate the corresponding temperature offsets. With values between about 20 and 40 K, the offsets appear to be significant. These findings highlight the very urgency to incorporate temperature corrections when performing synchrotron studies with custom-built furnaces.

Based on the two offset values, a linear correction function can be established, see Figure 6.8c), which is valid at least for the temperature range between both crystallization onsets. For the temperature scanning XPCS studies on the $Pt_{42.5}Cu_{27}Ni_{9.5}P_{21}$ alloy from Paper II, this is the case. The exceptionally good agreement between ex-situ DSC scans and the XPCS results in this publication speaks in favor of the whole correction approach.

6.2 Multiplicative versus additive KWW approaches to describe XPCS decorrelation in the non-equilibrium state

6.2.1 The multiplicative KWW approach in detail

The postulation of the KWW_{MULTI} fitting approach in Paper II might be the scientifically most outstanding aspect of this dissertation. While earlier works only differentiated between stretched decorrelation in the equilibrium [26,286–288] and compressed decorrelation in the non-equilibrium [30,259,261,262,265,269,270,286,288], the successful application of the KWW_{MULTI} model instead suggests a coexistence, or rather rivalry, of both these decorrelation types in the glass or glass transition state. This puts the fundamental understanding of atomic-scale dynamics of metallic glasses into perspective, as it implies that the non-equilibrium state is characterized by the superposition of two different styles of atomic motives. These are namely (sub-)diffusive motions known to be typical for the equilibrium supercooled liquid state as well as ballistic-like motions that are a consequence of the internal stress states that arise with vitrification.

The present chapter shall provide supplementary considerations that might help to understand why such a scenario is ultimately connected to the multiplicative formulation of the KWW_{MULTI} fitting function. To do so, we imagine a non-equilibrium state, in which particles are subject to the two named types of motions as illustrated on hand of three representative atoms in Figure 6.9. In general, the distance $\Delta\mathbf{r}_{j\text{-}k}(t)= \mathbf{r}_j(t)-\mathbf{r}_k(0)$ which an

atom j travels within the time t in relation to an atom k consists of a sub-diffusive component that causes the stretched decay, $\Delta\mathbf{r}_{\text{j-k,S}}(\text{t})$ and a ballistic-like component that causes the compressed decay, $\Delta\mathbf{r}_{\text{j-k,C}}(\text{t})$ as

$$\Delta\boldsymbol{r}_{j-k}(t) = \Delta\boldsymbol{r}_{j-k,S}(t) + \Delta\boldsymbol{r}_{j-k,C}(t). \tag{6.6}$$

Remembering Equation (4.32), the ISF then results as

$$f(\boldsymbol{q},t) = \left\langle \sum_{j}^{N}\sum_{k}^{N} a_j(\boldsymbol{q},t)\, a_k(\boldsymbol{q},0) \exp\left(-i\,\boldsymbol{q}\,\left(\Delta\boldsymbol{r}_{j-k,S}(t) + \Delta\boldsymbol{r}_{j-k,C}(t)\right)\right)\right\rangle. \tag{6.7}$$

As described in Chapter 4.3.3, the ISF consists of a self part (j=k) that regards the self-correlation of atoms over time, i.e. their individual dislocations in relation to themselves, and a distinct part (j≠k) that regards the dislocation of atoms in relation to their surroundings, i.e. to other atoms.

In the following, we will only consider self-correlation to illustrate the derivation of the $\text{KWW}_{\text{MULTI}}$ formula, since this simplification facilitates the mathematical treatment. First, we accommodate the heterogeneity of the sub-diffusive motions $\Delta\mathbf{r}_{\text{j-k,S}}(\text{t})$ by assuming a Gaussian distribution of $\Delta\mathbf{r}_{\text{j-k,S}}(\text{t})$, see Chapter 2.2.2. The ensemble averaging procedure then leads to the expression [90,91,271]

$$\left\langle \exp\left(-i\,\boldsymbol{q}\,\left(\Delta\boldsymbol{r}_{j-k,S}(t)\right)\right)\right\rangle = \exp\left(-\frac{\boldsymbol{q}^2\,\Delta\boldsymbol{r}^2_{j-k.S}(t)}{6}\right). \tag{6.8}$$

Here, the term $\Delta\mathbf{r}^2_{\text{j-k.S}}(\text{t})$ allows us to recapitulate Chapter 2.1.1 and substitute it with the mean squared displacement $\langle r_S^2(\text{t})\rangle$ of a sub-diffusive process according to Equation (2.3) as

$$\exp\left(-\frac{\boldsymbol{q}^2\,\langle r_S^2(\text{t})\rangle}{6}\right) = \exp\left(-\frac{\boldsymbol{q}^2\,K_S\,t^{\alpha_S}}{6}\right), \tag{6.9}$$

with a respective (sub-)diffusion coefficient K_S and a sub-diffusion-typical exponent α_S below unity (see also Figure 2.1). The same treatment for the ballistic-like motions $\Delta\mathbf{r}_{\text{j-k,C}}(\text{t})$ leads then to

$$\exp\left(-\frac{\boldsymbol{q}^2\,\langle r_C^2(\text{t})\rangle}{6}\right) = \exp\left(-\frac{\boldsymbol{q}^2\,K_C\,t^{\alpha_C}}{6}\right), \tag{6.10}$$

with a super-diffusion coefficient K_C and a super-diffusion-typical exponent α_C above unity. Further disregarding the individual scattering amplitudes (their influence was discussed in terms of the transit decorrelation in Chapter 6.1.2) and splitting the sum in the exponential term from Equation (6.7) brings us to the following expression

$$f(\boldsymbol{q},t) \propto \exp\left(-\frac{\boldsymbol{q}^2\, K_S\, t^{\alpha_S}}{6}\right) \exp\left(-\frac{\boldsymbol{q}^2\, K_C\, t^{\alpha_C}}{6}\right), \tag{6.11}$$

where we can already recognize the multiplicative interplay of the sub-diffusive and ballistic-like components. If we now commemorate the Siegert relation $f^2 \propto g_2$ from Equation (4.36) as well as the formulation of the KWW_{MULTI} function from Paper II,

$$g_2(\boldsymbol{q},t) = b + c \exp\left(-2\left(\frac{t}{\tau_S}\right)^{\beta_S}\right) \exp\left(-2\left(\frac{t}{\tau_C}\right)^{\beta_C}\right), \tag{6.12}$$

it becomes obvious that the diffusion exponents α_S and α_C directly predetermine the values of the shape exponents β_S and β_C. In other words, we here derived a quite direct relation between diffusion on the one hand and structural relaxation or decorrelation on the other hand, which was stated earlier but not further explained in Chapter 2.1.2.

It must be noted that strictly speaking, considering just the self part of the ISF is only valid in case of normal diffusion and when particles do not interact with each other, as it is e.g. found for classical Brownian motion [90,91,271]. In our case of a deeply undercooled or already vitrified liquid, this is hardly true, since atomic rearrangements have become heterogeneous, rather sub-diffusive, and highly cooperative so that the ISF is also determined by the distinct part. This is further underlined by considering that the present XPCS studies are performed at a q value of 2.86 $Å^{-1}$, hence directly at the FSDP of the $Pt_{42.5}Cu_{27}Ni_{9.5}P_{21}$ glass former. The FSDP incorporates structural information from short to medium range and the XPCS experiment therefore probes individual atomic motions as well as their motions in relation to the surroundings. Accordingly, the established direct relation between the two types of diffusive motion and the two decorrelation components of the KWW_{MULTI} must be handled with caution and should be seen as what it is, an approximation. Nevertheless, it can be argued that it still holds as a robust first order approach, since both motion types should manifest in the self as well as the distinct part of the ISF. Hence, the considerations based on self correlation should be sufficient to illustrate the principle.

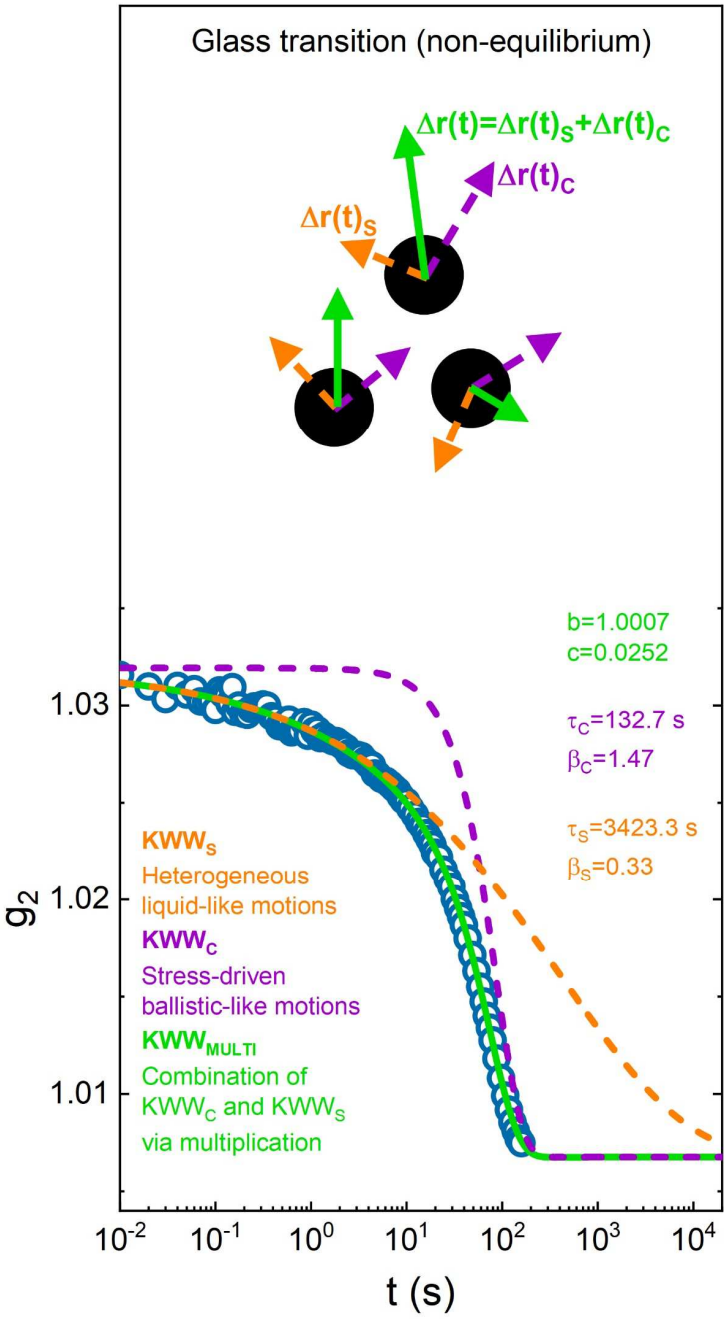

Figure 6.9: The KWW_{MULTI} approach assumes that individual atoms can be subject to stress-driven ballistic-like motions (purple vectors) as well as (sub-)diffusive liquid-like motions (orange vectors). Their total dislocation vector therefore results from a vector sum of both components (green vectors). The g_2 fit function then follows as a multiplicative formulation that allows a functional and physically meaningful description of the typical cut-off shape of the observed g_2 decorrelation in the non-equilibrium.

6.2.2 Additive KWW fitting as a situation-dependent alternative

Fit functions including a sum of two (or more) KWW expressions are found in literature [282,289–291]. These can be a functional approach to describe complex shapes in

decorrelation curves obtained by DLS or XPCS. During the writing process of Paper II, a vital debate among the authors arose, if such an additive model, further termed KWW_{ADD}, could be a more suitable alternative than the KWW_{MULTI} to describe the 'cut-off' behavior in the non-equilibrium g_2 data of the $Pt_{42.5}Cu_{27}Ni_{9.5}P_{21}$ alloy. In the following, the KWW_{ADD} model shall be briefly introduced and discussed. Similar considerations can be found in the Supplementary Information of Paper II. It shall be respectfully stated that credit must be given to Dr. Yuriy Chushkin, the ESRF researcher who initially advocated the use of an additive approach for the non-equilibrium g_2 data from Paper II.

The underlying conception would be that vitrification occurs as a kind of nucleation and growth process of vitrified regions. Picking up the spatial heterogeneity scenario used in Paper II and introduced in Chapter 2.2.2, the regions that vitrify first upon cooling would be those with slower dynamics, termed 'rigid domains' in the article and illustrated with a gray background in the respective figures. Vitrification would then be finished when the majority of the sample volume has changed from the liquid to the glassy state. The glass transition upon heating can be seen as the inverse process, namely nucleation and growth process of equilibrated liquid regions. The approach further assumes that stretched and compressed decay components stem from spatially exclusive regions, i.e. the stretched decay component is solely addressed to the liquid domains while the compressed decay is solely addressed to the vitrified domains. In other words, a region behaves eighter exclusively glass-like (compressed decay) or exclusively liquid-like (stretched decay). Here lies the fundamental difference to the KWW_{MULTI} conception, which assumes that atoms can be subjected to both types of motion, hence contributing to the stretched and compressed decorrelation components simultaneously, see Figure 6.9. The KWW_{ADD} concept is schematically illustrated in Figure 6.10.

We again consider only the self part for simplification reasons. It follows that the spatial segregation of the two exclusive types of motion allows a separation of the ISF into the sum of two independent ISFs, one for the liquid-like equilibrium regions including N atoms and one for the glass-like non-equilibrium regions including M atoms as

$$f(\boldsymbol{q}, t) = \tag{6.13}$$

$$\langle \sum_{j}^{N} \sum_{k}^{N} a_j(\boldsymbol{q},t)\, a_k(\boldsymbol{q},0) \exp\left(-i\, \boldsymbol{q}\, \Delta \boldsymbol{r}_{j-k,S}(t)\right)\rangle$$
$$+ \langle \sum_{o}^{M} \sum_{p}^{M} a_o(\boldsymbol{q},t)\, a_p(\boldsymbol{q},0) \exp\left(-i\, \boldsymbol{q}\, \left(-i\, \boldsymbol{q}\, \Delta \boldsymbol{r}_{o-p,C}(t)\right)\right)\rangle.$$

With the Siegert relation from Equation (4.36), the KWW_{ADD} model for the g_2 data then follows in form of

$$g_2(\boldsymbol{q},t) = b + c\, \left[x\, \exp\left(-\left(\frac{t}{\tau_{S,ADD}}\right)^{\beta_{S,ADD}}\right) + (x-1)\, \exp\left(-\left(\frac{t}{\tau_{C,ADD}}\right)^{\beta_{C,ADD}}\right)\right]^2. \quad (6.14)$$

If we finally expand the squared expression, we see that KWW_{ADD} consists of a stretched part $KWW_{S,ADD}$ (first term), a compressed part $KWW_{C,ADD}$ (third term), as well as a cross term (second term):

$$g_2(\boldsymbol{q},t) = b + c\, x^2\, \exp\left(-2\left(\frac{t}{\tau_{S,ADD}}\right)^{\beta_{S,ADD}}\right) + 2\, c\, (x-x^2) \exp\left(-\left(\frac{t}{\tau_{S,ADD}}\right)^{\beta_{S,ADD}} - \left(\frac{t}{\tau_{C,ADD}}\right)^{\beta_{C,ADD}}\right) + c\, (x-1)^2\, \exp\left(-2\left(\frac{t}{\tau_{C,ADD}}\right)^{\beta_{C,ADD}}\right). \quad (6.15)$$

The transition coefficient x quantifies the degree of equilibration with values between 0 and 1 and could for example reflect the (volume) portion of the equilibrated regions in relation to the whole illuminated sample volume. Accordingly, x=0 stands for a completely glassy state while x=1 indicates a completely equilibrated liquid state.

In practice, KWW_{ADD} was found to actually model the cut-off decorrelation shape of non-equilibrium g_2 data in a satisfying manner, as shown in Figure 6.10. The illustration further demonstrates that x effectively distributes the total decay contrast c among the three components of Equation (6.15), namely $KWW_{S,ADD}$, $KWW_{C,ADD}$, and the cross term.

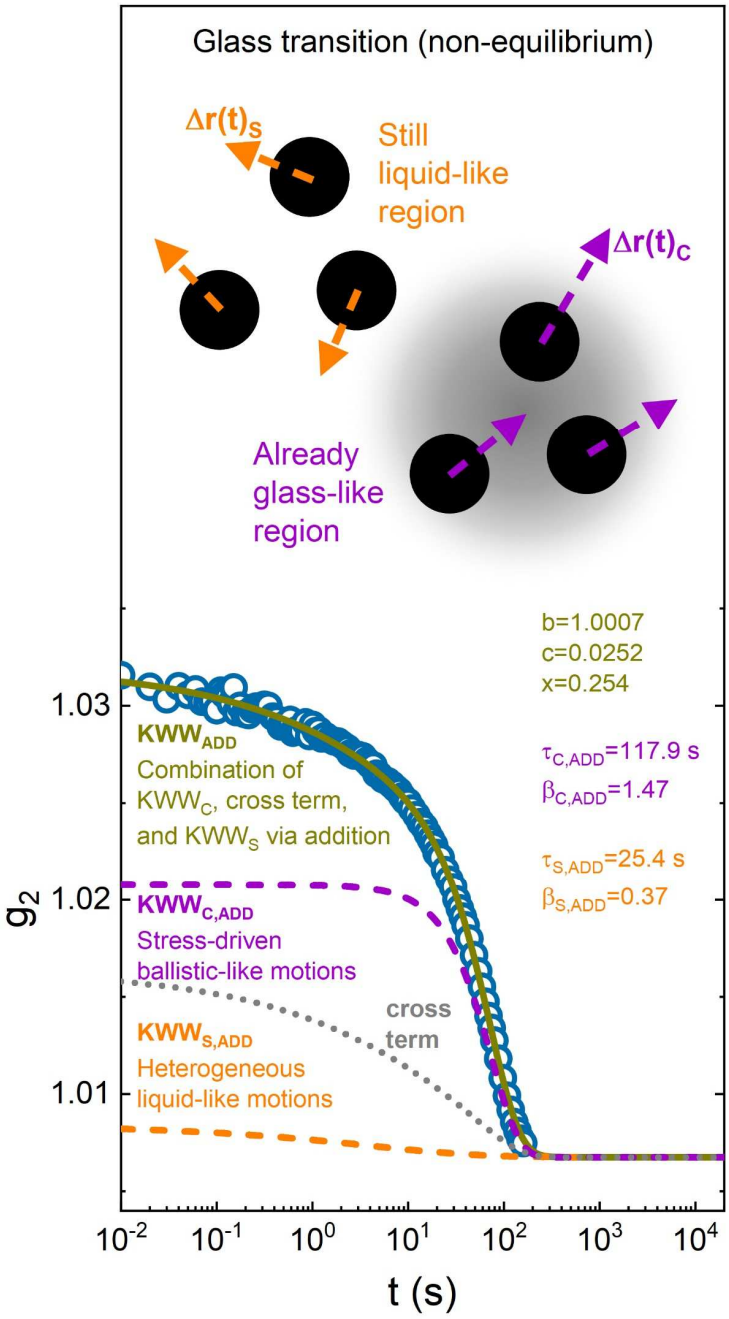

Figure 6.10: The KWW_{ADD} approach assumes that stress-driven ballistic-like motions (purple vectors) and (sub-)diffusive liquid-like motions (orange vectors) are well separated in different spatial regions. The g_2 fit function then follows as an additive formulation that also allows a functional description of the typical cut-off shape of the observed g_2 decorrelation in the non-equilibrium.

Figure 6.11 compares the KWW_{MULTI} fitting results published in Paper II with the KWW_{ADD} results. For KWW_{ADD} fitting, x is treated as a free parameter, see Figure 6.11a) and e). A comparison to the ex-situ DSC scans in Figure 6.11b) and f) shows that x roughly shows the expectable behavior by roughly mimicking the heat flow curve, hence showing high values around unity in the SCL state and a decrease towards zero in direction of the glassy state. The $KWW_{C,ADD}$ parameters, $\tau_{C,ADD}$ and $\beta_{C,ADD}$ are fairly similar to τ_C and β_C resulting

from the KWW_{MULTI} approach. The same applies for $\beta_{S,ADD}$, which retraces the course of β_S. Only $\tau_{S,ADD}$ differs significantly from its KWW_{MULTI} counterpart τ_S. Instead of following a steep liquid-typical temperature dependence throughout the glass transition region as τ_S does, $\tau_{S,ADD}$ behaves quite similar to $\tau_{C,ADD}$ and shows a less temperature-sensitive course as soon as the system leaves equilibrium. In other words, a large separation between the timescales of compressed and stretched components as we see it for KWW_{MULTI} is not observed. It shall be mentioned that these results cannot be fundamentally changed through altered fitting conditions like e.g. fixing x according to the sigmoidal shape of the calorimetric glass transition signal or alternations in the parameters b or c.

These findings demonstrate that the experimentally given cut-off shape of the non-equilibrium g_2 curves in combination with the mathematical construction of KWW_{ADD} forces both the timescales $\tau_{S,ADD}$ and $\tau_{C,ADD}$ to remain at fairly similar values (see e.g. the parameters shown in Figure 6.10). Any significant difference between $\tau_{S,ADD}$ and $\tau_{C,ADD}$ would inevitably lead to a loss of the single-step decay and instead, a double-step decay would arise, as it will be exemplarily shown later in Figure 6.12. Yet, in the present data set, we exclusively observed (cut-off) single-step decays. Moreover, it shall be mentioned that the timescale similarity dictated by the mathematical design allows to explain the large error bars found for $\tau_{S,ADD}$ in Figure 6.11. While the compressed part of the g_2 data is well defined and allows a robust determination of $KWW_{C,ADD}$, the data range that determines $KWW_{S,ADD}$ remains sparse, causing the large error bars and increased scatter.

The close link between both relaxation times predetermines unrealistically fast $\tau_{S,ADD}$ values throughout the whole non-equilibrium range. This leads to the counterintuitive situation that $\beta_{S,ADD}$ shows signs of equilibration (stretched), while the course pf $\tau_{S,ADD}$ rather indicates vitrified behavior. Accordingly, a physically meaningful picture as discussed in Paper II for the KWW_{MULTI} approach cannot be evolved here. KWW_{ADD} remains as a rather unphysical alternative, at least for the present data set obtained under the respective experimental conditions. Nevertheless, decorrelation in non-equilibrium metallic systems still remains far from being fully understood. Additive fitting or even combinations between additive and multiplicative approaches might emerge as meaningful alternatives, e.g. for XPCS studies at q values asides the FSDP or in case of alloy-specific transition effects.

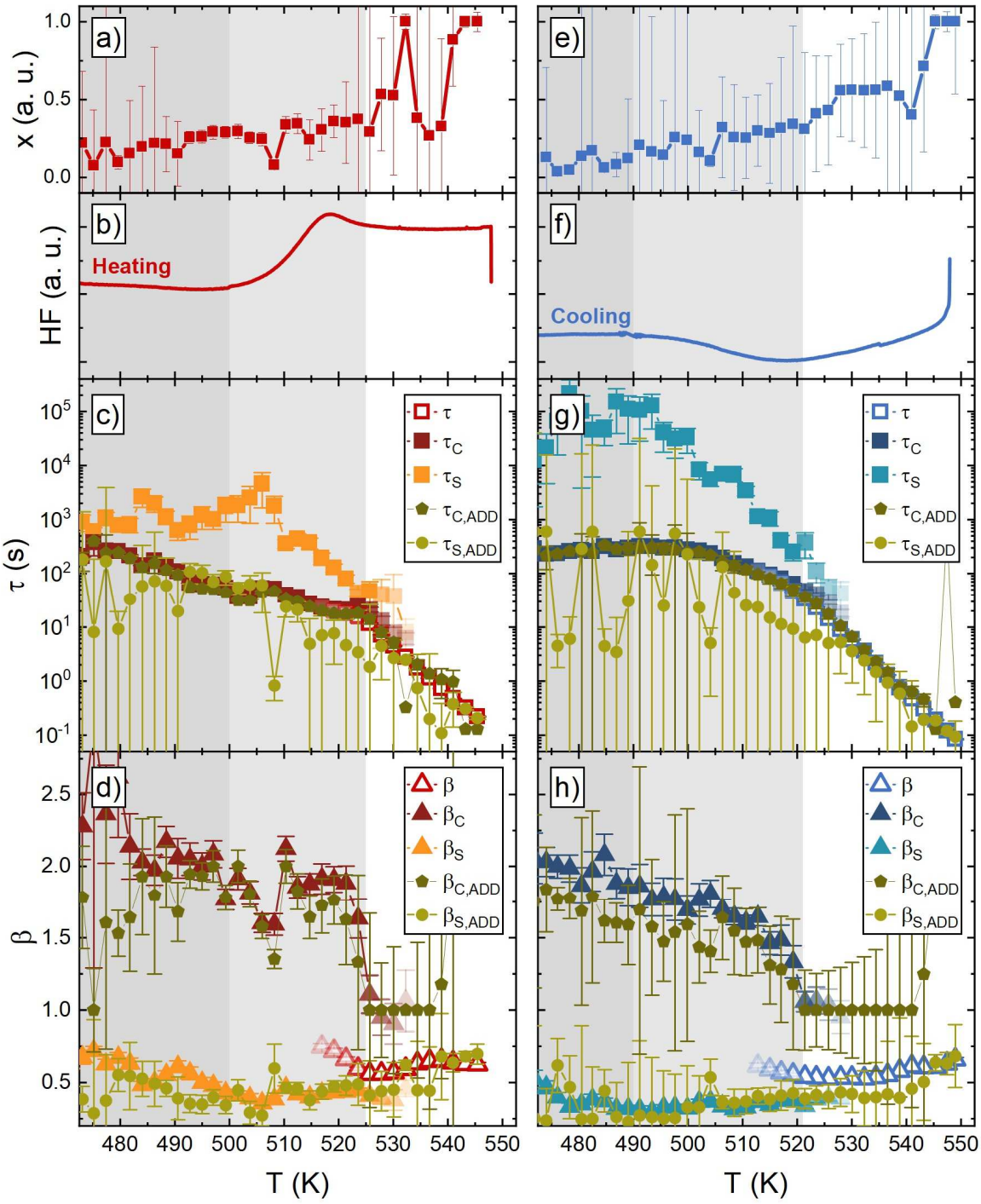

Figure 6.11: Comparison of the KWW_{MULTI} fit results from Paper II with the results from the present KWW_{ADD} fitting. The fitted f values roughly follow the heat flow curves, thereby indicating the fraction of liquid-like and glass-like material volume. The KWW_{MULTI} and KWW_{ADD} results largely agree, only $\tau_{S,ADD}$ behaves fundamentally different than and τ_S and rather follows the trend of $\tau_{C,ADD}$. This can be addressed to the mathematical construction of the KWW_{ADD} function.

A small thematical excursion shall provide an example of a scientific case where the additive model constitutes a very adequate option. It is well-known that phase separation and liquid-liquid transition effects can be found in PdNiP metallic glass formers [292–305]. Figure 6.12 grants a preview on so far unpublished g_2 decorrelation data of the

$Pd_{41.25}Ni_{41.25}P_{17.5}$ alloy, stemming from the same XPCS measurement campaign as the $Pt_{42.5}Cu_{27}Ni_{9.5}P_{21}$ results from Paper II.

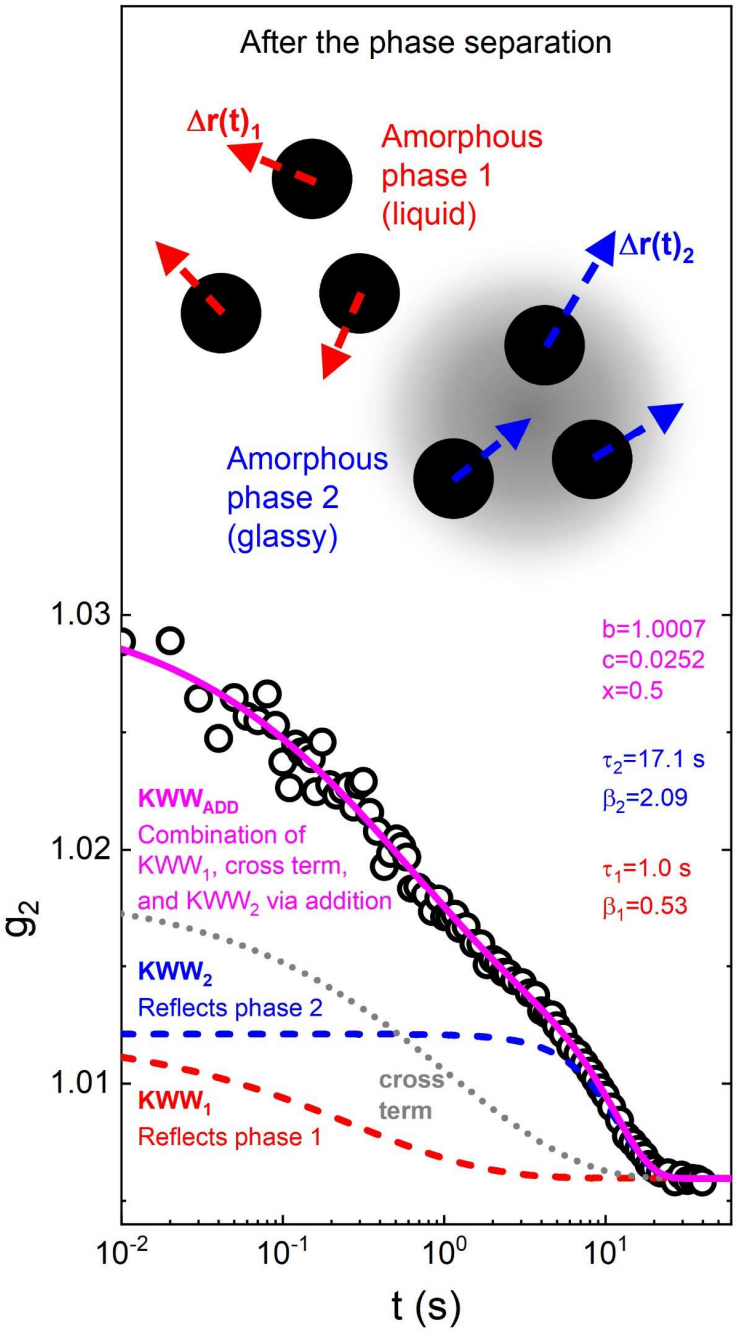

Figure 6.12: KWW_{ADD} is a suitable choice to describe the g_2 decorrelation observed for a $Pd_{41.25}Ni_{41.25}P_{17.5}$ sample that has previously undergone a phase separation, therefore showing a clear double-step decay. KWW_1 reflects the fast and stretched dynamics of the equilibrated phase 1, while KWW_2 reflects the slower and compressed dynamics of the still vitrified phase 2.

We observe a distinct double step appearance, which can be addressed to the phase separation that has previously occurred. Hence, the system consists of two different amorphous phases (phase 1 and phase 2) which come with distinctly separated

relaxation time distributions. At the temperature of the presented g_2 curve, phase 1 has already equilibrated in the SCL state, while phase 2 is still vitrified. Now, the additive KWW model can be adapted in the form of

$$g_2(\boldsymbol{q},t) = b + c\left[x\ \exp\left(-\left(\frac{t}{\tau_1}\right)^{\beta_1}\right) + (x-1)\ \exp\left(-\left(\frac{t}{\tau_1}\right)^{\beta_1}\right)\right]^2. \qquad (6.16)$$

Here, x reflects the (volume) fraction of the formed phase 1. The model allows for a well-adapted fit curve and furthermore provides physically meaningful results. While the equilibrated phase 1 shows fast dynamics with a relaxation time of τ_1=1.0 s and liquid-typical stretched shape (β_1=0.53), the still frozen phase 2 features (predominantly) slower and glass-typical compressed dynamics with τ_2=17.1 s and β_2=2.09, see Figure 6.12.

6.3 On the equilibrium supercooled liquid fragility of $Pt_{42.5}Cu_{27}Ni_{9.5}P_{21}$

This chapter will bundle all the fragility related results from Paper I (MDSC) and Paper II (XPCS) and combine them with additional DMA and FDSC data. Finally, a large-scale data comparison will be established, which allows a comprehensive evaluation of the $Pt_{42.5}Cu_{27}Ni_{9.5}P_{21}$ alloy's fragility and will further reveal a major issue of the VFT function.

6.3.1 Additional relaxation and transition time data from DMA and FDSC studies

The following chapter will present the results from isochronal DMA temperature scans as well as FDSC measurements of the dynamic glass transition and the fictive temperature, all performed on the $Pt_{42.5}Cu_{27}Ni_{9.5}P_{21}$ glass former. The respective methods and experimental details are described in the Chapters 4.1.3, 4.1.4 and 4.2.2. Fig. 6.13a) displays the normalized loss modulus E´´(ω,T) curves of all isochronal DMA temperature scans with applied modulation frequencies f between 0.1 and 30 Hz. The curves rise with temperature until a maximum is reached at the frequency-dependent dynamic glass transition $T_{g,dyn}(\omega)$, followed by a further decay in E´´(ω,T) with rising temperature. Here, the system's relaxation time equals the inverse angular frequency, see Equation (4.9). Naturally, $T_{g,dyn}(\omega)$ shifts to higher temperatures with increasing frequency and is indicated by filled pentagons in the respective curve color.

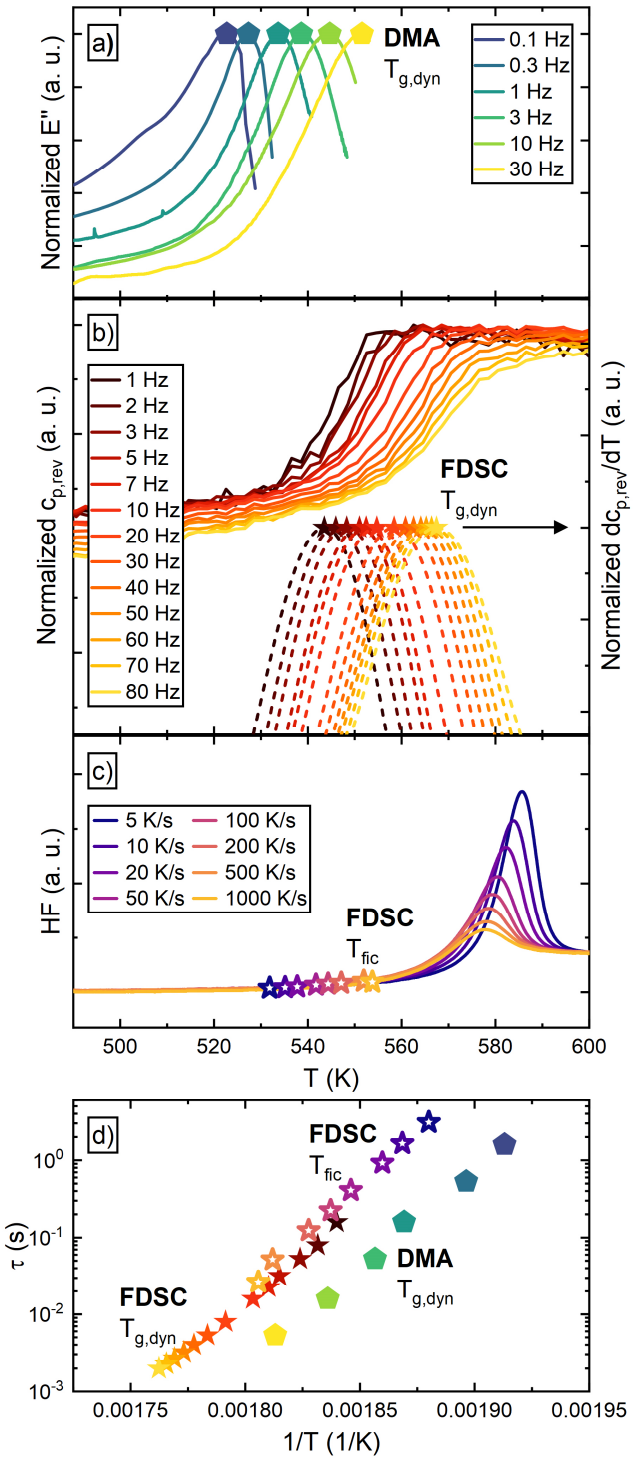

Fig. 6.13: In a), the normalized loss modulus curves of isochronal DMA temperature scans on the $Pt_{42.5}Cu_{27}Ni_{9.5}P_{21}$ metallic glass former are shown. $T_{g,dyn}$ depends on the measurement frequency f and manifests as the main peak of each curve, as highlighted. FDSC step response measurements on the same alloy are presented in b) as a function of the measurement frequency f. $T_{g,dyn}$ is reflected by a rise in the (normalized) $c_{p,rev}$. It is quantified by defining the inflection point (highlighted) via peak fitting of the derivative $dc_{p,rev}/dT$ (dashed lines). In c), 1000 K/s FDSC heating scans are shown, each one after cooling with different rates. T_{fic} (highlighted) is defined via the area matching method by Moynihan [306]. The Arrhenius diagram in d) compares the resulting data sets obtained by the three methods.

Fig. 6.13b) shows the reversing heat capacity $c_{p,rev}$ curves (solid lines) from the FDSC step response measurements normalized by their maximum value for best comparability. The dynamic glass transition manifests itself as a sigmoidal-like rise from the glassy level to the SCL level. This corresponds to a peak in the derivative $dc_{p,rev}/dT$ and can be fitted by a peak function, shown by the dotted lines in Fig. 6.13b). $T_{g,dyn}(\omega)$ is defined at the maximum of these peak fits (marking the inflection point of $c_{p,rev}$), analogous to the DMA evaluation. Again, Equation (4.9) accounts for the relationship between τ and ω. With rising frequency, $T_{g,dyn}(\omega)$ shifts to higher temperatures.

Fig. 6.13c) presents FDSC heating scans at a rate of 1000 K/s after cooling with different rates between 5 and 1000 K/s. As described in Chapter 4.1.4, the cooling rate-dependent T_{fic} values are determined using the Moynihan area matching method [240], while the corresponding transition times τ_{trans} are calculated according to Equation (4.14).

Finally, 6.12d) summarizes these results in an Arrhenius plot reflecting the temperature dependence of the apparent activation energy. The FDSC data sets, $T_{g,dyn}(\omega)$ and $T_{fic}(q_c)$, align very well and show the same steepness. The $T_{g,dyn}(\omega)$ data obtained by DMA features a practically identical slope as the FDSC data sets, but shows a distinct offset to them, which will be discussed in the next chapter.

6.3.2 Comparing timescales: On the fine differences between dynamics and kinetics as well as relaxation and retardation

In the following, we will establish a large-scale comparison of relaxation and transition times for the $Pt_{42.5}Cu_{27}Ni_{9.5}P_{21}$ alloy. This forms a comprehensive basis to demonstrate and discuss similarities as well as methodological differences among the various methods, which can be otherwise easily overlooked. Figure 6.14 combines the just introduced DMA and FDSC results with the MDSC and KWW-fitted XPCS relaxation time data from the Papers I and II. Further data from literature is added, namely relaxation times from isothermal XPCS studies by Neuber et al. [26] and transition times from DSC T_g shift studies by Gross et al. [70]. The first observation from this comparison would be the strikingly similar slopes among the different data sets. In other words, all methods seem to reflect the fragility of supercooled $Pt_{42.5}Cu_{27}Ni_{9.5}P_{21}$ in a nearly identical manner, which is an expected, but still encouraging outcome. We will focus on the quantification and modelling of the liquid's fragility in the next chapter. Nevertheless, offsets between the

obtained data sets are apparent and can be addressed to inherent methodological and physical differences, which shall be briefly discussed in the following.

To begin with, an offset between temperature scanning and isothermal XPCS τ data can be observed. Neuber et al. used temperature scans of 5 K/min to establish a crystallization-based correction for the isothermal measurements, as described in [26]. While this constitutes a robust first approach, it appears reasonable that the discrepancy of correcting isotherms with a temperature scanning approach causes a slight temperature error, which can explain the observed offset between the data sets in Figure 6.14. Here, simply shifting the isothermal data by about 5 K would lead to alignment.

Furthermore, we must consider that Figure 6.14 compares relaxation times from XPCS, MDSC, DMA, and FDSC step response with transition times from the DSC and FDSC $T_{fictive}$ measurements. While the former expresses the dynamics of the equilibrium SCL state, the latter characterizes the transition kinetics from equilibrium SCL to the non-equilibrium glass (or vice versa). For an in-depth discussion of the inherent differences between dynamics and kinetics, the reader may reconsider the Chapters 2.3 and 2.4. According to the Frenkel-Kobeko-Reiner (FKR) relation from Equation (2.24), liquid dynamics directly predetermine vitrification kinetics. Assuming a relatively temperature insensitive width of the kinetic glass transition event [227] and taking Equation (2.14) into account, the FKR relation can be reformulated to directly connect relaxation time τ and corresponding transition time τ_{trans} at a given (fictive) temperature via a proportionality factor C as

$$\left.\frac{\tau}{\tau_{trans}}\right|_{T=T_{fictive}} = C. \tag{6.17}$$

Reviewing the calorimetric data from Figure 6.14 shows that the kinetic τ_{trans} data from DSC and FDSC $T_{fictive}$ measurements show absolute values roughly twice as high as their dynamic counterparts, namely the τ values from MDSC and FDSC step response measurements. This implies a general C value of approximately 0.5. Such a value appears physically meaningful, since the timescale of vitrification at a given fictive temperature should be somewhat slower than the corresponding structural relaxation process of the equilibrium liquid at the same temperature. The effectively same slope of the compared data sets suggests that C is a constant, as it is often claimed in literature [137]. Yet, Monnier and Cangialosi [307] as well as Di Lisio et al. [32] recently showed that the concept of a temperature-independent C factor can be massively violated when

investigating the vitrification kinetics of small-scale samples via FDSC. Nevertheless, these effects were only found for sample masses below roughly 100 ng, and, therefore, the relatively large FDSC sample of 350 ng used in the present study should remain unaffected.

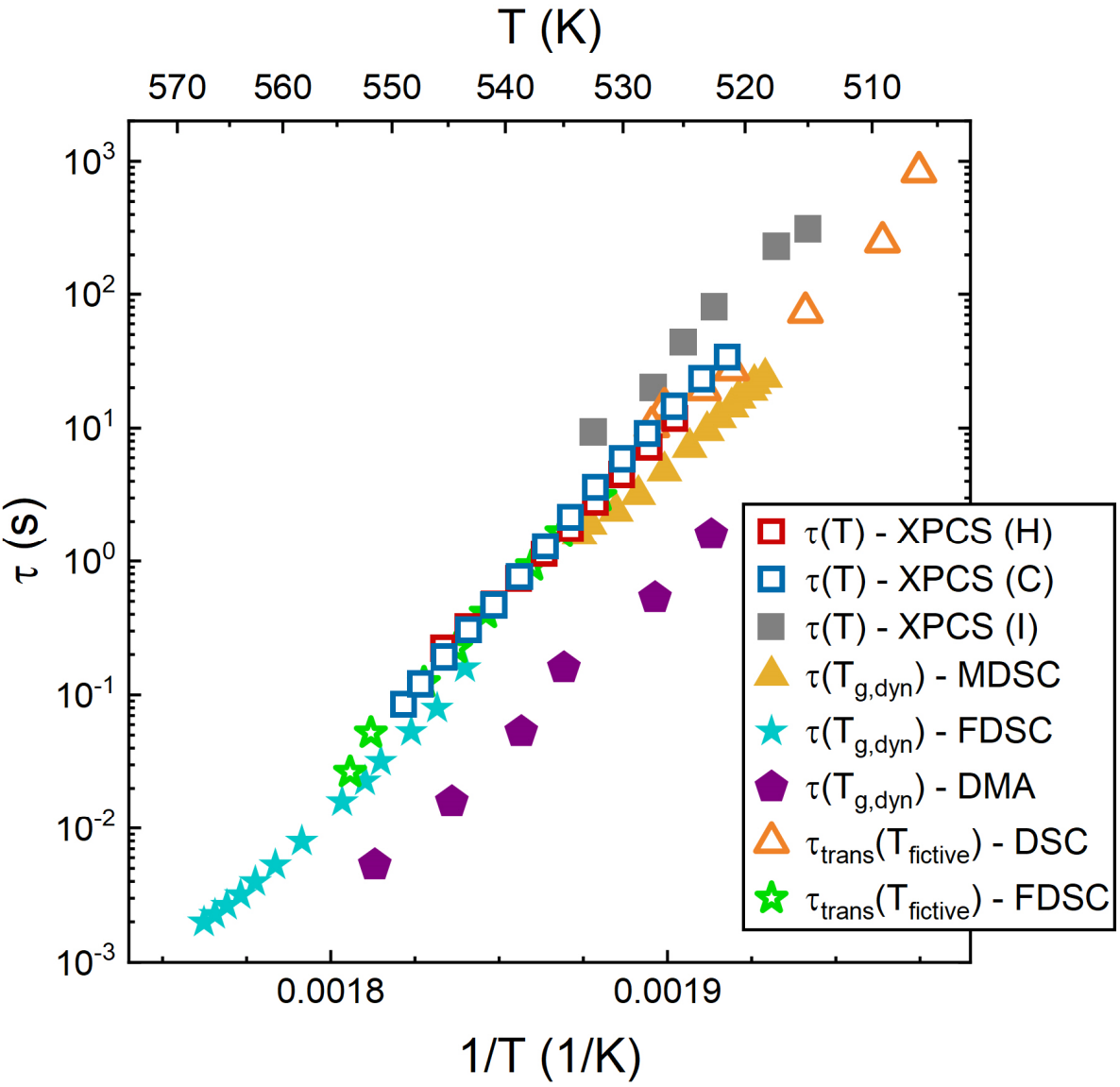

Figure 6.14: A large-scale comparison of all fragility-characterizing timescale data of the $Pt_{42.5}Cu_{27}Ni_{9.5}P_{21}$ alloy obtained in the frame of this work. Relaxation times from isothermal XPCS by Neuber et al. [26] (gray squares) and transition times obtained through T_g shift measurements by Gross et al. [70] (orange open triangles) are added to the comparison, too.

Finally, the DMA τ data shall be discussed, which stands out by ranging about one order of magnitude lower than the other data sets in Figure 6.14. To explain this striking offset, we have to reconsider Chapter 2.3.2, where the methodological differences between relaxation and retardation experiments were introduced. The DMA measurements are a relaxation experiments, which eventually determine a modulus-type property, namely

the complex elastic modulus $E^*(\omega,T)$ The other methods instead determine compliance-type properties, and hence they are retardation experiments [125,127]. It is well known that relaxation times determined by modulus measurements (relaxation experiments) are inherently lower than those determined by compliance measurements (retardation experiments) [125]. This aspect allows to explain the distinctly lower position of the DMA data in comparison to the other methods.

6.3.3 Fragility data comparison and adequate fitting models beyond the VFT equation

Paper I addresses the question of how to properly determine the fragility of a supercooled liquid from timescale data, in its particular case from relaxation times obtained by MDSC. Naturally, the well-known VFT function, see Equation (2.14), can applied. Yet, it was demonstrated that the preexponential factor τ_0 has a tremendous effect on the fitted values of D^* and T_0. If these two parameters shall be used for meaningful fragility comparisons, the preexponential factor must be defined in a consistent manner. To do so, Paper I suggests transforming the timescale data into viscosities using the Maxwell relation, see Equation (2.5). This way, the Nemilov relation from Equation (2.15) can be used to calculate and fix the preexponential factor η_0. The procedure has proven robust and was therefore also applied in Paper II. Nevertheless, the attentive reader may have noticed that the fit function has changed here from VFT to the cooperative shear model (CSM) introduced in Equation (2.18). The following considerations explain the reason for this change.

Figure 6.15a) shows the TMA equilibrium viscosities initially published by Gross et al. [70], which already served in Paper I and Paper II as reference. The VFT fit from Gross et al., which is also used in Paper I, is indicated with a dashed line and the CSM fit from Paper II is represented through a solid line. For both fits, the preexponential factor is calculated using Equation (2.15) and fixed as $\eta_0=4\times10^{-5}$ Pa s. Within the viscosity data range, both fits are practically identical, but significant differences are observed in the extrapolation behavior. The VFT fit appears distinctly more curved than the CSM fit, resulting in an offset of about one order of magnitude in viscosity at an extrapolation of roughly 50 K, see in the lower left corner of Figure 6.15a).

In Figure 6.15b) all the timescale data gathered in the previous Figure 6.14 have been transformed into the viscosity domain, creating an exceptionally large data range

spanning over more than 80 K. To do so, each data set is fitted with the CSM fit of the TMA data as

$$\tau(T) = \frac{\eta_0}{G}\exp\left(\frac{T_g^*}{T}\ln\left(\frac{\eta_g}{\eta_0}\right)\exp\left(2n\left(1-\frac{T}{T_g^*}\right)\right)\right), \qquad (6.18)$$

with the fixed parameters $\eta_0=4\times10^{-5}$ Pa s, T_g^* =498 K, $\eta_g=10^{12}$ Pa s, and n=1.153. Only the shear modulus G remains as a free fitting parameter, the results are listed in Table 6.1. All timescale values are then transformed into viscosities according to the Maxwell relation and by using the respective G values. For a more detailed description of the procedure, the reader is referred to Paper II.

We again see that all transformed timescale data show very similar slopes (i.e. fragilities) and align nicely with the TMA-determined CSM fit, which is therefore an adequate function to describe and extrapolate the alloy's fragility over the whole data range. The VFT fit shows a different picture as it is incapable of incorporating all data sets in a satisfying manner. As highlighted in the inset, it is especially unable to describe the rather straight, less curved path of the FDSC and temperature scanning XPCS results located at high temperatures. In other words, the VFT function seems to feature an inherent trend towards a too pronounced curviness, and hence it cannot model the almost Arrhenius-like trend of the measured relaxation times. This problem of excessive curvature is further substantiated by fitting all data sets together with one VFT fit, see the suboptimal gray dotted curve in Figure 6.15b).

In the context of Paper I, this issue was still hidden by the relatively small temperature range observed. With the introduction of modern FDSC analysis and the fast exposure times achievable with state of the art XPCS detectors, relaxation times in the sub-second regime can be obtained. This significantly expanses the accessible data range, see Figure 6.15b), and the inherent problem of the VFT equation becomes visible. Completely analogous observations can be found in case of e.g. four Mg-based metallic glass formers as reported by F. Vollmers [308]. Also, previous studies on Pd- and Zr-based metallic glass formers tend to show the same problem [309,310] Hence, the present issue of the VFT might prove as a general feature. Future studies might allow to draw clearer conclusions on this topic.

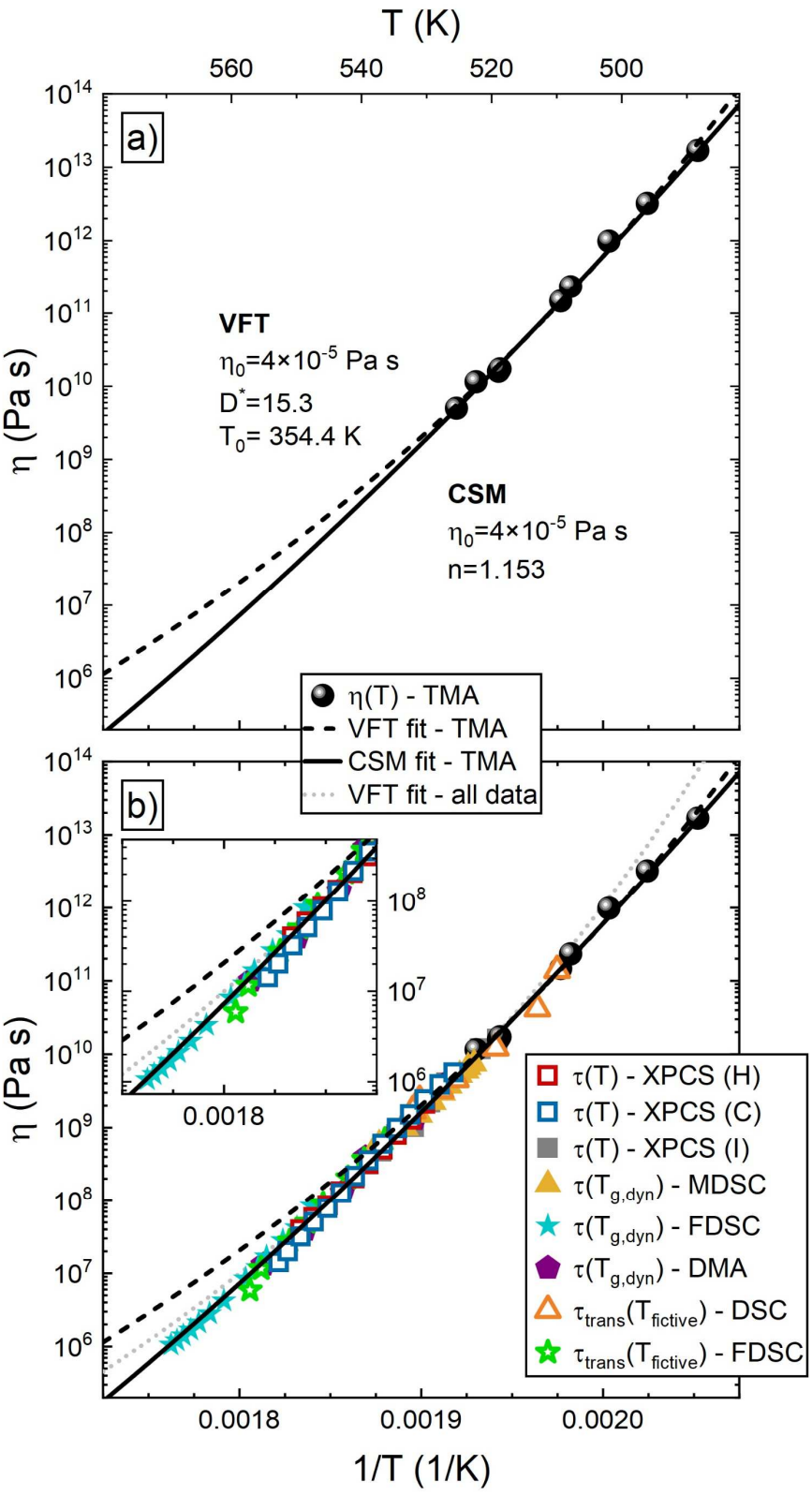

Figure 6.15: a) TMA-determined viscosities from Gross et al. [70] fitted with the VFT and the CSM model. b) Relaxation and transition times from various methods are transformed in the viscosity domain and aligned with the TMA data. While the CSM model allows to describe the whole data range, the VFT curve incorporates too much curvature, leading to distinct discrepancies between data and fit at higher temperature as highlighted in the inset. Fitting all data with the VFT equation also doesn't allow for a viable fit curve.

We see here that the methodological advances in fast scanning calorimetry and synchrotron technology mark significant progress in the investigation of the fragility of metallic glass forming liquids. These methods allow to advance deeper into the 'no-man's-land' of the supercooled liquid state, where structural relaxation and crystallization kinetics become so fast that conventional methods like TMA, DMA, or DSC cannot provide insights anymore. Here it shall be referred to the latest methodical advances that successfully combine synchrotron diffraction with in-situ FDSC [311,312]. With the upcoming generation of detector technology heading towards exposure times in the µs-regime, especially FDSC-XPCS combinations [312] will prove as a mighty tool to study ultra-fast liquid dynamics and transition kinetics at temperatures in the vicinity of the TTT crystallization nose.

Table 6.1: Comparison of the shear moduli used to transform the timescale data sets into viscosities.

Data type	**$\tau(T)$**	**$\tau(T)$**	**$\tau(T)$**	**$\tau(T_{g,dyn})$**	**$\tau(T_{g,dyn})$**	**$\tau(T_{g,dyn})$**	**$\tau(T_{fic})$**	**$\tau(T_{fic})$**
Method	XPCS (H)	XPCS (C)	XPCS (I)	MDSC	FDSC	DMA	DSC	FDSC
Reference	This work	This work	[26]	This work	This work	This work	[70]	This work
G (Pa s)	1.815×10^{8}	1.679×10^{8}	5.13×10^{7}	3.122×10^{8}	5.301×10^{8}	2.4567×10^{9}	1.667×10^{8}	2.230×10^{8}

6.4 Mechanical properties of metallic glasses additively formed via laser powder bed fusion

We will now leave the topics of XPCS, liquid dynamics, and transition kinetics behind and instead concentrate on the rather industry-related field of additively formed metallic glasses. At a first glance, this might look like a very large change of scope. Yet, it should be quickly reminded that liquid fragility is a major factor to predetermine crystallization kinetics, see Chapter 2.6, and knowledge about a metallic glass former's TTT diagram as exemplarily obtained in Paper III can be of large advantage to reach a deeper understanding or to even model various kinds of BMG processing routes. Fruitful combinations of FDSC-determined TTT diagrams with conventional casting [12,313] or also additive manufacturing [314–316] can be indeed found in literature and also in Paper III [2]. Indeed, the extensive knowledge about the crystallization behavior of $Pt_{42.5}Cu_{27}Ni_{9.5}P_{21}$ acquired in Paper III would create a formidable basis for a research project that aims to qualify this alloy for PBF-LB/M additive manufacturing. Use cases could be found in jewelry [317–319] or especially in catalytic applications, where Pd- and

Pt-based metallic glasses like the present $Pt_{42.5}Cu_{27}Ni_{9.5}P_{21}$ were shown to feature very promising characteristics [320,321].

Nevertheless, the present work is rather focused on structural applications of PBF-LB/M-formed BMGs, and hence, alloys based on cheaper, industry-typical elements like Zr, Cu, Ti, or Ni were investigated. The coming pages will shed light on the rather practical aspects of their formation via PBF-LB/M. Chapter 6.4.1 summarizes the work's findings on the mechanical properties of AM-formed BMGs, especially regarding the process-typical brittleness. In combination with further literature, an overview over the topic will be provided. Chapter 6.4.2 focusses on the step-wise increase in achievable maximum strength through purposeful alloy selection, which prefigures the rise of AM-formed NiNb-based metallic glasses with strength limits beyond 3 GPa in the near future. Finally, some possible application cases for additively formed metallic glasses that where tested within the periphery of this thesis will be presented, namely honeycomb light-weight applications in Chapter 6.5.1 and compliant mechanisms that functionalize the high elastic deformability of metallic glasses in Chapter 6.5.2.

6.4.1 On the brittle behavior of PBF-LB/M-formed metallic glasses

In the course of this work, three BMG families have been evaluated in terms of their applicability for additive manufacturing via PBF-LB/M, namely the Zr-based AMZ4 ($Zr_{59.3}Cu_{28.8}Al_{10.4}Nb_{1.5}$) in Paper IV (in conjunction with a closely related, coauthored work by J. Wegner et al. [17]), the CuTi-based Vit101 and its microalloyed derivates ($Cu_{47}Ti_{34}Zr_{11}Ni_8$, $Cu_{47}Ti_{33}Zr_{11}Ni_8Si_1$, and $Cu_{47}Ti_{34}Zr_{11}Ni_6Si_1Sn_2$) in Paper V, and finally $Ni_{62}Nb_{38}$ in Paper VI. Aiming for the application of these alloys as structural materials, one of the central goals of these publications was to achieve AM-formed BMGs with optimized mechanical properties. Based on the experience thereby gained, and by including coauthored publications by J. Wegner et al. [8,15,17] that are closely related to the present work as well as further literature sources, the following considerations shall provide an brief overview of the topic.

BMG parts formed via PBF-LB/M usually show brittle behavior [68,208,322–326]. In terms of the stress-strain diagram, this means that only elastic behavior is visible, as the material reaches strength levels below or (at best) at the level of the yield strength followed by a sudden fracture. Noteworthy degrees of plasticity can be observed only

under specific conditions, e.g. upon compression testing [325,327,328] or for beam bending on very thin beams [329,330], profiting from the well-known size effect of BMG mechanics [188,331,332] as demonstrated in Figure 6.16.

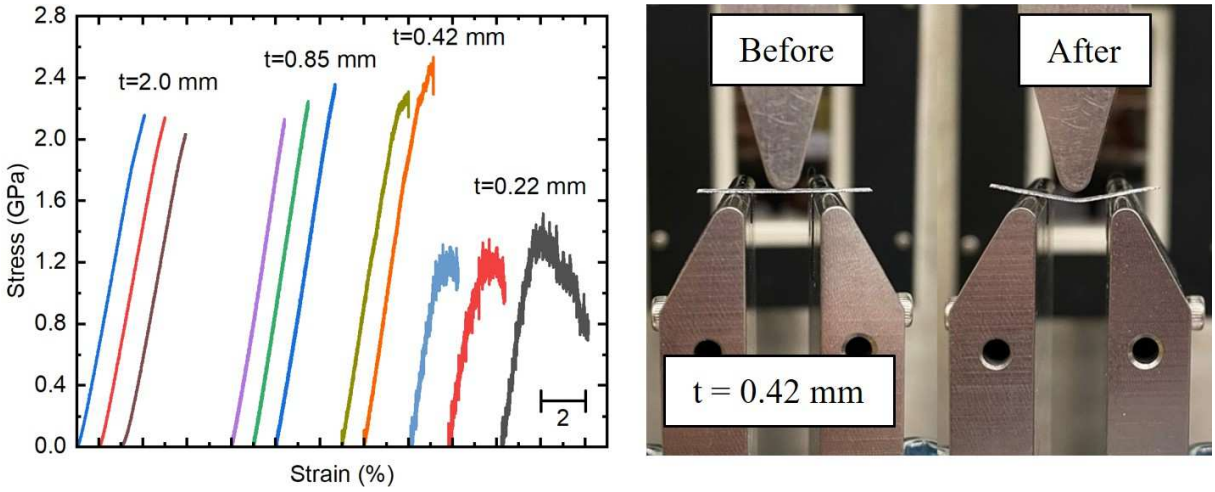

Figure 6.16: Stress-strain diagrams of PBF-LB/M-formed AMZ4 beams acquired via three-point beam bending. With decreasing thickness t, the BMG-typical size effect is observed, and the initially brittle material begins to feature significant plasticity, as further demonstrated in the photographs on the right. Taken from J. Wegner et al. [329].

To understand the interplay of the various factors that create this overall brittle mechanical behavior, we consider the stress intensity factor K_I (for mode I, crack opening), which quantifies the stress intensity at a given defect (e.g. at the tip of a crack). Under a certain stress σ, there exists a critical defect size a_C that will create a spontaneously growing crack leading to catastrophic failure. The corresponding critical stress intensity factor K_{IC} is known as the material's fracture toughness and can be calculated as

$$K_{IC} = \sigma\, Y \sqrt{\pi\, a_C}. \tag{6.19}$$

The geometry factor Y incorporates information about the sample geometry as well as the defect shape. The larger K_{IC}, the larger the defects that can be tolerated without material failure, or on the other hand, the larger the stresses that can be applied before fracture occurs. Basically, Equation (6.19) includes all aspects that determine how brittle a PBF-LB/M-formed BMG will be behave upon testing, as discussed in the following.

We start our considerations with the aspect of material compaction upon PBF-LB/M processing, which has a major impact on the internal defects, i.e. pores. As explained in Chapter 3.3.2 and demonstrated in numerous studies [4,17,68,206,208,325,333–336], too

low laser energy input will lead to poorly compacted samples with low relative densities. The resulting LOF creates large pores that are highly irregular in shape as demonstrated in Paper IV and exemplary shown in Figure 6.17 (taken from B. Li et al. [325]). Naturally, such low-density samples feature underwhelming strengths as the large and numerous pores act as stress risers, especially since their irregular shape affects the geometry factor Y unfavorably, see Equation (6.19). On the other hand, sufficiently high volume energy densities E_V will instead create high relative densities of 99% or above, and remaining porosity manifests as gas inclusions with mechanically less critical, spherical shapes, see Figure 6.17. In principle, thermoplastic post-processing could be used to further increase and optimize density by compressing the material to close remaining porosity, as mentioned in Paper IV. Indeed, hot isostatic pressing (HIP) on PBF-LB/M-formed AMZ4 was reported to reach this objective [337]. Nevertheless, embrittlement due to crystallization and aging of the glass must then be considered, as discussed later.

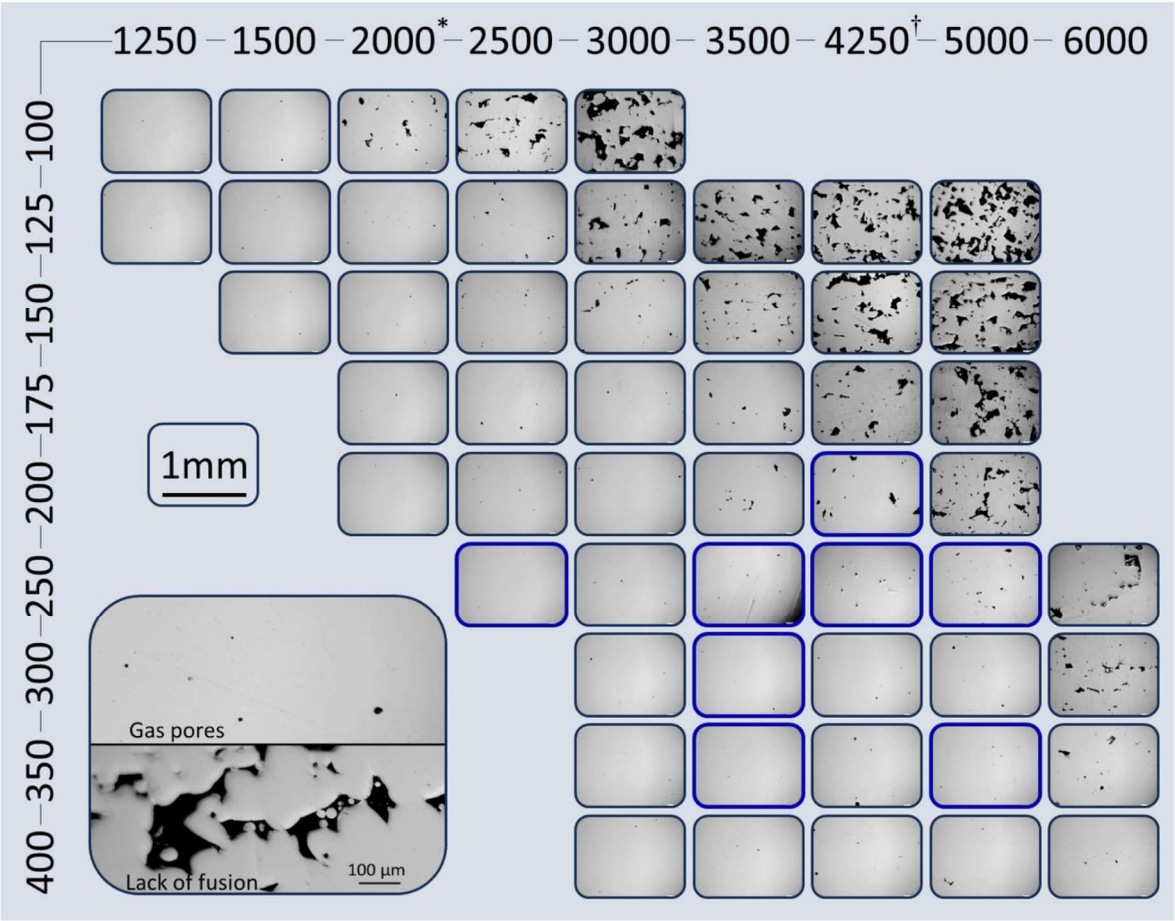

Figure 6.17: Light microscopy images of PBF-LB/M-formed AMZ4 samples created with different combinations of laser powers P (left axis, in W) and scan velocities v (upper axis, in mm/s). Poor compaction through irregularly shaped lack of fusion porosity is observed for low volume energy densities E_V (low P and high v, upper right corner), while higher E_V values lead to high relative densities with only a low degree of spherical gas pores remaining. Taken from [325].

Too excessive E_V input will eventually lead to crystallization effects as demonstrated in Paper VI for $Ni_{62}Nb_{38}$ or e.g. by the manifold studies on the most widely used BMG in additive manufacturing, the commercially available AMZ4 alloy [8,17,206,208,325,326,337,338]. In the context of Equation (6.19), crystallites act as internal defects that can start catastrophic crack propagation. Their highly detrimental effect on the mechanical performance is further amplified as primary crystalline phases are often found to be inherently brittle, thereby decreasing the overall fracture toughness of the material. Therefore, a PBF-LB/M process parameter evaluation must always aim for a balance between optimized density (requiring high E_V) and avoidance of significant crystallization (limiting E_V). Figure 6.18 from J. Wegner et al. [17] demonstrates such an evaluation process exemplary and shows that an adequate processing window can be surprisingly narrow, depending on the respective alloy.

This leads us directly to the next major influence factor, which are impurities like oxygen or carbon. During powder atomization, contamination with these elements is often unavoidable, due to the crucible material (often carbon), industry-typical vacuum and atmosphere conditions, and the large surface to volume ratio of the powder particles, which provides plenty of area for oxidation processes. The coauthored works of J. Wegner et al. [17] and E. Barreto et al. [23,27,33] analyze the issue in detail. Especially oxygen contamination is well known to alter the SRO and MRO of Zr-based BMGs. The result is an increasingly icosahedral [339], more rigid atomic structure that favors the formation of single catastrophic shear bands, leading to a harder, stronger, but also less though glass [340–345]. J. Best et al. indeed report a fracture toughness of about 26 MPa√m for highly oxygen-loaded PBF-LB/M-formed AMZ4, while the high-purity as-cast reference reaches values above 100 MPa√m [344]. Furthermore, contamination with oxygen and carbon can favor the formation of oxides and carbides, thereby accelerating the overall crystallization kinetics and narrowing down the suitable process parameter range as shown in Figure 6.18. For example, V. Pacheco et al. report that the high oxygen concentration triggers the formation of Zr_4Cu_2O instead of Zr_2Cu as the primary phase upon PBF-LB/M processing of AMZ4 [338].

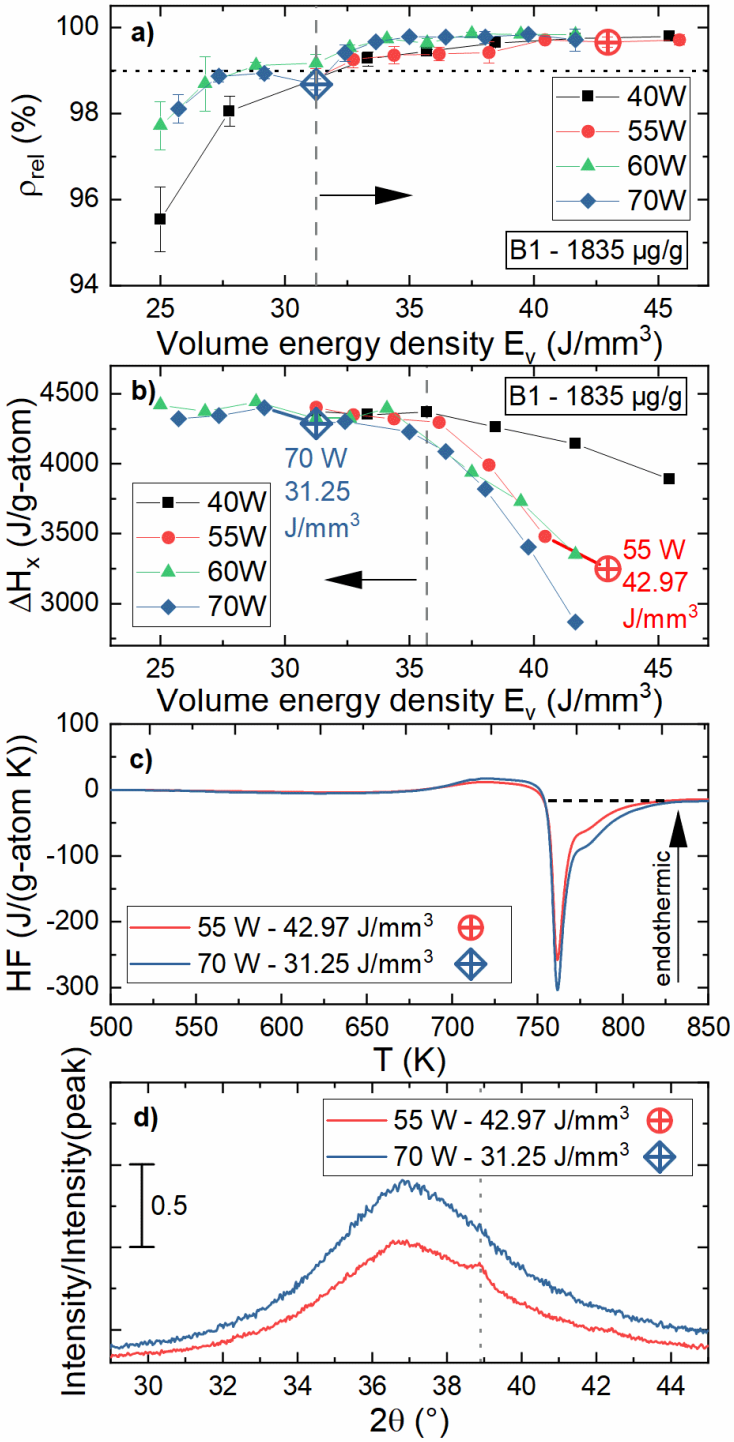

Figure 6.18: An example of a PBF-LB/M parameter evaluation process performed for AMZ4. a) Below E_V values of about 31 J/mm³, density remains insufficient. b) Yet, crystallization enthalpy evaluation reveals that E_V values higher than about 35 J/mm³ create partially crystalline samples, as further shown in the DSC scans and diffractograms in c) and d). The remaining parameter window for optimized samples is relatively narrow. Taken from [17].

In this context, the coauthored work by J. Wegner et al. investigated the structure and bending strength of PBF-LB/M-formed AMZ4 for different powder batches with varying

oxygen contents [17], some results are shown in Figure 6.19. For powders with oxygen contents below roughly 1600 µg/g, the combination of remaining porosity and oxygen contamination causes brittle fracture as soon as the yield strength is reached. Yet even higher oxygen loads result in premature fracture at strength levels below the yield strength.

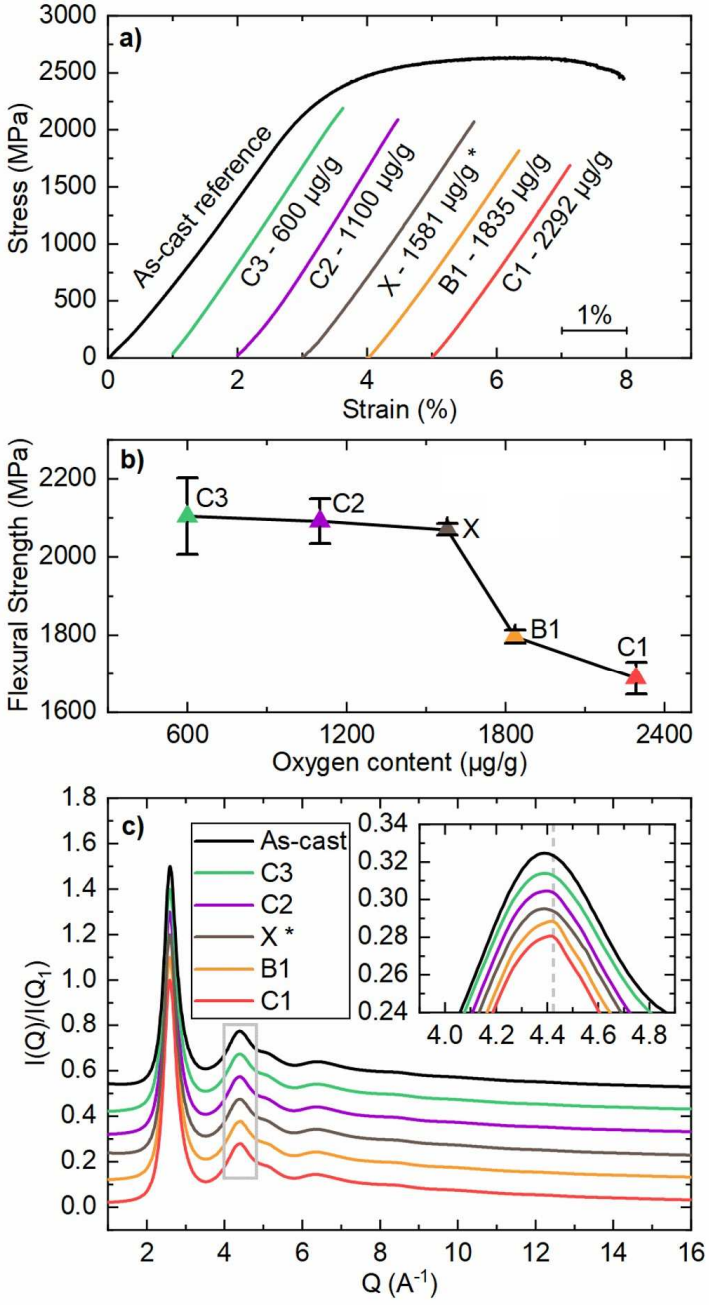

Figure 6.19: a) Depending on the oxygen concentration in the used powder feedstock, PBF-LB/M-formed AMZ4 samples may fracture before reaching the material's yield strength upon bending. b) The contamination threshold before premature fracture occurs can be roughly determined at 1600 µg/g. c) The respective embrittlement goes hand in hand with the emergence of first Bragg peaks in the HESXRD diffractogram, indicating beginning crystallization. Taken from [17].

For these samples, the HESXRD diffractogram reveals first Bragg peaks, see Figure 6.19c). These signalize emerging (nano-)crystallization, most likely in form of Zr_4Cu_2O precipitates induced by the high oxygen loads. It shall be mentioned at this point that major oxygen concentrations of up to 2292 µg/g (compare powder batch C1 in Figure 6.19) actually constitute a kind of micro-alloying. Converted into at%, the real composition of the additively formed AMZ4 would then be $Zr_{58.6}Cu_{28.5}Al_{10.3}Nb_{1.5}O_{1.1}$ instead of the original $Zr_{59.3}Cu_{28.8}Al_{10.4}Nb_{1.5}$. Such considerations put the massive differences in crystallization behavior, ductility, and fracture toughness between PBF-LB/M-formed and high-purity as-cast AMZ4 into perspective.

Finally, relaxation and residual stresses can be identified as a major influence factors for the mechanics of AM-formed BMGs. A relaxed glass with an accordingly low T_{fic} features a rather dense and rigid atomic structure, hence showing relatively brittle mechanical behavior [219]. While the results from Paper VI suggest that the fast thermal cycles of PBF-LB/M seem to create a glass with rather high free volume and T_{fic}, other works address embrittlement of the amorphous phase and even resulting crystallization to aging effects caused by the HAZ [68,346,347]. Furthermore, PBF-LB/M is known to create periodical alternations in structure and relaxation state due to the layer-wise built [348]. Such heterogeneity must also be seen critical in terms of the mechanical properties, as it introduces typical residual stress states [349] that can lead to crack formation as seen in Paper V and Paper VI. Here, thermal post-processing in form of equilibration in the SCL state followed by fast quenching and vitrification (similar to the thermal protocol used for TPF post-processing in Paper IV) might help to homogenize structure and relaxation state. Recent studies by D. Ouyang et al. [347] and L. Ruschel et al. [40] demonstrate the principle.

In conclusion, ductility and fracture toughness of PBF-LB/M-formed BMGs are challenged by the interplay of process-typical defects in form of remaining porosity as well as embrittlement due to crystallization, contamination issues, relaxation effects, and residual stresses. The problem could be addressed by BMG composites with an intentionally added crystalline phase that improves the overall ductility [350–353]. Yet, such approaches tend to be very challenging in terms of processing and might feature the issue of anisotropic properties. A different strategy for the future use of AM-formed BMGs would be to focus on the still impressive elastic properties of these materials. Chapter 6.5 will give some examples for respective part designs. In this case, optimizing the accessible

yield strength through reasonable alloy selection is a promising path, which will be discussed in the following chapter.

6.4.2 From Zr- to CuTi- and NiNb-based systems: Maximizing the accessible strength of AM-formed BMGs through alloy selection

The succession from Paper IV to V and VI displays a focus change from the medium-strength Zr-based AMZ4 to the significantly stronger and harder CuTi-based Vit101 system to finally consider the high-strength $Ni_{62}Nb_{38}$ glass former. Here, the underlying idea is to fathom and shift the limits of accessible mechanical properties for PBF-LB/M-formed BMGs. Paper IV and also J. Wegner et al. [17] show that additively formed AMZ4 can reproducibly reach its yield strength of 2.1 GPa upon bending, a value that has been identified as an interim world record by a review article from N. Sohrabi et al. in 2021 [68]. The bending tests on Vit101 from Paper V exceed this record by reaching the alloy's yield strength at up to 2.5 GPa. The small amount of available $Ni_{62}Nb_{38}$ powder feedstock [33] limits Paper VI to a preliminary parameter study and prohibits the formation of large beam samples for bending tests. Nevertheless, the found hardness values of more than 850 HV1 are practically identical to the hardness of as-cast $Ni_{62}Nb_{38}$ [31]. This agreement might foreshadow an overall promising mechanical performance of additively formed $Ni_{62}Nb_{38}$.

Figure 6.20 displays the stress-strain diagrams (measured upon bending) of PBF-LB/M-formed AMZ4 and Vit101 from Paper IV and V, which reach their alloy-specific yield strengths of 2.1 GPa and 2.5 GPa before brittle fracture occurs. Assuming the same behavior for PBF-LB/M-formed $Ni_{62}Nb_{38}$ would lead to an impressive maximum strength of roughly 3.5 GPa, as indicated on hand of the as-cast reference curve. This value would dwarf most metallic materials used today, including ultrahigh-strength steels [354].

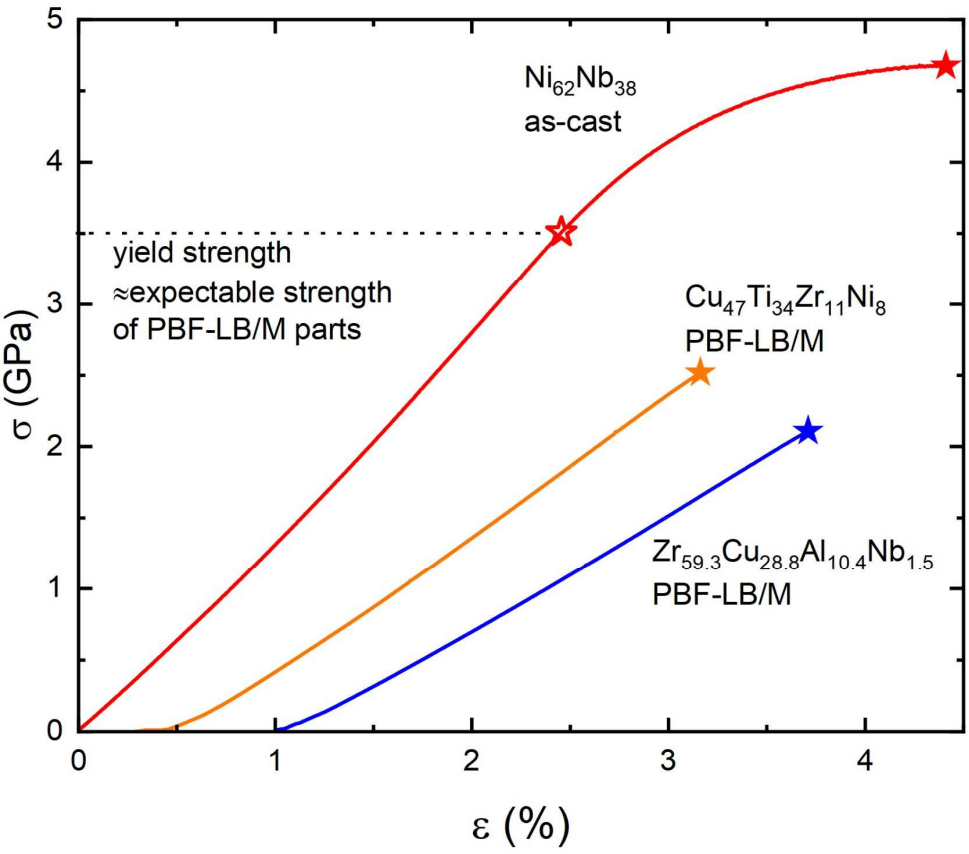

Figure 6.20: Stress-strain curves (bending) of PBF-LB/M-formed AMZ4 and Vit101 from Paper IV and V. When formed with optimized parameters, both systems can reproducibly reach the yield strength of the material before brittle fracture occurs. Assuming the same behavior for PBF-LB/M-formed $Ni_{62}Nb_{38}$ would lead to an impressive maximum strength of about 3.5 GPa, as indicated on hand of the as-cast reference curve for this alloy (this curve was measured with a bearing distance of 15 mm, the data was kindly provided by Lucas Ruschel).

Regarding the promising results in terms of high density and almost full amorphization in Paper VI, the alloy-inherent fracture toughness is probably the most crucial aspect that might allow or prohibit to reach such strength values for PBF-LB/M-formed $Ni_{62}Nb_{38}$. While AMZ4 and Vit101 feature fracture toughness values of roughly 100 MPa√m [344,355], a value of about 50 MPa√m was recently measured for $Ni_{62}Nb_{38}$ [43]. Ultimately, future studies must validate if the alloy can evolve its full mechanical potential in AM processing. It shall be mentioned that the GFA, hardness, and strength of the NiNb system can be significantly improved by alloying with various further elements, yet these optimizations come at the cost of ductility and toughness [31,43,58,59]. For example, B. Li et al. shows that microalloying with phosphor halves the determined fracture toughness [43]. This result agrees with the previously discussed embrittlement of PBF-LB/M-formed AMZ4 due to 'microalloying' with oxygen contamination [17] or the embrittlement of the Vit101 system due to minor additions of Si and Sn as reported in

Paper V and by G. Garrett et al. [355]. Seen in this context, the simple binary $Ni_{62}Nb_{38}$ alloy might be the most promising candidate to create high-strength PBF-LB/M-parts as it seems to offer the best fracture toughness in the NiNb BMG family.

6.5 Potential application cases of additively formed metallic glasses

Paper IV demonstrates that TPF-post-processing can be used to further functionalize PBF-LB/M-formed BMG parts, thereby implying applications in cases where the geometrical freedom of AM-processing meets the need for specifically structured surfaces. Nevertheless, the present work was part of several research projects on the PBF-LB/M of metallic glasses, and in the course of these projects, other potential applications were tested, evaluated and finally published by J. Wegner et al. [20,356,357]. These approaches can be summarized under the term DfAM, which stands for 'design for additive manufacturing'. The underlying principle of DfAM is to overcome designs that are optimized for traditional processing routes (casting, molding, machining etc.) by adapting to the conditions and advantages of additive manufacturing, especially the process-typical geometrical freedom. The following chapter will give a quick overview over the outcome of these test series.

6.5.1 Honeycomb structures as an archetypical example for AM lightweight structures

Honeycombs are natural structures that have been optimized by millions of years of evolution to provide an impressive balance between stiffness and strength on the one hand and material and space consumption on the other hand. Thus, honeycombs are often adapted as a biomorphic design in lightweight applications [358]. Due to the complex shape, they are rather difficult to manufacture by traditional routes but can be easily formed through AM-processes [359–361], making them a typical example for a DfAM structure. J. Wegner et al. tested PBF-LB/M-formed AMZ4 honeycomb structures in terms of their suitability for lightweight structural applications [356]. For this purpose, six types of beam samples with solid frames and inner structures in honeycomb design have been produced from AMZ4. The honeycomb cell heights h were varied between the different beam types as illustrated in Figure 6.21 (including a solid reference).

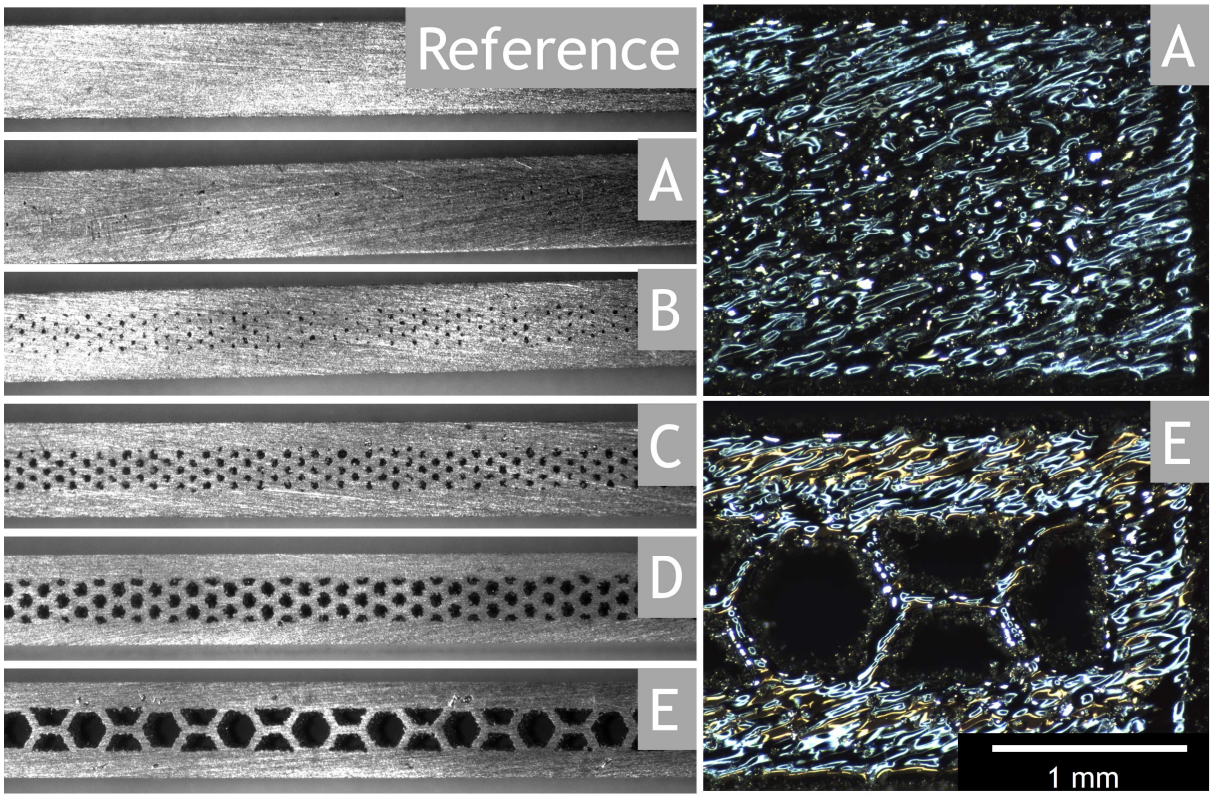

Figure 6.21: Microscopic pictures of the six types of beams created. The reference beam type features solid filling, the five honeycomb-structured ones are formed with increasing honeycomb cell heights h. Taken from [356].

The internal cavities act basically as large, intentionally introduced pores that reduce the relative density of the beams by up to 30%. Bending tests on these samples reveal that their specific strength (maximum strength normalized by the relative density) can exceed the specific strength of the solid PBF-LB/M-formed AMZ4, as shown in Figure 6.22. These results might be empirical and preliminary but demonstrate nevertheless the auspicious applicability of additively formed BMGs for lightweight DfAM designs. The interested reader might be referred to a recent publication by J. Wegner et al. that deepens the research on BMG lightweight designs in terms of lattice structures [329].

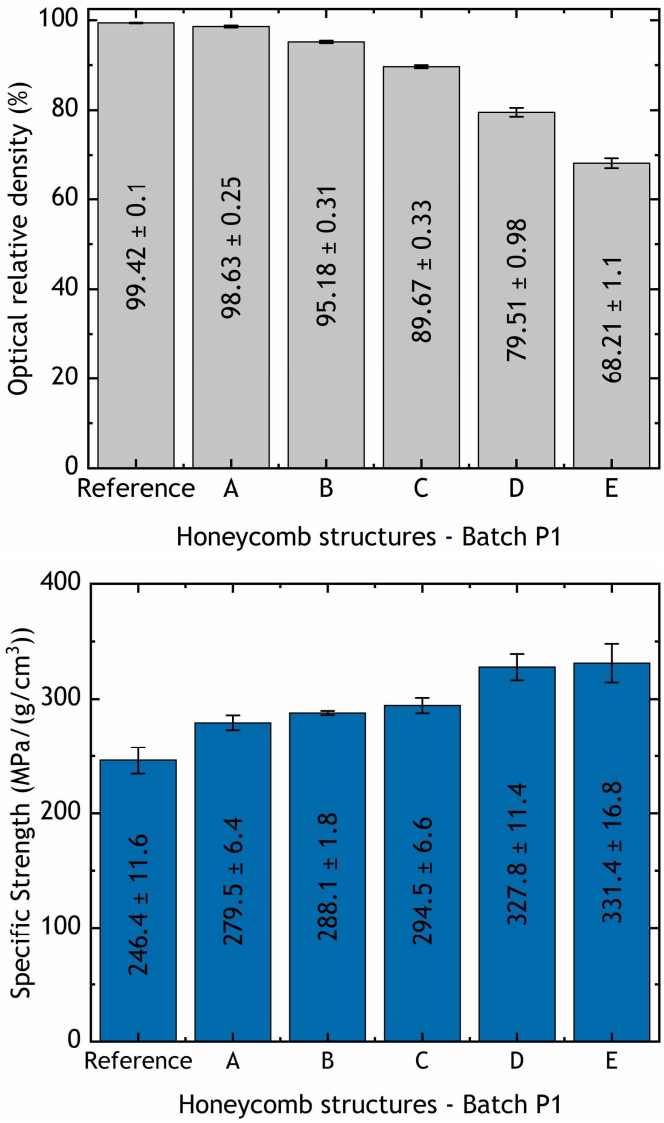

Figure 6.22: The relative density of the honeycomb-structured beams decreases with increasing cell size. Accordingly, the specific strength of these beams increases. Taken from [356].

6.5.2 Functionalizing the large elastic limit of metallic glasses trough AM-formed compliant mechanisms

Compliant mechanisms are designs that substitute hinges and joints trough elastic deformation within the part itself, allowing to reduce friction, wear, and the number of needed parts [362,363]. This requires specific shapes that might be difficult to machine, but can be easily created through AM, and hence, compliant mechanisms fit well within the DfAM concept. The superb elastic energy storability of BMGs, see Chapter 2.8.1, predestines them as material choice for such applications. We have seen that LPBF-formed AMZ4 with reasonable low oxygen contamination and produced with optimized process parameters is able to reach strength values in the order of the material's yield

strength of more than 2 GPa. In combination with more than 2% elastic deformability, an enormous potential to store elastic energy can be reached as demonstrated in Figure 6.23. AMZ4 can store more than three times the elastic energy of Ti6Al4V, a crystalline alloy that is known for its already high elasticity.

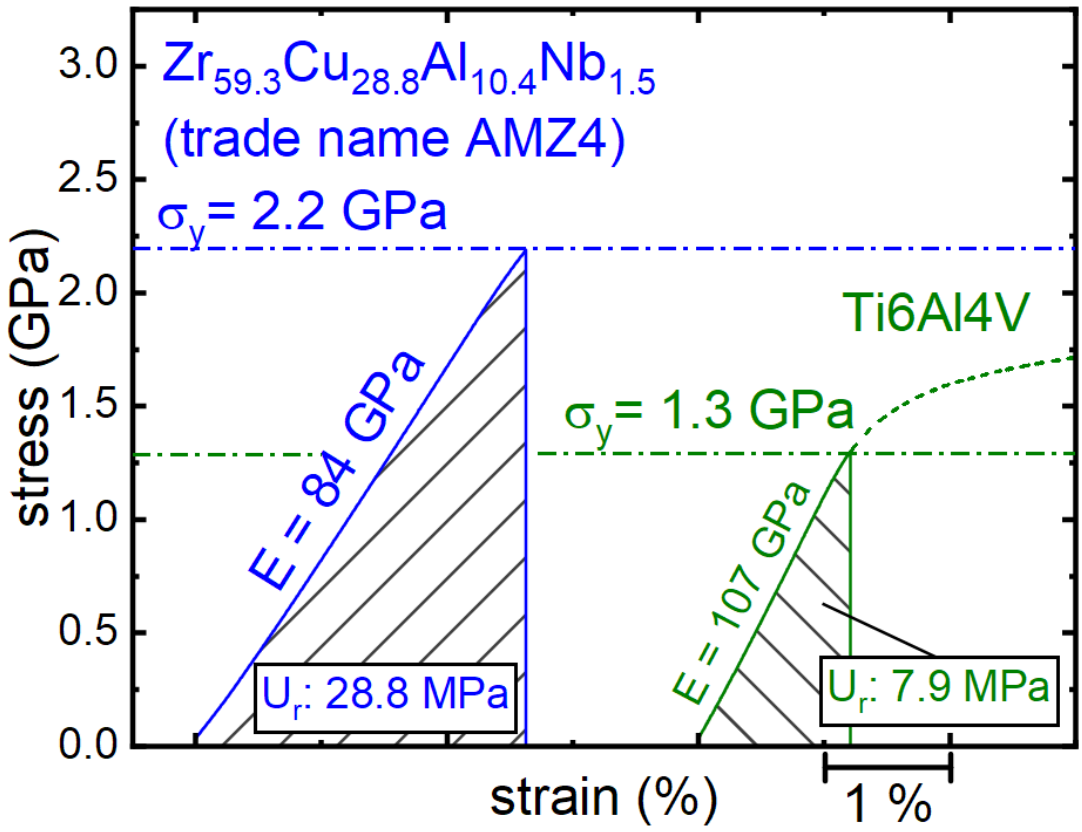

Figure 6.23: PBF-LB/M-formed AMZ4 allows to store more than three times the elastic energy as a Ti6Al4V reference, a crystalline alloy that is known for rather high elasticity. Taken from [20].

Accordingly, J. Wegner et al. functionalized this potential in a coauthored publication [20] by creating a compliant mechanism from additively formed AMZ4. A pincer tool was developed and realized through a deltoid Q-joint design. By pressing the two handle parts together, elastic bending occurs within the four hinges and allows to close the two clamps on the front of the tool, as illustrated in Figure 6.24.

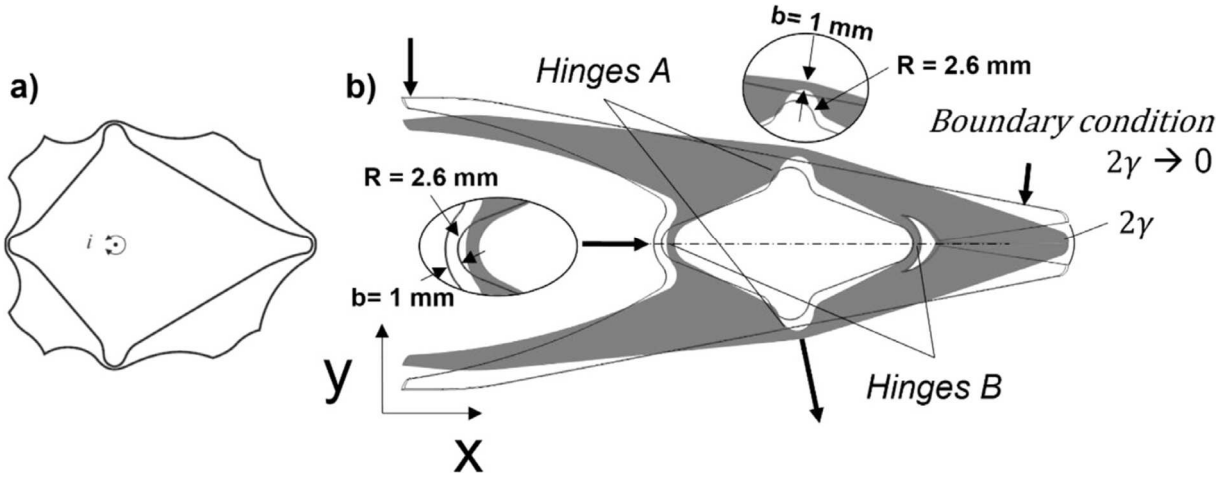

Figure 6.24: Schematic illustration of the deltoid Q-joint type compliant mechanism. Through compressing the handles, the clamps on the tip of the device can be closed. Elastic deformation localized in four hinges constitutes the basis for this effect. Taken from [20].

The design was created in two different sizes, photographs of the formed parts are shown in Figure 6.25. Considering the angle 2γ that spans between both clamps demonstrates the functionality of the used BMG material, see Figure 6.26. While AMZ4 allows for a full closure of the clamps while still preserving only elastic deformation in the highly loaded hinges, crystalline metals can only provide a small fraction of the 2γ=17.2° needed for full closure. Even the relatively elastic Ti6Al4V would only reach about one third of the needed motion range.

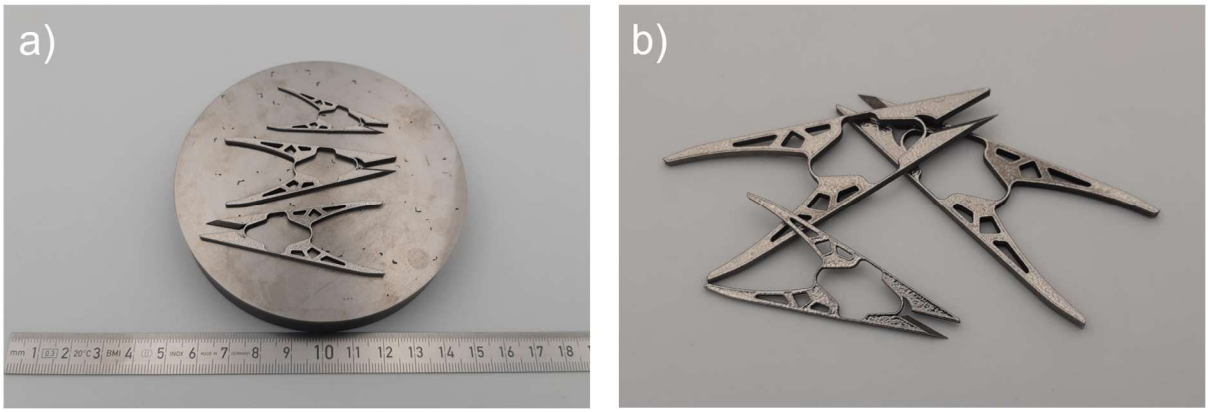

Figure 6.25: PBF-LB/M-formed pincer tools made from AMZ4. a) Still on the build plate and b) after separation and being ready to use. Taken from [20].

In order to achieve the same effect of clamp closure with the crystalline reference metals, the hinges and the whole part must be designed significantly larger. Using the PBF-LB/M formed BMG hence creates a striking advantage and encourages the use of similar devices e.g. as pincer tools in medicine.

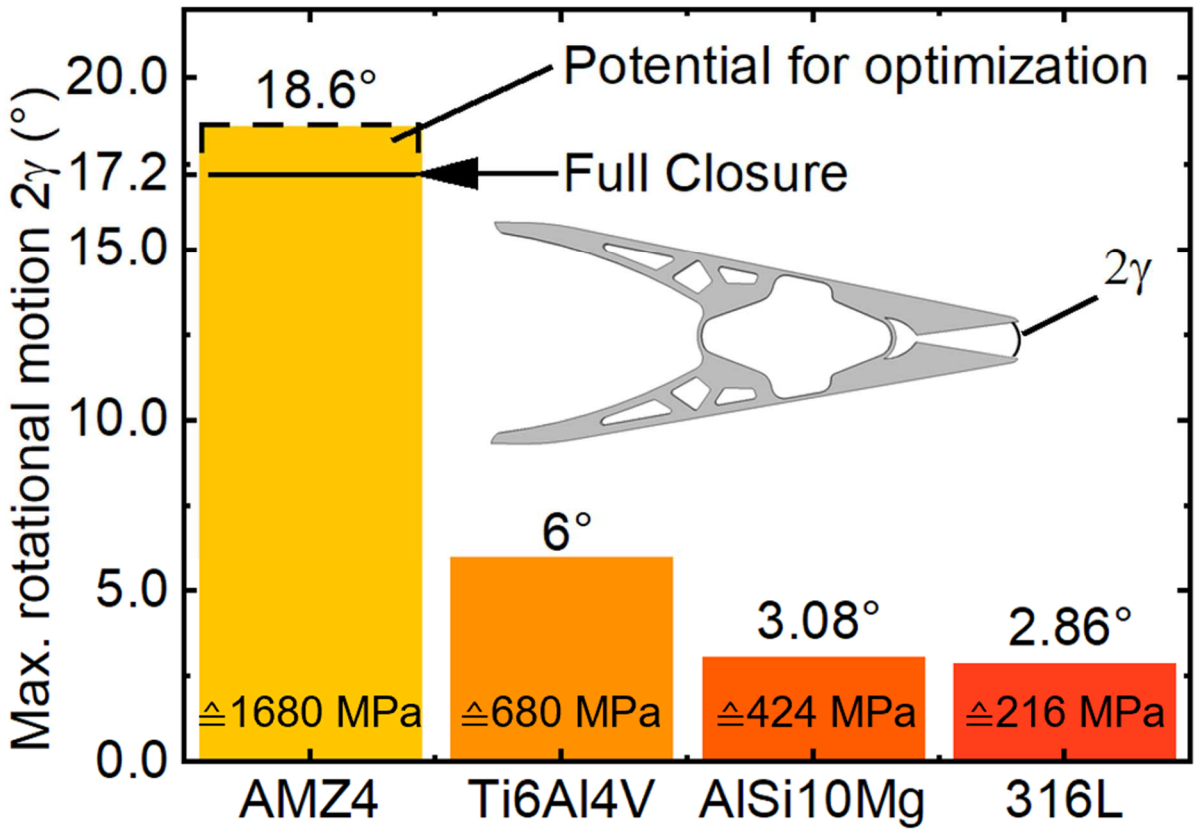

Figure 6.26: The maximum clamp angle 2γ that can be applied while remaining in the elastic deformation regime of the hinges. For the given design, only AMZ4 allows for full closure at 2γ=17.2°, while typical crystalline reference materials would show massive plastic deformation (or fracture) at the hinges in case of full closing. Taken from [20].

7. SUMMARY AND OUTLOOK

The present cumulative thesis includes six publications as well as additional results and considerations in the topical field of metallic glasses. The findings can be roughly grouped into three main categories.

7.1 Fragility of supercooled metallic liquids

The work focuses on the fragility of deeply supercooled metallic glass forming liquids. Here, the $Pt_{42.5}Cu_{27}Ni_{9.5}P_{21}$ alloy serves as a model system. Its liquid dynamics are characterized via MDSC in Paper I, via temperature scanning XPCS in Paper II and by using DMA and FDSC methods as additional methods. Especially the advanced methods of XPCS and FDSC allow to characterize temperature ranges that were mostly inaccessible in previous studies. Combining the resulting data with other experimental approaches leads to an exceptionally large fragility data set comparison and the question of an adequate model to describe, quantify, and extrapolate arises. Future studies, e.g. those that combine XPCS and FDSC to further increase the accessible temperature range might help to clarify the matter. Moreover, the work demonstrates the close connection between liquid dynamics and vitrification and also crystallization kinetics, which are modelled for the $Pt_{42.5}Cu_{27}Ni_{9.5}P_{21}$ alloy in Paper III by using state of the art FDSC methodology.

7.2 Revealing the coexistence of two types of atomic motions in the non-equilibrium state via temperature scanning XPCS

Paper II introduces the rather unconventional method of temperature scanning XPCS, which is a novelty in terms of metallic glass formers. By heating and cooling through the glass transition region of the $Pt_{42.5}Cu_{27}Ni_{9.5}P_{21}$ alloy, the work reveals for the first time that the non-equilibrium state seems to be characterized by the coexistence of two types of atomic motions, namely liquid-like (sub-)diffusive motions as well as glass-typical ballistic-like motions driven by internal stress states. It is found that this interplay can be mathematically modelled by a multiplication of two KWW functions. The presented method of temperature scanning XPCS will likely evolve to become a standard experimental approach for countless scientific cases, e.g. liquid-liquid transitions or phase separations. Furthermore, the developed multiplicative fitting approach might find its use

not only for out-of-equilibrium metallic systems, but for glass forming materials in general and its application is likely not limited to XPCS but could be also expanded to evaluate results stemming from much more prevalent dynamic light scattering experiments.

7.3 Laser powder bed fusion of metallic glass formers

Paper IV, V, and VI focus on the additive manufacturing of BMGs via laser powder bed fusion. Paper IV investigates the possibility of post-processing AM-formed parts via thermoplastic forming on hand of the Zr-based AMZ4 alloy. The approach appears promising, since it is able to optimize and functionalize part surfaces. Paper V provides a comprehensive evaluation of the CuTi-based Vit101 alloy system for PBF-LB/M. Paper VI finally presents a first evaluation of the binary $Ni_{62}Nb_{38}$ glass former in terms of AM. Given the case of optimized processing, it is demonstrated that the yield strength can be reproducibly reached for AMZ4 and Vit101 AM-formed parts, leading to record-bearing strength values of 2.1 GPa and 2.5 GPa, respectively. Extrapolating this trend to the $Ni_{62}Nb_{38}$ alloy would allow for PBF-LB/M-formed metallic glasses with extreme strength values beyond 3 GPa. Nevertheless, brittleness remains a challenge to be addressed. Furthermore, the work demonstrates that additively formed BMGs can be a promising choice for lightweight structures, but also for compliant mechanisms that functionalize the material-specific exceptional elastic deformability. The latter aspect would also be highly auspicious for e.g. auxetic structures.

8. COPYRIGHT PERMISSIONS

Copyright permissions for single figures

Figure 1.1: Taken from [64] under the license number 5994061251221

Figure 1.2: Taken from [68] via open access under CC BY 4.0

Figure 2.4: Taken from [89] under the license number 1591173-1

Figure 2.5: Taken from [96] via open access under CC BY 4.0

Figure 2.7: Taken from [110] under the license number 5994260863724

Figure 2.11: Taken from[142] under the license number 5994261495020

Figure 2.12: Taken from [142] under the license number 5994261495020

Figure 2.13: Taken from [158] under the license number 5994330059685

Figure 2.14: Taken from [160] under the license number 5994331256401

Figure 2.15: Taken from [164] via open access under CC BY 4.0

Figure 2.21: Taken from [71] under the license number 5994340921094

Figure 2.23: Taken from [188] under the license number 5994350398504

Figure 2.24: Taken from [196] under the license number 5994350961677

Figure 3.11: Taken from [211] under the license number 5994351270985

Figure 3.12: Taken from [65] under the license number 5994360274557

Figure 4.15: Taken from [244] under the license number 5994360526248

Figure 4.17: Taken from [251] under the license number 1591206-1

Figure 4.19: Taken from [6] via open access under CC BY 4.0

Figure 6.16: Taken from [329] under the license number 5994380159516

Figure 6.17: Taken from [325] via open access under CC BY 4.0

Figure 6.18: Taken from [17] via open access under CC BY 4.0

Figure 6.19: Taken from [17] via open access under CC BY 4.0

Figure 6.21: Taken from [356] via open access under CC BY 3.0

Figure 6.22: Taken from [356] via open access under CC BY 3.0

Figure 6.23: Taken from [20] as a co-author

Figure 6.24: Taken from [20] as a co-author

Figure 6.25: Taken from [20] as a co-author

Figure 6.26: Taken from [20] as a co-author

Copyright permissions for reprinted publications

Paper I: Reprinted from [1] under the license number 1592483-1

Paper II: Reprinted from [6] via open access under CC BY 4.0

Paper III: Reprinted from [3] via open access under CC BY 4.0

Paper VI: Reprinted from [2] via open access under CC BY 4.0

Paper V: Reprinted from [4] via open access under CC BY 4.0

Paper VI: Reprinted from [5] via open access under CC BY 4.0

9. REFERENCES

[1] M. Frey, N. Neuber, O. Gross, B. Zimmer, W. Possart, R. Busch, Determining the fragility of bulk metallic glass forming liquids via modulated DSC, J. Phys. Condens. Matter. 32 (2020). https://doi.org/10.1088/1361-648x/ab8526.

[2] M. Frey, J. Wegner, N. Neuber, B. Reiplinger, B. Bochtler, B. Adam, L. Ruschel, S.S. Riegler, H.-R. Jiang, S. Kleszczynski, G. Witt, R. Busch, Thermoplastic forming of additively manufactured Zr-based bulk metallic glass: A processing route for surface finishing of complex structures, Mater. Des. 198 (2021) 1–8. https://doi.org/10.1016/j.matdes.2020.109368.

[3] M. Frey, N. Neuber, M. Müller, O. Gross, S.S. Riegler, I. Gallino, R. Busch, Determining and Modelling a Complete Time-Temperature-Transformation Diagram for a Pt-based Metallic Glass Former through Combination of Conventional and Fast Scanning Calorimetry, Scr. Mater. 215 (2022). https://doi.org/10.1016/j.scriptamat.2022.114710.

[4] M. Frey, J. Wegner, E.S. Barreto, L. Ruschel, N. Neuber, B. Adam, S.S. Riegler, H.R. Jiang, G. Witt, N. Ellendt, V. Uhlenwinkel, S. Kleszczynski, R. Busch, Laser powder bed fusion of Cu-Ti-Zr-Ni bulk metallic glasses in the Vit101 alloy system, Addit. Manuf. 66 (2023). https://doi.org/10.1016/j.addma.2023.103467.

[5] M. Frey, J. Wegner, L.M. Ruschel, E.S. Barreto, S.S. Riegler, B. Adam, N. Ellendt, S. Kleszczynski, R. Busch, Additive manufacturing of $Ni_{62}Nb_{38}$ metallic glass via laser powder bed fusion, Prog. Addit. Manuf. 101 (2025). https://doi.org/10.1007/s40964-025-01007-6.

[6] M. Frey, N. Neuber, S.S. Riegler, A. Cornet, Y. Chushkin, F. Zontone, L.M. Ruschel, B. Adam, M. Nabahat, F. Yang, J. Shen, F. Westermeier, M. Sprung, D. Cangialosi, V. Di Lisio, I. Gallino, R. Busch, B. Ruta, Liquid-like versus stress-driven dynamics in a metallic glass former observed by temperature scanning X-ray photon correlation spectroscopy, Nat. Commun. 16 (2025). https://doi.org/10.1038/s41467-025-59767-2.

[7] M. Frey, R. Busch, W. Possart, I. Gallino, On the thermodynamics, kinetics, and sub-T_g relaxations of Mg-based bulk metallic glasses, Acta Mater. 155 (2018) 117–127. https://doi.org/10.1016/j.actamat.2018.05.063.

[8] J. Wegner, S. Kleszczynski, M. Frey, S. Hechler, G. Witt, R. Busch, Parameterstudie zur Verarbeitung metallischer Gläser auf Zr-Basis mit dem Laser-Strahlschmelzverfahren, in: Proc. 15th Rapid.Tech Conf., 2018. https://doi.org/10.3139/9783446458123.022.

[9] O. Gross, N. Neuber, A. Kuball, B. Bochtler, S. Hechler, M. Frey, R. Busch, Signatures of structural differences in Pt-P- and Pd-P-based bulk glass-forming liquids, Commun. Phys. 2 (2019) 1–8. https://doi.org/10.1038/s42005-019-0180-2.

[10] J. Wegner, M. Frey, P. Stiglmair, S. Kleszczynski, G. Witt, R. Busch, MECHANICAL PROPERTIES OF HONEYCOMB STRUCTURED ZR-BASED BULK METALLIC GLASS SPECIMENS FABRICATED BY LASER POWDER BED FUSION, South African J. Ind. Eng. 30 (2019). https://doi.org/\url{10.7166/30-3-2265}.

[11] H. Jiang, B. Bochtler, M. Frey, Q. Liu, X. Wei, Y. Min, S.S. Riegler, D. Liang, R. Busch, J. Shen, Equilibrium viscosity and structural change in the $Cu_{47.5}Zr_{45.1}Al_{7.4}$ bulk glass-forming liquid, Acta Mater. 184 (2020) 69–78. https://doi.org/10.1016/j.actamat.2019.11.039.

[12] N. Neuber, M. Frey, O. Gross, J. Baller, I. Gallino, R. Busch, Ultrafast scanning calorimetry of newly developed Au-Ga bulk metallic glasses, J. Phys. Condens. Matter. (2020). https://doi.org/10.1088/1361-648x/ab8252.

[13] H.-R. Jiang, B. Bochtler, S.S. Riegler, X.-S. Wei, N. Neuber, M. Frey, I. Gallino, R. Busch, J. Shen, Thermodynamic and kinetic studies of the Cu–Zr–Al(–Sn) bulk metallic glass-forming system, J. Alloys Compd. 844 (2020) 156126. https://doi.org/10.1016/j.jallcom.2020.156126.

[14] B. Ruta, S. Hechler, N. Neuber, D. Orsi, L. Cristofolini, O. Gross, B. Bochtler, M. Frey, A. Kuball, S.S.S. Riegler, M. Stolpe, Z. Evenson, C. Gutt, F. Westermeier, R. Busch, I. Gallino, Wave-Vector Dependence of the Dynamics in Supercooled Metallic Liquids, Phys. Rev. Lett. 125 (2020) 055701. https://doi.org/10.1103/PhysRevLett.125.055701.

[15] J. Wegner, M. Frey, S. Kleszczynski, R. Busch, G. Witt, Influence of process gas during powder bed fusion with laser beam of Zr-based bulk metallic glasses, in: 11th CIRP Conf. Photonic Technol. [LANE 2020], Elsevier B.V., 2020: pp. 205–210. https://doi.org/10.1016/j.procir.2020.09.039.

[16] H.R. Jiang, J.Y. Hu, N. Neuber, B. Bochtler, B. Adam, S.S. Riegler, M. Frey, L. Ruschel, W.F. Lu, A.H. Feng, R. Busch, J. Shen, Effect of sulfur on the glass-forming ability, phase

transformation, and thermal stability of Cu-Zr-Al bulk metallic glass, Acta Mater. 212 (2021) 116923. https://doi.org/10.1016/j.actamat.2021.116923.

[17] J. Wegner, M. Frey, M. Piechotta, N. Neuber, B. Adam, S. Platt, L. Ruschel, N. Schnell, S. Sebastian, H. Jiang, G. Witt, R. Busch, S. Kleszczynski, Influence of powder characteristics on the structural and the mechanical properties of additively manufactured Zr-based bulk metallic glass, Mater. Des. 209 (2021) 109976. https://doi.org/10.1016/j.matdes.2021.109976.

[18] E.S. Barreto, V. Uhlenwinkel, M. Frey, I. Gallino, R. Busch, A. Lüttge, Influence of Processing Route on the Surface Reactivity of $Cu_{47}Ti_{33}Zr_{11}Ni_6Sn_2Si_1$ Metallic Glass, Metals (Basel). 11 (2021) 1–13. https://doi.org/10.3390/met11081173.

[19] N. Neuber, O. Gross, M. Frey, B. Bochtler, A. Kuball, S. Hechler, I. Gallino, R. Busch, On the thermodynamics and its connection to structure in the Pt-Pd-Cu-Ni-P bulk metallic glass forming system, Acta Mater. 220 (2021) 117300. https://doi.org/10.1016/j.actamat.2021.117300.

[20] J. Wegner, M. Frey, R. Busch, S. Kleszczynski, Additive manufacturing of a compliant mechanism using Zr-based bulk metallic glass, Addit. Manuf. Lett. 1 (2021) 100019. https://doi.org/10.1016/j.addlet.2021.100019.

[21] H.-R. Jiang, J. Tseng, N. Neuber, J. Barrirero, B. Adam, M. Frey, A.-C. Dippel, S. Banerjee, I. Gallino, A.-H. Feng, G. Wang, F. Mücklich, R. Busch, J. Shen, On the devitrification of Cu–Zr–Al alloys: Solving the apparent contradiction between polymorphic liquid-liquid transition and phase separation, Acta Mater. 226 (2022) 117668. https://doi.org/10.1016/j.actamat.2022.117668.

[22] L. Thorsson, M. Unosson, M. Teresa Pérez-Prado, X. Jin, P. Tiberto, G. Barrera, B. Adam, N. Neuber, A. Ghavimi, M. Frey, R. Busch, I. Gallino, Selective laser melting of a Fe-Si-Cr-B-C-based complex-shaped amorphous soft-magnetic electric motor rotor with record dimensions, Mater. Des. 215 (2022) 110483. https://doi.org/10.1016/j.matdes.2022.110483.

[23] E. Soares Barreto, M. Frey, J. Wegner, A. Jose, N. Neuber, R. Busch, S. Kleszczynski, L. Mädler, V. Uhlenwinkel, Properties of gas-atomized Cu-Ti-based metallic glass powders for additive manufacturing, Mater. Des. 215 (2022) 110519. https://doi.org/10.1016/j.matdes.2022.110519.

[24] S. Bechtel, R. Schweitzer, M. Frey, R. Busch, H.-G. Herrmann, Material Extrusion of Structural Polymer-Aluminum Joints - Examining Shear Strength, Wetting, Polymer Melt Rheology and Aging, Materials (Basel). (2022). https://doi.org/10.3390/ma15093120.

[25] N. Neuber, M. Sadeghilaridjani, N. Ghodki, O. Gross, B. Adam, L. Ruschel, M. Frey, S. Muskeri, M. Blankenburg, I. Gallino, R. Busch, S. Mukherjee, Effect of composition and thermal history on deformation behavior and cluster connections in model bulk metallic glasses, Sci. Rep. 12 (2022) 1–14. https://doi.org/10.1038/s41598-022-20938-6.

[26] N. Neuber, O. Gross, M. Frey, B. Bochtler, A. Kuball, S. Hechler, F. Yang, E. Pineda, F. Westermeier, M. Sprung, F. Schäfer, I. Gallino, R. Busch, B. Ruta, Disentangling structural and kinetic components of the α-relaxation in supercooled metallic liquids, Commun. Phys. 5 (2022) 1–10. https://doi.org/10.1038/s42005-022-01099-4.

[27] E.S. Barreto, J. Wegner, M. Frey, S. Kleszczynski, R. Busch, V. Uhlenwinkel, L. Mädler, N. Ellendt, Influence of oxygen in the production chain of Cu-Ti-based metallic glasses via laser powder bed fusion, Powder Metall. 8 (2023) 1–12. https://doi.org/10.1080/00325899.2023.2179207.

[28] L.M. Ruschel, B. Adam, O. Gross, N. Neuber, M. Frey, H. Wachter, R. Busch, Development and optimization of novel sulfur-containing Ti-based bulk metallic glasses and the correlation between primarily crystallizing phases, thermal stability and mechanical properties, J. Alloys Compd. 960 (2023) 170614. https://doi.org/10.1016/j.jallcom.2023.170614.

[29] H. Jiang, J. Hu, N. Neuber, M. Frey, L. Xu, K. Sun, Y. Jia, G. Wang, R. Busch, J. Shen, Influence of sulfur addition on the glass formation, phase transformation and mechanical properties of $Cu_{50}Zr_{50}$ alloy, Acta Mater. 255 (2023) 119064. https://doi.org/10.1016/j.actamat.2023.119064.

[30] A. Cornet, G. Garbarino, F. Zontone, Y. Chushkin, J. Jacobs, E. Pineda, T. Deschamps, S. Li, A. Ronca, J. Shen, G. Morard, N. Neuber, M. Frey, R. Busch, I. Gallino, M. Mezouar, G. Vaughan, B. Ruta, Denser glasses relax faster: Enhanced atomic mobility and anomalous particle displacement under in-situ high pressure compression of metallic glasses, Acta Mater. 255 (2023) 119065. https://doi.org/10.1016/j.actamat.2023.119065.

[31] L.M. Ruschel, O. Gross, B. Bochtler, B. Li, B. Adam, N. Neuber, M. Frey, S. Jakovlev, F. Yang, H. Jiang, B. Gludovatz, J.J. Kruzic, R. Busch, Ni-Nb-P-based bulk glass-forming alloys:

Superior material properties combined in one alloy family, Acta Mater. accepted f (2023) 118968. https://doi.org/10.1016/j.actamat.2023.118968.

[32] V. Di Lisio, I. Gallino, S.S. Riegler, M. Frey, N. Neuber, G. Kumar, J. Schroers, R. Busch, D. Cangialosi, Size-dependent vitrification in metallic glasses, Nat. Commun. 14 (2023) 4698. https://doi.org/10.1038/s41467-023-40417-4.

[33] E.S. Barreto, M. Frey, L. Matthias, J. Wegner, S. Kleszczynski, R. Busch, N. Ellendt, Gas atomization of fully-amorphous $Ni_{62}Nb_{38}$ powder, Mater. Lett. 357 (2024) 135798. https://doi.org/10.1016/j.matlet.2023.135798.

[34] L.M. Ruschel, A. Kuball, B. Adam, M. Frey, R. Busch, $Zr_{56.5}Ti_{13.3}Ni_{13.6}Cu_{9.6}S_7$ bulk metallic glass-forming liquid, AIP Adv. 14 (2024). https://doi.org/10.1063/5.0192705.

[35] H. Schoenrath, J. Wegner, M. Frey, E. Soares Barreto, A. Elspaß, N. Schnell, B.H.R. Erdmann, J. Neises, N. Ellendt, R. Busch, S. Kleszczynski, Analytical Modeling of Cooling Rates in PBF-LB/M of Bulk Metallic Glasses, Solid Free. Fabr. 2023 Proc. (2024). https://doi.org/https://doi.org/10.26153/tsw/50980.

[36] S.S. Riegler, Y.H.S. Camposano, K. Jaekel, M. Frey, C. Neemann, S. Matthes, E. Vardo, M.R. Chegeni, H. Bartsch, R. Busch, J. Müller, P. Schaaf, I. Gallino, Nanocalorimetry of Nanoscaled Ni/Al Multilayer Films: On the Methodology to Determine Reaction Kinetics for Highly Reactive Films, Adv. Eng. Mater. 2302279 (2024). https://doi.org/10.1002/adem.202302279.

[37] L. Bruckhaus, J. Wegner, N. Schnell, H. Schönrath, E. Soares, B. Maximilian, N. Ellendt, R. Busch, S. Kleszczynski, Empirical calibration method for the thermal simulation of $Cu_{47}Ti_{34}Zr_{11}Ni_8$ single tracks in laser powder bed fusion, Prog. Addit. Manuf. 9 (2024) 593–600. https://doi.org/10.1007/s40964-024-00653-6.

[38] H. Schönrath, J. Wegner, M. Frey, M.A. Schroer, X. Jin, M. Teresa, P. Prado, R. Busch, S. Kleszczynski, Novel titanium-based sulfur-containing BMG for PBF-LB/M, Prog. Addit. Manuf. 9 (2024) 601–612. https://doi.org/10.1007/s40964-024-00668-z.

[39] B. Adam, A. Kuball, L.M. Ruschel, N. Neuber, M. Frey, R. Busch, Sulphuric precipitates in novel titanium-based, sulphur-bearing bulk metallic glass – a BMG composite?, Philos. Mag. Lett. (2024) 1–11. https://doi.org/10.1080/09500839.2024.2376614.

[40] L.M. Ruschel, S. Jakovlev, O. Gross, N. Neuber, B. Adam, M. Frey, B. Schmidt, B. Bochtler, R. Busch, Unraveling the role of relaxation and rejuvenation on the structure and deformation behavior of the Zr-based bulk metallic glass Vit105, Mater. Today Adv. 23 (2024) 100522. https://doi.org/10.1016/j.mtadv.2024.100522.

[41] H.R. Jiang, M. Frey, N. Neuber, Y.F. Gao, B. Zhang, J. Ren, G. Wang, R. Busch, J. Shen, In-situ scattering and calorimetric studies of crystallization pathway and kinetics in a Cu-Zr-Al bulk metallic glass, J. Alloys Compd. 1006 (2024) 176243. https://doi.org/10.1016/j.jallcom.2024.176243.

[42] H. Schönrath, J. Wegner, M.A. Schroer, M. Frey, R. Busch, S. Kleszczynski, Impact of processing parameters on mechanical properties of additively manufactured Ti-based BMGs, MATEC Web Conf. 406 (2024). https://doi.org/10.1051/matecconf/202440607003.

[43] B. Li, L.M. Ruschel, K. Nomoto, O. Gross, B. Adam, N. Neuber, M. Frey, S.P. Ringer, B. Gludovatz, R. Busch, J.J. Kruzic, Fracture behavior of NiNb and NiNbP bulk metallic glasses, J. Alloys Compd. 1010 (2025). https://doi.org/10.1016/j.jallcom.2024.177369.

[44] B. Adam, O. Kruse, L.M. Ruschel, N. Neuber, M. Frey, O. Gross, H.R. Jiang, B. Li, B. Gludovatz, J.J. Kruzic, R. Busch, Introduction of sulfur into an eutectic of the Zr-Ti-Ni-Cu system: Alloy development and characterization of the $(Zr_{50}Ti_{16.6}Ni_{18.3}Cu_{15})_{100-x}S_x$ bulk metallic glasses, J. Alloys Compd. 1025 (2025) 180307. https://doi.org/10.1016/j.jallcom.2025.180307.

[45] H.R. Jiang, M. Frey, N. Neuber, Q. Wang, W.F. Lu, L.M. Ruschel, G.Y. Sun, I. Gallino, B. Zhang, G. Wang, R. Busch, J. Shen, Y. Yang, Liquid-liquid phase transition and chemical phase separation in Cu-Zr-Al-Y bulk glass-forming supercooled liquid, Acta Mater. 293 (2025). https://doi.org/10.1016/j.actamat.2025.121090.

[46] C.A. Angell, Formation of glasses from liquids and biopolymers, Science. 267 (1995) 1924–1935. https://doi.org/10.1126/science.267.5206.1924.

[47] P. Richet, A History of Glass Science, in: Encycl. Glas. Sci. Technol. Hist. Cult., 2021: pp. 1413–1440. https://doi.org/10.1002/9781118801017.ch10.11.

[48] W. Klement, R.H. Willens, P. Duwez, Non-crystalline Structure in Solidified Gold–Silicon Alloys, Nature. 187 (1960) 869–870. https://doi.org/10.1038/187869b0.

[49] H.S. Chen, Thermodynamic considerations on the formation and stability of metallic glasses, Acta Metall. 22 (1974) 1505–1511. https://doi.org/10.1016/0001-6160(74)90112-6.

[50] H.S. Chen, Glassy Metals, Reports Prog. Phys. 43 (1980). https://doi.org/10.1007/978-3-662-47882-0.

[51] A.J. Drehman, A.L. Greer, D. Turnbull, Bulk formation of a metallic glass: Pd40Ni40P20, Appl. Phys. Lett. 41 (1982) 716–717. https://doi.org/10.1063/1.93645.

[52] H.W. Kui, A.L. Greer, D. Turnbull, Formation of Bulk Metallic Glass By Fluxing., Appl. Phys. Lett. 45 (1984) 615–616. https://doi.org/10.1063/1.95330.

[53] A. Inoue, T. Zhang, T. Masumoto, Zr-Al-Ni Amorphous Alloys with High Glass Transition Temperature and Significant Supercooled Liquid Region, Mater. Trans. JIM. 31 (1990) 177–183. https://doi.org/10.2320/matertrans1989.31.177.

[54] T. Zhang, A. Inoue, T. Masumoto, Amorphous Zr-Al-TM (TM=Co,Ni,Cu) alloys with significant supercooled liquid region of over 100 K, Mater. Trans. JIM. 32 (1991) 1005–1010. https://doi.org/10.2320/matertrans1989.32.1005.

[55] M.F. Ashby, A.L. Greer, Metallic glasses as structural materials, Scr. Mater. 54 (2006) 321–326. https://doi.org/10.1016/j.scriptamat.2005.09.051.

[56] W.H. Wang, The elastic properties, elastic models and elastic perspectives of metallic glasses, Prog. Mater. Sci. 57 (2012) 487–656. https://doi.org/10.1016/j.pmatsci.2011.07.001.

[57] W.H. Wang, C. Dong, C.H. Shek, Bulk metallic glasses, Mater. Sci. Eng. R Reports. 44 (2004) 45–90. https://doi.org/10.1016/j.mser.2004.03.001.

[58] H. Choi-Yim, D. Xu, W.L. Johnson, Ni-based bulk metallic glass formation in the Ni-Nb-Sn and Ni-Nb-Sn-X (X = B, Fe, Cu) alloy systems, Appl. Phys. Lett. 82 (2003) 1030–1032. https://doi.org/10.1063/1.1544434.

[59] H.T. Hu, L.Y. Chen, X.D. Wang, Q.P. Cao, J.Z. Jiang, Formation of Ni-Nb-Zr-X (X = Ti, Ta, Fe, Cu, Co) bulk metallic glasses, J. Alloys Compd. 460 (2008) 714–718. https://doi.org/10.1016/j.jallcom.2008.01.075.

[60] D. Meng, J. Yi, D.Q. Zhao, D.W. Ding, H.Y. Bai, M.X. Pan, W.H. Wang, Tantalum based bulk metallic glasses, J. Non. Cryst. Solids. 357 (2011) 1787–1790. https://doi.org/10.1016/j.jnoncrysol.2011.01.020.

[61] B. Bochtler, O. Gross, I. Gallino, R. Busch, Thermo-physical characterization of the $Fe_{67}Mo_6Ni_{3.5}Cr_{3.5}P_{12}C_{5.5}B_{2.5}$ bulk metallic glass forming alloy, Acta Mater. 118 (2016) 129–139. https://doi.org/10.1016/j.actamat.2016.07.031.

[62] C. Suryanarayana, A. Inoue, Iron-based bulk metallic glasses, Int. Mater. Rev. 58 (2013) 131–166. https://doi.org/10.1179/1743280412Y.0000000007.

[63] M. Telford, The case for bulk metallic glass, Mater. Today. 7 (2004) 36–43. https://doi.org/10.1016/S1369-7021(04)00124-5.

[64] J.F. Löffler, Bulk metallic glasses, Intermetallics. 11 (2003) 529–540. https://doi.org/10.1016/S0966-9795(03)00046-3.

[65] J. Schroers, The superplastic forming of bulk metallic glasses, JOM J. Miner. Met. Mater. (2005) 35–39. https://doi.org/10.1007/s11837-005-0093-2.

[66] J. Schroers, Processing of bulk metallic glass, Adv. Mater. 22 (2010) 1566–1597. https://doi.org/10.1002/adma.200902776.

[67] S. Pauly, L. Löber, R. Petters, M. Stoica, S. Scudino, U. Kühn, J. Eckert, Processing metallic glasses by selective laser melting, Mater. Today. 16 (2013) 37–41. https://doi.org/10.1016/j.mattod.2013.01.018.

[68] N. Sohrabi, J. Jhabvala, R.E. Logé, Additive manufacturing of bulk metallic glasses - Process , challenges and properties : A review, Metals (Basel). 11 (2021).

[69] J. Schroers, W.L. Johnson, Highly processable bulk metallic glass-forming alloys in the Pt-Co-Ni-Cu-P system, Appl. Phys. Lett. 84 (2004) 3666–3668. https://doi.org/10.1063/1.1738945.

[70] O. Gross, B. Bochtler, M. Stolpe, S. Hechler, W. Hembree, R. Busch, I. Gallino, The kinetic fragility of Pt-P- and Ni-P-based bulk glass-forming liquids and its thermodynamic and structural signature, Acta Mater. 132 (2017) 118–127. https://doi.org/10.1016/j.actamat.2017.04.030.

[71] O. Gross, S.S. Riegler, M. Stolpe, B. Bochtler, A. Kuball, S. Hechler, R. Busch, I. Gallino, On the high glass-forming ability of Pt-Cu-Ni/Co-P-based liquids, Acta Mater. 141 (2017) 109–119. https://doi.org/10.1016/j.actamat.2017.09.013.

[72] J. Heinrich, Massivglasbildende metallische Legierungen als Konstruktionswerkstoff Materialoptimierung und Technologieentwicklung zur Herstellung und Verarbeitung, 2012. https://doi.org/10.22028/D291-22841.

[73] J. Heinrich, R. Busch, B. Nonnenmacher, Processing of a bulk metallic glass forming alloy based on industrial grade Zr, Intermetallics. 25 (2012) 1–4. https://doi.org/10.1016/j.intermet.2012.02.011.

[74] Heraeus AMLOY, AMLOY-ZR01 datasheet, n.d.

[75] X.H. Lin, W.L. Johnson, Formation of Ti-Zr-Cu-Ni bulk metallic glasses, J. Appl. Phys. 78 (1995) 6514–6519. https://doi.org/10.1063/1.360537.

[76] L. Xia, W.H. Li, S.S. Fang, B.C. Wei, Y.D. Dong, Binary Ni-Nb bulk metallic glasses, J. Appl. Phys. 99 (2006) 58–61. https://doi.org/10.1063/1.2158130.

[77] R. Metzler, J.H. Jeon, A.G. Cherstvy, E. Barkai, Anomalous diffusion models and their properties: Non-stationarity, non-ergodicity, and ageing at the centenary of single particle tracking, Phys. Chem. Chem. Phys. 16 (2014) 24128–24164. https://doi.org/10.1039/c4cp03465a.

[78] R. Kohlrausch, Theorie des elektrischen Rückstandes in der Leidener Flasche, Ann. Phys. 167 (1854) 179–214.

[79] G. Williams, D.C. Watts, Non-symmetrical dielectric relaxation behaviour arising from a simple empirical decay function, Trans. Faraday Soc. 66 (1970) 80. https://doi.org/10.1039/tf9706600080.

[80] C. Maxwell, On the Dynamical Theory of Gases, Philos. Trans. R. Soc. London. 157 (1867) 49–88.

[81] D. Turnbull, M.H. Cohen, Free-volume model of the amorphous phase: Glass transition, J. Chem. Phys. 34 (1961) 120–125. https://doi.org/10.1063/1.1731549.

[82] M.H. Cohen, G.S. Grest, Liquid-glass transition, a free-volume approach, Phys. Rev. B. 20 (1979) 1077–1098. https://doi.org/10.1103/PhysRevB.20.1077.

[83] A. Meyer, J. Wuttke, W. Petry, O.G. Randl, H. Schober, Slow Motion in a Metallic Liquid, Phys. Rev. Lett. 80 (1998) 4454–4457. https://doi.org/10.1103/PhysRevLett.80.4454.

[84] Z. Evenson, F. Yang, G.G. Simeoni, A. Meyer, Self-diffusion and microscopic dynamics in a gold-silicon liquid investigated with quasielastic neutron scattering, Appl. Phys. Lett. 108 (2016). https://doi.org/10.1063/1.4944814.

[85] S. Wei, Z. Evenson, M. Stolpe, P. Lucas, C. Austen Angell, Breakdown of the Stokes-Einstein relation above the melting temperature in a liquid phase-change material, Sci. Adv. 4 (2018) 1–6. https://doi.org/10.1126/sciadv.aat8632.

[86] F. Faupel, W. Frank, M.-P. Macht, H. Mehrer, V. Naundorf, K. Rätzke, H.R. Schober, S.K. Sharma, H. Teichler, Diffusion in metallic glasses and supercooled melts, Rev. Mod. Phys. 75 (2003) 237–280. https://doi.org/10.1103/RevModPhys.75.237.

[87] B. Ruta, E. Pineda, Z. Evenson, Topical Review: Relaxation processes and physical aging in metallic glasses, J. Phys. Condens. Matter. 29 (2017) 503002. https://doi.org/10.1088/1361-648X/aa9964.

[88] M.D. Ediger, Spatially heterogeneous dynamics in supercooled liquids, Annu. Rev. Phys. Chem. 51 (2000) 99–128. https://doi.org/10.1146/annurev.physchem.51.1.99.

[89] R. Richert, Heterogeneous dynamics in liquids: Fluctuations in space and time, J. Phys. Condens. Matter. 14 (2002). https://doi.org/10.1088/0953-8984/14/23/201.

[90] P.N. Pusey, Liquids, Freezing and Glass Transition, in: Les Houches Sess. 51., 1991. https://books.google.co.uk/books?id=YC30nwEACAAJ.

[91] R. Pecora, Dynamic Light Scattering: Applications of Photon Correlation Spectroscopy, 2008. http://dx.doi.org/10.1007/978-1-4020-4465-6_13.

[92] G. Stokes, On the Effect of the Internal Friction of Fluids on the Motion of Pendulums, Trans. Cambridge Philos. Soc. 9 part II (1856) 8–106. https://doi.org/10.1007/BF03017698.

[93] W. Gotze, L. Sjogren, Relaxation processes in supercooled liquids, Reports Prog. Phys. 241 (1992). http://iopscience.iop.org/0034-4885/55/3/001.

[94] A. Arbe, J. Colmenero, M. Monkenbusch, D. Richter, Dynamics of glass-forming polymers: “Homogeneous” versus “heterogeneous” scenario, Phys. Rev. Lett. 81 (1998) 590–593. https://doi.org/10.1103/PhysRevLett.81.590.

[95] D. Chatterjee, A. Annamareddy, J. Ketkaew, J. Schroers, D. Morgan, P.M. Voyles, Fast surface dynamics on a metallic glass nanowire, ACS Nano. 15 (2021). https://doi.org/10.1021/acsnano.1c00500.

[96] P. Zhang, J.J. Maldonis, Z. Liu, J. Schroers, P.M. Voyles, Spatially heterogeneous dynamics in a metallic glass forming liquid imaged by electron correlation microscopy, Nat. Commun. 9 (2018) 1–7. https://doi.org/10.1038/s41467-018-03604-2.

[97] P. Chaudhuri, L. Berthier, W. Kob, Universal nature of particle displacements close to glass and jamming transitions, Phys. Rev. Lett. 99 (2007) 2–5. https://doi.org/10.1103/PhysRevLett.99.060604.

[98] E.R. Weeks, J.C. Crocker, A.C. Levitt, A. Schofield, D.A. Weitz, Three-dimensional direct imaging of structural relaxation near the colloidal glass transition, Science (80-.). 287 (2000) 627–631. https://doi.org/10.1126/science.287.5453.627.

[99] A. Bartsch, K. Rätzke, A. Meyer, F. Faupel, Dynamic arrest in multicomponent glass-forming alloys, Phys. Rev. Lett. 104 (2010) 1–4. https://doi.org/10.1103/PhysRevLett.104.195901.

[100] K. Ra, F. Faupel, A. Meyer, Diffusion in a Metallic Melt at the Critical Temperature of Mode Coupling Theory, (2003) 1–4. https://doi.org/10.1103/PhysRevLett.90.195502.

[101] A. Masuhr, T.A. Waniuk, R. Busch, W.L. Johnson, Time Scales for Viscous Flow, Atomic Transport, and Crystallization in the Liquid and Supercooled Liquid States of $Zr_{41.2}Ti_{13.8}Cu_{12.5}Ni_{10.0}Be_{22.5}$, Phys. Rev. Lett. 82 (1999) 2290–2293. https://doi.org/10.1103/PhysRevLett.82.2290.

[102] K.L. Ngai, S. Capaccioli, An explanation of the differences in diffusivity of the components of the metallic glass $Pd_{43}Cu_{27}Ni_{10}P_{20}$, J. Chem. Phys. 138 (2013). https://doi.org/10.1063/1.4793597.

[103] U. Geyer, S. Schneider, W.L. Johnson, Y. Qiu, T.A. Tombrello, M. M.-P., Atomic Diffusion in the Supercooled Liquid and Glassy States of the $Zr_{41.2}Ti_{13.8}Cu_{12.5}Ni_{10}Be_{22.5}$ Alloy, Phys. Rev. Lett. 75 (1995) 2364–2367.

[104] C. Chang, H.P. Zhang, R. Zhao, F.C. Li, P. Luo, M.Z. Li, H.Y. Bai, Liquid-like atoms in dense-packed solid glasses, Nat. Mater. 21 (2022) 1240–1245. https://doi.org/10.1038/s41563-022-01327-w.

[105] I. Gallino, R. Busch, Relaxation Pathways in Metallic Glasses, Jom. 69 (2017) 2171–2177. https://doi.org/10.1007/s11837-017-2573-6.

[106] G. Tarjus, D. Kivelson, Breakdown of the Stokes-Einstein relation in supercooled liquids, J. Chem. Phys. 103 (1995) 3071–3073. https://doi.org/10.4028/www.scientific.net/JMNM.20-21.541.

[107] F. Yang, T. Unruh, A. Meyer, Coupled relaxation processes in a glass forming ZrTiNiCuBe liquid, Epl. 107 (2014). https://doi.org/10.1209/0295-5075/107/26001.

[108] R. Pastore, T. Kikutsuji, F. Rusciano, N. Matubayasi, K. Kim, F. Greco, Breakdown of the Stokes-Einstein relation in supercooled liquids: A cage-jump perspective, J. Chem. Phys. 155 (2021). https://doi.org/10.1063/5.0059622.

[109] R. Böhmer, K.L. Ngai, C.A. Angell, D.J. Plazek, Nonexponential relaxations in strong and fragile glass formers, J. Chem. Phys. 99 (1993) 4201–4209. https://doi.org/10.1063/1.466117.

[110] R. Busch, J. Schroers, W.H. Wang, Thermodynamics and Kinetics of Bulk Metallic Glass, MRS Bull. 32 (2007) 620–623. https://doi.org/\url{10.1557/mrs2007.122}.

[111] C.A. Angell, Relaxation in liquids, polymers and plastic crystals - strong/fragile patterns and problems, J. Non. Cryst. Solids. 131–133 (1991) 13–31. https://doi.org/10.1016/0022-3093(91)90266-9.

[112] R. Busch, I. Gallino, Kinetics, Thermodynamics, and Structure of Bulk Metallic Glass Forming Liquids, Jom. 69 (2017) 2178–2186. https://doi.org/10.1007/s11837-017-2574-5.

[113] I. Gallino, O. Gross, G. Dalla Fontana, Z. Evenson, R. Busch, On the kinetic and thermodynamic fragility of the $Pt_{60}Cu_{16}Co_2P_{22}$ and $Pt_{57.3}Cu_{14.6}Ni_{5.3}P_{22.8}$ bulk metallic glasse, J. Alloys Compd. 615 (2015) S35–S39. https://doi.org/10.1016/j.jallcom.2013.12.006.

[114] N. Neuber, O. Gross, M. Eisenbart, M.N. Polyakov, J. Michler, U.E. Klotz, R. Busch, I. Gallino, A. Heiss, J.P. Best, The role of Ga addition on the thermodynamics, kinetics, and

tarnishing properties of the Au-Ag-Pd-Cu-Si bulk metallic glass forming system, Acta Mater. 165 (2018) 315–326. https://doi.org/10.1016/j.actamat.2018.11.052.

[115] G.S. Fulcher, Analysis of recent measurements of the viscosity of glasses-II, J. Am. Ceram. Soc. 8 (1925) 789–794. https://doi.org/10.1111/j.1151-2916.1925.tb16731.x.

[116] G. Tammann, W. Hesse, Die Abhängigkeit der Viscosistat von der Temperatur bei unterkühlten Flüssigkeiten', Zeitschrift Für Anorg. Und Allg. Chemie. 156 (1926) 245–257. https://doi.org/10.1002/zaac.19261560121.

[117] I. Gallino, On the fragility of bulk metallic glass forming liquids, Entropy. 19 (2017). https://doi.org/10.3390/e19090483.

[118] S. V. Nemilov, Structural aspect of possible interrelation between fragility (length) of glass forming melts and Poisson's ratio of glasses, J. Non. Cryst. Solids. 353 (2007) 4613–4632. https://doi.org/10.1016/j.jnoncrysol.2007.08.045.

[119] J.C. Mauro, Y. Yue, A.J. Ellison, P.K. Gupta, D.C. Allan, Viscosity of glass-forming liquids, Proc. Natl. Acad. Sci. U. S. A. 106 (2009) 19780–19784. https://doi.org/10.1073/pnas.0911705106.

[120] L. Hu, Y. Yue, J.C. Mauro, Fragile-to-Strong Transition in Metallic Glass-Forming Liquids, (2010). https://doi.org/10.1063/1.3457670.

[121] A.K. Doolittle, Studies in newtonian flow. II. the dependence of the viscosity of liquids on free-space, J. Appl. Phys. 22 (1951) 1471–1475. https://doi.org/10.1063/1.1699894.

[122] G.S. Grest, M.H. Cohen, Liquids, Glasses, and the Glass Transition: A Free-Volume Approach, Adv. Chem. Phys. XLVIII (1981).

[123] M.D. Demetriou, J.S. Harmon, M. Tao, G. Duan, K. Samwer, W.L. Johnson, Cooperative shear model for the rheology of glass-forming metallic liquids, Phys. Rev. Lett. 97 (2006) 41–44. https://doi.org/10.1103/PhysRevLett.97.065502.

[124] W.L. Johnson, M.D. Demetriou, J.S. Harmon, M.L. Lind, K. Samwer, Rheology and ultrasonic properties of metallic glassforming liquids: A potential energy landscape perspective, MRS Bull. 32 (2007) 644–650. https://doi.org/10.1557/mrs2007.127.

[125] E. Donth, The Glass Transition - Relaxation Dynamics in Liquids and Disordered Materials, 2001. https://doi.org/10.1002/9781119220510.ch13.

[126] D. Cangialosi, Glass Transition and Relaxation Phenomena, in: Therm. Anal. Polym. Mater., 2022: pp. 227–262. https://doi.org/10.1002/9783527828692.ch5.

[127] R. Richert, Perspective: Nonlinear approaches to structure and dynamics of soft materials, J. Chem. Phys. 149 (2018). https://doi.org/10.1063/1.5065412.

[128] H. Nyquist, Thermal agitation of electric charge in conductors, Phys. Rev. 32 (1928) 110–113. https://doi.org/10.1103/PhysRev.32.110.

[129] H.B. Callen, R.F. Greene, On a theorem of irreversible thermodynamics, Phys. Rev. 86 (1952) 702–710. https://doi.org/10.1103/PhysRev.86.702.

[130] R. Kubo, Statistical-Mechanical Theory of Irreversible Processes. I. General Theory and Simple Applications to Magnetic and Conduction Problems, J. Phys. Soc. Japan. 12 (1957) 570–586. https://doi.org/10.1143/JPSJ.12.570.

[131] M. Reiner, The Deborah Number, Phys. Today. 17 (1964) 62. https://doi.org/10.1063/1.3051374.

[132] I.S. Gutzow, J.W.P. Schmelzer, The Vitreous State, 2013. https://doi.org/10.1007/978-3-642-34633-0.

[133] J.W.P. Schmelzer, I.S. Gutzow, Glasses and the glass transition, 2011.

[134] J.E.K. Schawe, Vitrification in a wide cooling rate range: The relations between cooling rate, relaxation time, transition width, and fragility, 141 (2014). https://doi.org/10.1063/1.4900961.

[135] A.Q. Tool, Relation Between Inelastic Deformability and Thermal Expansion of Glass in Its Annealing Range, J. Am. Ceram. Soc. 29 (1946) 240–253. https://doi.org/10.1111/j.1151-2916.1946.tb11592.x.

[136] C.T. Moynihan, A.J. Easteal, M.A. Debolt, J. Tucker, Dependence of the Fictive Temperature of Glass on Cooling Rate, J. Am. Ceram. Soc. 8 (1975) 12–16. https://doi.org/10.1111/j.1151-2916.1976.tb09376.x.

[137] J.E.K. Schawe, Measurement of the thermal glass transition of polystyrene in a cooling rate range of more than six decades, Thermochim. Acta. 603 (2015) 128–134. https://doi.org/10.1016/j.tca.2014.05.025.

[138] J.D. Bernal, A geometrical approach to the structure Of liquids, Nature. 183 (1959) 141–147. https://doi.org/10.1038/183141a0.

[139] J.D. Bernal, Geometry of the Structure of Monatomic Liquids, Nature. 185 (1960) 68–70.

[140] J. Mason, J.D. Bernal, Packing of spheres: co-ordination of randomly packed spheres, Nature. 188 (1960) 910–911. https://doi.org/10.1038/188910a0.

[141] J.D. Bernal, The Bakerian Lecture, 1962 The structure of liquids, Proc. R. Soc. London. Ser. A. Math. Phys. Sci. 280 (1964) 299–322. https://doi.org/10.1098/rspa.1964.0147.

[142] Y.Q. Cheng, E. Ma, Atomic-level structure and structure-property relationship in metallic glasses, Prog. Mater. Sci. 56 (2011) 379–473. https://doi.org/10.1016/j.pmatsci.2010.12.002.

[143] F.C. Frank, Supercooling of liquids, Proc. R. Soc. London. Ser. A. Math. Phys. Sci. 215 (1952) 43–46. https://doi.org/10.1098/rspa.1952.0194.

[144] T. Schenk, V. Simonet, R. Bellissent, D.M. Herlach, Icosahedral Short-Range Order in Deeply Undercooled Metallic Melts, (2002) 1–4. https://doi.org/10.1103/PhysRevLett.89.075507.

[145] A. Hirata, L.J. Kang, T. Fujita, B. Klumov, K. Matsue, M. Kotani, A.R. Yavari, M.W. Chen, Geometric Frustration of Icosahedron in Metallic Glasses, Science (80-.). 341 (2013). https://doi.org/10.1126/science.1232450.

[146] D.R. Nelson, Order, frustration, and defects in liquids and glasses, Phys. Rev. B. 28 (1983) 5515–5535. https://doi.org/10.1103/PhysRevB.28.5515.

[147] D.R. Nelson, F. Sapaepen, Polyhedral order in condensed mater, Solid State Phys. 42 (1989).

[148] T.M. Hayes, J.W. Allen, J. Tauc, B.C. Giessen, J.J. Hauser, Short-Range Order in Metallic Glasses, Phys. Rev. Lett. 40 (1978). https://doi.org/10.1103/physrevlett.40.1282.

[149] P.H. Gaskell, A new structural model for transition metal-metalloid glasses, Nature. 276 (1978) 484–485. https://doi.org/10.1038/276484a0.

[150] P.H. Gaskell, A new structural model for amorphous transition metal silicides, borides, phosphides and carbides, J. Non. Cryst. Solids. 32 (1979) 207–224. https://doi.org/10.1016/0022-3093(79)90073-5.

[151] D. Holland-Moritz, T. Schenk, V. Simonet, R. Bellissent, P. Convert, T. Hansen, D.M. Herlach, Short-range order in undercooled metallic liquids, Mater. Sci. Eng. A. 375–377 (2004) 98–103. https://doi.org/10.1016/j.msea.2003.10.056.

[152] H. Tanaka, P. Se, General view of a liquid-liquid phase transition, Phys. Rev. E. 62 (2000) 6968–6976. https://doi.org/10.1103/PhysRevE.62.6968.

[153] H. Tanaka, Two-order-parameter description of liquids. I. A general model of glass transition covering its strong to fragile limit, J. Chem. Phys. 111 (1999) 3163–3174. https://doi.org/10.1063/1.479596.

[154] P.M. Derlet, H. Bocquet, R. Maaß, Viscosity and transport in a model fragile metallic glass, Phys. Rev. Mater. 5 (2021) 1–7. https://doi.org/10.1103/PhysRevMaterials.5.125601.

[155] D.B. Miracle, W.S. Sanders, O.N. Senkov, The influence of efficient atomic packing on the constitution of metallic glasses, Philos. Mag. 83 (2003) 2409–2428. https://doi.org/10.1080/1478643031000098828.

[156] D.B. Miracle, Efficient local packing in metallic glasses, J. Non. Cryst. Solids. 342 (2004) 89–96. https://doi.org/10.1016/j.jnoncrysol.2004.05.017.

[157] D.B. Miracle, The efficient cluster packing model - An atomic structural model for metallic glasses, Acta Mater. 54 (2006) 4317–4336. https://doi.org/10.1016/j.actamat.2006.06.002.

[158] D.B. Miracle, A structural model for metallic glasses, Nat. Mater. 3 (2004) 697–702. https://doi.org/10.1038/nmat1219.

[159] D.B. Miracle, A.L. Greer, K.F. Kelton, Icosahedral and dense random cluster packing in metallic glass structures, J. Non. Cryst. Solids. 354 (2008) 4049–4055. https://doi.org/10.1016/j.jnoncrysol.2008.05.006.

[160] H.W. Sheng, W.K. Luo, F.M. Alamgir, J.M. Bai, E. Ma, Atomic packing and short-to-medium-range order in metallic glasses, Nature. 439 (2006) 419–425. https://doi.org/10.1038/nature04421.

[161] T. Takagi, T. Ohkubo, Y. Hirotsu, B.S. Murty, K. Hono, D. Shindo, Local structure of amorphous $Zr_{70}Pd_{30}$ alloy studied by electron diffraction, Appl. Phys. Lett. 79 (2001) 485–487. https://doi.org/10.1063/1.1383055.

[162] D. Nagahama, T. Ohkubo, K. Hono, Crystallization of $Ti_{36}Zr_{24}Be_{40}$ metallic glass, Scr. Mater. 49 (2003) 729–734. https://doi.org/10.1016/S1359-6462(03)00337-3.

[163] G. Kumar, D. Nagahama, M. Ohnuma, T. Ohkubo, K. Hono, Structural evolution in the supercooled liquid of $Zr_{36}Ti_{24}Be_{40}$ metallic glass, Scr. Mater. 54 (2006) 801–805. https://doi.org/10.1016/j.scriptamat.2005.11.019.

[164] J. Ding, E. Ma, M. Asta, R.O. Ritchie, Second-nearest-neighbor correlations from connection of atomic packing motifs in metallic glasses and liquids, Sci. Rep. 5 (2015) 1–9. https://doi.org/10.1038/srep17429.

[165] M. Jankowski, V. Belova, Y. Chushkin, F. Zontone, M. Levantino, T. Narayanan, O. Konovalov, A. Pastore, The complex systems and biomedical sciences group at the ESRF: Current status and new opportunities after extremely brilliant source upgrade, Nucl. Instruments Methods Phys. Res. Sect. B Beam Interact. with Mater. Atoms. 538 (2023) 164–172. https://doi.org/10.1016/j.nimb.2023.02.034.

[166] O. Kubaschewski, C.B. Alcock, P.J. Spencer, Materials Thermochemistry, 6., Pergamon Press New York, 1993.

[167] R. Busch, Y.J. Kim, W.L. Johnson, Thermodynamics and Kinetics of the Undercooled Liquid and the Glass Transition of the $Zr_{41.2}Ti_{13.8}Cu_{12.5}Ni_{10.0}Be_{22.5}$ Alloy, J. Appl. Phys. 77 (1995) 4039–4043. https://doi.org/10.1063/1.359485.

[168] D. Turnbull, Kinetics of heterogeneous nucleation, J. Chem. Phys. 18 (1950) 198–203. https://doi.org/10.1063/1.1747588.

[169] D. Turnbull, Under what conditions can a glass be formed?, Contemp. Phys. 10 (1969) 473–488. https://doi.org/10.1080/00107516908204405.

[170] D.R. Uhlmann, A Kinetic Treatment of Glass Transition, J. Non. Cryst. Solids. 7 (1972) 337–348.

[171] K.F. Kelton, A.L. Greer, Nucleation in Condensed Matter - Applications in Materials and Biology, 2010. http://www.sciencedirect.com/science/article/B8GWY-4YPVB0X-7/2/16c2f80dbf71559afc7597219c6afb99.

[172] J.W. Christian, The Theory of Transformations in Metals and Alloys, Elsevier Ltd., 2002. https://www.sciencedirect.com/book/9780080440194/the-theory-of-transformations-in-metals-and-alloys?via=ihub=.

[173] W.L. Johnson, J.H. Na, M.D. Demetriou, Quantifying the origin of metallic glass formation, Nat. Commun. 7 (2016). https://doi.org/10.1038/ncomms10313.

[174] T. Kozieł, K. Pajor, Ł. Gondek, Cooling rate evaluation during solidification in the suction casting process, J. Mater. Res. Technol. 9 (2020) 13502–13508. https://doi.org/10.1016/j.jmrt.2020.09.082.

[175] A.L. Greer, Confusion by design, Nature. 366 (1993) 303–304.

[176] R. Busch, E. Bakke, W.L. Johnson, On the glass forming ability of bulk metallic glasses, in: Ismanam, 1996: pp. 327–335.

[177] a Inoue, Stabilization of supercooled liquid and opening-up of bulk glassy alloys, Proc. Japan Acad. Ser. B Phys. Biol. Sci. 73 (1997) 19–24. http://www.scopus.com/inward/record.url?eid=2-s2.0-0001952567&partnerID=40&md5=1a46ca495bc06507562b530298757b3b.

[178] Z.P. Lu, Y. Li, S.C. Ng, Reduced glass transition temperature and glass forming ability of bulk glass forming alloys, J. Non. Cryst. Solids. 270 (2000) 103–114. https://doi.org/10.1016/S0022-3093(00)00064-8.

[179] A. Kuball, O. Gross, B. Bochtler, B. Adam, L. Ruschel, M. Zamanzade, R. Busch, Development and characterization of titanium-based bulk metallic glasses, J. Alloys Compd. 790 (2019) 337–346. https://doi.org/10.1016/j.jallcom.2019.03.001.

[180] A. Kawashima, H. Habazaki, K. Hashimoto, Highly corrosion-resistant Ni-based bulk amorphous alloys, Mater. Sci. Eng. A. 304–306 (2001) 753–757. https://doi.org/10.1016/S0921-5093(00)01587-2.

[181] B. Schmidt, Comparative corrosion studies on bulk metallic glasses – on the influence of composition , production route , post- processing , and thermal history, Saarland University, 2024.

[182] J.J. Kruzic, Bulk Metallic Glasses as Structural Materials: A Review, Adv. Eng. Mater. 18 (2016) 1308–1331. https://doi.org/10.1002/adem.201600066.

[183] C. Suryanarayana, A. Inoue, Bulk Metallic Glasses, CRC Press, 2011.

[184] M. Telford, The case for bulk metallic glass, Materialstoday. 7 (2004) 36–43. https://doi.org/10.1016/S1369-7021(04)00124-5.

[185] M.K. Miller, P.K. Liaw, Bulk metallic glasses: An overview, Springer, New York, 2008.

[186] A. Inoue, B.L. Shen, C.T. Chang, Fe- and Co-based bulk glassy alloys with ultrahigh strength of over 4000 MPa, Intermetallics. 14 (2006) 936–944. https://doi.org/10.1016/j.intermet.2006.01.038.

[187] J. Wang, R. Li, N. Hua, T. Zhang, Co-based ternary bulk metallic glasses with ultrahigh strength and plasticity, J. Mater. Res. 26 (2011) 2072–2079. https://doi.org/10.1557/jmr.2011.187.

[188] C.A. Schuh, T.C. Hufnagel, U. Ramamurty, Mechanical behavior of amorphous alloys, Acta Mater. 55 (2007) 4067–4109. https://doi.org/10.1016/j.actamat.2007.01.052.

[189] F. Spaepen, A microscopic mechanism for steady state inhomogeneous flow in metallic glasses, Acta Metall. 25 (1977) 407–415. https://doi.org/10.1016/0001-6160(77)90232-2.

[190] A.S. Argon, Plastic deformation in metallic glasses, Acta Metall. 27 (1979) 47–58. https://doi.org/10.1016/0001-6160(79)90055-5.

[191] D. Klaumünzer, A. Lazarev, R. Maaß, F.H. Dalla Torre, A. Vinogradov, J.F. Löffler, Probing shear-band initiation in metallic glasses, Phys. Rev. Lett. 107 (2011) 1–5. https://doi.org/10.1103/PhysRevLett.107.185502.

[192] J. Bokeloh, S. V. Divinski, G. Reglitz, G. Wilde, Tracer measurements of atomic diffusion inside shear bands of a bulk metallic glass, Phys. Rev. Lett. 107 (2011) 1–5. https://doi.org/10.1103/PhysRevLett.107.235503.

[193] H. Rösner, M. Peterlechner, C. Kübel, V. Schmidt, G. Wilde, Density changes in shear bands of a metallic glass determined by correlative analytical transmission electron microscopy, Ultramicroscopy. 142 (2014) 1–9. https://doi.org/10.1016/j.ultramic.2014.03.006.

[194] M. Stolpe, J.J. Kruzic, R. Busch, Evolution of shear bands, free volume and hardness during cold rolling of a Zr-based bulk metallic glass, Acta Mater. 64 (2014) 231–240. https://doi.org/10.1016/j.actamat.2013.10.035.

[195] W.H. Wang, The elastic properties, elastic models and elastic perspectives of metallic glasses, Prog. Mater. Sci. 57 (2012) 487–656. https://doi.org/10.1016/j.pmatsci.2011.07.001.

[196] Y. Kawamura, T. Nakamura, A. Inoue, Superplasticity in $Pd_{40}Ni_{40}P_{20}$ metallic glass, Scr. Mater. 39 (1998) 301–306. https://doi.org/10.1016/S1359-6462(98)00163-8.

[197] O. Gross, Precious metal based bulk glass-forming liquids: Development, thermodynamics, kinetics and structure, (2018). https://doi.org/10.22028/D291-27993.

[198] N. Neuber, Connection of Thermodynamics, Kinetics, Mechanics and Structure in a model Pt-Pd-metallic glass-forming System, 2024.

[199] L. Sun, Q. Wu, Y. Xu, W. Wang, Study on solidification behaviour of $Pd_{40}Ni_{40}P_{20}$ alloy by fluxing method, Phys. B Condens. Matter. 240 (1997) 205–210. https://doi.org/10.1016/s0921-4526(97)00425-0.

[200] N. Ashgriz, Handbook of Atomization and Sprays, 2011. https://doi.org/10.1007/978-1-4419-7264-4.

[201] H. Henein, V. Uhlenwinkel, U. Fritsching, Metal sprays and spray deposition, 2017. https://doi.org/10.1007/978-3-319-52689-8.

[202] N. Ciftci, Cooling strategies for the atomization of glass-forming alloys, PHD Thesis. (2020) 153. https://doi.org/10.26092/elib/84.

[203] H.H. Liebermann, C.D. Graham, Production of amorphous alloy ribbons and effects of apparatus parameters on ribbon dimensions, IEEE Trans. Magn. 12 (1976) 921–923. https://doi.org/10.1109/TMAG.1976.1059201.

[204] H.H. Liebermann, The dependence of the Geometry of glassy alloy ribbons on the chill block melt-spinning process parameters, Mater. Sci. Eng. 43 (1980) 203–210. https://doi.org/10.1016/0025-5416(80)90103-2.

[205] U. Scipioni Bertoli, G. Guss, S. Wu, M.J. Matthews, J.M. Schoenung, In-situ characterization of laser-powder interaction and cooling rates through high-speed imaging of powder bed fusion additive manufacturing, Mater. Des. 135 (2017) 385–396. https://doi.org/10.1016/j.matdes.2017.09.044.

[206] J.J. Marattukalam, V. Pacheco, D. Karlsson, L. Riekehr, J. Lindwall, F. Forsberg, U. Jansson, M. Sahlberg, B. Hjörvarsson, Development of process parameters for selective

laser melting of a Zr-based bulk metallic glass, Addit. Manuf. 13 (2020) 101124. https://doi.org/10.1016/j.addma.2020.101124.

[207] V. Pacheco, D. Karlsson, J.J. Marattukalam, M. Stolpe, B. Hjörvarsson, U. Jansson, M. Sahlberg, Thermal stability and devitrification mechanism of a Zr-based Bulk Metallic Glass produced by Selective Laser Melting, Submitt. to J. Alloy. Compd. (2019) 153995. https://doi.org/10.1016/j.jallcom.2020.153995.

[208] S. Hadibeik, E. Gingl, L. Schretter, B. Bochtler, J. Li, C. Gammer, A. Hohenwarter, F. Spieckermann, J. Eckert, Semi-analytical and experimental heat input study of additively manufactured Zr-based bulk metallic glass: Insights into nano- and global-scale relaxation and crystallization, Addit. Manuf. 89 (2024) 104295. https://doi.org/10.1016/j.addma.2024.104295.

[209] S. Hadibeik, H. Ghasemi-Tabasi, A. Burn, S. Lani, F. Spieckermann, J. Eckert, Controlling the Glassy State toward Structural and Mechanical Enhancement: Additive Manufacturing of Bulk Metallic Glass Using Advanced Laser Beam Shaping Technology, Adv. Funct. Mater. 34 (2024) 1–16. https://doi.org/10.1002/adfm.202311118.

[210] H. Zhu, H. Ou, A. Popov, Incremental sheet forming of thermoplastics: a review, Int. J. Adv. Manuf. Technol. 111 (2020) 565–587. https://doi.org/10.1007/s00170-020-06056-5.

[211] B. Bochtler, M. Stolpe, B. Reiplinger, R. Busch, Consolidation of amorphous powder by thermoplastic forming and subsequent mechanical testing, Mater. Des. 140 (2018) 188–195. https://doi.org/10.1016/j.matdes.2017.11.058.

[212] B. Bochtler, O. Kruse, R. Busch, Thermoplastic Forming of Amorphous Metals., J. Phys. Condens. Matter. 32 (2020) 1–11. https://doi.org/10.1088/1361-648X/ab7ad7.

[213] J. Schroers, B. Lohwongwatana, W.L. Johnson, A. Peker, Precious bulk metallic glasses for jewelry applications, Mater. Sci. Eng. A. 448–451 (2007) 235–238. https://doi.org/10.1016/j.msea.2006.02.301.

[214] T. He, N. Ciftci, V. Uhlenwinkel, S. Scudino, Synthesis of bulk $Zr_{48}Cu_{36}Al_8Ag_8$ metallic glass by hot pressing of amorphous powders, J. Manuf. Mater. Process. 5 (2021). https://doi.org/10.3390/jmmp5010023.

[215] J. Schroers, Processing of bulk metallic glass, Adv. Mater. 22 (2010) 1566–1597. https://doi.org/10.1002/adma.200902776.

[216] J. Schroers, T.M. Hodges, G. Kumar, H. Raman, A.J. Barnes, Q. Pham, T.A. Waniuk, Thermoplastic blow molding of metals, Mater. Today. 14 (2011) 14–19. https://doi.org/10.1016/S1369-7021(11)70018-9.

[217] R.M. Ojeda Mota, N. Liu, S.A. Kube, J. Chay, H.D. McClintock, J. Schroers, Overcoming geometric limitations in metallic glasses through stretch blow molding, Appl. Mater. Today. 19 (2020) 100567. https://doi.org/10.1016/j.apmt.2020.100567.

[218] B. Sarac, J. Eckert, Thermoplasticity of metallic glasses: Processing and applications, Prog. Mater. Sci. 127 (2022). https://doi.org/10.1016/j.pmatsci.2022.100941.

[219] G. Kumar, P. Neibecker, Y.H. Liu, J. Schroers, Critical fictive temperature for plasticity in metallic glasses, Nat. Commun. 4 (2013) 1536. https://doi.org/10.1038/ncomms2546.

[220] G.W.H. Höhne, W.F. Hemminger, H.-J. Flammersheim, Differential Scanning Calorimetry, 2003. https://doi.org/10.1007/978-3-662-06710-9_1.

[221] S.L. Lai, J.Y. Guo, V. Petrova, G. Ramanath, L.H. Allen, Size-dependent melting properties of small tin particles: Nanocalorimetric measurements, Phys. Rev. Lett. 77 (1996) 99–102. https://doi.org/10.1103/PhysRevLett.77.99.

[222] M. Zhang, M.Y. Efremov, F. Schiettekatte, E.A. Olson, A.T. Kwan, S.L. Lai, T. Wisleder, J.E. Greene, L.H. Allen, Size-dependent melting point depression of nanostructures: Nanocalorimetric measurements, Phys. Rev. B - Condens. Matter Mater. Phys. 62 (2000) 10548–10557. https://doi.org/10.1103/PhysRevB.62.10548.

[223] S.A. Adamovsky, A.A. Minakov, C. Schick, Scanning microcalorimetry at high cooling rate, Thermochim. Acta. 403 (2003) 55–63. https://doi.org/10.1016/S0040-6031(03)00182-5.

[224] A. Gradys, P. Sajkiewicz, S. Adamovsky, A. Minakov, C. Schick, Crystallization of poly(vinylidene fluoride) during ultra-fast cooling, Thermochim. Acta. 461 (2007) 153–157. https://doi.org/10.1016/j.tca.2007.05.023.

[225] C. Schick, V. Mathot, Fast scanning calorimetry, 2016. https://doi.org/10.1007/978-3-319-31329-0.

[226] J. Schawe, The revolutionary new Flash DSC1: Optimum performance for metastable materials, METTLER TOLEDO Therm. Anal. UserCom. 1 (2010) 1–6. http://scholar.google.com/scholar?hl=en&btnG=Search&q=intitle:The+revolutionary+new+Flash+DSC+1:+Optimum+performance+for+metastable+materials#0.

[227] Z. Evenson, I. Gallino, R. Busch, The effect of cooling rates on the apparent fragility of Zr-based bulk metallic glasses, J. Appl. Phys. 123529 (2010). https://doi.org/10.1063/1.3452381.

[228] H. Gobrecht, K. Hamann, G. Willers, Complex plane analysis of heat capacity of polymers in the glass transition region, J. Phys. E. 4 (1971) 21–23. https://doi.org/10.1088/0022-3735/4/1/004.

[229] P.S. Gill, S.R. Sauerbrunn, M. Reading, Modulated differential scanning calorimetry, J. Therm. Anal. 40 (1993) 931–939. https://doi.org/10.1007/BF02546852.

[230] M. Reading, A. Luget, R. Wilson, Modulated differential scanning calorimetry, Thermochim. Acta. 238 (1994) 295–307. https://doi.org/10.1016/S0040-6031(94)85215-4.

[231] F. Cser, F. Rasoul, E. Kosior, Modulated Differential Scanning Calorimetry - The effect of experimental variables, J. Therm. Anal. 50 (1997) 727–744. https://doi.org/10.1007/BF01979203.

[232] Z. Jiang, C.T. Imrie, J.M. Hutchinson, An introduction to temperature modulated differential scanning calorimetry (TMDSC): A relatively non-mathematical approach, Thermochim. Acta. 387 (2002) 75–93. https://doi.org/10.1016/S0040-6031(01)00829-2.

[233] E. Shoifet, G. Schulz, C. Schick, Temperature modulated differential scanning calorimetry – extension to high and low frequencies, Thermochim. Acta. 603 (2015) 227–236. https://doi.org/10.1016/j.tca.2014.10.010.

[234] N.G. Perez-de-Eulate, V. Di Lisio, D. Cangialos, Glass transition and molecular dynamics in polystyrene nanospheres by fast scanning calorimetry, ACS Macro Lett. 6 (2017) 859–863. https://doi.org/10.1021/acsmacrolett.7b00484.

[235] M. Merzlyakov, C. Schick, Step response analysis in DSC - A fast way to generate heat capacity spectra, Thermochim. Acta. 380 (2001) 5–12. https://doi.org/10.1016/S0040-6031(01)00631-1.

[236] X. Monnier, D. Cangialosi, B. Ruta, R. Busch, I. Gallino, Vitrification decoupling from α-relaxation in a metallic glass, Sci. Adv. 6 (2020). https://doi.org/10.1126/sciadv.aay1454.

[237] S. Pogatscher, D. Leutenegger, A. Hagmann, P.J. Uggowitzer, J.F. Löffler, Reprint of: Characterization of bulk metallic glasses via fast differential scanning calorimetry, Thermochim. Acta. 603 (2015) 46–52. https://doi.org/10.1016/j.tca.2014.12.012.

[238] J.Q. Wang, Y. Shen, J.H. Perepezko, M.D. Ediger, Increasing the kinetic stability of bulk metallic glasses, Acta Mater. 104 (2016) 25–32. https://doi.org/10.1016/j.actamat.2015.11.048.

[239] J.E.K. Schawe, Temperature correction at high heating rates for conventional and fast differential scanning calorimetry, Thermochim. Acta. 698 (2021) 178879. https://doi.org/10.1016/j.tca.2021.178879.

[240] C.T. Moynihan, P.B. Macedo, C.J. Montrose, P.K. Gupta, M.A. DeBolt, J.F. Dill, B.E. Dom, P.W. Drake, A.J. Easteal, P.B. Elterman, R.P. Moeller, H. Sasabe, J.A. Wilder, Structural relaxation in vitreous materials, Ann. N. Y. Acad. Sci. 279 (1976) 15–35. https://doi.org/10.1111/j.1749-6632.1976.tb39688.x.

[241] A.A. Abate, D. Cangialosi, S. Napolitano, High throughput optimization procedure to characterize vitrification kinetics, Thermochim. Acta. 707 (2022) 179084. https://doi.org/10.1016/j.tca.2021.179084.

[242] K.P. Menard, Dynamic Mechanical Analysis - A Practical Introduction, 1999. https://doi.org/10.1201/9781420049183.ch2.

[243] W.H. Bragg, W.L. Bragg, The reflection of X-rays by crystals, Proc. R. Soc. London A Math. Phys. Eng. Sci. 88 (1913) 428–438.

[244] J. Als-Nielsen, D. McMorrow, Elements of Modern X-ray Physics, Wiley Online Library, 2011.

[245] M. Sutton, S.G.J. Mochrie, T. Greytak, S.E. Nagler, L.E. Berman, G.A. Held, G.B. Stephenson, Observation of speckle by diffraction with coherent X-rays, Nature. 352 (1991) 608–610. https://doi.org/10.1038/352608a0.

[246] G. Grübel, F. Zontone, Correlation spectroscopy with coherent X-rays, J. Alloys Compd. 362 (2004) 3–11. https://doi.org/10.1016/S0925-8388(03)00555-3.

[247] E. Takeshi, S.J.L. Billinge, Underneath the Bragg Peaks, Elsevier Ltd, 2003. https://doi.org/10.1016/B978-0-08-097133-9.00013-7.

[248] X. Qiu, J.W. Thompson, S.J.L. Billinge, PDFgetX2: A GUI-driven program to obtain the pair distribution function from X-ray powder diffraction data, J. Appl. Crystallogr. 37 (2004) 678. https://doi.org/10.1107/S0021889804011744.

[249] B. Bochtler, Thermophysical and Structural Investigations of a CuTi- and a Zr-based Bulk Metallic Glass, the Influence of Minor Additions, and the Relation to Thermoplastic Forming, Saarland University, 2019.

[250] M. Stolpe, Synchrotron x-ray diffraction studies of bulk metallic glass forming liquids and glasses, Saarlan University, 2019.

[251] F. Van Der Veen, F. Pfeiffer, Coherent x-ray scattering, J. Phys. Condens. Matter. 16 (2004) 5003–5030. https://doi.org/10.1088/0953-8984/16/28/020.

[252] L. Cipelletti, L. Ramos, S. Manley, E. Pitard, D.A. Weitz, E.E. Pashkovski, M. Johansson, Universal non-diffusive slow dynamics in aging soft matter, Faraday Discuss. 123 (2003) 237–251. https://doi.org/10.1039/b204495a.

[253] M. Bouzid, J. Colombo, L.V. Barbosa, E. Del Gado, Elastically driven intermittent microscopic dynamics in soft solids, Nat. Commun. 8 (2017) 1–8. https://doi.org/10.1038/ncomms15846.

[254] J. Gabriel, T. Blochowicz, B. Stühn, Compressed exponential decays in correlation experiments: The influence of temperature gradients and convection, J. Chem. Phys. 142 (2015). https://doi.org/10.1063/1.4914092.

[255] J. Stetefeld, S.A. McKenna, T.R. Patel, Dynamic light scattering: a practical guide and applications in biomedical sciences, Biophys. Rev. 8 (2016) 409–427. https://doi.org/10.1007/s12551-016-0218-6.

[256] T. Böhmer, J.P. Gabriel, L. Costigliola, J.N. Kociok, T. Hecksher, J.C. Dyre, T. Blochowicz, Time reversibility during the ageing of materials, Nat. Phys. (2024). https://doi.org/10.1038/s41567-023-02366-z.

[257] G. Grübel, A. Madsen, A. Robert, X-ray photon correlation spectroscopy, J. Synchrotron Radiat. 21 (2014) 1057–1064. https://doi.org/10.1107/S1600577514018232.

[258] A. Madsen, R.L. Leheny, H. Guo, M. Sprung, O. Czakkel, Beyond simple exponential correlation functions and equilibrium dynamics in x-ray photon correlation spectroscopy, New J. Phys. 12 (2010). https://doi.org/10.1088/1367-2630/12/5/055001.

[259] A. Das, P.M. Derlet, C. Liu, E.M. Dufresne, R. Maaß, Stress breaks universal aging behavior in a metallic glass, Nat. Commun. 10 (2019) 1–9. https://doi.org/10.1038/s41467-019-12892-1.

[260] T. Xu, X.D. Wang, E.M. Dufresne, Y. Ren, Q. Cao, D. Zhang, J.Z. Jiang, Anomalous fast atomic dynamics in bulk metallic glasses, Mater. Today Phys. 17 (2021) 100351. https://doi.org/10.1016/j.mtphys.2021.100351.

[261] X.D. Wang, B. Ruta, L.H. Xiong, D.W. Zhang, Y. Chushkin, H.W. Sheng, H.B. Lou, Q.P. Cao, J.Z. Jiang, Free-volume dependent atomic dynamics in beta relaxation pronounced La-based metallic glasses, Acta Mater. 99 (2015) 290–296. https://doi.org/10.1016/j.actamat.2015.08.010.

[262] Z. Evenson, B. Ruta, S. Hechler, M. Stolpe, E. Pineda, I. Gallino, R. Busch, X-ray photon correlation spectroscopy reveals intermittent aging dynamics in a metallic glass, Phys. Rev. Lett. 115 (2015). https://doi.org/10.1103/PhysRevLett.115.175701.

[263] A. Das, E.M. Dufresne, R. Maaß, Structural dynamics and rejuvenation during cryogenic cycling in a Zr-based metallic glass, Acta Mater. 196 (2020) 723–732. https://doi.org/10.1016/j.actamat.2020.06.063.

[264] B. Ruta, G. Baldi, G. Monaco, Y. Chushkin, Compressed correlation functions and fast aging dynamics in metallic glasses, J. Chem. Phys. 138 (2013). https://doi.org/10.1063/1.4790131.

[265] B. Ruta, Y. Chushkin, G. Monaco, L. Cipelletti, E. Pineda, P. Bruna, V.M. Giordano, M. Gonzalez-Silveira, Atomic-scale relaxation dynamics and aging in a metallic glass probed

by X-ray photon correlation spectroscopy, Phys. Rev. Lett. 109 (2012) 1–5. https://doi.org/10.1103/PhysRevLett.109.165701.

[266] M. Leitner, B. Sepiol, L.M. Stadler, B. Pfau, Time-resolved study of the crystallization dynamics in a metallic glass, Phys. Rev. B - Condens. Matter Mater. Phys. 86 (2012) 1–7. https://doi.org/10.1103/PhysRevB.86.064202.

[267] B. Ruta, Y. Chushkin, G. Monaco, L. Cipelletti, V.M. Giordano, E. Pineda, P. Bruna, Relaxation dynamics and aging in structural glasses, AIP Conf. Proc. 1518 (2013) 181–188. https://doi.org/10.1063/1.4794566.

[268] B. Ruta, V.M. Giordano, L. Erra, C. Liu, E. Pineda, Structural and dynamical properties of $Mg_{65}Cu_{25}Y_{10}$ metallic glasses studied by in situ high energy X-ray diffraction and time resolved X-ray photon correlation spectroscopy, J. Alloys Compd. 615 (2014) 45–50. https://doi.org/10.1016/j.jallcom.2013.12.162.

[269] V.M. Giordano, B. Ruta, Unveiling the structural arrangements responsible for the atomic dynamics in metallic glasses during physical aging, Nat. Commun. 7 (2016) 1–8. https://doi.org/10.1038/ncomms10344.

[270] Z. Evenson, A. Payes-Playa, Y. Chushkin, M. Di Michiel, E. Pineda, B. Ruta, Comparing the atomic and macroscopic aging dynamics in an amorphous and partially crystalline $Zr_{44}Ti_{11}Ni_{10}Cu_{10}Be_{25}$ bulk metallic glass, J. Mater. Res. 32 (2017) 2014–2021. https://doi.org/10.1557/jmr.2017.187.

[271] E.J. Jaeschke, Synchrotron Light Sources and Free-Electron Lasers, 2016. https://doi.org/10.1007/978-3-319-14394-1.

[272] S. Busch, T.H. Jensen, Y. Chushkin, A. Fluerasu, Dynamics in shear flow studied by X-ray Photon Correlation Spectroscopy, Eur. Phys. J. E. 26 (2008) 55–62. https://doi.org/10.1140/epje/i2007-10305-2.

[273] S. Hechler, B. Ruta, M. Stolpe, E. Pineda, Z. Evenson, O. Gross, A. Bernasconi, R. Busch, I. Gallino, Microscopic evidence of the connection between liquid-liquid transition and dynamical crossover in an ultraviscous metallic glass former, Phys. Rev. Mater. 2 (2018) 1–15. https://doi.org/10.1103/PhysRevMaterials.2.085603.

[274] Y. Chushkin, C. Caronna, A. Madsen, A novel event correlation scheme for X-ray photon correlation spectroscopy, J. Appl. Crystallogr. 45 (2012) 807–813. https://doi.org/10.1107/S0021889812023321.

[275] S. Sarker, ATOM DYNAMICS OF AMORPHOUS MATERIALS BY X-RAY PHOTON CORRELATION SPECTROSCOPY (XPCS) & NEUTRON SPECTROSCOPY, University of Nevada, 2017. http://hdl.handle.net/11714/2064.

[276] T. Narayanan, W. Chèvremont, T. Zinn, F. Meneau, Small-angle X-ray scattering in the era of fourth-generation light sources, J. Appl. Crystallogr. 56 (2023) 939–946. https://doi.org/10.1107/S1600576723004971.

[277] Y. Leng, Light Microscopy, Wiley Online Library, 2008. https://doi.org/10.1002/9780470823002.ch1.

[278] L. Reimer, Scanning Electron Microscopy, Springer, 1998. https://doi.org/https://doi.org/10.1007/978-3-540-38967-5.

[279] DIN Deutsches Institut für Normung e.V., HÄRTEPRÜFUNG NACH VICKERS UND KNOOP DIN EN ISO 6507-1 (1998-01-00), 1998.

[280] X. Lu, S.G.J. Mochrie, S. Narayanan, A.R. Sandy, M. Sprung, How a liquid becomes a glass both on cooling and on heating, Phys. Rev. Lett. 100 (2008) 5–8. https://doi.org/10.1103/PhysRevLett.100.045701.

[281] A. Ricci, G. Campi, B. Joseph, N. Poccia, D. Innocenti, C. Gutt, M. Tanaka, H. Takeya, Y. Takano, T. Mizokawa, M. Sprung, N.L. Saini, Intermittent dynamics of antiferromagnetic phase in inhomogeneous iron-based chalcogenide superconductor, Phys. Rev. B. 101 (2020) 1–6. https://doi.org/10.1103/PhysRevB.101.020508.

[282] A. Jain, F. Schulz, F. Dallari, V. Markmann, F. Westermeier, Y. Zhang, G. Grübel, F. Lehmkühler, Three-step colloidal gelation revealed by time-resolved x-ray photon correlation spectroscopy, J. Chem. Phys. 157 (2022). https://doi.org/10.1063/5.0123118.

[283] Q. Zhang, D. Bahadur, E.M. Dufresne, P. Grybos, P. Kmon, R.L. Leheny, P. Maj, S. Narayanan, R. Szczygiel, S. Ramakrishnan, A. Sandy, Dynamic Scaling of Colloidal Gel Formation at Intermediate Concentrations, Phys. Rev. Lett. 119 (2017) 1–6. https://doi.org/10.1103/PhysRevLett.119.178006.

[284] D.P. Chowdhury, Application of photon correlation spectroscopy to flowing Brownian motion systems, Kansas State University, 1985.

[285] M. Cammarata, ESRF ID10 Newsletter (February 2024), (2024). https://confluence.esrf.fr/display/ID10COHERENCEKW/2024.02.24.

[286] B. Ruta, Y. Chushkin, G. Monaco, L. Cipelletti, V.M. Giordano, E. Pineda, P. Bruna, Relaxation dynamics and aging in structural glasses, AIP Conf. Proc. 1518 (2013) 181–188. https://doi.org/10.1063/1.4794566.

[287] S. Hechler, B. Ruta, M. Stolpe, E. Pineda, Z. Evenson, O. Gross, A. Bernasconi, R. Busch, I. Gallino, Microscopic evidence of the connection between liquid-liquid transition and dynamical crossover in an ultraviscous metallic glass former, Phys. Rev. Mater. 2 (2018) 1–6. https://doi.org/10.1103/PhysRevMaterials.2.085603.

[288] N. Amini, F. Yang, E. Pineda, B. Ruta, M. Sprung, A. Meyer, Intrinsic relaxation in a supercooled ZrTiNiCuBe glass forming liquid, Phys. Rev. Mater. 5 (2021) 1–8. https://doi.org/10.1103/PhysRevMaterials.5.055601.

[289] F. Liénard, É. Freyssingeas, P. Borgnat, A multiscale time-Laplace method to extract relaxation times from non-stationary dynamic light scattering signals, J. Chem. Phys. 156 (2022). https://doi.org/10.1063/5.0088005.

[290] D. Parisi, J. Ruiz-Franco, Y. Ruan, C.Y. Liu, B. Loppinet, E. Zaccarelli, D. Vlassopoulos, Static and dynamic properties of block copolymer based grafted nanoparticles across the non-ergodicity transition, Phys. Fluids. 32 (2020). https://doi.org/10.1063/5.0031862.

[291] F.A.D.M. Marques, R. Angelini, E. Zaccarelli, B. Farago, B. Ruta, G. Ruocco, B. Ruzicka, Structural and microscopic relaxations in a colloidal glass, Soft Matter. 11 (2015) 466–471. https://doi.org/10.1039/c4sm02010c.

[292] A.R. Yavari, S. Hamar-Thibault, H.R. Sinning, On the microstructure of amorphous Pd46Ni36P18 with two glass transitions, Scr. Metall. 22 (1988) 1231–1234. https://doi.org/10.1016/S0036-9748(88)80137-6.

[293] S. V. Madge, H. Rösner, G. Wilde, Transformations in supercooled $Pd_{40.5}Ni_{40.5}P_{19}$, Scr. Mater. 53 (2005) 1147–1151. https://doi.org/10.1016/j.scriptamat.2005.07.020.

[294] S. Fu, S. Liu, J. Ge, J. Wang, H. Ying, S. Wu, M. Yan, L. Zhu, Y. Ke, J. Luan, Y. Ren, X. Zuo, Z. Wu, Z. Peng, C.-T. Liu, X.-L. Wang, T. Feng, S. Lan, In situ study on medium-range order

evolution during the polyamorphous phase transition in a Pd-Ni-P nanostructured glass, J. Mater. Sci. Technol. (2022). https://doi.org/10.1016/j.jmst.2022.01.038.

[295] Q. Du, X.J. Liu, Y. Cao, Q. Zeng, H. Wang, Y. Wu, S. Jiang, X. Zhang, Z.P. Lu, Composition dependence of polyamorphic transition in Pd–Ni–P metallic glasses, Sci. China Mater. (2023) 1–8. https://doi.org/10.1007/s40843-023-2507-6.

[296] L.F. Ouyang, J. Shen, Y. Huang, Y.H. Sun, H.Y. Bai, W.H. Wang, Strong-to-fragile transition in a metallic-glass forming supercooled liquid associated with a liquid-liquid transition, J. Appl. Phys. 133 (2023). https://doi.org/10.1063/5.0137847.

[297] T. Xu, X.D. Wang, E.M. Dufresne, K.A. Beyer, P. An, J. Ma, N. Wang, S. Liu, Q.P. Cao, S.Q. Ding, D.X. Zhang, L. Zheng, J. Zhang, T.D. Hu, Z. Jiang, Y. Huang, J.Z. Jiang, Unveiling the Structural Origins of Dynamic Diversity in Pd-Based Metallic Glasses, Small. 20 (2024) 1–12. https://doi.org/10.1002/smll.202309331.

[298] S. Lan, Y.L. Yip, M.T. Lau, H.W. Kui, Direct imaging of phase separation in $Pd_{41.25}Ni_{41.25}P_{17.5}$ bulk metallic glasses, J. Non. Cryst. Solids. 358 (2012) 1298–1302. https://doi.org/10.1016/j.jnoncrysol.2012.02.034.

[299] Z.D. Wu, X.H. Lu, Z.H. Wu, H.W. Kui, Spinodal decomposition in Pd41.25Ni41.25P 17.5 bulk metallic glasses, J. Non. Cryst. Solids. 385 (2014) 40–46. https://doi.org/10.1016/j.jnoncrysol.2013.10.009.

[300] Z.D. Wu, W.Z. Zhou, Y.F. Lo, S. Lan, H.W. Kui, On the short-range orders in spinodal Pd-Ni-P bulk metallic glasses, J. Non. Cryst. Solids. 410 (2015) 51–57. https://doi.org/10.1016/j.jnoncrysol.2014.12.017.

[301] S. Lan, Y. Ren, X.Y. Wei, B. Wang, E.P. Gilbert, T. Shibayama, S. Watanabe, M. Ohnuma, X.L. Wang, Hidden amorphous phase and reentrant supercooled liquid in Pd-Ni-P metallic glasses, Nat. Commun. 8 (2017) 1–8. https://doi.org/10.1038/ncomms14679.

[302] W.Z. Zhou, X.C. Wang, Y.F. Lo, H.W. Kui, Z.D. Wu, Direct imaging of a first-order liquid-liquid phase transition in undercooled molten PdNiP alloys and its thermodynamic implications, J. Non. Cryst. Solids. 472 (2017) 75–85. https://doi.org/10.1016/j.jnoncrysol.2017.07.020.

[303] J. Shen, Y.H. Sun, J. Orava, H.Y. Bai, W.H. Wang, Liquid-to-liquid transition around the glass-transition temperature in a glass-forming metallic liquid, Acta Mater. 225 (2022) 117588. https://doi.org/10.1016/j.actamat.2021.117588.

[304] J. Shen, S.-L. Liu, Y. Sun, W.H. Wang, Metallic Glacial Glass, Natl. Sci. Open. 012110 (2022) 59–70. https://doi.org/10.1360/nso/20220049.

[305] J. Shen, H.P. Zhang, Z.Q. Chen, L.F. Ouyang, F.R. Wang, Z. Lu, M.Z. Li, Y.H. Sun, H.Y. Bai, W.H. Wang, The Kinetics of Reentrant Glass Transition in Metallic Liquids, Acta Mater. 244 (2022) 1–7. https://doi.org/10.1016/j.actamat.2022.118554.

[306] C.T. Moynihan, P.B. Macedo, C.J. Montrose, P.K. Gupta, P.B. Elterman, R.P. Moeller, H. Sasabe, J.A. Wilder, Structural relaxation in vitreous materials, Ann. New York Acad. Sci. 279 (2006) 15–35.

[307] X. Monnier, D. Cangialosi, Thermodynamic Ultrastability of a Polymer Glass Confined at the Micrometer Length Scale, Phys. Rev. Lett. 121 (2018) 137801. https://doi.org/10.1103/PhysRevLett.121.137801.

[308] F. Vollmers, Untersuchung von Magnesium basierten metallischen Gläsern mittels Chip-Kalorimetrie, Saarland University, 2025.

[309] G. Wilde, R. Willnecker, H.-J. Fecht, Calorimetric, thermomechanical, and rheological characterizations of bulk glass-forming $Pd_{40}Ni_{40}P_{20}$, J. Appl. Phys. 87 (2000) 1141. https://doi.org/https://doi.org/10.1063/1.371991.

[310] R. Al-Mukadam, I.K. Götz, M. Stolpe, J. Deubener, Viscosity of metallic glass-forming liquids based on Zr by fast-scanning calorimetry, Acta Mater. 221 (2021) 117370. https://doi.org/10.1016/j.actamat.2021.117370.

[311] F. Römer, P. Ramasamy, I. Steffny, M. Stoica, U. Lienert, C. Quick, Z. Hegedüs, J. Eckert, F. Spieckermann, Crystallization of $Fe_{74}Mo_4P_{10}C_{7.5}B_{2.5}Si_2$ metallic glass: Insights from in-situ synchrotron diffraction and Flash DSC, Mater. Today Adv. 25 (2025). https://doi.org/10.1016/j.mtadv.2024.100550.

[312] A. Martinelli, J. Baglioni, P. Sun, F. Dallari, E. Pineda, Y. Duan, T. Spitzbart-silberer, F. Westermeier, M. Sprung, A new experimental setup for combined fast differential scanning calorimetry and X-ray photon correlation spectroscopy, J. Synchrotron Radiat. 31 (2024) 1–9. https://doi.org/10.1107/S1600577524002510.

[313] S. Pogatscher, P.J. Uggowitzer, J.F. Löffler, In-situ probing of metallic glass formation and crystallization upon heating and cooling via fast differential scanning calorimetry, Appl. Phys. Lett. 104 (2014) 1–5. https://doi.org/10.1063/1.4884940.

[314] N. Sohrabi, J.E.K. Schawe, J. Jhabvala, J.F. Löffler, R.E. Logé, Critical crystallization properties of an industrial-grade Zr-based metallic glass used in additive manufacturing, Scr. Mater. 199 (2021) 113861. https://doi.org/10.1016/j.scriptamat.2021.113861.

[315] N. Sohrabi, J. Jhabvala, G. Kurtuldu, R. Frison, A. Parrilli, M. Stoica, A. Neels, J.F. Löffler, R.E. Logé, Additive manufacturing of a precious bulk metallic glass, Appl. Mater. Today. 24 (2021) 101080. https://doi.org/10.1016/j.apmt.2021.101080.

[316] N. Sohrabi, T. Ivas, J. Jhabvala, J.E.K. Schawe, J.F. Löffler, H. Ghasemi-Tabasi, R.E. Logé, Quantitative prediction of crystallization in laser powder bed fusion of a Zr-based bulk metallic glass with high oxygen content, Mater. Des. 239 (2024). https://doi.org/10.1016/j.matdes.2024.112744.

[317] M. Eisenbart, U.E. Klotz, R. Busch, I. Gallino, On the abnormal room temperature tarnishing of an 18 karat gold bulk metallic glass alloy, J. Alloys Compd. 615 (2014) S118–S122. https://doi.org/10.1016/j.jallcom.2013.11.167.

[318] O. Gross, M. Eisenbart, L.-Y. Schmitt, N. Neuber, L. Ciftci, U.E. Klotz, R. Busch, I. Gallino, Development of novel 18-karat, premium-white gold bulk metallic glasses with improved tarnishing resistance, Mater. Des. 140 (2018) 495–504. https://doi.org/10.1016/j.matdes.2017.12.007.

[319] N. Neuber, O. Gross, M. Eisenbart, A. Heiss, U.E. Klotz, J.P. Best, M.N. Polyakov, J. Michler, R. Busch, I. Gallino, The role of Ga addition on the thermodynamics, kinetics, and tarnishing properties of the Au-Ag-Pd-Cu-Si bulk metallic glass forming system, Acta Mater. 165 (2018) 315–326. https://doi.org/10.1016/j.actamat.2018.11.052.

[320] Y. Yan, C. Wang, Z. Huang, J. Fu, Z. Lin, X. Zhang, J. Ma, J. Shen, Highly efficient and robust catalysts for the hydrogen evolution reaction by surface nano engineering of metallic glass, J. Mater. Chem. A. 9 (2021) 5415–5424. https://doi.org/10.1039/d0ta10235k.

[321] C. Mahajan, V. Hasannaeimi, N. Neuber, X. Wang, R. Busch, I. Gallino, S. Mukherjee, Model Metallic Glasses for Superior Electrocatalytic Performance in a Hydrogen Oxidation

Reaction, ACS Appl. Mater. Interfaces. 15 (2023) 6697–6707. https://doi.org/10.1021/acsami.2c18266.

[322] S. Pauly, C. Schricker, S. Scudino, L. Deng, U. Kühn, Processing a glass-forming Zr-based alloy by selective laser melting, Mater. Des. 135 (2017) 133–141. https://doi.org/10.1016/j.matdes.2017.08.070.

[323] P. Bordeenithikasem, M. Stolpe, A. Elsen, D.C. Hofmann, Glass forming ability, flexural strength, and wear properties of additively manufactured Zr-based bulk metallic glasses produced through laser powder bed fusion, Addit. Manuf. 21 (2018) 312–317. https://doi.org/10.1016/j.addma.2018.03.023.

[324] J.P. Best, J. Ast, B. Li, M. Stolpe, R. Busch, F. Yang, X. Li, J. Michler, J.J. Kruzic, Relating fracture toughness to micro-pillar compression response for a laser powder bed additive manufactured bulk metallic glass, Mater. Sci. Eng. A. 770 (2020) 138535. https://doi.org/10.1016/j.msea.2019.138535.

[325] B. Li, V. Yakubov, K. Nomoto, S.P. Ringer, B. Gludovatz, X. Li, J.J. Kruzic, Superior mechanical properties of a Zr-based bulk metallic glass via laser powder bed fusion process control, Acta Mater. 266 (2024) 119685. https://doi.org/10.1016/j.actamat.2024.119685.

[326] N. Sohrabi, A. Parrilli, J. Jhabvala, A. Neels, R.E. Logé, Tensile and Impact Toughness Properties of a Zr-Based Bulk Metallic Glass Fabricated via Laser Powder-Bed Fusion, Materials (Basel). 14 (2021). https://doi.org/10.3390/ma14195627.

[327] L. Deng, K. Kosiba, R. Limbach, L. Wondraczek, U. Kühn, S. Pauly, Plastic deformation of a Zr-based bulk metallic glass fabricated by selective laser melting, J. Mater. Sci. Technol. 60 (2021) 139–146. https://doi.org/10.1016/j.jmst.2020.06.007.

[328] L. Deng, A. Gebert, L. Zhang, H.Y. Chen, D.D. Gu, U. Kühn, M. Zimmermann, K. Kosiba, S. Pauly, Mechanical performance and corrosion behaviour of Zr-based bulk metallic glass produced by selective laser melting, Mater. Des. 189 (2020). https://doi.org/10.1016/j.matdes.2020.108532.

[329] J. Wegner, L. Bruckhaus, H. Schoenrath, S. Kleszczynski, Fabrication of bulk metallic glass lattice structures using laser powder bed fusion, MATEC Web Conf. 406 (2024) 1–11. https://doi.org/10.1051/matecconf/202440607001.

[330] J. Wegner, L. Bruckhaus, M.A. Schroer, M. Rayer, H. Schoenrath, S. Kleszczynski, Zr - based bulk metallic glasses in PBF - LB / M : near - polished surface quality in the as - built state, Prog. Addit. Manuf. (2024) 21–25. https://doi.org/10.1007/s40964-024-00667-0.

[331] Q. He, J. Xu, Locating Malleable Bulk Metallic Glasses in Zr-Ti-Cu-Al Alloys with Calorimetric Glass Transition Temperature as an Indicator, J. Mater. Sci. Technol. 28 (2012) 1109–1122. https://doi.org/10.1016/S1005-0302(12)60180-7.

[332] B. Gludovatz, S.E. Naleway, R.O. Ritchie, J.J. Kruzic, Size-dependent fracture toughness of bulk metallic glasses, Acta Mater. 70 (2014) 198–207. https://doi.org/10.1016/j.actamat.2014.01.062.

[333] H.Y. Jung, S.J. Choi, K.G. Prashanth, M. Stoica, S. Scudino, S. Yi, U. Kühn, D.H. Kim, K.B. Kim, J. Eckert, Fabrication of Fe-based bulk metallic glass by selective laser melting: A parameter study, Mater. Des. 86 (2015) 703–708. https://doi.org/10.1016/j.matdes.2015.07.145.

[334] Z. Mahbooba, L. Thorsson, M. Unosson, P. Skoglund, H. West, T. Horn, C. Rock, E. Vogli, O. Harrysson, Additive manufacturing of an iron-based bulk metallic glass larger than the critical casting thickness, Appl. Mater. Today. 11 (2018) 264–269. https://doi.org/10.1016/j.apmt.2018.02.011.

[335] X.D. Nong, X.L. Zhou, Y.X. Ren, Fabrication and characterization of Fe-based metallic glasses by Selective Laser Melting, Opt. Laser Technol. 109 (2019) 20–26. https://doi.org/\url{10.1016/j.optlastec.2018.07.059}.

[336] P. Zhang, J. Tan, Y. Tian, H. Yan, Z. Yu, Research progress on selective laser melting (SLM) of bulk metallic glasses (BMGs): a review, Int. J. Adv. Manuf. Technol. (2021). https://doi.org/10.1007/s00170-021-07990-8.

[337] Ł. Żrodowski, R. Wróblewski, M. Leonowicz, B. Morończyk, T. Choma, J. Ciftci, W. Święszkowski, A. Dobkowska, E. Ura-Bińczyk, P. Błyskun, J. Jaroszewicz, A. Krawczyńska, K. Kulikowski, B. Wysocki, T. Cetner, G. Moneta, X. Li, L. Yuan, A. Małachowska, R. Chulist, C. Żrodowski, How to control the crystallization of metallic glasses during laser powder bed fusion? Towards part-specific 3D printing of in situ composites, Addit. Manuf. 76 (2023). https://doi.org/10.1016/j.addma.2023.103775.

[338] V. Pacheco, D. Karlsson, J.J. Marattukalam, M. Stolpe, B. Hjörvarsson, U. Jansson, M. Sahlberg, Thermal stability and crystallization of a Zr-based metallic glass produced by suction casting and selective laser melting, J. Alloys Compd. 825 (2020) 153995. https://doi.org/\url{10.1016/j.jallcom.2020.153995}.

[339] Z.H. Han, L. He, Y.L. Hou, J. Feng, J. Sun, Understanding the mechanism for the embrittlement of a monolithic Zr-based bulk metallic glass by oxygen, Intermetallics. 17 (2009) 553–561. https://doi.org/10.1016/j.intermet.2009.01.011.

[340] V. Keryvin, C. Bernard, J.C. Sanglebœuf, Y. Yokoyama, T. Rouxel, Toughness of $Zr_{55}Cu_{30}Al_{10}Ni_5$ bulk metallic glass for two oxygen levels, J. Non. Cryst. Solids. 352 (2006) 2863–2868. https://doi.org/10.1016/j.jnoncrysol.2006.02.102.

[341] Y. Yokoyama, A. Kobayashi, K. Fukaura, A. Inoue, Oxygen embrittlement and effect of the addition of Ni element in a bulk amorphous Zr-Cu-Al alloy, Mater. Trans. 43 (2002) 571–574. https://doi.org/10.2320/matertrans.43.571.

[342] X.H. Lin, W.L. Johnson, W.K. Rhim, Effect of Oxygen Impurity on Crystallization of an Undercooled Bulk Glass Forming Zr–Ti–Cu–Ni–Al Alloy, Mater. Trans. JIM. 38 (1997) 473–477. doi.org/10.2320/matertrans1989.38.473.

[343] Z.P. Lu, H. Bei, Y. Wu, G.L. Chen, E.P. George, C.T. Liu, Oxygen effects on plastic deformation of a Zr-based bulk metallic glass, Appl. Phys. Lett. 92 (2008) 1–4. https://doi.org/10.1063/1.2828981.

[344] J.P. Best, H.E. Ostergaard, B. Li, M. Stolpe, F. Yang, K. Nomoto, M.T. Hasib, O. Muránsky, R. Busch, X. Li, J.J. Kruzic, Fracture and fatigue behaviour of a laser additive manufactured Zr-based bulk metallic glass, Addit. Manuf. (2020) 101416. https://doi.org/10.1016/j.addma.2020.101416.

[345] J. Shi, S. Ma, S. Wei, J.P. Best, M. Stolpe, B. Markert, Connecting structural defects to tensile failure in a 3D-printed fully-amorphous bulk metallic glass, Mater. Sci. Eng. A. 813 (2021) 141106. https://doi.org/10.1016/j.msea.2021.141106.

[346] X. Lin, Y. Zhang, G. Yang, X. Gao, Q. Hu, J. Yu, L. Wei, W. Huang, Microstructure and compressive/tensile characteristic of large size Zr-based bulk metallic glass prepared by laser solid forming, J. Mater. Sci. Technol. 35 (2019) 328–335. https://doi.org/10.1016/j.jmst.2018.10.033.

[347] D. Ouyang, Q. Zheng, L. Wang, H. Wang, C. Yang, P. Zhang, N. Li, The brittleness of post-treatment of 3D printed Zr-based metallic glasses in supercooled liquid state, Mater. Sci. Eng. A. 782 (2020) 139259. https://doi.org/10.1016/j.msea.2020.139259.

[348] J.P. Best, Z. Evenson, F. Yang, A.-C. Dippel, M. Stolpe, O. Gutowski, M.T. Hasib, X. Li, J.J. Kruzic, Structural periodicity in laser additive manufactured Zr-based bulk metallic glass, Appl. Phys. Lett. 115 (2019) 031902. https://doi.org/10.1063/1.5100050.

[349] N. Sohrabi, J. Jhabvala, G. Kurtuldu, M. Stoica, A. Parrilli, S. Berns, E. Polatidis, S. Van Petegem, S. Hugon, A. Neels, J.F. Löffler, R.E. Logé, Characterization, mechanical properties and dimensional accuracy of a Zr-based bulk metallic glass manufactured via laser powder-bed fusion, Mater. Des. 199 (2021). https://doi.org/10.1016/j.matdes.2020.109400.

[350] P. Zhang, Ouyang, Di, L. Liu, Enhanced mechanical properties of 3D printed Zr-based BMG composite reinforced with Ta precipitates, J. Alloys Compd. 803 (2019) 476–483. https://doi.org/\url{10.1016/j.jallcom.2019.06.303}.

[351] S. Su, Y. Lu, Laser directed energy deposition of Zr-based bulk metallic glass composite with tensile strength, Mater. Lett. 247 (2019) 79–81. https://doi.org/10.1016/j.matlet.2019.03.111.

[352] Y. Lu, S. Su, S. Zhang, Y. Huang, Z. Qin, X. Lu, W. Chen, Controllable additive manufacturing of gradient bulk metallic glass composite with high strength and tensile ductility, Acta Mater. 206 (2021) 116632. https://doi.org/10.1016/j.actamat.2021.116632.

[353] P. Zhang, C. Zhang, D. Ouyang, L. Liu, Enhancement of plasticity and toughness of 3D printed binary $Zr_{50}Cu_{50}$ bulk metallic glass composite by deformation-induced martensitic transformation, Scr. Mater. 192 (2021) 7–12. https://doi.org/10.1016/j.scriptamat.2020.09.044.

[354] J. Tian, Z. Jiang, Exploring New Strategies for Ultrahigh Strength Steel via Tailoring the Precipitates, Front. Mater. 8 (2021) 1–7. https://doi.org/10.3389/fmats.2021.797798.

[355] G.R. Garrett, M.D. Demetriou, J. Chen, W.L. Johnson, Effect of microalloying on the toughness of metallic glasses, Appl. Phys. Lett. 101 (2012) 101–104. https://doi.org/10.1063/1.4769997.

[356] J. Wegner, M. Frey, P. Stiglmair, S. Kleszczynski, G. Witt, R. Busch, MECHANICAL PROPERTIES OF HONEYCOMB STRUCTURED ZR-BASED BULK METALLIC GLASS SPECIMENS FABRICATED BY LASER POWDER BED FUSION, South African J. Ind. Eng. 30 (3) (2019) 32–40. https://doi.org/10.7166/30-3-2265.

[357] J. Wegner, Funktionalisierung der prozessinhärenten Abkühlraten des Laser-Strahlschmelzens zur Verarbeitung metallischer Massivgläser, (2023). https://doi.org/10.17185/duepublico/78650.

[358] C. Qi, F. Jiang, S. Yang, Advanced honeycomb designs for improving mechanical properties: A review, Compos. Part B Eng. 227 (2021) 109393. https://doi.org/10.1016/j.compositesb.2021.109393.

[359] T. Goldmann, W.C. Huang, S. Rzepa, J. Džugan, R. Sedláček, M. Daniel, Additive Manufacturing of Honeycomb Lattice Structure—From Theoretical Models to Polymer and Metal Products, Materials (Basel). 15 (2022). https://doi.org/10.3390/ma15051838.

[360] S.O. Obadimu, K.I. Kourousis, In-plane compression performance of additively manufactured honeycomb structures: a review of influencing factors and optimisation techniques, Int. J. Struct. Integr. 14 (2023) 337–353. https://doi.org/10.1108/IJSI-10-2022-0130.

[361] J. Li, H. Wang, X. Kong, Z. Jiao, W. Yang, Additively Manufactured Bionic Corrugated Lightweight Honeycomb Structures with Controlled Deformation Load-Bearing Properties, Materials (Basel). 17 (2024). https://doi.org/10.3390/ma17102274.

[362] S. Shuib, M.I.Z. Ridzwan, A.H. Kadarman, Methodology of compliant mechanisms and its current developments in applications: A review, Am. J. Appl. Sci. 4 (2007) 160–167. https://doi.org/10.3844/ajassp.2007.160.167.

[363] S.P. Jagtap, B.B. Deshmukh, S. Pardeshi, Applications of compliant mechanism in today's world - A review, J. Phys. Conf. Ser. 1969 (2021). https://doi.org/10.1088/1742-6596/1969/1/012013.